Transactions of the ASME, Journal of Fluids Engineering (ISSN 0098-2202) is published bimonthly (Jan., Mar., May, July, Sept., Nov.) by The American Society of Mechanical Engineers, Three Park Avenue, New York, NY 10016. Periodicals postage paid at New York, NY and additional mailing offices.
POSTMASTER: Send address changes to Transactions of the ASME, Journal of Fluids Engineering, c/o THE AMERICAN SOCIETY OF MECHANICAL ENGINEERS, 22 Law Drive, Box 2300, Fairfield, NJ 07007-2300.
CHANGES OF ADDRESS must be received at Society headquarters seven weeks before they are to be effective. Please send old label and new address.

INDEXED by Applied Mechanics Reviews and Engineering Information, Inc. Canadian Goods & Services Tax Registration #126148048.

Journal of Fluids Engineering

Published Bimonthly by ASME

VOLUME 126 • NUMBER 1 • JANUARY 2004

TECHNICAL PAPERS

(Contents continued on inside back cover)

This journal is printed on acid-free paper, which exceeds the ANSI Z39.48-1992 specification for permanence of paper and library materials. ♾™
♻ 85% recycled content, including 10% post-consumer fibers.

The ASME Journal of Fluids Engineering is abstracted and indexed in the following:

Applied Science & Technology Index, AMR Abstracts Database, Chemical Abstracts, Chemical Engineering and Biotechnology Abstracts (Electronic equivalent of Process and Chemical Engineering), Civil Engineering Abstracts, Computer & Information Systems Abstracts, Corrosion Abstracts, Current Contents, Ei EncompassLit, Electronics & Communications Abstracts, Engineered Materials Abstracts, Engineering Index, Environmental Engineering Abstracts, Environmental Science and Pollution Management, Excerpta Medica, Fluidex, Index to Scientific Reviews, INSPEC, International Building Services Abstracts, Mechanical & Transportation Engineering Abstracts, Mechanical Engineering Abstracts, METADEX (The electronic equivalent of Metals Abstracts and Alloys Index), Petroleum Abstracts, Process and Chemical Engineering, Referativnyi Zhurnal, Science Citation Index, SciSearch (The electronic equivalent of Science Citation Index), Shock and Vibration Digest, Solid State and Superconductivity Abstracts, Theoretical Chemical Engineering

Computational Analysis of Wall Roughness Effects for Liquid Flow in Micro-Conduits

C. Kleinstreuer
e-mail: ck@eos.ncsu.edu

J. Koo

Department of Mechanical & Aerospace Engineering,
North Carolina State University,
Raleigh, NC 27695-7910

Fluid flow in microchannels or microtubes may differ in terms of wall frictional effects, and hence flow rates, when compared to macrochannels. Focusing on steady laminar fully developed flow of a liquid in different micro-conduits, relative surface roughness is captured in terms of a porous medium layer (PML) model. The new approach allows the evaluation of microfluidics variables as a function of PML characteristics, i.e., layer thickness and porosity, uncertainties in measuring hydraulic diameters as well as the inlet Reynolds number. Specifically, realistic values for the PML Darcy number, relative surface roughness, and actual flow area are taken into account to match observed friction factors in micro-conduits. The model predictions compared well with measured data sets for systems with significant relative roughness values. Although other surface effects may have influenced the experimental results as well, surface roughness is found to affect the friction factor and hence the flow parameters in relatively rough channels, e.g., those which are made of aluminum or stainless steel by way of micro-cutting processes.
[DOI: 10.1115/1.1637633]

1 Introduction

In recent reviews of experimental contributions to liquid flow in microchannels (c.f. Gad-el-Hak [1]; Sobhan and Garimella [2]; Koo and Kleinstreuer [3]), it was documented that there are two conflicting bodies of evidence (see Table 1 in [3]). For example, Peng et al. [4,5], Qu et al. [6] and Guo and Li [7] indicated that the friction factor in microchannel flow is augmented when compared to macrochannels, while Sharp [8], Judy et al. [9], Wu and Cheng [10] and Gao et al. [11] claimed that it is unaltered and hence there is no deviation from conventional theory. However, there is measured evidence, even in Sharp's data, that wall effects may change the flow behavior; still, an enhanced form of the Navier-Stokes equation can be employed to analyze liquid flow in micro-conduits.

In general, as the flow cross section becomes smaller, the surface-to-volume ratio increases and the effects of wall phenomena, such as surface roughness, van der Waals force, and electrokinetic force, may play an important role in the fluid mechanics (c.f. Li [12]; Mala and Li [13]). Focusing on surface roughness impact, Mala and Li [13] and Qu et al. [6] proposed a ''roughness viscosity'' model, whereas Tichy [14] replaced the roughness surface with a porous film governed by Darcy's law, while Li and Hwang [15] employed a Brinkman-extended Darcy model for near-wall flow simulations of rarefied gas in long microtubes (Li et al. [16]). Hamrock [17] classified the geometric characteristics of actual surfaces into three categories, i.e., error of form, waviness, and roughness. Waviness stems from relatively long waves in a surface profile, which is associated with unwanted vibrations that typically occur in machine tool systems. Roughness results from irregularities, excluding error of form and waviness, which are inherent in the cutting and polishing processes during production. Both waviness and roughness are regarded as ''relative roughness'' in the present model.

The varying experimental observations and data analyses are the impetus for the development of a micro-conduit flow hypothesis which correlates actual micro-scale flow behavior with significant effects of relative surface roughness as well as hydraulic diameter uncertainties, in order to provide a flexible model for proper experimental data interpretation.

Contributed by the Fluids Engineering Division for publication in the JOURNAL OF FLUIDS ENGINEERING. Manuscript received by the Fluids Engineering Division January 27, 2003; revised manuscript received August 16, 2003. Associate Editor: T. B. Gatski.

2 Theory

Surface roughness can be described as random distributions of wall peaks and valleys, which, in the average, could be modeled as a homogeneous porous medium layer (PML) characterized by porosity α (or permeability κ) and height h. Figures 1(a–c) depict the evolution of the PML model from a random wall roughness region (Fig. 1(a)) via an ordered roughness layer (Fig. 1(b)) to a homogeneous porous medium layer (Fig. 1(c)). Specifically, a representative microchannel of half-height (or half-width) $H/2$ is depicted in Fig. 1(c). The nominal value of channel height is determined as the distance between the center of the layer and the center of the channel (Hamrock [17]) This thin porous layer, h, generates two phenomena, i.e., generally an enhanced flow resistance when h and α are measurable as well as a reduced channel cross section when h is substantial and α is very small. Clearly, when h is finite, and $\alpha \rightarrow 1$, the surface roughness effect is negligible and the flow area increases slightly. In order to elucidate the capabilities of the proposed PML model on the friction factor, various liquid flow fields in different micro-conduits have been analyzed.

Starting with a generalized transport equation describing fluid flow in any conduit as well as porous medium layer, the systemic equations are derived, assuming steady fully developed flow in 2-D microchannels, microtubes, and micro-journal bearings.

2.1 Modeling Equation. A generalized transport equation (c.f. Kleinstreuer [18,19]) for flow in a porous medium layered micro-conduit can be written as

$$\frac{\partial}{\partial t}(\alpha\rho\Phi) + \nabla\cdot(\rho\vec{\vec{K}}\cdot\vec{u}\Phi) - \nabla\cdot(\mu\vec{\vec{K}}\cdot\nabla\Phi) = \alpha S \qquad (1)$$

where Φ is an arbitrary transport quantity, α is the porosity, $\vec{\vec{K}} = \alpha\vec{\vec{\delta}}$ is an area porosity tensor, $\vec{u}$ is the velocity vector, ρ is the fluid density, μ is the fluid viscosity, and S is a source term.

Setting $\Phi \equiv 1$, $S \equiv 0$ and $\Phi \equiv \vec{u}$, $S \equiv \vec{R}$, the corresponding continuity and momentum equations are as follows.

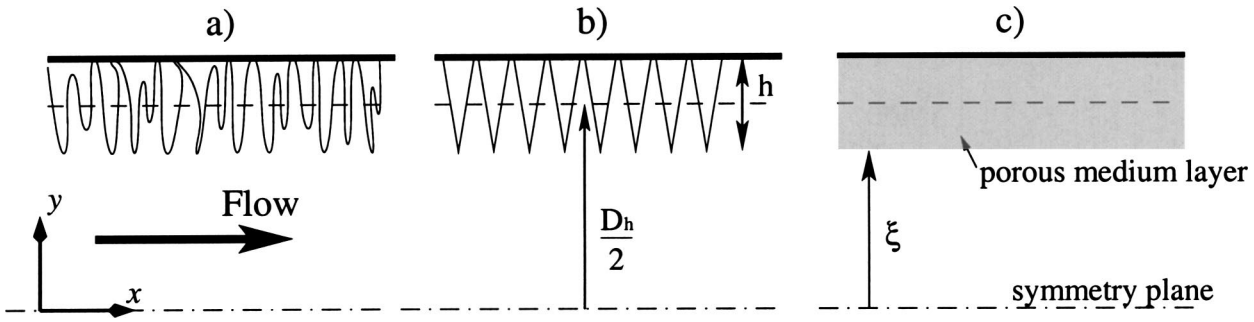

Fig. 1 Porous medium layer equivalent to surface roughness and simple microchannel geometry: (*a*) real surface roughness; (*b*) homogeneous distribution of identical roughness elements; and (*c*) mid-plane view of conduit with idealized roughness layer, or porous medium layer (PML).

Continuity Equation.

$$\frac{\partial}{\partial t}(\alpha\rho)+\nabla\cdot(\rho\vec{\vec{K}}\cdot\vec{u})=0 \tag{2}$$

Momentum Equation.

$$\frac{\partial}{\partial t}(\alpha\rho\vec{u})+\nabla\cdot(\rho(\vec{\vec{K}}\cdot\vec{u})\otimes\vec{u})-\nabla\cdot(\mu\vec{\vec{K}}\cdot(\nabla\vec{u}+\nabla\vec{u}^T))$$
$$=-\alpha\vec{R}-\alpha\nabla p \tag{3}$$

where p is the pressure, and $\vec{R}$ is the resistance vector to flow in the porous medium layer. On the right-hand side of Eq. (3), the first term captures the augmented surface forces induced by wall effects in micro-systems, and the last term is the pressure force acting on the fluid. In the open conduit $\alpha=1$ and $\vec{R}=0$, whereas inside the porous medium layer, α may vary, $0\leqslant\alpha<1$, and the resistance vector, $\vec{R}$, can be represented as

$$\vec{R}=(R_C+R_F|\vec{u}|^{\beta})\vec{u} \tag{4}$$

where R_C is a resistance constant, R_F is the resistance speed factor, and β is a "resistance speed power" as summarized in Table 1.

Assuming constant fluid and material properties, Eq. (3) can be written as

$$\alpha\frac{\partial\vec{u}}{\partial t}+\nabla\cdot((\alpha\vec{u})\otimes\vec{u})=-\frac{\alpha}{\rho}\nabla p+\frac{\mu}{\rho}\alpha\nabla\cdot(\nabla\vec{u}+\nabla\vec{u}^T)$$
$$-\frac{\alpha}{\rho}(R_C+R_F|\vec{u}|)\vec{u} \tag{5}$$

With fully-developed (parabolic) velocity profiles for 2-D channel flow, the viscous and resistance terms have the same sign, i.e., considering:

$$\vec{u}(y)=c_1y^2+c_2y+c_3>0; \tag{6a}$$

$$\frac{d^2\vec{u}}{dy^2}=2c_1<0; \quad c_1<0 \tag{6b}$$

where the c_i's are constants, so that:

$$\text{sign}\left(\frac{\mu}{\rho}\alpha\nabla\cdot(\nabla\vec{u}+\nabla\vec{u}^T)\right)=\text{sign}\left(-\frac{\alpha}{\rho}R_C\cdot\vec{u}\right)$$
$$=\text{sign}\left(-\left(\frac{\alpha}{\rho}R_F|\vec{u}|\right)\vec{u}\right) \tag{6c}$$

This implies that the porous medium generates augmented viscous flow effects in the wall layer directly proportional to channel flow rate and porous layer resistance $R_C=R_C(\alpha,h)$.

Now, in order to readily elucidate the porous medium layer, or roughness, effects in a microchannel and the relative importance of the resistance speed factor, R_F, a simplified version of Eq. (5) was numerically solved, employing MATLAB (MathWorks [20]) with a user-supplied program. Specifically, assuming steady, fully-developed 2-D flow in an isotropic porous medium, Eq. (5) reduces to the 2-D Brinkman-Forchheimer-extended-Darcy equation.

$$0=-\frac{dp}{dx}+\mu\frac{d^2u}{dy^2}-\left\{\frac{\mu}{\kappa}u+\frac{\rho C_F}{\kappa^{1/2}}u^2\right\}_{\text{PML}} \tag{7}$$

where, with respect to Eq. (5), the L.H.S. is zero, $\nabla p\rightarrow dp/dx$ = constant, $\nabla\cdot(\mu(\nabla\vec{u}+\nabla\vec{u}^T))\rightarrow\mu\,d^2u/dy^2$, $R_C=\mu/\kappa$, $R_F=\rho C_F/\kappa^{1/2}$, and $C_F=0.55$ (Nield and Bejan [21]).

In dimensionless form,

$$0=-\frac{dp^*}{dx^*}+\frac{4}{\text{Re}_{D_h}}\frac{d^2u^*}{dy^{*2}}-\left\{\frac{4}{\text{Da}\cdot\text{Re}_{D_h}}+\frac{C_F}{\text{Da}^{1/2}}u^{*2}\right\}_{\text{PML}} \tag{8}$$

where $p^*=p/\rho U_0^2$, $u^*=u/U_0$, $x^*=x/H$, $y^*=y/H$, Da $=\kappa/H^2$, $\text{Re}_{D_h}=4\rho U_0H/\mu$, H is the half-channel height, U_0 is the

Table 1 Porous medium constants, coefficients, and parameters (Reprinted from Ref. [3] with written permission from IOP, Bristol, UK)

Symbol	Meaning	Typical values/formats
α	(Volume) porosity	$0.0\leqslant\alpha\leqslant1.0$
κ	Permeability	10^{-4} cm$^2<\kappa<\infty$
K	Area porosity tensor	For isotropic porous media, $K_{ij}=\alpha\delta_{ij}$
Γ	Fluid viscosity	For laminar flow, $\Gamma\equiv\mu$
R_C	Resistance constant	$R_C=f(\text{Da},\text{Re})$
R_F	Resistance speed factor	$R_F=f(\text{Da},\|\vec{u}\|)$
β	Resistance speed power	$\beta\approx1.0$

Table 2 Typical values of relative surface roughness ($h/D_h\times100\%$)

Author	Relative surface roughness (%)	Material
Pfhaler et al. [22,23]	~1%	Silicon
Peng et al. [4,5]	~0.6–1%	Silicon
Mala & Li [13]	~3.5%	Stainless steel/Fused silica
Papautsky et al. [24]	~2%	Silicon
Wu & Cheng [10]	~0.12%	Silicon
Guo & Li [7]	~3–4.3%	Stainless steel
Xu et al. [25,26]	~0–1.7%	Aluminum, Silicon

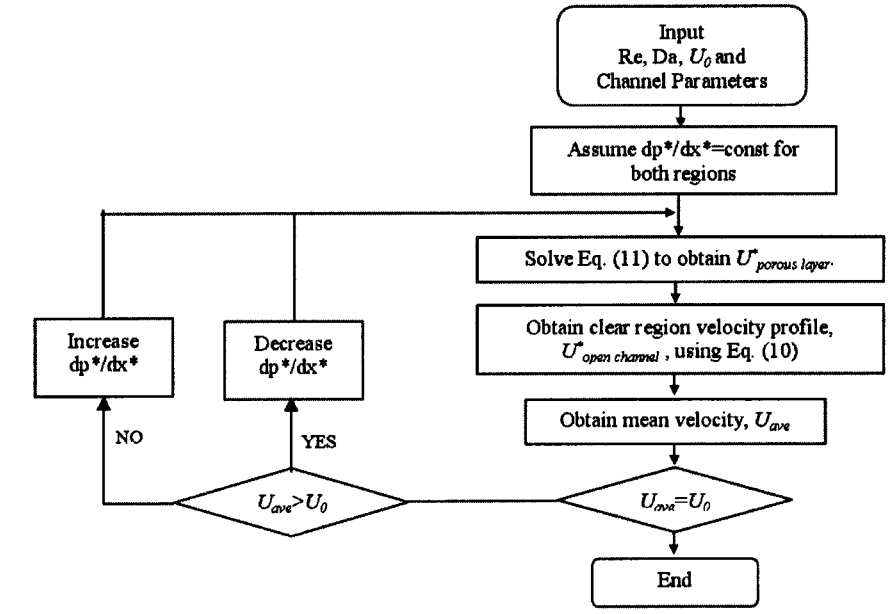

(*a*)

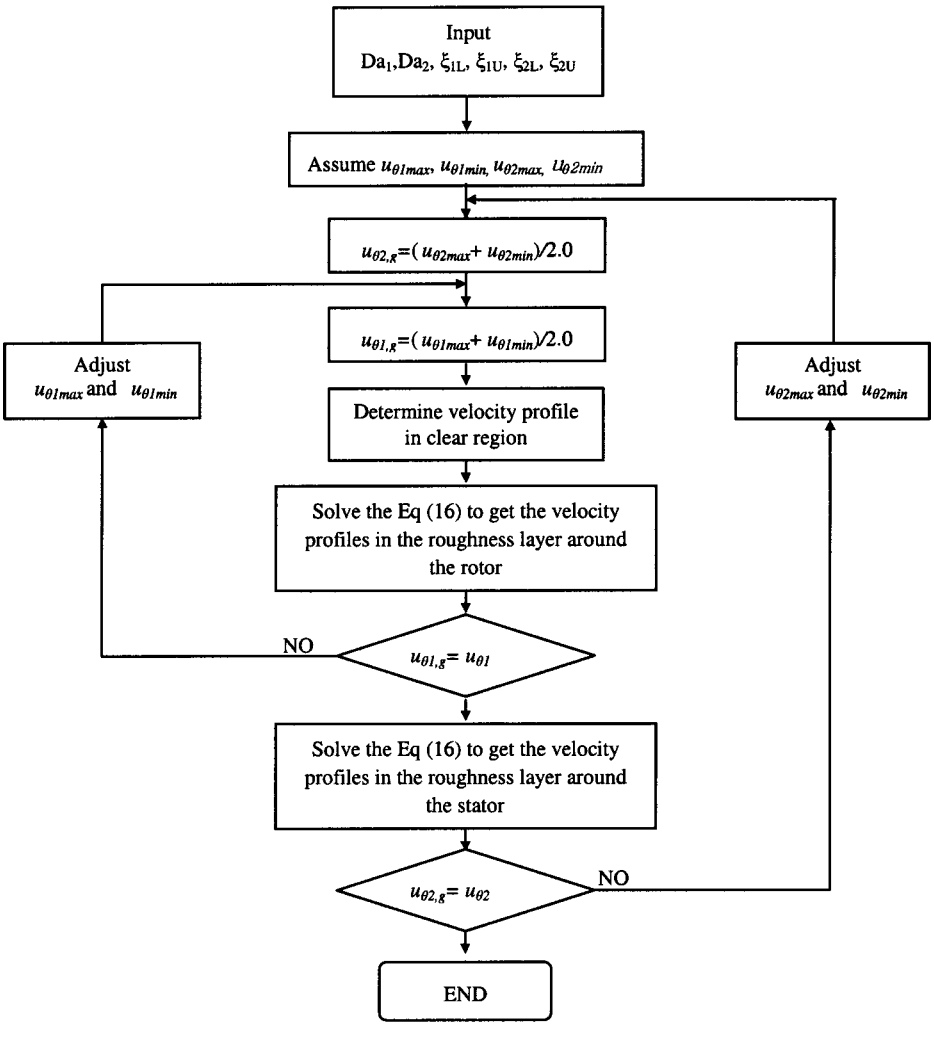

(*b*)

Fig. 2 Flowcharts: (*a*) Flow field solution in a microchannel with constant homogeneous porous wall layers; and (*b*) Velocity profiles in the annulus between the rotor and the stator (see Fig. 3 for the definition of symbols)

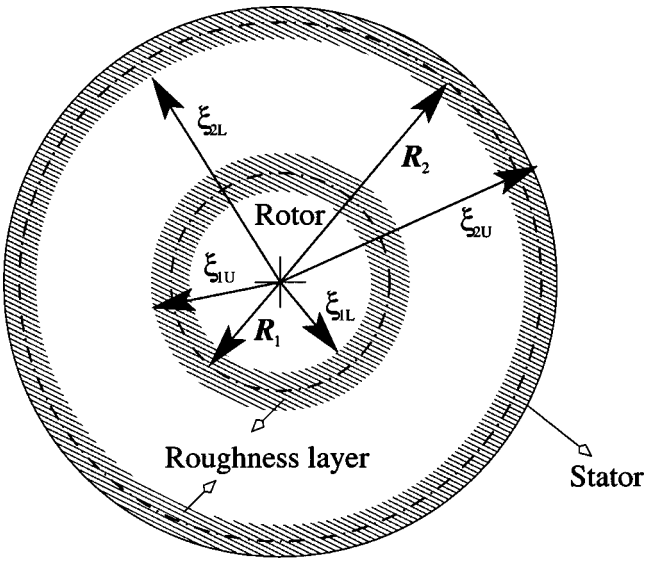

Fig. 3 Schematics of the micro-journal bearing: R_1 and R_2 represent radii of the rotor and stator, respectively, whereas ξ_{1L}, ξ_{1U}, ξ_{2L} and ξ_{2U} are the interface coordinates of the inner and outer porous layers

average velocity, D_h is the hydraulic diameter, C_F is a drag coefficient, α is the porosity of the PML in the channel, and κ is the permeability where $\kappa \sim \alpha^3(1-\alpha)^{-2}$.

Typical relative surface roughness values for micro-conduits are listed in Table 2. Generally, surface roughness depends on the wall material and machining process, where micromachining (or micro-cutting) results in higher roughness than etching processes; furthermore, microchannels of stainless steel or aluminum have higher values of surface roughness than those of silicon. For example, Xu et al. [25,26] measured typical roughness heights for etching processes to be 20 nm, which is negligible in most microchannels where $D_h > 10\ \mu$m, while a channel milled into an aluminum plate by micro-end-mills produced roughness of about 0.5 μm. It shows the dependence of the relative roughness on the channel material and manufacturing method (see Table 2).

2.2 Microchannels. For the clear, i.e., porous medium-free region of the channel, Eq. (8) reduces to (Da$\to\infty$):

$$0 = -\frac{dp^*}{dx^*} + \frac{4}{\mathrm{Re}_{D_h}} \frac{d^2u^*}{dy^{*2}} \tag{9}$$

Double integration yields:

$$u^*(y^*) = \frac{\mathrm{Re}_{Dh}}{4} \frac{dp^*}{dx^*}(y^{*2} - \xi^2) + u^*_{\mathrm{int}} \tag{10}$$

where ξ is the non-dimensionalized coordinate for the open channel-porous medium layer interface, and u^*_{int} is the flow velocity at the interface, which depends on the iterative solution to the PML-flow problem.

The velocity profile in the porous region is obtained by solving Eq. (11), using a boundary-value-problem ordinary differential equation (ODE) solver routine that is provided in MATLAB 6.0. 400 elements were evenly distributed in the porous medium layer and 2,000 elements in the open region.

$$0 = -\frac{dp^*}{dx^*} + \frac{4}{\mathrm{Re}_{D_h}} \frac{d^2u^*}{dy^{*2}} - \frac{4}{\mathrm{Da} \cdot \mathrm{Re}_{D_h}} - \frac{C_F}{\mathrm{Da}^{1/2}} u^{*2} \tag{11a}$$

The boundary conditions are no-slip velocity ($u=0$) at the channel wall, and matching velocity gradients at the interface between clear and porous regions, i.e.,

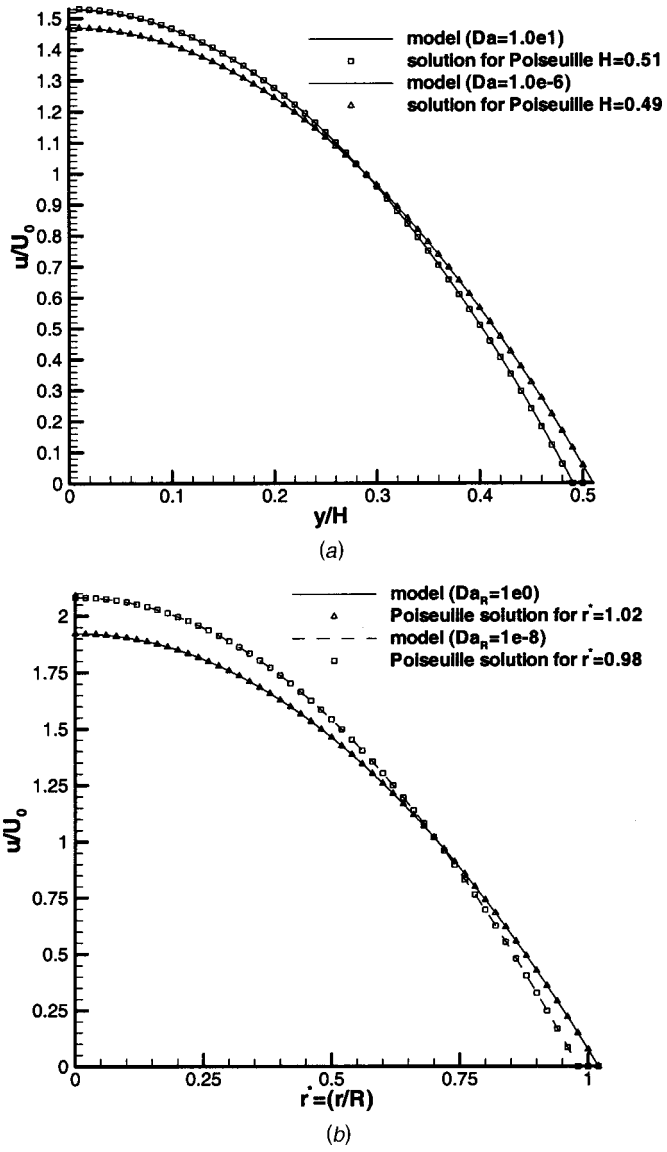

Fig. 4 Comparison of modeling results with Poiseuille flow for (*a*) PML microchannel; and (*b*) PML microtube

$$\left.\frac{du^*}{dy^*}\right|_{y^*=\xi} = \frac{\mathrm{Re}_{Dh}}{4} \frac{dp^*}{dx^*} \xi \tag{11b}$$

Based on global mass conservation, the velocity gradient at the interface was iteratively obtained using the shooting method by assuming a reasonable pressure gradient for the flow field. After computing the velocity field, the average flow velocity was obtained for each iteration. Comparing it with the given average velocity, the pressure gradient, dp^*/dx^*, was adjusted to match the average velocity from each iteration to the given average velocity (cf. Fig. 2). It took about five minutes to obtain a solution per case on a Sun Ultra 60 workstation.

2.3 Microtubes. Equation (11) in cylindrical coordinates reads

$$0 = -\frac{dp^*}{dx^*} + \frac{2}{\mathrm{Re}_D}\left(\frac{d^2u^*}{dr^{*2}} + \frac{1}{r^*}\frac{du^*}{dr^*}\right) - \frac{2}{\mathrm{Da} \cdot \mathrm{Re}_D} - \frac{C_F}{\mathrm{Da}^{1/2}} u^{*2} \tag{12}$$

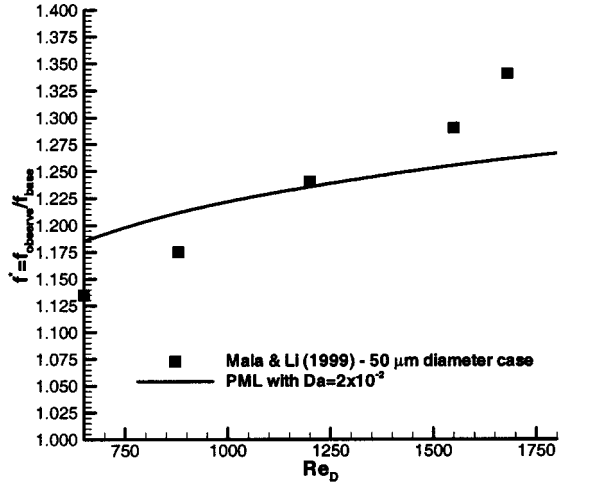

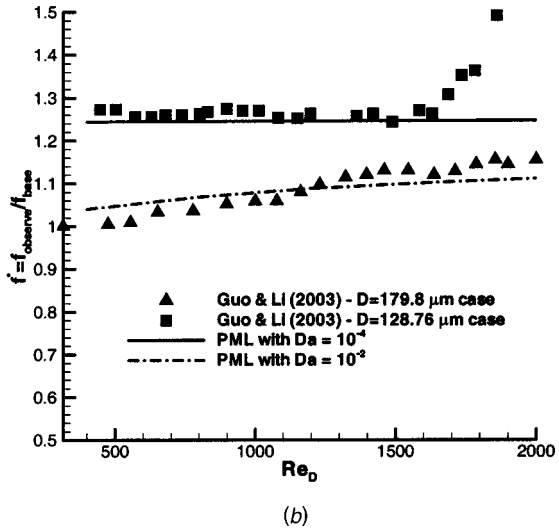

Fig. 5 Comparisons of porous medium layer (PML) model predictions with experimental data: (*a*) Mala and Li (1999); and (*b*) Guo and Li (2003) (Reprinted from Ref. [3] with written permission from IOP, Bristol, UK)

subject to the no-slip velocity ($u=0$) condition at the wall, and velocity gradient matching at the interface between clear and porous regions, i.e.,

$$\left.\frac{du^*}{dr^*}\right|_{r^*=\xi} = \frac{\mathrm{Re}_D}{2}\frac{dp^*}{dx^*}\xi \tag{13}$$

The velocity profiles can be obtained with the same procedure used for the microchannel (or parallel plate) case.

2.4 Micro-Journal Bearings. Figure 3 shows the schematics for a rotating cylinder in a tube, with roughness layers on both surfaces. The PML thickness was calculated based on the nominal clearance between the rotor and the stator. Eight hundred grid points were placed in both roughness layers. Again, the flow is assumed to be steady, fully developed, and axi-symmetric and can be described by

$$0=\mu\left(\frac{d^2u_\theta}{dr^2}+\frac{1}{r}\frac{du_\theta}{dr}-\frac{u_\theta}{r^2}\right)-\frac{\mu}{\kappa}(u_\theta-u_R)-\frac{\rho C_F}{\mu\kappa^{1/2}}(u_\theta-u_R)^2 \tag{14}$$

where u_R is the rotor speed, and u_θ is the fluid velocity in the roughness layer. In the roughness layer on the stator, $u_R=0$.

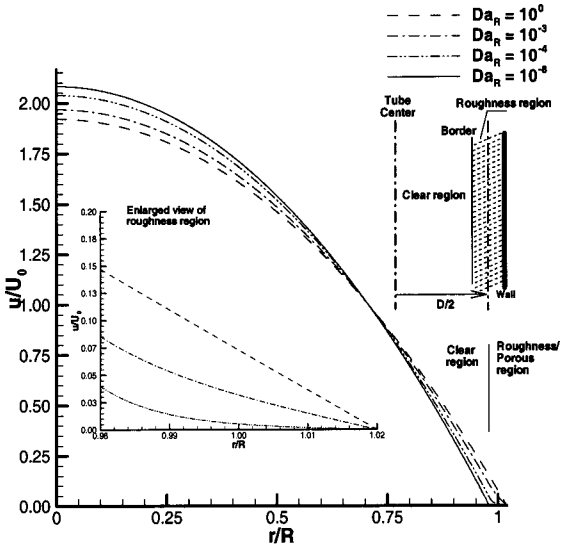

Fig. 6 Effect of Darcy number on microtubular velocity profile ($\mathrm{Re}_D=2000$, $h/D_h=0.02$, the Forchheimer term is retained). (Reprinted from Ref. [3] with written permission from IOP, Bristol, UK)

In dimensionless form, with $U_0=R_{1\omega 0}$, we have for the open region:

$$0=\frac{d^2u_\theta^*}{dr^{*2}}+\frac{1}{r^*}\frac{du_\theta^*}{dr^*}-\frac{u_\theta^{*2}}{r^{*2}} \tag{15}$$

and for the PML:

$$0=\frac{d^2u_\theta^*}{dr^{*2}}+\frac{1}{r^*}\frac{du_\theta^*}{dr^*}-\frac{u_\theta^*}{r^{*2}}-\frac{u_\theta^*-u_R^*}{\mathrm{Da}_R}-\frac{\mathrm{Re}_R C_F}{\mathrm{Da}_R^{1/2}}(u_\theta^*-u_R^*)^2 \tag{16}$$

subject to the no-slip conditions at ξ_{1L} and ξ_{2U} as well as interface matching conditions (cf. Fig. 2(*b*)). Here, $\mathrm{Re}_R=\rho u_0 R_2/\mu$, $u_0=R_{1\omega 0}$, ω_0 is the rotor angular velocity. The velocities are nondimensionalized by dividing by u_0. The torque per unit length required to overcome frictional effects is

$$T=\vec{F}\times\vec{r}:=2\pi(r^2\tau)_{\mathrm{wall}} \tag{17}$$

3 Results and Discussion

3.1 Model Validations. For large Darcy numbers, the PML is permeable and hence the additional friction effect vanishes so that the flowing liquid experiences a half-channel of $y^*=0.51$, or a fixed tube radius of $r^*=1.02$. In the other extreme case when the Darcy number approaches zero, the PMLs act as solid ''coatings'' and hence the flow areas are slightly reduced to $y^*=0.49$ or $r^*=0.98$. Figures 4(*a*) and 4(*b*) depict a comparison between the modeling results and the exact flow solutions for both cases.

Figure 5 shows comparisons between the PML model predictions and selected experimental results. Specifically, the experimental results of Mala and Li [13], which fall into the region predicted by the PML model, indicate a strong $f^*(\mathrm{Re}_D)$ dependence (Fig. 5(*a*)). The experimental data sets of Guo and Li [7] are well matched with the PML model (Fig. 5(*b*)). Clearly, roughness elements of the 179.8 μm diameter tube have a higher Darcy number when compared to the 128.8 μm diameter tube. The

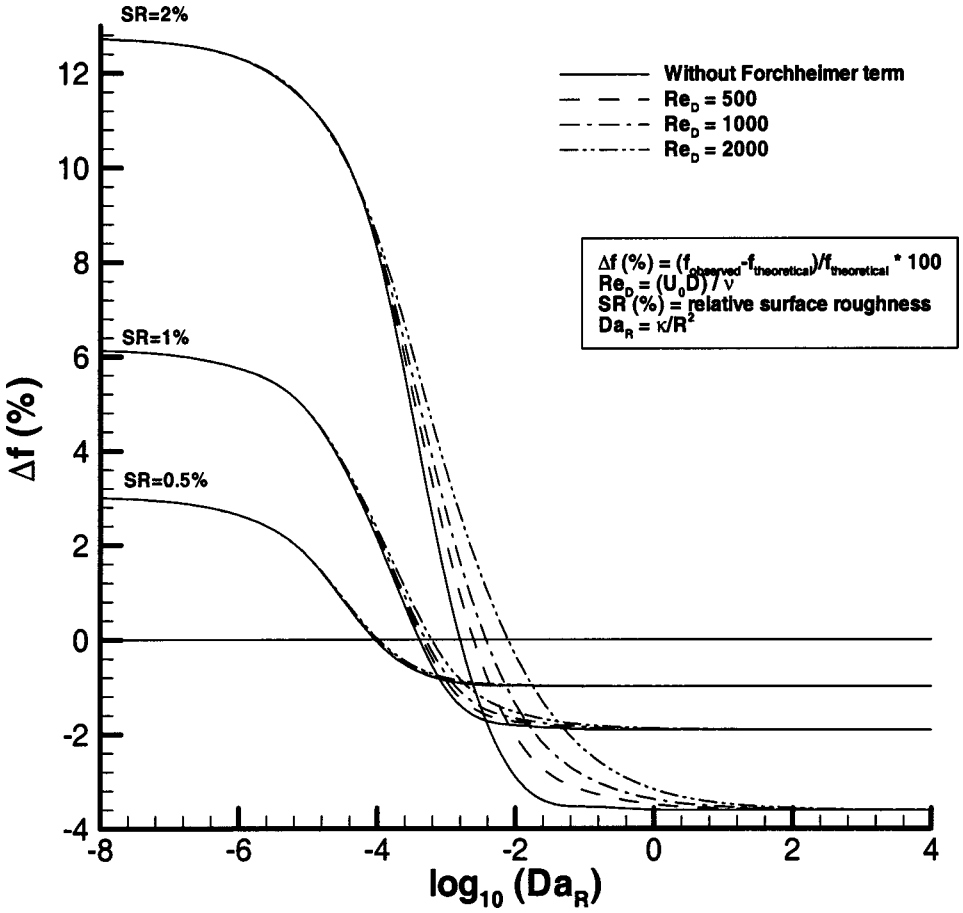

Fig. 7 Effects of Reynolds number, surface roughness, Darcy number, and Forchheimer drag term on the change in friction factor for microtubular flows

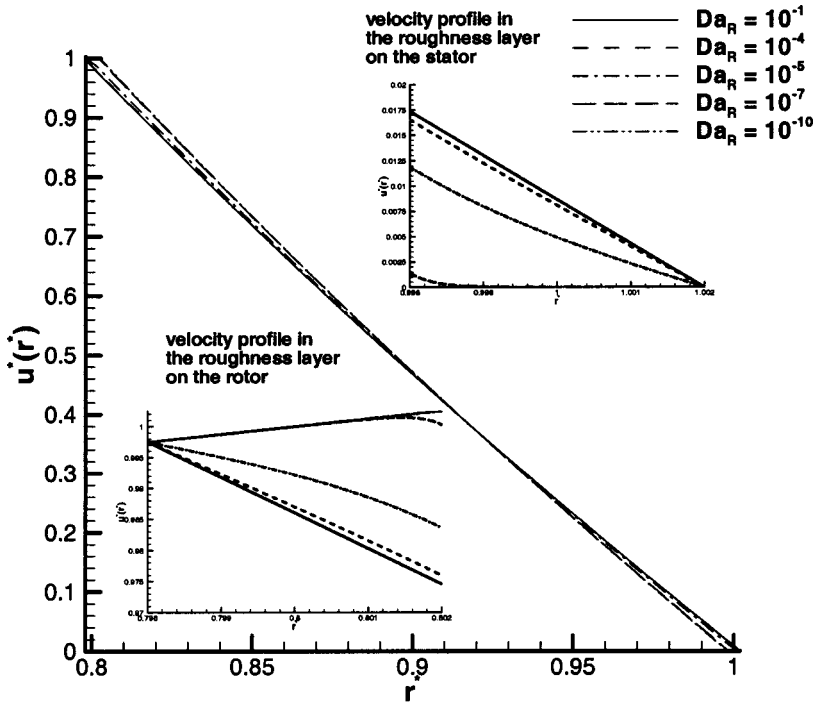

Fig. 8 The effect of Darcy number, Da_R, on the velocity profiles in the gap

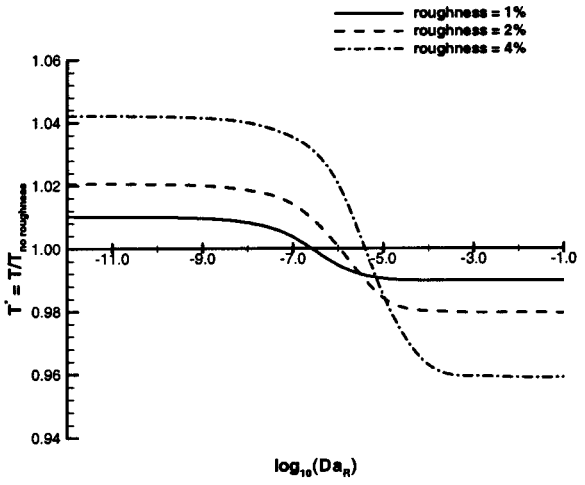

(*a*)

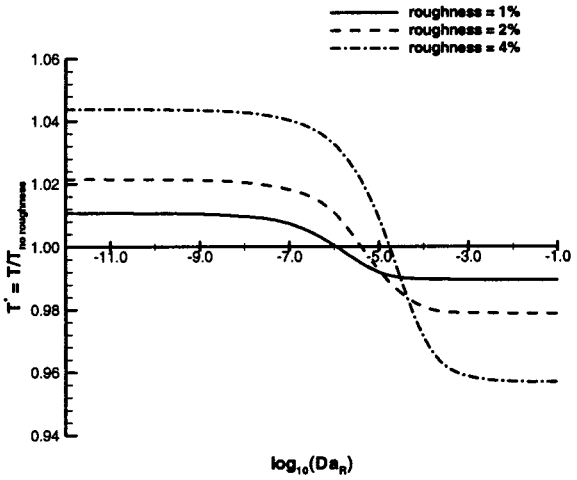

(*b*)

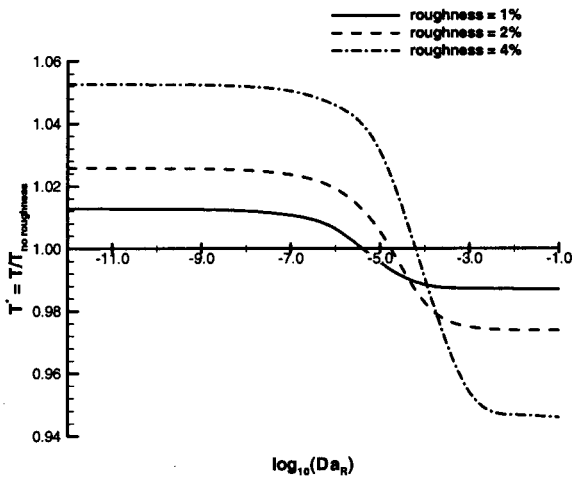

(*c*)

Fig. 9 The effect of roughness layer on the torque required to maintain flow field: (*a*) 10% clearance case; (*b*) 20% clearance case; and (*c*) 40% clearance case

$f^*(\mathrm{Re}_D)$ data for the 179.8 μm diameter tube seems to indicate the effect of laminar-to-turbulent flow transition, when $\mathrm{Re}_D > 1700$. They [7] claimed that "the form drag resulting from the roughness is one reason leading to the increased friction factor;" the form drag is captured by the Forchheimer term in the PML model.

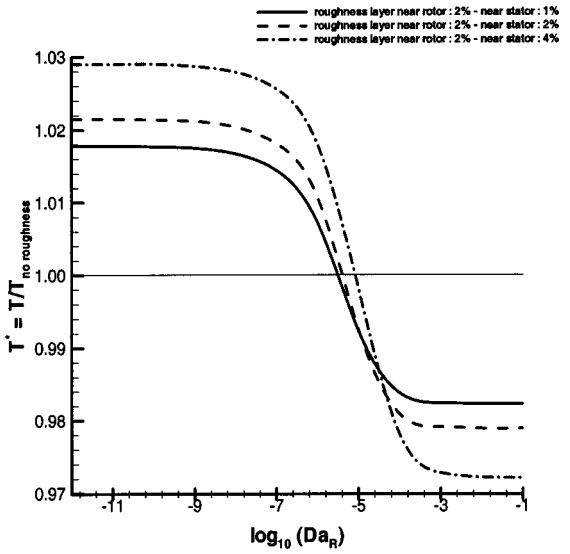

Fig. 10 The effect of clearance width on the torque: *R* is the nominal radius of the stator

3.2 Porous Medium Layer Effects. There are several PML effects of interest in terms of porous medium permeability, and height as well as actual flow are influencing the local velocity, friction factor, and torque. It should be noted that changes in friction factor and the influence of the Forchheimer term, $C_F \mathrm{Da}^{-1/2} u^{*2}$, are more pronounced in microtubes than in microchannels so that only solutions to systems of sections 2.3 and 2.4 are shown. Specifically, the velocity inside the PML of a microtube is somewhat larger than in the parallel plate case (see Fig. 4 in [3]), and hence the flow resistance is greater in a microtube. Thus, the PML thickness plays a measurable role concerning the type of conduit, impact of the Forchheimer term, and ultimately the flow resistance.

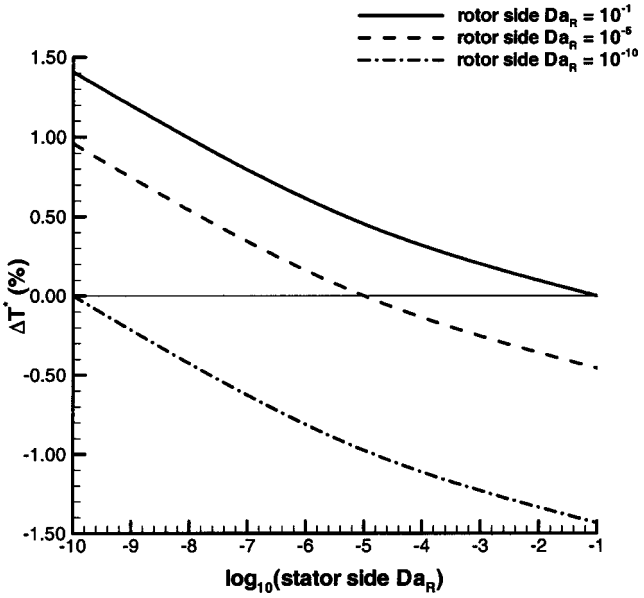

Fig. 11 The effect of the Darcy number difference on the required torque

3.2.1 Microtube Results. For a given Reynolds number ($\mathrm{Re}_D=2{,}000$) and PML-height $h/R=0.04$, while neglecting for this test run the Forchheimer term in Eq. (12), the impact of the Darcy number on the axial velocity profile is twofold (Fig. 5). With increasing PML permeability, the velocity profile: (a) flattens in the tube-center region, and (b) migrates into the PML with a profile ''cross-over'' point at $r^*\approx 0.7$. Of special interest is the PML-flow effect, with and without the Forchheimer term, on the change in friction factor, i.e.,

$$f^*=\frac{\Delta f}{f_{\text{theory}}}=\frac{f_{\text{observed}}-f_{\text{theoretical}}}{f_{\text{theory}}}\times 100\% \tag{18}$$

where $f_{\text{theoretical}}$ is obtained from conventional theory, i.e.,

$$f_{\text{theory}}=\frac{2\tau_{\text{wall}}}{\rho\overline{u}^2}, \tag{19a}$$

$$\overline{u}=Q/(r_0^2\pi) \tag{19b}$$

and $f_{\text{observed}}=\text{fct}(\text{SR},\text{Da},\text{Re})$ results from our computer experiments, where SR represents relative surface roughness ($\text{SR}=h/D_h$). Clearly, the Forchheimer term is important for significant relative surface roughness values and Darcy numbers, i.e., $\text{SR}\geqslant 0.02$ and $10^{-4}\leqslant \text{Da}\leqslant 1$, even for low Reynolds numbers (Fig. 7). When using only the Brinkman term, $2(\text{Da}\,\text{Re}_D)^{-1}$, the Reynolds number has no measurable influence on f^*. As already implicit in Fig. 6, the Darcy number affects f^* in a major fashion (see Fig. 7). For example, for $\text{SR}=0.02$, the friction factor increases about 12.7% for low PML Darcy numbers and decreases by 3.6% for high Darcy numbers. The reason is that when $\text{Da}\rightarrow\infty$ the cross sectional area increases slightly ($r=r_0+h/2$) while the average velocity is somewhat reduced and hence $f_{\text{observed}}<f_{\text{theoretical}}$.

According to laboratory measurements by Mala and Li [13], the normalized friction constant, $C^*(=f_{\text{observed}}/f_{\text{theory}})$, increases up to 20% for different Reynolds numbers, up to $\text{Re}=1{,}200$ (Above $\text{Re}\approx 1{,}200$, additional effects, such as nonuniform inlet conditions and complex conduit geometries, may come into play [3,8]. Specifically, Mala and Li [13] reported relative roughness values varying from 1.15% for the 152 μm diameter tube to 3.5% for the 50 μm diameter tube. For a particular case study, assuming $\kappa=10^{-3}$, the PML model predicted a 20% higher friction factor, exactly as observed by Mala and Li [13], using their definition of the nominal tube diameter. Data from Qu et al. [6], who were part of the Mala and Li research group, as well as Xu et al. [25,26] showed a measurable dependence of the friction factor on the Reynolds number. This $f^*(\text{Re})$ effect can be captured with the Forchheimer term in Equation (12).

In contrast, Judy et al. [9] measured mostly smaller friction factors than the corresponding theoretical values without any dependence on the Reynolds number. Our PML model can reproduce this observation by means of a high Darcy number; for example, when $\text{Da}\rightarrow\infty$ their largest friction factor deviation, i.e., $f^*=-15\%$, can be simulated. Clearly, their photographs of the tube cross sections indicate ''wavy'' surfaces, which imply strong uncertainties with respect to the measured nominal tube diameter and hence possibly larger actual flow areas than observed.

3.2.2 Micro-Journal Bearing. Figure 8 shows the velocity profiles in micro-journal bearings. From the enlarged view of the velocity profile in the roughness layer on the rotor, the fluid is found to have higher velocity, as the PML-Darcy number increases. The effects of surface roughness thickness, Darcy number, and clearance width on the torque is shown in Fig. 9. In contrast to the previous cases, the maximum torque increase and decrease are the same, i.e., around 4% in relative magnitude. However, the surface roughness is calculated based on the clearance width which is much smaller than the hydraulic diameter as previously employed.

Figure 10 shows the effect of gap size on the torque. The change in required torque increases with gap size. The maximum Darcy number to which the required torque decreases also increases with clearance width. Furthermore, the effect of difference in roughness layer thicknesses is shown in Fig. 10. If the roughness layer on the stator is thinner than that on the rotor, the required torque change decreases; if the roughness layer on the stator is thicker than on the rotor, the required torque change increases. The maximum Darcy number for which the required torque decreases, shifts to the left or decreases with thinner stator PMLs.

The Darcy number effect on the change in torque is shown in Fig. 11. Each line depicts the effect of the stator-side Darcy number on the required torque variation for the fixed Darcy number of the rotor PML. The maximum variation is about 1.5%, which is calculated based on the required torque for the case that the stator-side roughness layer has the same Darcy number as that for the rotor-side roughness layer. The required torque increases when the stator-Da is greater than that of the rotor-Da.

4 Conclusions

Laminar flow of liquids in micro-conduits, such as straight channels, tubes and rotating cylinders, may differ in terms of wall frictional effects, and hence flow rates, when compared to macro-channels. Specifically, some experimentalists claimed that friction factors in microchannels are higher, and perhaps require a new (molecular) modeling approach, whereas others noted that the conventional, i.e., macro-scale theory is adequate to predict all transport phenomena. Clearly, higher uncertainties are associated with micro-scale measurements, and experimental errors may lead to unrealistic interpretations of flow phenomena.

Focusing on steady laminar fully-developed flow of a liquid in different micro-conduits, relative surface roughness and actual diameter (or channel height) variations are captured in terms of a porous medium layer (PML) model. The new approach allows the evaluation of microfluidics variables as a function of PML characteristics, i.e., layer thickness and porosity, uncertainties in measuring hydraulic diameters, as well as the inlet Reynolds number.

Specifically, realistic values for the PML Darcy number, $0<\text{Da}<\infty$, relative surface roughness, $0.5\leqslant \text{SR}\leqslant 2\%$, and actual flow area, $D_h=D_{h,\text{nominal}}\pm 4\%$, are taken into account to match observed friction factor values in micro-conduits.

The model predictions compared well with measured data sets [7–9,13] where the relative roughness were measured to be significant. Although other surface effects may have influenced the experimental results as well, surface roughness is found to affect the friction factor and hence the flow parameters in relatively rough channels, which are made of aluminum or stainless steel by way of micro-cutting processes. However, further experiments to provide accurate values for the drag coefficient, C_f, which depends on the configuration of the surface roughness elements, would be desirable to refine the PML model.

Acknowledgments

The authors want to express their thanks to Dr. Joseph P. Archie and Mrs. Sarah Archie for the endowment of the McDonald-Kleinstreuer fellowship, presently awarded to Junemo Koo.

References

[1] Gad-el-Hak, M., 1999, ''The Fluid Mechanics of Microdevices-The Freeman Scholar Lecture,'' ASME J. Fluids Eng., **121**, pp. 5–33.
[2] Sobhan, C. B., and Garimella, S. V., 2001, ''A Comparative Analysis of Studies on Heat Transfer and Fluid Flow in Microchannels,'' Microscale Thermophys. Eng., **5**, pp. 293–311.
[3] Koo, J., and Kleinstreuer, C., 2003, ''Liquid Flow in Microchannels: Experimental Observations and Computational Analyses of Microfluidics Effects,'' J. Micromech. Microeng., **13**, 568–579.
[4] Peng, X. F., Peterson, G. P., and Wang, B. X., 1994, ''Frictional Flow Characteristics of Water Flowing Through Rectangular Microchannels,'' Exp. Heat Transfer, **7**, pp. 249–264.

[5] Peng, X. F., and Peterson, G. P., 1996, ''Convective Heat Transfer and Flow Friction for Water Flow in Microchannel Structures,'' Int. J. Heat Mass Transfer, **39**(12), pp. 2599–2608.
[6] Qu, W., Mala, G. M., and LI, D., 2000, ''Pressure-driven Water Flows in Trapezoidal Silicon Microchannels,'' Int. J. Heat Mass Transfer, **43**, pp. 353–364.
[7] Guo, Z., and Li, Z., 2003, ''Size Effect on Microscale Single-Phase Flow and Heat Transfer,'' Int. J. Heat Mass Transfer, **46**, pp. 149–159.
[8] Sharp, K. V., 2001 ''Experimental Investigation of Liquid and Particle Laden Flows in Microtubes,'' Ph.D. thesis, University of Illinois, Urbana-Champaign, IL.
[9] Judy, J., Maynes, D., and Web, B. W., 2002, ''Characterization of Frictional Pressure Drop for Liquid Flows Through Microchannels,'' Int. J. Heat Mass Transfer, **45**(17), pp. 3477–3489.
[10] Wu, H. Y., and Cheng, P., 2003, ''Friction Factors in Smooth Trapezoidal Silicon Microchannels with Different Aspect Ratios,'' Int. J. Heat Mass Transfer, **46**, pp. 2519–2525.
[11] Gao, P., Person, S., and Favre-Marinet, M., 2002, ''Scale Effects on Hydrodynamics and Heat Transfer in Two-Dimensional Mini and Microchannels,'' Int. J. Heat Mass Transfer, **41**, pp. 1017–1027.
[12] Li, D., 2001, ''Electro-Viscous Effects on Pressure-Driven Liquid Flow in Microchannels,'' Colloids Surf., A, **195**, pp. 35–57.
[13] Mala, G. M., and Li, D., 1999, ''Flow Characteristics of Water in Microtubes,'' Int. J. Heat Mass Transfer, **20**, pp. 142–148.
[14] Tichy, J. A., 1995, ''A Porous Media Model for Thin Film Lubrication,'' ASME J. Tribol., **117**, pp. 16–21.
[15] Li, W., and Hwang, C., 1999, ''Derivation of the Modified Molecular Gas Lubrication-a Porous Media Model,'' J. Phys. D, **32**, pp. 1421–1427.
[16] Li, W., Lin, J., Lee, S., and Chen, M., 2002, ''Effects of Roughness on Rarefied Gas Flow in Long Microtubes,'' J. Micromech. Microeng., **12**, pp. 149–156.
[17] Hamrock, B. J., 1994, *Fundamentals of Fluid Film Lubrication*, McGraw-Hill, New York.
[18] Kleinstreuer, C., 2003, *Two-Phase Flow—Theory and Applications*, Taylor & Francis Publishers, Washington, DC and London, UK.
[19] Kleinstreuer, C., 1997, *Engineering Fluid Dynamics*, Cambridge University Press, New York.
[20] MathWorks, 2002, ''Using MATLAB,'' MathWorks Inc., Natick, MA, USA.
[21] Nield, D. A., and Bejan, A., 1992, *Convection in Porous Media*, Springer-Verlag, New York, Chap. 1.
[22] Pfhaler, J., Harley, J., and Bau, H., 1990, ''Liquid Transport in Micron and Submicron Channels,'' Sens. Actuators, **A21–A23**, pp. 431–434.
[23] Pfhaler, J., Harley, J., Bau, H., and Zemel, J. N., 1991, ''Gas and Liquid Flow in Small Channels,'' *Micromechanical Sensors, Actuators, and Systems*, ASME Winter Annual Meeting, Atlanta, GA, Dec. 1–6, 1991, DSC Series **32**, pp. 49–60.
[24] Papautsky, I., Brazzle, J., Ameel, T., and Frazier, A. B., 1999, ''Laminar Fluid Behavior in Microchannels Using Micropolar Fluid Theory,'' Sens. Actuators, **73**, pp. 101–108.
[25] Xu, B., Ooi, K. T., Wong, N. T., and Choi, W. K., 1999, ''Liquid Flow in Microchannels,'' *Proceedings of the 5th ASME/JSME Joint Thermal Engineering Conference*, San Diego, California.
[26] Xu, B., Ooi, K. T., Wong, N. T., and Choi, W. K., 2000, ''Experimental Investigation of Flow Friction for Liquid Flow in Micro Channels,'' Int. Commun. Heat Mass Transfer, **27**(8), pp. 1165–1176.

Interfacial Electrokinetic Effect on the Microchannel Flow Linear Stability

Sedat Tardu
Laboratoire des Ecoulements Géophysiques et Industriels, LEGI
B.P. 53 X, 38041 Grenoble, Cédex France
e-mail: Sedat.Tardu@hmg.inpg.fr

The electrostatic double layer (EDL) effect on the linear hydrodynamic stability of microchannel flows is investigated. It is shown that the EDL destabilizes the Poiseuille flow considerably. The critical Reynolds number decreases by a factor five when the non-dimensional Debye-Huckel parameter κ is around ten. Thus, the transition may be quite rapid for microchannels of a couple of microns heights in particular when the liquid contains a very small number of ions. The EDL effect disappears quickly for $\kappa \geqslant 150$ corresponding typically to channels of heights 400 μm or larger. These results may explain why significantly low critical Reynolds numbers have been encountered in some experiments dealing with microchannel flows. [DOI: 10.1115/1.1637927]

Introduction

Both the rapid development of MEMS, and the need for high rates of heat removal of micro electronic devices require a clear understanding of micro flows in channels of heights ranging from some 100 to a couple of μm. It is not clear whether the classical macro-approaches are still valid or not in such small devices. Several experimental studies published so far are quite inconsistent, and no clear answer to these questions has been given yet. (Gad-el Hak [1], Tardu [2]).

In liquid flows, the molecular effects inducing slip boundary conditions become important only for microchannels of hydraulic diameters smaller than 1 μm [1,2]. Thus, it is rather difficult to explain the large departures from conventional transport theory observed in some microchannel flows of larger heights [3,4]. One of the micro-effects that may play an important role is the interfacial effect caused by the electric double layer (EDL) at the solid/liquid interface. The electrostatic charges present on the solid surface attract the counterions to establish an electrical field. In the compact layer next to the wall and less than 1 nm thick the ions are immobile. In the diffuse EDL layer however, the ions are less affected by the electrical field and can move. The counterion concentration near the wall is larger than in the bulk of the fluid. That results in a net charge density in a unit volume resulting from the concentration difference between cations and anions, according to the Boltzmann equation. The electrostatic potential at any point near the surface, provided that it is small compared to the energy of ions, may be obtained by a linear approximation of the Poisson-Boltzmann equation. Its value at the wall can be related to the Zeta potential between the compact layer and diffuse layer, when the EDLs near the opposite walls do not overlap. The Zeta potential is a property of the solid-liquid pair and can be determined experimentally [5]. The imposed pressure gradient accumulates the mobile ions downstream and sets up an electrical field whose potential is called the streaming or electrokinetic potential. The streaming potential and the net charge density induces a streamwise external force. In the steady state, the streaming current due to the transport of charges is in equilibrium with the conduction current in the opposite direction. That allows the determination of the streaming potential and of the velocity profiles under the EDL effect. In macro scale flows, these effects are negligible, as well as the thickness of the EDL is very small compared to the height of the channel.

Contributed by the Fluids Engineering Division for publication in the JOURNAL OF FLUIDS ENGINEERING. Manuscript received by the Fluids Engineering Division May 16, 2003; revised manuscript received September 11, 2003. Associate Editor: J. S. Marshall.

The velocity profile under the electrokinetic EDL effect obtained by Mala et al. [6] in the Debye-Hückel approximation, can be put in non-dimensional form as [2];

$$u = 1 - y^2 - 4\,\frac{I_1 - I_2}{\dfrac{\kappa^2 \sinh\kappa}{\overline{\zeta}^2 G} + 4\left(I_3 - \dfrac{I_4}{\sinh\kappa}\right)}\left\{1 - \left|\frac{\sinh\kappa\ y}{\sinh\kappa}\right|\right\} \tag{1}$$

where the scaling velocity is the centerline velocity of the Poiseuille component, i.e. $-a^2 dp/dx/2\mu$ and the scaling length is the half channel height a. There are several parameters in this equation, for instance $G = (n_0 z\ e\ a)^2/\lambda_0 \mu$, with n_0 standing for the ionic number concentration, z for the valence of positive or negative ions, e for the electron charge λ_0 the electric conductivity of the fluid, and μ for its dynamic viscosity. One of the most important quantities involving in (1) is the non dimensional Debye-Hückle parameter $\kappa = a\ k = a(2\,n_0 z^2\ e^2/\varepsilon\varepsilon_0 k_b\ T)^{1/2}$ with ε and ε_0 being respectively the dielectric constant of the medium and the permittivity of vacuum, k_b the Boltzmann constant and T the absolute temperature. The characteristic EDL thickness is $1/k$. The non-dimensional Zeta potential reads for $\overline{\zeta} = z\ e\zeta/k_b T$. The quantities I in (1) are given by:

$$I_1 = I_3 = \frac{\cosh\kappa - 1}{\kappa},\quad I_2 = \left(\frac{1}{\kappa} + \frac{2}{\kappa^3}\right)\cosh\kappa - \frac{2}{\kappa^2}\sinh\kappa - \frac{2}{\kappa^3},$$

$$I_4 = \frac{\sinh\kappa\cosh\kappa}{2\kappa} - \frac{1}{2} \tag{2}$$

Fig. 1a compares the velocity profile of an ''EDL flow'' with the conventional Poiseuille flow, when $\kappa = 41$, $G = 12720$ and $\overline{\zeta} = 2.1254$. This case corresponds to the flow of an *infinitely* diluted aqueous KCl solution ($n_0 = 3.764 \times 10^{19}$ m^{-3}, $\lambda_0 = 7.89 \times 10^{-9}$ S/m) through a microchannel of height 100 μm subjected to a Zeta potential of 50 mV. The parameters G $\overline{\zeta}$ and κ are exactly those used by Mala et al. [6] who analyzed the electrokinetic effects of the double layer. The Debye length is 1.2 μm which is close to the value corresponding to the de-ionized ultra-filtered water experiments of Ren et al. [5] The first impression one has from Fig. 1a is the close similarity between the EDL and Poiseuille profiles with a decrease of the centreline velocity typical to the EDL flows. The important difference however is the presence of an inflexional point at $y \approx 1/\kappa \arcsin h\{-2/r\kappa^2 \sinh(\kappa)\}$ in the EDL profile where r is the ratio of the

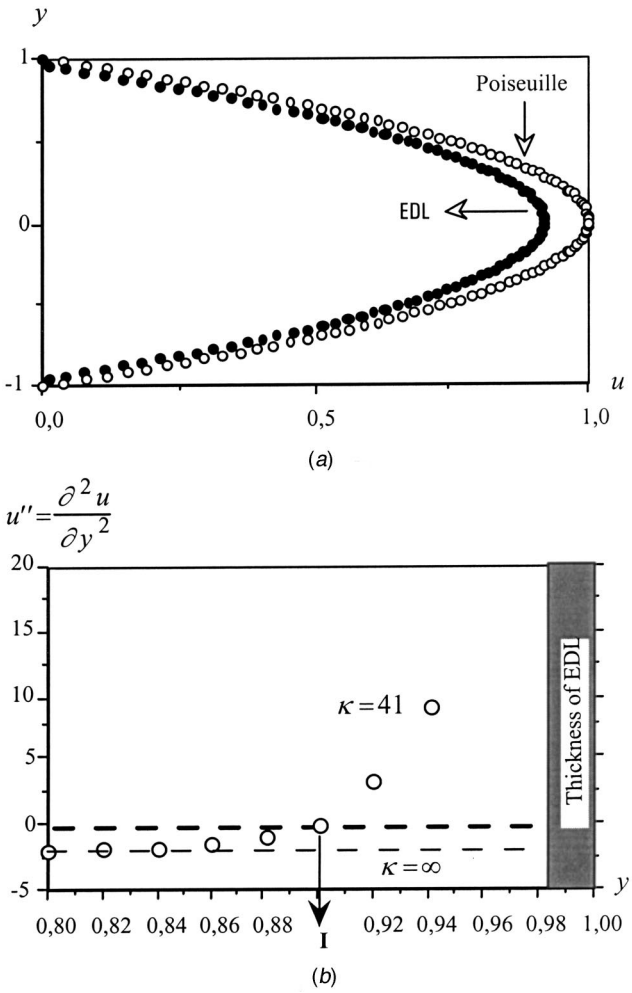

Fig. 1 EDL and Poiseuille velocity profiles (*a*), and the inflexional instability of Fjortoft type (*b*). The parameters of the EDL flow are given in the text. The broken line in (*b*) corresponds to Poiseuille flow with $\kappa=\infty$ and the circles to the $\kappa=41$ EDL flow. The inflexion point is shown by I. The inviscid instability is of Fjortoft type because after the inflexion point near the wall, $u''>0$ and the velocity is smaller than the velocity at the inflexion point u_I, resulting in $u''(u-u_I)<0$ in this zone.

EDL and Poiseuille flows centerline velocities. This makes the flow inviscidly unstable, according to the Fjortoft's criteria.

The linear hydrodynamic stability under the EDL effect is studied through classical methods. The Orr-Sommerfeld equation is solved by a Galerkin-like procedure [7]. The stream function is expanded in a Chebyshev polynomial series with up to 256 terms. The τ-method described by Orszag [8] is used. The disturbances with symmetric streamfunctions are considered only. The eigenvalues of the matrices were numerically computed by the QR algorithm. The method gave very close results to Grosch and Salwen [9] who used different sets of expansion functions.

Figure 2 shows the neutral curve corresponding to the microchannel-flow with the parameters given below, together with a "macro" Poiseuille flow (i.e. $\bar{\zeta}=0$ or $\kappa\to\infty$). It is clearly seen that the critical Reynolds number decreases by *a factor nearly equal to 2* under the effect of EDL: the critical wave and Reynolds numbers of the microflow are respectively $\alpha_c=1.10$ and $\mathrm{Re}_c=3190$ to be compared with $\alpha_c=1.02$ and $\mathrm{Re}_c=5772$ of the conventional Poiseuille flow. Due to its inviscid inflexional instability (unstable for $\mathrm{Re}\to\infty$ for a given α), the band of unstable wave numbers of the EDL-microflow is significantly larger compared with the Poiseuille-macroflow. The destabilizing EDL effect disappears quickly when the height of the channel is increased by a factor of 4 (400 μm) (triangle in Fig. 2 corresponding to $\kappa=163$). This goes in the same line as previous experimental results showing the lack of micro-effects for the microchannels of height larger than typically 100 μm. For smaller values of κ, in return, the effect of the interfacial effects caused by EDL on the transition may be much more severe. For instance, the critical Reynolds number decreases up to $\mathrm{Re}_c=1042$ for a channel with a 40 μm separation distance subject to the same conditions (the square in Fig. 2 with $\kappa=16$), and to a value as small as $\mathrm{Re}_c=496$ when $\kappa=8$. This effect, combined with the influence of the roughness that can be critical in microchannel flows, may be the explanation of significantly small transitional Reynolds numbers reported in some studies, and the decrease of Re_c with the decrease of channel size [3,4].

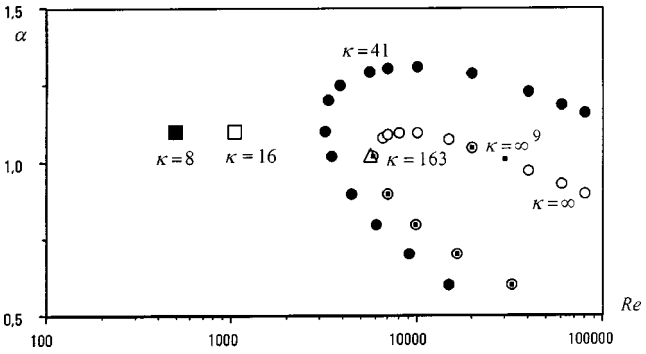

Fig. 2 Neutral curves of the EDL flow compared with the Poiseuille flow. The open circles correspond to Poiseuille flow with $\kappa=\infty$. The results of Grosh and Salwen [9] are shown by small bold squares. Bold circles correspond to $\kappa=41$, $G=12720$ and $\bar{\zeta}=2.1254$. The rest of the results are obtained by changing the microchannel height and keeping constant the rest of the parameters.

The second parameter that plays an important role in the stability mechanism under the EDL effect is $G\bar{\zeta}^2$ (Eq. 1). It is clear that EDL will play a negligible role as $G\bar{\zeta}^2\to 0$, that is, when the Zeta potential becomes very small. Yet, the inflexional instability effect is so strong that the critical Reynolds number is affected even when the electroviscous effects are negligibly small. Figure 3 shows the critical Reynolds number variation versus $G\bar{\zeta}^2$ for $\kappa=16$ and $\alpha=1.02$. It is seen that there is a decrease of 30% in Re_c already at $G\bar{\zeta}^2=100$. The EDL and macro-Poiseuille velocity profiles coincide almost perfectly at this low value of $G\bar{\zeta}^2$ (not shown here). The second striking feature of Fig. 3 is the rapid decrease of the critical Reynolds number as $G\bar{\zeta}^2$ increases, before reaching a plateau region at $G\bar{\zeta}^2\approx 10^4$.

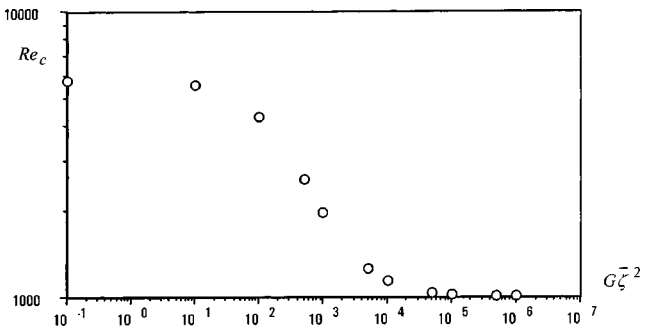

Fig. 3 The critical Reynolds number versus $G\bar{\zeta}^2$ for $\kappa=16$ and $\alpha=1.02$.

The macroscale Poiseuille flow is **metastable**; i.e., the corresponding stability is **subcritical**. Nonlinear analysis shows that the instability may occur with finite amplitude when all infinitesimal disturbances are stable [10]. There is a significantly lower critical value of the Reynolds number Re_G compared to Re_c, above which the flow is unstable and below which there is no bifurcation. The exact theoretical determination of Re_G is still a matter of research. Experiments show that $\mathrm{Re}_G/\mathrm{Re}_c \approx 1000/5772 \approx 1/6$. The transitional Reynolds number depends on the shape and shape factors of the channels.

The Poiseuille flow is monotonically stable only for $\mathrm{Re}<100$ to be compared with 5772. The lower limit of the transitional Reynolds number Re_t of channel flows is about 400 according to experiments and the growth rate of three-dimensional disturbances of linear secondary instability [11] (1100 based on the hydraulic diameter and channel averaged velocity). Thus, the ratio $\mathrm{Re}_t/\mathrm{Re}_c < \frac{1}{15}$ in macroscale Poiseuille flows.

The main non-linear stability mechanism in macro-Poiseuille flow is due to a secondary instability with the development of mean spanwise profiles inflexion with strong shear [12,13]. In the EDL flow there is already a streamwise inflexion point in the base flow. Thus, the Reynolds numbers Re_G and Re_t should be much lower under the EDL effect. A nonlinear analysis is necessary to check out this point but the first stage is then the determination of the marginal curve which is done here. The nonlinear saturation of the primary stability and formation of a secondary flow, together with the secondary instability processes have to be analyzed in EDL flow similarly to the Poiseuille macro-flow [11]. Some arguments on the reinforcing effect of the EDL on the subcritical nature of the macro Poiseuille flow may however already be given. The square of the amplitude of a finite disturbance is given by:

$$\frac{d|A_1^2|}{dt} = 2\alpha c_i |A_1|^2 + (k_1 + k_2 + k_3)|A_1|^4 \tag{3}$$

according to Stuart [14]. The flow reaches a subcritical equilibrium state when $k_1+k_2+k_3>0$. The coefficient k_1 represents the distortion of the mean motion: it is related to the eigenfunctions of the linear stability problem, and it is negative. The coefficient k_2 is linked to the generation of the harmonic of the fundamental and is also likely negative. The wall normal distortion of the fundamental (k_3) must ''be positive and outweigh the combined negative effect of k_1 and k_2 to reach a subcritical state'' [14]. Now, k_1 is proportional to $\mathrm{Re}_c\alpha_c^2$ (Eq. 6.3 of [14]). It has therefore a significantly smaller negative contribution to $k_1+k_2+k_3$ under the EDL effect. Furthermore, part of the terms involving in the coefficient k_3 is inversely proportional to Re_c according to the Eq. 6.5 of [14] and the EDL presumably reinforces the positive character of k_3 in the subcritical state.

The experimental verification of the linear stability results is difficult because of the subcritical character of the stability mechanism, and the difficult control of the level of turbulence at the inlet. That also rises the question of the EDL effect on the stability in the developing region. It is also somewhat difficult to reach such high Reynolds numbers in microchannels, even though one may consider the possibility of Debye lengths larger than 1 μm, thus higher channels compared with the numerical example given before. Well-controlled experiments are certainly more difficult in microchannels. Yet, it should be possible to detect the EDL effects on the transitional Reynolds number by classical Repressure gradient curves. Table 1 shows the expected transitional Reynolds numbers under the EDL effect as a function of κ. The ratio $\mathrm{Re}_t/\mathrm{Re}_c = 1/15$ is taken same as in macro channels, although, it is more than likely that $\mathrm{Re}_t/\mathrm{Re}_c$ is presumably smaller under the EDL effect according to the arguments given above. Table 1 also shows the Reynolds numbers achieved in some experiments. It is seen that the expected transitional Reynolds number is within the range of experimental possibilities. For larger channel of typical height 100 μm or so, the critical Reynolds number should also be measured, at least in principle. The experiments are limited to small Reynolds numbers for microchannels of height smaller than 20 μm, because very high pressure is then necessary and the channels will then break.

Table 1 Estimated values of the transitional numbers under the EDL effect compared with some experiments and the range of Re numbers that can be reached in microchannels. *1*: Mala and Li [15], microtubes, the transitional Re number of 150 (second line, last column) correspond to $D_h/2=65$ μm. *2*: Gao et al. [18], 2-D microchannels, *3*: Qu et al. [19], trapezoidal silicon microchannels. Profiles at $D_h/2$-71 μm (their Fig. 8) suggest a transitional number of 200. *4*: Wang and Peng [4] microchannels. This is a particularly low transitional Reynolds number. The exact value of $D_h/2$ is 150 μm. The value of κ is larger than 120 for other microchannels these authors investigated. Although their experiments have been conducted with distilled water (so that roughly $1/k=1\mu$m) the low transitional Reynolds numbers they report for higher channels cannot be explained by the EDL effect. Strong effect of roughness in the inlet region is suspected in these experiments.

Channel height, or $D_h/2$ (μm)	κ ($\frac{1}{k}=1\,\mu m$)	Critical Reynolds number (**Transitional Reynolds number, estimated**) $Re_{t\kappa=\infty}=400$	Re reached in some experiments reported in the literature (Exact $D_h/2$ values in μm)	Reynolds number in early transition reported in some investigations
100	41	3190 (**213**)	400[1] (102.5), 400[2] (100)	50 [4](see the text) 200[3]* (see the text)
40	16	1042 (**70**)	360[1] (50.5), 70[2] (53), 95[3] (33)	150[1]
20	8	496 (**33**)	250[1] (25), 23[3] (23.5)	56–170[1]

The last column of Table 1 shows transitional Reynolds numbers reported by some authors indicating early transition in microchannel liquid flows. All of these experiments have been conducted with DIUF-W but the channel wall material may be different from one experiment to the other. In lack of experimental details it is hard to give definitive conclusions. Yet, there is a satisfactory agreement between the estimated theoretical Re_t and the measurements, in particular with those of Mala and Li [15]. There is only one value reported by them on which we are sure, but unfortunately other details are not available. They, however, clearly indicated that ''there is an early transition from laminar to turbulent flow at $\mathrm{Re}_t \geqslant 56-168$'' and that ''the range of Re_t values varies somewhat, depending on the diameter and the material of the wall'' pointing at a plausible EDL effect. Note that these experiments have been conducted in micro tubes, and that the Poiseuille-Hagen flow is linearly stable. That does not matter for the qualitative comparisons made here, since the nonlinear character of the stability is similar in planar and cylindrical channels.

To conclude, the EDL destabilizes the linear modes of the Poiseuille channel flow and early transition in microchannels is plausible. This effect can be experimentally checked, provided that the liquid contains a very small amount of ions, the Zeta potential is high enough and the channel height is sufficiently small. In practice that would require the use of DIUF-W or organic liquids, and channel heights larger than 20 μm (but smaller than typically 100 μm) for feasibility problems (microchannel failure at high pressures). There is no effect on stability for liquids with high ionic concentration and/or mini channels. The nonlinear stability analysis of the EDL flow is necessary, although physical considerations indicate a much more rapid transition compared to macro flows. Direct Numerical Simulations can also be helpful to this end. Controlled experiments in a way similar to those reported by Ren et al. [5] have to be conducted, by keeping the same channel with the same roughness distribution, and changing the ionic concentration of the liquid. The fact that the channels cross-section shape, in particular the corners have important contribution to the EDL field have also to be considered (Yang et al., [16,17]). These results may imply important industrial applications, in particular in the control and manipulation of the heat transfer process in

microchannels. The complete parametrical study including the EDL effects on amplification and decay rates, and the eigenvalue spectrum is under investigation. The nonlinear stability analysis of EDL flow is also currently investigated.

References

[1] Gad-el-Hak, M., 1999, ''The Fluid Mechanics of Microdevices,'' J. Fluids Eng., **121**, pp. 5–33.

[2] Tardu, S., 2003, ''Transferts thermiques dans les microcanaux,'' *Traité EGEM*, Tome 6 Ch. 6, Microfluidique, 36p., Hermès.

[3] Peng, X. F., Peterson, G. P., and Wang, B. X., 1994, ''Heat Transfer Characteristics of Water Flowing through Microchannels,'' Exp. Heat Transfer, **7**, 265–283.

[4] Wang, B. X., and Peng, X. F., 1994, ''Experimental Investigation on Liquid Forced Convection Heat Transfer through Microchannels,'' Int. J. Heat Mass Transfer, **37**, 73–82.

[5] Ren, L., Qu, W., and Li, D., 2001, ''Interfacial Electrokinetic Effects on Liquid Flow in Microchannels,'' Int. J. Heat Mass Transfer, **44**, 3125–3134.

[6] Mala, G. M., Li, D., and Dale, J. D., 1997, ''Heat Transfer and Fluid Flow in Microchannels,'' Int. J. Heat Mass Transfer, **40**(13), 3079–3088.

[7] Von Kerczek, C. H., 1982, ''The Instability of Oscillatory Poiseuille Flow,'' J. Fluid Mech., **116**, 91–114.

[8] Orszag, S. A., 1971, ''Accurate Solution of Orr-Somerfeld Stability Equation,'' J. Fluid Mech., **50**, 689–703.

[9] Grosch, C. E., and Salwen, H., 1968, ''The Stability of Steady and Time-dependent Plane Poiseuille Flow,'' J. Fluid Mech., **34**, pp. 177–205.

[10] Drazin, P. G., and Reid, W. H., 1981, *Hydrodynamic Stability*, Cambridge University Press, Cambridge, UK, pp. 370–464.

[11] Orszag, S. A., and Patera, A. T., 1983, ''Secondary Instability of Wall-Bounded Shear Flows,'' J. Fluid Mech., **128**, pp. 347–385.

[12] Henningson, D. S., and Kim, J., 1991, ''On Turbulent Spots in Plane Poiseuille Flow,'' J. Fluid Mech., **228**, pp. 183–205.

[13] Itoh, N., 1974, ''Spatial Growth of Finite Wave Disturbances in Parallel and Nearly Parallel Flows. Part 1: The Theoretical Analysis and the Numerical Results for Plane Poiseuille Flow,'' Transactions of the Japan Society of Aeronautics and Space Sciences, **17**, 160–174.

[14] Stuart, J. T., 1960, ''On the Nonlinear Mechanics of Wave Disturbances in Stable and Unstable Parallel Flows. Part 1: The Basic Behavior in Plane Poiseuille Flow,'' J. Fluid Mech., **9**, 353–370.

[15] Mala, G. M., and Li, D., 1999, ''Flow Characteristics of Water in Microtubes,'' Int. J. Heat Fluid Flow, **20**, 142–148.

[16] Yang, C., and Li, D., 1997, ''Electrokinetic Effects on Pressure-driven Liquid Flows in Rectangular Microchannels,'' J. Colloid Interface Sci., **194**, 95–107.

[17] Yang, C., and Li, D., 1998, ''Analysis of Electrokinetic Effects on the Liquid Flow in Rectangular Microchannels,'' Colloids Surf., **143**, 339–353.

[18] Gao, P., Le Person, S., and Favre Marinet, M., 2002, ''Scale effects on Hydrodynamics and Heat Transfer in Two-Dimensional Mini and Microchannels,'' Int. J. Therm. Sci., **41**, p. 10.

[19] Qu, W., Mala, G. M., Li, D., 2000, ''Pressure-driven Water Flows in Trapezoidal Silicon Microchannels,'' Int. J. Heat Mass Transfer, **43**, 353–364.

Low-Reynolds Number Turbulence Models: An Approach for Reducing Mesh Sensitivity

Jonas Bredberg
Volvo Aero Corporation,
Engines Division
SE-461 81 Trollhättan, Sweden
e-mail: jonas.bredberg@volvo.com

Lars Davidson
Chalmers University of Technology
Department of Thermo and Fluid Dynamics
SE-412 96 Gothenburg, Sweden

This study presents a new near-wall treatment for low-Reynolds number (LRN) turbulence models that maintains accuracy in 'coarse' mesh predictions. The method is based on a thorough examination of approximations made when integrating the discretized equations in the near-wall region. A number of modifications are proposed that counteract errors introduced when an LRN-model is used on meshes for which the first interior node is located at $y^+ \approx 5$. Here the methodology is applied to the $k-\omega$ turbulence model by Bredberg et al. [1], although similar corrections are relevant for all LRN models. The modified model gives asymptotically, in the sense of mesh refinement, identical results to the baseline model. For coarser meshes ($y^+ \leqslant 10$), the present method improves numerical stability with less mesh-dependency than the non-modified model. Results are included for fully developed channel flow, a backward-facing step flow and heat transfer in a periodic rib-roughened channel. [DOI: 10.1115/1.1638791]

1 Introduction

With respect to computing the near-wall behavior of complex turbulent flow, two different methods are commonly employed in computational fluid dynamics codes. These are referred to as the integrated method and the wall function method. Using the former type necessitates a low-Reynolds number (LRN) turbulence model in which modifications are made to account for the viscous effects found in the wall vicinity (viscous sub-layer). LRN-models require that the near-wall region is resolved using a sufficient number of computational cells to capture the strong gradients usually found there. The end result is enhanced predictions, especially for near-wall sensitive parameters such as the Nusselt number and skin friction. The computational efforts are however substantially higher than when using the alternative wall function approach. With the latter strategy, high-Reynolds number (HRN) turbulence models are employed that utilize algebraic functions to bridge the near-wall region, that substantially relax the mesh requirements.

Wall functions (Patankar and Spalding [2]) are derived assuming that a Couette flow prevails, i.e. that the variation of the dependent parameters with respect to the streamwise direction can be neglected. For impermeable walls the flow equations can be solved analytically to yield the well-known, law-of-the-walls:

$$U^+ = \frac{1}{\kappa}\ln(y^+) + B \tag{1}$$

$$T^+ = \frac{\mathrm{Pr}_t}{\kappa}\ln(y^+) + B_T \tag{2}$$

Similar wall functions can be derived for turbulence quantities (Wilcox [3]). Employing these equations permits us to simplify the near-wall treatment to an one-dimensional analysis for which the solution of the dependent variables is only a function of the normalized wall-distance. Naturally such a simplification reduces the computational storage and time, through a reduction of the number of nodes, in addition the convergence rate is increased as a result of the simplified equations.

The universality of these wall functions is however limited, as they are derived from simplified governing equations. Their use has also frequently been questioned (Launder [4]). In spite of their lack of physics, they have often out of necessity been employed and have in many cases performed admirably. It should also be emphasized that in many cases of industrial relevance the use of wall functions is the only affordable method.

A simple and yet effective improvement for the wall function is to substitute the usage of the friction velocity, u_τ, with $C_\mu^{1/4}\sqrt{k}$ in the scaling for the velocity log-law. In flows that involve recirculation, for which u_τ is unsuitable as a velocity scale, the improvement is significant. In addition, Launder and Spalding [5] (LS) suggested that the turbulent kinetic energy should to be solved in the first interior node, rather than being a priori set using a wall function. The latter is especially important as k varies considerably in the near-wall region, hence the cell-averaged values (as given in a finite volume method) is difficult to specify in a universal manner.

In an attempt to improve the initial assumption of a constant shear-stress and a linear length-scale variation across the first interior cell, Chieng and Launder [6] (CL) extended the wall function treatment to a zonal approach. Their method assumes that the near-wall region can be divided into two layers, for which the sublayer thickness ($y^+ \approx 11$) acts as a partition line. Johnson and Launder [7] (JL), and also Ciofalo and Collins [8], further improved the model by making the viscous sub-layer thickness dependent on local turbulence levels. The zonal idea was taken further by Amano and his colleagues [9,10]. In addition to solving the k-equation Amano et al. also included cell-averaged generation and destruction terms in the ε-equation. In their 1983 paper [9], the treatment was extended to a three-layer model, where the first interior cell was divided into three regions: the viscous sublayer, the buffer layer and the fully turbulent layer, in which k, ε and $\rho\overline{uv}$ had their respective variations.

Acharya et al. [11] evaluated the three models proposed by Launder et al. (LS, CL, JL) for a surface mounted rib case and found only marginal differences between the LS and the CL models, both yielding an underestimation of the heat transfer. The Johnson-Launder modification improved the predictions in the recirculating zone but resulted in an overestimation of the heat transfer in the downstream region. Heyerichs and Pollard [12] compared the LS, CL and the two-layer Amano model for the same BFS-case with good agreement in the predicted Stanton number. Despite the documented improvements made through the various refinements, the LS model is still the standard wall function for commercial CFD-codes. It should be noted that it is nu-

Contributed by the Fluids Engineering Division for publication in the JOURNAL OF FLUIDS ENGINEERING. Manuscript received by the Fluids Engineering Division March 13, 2002; revised manuscript received September 11, 2003. Associate Editor. I. Celik.

merically awkward to implement the most elaborated zonal-schemes, and the authors have reported problems with numerical stability for nontrivial flows using these models (Bredberg [13].)

An alternative to the wall function approach is to solve for a parabolic equation in the near-wall region (Launder [4]). In the mid-1980s researchers at UMIST developed the parabolic sub-layer (PSL) scheme (Iacovides and Launder [14]). PSL assumes a constant static pressure across the wall affected region where the pressure-velocity coupling is neglected and the wall normal velocity is given from continuity. While such a scheme is computationally more expensive than a wall function approach, it is still significantly cheaper than LRN-models. For complex situations, such as the simulation of a U-bend (Choi et al. [15]) it was, however found that the PSL approximation introduced serious errors.

A third methodology for reducing computational requirements, can loosely be denoted as an enhanced representation of the dependent variables through analytical integration of the near-wall region. This may be done at two levels: 1) integration of the individual terms or 2) integrated solution of the differential equations. The former route is used for the zonal models, in which a cell-averaged, i.e., an integrated value, is required in the specification of the source and sink terms in the solved turbulence equations. The analytic solution, via integration of the differential equations, was experimented with in the beginning of CFD (Spalding [16], Wolfshtein [17]). The complexity of the equation system however necessitates that severe simplification being made for the successful conclusion of such a project. The law-of-the-wall may be given as an example. Only recently have there been attempts to incorporate a more advanced scheme in which convective terms are included in the analysis (Craft et al. [18,19]). The route embarked upon here is however to improve the analytic integration of the individual terms in the transport equations.

In a previous investigation the authors devised a model based on the Chieng-Launder zonal approach, however applied to the Wilcox [20] standard $k-\omega$ model (Bredberg et al. [21]) (BPD). Although there are similarities between the BPD model and the CL model, a significant difference is the treatment of the generation and dissipation terms for the *k*-equation. In the BPD model the integration of each term is done separately in the viscous sub-layer and the fully turbulent region. The two volume-averaged values are then blended together using an exponential function that ensures that an LRN-model is obtained in the limit of a fine mesh while wall functions are retrieved for a coarse mesh. A complete discussion and analysis of the model is found in Bredberg [22]. Although the model predicted heat transfer with reasonable accuracy, the aim of a mesh insensitive model was not fulfilled.

In finite-volume method codes the evaluated source terms in the transport equations represent the volume average of a cell. In cases when the source terms are composed of non-linear variables, the simplified assumption that the cell-centered value is equal to the volume-weighted average of the cell could lead to large discrepancies in the predicted results. Rautaheimo and Siikonen [23] however showed significant improvements in the predicted skin friction for cells with the node location of $5 \leqslant y^+ \leqslant 10$, through studying higher order differencing schemes and the near-wall variation of the dependent variables. The method is based on a flux-correction scheme which was also adopted by Grotjans and Menter [24]. By shifting the computational domain, the boundary condition is applied at the edge of the viscous sub-layer, and the effect of the near-wall region is modelled using modified wall fluxes. They showed a significant improvement in grid-independence as compared with standard wall functions.

Using a slightly different approach the present study investigate the effects of numerical approximations made to the volume-averaged terms when coarsening the mesh. On the basis of simplified flow equations, functions for the near-wall variations of the turbulent quantities and velocity are established. In cases in which these functions depend only on the wall normal distance, it is shown that the source terms in the transport equations can be analytically integrated. To diminish the sensitivity to the location of the near-wall node, some empirical corrections are applied to these terms. The DNS database for channel flow, Reynolds number of 13,750, is used for validation and numerical optimization of the integrating functions. Considering previous studies (Bredberg et al. [21], and Rautaheimo and Siikonen [23]), the range of applicability for the present model is limited to the viscous sub-layer and the lower part of the buffer layer, $y^+ \leqslant 10$.

Predictions are included for a higher Reynolds number case, a backward-facing step flow and a rib-roughened channel flow, where the new model produces very good results as compared with DNS-data and measurements. The inclusion of the near-wall treatment shows improved mesh independence with little sensitivity to the first near-wall node location. Compared to models based on wall functions the present method still requires a finer mesh. However, the number of nodes may be significantly decreased compared to an LRN approach. The nodes employed within the viscous sub-layer can be reduced from (7–10), as recommended by Wilcox [3], to only one through the use of these analytically derived modifications.

2 Model Formulation

2.1 Flow Equations. The governing equations for an incompressible flow are the continuity equation, the momentum equations and the temperature equation. These are respectively:

$$\frac{\partial U_i}{\partial x_i} = 0 \tag{3}$$

$$\frac{DU_i}{D\tau} = -\frac{\partial P}{\partial x_i} + \frac{\partial}{\partial x_j}\left(\mu \frac{\partial U_i}{\partial x_j} - \rho\overline{u_i u_j}\right) \tag{4}$$

$$\frac{DT}{D\tau} = \frac{\partial}{\partial x_i}\left(\frac{\mu}{\mathrm{Pr}}\frac{\partial T}{\partial x_i} - \rho\overline{u_i t}\right) \tag{5}$$

This equation system is not closed due to the Reynolds stress tensor, $\overline{u_i u_j}$, in the momentum equations and the heat flux vector, $\overline{u_i t}$, in the temperature equation. Employing an eddy-viscosity model (EVM), the Reynolds stress tensor is modelled through the Boussinesq hypothesis:

$$-\overline{u_i u_j} = \nu_t\left(\frac{\partial U_i}{\partial x_j} + \frac{\partial U_j}{\partial x_i}\right) - \frac{2}{3}k\,\delta_{ij} \tag{6}$$

where the eddy-viscosity is described using a turbulence model. The turbulent heat-flux vector is modelled as

$$-\overline{u_i t} = \frac{\nu_t}{\mathrm{Pr}_t}\frac{\partial T}{\partial x_i} \tag{7}$$

where the turbulent Prandtl number, Pr_t, can either be set as a constant, or as a function on some flow quantity, see e.g. Kays [25]. For the predictions in this paper, $\mathrm{Pr}_t = 0.9$.

For fully developed channel flow, the Reynolds-averaged streamwise momentum equation and temperature equation can be simplified to (Tennekes and Lumley [26]):

$$\tau_w\left(1 - \frac{y}{h}\right) = (\mu + \mu_t)\frac{dU}{dy} \tag{8}$$

$$q_w = C_p\left(\frac{\mu}{\mathrm{Pr}} + \frac{\mu_t}{\mathrm{Pr}_t}\right)\frac{dT}{dy} \tag{9}$$

Neglecting the molecular viscosity, assuming an eddy-viscosity variation of $\nu_t = u_\tau \kappa y$, and with the definition of the friction velocity, $u_\tau \equiv \sqrt{\tau_w/\rho}$, the law-of-the-wall, Eqs. (1) and (2) are obtained, see e.g. Bredberg [22].

If instead the eddy-viscosity is set to zero, as in the limit of the wall, these equations (Eqs. (8) and (9)) reduce to the definitions of the wall-shear and heat-flux as:

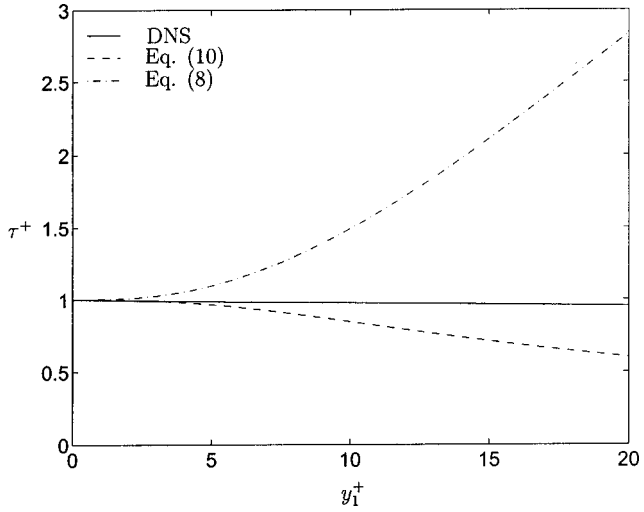

Fig. 1 Total wall shear stress, evaluated at y_1^+. y^+-value of cell center along abscissa. DNS-data [28], fully developed channel flow at Re_τ=395.

$$\tau_w \equiv \mu \left.\frac{dU}{dy}\right|_{y=0} \tag{10}$$

$$q_w \equiv \frac{\mu C_p}{\mathrm{Pr}} \left.\frac{dT}{dy}\right|_{y=0} \tag{11}$$

The above definitions are used for computing relevant wall parameters when the first node is located within the viscous sublayer ($y^+ \leqslant 5$).

Employing LRN-models with no-slip conditions at the wall, the discretized equations will predict a linear relation for the velocity and temperature profiles at the first interior node. In situations when the first node is located outside the viscous sub-layer, for which the linear law is no longer valid, CFD-codes will underestimate the velocity and temperature gradients at the wall, and, through the usage of Eqs. (10) and (11) also the shear stress and heat flux.

It is here investigated whether the use of Eqs. (8) and (9) may possibly improve the results when applied to coarse mesh computations. The shear stress and the wall normal heat flux are constant, as long as the advective terms are negligible. Thus if localized values are employed, it is equally valid to use e.g. Eq. (8) as it is to use Eq. (10).

Figure 1 compares the estimated wall shear stress using DNS-data for fully developed channel flow, via Eqs. (8) and (10). It can clearly be seen in the figure that neither of the two formulations is accurate beyond $y^+ \geqslant 5$, with the standard procedure (10) being the preferable one. The laminar relation is thus used throughout the paper, with the wall shear stress calculated as: $\tau_w = \tau = \mu U_1 / y_1$.

For the temperature equation, Eq. (9) is used however, as a slight improvement in the predicted Nusselt number for coarser meshes can be noted, (see Fig. 10). No degeneration is apparent for refined meshes as the eddy-viscosity is negligible at the first node.

2.2 Turbulence Equations. The above discussion is of importance in estimating the correct wall shear stress and wall heat flux. The flow equations do however not include any volume averaged source or sink terms, whereas the generation and destruction terms in the turbulence equations do. The standard method is to use the cell-centered value multiplied with the cell-volume to represent the integrated quantities. This praxis fails for a coarse meshes if the quantities involved do not behave in an orderly fashion, that is with no or linear variation. Using the results of Hanjalic and Launder [27], it is possible to derive the near-wall dependency of the important variables as:

$$U \sim y^1, \quad \mu_t \sim y^3, \quad k \sim y^2, \quad \varepsilon \sim y^0, \quad \omega \sim y^{-2} \tag{12}$$

Thus terms involving the eddy-viscosity, μ_t, the turbulent kinetic energy, k, or the specific dissipation rate, ω, may be inaccurate unless the variation are resolved on a fine mesh, as is done with an LRN-model. The integration of the production and dissipation term in the turbulence kinetic energy equation gives, using Eq. (12):

$$\int_0^{\Delta V} P_k dV = \Delta x \Delta z \int_0^{\Delta y} \mu_t \left(\frac{dU}{dy}\right)^2 dy = \left\{ \begin{matrix} \mu_t = C_1 y^3 \\ dU/dy = C_2 y^0 \end{matrix} \right\}$$
$$= \Delta x \Delta z \int_0^{\Delta y} C_1 y^3 (C_2)^2 dy = C_1 C_2^2 \frac{(\Delta y)^3}{4} \Delta V \tag{13}$$

$$\int_0^{\Delta V} \varepsilon dV = \Delta x \Delta z \int_0^{\Delta y} \varepsilon dy = \{\varepsilon = C_3 y^0\} = C_3 \Delta V \tag{14}$$

The assumed relations for the velocity and eddy-viscosity are a fair approximation, however less so for the dissipation rate. Data of Moser et al. [28] indicate that the boundary condition for ε depends on the Reynolds number, and that the constant relation is valid only in a very thin layer close to the wall (Mansour et al. [29]). An alternative to ε as the length-scale determining equation is the specific dissipation rate, ω. For ω_w^+ and ε_w^+ we can write:

$$\omega_w^+ \equiv \omega_w \frac{\nu}{u_\tau^2} \overset{!}{=} \frac{6\nu}{C_k y^2} \frac{\nu}{u_\tau^2} = \frac{6}{C_k y^{+2}} \tag{15}$$

$$\varepsilon_w^+ \equiv \varepsilon_w \frac{\nu}{u_\tau^4} \overset{!}{=} 2\nu \frac{k}{y^2} \frac{\nu}{u_\tau^4} = 2 \frac{k^+}{y^{+2}} \tag{16}$$

where the identities, $(\overset{!}{=})$, assume common approximations made in CFD-codes. An alternative to Eq. (15) is used in the newly developed $k-\omega$ model by Bredberg et al. [1]. The boundary condition for ε, in contrast to ω, is coupled to the k-equation, which may be of concern in coarse mesh simulations where a high degree of accuracy for the first node is not guaranteed. Hanjalic [30] also noted that, although both k^+ and ε^+ are Reynolds number dependent, their ratio (i.e., ω^+) is less flow dependent. Consequently, we believe that improved numerical stability can be achieved through the use of ω as the length-scale determining equation. Previous studies (Huang and Bradshaw [31]) have also showed that the $k-\omega$ model is preferable to the $k-\varepsilon$ model in wall-bounded turbulent flows. On the grounds of this it was decided to adopt the present treatment to the $k-\omega$ model of Bredberg et al. [1]. Using a $k-\omega$ model, the destruction term is modelled as $\varepsilon = C_k k \omega$, with the integration as:

$$\int_0^{\Delta V} C_k k \omega dV = \Delta x \Delta z \int_0^{\Delta y} C_k k \omega dy = \left\{ \begin{matrix} k = C_4 y^2 \\ \omega = C_5 y^{-2} \end{matrix} \right\} = C_k C_4 C_5 \Delta V \tag{17}$$

The exact integrations (Eqs. 13 and 17) should be compared with the numerical approximation using cell-centered values (ϕ_p) in a CFD-code:

$$\overline{P_k} \Delta V \approx \mu_p \left(\frac{U_p}{y_p}\right)^2 \Delta V = C_1 \left(\frac{\Delta y}{2}\right)^3 (C_2)^2 \Delta V = C_1 C_2^2 \frac{(\Delta y)^3}{8} \Delta V \tag{18}$$

$$\overline{\varepsilon} \Delta V \approx C_k k_p \omega_p \Delta V = C_k C_4 \left(\frac{\Delta y}{2}\right)^2 C_5 \left(\frac{2}{\Delta y}\right)^2 \Delta V = C_k C_4 C_5 \Delta V \tag{19}$$

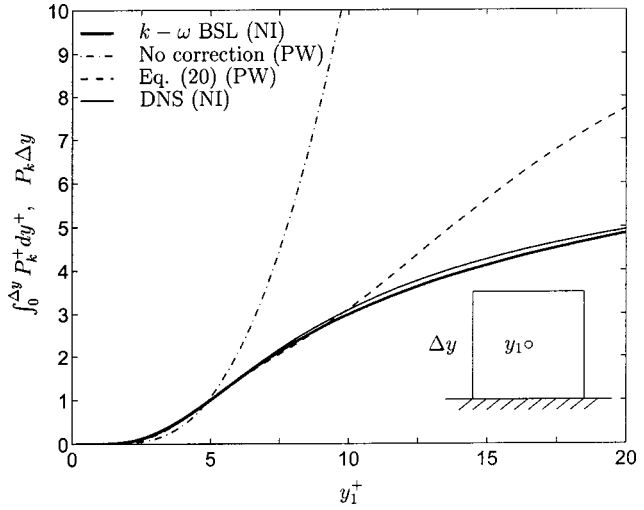

Fig. 2 Averaged production in first near-wall computational cell. Numerical integration (NI) versus point-wise (PW) evaluation (using node value). y^+-value of cell center along abscissa. DNS-data [28] and $k-\omega$ BSL model [1], fully developed channel flow at $Re_\tau=395$.

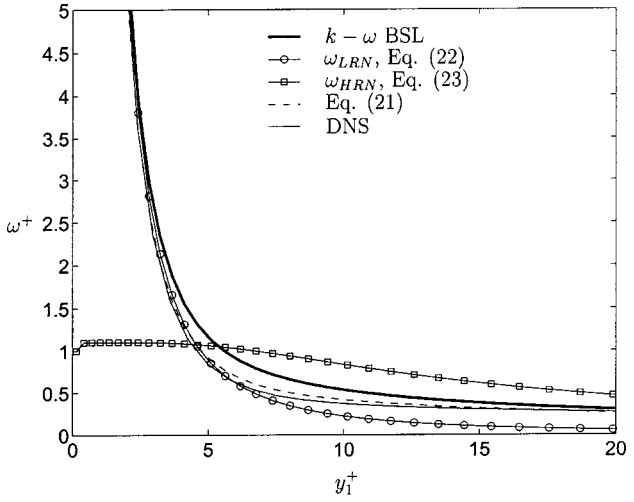

Fig. 3 ω in first near-wall computational cell. y^+-value of cell center along abscissa. DNS-data [28] and $k-\omega$ BSL model [1], fully developed channel flow at $Re_\tau=395$.

In the case of the production term, the finite-volume code underestimates the volume integral by a factor of two as a result of using cell-centered values. The present study includes this factor in the numerical scheme. To extend the accuracy of the model to regions in which the near-wall relation (Eq. 12) fails, an empirical damping function is added to the production term. A similar numerical optimization was attempted for the dissipation term, but improvements were restricted to the channel flow. Thus the only modification made to the *k*-equation is given as:

$$P_k^{mod}=\frac{2}{1+0.9R_t}P_k^{std} \tag{20}$$

where $R_t=k/(\nu\omega)$ is the turbulent Reynolds number. The accuracy of this model is evaluated for fully developed channel flow. The numerically integrated production term on a refined (LRN) mesh is compared in Fig. 2 with cell-centered, point-wise values on coarse meshes. The importance of the additional factor on a $y_1^+ \geqslant 5$ mesh is evident. The standard method ($\overline{P_k}=\mu_{t,1}(U_1/y_1)^2$) overestimates the production outside the viscous sub-layer and will commonly result in non-convergent solutions if used on a $y_1^+ \approx 10$ mesh.

Using a $k-\omega$ model, the ω-equation is not solved for the first near-wall node and hence the above manipulation is not applicable. To improve coarse mesh predictions, a route similar to that one used in Bredberg et al. [21] is adopted. The wall value of ω is set by combining a low-Reynolds number (LRN) and a wall function (HRN) approach:

$$\omega_w=f\omega_{LRN}+(1-f)\omega_{HRN} \tag{21}$$

where ω_{LRN} and ω_{HRN} are the solutions to the ω-equation, Eq. (25), in the viscous sub-layer and fully turbulent regime, respectively:

$$\omega_{LRN}=\frac{2\nu}{C_k y^2} \tag{22}$$

$$\omega_{HRN}=\frac{u_\tau}{\sqrt{C_k}\kappa y} \tag{23}$$

Following Launder and Spalding [5], the friction velocity, u_τ, is substituted by $\sqrt{k}C_k^{1/4}$. The smoothing function, *f*, is numerically optimized to $f=\exp(-y^*/17)$, where $y^*=u_\varepsilon y/\nu$ is the non-dimensional wall distance, using the Kolmogorov velocity scale, $u_\varepsilon=(\varepsilon\nu)^{1/4}$, as suggested by Abe et al. [32]. A comparison with DNS-data on the proposed model for the near-wall specific dissipation rate is given in Fig. 3. Note that the above modifications are applied only to the first interior node, substituting procedures used for wall function based models. The additional implementation complexity is marginal, as most codes already include special routines for walls, eg. in the specification of ω_w. It should be noted that the assumed near-wall variations in Eq. (12) are strictly valid only in the viscous sub-layer, and thus the use of the current model when the first node is located in the logarithmic layer is strongly discouraged.

2.3 The Baseline Turbulence Model. The new boundary treatment is applicable to any turbulence model. However, when mated with a $k-\omega$, there is a numerical advantage in the specification of the secondary turbulence quantity, as discussed above. In this paper, the $k-\omega$ turbulence model by Bredberg et al. [1] is used. The model was developed in the following form:

$$\frac{Dk}{Dt}=P_k-C_k k\omega+\frac{\partial}{\partial x_j}\left[\left(\nu+\frac{\nu_t}{\sigma_k}\right)\frac{\partial k}{\partial x_j}\right] \tag{24}$$

$$\frac{D\omega}{Dt}=C_{\omega 1}\frac{\omega}{k}P_k-C_{\omega 2}\omega^2+C_\omega\left(\frac{\nu}{k}+\frac{\nu_t}{k}\right)\frac{\partial k}{\partial x_j}\frac{\partial \omega}{\partial x_j}+\frac{\partial}{\partial x_j}\left[\left(\nu+\frac{\nu_t}{\sigma_\omega}\right)\frac{\partial \omega}{\partial x_j}\right] \tag{25}$$

with the turbulent viscosity given by:

$$\nu_t=C_\mu f_\mu\frac{k}{\omega}$$

$$f_\mu=0.09+\left(0.91+\frac{1}{R_t^3}\right)\left[1-\exp\left\{-\left(\frac{R_t}{25}\right)^{2.75}\right\}\right] \tag{26}$$

R_t is the turbulent Reynolds number defined as $R_t=k/(\omega\nu)$. The constants in the model are given as:

$$C_k=0.09,\quad C_\mu=1,\quad C_\omega=1.1,\quad C_{\omega 1}=0.49,$$
$$C_{\omega 2}=0.072,\quad \sigma_k=1,\quad \sigma_\omega=1.8$$

3 Results and Discussion

The new near-wall treatment is evaluated for four different test cases: fully developed turbulent channel flow at $Re_\tau=395$ (Moser

Table 1 Predicted skin friction, friction-velocity and y_1^+ using different number of cell (N). DNS-data [28] and $k-\omega$ BSL model [1] fully developed channel flow at $Re_\tau=395$.

Mesh	DNS	$k-\omega$ BSL	$N=100$	$N=50$	$N=50$	$N=20$
y_1^+	0.03	0.14	0.14	1.0	4.0	10.0
u_τ/U_B	0.0575	0.0573	0.0573	0.0569	0.058	0.0582
$1000\times C_f$	6.61	6.57	6.57	6.48	6.73	6.77

et al. [28]), and at $Re_H=250,000$, the backward-facing step (BFS) flow, $Re_h=5100$ (Le et al. [33]), and a rib-roughened channel flow, $Re_H=30{,}000$ (Rau et al. [34]).

The modifications were implemented in the incompressible finite-volume method code CALC-BFC (Davidson and Farhanieh [35]). The code employs a second-order bounded differencing scheme (van Leer [36]) for the convective derivates and second-order central differencing scheme for the other terms. The SIMPLE-C algorithm is used to deal with the velocity-pressure coupling. CALC-BFC uses Boundary-Fitted-Coordinates, on a non-staggered grid with the Rhie-Chow [37] interpolation to smooth nonphysical oscillations. In order to improve the diagonal domination in the TDMA solver, the cross-diffusion terms (in the ω-equation) are added to the left-hand side if they are negative and to the right-hand side otherwise. For the fully developed channel flows and the rib-roughened channel flow, periodic boundary conditions were used for the inlet and outlet sections. All variables were prescribed in the inlet for the backward-facing step flow, while the Neumann condition was used at the outlet. A no-slip condition was used on the walls, $U_i=0, k=0$. The boundary condition for ω was set using the relation in Eq. (21).

The objective of the present study is to validate the new boundary condition's insensitiveness to the location of the first interior node through a comprehensive mesh study. The performance of the baseline model, i.e., the asymptotic result using the present method, and comparisons with contemporary turbulence models are discussed in Bredberg et al. [1].

3.1 Fully Developed Channel Flow, $Re_\tau=395$. The model was validated using DNS-data (Kim, 1988, unpublished work, also Moser et al. [28]) for a fully developed turbulent channel flow with $Re_\tau=395$. It is attractive to include this test-case in spite of its simplicity, since the important wall effects are present in the flow. Only half of the channel needs to be simulated, with symmetry conditions applied along the centerline of the channel. The number of nodes in the wall-normal direction range from $N=20$ (uniformly distributed) to a near-wall clustered 100-node mesh. The location of the first interior node is given in Table 1. Both the streamwise velocity, Fig. 4, and the turbulent kinetic energy, Fig. 5, are normalized using the friction velocity, u_τ, which is also found in Table 1. DNS-data give $u_\tau/U_B=0.0575$, which is excellently reproduced by the baseline model. The deviation in u_τ/U_B using the new wall treatment is zero for the refined mesh and small for coarser meshes, as indicated by the table. The skin friction, C_f, is calculated as $C_f=2\tau_w/\rho U_B^2=2(u_\tau/U_B)^2$.

The normalized streamwise velocity, $U^+=U/u_\tau$, is shown in Fig. 4, while the normalized turbulent kinetic energy, $k^+=k/u_\tau^2$, is found in Fig. 5. The figures includes both DNS data and the results of the non-modified $k-\omega$ turbulence model (Bredberg et al. [1]). The predicted results using the near-wall modification are shown as the deviation as compared with the non-modified model and listed as a percentage, $(\phi-\phi_{ref})/\phi_{ref}$, on the right-hand side of the figures. For both parameters the discrepancies with a low-Reynolds number mesh are negligible.

The velocity profile is severely overestimated for the mesh with a $y_1^+=10$. This can however be explained as a direct consequence of the definitions of y^+ and U^+ and the relation used for the wall shear stress, Eq. (10). This equation will inherently predict a linear-law for the velocity, regardless of the first node location, as:

$$y_1^+\equiv\frac{y_1u_\tau}{\nu}=\{\text{Eq. (10)}\}=\frac{y_1\sqrt{\tau_w/\rho}}{\nu}=\frac{y_1\sqrt{\nu U_1/y_1}}{\nu}=\sqrt{\frac{y_1U_1}{\nu}} \tag{27}$$

$$U_1^+\equiv\frac{U_1}{u_\tau}=\{\text{Eq. (10)}\}=\frac{U_1}{\sqrt{\tau_w/\rho}}=\frac{U_1}{\sqrt{\nu U_1/y_1}}=\sqrt{\frac{y_1U_1}{\nu}}$$

The deviation for $y_1^+=10$ is 20%, which must be considered when constructing models that assume a linear relation for the velocity profile, via Eq. (10). The work by George [38] suggests alternatives to this simplified idea.

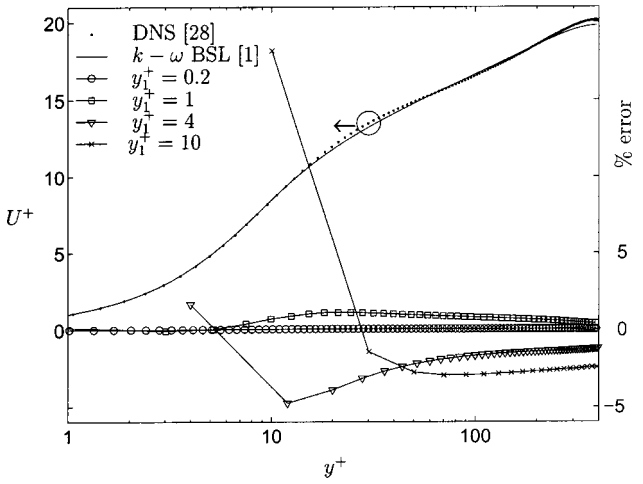

Fig. 4 Fully developed channel flow at $Re_\tau=395$. Velocity profile (left) and error $(U^+-U^+_{ref})/U^+_{ref}$ (right).

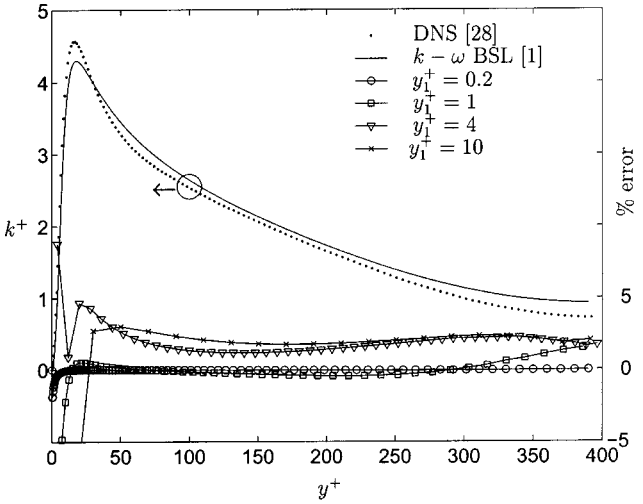

Fig. 5 Fully developed channel flow at $Re_\tau=395$. Turbulent kinetic energy profile (left) and error $(k^+-k^+_{ref})/k^+_{ref}$ (right).

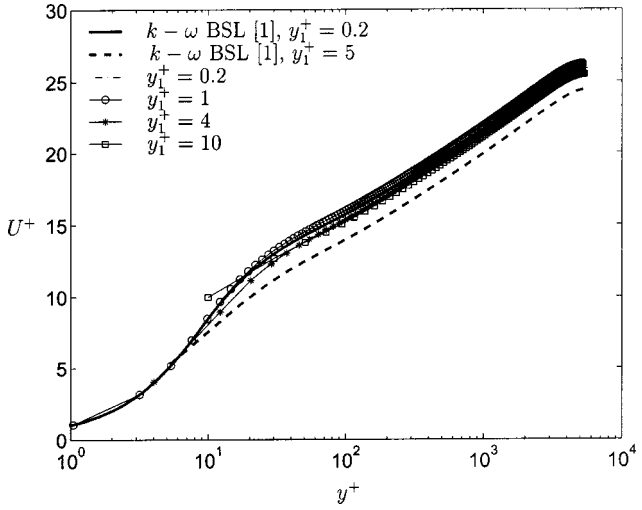

Fig. 6 Fully developed channel flow at Re_H=250, 000. Velocity profile.

3.2 Fully Developed Channel Flow, Re_H=250,000. For industry application it is of interest to validate the performance of the modification at a substantial higher Reynolds number. In Fig. 6 the predicted velocity profile on different mesh refinement with the baseline $k-\omega$ model is compared with the near-wall modified $k-\omega$ model as given in the previous section is shown. Using the baseline model no converged solution was achievable for meshes with a first node location at $y_1^+ > 5$. Modifying the near-wall treatment, as proposed here, greatly improve the stability and also accuracy when coarsing the mesh.

3.3 Backward-Facing Step. For a backward-facing step (BFS) case, the flow undergoes separation, recirculation and reattachment followed by a redeveloping boundary layer. In addition, this case involves a shear-layer mixing process, and an adverse pressure gradient. The BFS is thus an attractive flow for evaluations of turbulence models.

The case used here is the one studied by Le et al. [33] using DNS. In the present computation the inflow condition is specified using DNS data at $x/h=-10$. The Neumann condition was applied for all variables at the outlet located at $x/h=30$. The overall calculation domain ranges from $x/h=-10$ to $x/h=30$, with the step located at $x=0$. The channel height is $5h$ in the inlet section and $6h$ after the step, yielding an expansion ratio of 1.2, see Fig. 7.

Due to the relatively low Reynolds number, Re_h=5100, a fair mesh comparison is difficult to make as the number of nodes spanning the step will be too few to resolve even the larger flow structures when coarse meshes are employed. Thus the meshes used in the present computations, presented in Table 2, all have a significant number of nodes, especially in the streamwise direction. The computation made using the 200×180 mesh (streamwise by wall normal) with a first interior node at $y^+=0.2$ can be considered as a mesh independent solution.

Table 2 Re-attachment point, BFS-case. Present model compared with DNS-data [33] and $k-\omega$ BSL model [1].

Mesh	DNS	$k-\omega$ BSL	200×180	100×90	100×70	100×30
y_1^+	0.1	0.22	0.21	1.1	3.9	10.0
x_r/h	6.28	6.34	6.32	6.25	5.90	4.68

The computed skin friction coefficient, $C_f=2\tau_w/\rho U_\infty^2$, using the different meshes are shown in Fig. 8. Included in the figure are the results of the baseline $k-\omega$ turbulence model (Bredberg et al. [1]) and DNS-data. The computed C_f with the modified near-wall treatment gives only a marginal difference for the two most refined meshes (200×180 and 100×90). Coarsening the mesh further to a first node location at $y^+=4$ gives a small deviation in the predicted C_f and a slight re-location of the reattachment point. The result with the 100×30 mesh gives a substantially smaller recirculation zone. One of the commonly used quantities to justify the accuracy of a turbulence model in a BFS-case is the reattachment length of the main separation. The present model gives results close to those of the DNS data, $x_r/h=6.28$, for all meshes apart from the $y_1^+=10$ mesh, see Table 2.

3.4 Rib-Roughened Channel. The heat transfer performance of the present method is evaluated in the rib-roughened case of Rau et al. [34], see Fig. 9. The Reynolds number, based on the mean velocity and the channel height, H, is Re_H=30,000. A constant heat flux boundary condition was applied at the walls,

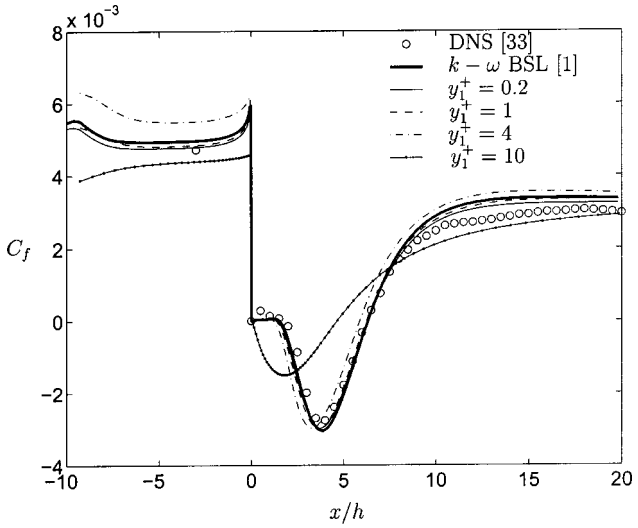

Fig. 8 Friction coefficient, BFS-case

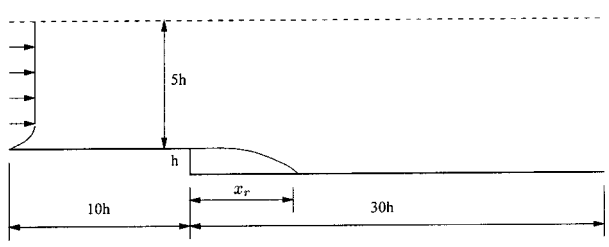

Fig. 7 Geometrical conditions, not to scale, BFS-case

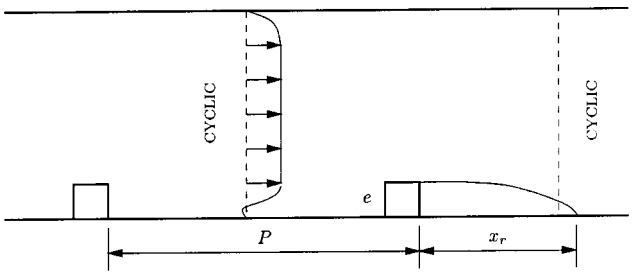

Fig. 9 Geometry, rib-roughened channel

Table 3 Re-attachment point, rib-roughened channel. Present model compared with experiment [34] and $k-\omega$ BSL model [1].

Mesh	Experiment	$k-\omega$ BSL	100×120	100×120	50×60	50×55
y_1^+	-	0.2	0.2	1.0	4.0	10
x_r/e	4→4.25	4.1	4.1	4.2	4.2	5.7

with the rib insulated. The rib-height-to-channel-height, e/H, is 0.1, and the pitch-to-height ratio, P/e, is 9. The single rib is located along the lower wall as shown in Fig. 9.

The measured Nusselt numbers are normalized with the Dittus-Boelter equation (Dittus and Boelter [39]), as introduced by McAdams [40]:

$$Nu_\infty = 0.023 \cdot \mathrm{Re}_H^{0.8} \cdot \mathrm{Pr}^{0.4} \tag{28}$$

The computations were made using a periodic boundary condition at the streamwise boundaries.

The following meshes were used for this case: two 100×120 meshes, one 50×60 mesh and one 50×55 mesh (streamwise ×wall normal). The two 100×120 meshes were constructed using different stretching in the wall normal direction, resulting in a first interior node distance at $y_1^+ = 0.2$ and $y_1^+ = 1$, respectively. In a ribbed channel, the use of y^+ is unsuitable as an indicator of the wall distance. The definition of y^+ uses the friction velocity, which will be undefined in reattachment and separation points. Thus y^+ will vary substantially along the lower wall even though the nodes are located at the same distance from the wall. To enable a valid comparison with the other cases, y_1^+ for the upper wall is used instead. The non-normalized distance for the first interior node is the same for the upper and lower walls for all meshes used here. The actual y_1^+ value of the lower wall will generally be smaller, owing to the reduced velocity in recirculating areas.

The predicted normalized Nusselt number along the lower wall using the different meshes is compared in Fig. 10 with the baseline model of Bredberg et al. [1]. The zero heat transfer for $4 \leqslant x/e \leqslant 5$ indicates the location of the insulated rib. Employing the modified wall treatment on the same $y_1^+ = 0.2$ mesh yields results identical to those of the baseline model, with the curves overlaying each other. For the $y_1^+ = 1$ and $y_1^+ = 4$ meshes the present predictions are within 5% of the grid independent result. Note, however, that there is a qualitative difference using the coarsest mesh, with a downstream shift of the location of the maximum *Nu* that is accompanied by a similar shift in the reattachment point of the main recirculating bubble, Table 3.

Two different relations were used in the estimation of the wall temperature corresponding to Eqs. (9) and (11). In Fig. 10, the result using the former is labeled with ν_t. For the $y_1^+ = 1$ mesh, the difference between the two formulations is negligible. However, with the $y_1^+ = 10$ mesh, the inclusion of the eddy-viscosity, ν_t, improves the predicted Nusselt number. Even though the results in the case of the coarsest mesh deviate by more than 25% from the experimental data, they are still encouraging as compared with other turbulence models, especially when using wall function based models, see Bredberg [13].

4 Summary

This study presents an improved near-wall treatment for turbulence models. The method is based on a thorough examination of approximations made when integrating the discretized equations in the near-wall region. A number of modifications are proposed which counteract errors introduced when using an LRN-model on meshes for which the first interior node is located at $y^+ \geqslant 5$. Here the methodology is applied to the $k-\omega$ turbulence model by Bredberg et al. [1], although similar corrections are relevant for all LRN models. For a fine mesh, the model gives asymptotically identical results to those of the baseline model. The present method improves numerical stability for coarser meshes, and also shows less mesh dependency than a non-modified model. Results for fully developed channel flow, backward-facing step flow and rib-roughened channel are presented. For the four cases considered, the predicted results are only weakly grid dependent for meshes with a first interior node located below $y^+ < 10$. This is a great improvement over traditional low-Reynolds number models, which necessitate at least five nodes within this range.

The proposed modifications can give a twofolded reduction in the computational resources needed in each dimension with maintained fidelity in the predicted results. It should be noted however that the method is not a substitute for turbulence models based on wall functions, owing to the limited validity of the near-wall corrections used.

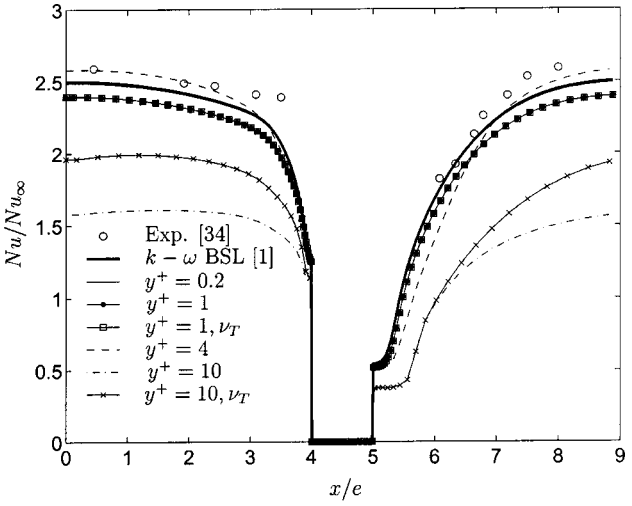

Fig. 10 Nusselt number, rib-roughened channel

Acknowledgments

Funding for the present work has been provided by STEM, Volvo Aero Corporation and ALSTOM Power via the Swedish Gas Turbine Center (GTC).

Nomenclature

C_p = Specific heat
C = Various constants
h = Step-height
H = Channel height
Nu = Nusselt number, $q\nu/\mathrm{Pr}(T_w - T_{bulk})$
p = Static pressure
Pr = Prandtl number
q = Heat flux
Re = Reynolds number, UH/ν
R_t = Turbulent Reynolds number, $k/(\omega\nu)$
Re_τ = u_τ based Reynolds number, yu_τ/ν
T = Temperature
U_i = Velocity
$\overline{u_i' u_j'}$ = Reynolds stresses
u_τ = Friction velocity, $\sqrt{\tau_w/\rho}$
y = Wall normal distance

Greek Symbols

ε = Dissipation rate
κ = Van Karman constant
ν = Kinematic viscosity
μ = Dynamic viscosity
ρ = Density

ω = Specific dissipation rate
σ_k, σ_ω = Turbulence model coefficients
τ = Time
τ = Shear stress

Subscripts

1 = First interior node
t = Turbulent quantity
T = Thermal quantity
w = Wall value

References

[1] Bredberg, J., Peng, S-H., and Davidson, L., 2002, An Improved $k-\omega$ Turbulence Model Applied to Recirculating Flows. Int. J. Heat Fluid Flow, **23**, 731–743.

[2] S. V. Patankar, and D. B. Spalding, 1970, *Heat and Mass Transfer in Boundary Layers*. Intertext Books, London.

[3] D. C. Wilcox, 1993, *Turbulence Modeling for CFD*. DCW Industries, Inc.

[4] Launder, B. E., 1984, Numerical Computation of Convective Heat Transfer in Complex Turbulent Flows: Time to Abandon Wall Functions? Int. J. Heat Mass Transfer, **27**, 1485–1491.

[5] Launder, B. E., and Spalding, D. B., 1974, The Numerical Computation of Turbulent Flows. Comput. Methods Appl. Mech. Eng., **3**, 269–289.

[6] Chieng, C. C., and Launder, B. E., 1980, On the Calculation of Turbulent Heat Transfer Transport Downstream an Abrupt Pipe Expansion. Numer. Heat Transfer, **3**, 189–207.

[7] Johnson, R. W., and Launder, B. E., 1982, Discussion of: On the Calculation of Turbulent Heat Transfer Transport Downstream an Abrupt Pipe Expansion. Numer. Heat Transfer, **5**, 493–496.

[8] Ciofalo, M., and Collins, M. W., 1989, $k-\varepsilon$ Predictions of Heat Transfer in Turbulent Recirculating Flows Using an Improved Wall Treatment. Numer. Heat Transfer, **15**, 21–47.

[9] Amano, R. S., Jensen, M. K., and Goel, P., 1983, A Numerical and Experimental Investigation of Turbulent Heat Transport Downstream From an Abrupt Pipe Expansion. J. Heat Transfer, **105**, 862–869.

[10] Amano, R. S., 1984, Development of a Turbulence Near-wall Model and its Application to Separated and Reattached Flows. Numer. Heat Transfer, **7**, 59–75.

[11] Acharya, S., Dutta, S., and Myrum, T. A., 1998, Heat Transfer in Turbulent Flow Past a Surface-mounted Two-dimensional Rib. J. Heat Transfer, **120**, 724–734.

[12] Heyerichs, K., and Pollard, A., 1996, Heat transfer in Separated and Impinging Turbulent Flows. Int. J. Heat Mass Transfer, **39**, 2385–2400.

[13] J. Bredberg, 2002, *Turbulence Modelling for Internal Cooling of Gas-Turbine Blades*. Ph.D. thesis, Dept. of Thermo and Fluid Dynamics, Chalmers University of Technology, Gothenburg. Also available at www.tfd.chalmers.se/~lada.

[14] Iacovides, H., and Launder, B. E., 1984, PSL-an Economical Approach to the Numerical Analysis of Near-wall, Elliptic Flow. J. Fluids Eng., **106**, 241–242.

[15] Choi, Y. D., Iacovides, H., and Launder, B. E., 1989, Numerical Computation of Turbulent Flow in a Square-sectioned 180 Deg Bend. J. Fluids Eng., **111**, 59–68.

[16] Spalding, D. B., 1967, Heat Transfer from Turbulent Separated Flows. J. Fluid Mech., **27**, 97–109.

[17] Wolfshtein, M., 1969, The Velocity and Temperature Distribution in One-dimensional Flow with Turbulence Augmentation and Pressure Gradient. Int. J. Heat Mass Transfer, **12**, 301–318.

[18] T. J. Craft, A. V. Gerasimov, H. Iacovides, and B. E. Launder, 2001, Progress in the Generalization of Wall-function Treatments. Report, Dept. of Mechanical Engineering, UMIST, Manchester.

[19] T. J. Craft, A. V. Gerasimov, H. Iacovides, B. E. Launder, and C. Robinson, 2001, A New Wall Function Strategy for Forced and Mixed Convection. In: *2nd Int. Symp. on Turbulent Shear Flow Phenomena*, pages 1–20, Stockholm.

[20] Wilcox, D. C., 1988, Reassessment of the Scale-determining Equation for Advanced Turbulence Models. AIAA J., **26**, 1299–1310.

[21] J. Bredberg, S-H. Peng, and L. Davidson, 2000, On the Wall Boundary Condition for Computing Heat Transfer with $k-\omega$ Models. In: J. H. Kim, editor, *HTD-Vol. 366-5, ASME Heat Transfer Division-2000*, **5**, pages 243–250, Orlando. The American Society of Mechanical Engineers.

[22] J. Bredberg, 2000, On the Wall Boundary Condition for Turbulence Model. Report 00/4, Dept. of Thermo and Fluid Dynamics, Chalmers University of Technology, Gothenburg. Also available at www.tfd.chalmers.se/~lada.

[23] P. Rautaheimo, and T. Siikonen, 2000, Improved Solid-wall Boundary Treatment in Low-Reynolds Number Turbulent Models. AIAA Paper 2000–0136, Reno, NV, USA.

[24] H. Grotjans, and F. R. Menter, 1998, Wall Functions for General Application CFD Codes. In: *CD-ROM Proceedings of ECCOMAS*, pages 1112–1117, Athens.

[25] Kays, W. M., 1994, Turbulent Prandtl Number-where Are We? J. Heat Transfer, **116**, 284–295.

[26] H. Tennekes, and J. L. Lumley, 1972, *A First Course in Turbulence*. Massachusetts Institute of Technology, Cambridge.

[27] Hanjalić, K., and Launder, B. E., 1976, Contribution Towards a Reynolds-stress Closure for Low-Reynolds-number Turbulence. J. Fluid Mech., **74**, 593–610.

[28] R. D. Moser, J. Kim, and N. N. Mansour, 1999, Direct Numerical Simulation of Turbulent Channel Flow up to Re=590. Physics of Fluids, **11**: 943–945. Data available at www.tam.uiuc.edu/Faculty/Moser/.

[29] Mansour, N. N., Kim, J., and Moin, P., 1988, Reynolds-stress and Dissipation-rate Budgets in a Turbulent Channel Flow. J. Fluid Mech., **194**, 15–44.

[30] K. Hanjalić, 2002, Near-wall behavior of ε and ω. Private Communication, Dept. of Thermo and Fluid Dynamics, Chalmers University of Technology, Gothenburg.

[31] Huang, P. G., and Bradshaw, P., 1995, Law of the Wall for Turbulent Flows in Pressure Gradients. AIAA J., **33**, 624–632.

[32] Abe, K., Kondoh, T., and Nagano, Y., 1994, A New Turbulence Model for Predicting Fluid Flow and Heat Transfer in Separating and Reattaching Flows-I. Flow Field Calculations. Int. J. Heat Mass Transfer, **37**, 139–151.

[33] Le, H., Moin, P., and Kim, J., 1997, Direct Numerical Simulation of Turbulent Flow Over a Backward-facing Step. J. Fluid Mech., **330**, 349–374.

[34] Rau, G., Cakan, M., Moeller, D., and Arts, T., 1998, The Effect of Periodic Ribs on the Local Aerodynamic and Heat Transfer Performance of a Straight Cooling Channel. J. Turbomach., **120**, 368–375.

[35] L. Davidson, and B. Farhanieh, 1995, CALC-BFC. Report 95/11, Dept. of Thermo and Fluid Dynamics, Chalmers University of Technology, Gothenburg.

[36] van Leer, B., 1974, Towards the Ultimate Conservative Difference Monotonicity and Conservation Combined in a Second-order Scheme. J. Comput. Phys., **14**, 361–370.

[37] Rhie, C. M., and Chow, W. L., 1983, Numerical Study of the Turbulent Flow Past an Airfoil with Trailing Edge Separation. AIAA J., **21**, 1525–1532.

[38] W. B. George, 2001, Lecture notes, Turbulence Theory. Report, Dept. Thermo and Fluid Dynamics, Chalmers University of Technology, Gothenburg.

[39] Dittus, F. W., and Boelter, L. M. K., 1930, Heat Transfer in Automobile Radiators of the Tubular Type. Univ. Calif. Publ. Eng., **2**, 443–461.

[40] W. H. McAdams, 1942, *Heat Transmission*. McGraw-Hill, New York, 2nd edition.

Multi-Modal Forcing of the Turbulent Separated Shear Flow Past a Rib

P. K. Panigrahi

S. Acharya

Department of Mechanical Engineering,
Louisiana State University,
Baton Rouge, LA 70803

Experiments have been conducted to study the development of flow behind a surface mounted rib under different phase controlled excitation. Single mode excitation and multi-mode excitation with different relative phases are studied. The results presented include the coherent and random components of the turbulent energy and shear stresses, the energy exchange with the mean flow and between the modes, and the phase decorrelation of the coherent components. The fundamental-subharmonic excitation does not provide any significant improvements in the shear layer growth over the fundamental excitation. The shear layer growth correlates with the subharmonic mode development. The large scale structures are significant even after the reattachment region as evident from the magnitude of the coherent components of the turbulent energy and the shear stress. The binary exchange terms are significant in the near-field region whose sign is phase dependent, i.e., it reverses its sign based on the phase difference between the fundamental and 1st subharmonic mode. The location of the fundamental and subharmonic peaks are different from the peak location of their respective energy exchange with the mean flow; this is attributed to the significance of the binary energy exchange between the fundamental and the subharmonic mode in this region. The excitation regularizes the flow leading to low phase jitter in the near field region. The origin and development of phase decorrelation is attributed primarily to the subharmonic instability. [DOI: 10.1115/1.1637634]

1 Introduction

It is a well known fact that coherent, vortical structures play a dominant role in the development of shear layers such as plane mixing layers, jets, and reattaching shear layers. The growth, evolution, and interaction between these vortical structures is primarily responsible for the near-field development of the shear layer. The most extensively studied shear layer is that of a plane mixing layer past a splitter plate. Ho and Huang [1] observed that the spreading rate of a mixing layer can be greatly manipulated by low level forcing at the subharmonic of the most unstable frequency, which was attributed to the merging of vortices. Yang and Karlsson [2] studied the instability of a plane shear layer influenced by the superposition of the fundamental frequency and its first subharmonic frequency. For the two mode forcing, greater shear layer growth was observed relative to the single-mode forcing, and was attributed to the vortex merging mechanism. The vortex merging termed as either ''pairing'' or ''tearing'' was observed to be dependent on the phase difference between the two modes.

Raman and Rice [3] studied the axisymmetric jet under controlled perturbation with fundamental and subharmonic tones and observed that the two frequency excitation is more effective than the single frequency excitation. Gordeyev and Thomas [4] investigated the temporal aspects of fundamental-subharmonic phase locking of a jet shear layer excited using single-mode forcing and dual-mode forcing. They characterized the temporal amplitude and phase behavior of the subharmonic from application of the wavelet transform and observed intermittent π-shifts in phase between two fixed values. This temporal phase behavior of the subharmonic was considered to be responsible for intermittently disrupting the phase lock with the fundamental.

The influence of shear layer excitation on the development and evolution of coherent structures behind a backward facing step has also been investigated by several investigators (Roos and Kegelman [5], Bhattacharjee et al. [6], and Hasan [7]). Bhattacharjee et al. [6] observed that the spreading rate can be increased most effectively by forcing at a non-dimensional frequency St_h (based on step height and free stream velocity) between 0.2 and 0.4. Roos and Kegelman [5] observed sufficient reduction in the reattachment length when forcing at St_h greater than 0.25 due to the completion of at least one stage of pairing prior to the reattachment. Hasan [7] for a backward facing step, observed two distinct modes of instability: the shear layer mode ($St_\theta \simeq 0.012$) and the step mode ($St_h \simeq 0.185$). The above-noted studies dealing with the effect of excitation on the development of reattaching shear layer past a back-step are all limited to single frequency studies.

In the present paper, the configuration of interest is that of a ribbed duct flow characterized by a reattaching shear layer. This flow configuration is different from that past a backward facing step due to flow separation upstream of the rib. The effect of single-mode and multi-mode excitation on the reattaching shear layer past a surface-mounted rib has not yet been investigated, and is the main objective of the present paper. In order to investigate the periodic and nonperiodic aspects of the reattaching shear layer evolution, the pattern recognition technique (Zhou et al. [8], Acharya and Panigrahi [9]) is applied to the velocity-time data for presenting the coherent and random component of turbulent energy and shear stresses. In addition, the pattern recognition technique (Acharya and Panigrahi [9]) and the method introduced by Ho et al. [10] (HZFB method) are applied to study the phase decorrelation evolution. Detailed information regarding the modal development, the energy exchanges of the mean flow with the odd and even modes as well as binary energy exchange between the modes are presented. The effect of excitation on the phase jitter or phase decorrelation magnitude is also reported to show the zone of influence within which the control signal is phase locked to the vortex shedding or vortex merging.

Contributed by the Fluids Engineering Division for publication in the JOURNAL OF FLUIDS ENGINEERING. Manuscript received by the Fluids Engineering Division April 30, 2002; revised manuscript received August 8, 2003. Associate Editor: M. V. Ötügen.

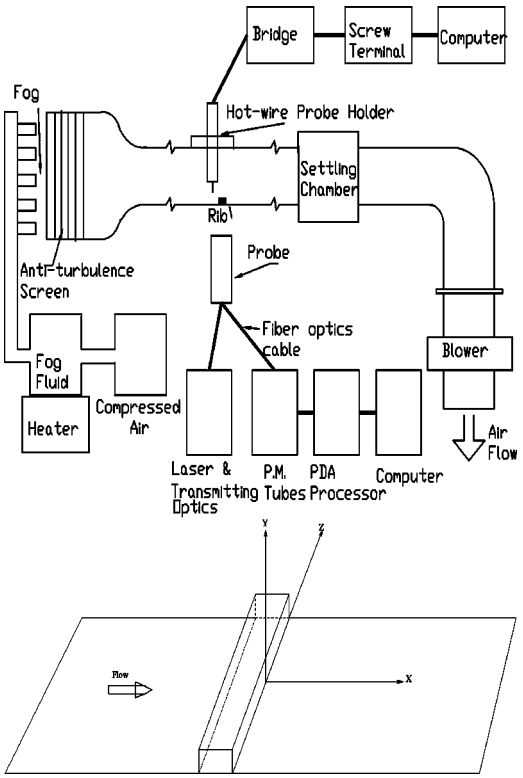

Fig. 1 Schematic of the experimental setup (top) and coordinate system of the rib (bottom)

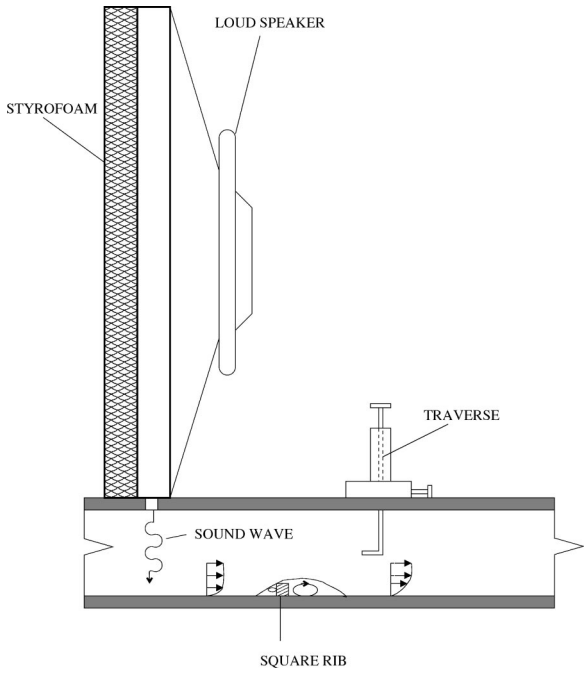

Fig. 2 Schematic of the flow excitation arrangement

2 Description of the Experiment

The schematic of the experimental setup is shown in Figure 1. Air is drawn into a rectangular channel of 0.3 m by 0.06 m cross section through a 5.25 to 1 contraction section, honeycomb and wire-mesh screens by a blower operating in the suction mode. The Reynolds number based on the average velocity (U_{av}) and hydraulic diameter of the channel is set equal to 14,600. The free stream turbulence at the exit of the contraction section measured using a hot wire anemometer is equal to 0.4%. The ratio of the channel width to rib height (h) is 47.2, which is larger than the required aspect ratio (12) to minimize three-dimensional effects. The blockage ratio due to the rib is 9.5%. At Re=14600, the boundary layer thickness in a smooth channel is 6 mm at the rib location and the corresponding shape factor is equal to 1.42. The rib is located near the entrance of the channel, i.e., about 18 rib height from the exit of the contraction cone. The developing boundary layer at the location where the rib is mounted compares well with the law of the wall and therefore is turbulent in nature.

Hotwire anemometry and laser-Doppler velocimetry (LDV) were both used for the velocity measurements. The two-channel hot wire anemometer was operated in the constant temperature mode with a 70% overheat ratio. The anemometer output was connected to a Keithley Metrabyte data acquisition card (DAS-16) through a screw terminal accessory board (STA-16). The Streamer package supplied by Keithley Metrabyte was used to enable direct storage of data from the DAS-16 board to the hard disk of the computer. The X-wire was calibrated using a Model 1125 calibrator supplied by TSI. The calibration accuracy was confirmed by comparing the hot wire data with the LDV data and the measured mean velocities with the two different techniques were within 1%. The hot wire data acquisition sampling rate was 4160 Hz/channel and the total number of samples recorded per channel was 16,384. The voltage input to the loud speaker was simultaneously collected with the two channel output from the X-wire. Thus, the total number of samples for a single point measurement was 48K.

The laser-Doppler velocimetry measurements were performed using a two-color DANTEC fiber-optic system. The Argon-Ion laser beam was split into a pair of 488 nm (blue) and 514.5 nm (green) wavelength beams using a color separator and a beam splitter. One beam from each of the two pairs was shifted by 40 MHz using a Bragg cell to eliminate the directional ambiguity in velocity measurements. A 400 mm focal length lens focused the resulting pair of beams to a measurement volume of less than 0.2 mm waist diameter. The flow was seeded with an aerosol mist, obtained by heating a fog fluid supplied by Rosco Inc. Backscattered light was collected by photomultiplier tubes and processed using the PDA signal processor and SIZEware software supplied by Dantec. The sampling rate of the LDV signal was varied depending on the rate of supply and diameter of the seeding particle and was within the range of 100 Hz to 2000 Hz. For the LDV measurements, the total number of filtered samples with high signal to noise ratio per point was 10,000 or greater. The reattachment length was determined by measuring the velocity at a location close to the bottom wall (2 mm away from the surface) at various streamwise locations (X/h). The location where the velocity changed sign from negative to positive was termed as the reattachment point. From the LDV measurements, it was observed that the reversed flow intermittency (fraction of time for which the flow is negative) is zero for the transverse location where $U/U_{\max}$ is greater than 0.65. Therefore, the hot wire measurements were made at or above the transverse location where $U/U_{\max}=0.65$. The Reynolds stresses and the shear layer growth measurements have been acquired using both hot wire anemometry and laser-Doppler velocimetry. The maximum differences in their peak magnitude were observed to be within 5% and this paper has reported these measurements from the hot wire data. The coherent contribution of the total turbulent energy, modal energy exchange, binary energy exchange and phase jitter results reported in this paper have been calculated from the hot wire measurements. The reattachment length has been measured using laser Doppler velocimetry.

For flow excitation, a loudspeaker was used in an arrangement similar to that of Fiedler and Mensing [11] in their study of plane turbulent shear layer excitation (see Fig. 2). Excitation using a loudspeaker was chosen because the arrangement is simple and a

repeatable range of amplitude and frequency can be obtained. The two channel PCI-312 signal generator from PC Instruments provided the required type of signal (single mode or two modes at different phase differences) to the loudspeaker through a power amplifier from Velodyne Acoustics (Model OLD-12-N). The loudspeaker was connected to a rectangular cavity of dimension 0.5969 m$\times$0.3048 m$\times$0.0222 m. The cavity was padded with styrofoam to minimize the effect from multiple reflection of acoustic waves inside the cavity. The acoustic beam enters through a 4.76 mm wide slot located at about $9h$ upstream of the rib.

2.1 Forcing Criteria. It is expected that both the forcing frequency and the forcing amplitude would play an equally important role in the modification of the large scale structures. The fundamental frequency of 52 Hz is observed to be the dominant frequency (see Fig. 2) in the near field of the rib and has been selected for single mode fundamental excitation. The subharmonic (26 Hz) manifests at a later stage in the downstream direction. Phase difference between the fundamental and subharmonic is expected to play a crucial role in the shear layer development and therefore, for the fundamental-subharmonic excitation, phase differences of 0°, 90°, 180°, and 270° have been used. The phase angle here is defined as the difference between twice the phase angle of the subharmonic wave and phase angle of the fundamental wave.

The forcing level is defined here as the ratio between the root-mean-square (rms) velocity of the large scale fluctuations due to the excitation and the average velocity measured at the downstream edge of the rib at a Y/h equal to 2.0. This location represents the external free stream at the downstream edge of the rib. Different forcing levels were obtained by adjusting the voltage input to the power amplifier of the loud speaker. For a desired amplitude and phase difference, the input to the function generator depends on the frequency response of the loud speaker chamber. Hence, initial calibration of the loud speaker was performed by plotting and curve fitting the forcing level versus the voltage supplied from the function generator. This helped in the selection of the correct input from the function generator to the power amplifier for a particular forcing frequency and forcing level. To select the forcing level for this study, the momentum thickness at $X/h=8$ was examined at different forcing level. It was observed that the rate of increase in momentum thickness reduces significantly after the forcing level reaches 2%. Therefore, the 2% forcing level is considered as the optimum forcing level and the flow is excited at 2% forcing level in this study. For the two frequency forcing, the forcing level for each mode was selected to be equal to 1%, such that the total forcing level was 2%.

2.2 Uncertainty. The uncertainty in the measurements were obtained using the method described by Moffat [12]. The uncertainty in momentum thickness is calculated to be 7.1%. The Strouhal number based on momentum thickness has an uncertainty of about 8.0%. Uncertainty of the most amplified frequency is estimated to be the spectral resolution of the power spectrum (reciprocal of signal observation time in second), i.e., about 1.0 Hz. From the repeated measurements of the reattachment length, the uncertainty in reattachment length is observed to be 4.0%. The maximum uncertainty of the Reynolds stresses ($u^2_{\mathrm{rms}}, v^2_{\mathrm{rms}}, \overline{u'v'}$) from repeated measurements is estimated to be 4.5%. The uncertainty of $Y_{0.7}$, $Y_{0.9}$, i.e., the Y-location at which $U/U_{\max}=0.7$ and 0.9, respectively is estimated from the uncertainty of velocity measurements to be equal to 2.1%. The uncertainty of the shear layer growth parameter $((Y_{0.9}-Y_{0.7})/h)$ is equal to 3.0%. The uncertainty of the coherent component of Reynolds stresses (u_f^2 and $\overline{u_f v_f}$) is equal to 5.6%, which has been estimated as the combination of uncertainty in the Reynolds stress measurements and the error in assumption of the coherent mode in the pattern recognition approach. The uncertainty of energy exchange with the mean flow is equal to 6.0% which has been estimated as the combination of coherent shear stress and velocity gradient uncertainty. The uncertainty of the binary energy exchange with the mean flow from the combined uncertainty of coherent shear stress and the gradient of the coherent velocity is equal to 6.4%. The uncertainty of phase jitter from modified HZFB method is equal to 3.6%, which has been estimated as the combined effect of the error in the estimation of the normalized time period and the error due to log-normal curve fitting. The uncertainty of the phase jitter from the pattern recognition approach is equal to 3.3%, which has been estimated as the combined effect of phase estimation error and normal curve fitting error.

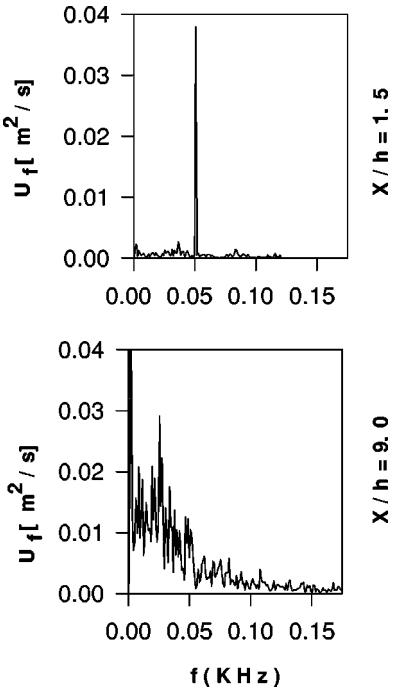

Fig. 3 The power spectrum of the streamwise *u*-velocity behind the rib turbulator for the unexcited flow

3 Data Analysis Procedure

In the following sections, the data analysis techniques for the evaluation of the coherent structure magnitude and phase jitter magnitude are discussed. For the coherent structure magnitude calculation, the pattern recognition method (Zhou et al. [8] and Acharya and Panigrahi [9]) has been used. For the phase jitter magnitude calculation, the modified HZFB method (Acharya and Panigrahi [13]) and the pattern recognition method (Acharya and Panigrahi [9]) have been used.

3.1 Coherent Structure Magnitude. Both the random and coherent eddies contribute to the total velocity fluctuation of a turbulent flow. The pattern recognition technique calculates these individual contributions. The advantage of pattern recognition technique over traditional ensemble average technique is that the former is insensitive to phase jitter while the later is not. The coherent velocity component is approximated to be the combined contribution from several modes and to identify these dominant modes, the power spectral density of u-velocity at different X/h locations have been presented in Fig. 3. The fundamental and subharmonics are observed to be the dominant modes. In addition, the 3/2 fundamental may show up due to the nonlinear interaction between the fundamental and its subharmonic. Similarly, the 5/2 fundamental may result due to the nonlinear interaction between the 3/2 fundamental and the fundamental. The second (1/4 fundamental) and third subharmonic (1/8 fundamental) modes may result from vortex mergings, while the 1st harmonic (2 fundamental)

may appear from vortex breakup. Therefore, the coherent velocity is assumed to be the combined contribution of the 5/2 fundamental, the 1st harmonic, the 3/2 fundamental, the fundamental, the 1st subharmonic, the 2nd subharmonic and the 3rd subharmonic. Any contribution from frequency larger than the maximum frequency (here the 5/2 fundamental) is regarded as the random small scale motion. The details on the evaluation of the individual modes of the coherent component have been discussed in Acharya and Panigrahi [9]. The total coherent structure amplitude is calculated by summing the amplitudes of all modes (5/2 fundamental, 1st harmonic, 3/2 fundamental, fundamental, 1st subharmonic, 2nd subharmonic, and 3rd subharmonic).

3.2 Phase Jitter Magnitude. Ho et al. [10] used a technique (referred here as HZFB technique) to evaluate the phase jitter magnitude of mixing layer. In this technique, the period of the coherent structure passage is calculated from the fluctuating velocity signal as the distance between the positively sloped zero crossing points. These time periods of structure passages are then used to construct a histogram of the normalized time periods. The log-normal probability distribution is used to curve fit the histogram. The standard deviation of the log normal distribution is used as a measure of the phase jitter in the signal. Acharya and Panigrahi [13] observed that the small scale structures can erroneously affect the coherent structure histogram and proposed a simple modification of the HZFB method. This modified HZFB method has been used for phase jitter calculation.

The pattern recognition technique (Acharya and Panigrahi [9]) for coherent structure magnitude calculation has been used for phase jitter determination. In this approach, the phase jitter present in the large scale structure is assumed to be mainly from the discrete large scale modes predominant in the fluctuating signal. For a single-frequency forcing, the jitter manifests in the forcing wave frequency itself. For the two-mode forcing, (i.e., fundamental and 1st subharmonic) the phase jitter manifests in both modes. A histogram is constructed from the whole population of the phase angles and the standard deviation of the histogram is calculated by fitting the histogram with a normal distribution using the least square method. The standard deviation of this distribution is used as a quantitative measure of the phase jitter.

4 Results and Discussions

The results are discussed in the following sequence: (a) unforced flow, (b) modal energy development, (c) energy exchange with the mean flow, (d) binary mode interactions, and (e) phase decorrelation.

4.1 Unforced Flow. Figure 4 presents the streamwise velocity spectra of the unforced flow at two X/h locations; $X/h=1.5$ corresponding to a location downstream of the rib, and $X/h=9$ which is downstream of the reattachment point. At $X/h=1.5$, the spectrum reveals the presence of a clear shear layer instability at about 52 Hz (fundamental). The spectrum is taken at a Y/h location where this instability peak is the strongest, and the background turbulence is relatively low. No other peaks are seen in this spectrum indicating a relatively clean flow with low freestream turbulence uncontaminated by other spurious frequencies arising from the blower or the honeycombs. As the flow develops, additional frequencies manifest themselves, and at $X/h=9$, the fundamental has diminished considerably in magnitude, while the first and second subharmonic appear to have manifested themselves.

Figure 4 shows the turbulence intensity in the streamwise and cross-stream directions and the turbulent shear stress at $X/h=6$ (close to reattachment) and at $X/h=9$ and 11.5 (downstream of reattachment). In all cases, the freestream values are quite low ($u^2_{\rm rms}/U^2_{av}=0.0003$, turbulence intensity$=1.8\%$). The peak streamwise turbulence intensity at $X/h=6$, by comparison, is nearly 30% ($u^2_{\rm rms}/U^2_{av}=0.09$). Thus clearly, the fluctuations in the unperturbed freestream are relatively small (compared to the peak turbulence levels in the shear layer), they do not have any additional discrete frequency components, and are therefore not expected to significantly alter the natural dynamics of the coherent structures in the flow. With forcing, the discrete forcing frequencies introduced into the freestream are expected to interact with the coherent structures, and the effect of this interaction is presented later.

With flow development, the intensity values drop off rapidly between $X/h=6$ and 9, with a nearly twofold decrease in the peak value of $u^2_{\rm rms}/U^2_{av}$ and $v^2_{\rm rms}/U^2_{av}$. Thus, there is a fairly strong recovery in the flow downstream of reattachment till about $X/h=9$, beyond which the recovery appears to be considerably reduced. The turbulent shear stresses also show the same behavior with nearly a threefold reduction in the peak shear stresses between $X/h=6$ and 9.

4.2 Modal Energy Development. The large scale structures are assumed to be composed of several instability waves (modes) which propagate, interact with each other and amplify in the downstream direction. The growth of the shear layer is best explained by the streamwise development of the fundamental and 1st subharmonic modes (Ho and Huang [1], Nikitopoulos and Liu [14]). In this section, we try to correlate the growth of the reattaching shear layer to the development of fundamental and subharmonic modes.

The $(Y_{0.9}-Y_{0.7})/h$ value plotted in Fig. 5 is used here as a measure of the shear layer growth, where $Y_{0.7}$ and $Y_{0.9}$ are the respective Y locations corresponding to $U/U_{\max}=0.7$ and 0.9. The slope of the plots in Fig. 5 may be assumed to represent the shear layer growth rate. At $X/h=11.5$, the forced flow exhibits values of $((Y_{0.9}-Y_{0.7})/h)$ in excess of 0.9 while the corresponding values for the unexcited flow are only about 0.6 indicating greater growth of the excited flow. Both the unexcited and excited flow exhibit an initial region of slow growth (in the range of $0\leqslant X/h\leqslant 1.5-2.5$) followed by a region of nearly linear growth ($X/h\geqslant 1.5-2.5$). To compare the growth rate for different excitation, the shear layer growth ($(Y_{0.9}-Y_{0.7})/h$) is linear curve fitted in Fig. 6. The excited flow exhibits higher growth rate (slope$=0.056-0.067$) than the unexcited flow (slope$=0.038$) and the fundamental excitation exhibits the maximum growth rate (slope $=0.067$) among all excitation. For the fundamental-subharmonic excitation, the phase difference $\Delta\phi=90°$ exhibits higher growth rate (slope$=0.063$) in comparison to other phase differences i.e. $\Delta\phi=0°$, 180°, and 270° (slope$=0.056-0.058$).

In Fig. 7, the $Y_{0.7}$ and $Y_{0.9}$ locations and the corresponding magnitude of fundamental and subharmonic mode are presented. An upward rise or positive slope of the $Y_{0.7}$ and $Y_{0.9}$ location indicates that the shear layer is deflected in the upward direction, i.e., away from the bottom channel surface. For both the unexcited and excited flow, the upward deflection of the shear layer at $Y_{0.9}$ occurs till a later X/h location in comparison to $Y_{0.7}$ location. There is no appreciable change in the $Y_{0.9}$ variation of the excited flow in comparison to that of the unexcited flow. The positive slope of $Y_{0.7}$ for the fundamentally excited flow is observed till $X/h\simeq 1$ in comparison to $X/h\simeq 3$ for the unexcited flow indicating that the downward deflection of the fundamentally excited shear layer begins about two rib heights earlier in comparison to the unexcited flow. The reattachment length of the shear layer (obtained based on LDV measurements) for the excited flow is $X/h=4.0$ compared to 5.5 for the natural unforced flow and this drop in the reattachment length correlates with the earlier downward deflection of the excited shear layer.

From the modal energy development at the $Y_{0.7}$ location for the fundamental excitation (Fig. 8), the fundamental wave is seen to grow and attain a maximum value at $X/h=0.5$ and then decreases till $X/h=3$. Beyond $X/h=3$, the energy in the fundamental mode is almost constant and the subharmonic shows a weak growth till $X/h=3$ after which it grows at a faster rate before saturation at $X/h\simeq 6$. The maximum modal amplitudes at $Y_{0.7}$ is larger than

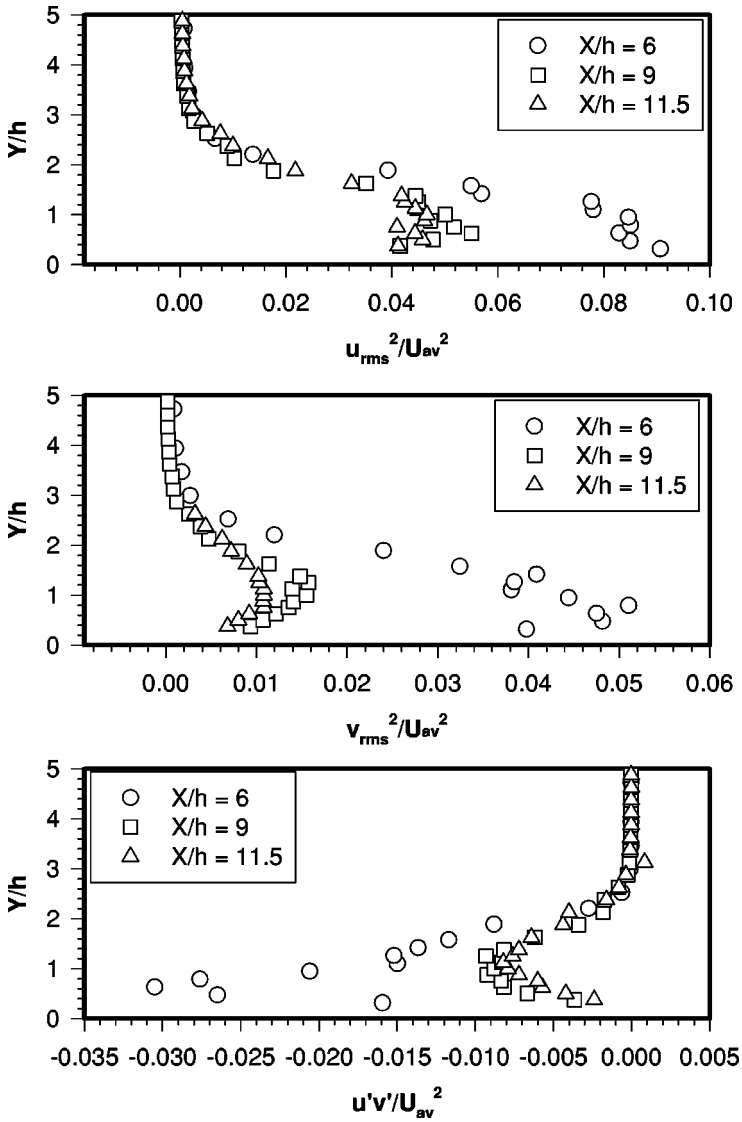

Fig. 4 The normalized streamwise fluctuation (top), normalized cross-stream fluctuation (middle), and normalized shear stress (bottom) profiles for the unexcited flow

that at $Y_{0.9}$ location due to the larger velocity gradient at the former location. At $Y_{0.9}$, the maximum fundamental amplitude takes place at $X/h=3$ compared to $X/h=0.5$ value for the $Y_{0.7}$ location and after that the fundamental magnitude drops till $X/h=5.0$ where the subharmonic starts growing at a larger rate. Thus, the growth of the subharmonic at $Y_{0.9}$ location is delayed relative to the $Y_{0.7}$ location (note the different vertical scales in the two plots). For a mixing layer, Hajj et al. [15] observed that the subharmonic mode grows at a faster rate after the saturation of the fundamental and the saturation amplitude of the fundamental and subharmonic have same order of magnitude. Similar to the mixing layer, the subharmonic mode grows at a faster rate after the saturation of the fundamental for both $Y_{0.9}$ and $Y_{0.7}$ locations. The saturation magnitude of the subharmonic has same order of magnitude as the fundamental for $Y_{0.9}$ location while for $Y_{0.7}$ location, the saturation amplitude of the subharmonic is smaller than that of the fundamental.

In fundamental-subharmonic excitation, the subharmonic mode is a stronger function of phase difference ($\Delta\phi$) in comparison to the fundamental mode. The maximum subharmonic mode magnitude at $Y_{0.7}$ is highest for $\Delta\phi=90°$ and lowest for $\Delta\phi=270°$. Similarly, the shear layer growth is highest for $\Delta\phi=90°$ in comparison to that for $\Delta\phi=270°$ indicating some kind of correlation

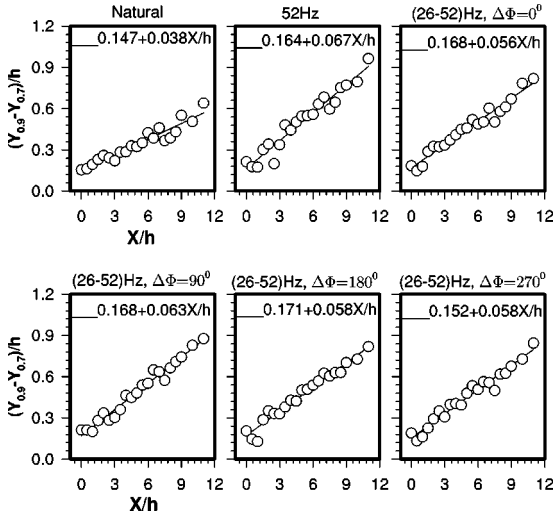

Fig. 5 The streamwise shear layer growth ($(Y_{0.9}-Y_{0.7})/h$) with its linear curve fit for the unexcited and excited flow

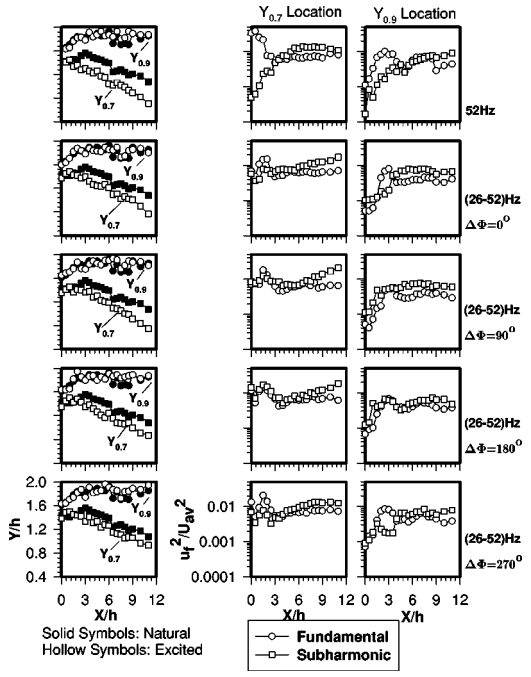

Fig. 6 The development of $Y_{0.7}$ and $Y_{0.9}$ locations and corresponding modal (fundamental and subharmonic) magnitude for the unexcited and excited flow

between the subharmonic mode and the shear layer growth. The subharmonic has one peak in the near field due to the natural amplification and has a second peak in the far field possibly due to random pairing. It may be mentioned that for a backward facing step, Eaton and Johnston [16] observed a drop in Strouhal number value by about 50% at around the reattachment region suggesting the importance of subharmonic after reattachment. Our present observation also support the importance of the subharmonic after reattachment for a shear layer behind the surface mounted rib.

To supplement the above observations, Fig. 9 shows the development of the $U_{\rm rms}$, $V_{\rm rms}$, $\overline{u'v'}$ and their coherent and random components for the fundamentally excited flow. Both the $U_{\rm rms}$ and $V_{\rm rms}$ increase with X/h, but reach their peak values at different X/h locations. At $Y_{0.7}$, the $U_{\rm rms}$ peaks just downstream of the rib, then decays to a minimum at $X/h \simeq 2$. At this location, $V_{\rm rms}$ peaks followed by a decay. Along with the decay in $V_{\rm rms}$ there is an increase in $U_{\rm rms}$ which again peaks at a X/h location of about eight. A similar behavior is observed for $Y_{0.9}$ except that the first $U_{\rm rms}$ peak occurs further downstream. The growth of the forcing frequency (the fundamental) at $Y_{0.7}$ and $Y_{0.9}$ occurs at a different rate in the streamwise direction. The X/h location at which the saturation of the fundamental takes place is earlier ($X/h \simeq 0.5$) for $Y_{0.7}$ location in comparison to the $X/h \simeq 2.5$ for $Y_{0.9}$ location. This may be due to the larger mean strain at $Y_{0.7}$ location, which leads to a larger growth rate resulting in earlier saturation. After the completion of fundamental growth, the subharmonic growth rate increases and is the primary contributor to the total coherent turbulent kinetic energy. The random scale motions are small even after reattachment. The coherent and random Reynolds stress at $Y_{0.7}$ and $Y_{0.9}$ locations plotted in Fig. 5 indicate that most of the Reynolds stresses are due to the large scale structures. Similar to the coherent energy in the streamwise fluctuation (see Fig. 5), the coherent Reynolds stress at $Y_{0.7}$ takes place at an earlier X/h location than that for $Y_{0.9}$.

4.3 Energy Exchange With the Mean Flow. In the previous section, the coherent component of turbulent energy was shown to be the dominant contributor to the total energy in the shear layer. In this section, the energy exchange of different

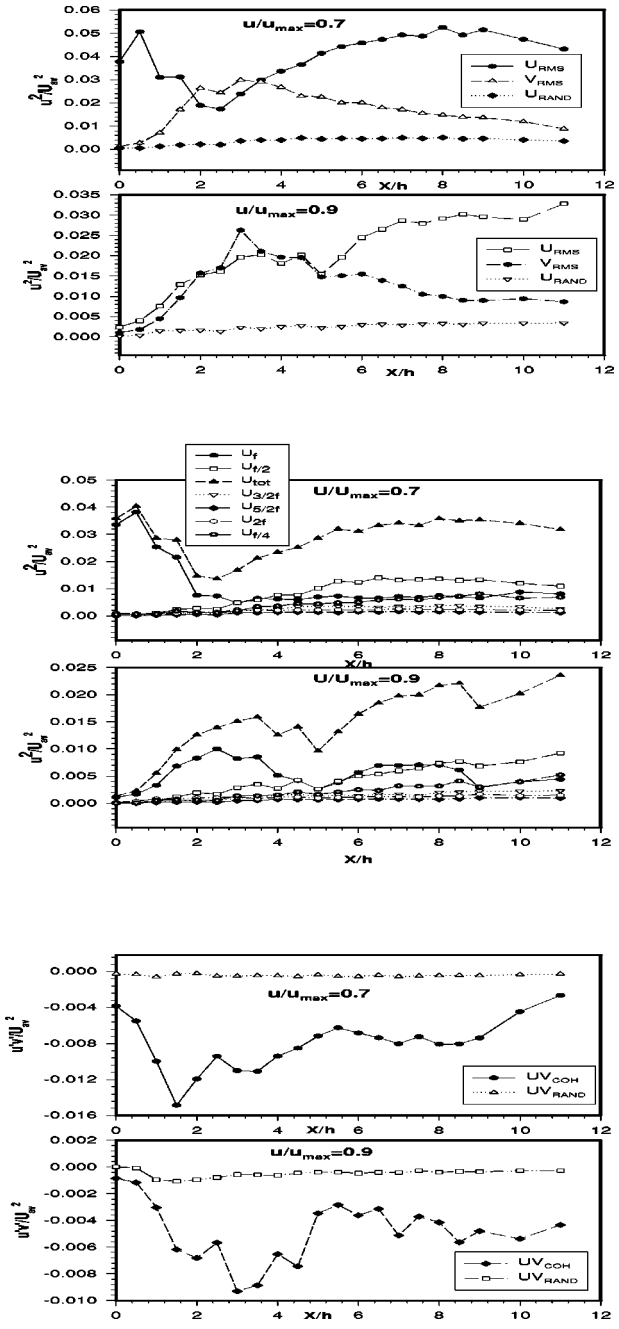

Fig. 7 The development of turbulent energy (both stream-wise and cross-stream) (top), coherent energy and its constituent modes (middle), and coherent and random shear stress (bottom) for the fundamental excitation, at $Y_{0.7}$ and $Y_{0.9}$ location

modes with the mean motion, i.e., the production of the modal energy is discussed. The energy exchange of different modes with the mean flow is calculated from using

$$-\overline{u_n v_n \frac{\delta U}{\delta Y}} \tag{1}$$

where "n" represents the index of predominant modes present in the flow. A positive value of the energy exchange term indicates the transfer of energy from the mean motions.

The modal energy exchange with the mean flow for the fundamental excitation and the fundamental-subharmonic excitation are shown in Fig. 8. For the fundamental excitation, the energy exchange of the subharmonic with the mean flow grows after the

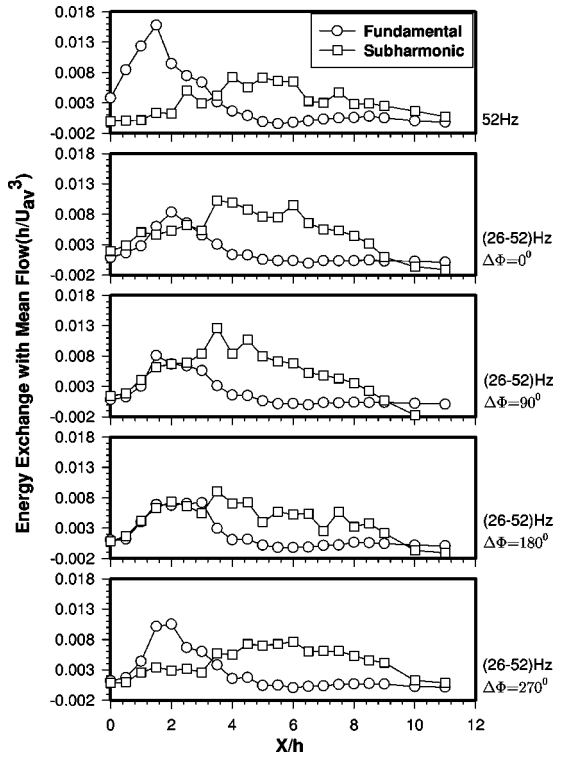

Fig. 8 The modal energy exchange with the mean flow at $Y_{0.7}$ location for the excited flow

energy exchange with the fundamental reaches its maximum value at $X/h \simeq 1.6$. The saturation of the fundamental mode takes place at an earlier ($X/h \simeq 0.6$) location (Fig. 5) than the ($X/h \simeq 1.6$) location at which the mean flow energy exchange with the fundamental reaches its maximum value (Fig. 5). This indicates the possible importance of binary energy exchange which has been presented in the following section.

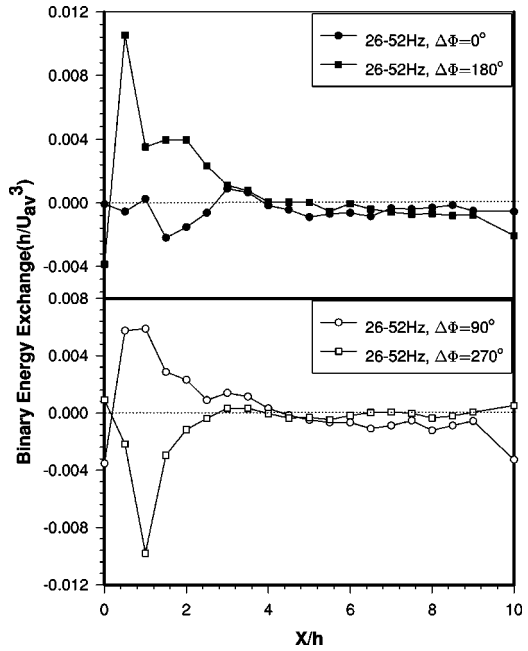

Fig. 9 The binary energy exchange between the fundamental and subharmonic mode at $Y_{0.7}$ location for the fundamental-subharmonic excitation

For fundamental-subharmonic excitation, the energy transfer from the mean flow to both the subharmonic and the fundamental frequencies is equally important in the near field region ($X/h < 4$) (see Fig. 5). The energy exchange with the fundamental peaks first at $X/h \simeq 2$ and that for the subharmonic occurs later at $X/h \simeq 4$. The maximum magnitude of the subharmonic energy exchange with the mean flow is larger than that of the fundamental for $\Delta\phi = 0°$ and 90°. The maximum magnitude of the fundamental and subharmonic energy exchange are equal to each other for $\Delta\phi = 180°$ and the maximum magnitude of the subharmonic energy exchange with the mean flow is lower than that of the fundamental for $\Delta\phi = 270°$. The maximum fundamental and subharmonic magnitude in Fig. 5 correlates with the magnitude of energy exchange in Fig. 5. However, the subharmonic energy exchange with the mean flow and the subharmonic mode do not correlate with each other in the far field indicating the possible role played by other mechanisms, i.e., convection and diffusion.

For all the two-mode excitation cases, the mean-fundamental energy exchange increases rapidly in the near field region reaching a peak at $X/h \simeq 2$, and decays monotonically downstream. The fundamental energy levels shown in Figs. 5 show a similar trend. The energy exchange of the subharmonic with the mean flow occurs more gradually with a flat peak at $X/h \simeq 4$ and is observed to be more sensitive to the phase difference. Rajaee and Karlsson [17] for a mixing layer, observed that the energy exchange of the subharmonic with the mean flow is negligible for the tearing type of vortex merging, and substantial for the pairing type of vortex merging. Gordeyev and Thomas [4] in their bimodal forcing experiments of jet shear layer, observed that the subharmonic amplitude remains virtually constant for a broad range of phase difference, i.e., most $\Delta\phi$ favors vortex pairing. For a limited range of $\Delta\phi$, the subharmonic amplitude decreases (around 260° in their experiment). From Fig. 5, the subharmonic production is observed to have the lowest magnitude for $\Delta\phi = 270°$. It should be recalled here that among all the fundamental-subharmonic excitation cases studied here, the $\Delta\phi = 270°$ case had the minimum mixing enhancement, possibly due to the relatively small subharmonic production (see Fig. 5).

4.4 Binary-Mode Interactions. The evolution of two wave interactions is expected to explain the dominant physical mechanism in the growth and decay of the fundamental and subharmonic disturbances and the significance of initial conditions and phase angle. The mode interaction term, i.e., the rate of energy transfer from the fundamental to the subharmonic is given by (Nikitopoulos and Liu [14]):

$$-\overline{u_i^o u_j^o \frac{\delta u_i^e}{\delta x_j}} \tag{2}$$

where, the superscript "*o*" stands for the subharmonic mode and "*e*" stands for the fundamental mode. This energy interaction term represents the work done by the Reynolds stress of the subharmonic mode with the strain field of the fundamental modes. The estimation of spatial derivatives ($\delta u_i^e/\delta x_j$) of the fundamental mode is only possible when the instantaneous spatial fluctuation can be measured with the help of large array of probes. In this work, the spatial derivatives of the even mode are calculated assuming the validity of Taylors hypothesis. Thus, the binary mode energy exchange is calculated from:

$$-\overline{u_i^o u_j^o \left(\frac{\delta u_i^e}{V\delta t} + \frac{\delta u_j^e}{U\delta t} \right)} \tag{3}$$

The validity of Taylors hypothesis is justified as follows. Antonia and Luxton [18] investigated the structure of boundary layer which forms downstream of a sudden change from smooth to

rough surface by mounting roughness elements of 1/8 inch square cross section with a pitch of 1/2 inch. They obtained the longitudinal length scale by using autocorrelation and two-point space time correlation measurements. The length scales obtained from the two techniques were in good agreement with each other. Taylors hypothesis assumes that the correlation $\overline{u(t')u(t'-t)}$ (where $\overline{\ }$ represents averaging with respect to t') must be identical to $\overline{u(\zeta)u(\zeta-x)}$ (where, $\overline{\ }$ represents averaging with respect to ζ). The comparable length scale results obtained from autocorrelation and space time correlation indicated the validity of Taylors hypothesis even in a region where mean velocity gradient and turbulence intensities are high. Antoniou and Bergeles [19] assumed the validity of Taylors hypothesis and presented the length scale obtained from autocorrelation measurement behind surface-mounted prism of varying length cross section and compared with the integral length scale results obtained by Antonia and Luxton [18]. The agreement between the length scales obtained for different size of surface roughness from separate measurements indicate the general validity of Taylors hypothesis in these geometries. Therefore, in the present case, the general validity of Taylors hypothesis is assumed.

The subharmonic-fundamental energy exchange for the fundamental-subharmonic excitation at different phase differences is plotted in Fig. 5. The positive sign of the energy exchange terms indicate the transfer of energy from the fundamental to the subharmonic while the negative sign indicates the loss of energy to the fundamental. The effectiveness of the phase angle difference can be observed in the near field of the separated shear layer region ($X/h \leqslant 3$), while away from the separated region ($X/h > 3$), the binary exchange of the coherent modes is small and no effect of phase difference can be ascertained. The importance of the binary exchange term in the near field region indicates the importance of the nonlinear interaction close to the downstream edge of the rib. The small values of the binary exchange terms in the far field may be attributed to the phase decorrelation in the near reattachment region. This will be made clear in the following section describing the results of phase decorrelation.

The mode interaction term is mostly positive for $\Delta\phi$ equal to 90° and 180°, and negative for 0° and 270°. This behavior is consistent with the mode interaction integral behavior of a mixing layer (Nikitopoulos and Liu [14]), where, it was noted that the sign of the intermodal energy terms was phase dependent i.e. it reverses its sign based on the phase difference. Comparing Fig. 5 with Fig. 5, it may be observed that in the near field region, the binary energy exchange and the energy exchange with the mean flow are equally dominant. Thus, the net amplification rate and modal energy development is not primarily dependent upon the production from the mean flow only but also on the binary exchange terms. From Fig. 5 it is observed for the fundamental-subharmonic excitation that the 1st peak of the subharmonic mode takes place at about $X/h=1.6$. However, Fig. 5 shows that the maximum energy exchange of the subharmonic with the mean flow takes place at a later location ($X/h \simeq 3.6$). The binary exchange terms in Fig. 5 peak at about $X/h=0.6$. Thus, the shift in peak of the subharmonic mode to an earlier location in comparison to the peak of the energy exchange with the mean flow may be attributed to the importance of the binary exchange terms. For the $\Delta\phi=180°$ case, the binary energy exchange term shown in Fig. 5 is positive, and correspondingly the subharmonic mode show the highest amplification in Fig. 5. Similarly, for the $\Delta\phi=270°$ case, the binary energy exchange term is negative in Fig. 5 and the subharmonic mode has minimum growth. This is directly related to the transfer of energy from the subharmonic to the fundamental, since both modes draw energy from the mean.

4.5 Phase Decorrelation. In the mixing layer studies, it has been observed that the spreading rate changes due to forcing in the region where the flow is locked to the forcing signal (see Ho et al. [10]). Forcing loses its influence when the flow is not locked to the forcing signal. Subharmonic forcing is effective in increasing the zone of influence. This zone of influence or region of phase locking can be represented by showing the evolution of phase jitter. The evolution of phase jitter in a reattaching shear layer undergoing both single frequency and two frequency excitation are discussed in this section.

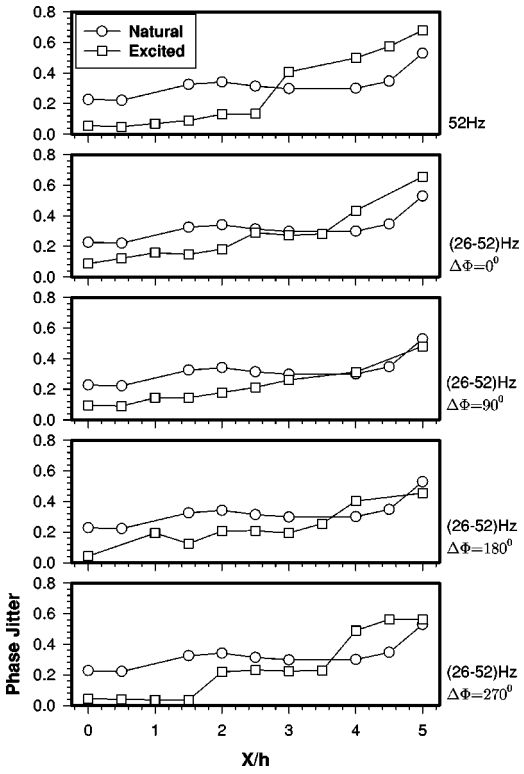

Fig. 10 The development of phase jitter from modified HZFB method at $Y_{0.7}$ location for the unexcited and excited flow

The effect of fundamental and fundamental-subharmonic excitation ($\Delta\phi=0°$, 90°, 180° and 270°) on phase jitter evolution at $Y_{0.7}$ location is presented in Fig. 10. The phase jitter values of the unforced reattaching shear layer are larger than that of the unforced mixing layer, presented by Ho et al. [10] indicating weaker coherence of the former than the later. The maximum value of phase jitter$\simeq$0.53 observed in the far field ($X/h \simeq 5$) of the reattaching shear layer is greater than phase jitter$\simeq$0.38 observed in a free shear layer (Ho et al. [10]). There is a drop in the phase jitter magnitude due to excitation in the near field region indicating greater coherence. When forced at the fundamental, the phase jitter in the near field region of the reattaching shear layer and free shear layer (Ho et al. [10]) are comparable in magnitude ($\simeq$0.05).

The complete phase decorrelation takes place earlier ($X/h \simeq 2.5$) for the fundamental excitation in comparison to the fundamental-subharmonic excitation ($X/h \simeq 3.5$). The fast subharmonic growth at an earlier X/h location for the fundamental excitation than the fundamental-subharmonic excitation in Fig. 5 indicates a possible correlation between the phase jitter and the subharmonic. For the fundamental-subharmonic excitation, the significant increase in phase jitter takes place at $X/h \simeq 3.5$ in Fig. 5 at about same location where the subharmonic mode has steep growth in Fig. 11. In the near field region ($X/h \leqslant 2.5$), the phase jitter magnitude of the fundamental excitation is lower than that of the fundamental-subharmonic excitation ($\Delta\phi=0°$, 90°, and 180°) in Fig. 5; which correlates to the corresponding lower subharmonic magnitude for the fundamental excitation in comparison to the fundamental-subharmonic excitation in Fig. 5. The phase jitter magnitude of the fundamental excitation and fundamental-

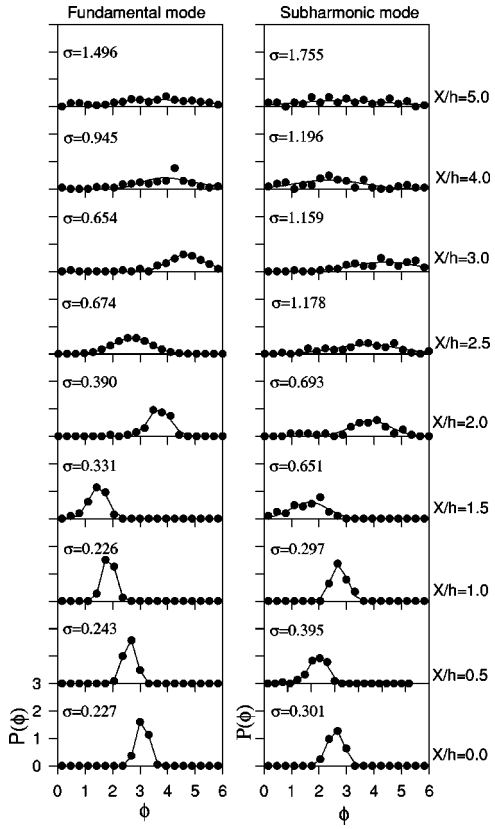

Fig. 11 The development of fundamental and subharmonic mode phase decorrelation for fundamental-subharmonic excitation ($\Delta\phi=90°$) using the pattern recognition approach at $Y_{0.7}$ location. The symbols corresponds to the actual data and the solid lines correspond to the curve fit and the σ is the standard deviation (phase jitter).

subharmonic excitation ($\Delta\phi=270°$) are comparable at $X/h \leqslant 1.5$ region in Fig. 5 as they have similar subharmonic magnitude in Fig. 5. Therefore, it may be construed that the phase jitter and the subharmonic mode development are correlated.

To better illustrate the role of subharmonic mode on phase jitter magnitude, the phase jitter evolution of fundamental and subharmonic mode using pattern recognition approach have been presented in Fig. 5 for the fundamental-subharmonic excitation ($\Delta\phi=90°$). The complete phase decorrelation of the fundamental mode occurs earlier ($X/h\simeq 2.0$) than that of the subharmonic ($X/h=3.5$). The phase jitter magnitude of the subharmonic frequency is consistently higher than that of the fundamental frequency indicating that the subharmonic mode is the primary cause of phase jitter in a reattaching layer. Comparing with the Fig. 5, it is observed that the effect of phase difference on the binary energy exchange terms is significant in the region of strong phase correlation or coupling between the fundamental and subharmonic modes. There is negligible coherent energy exchange in the region of complete phase decorrelation between the two modes. The random turbulent fluctuations shown in Fig. 5 being negligible in magnitude, the importance of small scales on the origin of phase decorrelation is ruled out. Ho et al. [10] for a mixing layer also concluded that the phase decorrelation is a two dimensional phenomenon and the three dimensional effects such as small scale transition is not the primary cause of phase decorrelation. In a jet shear layer, Gordeyev and Thomas [4] observed intermittent π shift in subharmonic phase between two fixed phase values. They attributed this phase behavior of the subharmonic mode to the disruption of phase lock with the fundamental. Thus, our observation about the crucial role of subharmonic instability on phase decorrelation is supported by the results from Gordeyev and Thomas [4] for a jet shear layer case. However, no intermittent π shift in subharmonic phase is observed in this work. This may be due to the difference in geometry of study between the two investigations and the reattaching shear layer investigated in the present work is strongly influenced by the recirculating region and is turbulent in nature as opposed to the laminar nature of the jet shear layer.

5 Summary

The effect of the single (fundamental) and two frequency (fundamental and subharmonic) excitation on the development of the reattaching shear layer past a surface mounted rib has been studied in this paper. Phase differences of 0°, 90°, 180°, and 270° between the fundamental and subharmonic have been considered. The modal energy development, energy exchange with the mean flow, binary energy exchange and the phase decorrelation behavior are discussed. The main findings from this work can be summarized as follows:

- The large scale motions are significant even after reattachment, which is evident from the magnitude of coherent component of turbulent energy and the coherent component of the turbulent shear stress.
- For the fundamental excitation, the subharmonic mode grows after the saturation of the fundamental and for the subharmonic-fundamental excitation, the subharmonic and fundamental modes grow into one peak in the near field at about same X/h location and subsequently the subharmonic mode grows again after reattachment.
- The binary energy exchange is significant in the near field and its sign is phase dependent i.e. it reverses its sign based on the phase difference. The significant value of the binary exchange terms in the near field region is responsible for the location of the fundamental and subharmonic peaks being different from their respective peaks of energy exchange with the mean flow.
- Excitation improves the coherence with low value of phase jitter in the near field region leading to complete phase decorrelation in the far field region ($X/h>3$).
- From the phase jitter evolution of the fundamental and subharmonic mode, the origin of phase decorrelation is attributed to the subharmonic instability.
- The fundamental-subharmonic excitation does not offer significant improvement on the zone of influence compared to the fundamental excitation.

References

[1] Ho, C. M., and Huang, L. S., 1982, "Subharmonics and Vortex Merging in Mixing Layers," J. Fluid Mech., **119**, pp. 443–473.
[2] Yang, Z., and Karlsson, S. K. F., 1991, "Evolution of Coherent Structures in a Plane Shear Layer," Phys. Fluids A, **3**(9), pp. 2207–2219.
[3] Raman, G., and Rice, E. J., 1991, "Axisymmetric Jet Forced by Fundamental and Subharmonic Tones," AIAA J., **29**(7), pp. 1114–1122.
[4] Gordeyev, S. V., and Thomas, F. O., 1999, "Temporal Subharmonic Amplitude and Phase Behavior in a Jet Shear Layer: Wavelet Analysis and Hamiltonian Formulation," J. Fluid Mech., **394**, pp. 205–240.
[5] Roos, F. W., and Kegelman, J. T., 1986, "Control of Coherent Structures in Reattaching Laminar and Turbulent Shear Layers," AIAA J., **24**(12), pp. 1956–1963.
[6] Bhattacharjee, S., Scheelke, B., and Troutt, T. R., 1986, "Modification of Vortex Interactions in a Reattaching Separated Flow," AIAA J., **24**(4), pp. 623–629.
[7] Hasan, M. A. Z., 1992, "The Flow Over a Backward Facing Step Under Controlled Perturbation: Laminar Separation," J. Fluid Mech., **238**, pp. 73–96.
[8] Zhou, M. D., Heine, C., and Wygnanski, I., 1996, "The Effects of Excitation on the Coherent and Random Motion in a Plane Wall Jet," J. Fluid Mech., **310**, pp. 1–37.
[9] Acharya, S., and Panigrahi, P. K., 2003, "Analysis of Large Scale Structures in Separated Shear Layer," Exp. Therm. Fluid Sci., **27**(7), pp. 817–828.
[10] Ho, C. M., Zohar, Y., Foss, J. K., and Buell, J. C., 1991, "Phase Decorrelation of Coherent Structures in a Free Shear Layer," J. Fluid Mech., **230**, pp. 319–337.
[11] Fiedler, H. E., and Mensing, P., 1985, "The Plane Turbulent Shear Layer with Periodic Excitation," J. Fluid Mech., **150**, pp. 281–309.
[12] Moffat, R. J., 1982, "Contributions to the Theory of Single-Sample Uncertainty Analysis," ASME J. Fluids Eng., **104**, pp. 250–260.

[13] Acharya, S., and Panigrahi, P. K., 2003, ''Analysis of Phase Jitter Evolution in a Reattaching Shear Layer,'' Exp. Fluids, **35**(3), 237–239.
[14] Nikitopoulos, D. E., and Liu, J. T. C., 1987, ''Nonlinear Binary-Mode Interactions in a Developing Mixing Layer,'' J. Fluid Mech., **179**, pp. 345–370.
[15] Hajj, M. R., Miksad, R. W., and Powers, E. J., 1992, ''Subharmonic Growth by Parametric Resonance,'' J. Fluid Mech., **236**, pp. 385–413.
[16] Eaton, J. K., and Johnston, J. P., 1981, ''Low Frequency Unsteadiness of a Reattaching Turbulent Shear Layer,'' *Proceedings of the Third International Symposium on Turbulent Shear Flows*, Davis, CA, pp. 162–170.
[17] Rajaee, M., and Karlsson, S. K. F., 1992, ''On the Fourier Space Decomposition of Free Shear Flow Measurements and Mode Generation in the Pairing Process,'' Phys. Fluids A, **4**(2), pp. 321–339.
[18] Antonia, R. A., and Luxton, R. E., 1971, ''The Response of a Turbulent Boundary Layer to an Upstanding Step Change in Surface Roughness,'' J. Fluid Mech., **48**(4), pp. 721–761.
[19] Antoniou, J., and Bergeles, G., 1988, ''Development of the Reattached Flow Behind Surface-Mounted Two Dimensional Prisms,'' ASME J. Fluids Eng., **110**, pp. 127–133.

Compressibility Effects on the Extended Crocco Relation and the Thermal Recovery Factor in Laminar Boundary Layer Flow

B. W. van Oudheusden
Department of Aerospace Engineering,
Delft University of Technology,
PO Box 5058, 2600 GB Delft, The Netherlands
e-mail: B.W.vanOudheusden@LR.TUDelft.nl

The relation between velocity and enthalpy in steady boundary layer flow is known as the Crocco relation. It describes that for an adiabatic wall the total enthalpy remains constant throughout the boundary layer, when the Prandtl number (Pr) is one, irrespective of pressure gradient and compressibility. A generalization of the Crocco relation for Pr near one is obtained from a perturbation approach. In the case of constant-property flow an analytic expression is found, representing a first-order extension of the standard Crocco relation and confirming the asymptotic validity of the square-root dependence of the recovery factor on Prandtl number. The particular subject of the present study is the effect of compressibility on the extended Crocco relation and, hence, on the thermal recovery in laminar flows. A perturbation analysis for constant Pr reveals two additional mechanisms of compressibility effects in the extended Crocco relation, which are related to the viscosity law and to the pressure gradient. Numerical solutions for (quasi-)self-similar as well as non-similar boundary layers are presented to evaluate these effects quantitatively.
[DOI: 10.1115/1.1637626]

1 Introduction

1.1 The Crocco Relation. The similarity which exists between the diffusive transport of momentum and heat in a boundary layer flow establishes a close link between the local values of flow velocity and enthalpy. This relation is usually reffered to as the Crocco-(Busemann) relation. Its derivation can be found in several standard text books covering the topic of high-speed viscous flow, like [1–5], and states, in essence, that for steady laminar boundary layer flow the enthalpy (h) can be expressed as a function of the velocity (u, in case of two-dimensional flow), for any viscosity function $\mu(T)$. It is strictly valid when the Prandtl number $Pr=1$ and with either an adiabatic wall (zero heat transfer), or zero pressure gradient. For two-dimensional flow and an adiabatic wall, which are the conditions considered here, the Crocco relation reduces to:

$$h=h_e+\frac{1}{2}(u_e^2-u^2) \tag{1}$$

where a subscript e refers to the conditions in the external stream. Hence, the Crocco relation reveals that for $Pr=1$ and in the absence of heat transfer at the wall, the total enthalpy $H=h+(1/2)u^2$ is constant across the boundary layer. Accordingly, the (wall) recovery factor r is equal to one, where r is defined as:

$$r=\frac{h_{aw}-h_e}{\frac{1}{2}u_e^2} \tag{2}$$

with h_{aw} the adiabatic wall enthalpy, which is equal in this case to H_e, the constant total enthalpy of the inviscid freestream. This result visualizes the concept of ''recovery'' as the conversion of meanflow kinetic energy into thermal energy in the decelerated viscous flow. In the case of the recovery factor being one, a perfect energy conversion hence takes place.

Contributed by the Fluids Engineering Division for publication in the JOURNAL OF FLUIDS ENGINEERING. Manuscript received by the Fluids Engineering Division Feb. 20, 2003; revised manuscript received Aug. 27, 2003. Associate Editor: T. B. Gatski.

The powerful concept of the Crocco relation is that, given the restrictions mentioned, it has a further general validity, in that it applies also under three-dimensional and compressible flow conditions. The Crocco relation may be further valid for turbulent flow as well, provided that in addition the turbulent Prandtl number is one [3,4]. The case of turbulent flow, however, is outside the scope of the present discussion [1].

1.2 The Extended Crocco Relation for $Pr\neq 1$. For arbitrary Prandtl number, the effect of Pr is commonly incorporated by applying a direct generalization of Eq. (1), which corresponds to the assumption that a constant recovery factor r can be applied throughout the entire viscous layer, implying:

$$h=h_e+r\frac{1}{2}(u_e^2-u^2) \tag{3}$$

$$H=H_e+(r-1)\frac{1}{2}(u_e^2-u^2). \tag{4}$$

The above result is exact for (compressible) Couette flow with constant Pr, see e.g., [6], in which case the convective derivatives are zero. The recovery factor r is then equal to the Prandtl number Pr.

For boundary layer flows this ''generalized Crocco relation'' has no exact validity, and is obtained only in an approximate sense [7]. In this approach the value of r is based on the thermal recovery at the wall, derived from theoretical studies of self-similar boundary layer solutions in constant-property flow to be approximately $r=Pr^{1/2}$, also in pressure gradient [8–10,5], while being valid with good approximation for compressible flow in zero pressure gradient as well [11,12].

A serious objection to this modification of the Crocco relation in boundary layer flows, however, is that the resulting enthalpy distribution violates the conservation of energy. According to this principle, the reduction of the total enthalpy near the wall due to the incomplete heat recovery ($r<1$ for realistic gases where $Pr<1$), must be balanced by a flow region where $H>H_e$, see [7,13], an effect which is not reproduced by an expression like Eq. (4). The creation of nonuniformities in total enthalpy in a flow is

also known as "energy separation" [13]. Apart from the diffusive effect considered here, unsteady pressure work may be a further and powerful mechanism for this, but unsteady effects are not considered here.

In an earlier paper [14], a modified expression was derived for the Crocco relation with Pr different from one, which establishes an asymptotically-complete first-order extension of the original Crocco relation. Its derivation was based on a perturbation analysis of self-similar solutions of the constant-property boundary layer equations, but showed to be valid for nonsimilar flows as well. The result of the analysis further confirmed the general asymptotic validity of the approximation $r=Pr^{1/2}$.

1.3 Compressibility Effects on the Recovery Factor. In the above mentioned study it was found, furthermore, that the effect of compressibility on the extended Crocco relation was only small in the case of zero pressure gradient flow. This result agrees with other analytical and experimental findings on the laminar recovery factor, as mentioned above, and which have led to the common notion that the $r=Pr^{1/2}$ approximation possesses a similar validity in compressible flows as well. As suggested by a number of sources, the compressibility effect may then sufficiently be described by taking only the temperature dependence of Pr into account ("the reference temperature method," see [2–4]). However, this effect is known to be only small in real gases and may be of the same order as the viscous effect for larger Mach numbers, as shown by Van Driest [13]. Furthermore, this finding of small compressibility effect may be only a fortuitous result, not amendable to more general compressible flow situations, as the flat-plate case on which it is based contains only a limited aspect of compressibility, in that only thermal effects are present but no pressure effects [15].

Relatively little attention appears to have been given to the systematic study of the pressure-gradient effect on the recovery factor in compressible flow. In the investigation of Herwig ([15], see also [5]) the effect of compressibility on the boundary layer was treated as a perturbation of incompressible (self-similar) solutions, by allowing for variable properties (viscosity, conductivity, density and specific heat). Equations were derived with which the sensitivity of the (velocity and temperature) solution to property variation can be assessed, as function of the Prandtl number and the pressure-gradient parameter β. Numerical data were provided for a limited number of combinations of Pr and β. Although quite general in its approach to the possible (independent) variation of fluid properties, the scope of the study is limited to small Mach numbers, while also the effect of pressure gradient on recovery is not clearly revealed. As to the effect of compressibility on recovery, only the flat-plate case is discussed explicitly, in which it agrees with other studies in literature regarding the effect of the variation of viscosity. The data provided in the paper further allow only a limited assessment of the effect of pressure gradient, as results are given only for a selected number of self-similar solutions with positive β. These results indicate that with increasing Mach number there is an additional decrease of the recovery factor, but that the effect is rather small.

An example of possible evidence of a noticeable effect of pressure gradient on the recovery in compressible flow, on the other hand, was discussed by White [3]. Results were given of numerical computations of the laminar boundary layer with a linearly decreasing freestream Mach number, which can be seen as the compressible extension of the Howarth boundary layer. An interesting result in particular was that the recovery factor near separation was reported to drop significantly, from the value $r=0.84$ under incompressible conditions to a value of $r=0.51$ for a reference freestream Mach number of 6. White explicitly attributes this effect to the pressure gradient. His explanation, viz. that the viscous dissipation at the wall is reduced near separation, however, cannot be the reason as this would equally apply to (compressible) flow with $Pr=1$, for which the strict Crocco relation (1) still applies. Moreover, viscous dissipation represents a direct transfer of mechanical into thermal energy and is therefore in itself not responsible for an incomplete recovery. Rather, it is the imbalance between thermal and mechanical diffusion which occurs when $Pr\neq 1$, which gives rise to variations in the total enthalpy [13].

The present study addresses the effect of compressibility in a systematic approach, based on the analysis of the transformed equations for general (non-similar) boundary layer flow. To reveal what are believed to be the basic mechanisms responsible for the compressibility effect, the analysis allows for variable density, conductivity and viscosity, while keeping the Prandtl number and specific heat constant, a common assumption in non-hypersonic flow applications. Apart from this limitation, the analytical approach is not restricted to small Mach numbers, in contrast to Herwig's study [15], of which some results will be used to corroborate findings of the present analysis. For comparison the analysis of constant-property ("incompressible") flow is included, which reproduces the results for general, non-similar flow obtained earlier [14]. In the case of compressible flow, two major mechanisms are identified that may invalidate the incompressible results, viz. the variation of fluid properties (density and viscosity) themselves, and a direct Mach number effect through the pressure gradient. Numerical computations of (quasi-) self-similar as well as non-similar boundary-layer solutions are presented to evaluate and illustrate the extent of these effects.

2 Governing Equations

The continuity, momentum and energy equations governing steady two-dimensional laminar compressible boundary layer flow with respect to a Cartesian coordinate frame (x,y), with (u,v) the corresponding velocity components, are given by:

$$\frac{\partial \rho u}{\partial x}+\frac{\partial \rho v}{\partial y}=0 \tag{5}$$

$$\rho u\frac{\partial u}{\partial x}+\rho v\frac{\partial u}{\partial y}=-\frac{\mathrm{d}p}{\mathrm{d}x}+\frac{\partial}{\partial y}\mu\frac{\partial u}{\partial y} \tag{6}$$

$$\rho u\frac{\partial h}{\partial x}+\rho v\frac{\partial h}{\partial y}=u\frac{\mathrm{d}p}{\mathrm{d}x}+\mu\left(\frac{\partial u}{\partial y}\right)^2+\frac{\partial}{\partial y}\frac{\mu}{Pr}\frac{\partial h}{\partial y}, \tag{7}$$

where p is the pressure, ρ the density and μ the dynamic viscosity. The external flow is adiabatic so that: $\mathrm{d}p/\mathrm{d}x=-\rho_e u_e \mathrm{d}u_e/\mathrm{d}x=\rho_e \mathrm{d}h_e/\mathrm{d}x$. Constant Prandtl number and specific heat is assumed, and the fluid is considered to behave as a perfect gas with enthalpy $h=c_pT$ and γ the ratio of specific heats.

2.1 Compressibility Transformation. The equations are subjected to a standard compressibility transformation, see e.g., [2] or [4], with transformed coordinates $\xi(x)$ and $\eta(x,y)$ defined according to:

$$\frac{\mathrm{d}\xi}{\mathrm{d}x}=\rho_e\mu_e u_e, \quad \frac{\partial\eta}{\partial y}=\frac{u_e}{\sqrt{2\xi}}\rho \tag{8}$$

Introducing the transformed stream function $f(\xi,\eta)$ defined by $f'(\eta)=u/u_e$, and the enthalpy function $g(\xi,\eta)=h/h_e$, the momentum and energy equations are given by:

$$(Cf'')'+ff''+\beta(g-f'^2)=2\xi\left(f'\frac{\partial f'}{\partial\xi}-f''\frac{\partial f}{\partial\xi}\right) \tag{9}$$

$$\frac{(Cg')'}{Pr}+fg'+\frac{u_e^2}{he}Cf''^2=2\xi\left(f'\frac{\partial g}{\partial\xi}-g'\frac{\partial f}{\partial\xi}\right) \tag{10}$$

A prime denotes differentiation with respect to η. The Chapman-Rubesin function C and the pressure-gradient parameter β are defined by:

$$C(\xi,\eta)=\frac{\mu\rho}{\mu_e\rho_e}, \quad \beta(\xi)=\frac{2\xi}{u_e}\frac{\mathrm{d}u_e}{\mathrm{d}\xi} \tag{11}$$

For the present study it is convenient and more appropriate to replace the enthalpy function g by an enthalpy recovery function θ [5,15,14]:

$$\theta = \frac{h - h_e}{\frac{1}{2}u_e^2} \tag{12}$$

It may be noted that the value of θ at the wall corresponds directly to the recovery factor r. The momentum Eq. (9) and the energy Eq. (10) can now be written as:

$$(Cf'')' + ff'' + \tilde{\beta}(G - f'^2) = 2\xi\left(f'\frac{\partial f'}{\partial \xi} - f''\frac{\partial f}{\partial \xi}\right) \tag{13}$$

$$\frac{(C\theta')'}{Pr} + f\theta' - 2\tilde{\beta}f'\theta + 2Cf''^2 = 2\xi\left(f'\frac{\partial \theta}{\partial \xi} - \theta'\frac{\partial f}{\partial \xi}\right) \tag{14}$$

with $\tilde{\beta}$ expressing the pressure gradient in terms of the freestream Mach number M_e:

$$\tilde{\beta} = \frac{2\xi}{M_e}\frac{\mathrm{d}M_e}{\mathrm{d}\xi} = (1 + \epsilon_M)\beta \tag{15}$$

The boundary conditions at the (adiabatic) wall are: $f = 0$, $f' = 0$ and $\theta' = 0$, while near the external flow ($\eta = \infty$) $f' = 1$ and $\theta = 0$ apply. The scaled enthalpy $g = h/h_e$ and total enthalpy $G = H/H_e$ relate to θ as:

$$g = 1 + \epsilon_M \theta \tag{16}$$

$$G = 1 + \alpha_M(\theta + f'^2 - 1) \tag{17}$$

where $\epsilon_M = (1/2)u_e^2/h_e = (1/2)(\gamma - 1)/M_e^2$ and $\alpha_M = (1/2)u_e^2/H_e = \epsilon_M/(1 + \epsilon_M)$, so that $\alpha_M < 1$. Note that $\epsilon_M = \alpha_M = 0$ for $M_e = 0$, and that as the Mach number increases to infinity, ϵ_M increases indefinitely as well, whereas α_M remains bounded. Regarding the above expressions, the same applies to g and G, respectively, as θ remains $\mathcal{O}(1)$ for an adiabatic wall. Because of this, the Mach number effect on the solution through the pressure gradient, as expressed in either (9) or (13), is likely to be smaller for the latter. Indeed, for a linear viscosity law and unity Prandtl number (hence, $C = 1$ and $G = 1$), this form of the f-equation then reduces exactly to the incompressible Falkner-Skan equation, cf. [16]. This indicates that $\tilde{\beta}$, rather than β, is the proper choice for the self-similarity pressure-gradient parameter for compressible flow, in that similarity may be obtained (approximately) for a constant value of $\tilde{\beta}$, rather than β.

2.2 Viscosity Law. As will be shown later on, the viscosity-temperature relation is very important for the compressibility influence on the Crocco relation. For Sutherland's viscosity law C can be evaluated as:

$$C = g^{1/2}\frac{1 + \overline{S}}{g + \overline{S}} \tag{18}$$

where: $\overline{S} = S/T_e = (1 + \epsilon_M)S/T_t$, with T_t the total temperature in the external flow and $S = 111$ K for air. For a general viscosity law, such as Sutherland's, the solution is a function of both M_e and T_e, but when the viscosity is expressed as a power law, $\mu/\mu_e = (T/T_e)^\omega$, the direct effect of T_e vanishes:

$$C = g^{\omega - 1} = (1 + \epsilon_M \theta(\eta))^{\omega - 1}. \tag{19}$$

It is for this convenient reason that the power-law function is often employed in analytical studies of the effect of varying properties. It should be remembered, however, that the accuracy of this expression is only limited in describing the true viscosity behavior, although an appropriately chosen value of ω may suffice as an approximate description of the variation of μ over a limited temperature range. Note furthermore from (19), that C increases with T when $\omega > 1$ and decreases when $\omega < 1$.

2.3 Asymptotic Solution Approach. A perturbation approach is used to investigate the effect of Prandtl number on the solution of the energy equation for Pr different from unity, in which the enthalpy function is expanded in an asymptotic series:

$$\theta(\eta) = \theta_0(\eta) + \epsilon\theta_1(\eta) + \epsilon^2\theta_2(\eta) + \ldots \tag{20}$$

with respect to the perturbation parameter $\epsilon = Pr - 1$. Substitution of the series into the enthalpy equation and collecting equal powers of ϵ then provides the equations which the subsequent terms have to satisfy. For each function θ_i the same boundary conditions apply, viz. $\theta_i' = 0$ at $\eta = 0$ and $\theta_i = 0$ for $\eta \to \infty$.

The particular purpose of this analysis is to relate enthalpy directly to velocity, by finding expressions for the first two terms of the asymptotic series for θ in relation to f. This approach provides a consistent asymptotic extension of the Crocco relation for Prandtl number different from (but near) unity. The procedure will first be applied in the next section to constant property flow, after which the case of variable properties will be addressed.

3 Constant Property (Incompressible) Flow

In constant property flow ρ and μ are taken constant so $C = 1$. A necessary requirement for this assumption is that the Mach number becomes vanishingly small ($M_e \to 0$). Hence, $g = G = 1$ and $\tilde{\beta} = \beta$, so that Eqs. (13) and (14) simplify to:

$$f''' + ff'' + \beta(1 - f'^2) = 2\xi\left(f'\frac{\partial f'}{\partial \xi} - f''\frac{\partial f}{\partial \xi}\right) \tag{21}$$

$$\frac{\theta''}{Pr} + f\theta' - 2\beta f'\theta + 2f''^2 = 2\xi\left(f'\frac{\partial \theta}{\partial \xi} - \theta'\frac{\partial f}{\partial \xi}\right) \tag{22}$$

Applying the asymptotic solution approach in this case, yields the following equations for the first two terms θ_0 and θ_1 of the expansion, Eq. (20):

$$\theta_0'' + f\theta_0' - 2\beta f'\theta_0 + 2f''^2 = 2\xi\left(f'\frac{\partial \theta_0}{\partial \xi} - \theta_0'\frac{\partial f}{\partial \xi}\right) \tag{23}$$

$$\theta_1'' + f\theta_1' - 2\beta f'\theta_1 - \theta_0'' = 2\xi\left(f'\frac{\partial \theta_1}{\partial \xi} - \theta_1'\frac{\partial f}{\partial \xi}\right) \tag{24}$$

The equations for subsequent terms can be obtained in a recursive way, as was shown in [14]. The zero-order solution θ_0 is identical to the solution for $Pr = 1$, so in correspondence with the original Crocco relation:

$$\theta_0 = 1 - f'^2 \tag{25}$$

which can be verified by evaluating Eq. (23). Substituting $\theta_0'' = -2f'f''$ into Eq. (24), the first-order problem reads:

$$\theta_1'' + f\theta_1' - 2\beta f'\theta_1 + 2(f'f'')' = 2\xi\left(f'\frac{\partial \theta_1}{\partial \xi} - \theta_1'\frac{\partial f}{\partial \xi}\right) \tag{26}$$

The solution for θ_1 found in [14]:

$$\theta_1 = \frac{1}{2}(1 - f'^2) - ff'' \tag{27}$$

can be verified to satisfy Eq. (26) in general.

3.1 Interpretation in Dimensional Properties. Returning to dimensional properties, and with substitution of the results that were obtained for θ_0 and θ_1, the Crocco relation and the recovery factor are expressed explicitly up to first order in ϵ as:

$$h = h_e + \frac{1}{2}(u_e^2 - u^2) + \frac{\epsilon}{2}\left(\frac{1}{2}(u_e^2 - u^2) - \frac{\psi}{\rho}\frac{\partial u}{\partial y}\right) + \mathcal{O}(\epsilon^2) \tag{28}$$

$$r = 1 + \frac{\epsilon}{2} + \mathcal{O}(\epsilon^2) \tag{29}$$

where ψ is the stream function defined by $\rho u = \partial\psi/\partial y$, with ρ constant in the case under consideration. The result Eq. (29) confirms the expression $r \approx Pr^{1/2}$ as an asymptotically correct first-order approximation for two-dimensional constant-property flow in general. After truncation of both series by neglecting the $\mathcal{O}(\epsilon^2)$ terms and subsequent elimination of ϵ, the relation between enthalpy and velocity can be written alternatively as:

$$h = h_e + r\frac{1}{2}(u_e^2 - u^2) - (r-1)\frac{\psi}{\rho}\frac{\partial u}{\partial y} \tag{30}$$

$$H = H_e + (r-1)\left(\frac{1}{2}(u_e^2 - u^2) - \frac{\psi}{\rho}\frac{\partial u}{\partial y}\right) \tag{31}$$

Comparison with the classic forms of the modified Crocco relation, see Eqs. (3) and (4), reveals that the classic modification incorporates only the first recovery part of the first-order term, but that the second part that expresses the energy migration towards the outer flow, is absent in them.

4 Variable Property (Compressible) Flow

The analysis of variable-property flow starts by the observation that also in this case $\theta_0 = 1 - f'^2$ must be the correct $\mathcal{O}(1)$ term of the expansion, as a direct consequence of the fact that the original Crocco relation (1) for $Pr = 1$ is valid for compressible flow as well. The equation for the first-order perturbation term θ_1 is now obtained by the same asymptotic solution approach, i.e. substitution of the expansion for θ, Eq. (20), into Eq. (14) with θ_0 given explicitly by Eq. (25).

When, following the constant-property analysis, we add to this the momentum Eq. (13) multiplied by $2f'$, all terms of $\mathcal{O}(1)$ are cancelled, where with reference to Eq. (17) G has been substituted by: $G = 1 + \epsilon\alpha_M\theta_1 + \mathcal{O}(\epsilon^2)$. Grouping in the remaining expression all terms of $\mathcal{O}(\epsilon)$ then yields the following equation for θ_1:

$$(C\theta_1')' + f\theta_1' - 2\tilde{\beta}(1-\alpha_M)f'\theta_1 + 2(Cf'f'')' = 2\xi\left(f'\frac{\partial\theta_1}{\partial\xi} - \theta_1'\frac{\partial f}{\partial\xi}\right) \tag{32}$$

To investigate the compressibility effects on θ_1, let the incompressible solution Eq. (27) be enhanced as:

$$\theta_1 = \frac{1}{2}(1 - f'^2) - ff'' + \theta_{1,c} \tag{33}$$

where $\theta_{1,c}$ is the additional component of θ_1 due to compressibility. By substituting Eq. (33) into Eq. (32) and adding to it, again following the constant-property analysis, the derivative of the product of the momentum Eq. (13) and f, the following transport equation for $\theta_{1,c}$ is obtained, neglecting $\mathcal{O}(\epsilon)$ terms:

$$(C\theta_{1,c}')' + f\theta_{1,c}' - 2\tilde{\beta}(1-\alpha_M)f'\theta_{1,c} + [C'ff'']' + 2\tilde{\beta}\alpha_M f'\left[\frac{1}{2}(1 - f'^2) - ff''\right] = 2\xi\left(f'\frac{\partial\theta_{1,c}}{\partial\xi} - \theta_{1,c}'\frac{\partial f}{\partial\xi}\right) \tag{34}$$

The last two terms on the left-hand-side of the equation act as source terms in the transport of $\theta_{1,c}$ and hence reveal the mechanisms responsible for deviations from the incompressible solution. To have these terms vanish irrespective of f, it is necessary that C is constant and either α_M or $\tilde{\beta}$ is zero. This is indeed obtained for the incompressible limit (with $C = 1$, $\alpha_M = 0$ and $\tilde{\beta}$ arbitrary), in which case Eq. (32) reduces to Eq. (26). Under compressible flow conditions it is fulfilled only in the case of zero pressure-gradient flow ($\tilde{\beta} = 0$) in combination with a linear dependence of viscosity on temperature ($C = 1$). A further interpretation of the individual source terms allows already at this point of the analysis a preliminary assessment of how the effects under consideration will qualitatively affect the incompressible results.

1. The first term expresses the direct effect of varying properties, which are the consequence of the temperature variation across the boundary layer. The fact that it is only the variation of the product $\rho\mu$ which is relevant, alleviates this ''thermal compressibility effect'' to a large extent, as ρ and μ show opposite thermal behavior: ρ decreases with temperature whereas μ increases. Indeed, for a linear viscosity-temperature relation the effect vanishes completely ($C = 1$). With the temperature gradient being negative everywhere in the boundary layer, C' is positive when the temperature-dependence of the viscosity is less than linear ($\omega < 1$) and negative when $\omega > 1$. Combination of Eq. (19) and (25) yields for the first source term in Eq. (34):

$$(C'ff'')' = -2\epsilon_M(\omega - 1)(g^{\omega-2}ff'f''^2)' + \mathcal{O}(\epsilon) \tag{35}$$

Near an adiabatic wall $(g^{\omega-2}ff'f''^2)'$ is positive. As a result, this effect will be to increase the local value of θ_1, and hence to increase the Prandtl number effect on the recovery factor, when $\omega < 1$. Concluding, for $Pr < 1$ a decrease of the recovery factor with freestream Mach number is predicted to occur when $\omega < 1$, and similarly, an increase when $\omega > 1$.

2. The second term reflects the effect of pressure gradient in combination with a direct Mach number influence through α_M. Its contribution to the recovery effect is easily interpreted, as to increase with both $\tilde{\beta}$ and α_M. For positive $\tilde{\beta}$ (negative pressure gradient) the compressibility effect therefore increases the Prandtl dependence, whereas for a negative $\tilde{\beta}$ (positive pressure gradient) it has a decreasing effect. Hence, again for $Pr < 1$, the recovery factor is expected to decrease in a negative pressure gradient, and to increase in a positive pressure gradient.

5 Numerical Investigation

A numerical investigation was made to obtain accurate solutions to the f- and θ-equations, in order to quantify the compressibility effects on the extended Crocco relation, in particular the influence of the pressure gradient and the viscosity relation on the recovery factor.

Numerical solutions are first presented for (quasi-)self-similar flow solutions, with the purpose of evaluating and illustrating the extent of the different effects that have been identified in the theoretical analysis. This may then serve for comparison when interpreting more general, i.e. nonsimilar, boundary layer solutions of which two examples will be considered in the present study.

5.1 Self-Similar Boundary Layer Calculations

Self-Similarity in Compressible Boundary Layers. From an analytical point of view the study of self-similar solutions is especially attractive as this allows the boundary layer problem to be treated in the form of a set of ordinary differential equations. A first requirement for self-similarity to be obtained in the (f,θ) formulation is that $\tilde{\beta}$ is constant, implying: $M_e \propto \xi^{\tilde{\beta}/2}$. However, for compressible flow the additional requirement is that G and C, hence g, must be self-similar as well. Regarding Eqs. (16) and (17) this means that both ϵ_M and α_M must be constants. Strict self-similarity in compressible flow is therefore only possible when M_e is constant, i.e. for zero pressure-gradient flow.

For a linear viscosity law, hence $C = 1$, further possibilities exist for self-similarity for the boundary layer problem in essentially the (f,G) formulation, as shown by Chapman and Rubesin [17]. In the present case, the use of a linear viscosity law relaxes the additional requirement to only G being self-similar, which can be achieved when any of the following conditions is satisfied:

1. $M_e \approx 0$: incompressible flow, with $G \approx 1$ as $\alpha_M \approx 0$.

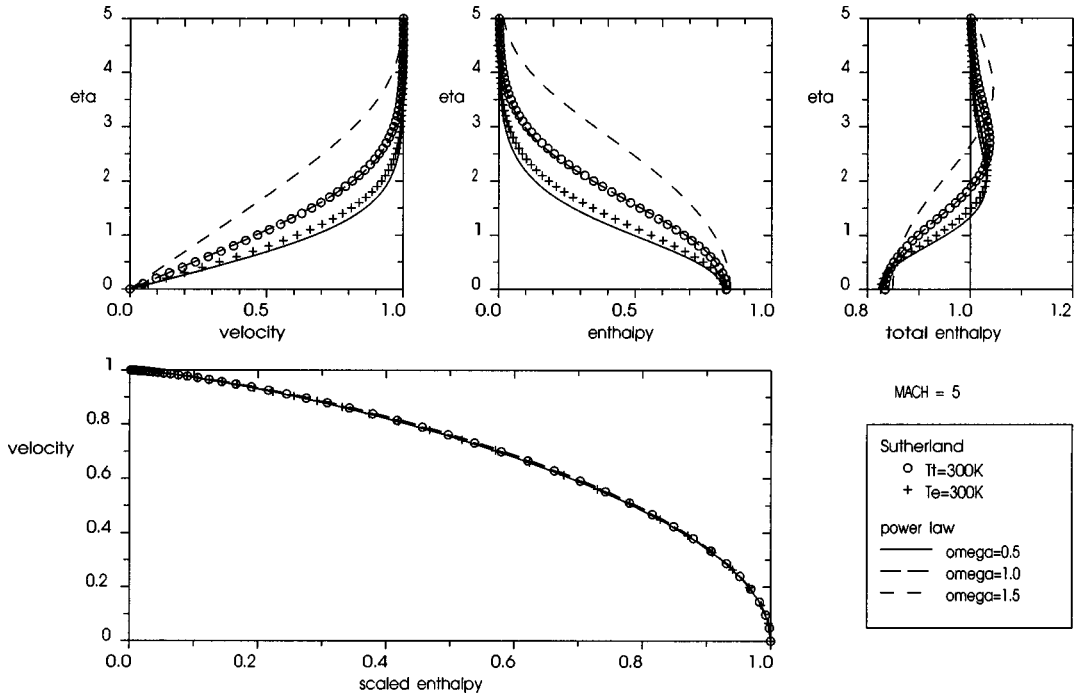

Fig. 1 Self-similar solutions for the transformed profiles of the velocity f', the enthalpy θ and the total enthalpy $\theta+f'^2$. Symbols indicate calculations with Sutherland's viscosity law, lines for the power-law, see legend in the figure ($Pr=0.7$, $\tilde{\beta}=0$, $M_e=5$).

2. $Pr=1$: in that case $G=1$ according to the original Crocco relation. The equations become identical to their incompressible form.

3. $M_e \gg 1$: $\alpha_M \approx 1$ remains nearly constant at large values of the Mach number. Hence, $G=\theta+f'^2$ is self-similar as well.

Evidently, for our present interest, which is the combined effect of compressibility and Prandtl number on thermal recovery, only the last case bears relevance.

The possibility of obtaining strict self-similarity in compressible flow, therefore, is very limited [18]. However, if the effect of changing M_e on the solution (in the transformed variables) is only small, self-similarity may occur in an approximate sense, referred to as "local similarity" [2]. It assumes that the solution is dominated by the effects which are represented by the local values of $\tilde{\beta}$ and M_e and that history effects, expressed by the terms involving ξ-derivatives, may be neglected. This concept will be exploited here for the study of the effect of the pressure gradient.

Results of the Calculations. For the calculations of the (quasi-) self-similar solutions a 5-point equidistant finite-difference scheme with fourth-order accuracy was employed. The coupled equations are solved iteratively by means of subsequent approximations. Convergence of the solutions is assumed when the value of $f''(0)$ between subsequent iterations does not change within a prescribed small value (typically taken 10^{-8}). Outer flow boundary conditions are applied at a finite value $\eta_{\max}$ taken sufficiently large so as to ensure that the final solution does not depend on it within the desired numerical accuracy. The results reported here have been obtained mostly with $\eta_{\max}=10$ and $\Delta\eta=0.1$ or 0.05 with grid refinement studies verifying that the error in the recovery factor was less than 10^{-6} for all cases considered.

All calculations have been performed for $Pr=0.7$ and $\gamma=1.4$, with variation of the free stream Mach number M_e and pressure-gradient parameter $\tilde{\beta}$. Different viscosity relations have been applied, such as Sutherland's law with $S=111$ K and taking either $T_t=300$ K or $T_e=300$ K constant (representative of either wind-tunnel or free flight conditions), as well as the power-law expression with different values for the exponent ω.

As an illustration, the (transformed) profiles of the velocity, enthalpy and total enthalpy, are given in Fig. 1 for the case $M_e=5$ and $\tilde{\beta}=0$ (flat plate flow). Note that for this specific case, the result for the linear viscosity law ($\omega=1$) is identical to the incompressible (=Blasius) solution, and all compressibility effects are contained in the coordinate transformation, Eq. (8).

The viscosity law is seen to have quite a strong effect on the boundary layer scaling, notwithstanding the use of transformed coordinates, with the thickness scale increasing with ω in approximate proprotion to $\sqrt{C_w}$, see [3]. This stretching can be explained by introducing in Eq. (13) the approximation $C(\eta)\approx C_w$ (for the adiabatic wall case the temperature in a large part of the boundary layer is approximately equal to that at the wall). The solution is then given by $f(\eta)=\sqrt{C_w}f_0(\eta/\sqrt{C_w})$ where f_0 is the incompressible solution satisfying the Blasius equation: $f_0'''+f_0f_0''=0$.

Although this stretching evidently affects the value of $f''(0)$ directly, the recovery factor $r=\theta(0)$ is seen to vary only slightly. It may be noted further, that the result for Sutherland's viscosity law with $T_t=300$ K resembles closely that for the linear viscosity law, whereas for $T_e=300$ K the results are close to the high-temperature approximation $\omega=0.5$. The lower graph confirms that the effect is basically a stretching of the normal coordinate and that the normalized velocity-enthalpy correlation (where the enthalpy variation has been scaled with its value at the wall) is virtually the same for all cases. Very similar results were obtained for other values of $\tilde{\beta}$.

The compressibility effect on $f''(0)$ and r, as a function of Mach number, pressure gradient and viscosity law, is further illustrated in Fig. 2 for three different values of $\tilde{\beta}$, viz. $\tilde{\beta}=0$ (top), $\tilde{\beta}=1$ (center) and $\tilde{\beta}=-0.15$ (bottom). The labeled curves correspond to the power-law viscosity with different values of ω, while the dashed line indicates the results for Sutherland's law with T_t

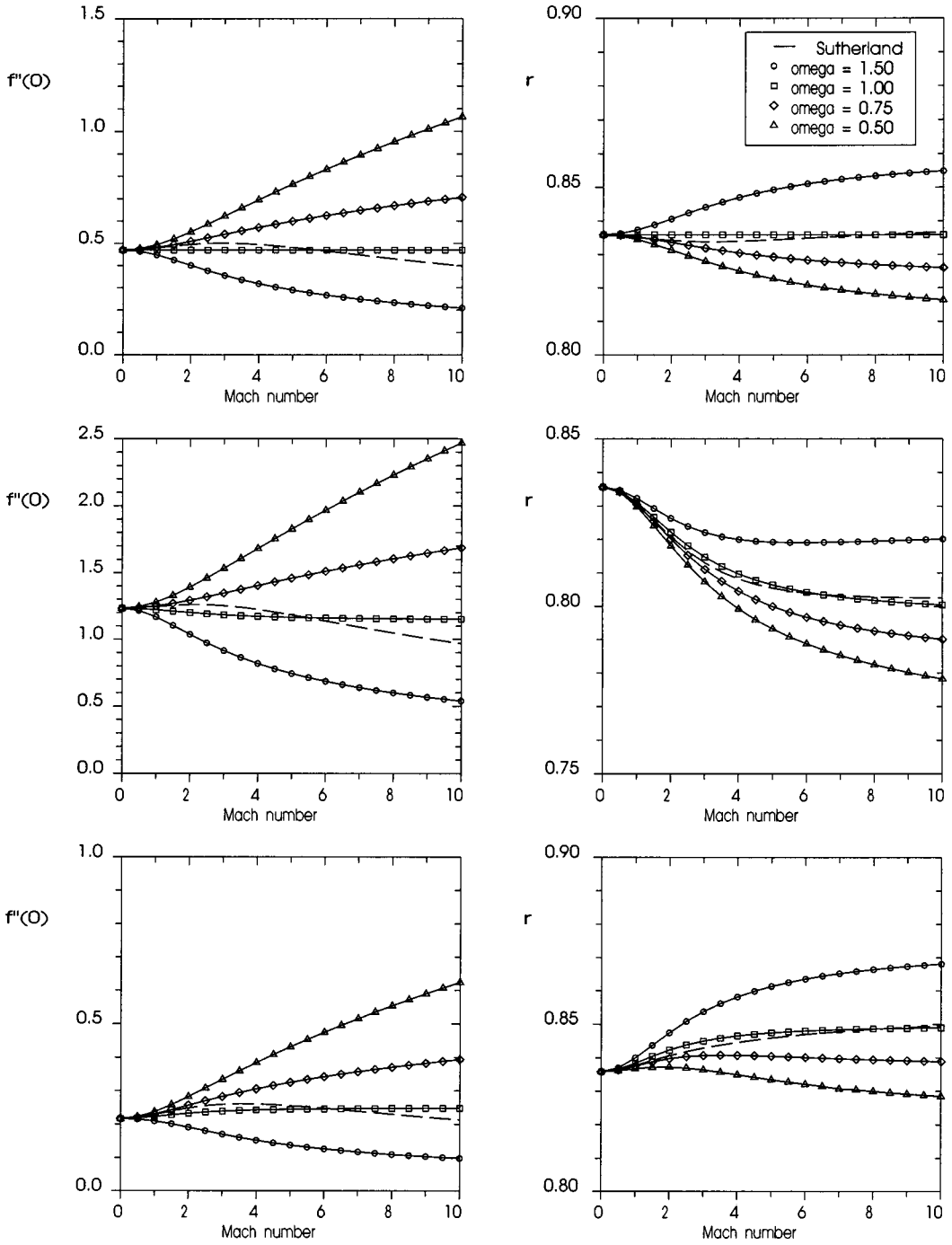

Fig. 2 Effect of Mach number, viscosity law and pressure gradient on $f''(0)$ and recovery factor r; top: $\tilde{\beta}=0$, center: $\tilde{\beta}=1$, bottom: $\tilde{\beta}=-0.15$; dashed lines indicate results for Sutherlands's law with $T_t=300$ K ($Pr=0.7$).

$=300$ K. The latter is seen to agree approximately with the power law for $\omega=1$, as had been also observed in Fig. 1. The influence of the viscosity law is most clearly revealed for the zero pressure-gradient case $\tilde{\beta}=0$, where only the thermal compressibility effect is present. The effect on the recovery factor is seen to agree with the predicted behavior, viz. that r increases with M_e when $\omega>1$, whereas r decreases with M_e when $\omega<1$.

Comparing in the diagrams for different $\tilde{\beta}$ the specific curve for the linear viscosity law ($\omega=1$) is of special interest to the present study, as here only the pressure-gradient effect is present. It can be observed that the f solution does not vary strongly with M_e, as evidenced by the values of $f''(0)$ which are nearly constant. This is in agreement with the remarks made earlier regarding the choice of $\tilde{\beta}$ as the proper similarity pressure-gradient parameter. The prediction that r increases with M_e when $\tilde{\beta}$ is negative and that r decreases with M_e when $\tilde{\beta}$ is positive is indeed confirmed by the numerical results.

The other curves reveal the results of combined thermal and pressure-gradient compressibility effects. It is observed that when

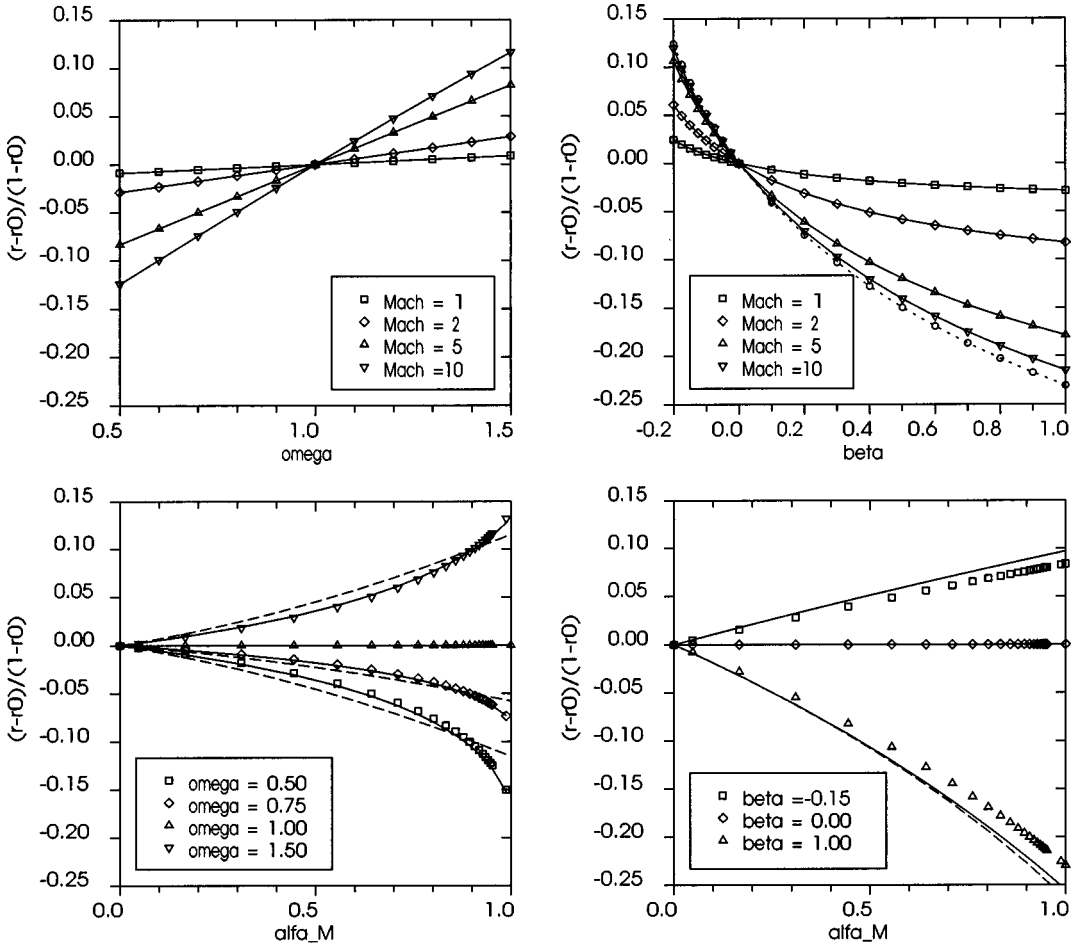

Fig. 3 Normalized recovery factor data and Mach number scaling; left: effect of viscosity-law exponent ω in flat-plate flow ($\tilde{\beta}=0$); right: effect of pressure-gradient parameter $\tilde{\beta}$ with linear viscosity law ($\omega=1$), dotted line indicates $M_e=\infty$. Symbols apply to numerical data for $Pr=0.7$. Lines in the bottom diagrams represent the exact (solid) or approximate (dashed) results of the perturbation analysis.

$\tilde{\beta}<0$ and $\omega>1$ both effects act to amplify each other in increasing the recovery factor, whereas when $\tilde{\beta}>0$ and $\omega<1$ they both act to decrease the recovery factor.

In the lower Mach number range, up to about 2, the present data find quantitative support from Herwig's results [15] under the same conditions ($Pr=0.7$, $\gamma=1.4$), for example regarding the effect of viscosity law on the flat-plate recovery factor (Herwig: $r=0.8358-0.0032(1-\omega)M_e^2$) and the stagnation-point recovery factor with linear viscosity law (Herwig: $r=0.8356-0.0041M_e^2$).

Normalized Results and Mach Number Scaling. The results for these two cases that reveal each of the compressibility mechanisms separately, that is variation of ω with $\tilde{\beta}=0$ or variation of $\tilde{\beta}$ when $\omega=1$, have been normalized in Fig. 3. The recovery data have been scaled as $(r-r_0)/(1-r_0)$, where r_0 is the incompressible recovery factor at this value of Pr. According to the preceding theory this removes the first order dependence on Pr, as:

$$\frac{r-r_0}{1-r_0}\approx -2\,\theta_{1,c}(0)+\mathcal{O}(\epsilon) \tag{36}$$

making the results only a function of ω, $\tilde{\beta}$ and M_e. The left diagram on the top row shows the effect of the power-law exponent ω on the recovery factor, for different values of the Mach number. The right diagram similarly shows the effect of the pressure-gradient parameter $\tilde{\beta}$. The dotted line indicates the result for infinitely large Mach number (note that with $C=1$, the present formulation allows to take the theoretical limit $M_e=\infty$, hence $\alpha_M=1$, without introducing singular behavior of the boundary layer scaling). For a constant value of the Mach number, the variation of r with ω (for $\tilde{\beta}=0$) is observed to be very nearly linear, whereas for the variation with $\tilde{\beta}$ (for $\omega=1$) there is a distinct nonlinearity.

An analysis of scaling effects is undertaken by a further scrutinization of Eq. (34). It has to be noted that, although the perturbation expansion approach of Eq. (20) has removed the direct Pr dependence, the coefficients in Eq. (34) still contain an implicit dependence on Pr, through the functions f and C, in addition to the explicit and implicit dependence on $\tilde{\beta}$, Mach number and viscosity law. For the flat-plate case ($\tilde{\beta}=0$) it was already observed that the major effect of the visosity law is that of producing a stretching of the boundary layer scale. Introducing the same stretching into Eq. (34) together with the approximations $C\approx C_\omega$ applied to the first term and $C'\approx(\omega-1)C_\omega(g'/g)$ applied to the fourth term, yields:

$$\theta''_{1,c}+f_0\theta'_{1,c}-2\tilde{\beta}(1-\alpha_M)f'_0\theta_{1,c}-(\omega-1)\alpha_M\left[\frac{2f_0f'_0f''^2_0}{1-\alpha_Mf'^2_0}\right]'$$
$$+\tilde{\beta}\alpha_Mf'_0[1-f'^2_0-2f_0f''_0]=0 \tag{37}$$

where Eqs. (19) and (25) have been used to evaluate g, neglecting terms of $\mathcal{O}(\epsilon)$ and higher. Similarly, with $G=1+\mathcal{O}(\epsilon)$, to the

Table 1 Sensitivity parameters for ω and $\tilde{\beta}$ effect on the recovery factor according to the approximate approach of Eq. (37).

	$\tilde{\beta}=-0.15$		$\tilde{\beta}=0$		$\tilde{\beta}=1$	
	c_1	c_2	c_1	c_2	c_1	c_2
$\alpha_M=0$	0.149	0.724	0.131	0.518	0.110	0.183
$\alpha_M=0.25$	0.177	0.703	0.156	0.518	0.134	0.197
$\alpha_M=0.5$	0.199	0.684	0.181	0.518	0.166	0.215
$\alpha_M=0.75$	0.216	0.665	0.206	0.518	0.213	0.237
$\alpha_M=1$	0.229	0.647	0.231	0.518	0.297	0.265

same order of approximation f_0 corresponds to the incompressible solution for this value of $\tilde{\beta}$, satisfying the equation $f_0'''+f_0f_0''+\tilde{\beta}(1-f_0'^2)=0$. In the above approximate form of the transport equation for $\theta_{1,c}$ the dependence on $\tilde{\beta}$, ω and Mach number (the latter through α_M) has been made explicit, apart from the implicit effect of $\tilde{\beta}$ on f_0. This means that for a given value of $\tilde{\beta}$ the equation is linear in $\theta_{1,c}$, allowing the effect of the source terms to be evaluated independently of each other. This observation suggests the following functional form for the normalized recovery factor:

$$\frac{r-r_0}{1-r_0}\approx(\omega-1)\alpha_M\cdot c_1(\tilde{\beta},\alpha_M)-\tilde{\beta}\alpha_M\cdot c_2(\tilde{\beta},\alpha_M) \qquad (38)$$

where the parameters c_1 and c_2 are positive-valued functions of $\tilde{\beta}$ and α_M (hence, M_e). Table 1 gives some computed values for c_1 and c_2 obtained from solving Eq. (37).

To illustrate the Mach number scaling the diagrams in the bottom row of Fig. 3 display the normalized recovery data versus α_M for the two cases considered. The symbols refer to the exact numerical data obtained at $Pr=0.7$ while the lines indicate the results of the perturbation analysis; solid lines are for the exact approach of Eq. (34), while the dashed lines indicate the approximate approach of Eq. (37) using the incompressible velocity profile. It is seen that for the viscosity-law effect the exact perturbation approach corresponds closely with the numerical data indicating that the contribution of the higher order terms of the perturbation in Eq. (36) is small. The approximate approach, although capturing all basic features, differs notably as a result of the approximate modeling of the *C*-terms in Eq. (34). For the pressure-gradient effect, on the other hand, there is only little difference between exact and approximate perturbation results, which is not surprising as the *C*-effect is absent here and the approximation only involves replacing the true velocity profile by the incompressible solution, which are very similar. The deviation between perturbation results and the numerical data, however, is larger in this case, suggesting that here higher-order terms have a larger influence. The latter assumption was verified by repeating the analysis for a value of Pr closer to unity (results not shown), where indeed resulted in smaller differences between the numerical data and the first-order perturbation results.

5.2 Nonsimilar Boundary Layer Calculations. In order to investigate nonsimilar boundary-layer development the numerical scheme was extended by replacing the ξ-derivatives in Eqs. (13) and (14) by backward finite-differences, which allows the boundary development to be computed by means of downstream marching from the appropriate self-similar solution at the initial station $\xi=0$. For the present computations, a three-point backward scheme was used, which is second-order accurate in the step size $\Delta\xi$. Grid studies were used to verify that the results obtained for the recovery factor remained accurate within 10^{-4}, with the possible exception of the direct environment of the separation location where the boundary layer equations develop singular behavior [3].

Regarding the present formulation of the equations, the external flow is most conveniently expressed as $M_e(\xi)$, as this allows all relevant freestream-related parameters required for the computation to be determined without the need to explicitly evaluate the (Mach number and viscosity-law dependent) coordinate transformation, Eq. (8). Two different cases will be considered: $M_e=M_0(1+\xi)$ and $M_e=M_0(1-\xi)$. Both start as a flat plate flow, but the first is an accelerating flow, while the second is a flow decelerating towards separation. For incompressible flow ($M_0=0$) the corresponding velocity distribution in physical coordinates are $u_e=U_0e^x$ and $u_e=U_0e^{-x}$, respectively, starting from $x=0$. The accelerated flow is computed on the interval $0\leqslant\xi\leqslant1$, over which the Mach number doubles and $\tilde{\beta}$ increases from 0 to 1. The decelerated flow is computed until separation occurs. The results of the computations (again with $Pr=0.7$ and $\gamma=1.4$) have been depicted in Fig. 4. The diagrams on the left show the development of $f''(0)$, the nondimensional velocity gradient at the wall, while the diagrams on the right give the results for the recovery factor *r*. The solid lines indicate the computational results for the linear viscosity law, for different values of the reference Mach number M_0, with the dotted line corresponding to $M_0=\infty$. The dashed lines depict the results for $\omega=0.75$, for two values of the Mach number.

The computations show that the Mach number effect on the velocity solution is small, due to the use of transformed coordinates, especially for the linear viscosity law (in that case it is completely absent when in addition $Pr=1$, see [16]). The results for the recovery factor confirm the findings of the self-similar analysis, in that the recovery factor decreases in a favorable pressure gradient and increases in an adverse pressure gradient, to a similar extent as in the self-similar solutions.

6 Conclusions

The effect of compressibility on the validity of the extended Crocco relation for laminar flow was investigated. The original Crocco relation, which applies when $Pr=1$ is valid for both compressible and incompressible flow alike. For constant-property flow a generally valid, first-order extension of the Crocco relation can be formulated, which describes the effect of non-unity Prandtl number. Two compressibility effects were identified, which give rise to deviations from this general constant-property result.

Firstly, there is a thermal compressibility effect, which is caused directly by the variation of viscosity and density across the boundary layer. In flat-plate flow, this is the only effect present. The way in which this affects the Crocco relation, and in particular the recovery factor, depends on the viscosity law. For a power-law relation between viscosity and temperature, and assuming that $Pr<1$, we find that *r* increases with M_e when $\omega>1$, and decreases with M_e when $\omega<1$.

The second compressibility effect is that of the pressure gradient in combination with a direct Mach number influence. As a result of this, the recovery factor is expected to decrease in a negative pressure gradient, and to increase in a positive pressure gradient, again for $Pr<1$.

These analytical predictions were confirmed by numerical solutions for (quasi) self-similar boundary layer solutions. These reveal the magnitude of both effects to be of the same order for typical situations. For the range of parameter values studied, these effects are observed to increase or decrease the Pr-effect on the recovery factor by an amount of 10% to 20%. In absolute sense, hence, the pressure-gradient effect is concluded to be only limited. For example, with $Pr=0.7$ and a linear viscosity law, the recovery factor in stagnation point flow $\tilde{\beta}=1$ is found to decrease from 0.836 at incompressible conditions to a minimum value of 0.798 in the limit of $M_e=\infty$, which is a change of 4.5%. Similarly, for $\tilde{\beta}=-0.20$ which is for a self-similar laminar flow near separation, it increases to a maximum value of 0.856 (2.4% change).

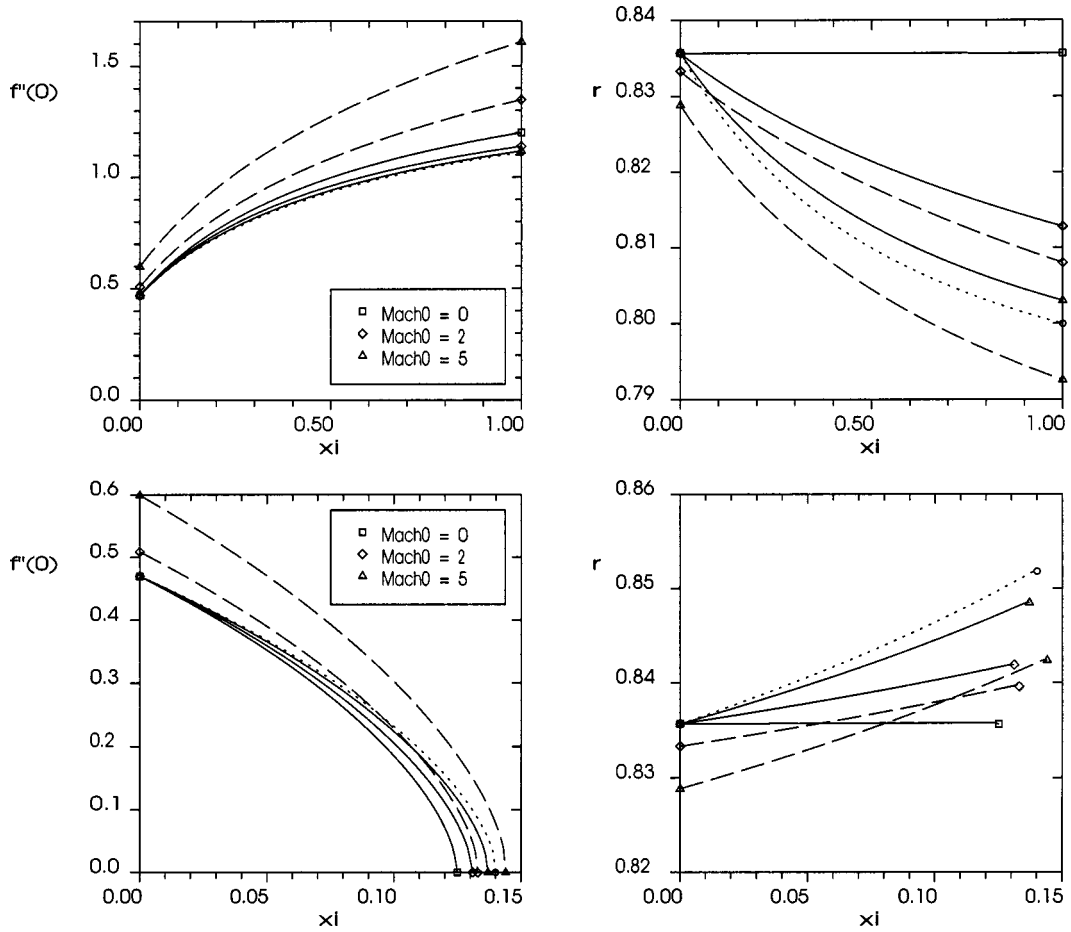

Fig. 4 Nonsimilar boundary layer development ($Pr=0.7$); top: $M_e=M_0(1+\xi)$; bottom: $M_e=M_0(1-\xi)$. Solid lines are for $\omega=1$ (dotted line indicates $M_0=\infty$), dashed lines are for $\omega=0.75$.

Additional computations for non-similar (developing) boundary layers revealed no significant effect of nonsimilarity on the above conclusions.

Reduced Recovery Factors Near Separation. To come back to the reduction of recovery factors near separation, as reported by White and referred to in the introduction, the present results are not in support of such a trend. Flow separation occurs in an adverse pressure gradient, which on the contrary is predicted to increase the recovery factor. The present analysis further suggests the pressure gradient effect to be only moderate, and that there is no strong effect of nonsimilarity.

Closer study reveals that this discrepancy with White's findings can be attributed to the difference in the modeling of the temperature dependence of the fluid properties, notably that of the specific heat. In the present analysis both the Prandtl number and the specific heat are assumed to be constant, so that conductivity and viscosity follow the same law. In White's calculations, on the other hand, also a constant Prandtl number was taken, but the viscosity and thermal conductivity were each modeled by a power law with different values of the exponent. This implies that the specific heat, $c_p=Pr\cdot k/\mu$, is not constant, but instead increases with temperature. As a consequence, a certain rise in enthalpy corresponds to a smaller increase in temperature than with a constant specific heat. This may then, incorrectly, be interpreted as a reduction in the recovery factor. If the recovery mechanism is assumed to be described by a relation of the type: $c_p(T)\mathrm{d}T=-r\mathrm{d}((1/2)u^2)$, then, taking $r=r_0$ constant and $c_p\propto T^n$, the apparent value $\tilde{r}$ of the recovery factor, based on the adiabatic wall temperature increase, would then be:

$$\tilde{r}=\frac{T_{aw}/T_e-1}{\epsilon_M}=\frac{(1+r_0(n+1)\epsilon_M)^{1/n+1}-1}{\epsilon_M} \tag{39}$$

With the values used by White, $Pr=0.71$, $n=0.144$ and taking $r_0=\sqrt{Pr}=0.84$, the apparent recovery factor $\tilde{r}$ would then be found to drop to 0.71 at $M_e=6$ ($\epsilon_M=7.2$). Also, expanding Eq. (39) for small Mach numbers gives an approximation $\tilde{r}\approx r_0-0.07nM_e^2$, which is similar to what is obtained when evaluating Herwig's results [15] for these conditions ($\tilde{r}\approx 0.836-0.07nM_e^2$). This confirms that the observed reduction of the recovery factor is not to be attributed to the effect of the pressure gradient, as originally suggested, but to that of varying specific heat.

References

[1] Dorrance, W. H., 1962, *Viscous Hypersonic Flow*, McGraw-Hill.
[2] Anderson, J. D., 1989, *Hypersonic and High Temperature Gas Dynamics*, McGraw-Hill.
[3] White, F. M., 1991, *Viscous Fluid Flow*, 2nd edn. McGraw-Hill.
[4] Schetz, J. A., 1993, *Boundary Layer Analysis*, Prentice Hall.
[5] Schlichting, H., and Gersten, K., 1979, *Boundary-Layer Theory*, 8th edn. Springer.
[6] Smits, A. J., and Dussauge, J. P., 1996, *Turbulent Shear Layers in Compressible Flow*, American Institute of Physics.
[7] Van Driest, E. R., 1952, "Investigation of the Laminar Boundary Layer in Compressible Flow Using the Crocco Method," *NACA TN 2597*.
[8] Tifford, A. N., and Chu, S. T., 1952, "On Heat Transfer, Recovery Factors, and Spin for Laminar Flows," J. Aeronaut. Sci., **19**, pp. 787–789.
[9] Brun, E. A., 1956, "Quelques considérations sur la convection de la chaleur aux grandes vitesses et aux températures élevées," *Selected Combustion Problems, Vol II*, AGARD, Pergamon Press, pp. 185–198.
[10] Le Fur, B., 1960, "Convection de la chaleur en régime laminaire dans le cas

d'un gradient de pression et d'une température de paroi quelconques, le fluide étant à propriétés physiques constantes,'' Int. J. Heat Mass Transfer, **1**, pp. 68–80.
[11] Kaye, J., 1954, ''Survey of Friction Coefficients, Recovery Factors and Heat-Transfer Coefficients for Supersonic Flow,'' J. Aeronaut. Sci., **21**, pp. 117–129.
[12] Van Driest, E. R., 1959, ''Convective Heat Transfer in Gasses,'' *High Speed Aerodynamics and Jet Propulsion, Volume V, Turbulent Flows and Heat Transfer*, C. C. Lin, ed., Princeton University Press, pp. 339–427.
[13] Eckert, E. R. G., 1986, ''Energy Separation in Fluid Flows,'' Int. Commun. Heat Mass Transfer, **13**, pp. 127–143.
[14] Van Oudheusden, B. W., 1997, ''A Complete Crocco Integral for Two-Dimensional Laminar Boundary Layer Flow Over an Adiabatic Wall for Prandtl Numbers Near Unity,'' J. Fluid Mech., **353**, pp. 313–330.
[15] Herwig, H., 1987, ''An Asymptotic Approach to Compressible Boundary-Layer Flow,'' Int. J. Heat Mass Transfer, **30**, pp. 59–68.
[16] Cohen, C. B., and Reshotko, E., 1956, ''Similarity Solutions for the Compressible Laminar Boundary Layer With Heat Transfer and Arbitrary Pressure Gradient,'' *NACA Rept 1293*.
[17] Chapman, D. R., and Rubesin, M. W., 1949, ''Temperature and Velocity Profiles in the Compressible Laminar Boundary Layer With Arbitrary Distribution of Surface Temperature,'' J. Aeronaut. Sci., **16**, pp. 547–565.
[18] Li, T. Y., and Nagamatsu, H. T., 1955, ''Similar Solutions of Compressible Boundary-Layer Equations,'' J. Aeronaut. Sci., **22**, pp. 607–616.

Circular Dynamic Stereoscopy and Its Application for Fluid Measurement

Kikuhito Kawasue
e-mail: kawasue@cc.miyazaki-u.ac.jp
Miyazaki University,
1-1 Gakuen Kibanadai Nishi,
Miyazaki, 889-2192 Japan

Yuichiro Oya
Japan Fluid Engineering Laboratory,
339-30 Kosasa, Kitamatsuura,
Nagasaki 857-0401 Japan

Takakazu Ishimatsu
Nagasaki University,
1-14 Bunkyo,
Nagasaki, 852-8521 Japan

By attaching a refractor to the lens of a Video Capture Device (e.g., CCD Video Camera) it is possible to record optical displacements from the original position of any object (tracer particle) within the image plane. If the refractor is physically rotated around the optical axis at high speed, the tracer particles create annular streaks due to the effect caused by the refractor's circular shift. The perceived displacements are added to the image being recorded by the Video Capture Device (VCD). Additionally, these displacements are directly related to the distance between the VCD and the particle being measured: the magnitude of displacement on the image plane being inversely proportional to the distance between the VCD and point of measurement. Since the radius of each annular streak, of a point being measured, is inversely proportional to its distance from the VCD, it is therefore possible by analyzing these annular streaks, to determine the three dimensional positional information of the point. Thus the radius of the annular streaks on the image plane determines the z coordinate, while the geometric center provides the x and y coordinates. The theory and setup of such a measuring system is subsequently presented, and the measurement of a moving surface, such as moving water, is used to demonstrate a typical application of such a system. [DOI: 10.1115/1.1637632]

1 Introduction

The use of 3-D information obtainable by computer imaging systems is attractive in various fields. Moreover, automatic detection of such information has been, and continues to be, one of the primary aims of computer engineering. However, up to now, only a few typical methods have been developed for obtaining 3-D information. One such system is based on stereovision, using two or more CCD cameras [1,2], yet another is based on the slit-ray projection method [3,4]. The stereovision system measures the difference between matching pairs of points in frames viewed from different angles. However, one difficulty related to this type of system is accurately determining the matching pairs of points in each frame. This can also be problematic for computer processing because there may be several possible choices of matching points. In the slit-ray projection method, the object being measured is reconstructed from multiple images each of which consists of a slice (slit-ray) of the original image taken at various different positions. Quantitative measurement is established by taking into consideration the geometric relationship between the VCD and the structured light (slit-ray). Using this method, the object being measured must remain stationary while the structured light is scanned over the surface of the object. Therefore in general, moving objects cannot be measured using the slit-ray projection method. However, some systems are capable of indirectly measuring a moving surface, such as water, by projecting a color-coded pattern onto the surface which is subsequently used as points of reference [5–8]. These systems are capable of measuring the gradient of the water surface at high spatial resolutions, but as such systems are easily influenced by outside light disturbances, special precautions must be taken. Other three-dimensional measurement systems, that use a single CCD-Camera employing specialized aperture masks, have been used in robot vision applications [9] and in fluid measurement [10], etc. These are based on the use of a pattern projected onto the objects and an annular-hole or multi-pin-hole mask placed in the aperture of the camera lens. Any illuminated point, which is not in the plane of focus, is viewed as a circle in the case of the annular-aperture mask method and as multiple points in the case of the multi-pin-hole aperture mask method. The diameter of the circle or the distance between the points in the (CCD) image gives the depth (z), and the geometrical center provides the x and y coordinates. While the system is compact and consists of a low number of components, lack of clarity in the image cannot be avoided since this method relies on the blurring phenomenon to obtain its depth.

In this paper, a new technique for measuring the instantaneous three-dimensional positions of multiple points by analyzing a single image is introduced. The main feature of this technique is the use of a single VCD attached to an image shifting apparatus [11]. By introducing a refractor onto the VCD lens, the image of any point being measured is displaced on the image plane; this displacement is directly related to the distance between the VCD and the point being measured [12,13]. The magnitude of displacement on the image plane is inversely proportional to the distance between the VCD and the point being measured. When the refractor is rotated physically at high speed, the points being measured appear in the image as annular streaks. This is due to the change in focal position induced by the rotational shift; which is added to the image by the VCD during the recording process. Since the radius of each annular streak is inversely proportional to the distance of the point being measured from the VCD, each annular streak thus describes the 3-D information of the point. Three-dimensional information can therefore be calculated by analyzing each of the annular streaks. That is, the centers and radii of each annular streak in the image can be converted into their respective 3-D world coordinates (x,y,z). A high level of confidence and reliability is possible because the difficult task of matching the relative points between different frames is not necessary. This method has been applied to the measurement of moving tracer particles in flow analysis—with satisfactory results being obtained. The measurement of a moving surface, such as moving water, is subsequently presented as an application of the proposed measurement system. Measurement is possible using the phenomenon of this circular dynamic method and a multi laser spot projector; the results obtained suitably demonstrating the feasibility of this method.

Contributed by The Fluids Engineering Division for publication in the ASME JOURNAL OF FLUIDS ENGINEERING. Manuscript received by the Fluids Engineering Division December 4, 2002; revised manuscript received September 11, 2003. Associate Editor: A. K. Prasad.

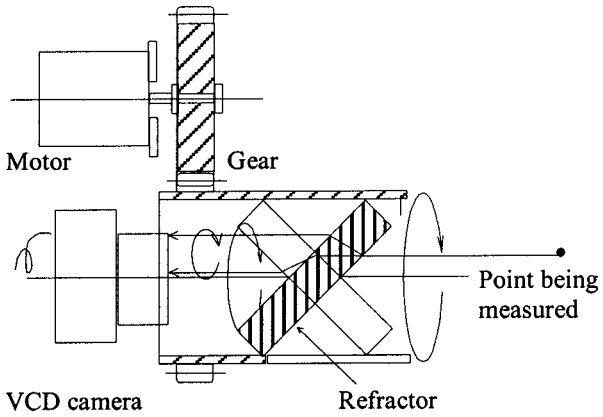

Fig. 1 System setup

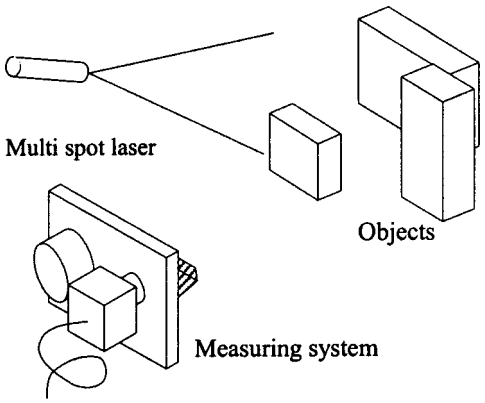

Fig. 3 Experimental setup using multiple laser spots

2 Circular Dynamic Stereoscopy

A simplified setup of the imaging system is shown in Fig. 1. Introducing a refractor onto the VCD lens displaces any point being measured in the image by a distance corresponding to the distance between the VCD and the actual point being measured. The displacement r in the image is inversely proportional to the distance D between the point being measured and the VCD. This is given by:

$$D = \frac{f \cdot d}{r} \tag{1}$$

where f is the focal length of the VCD and d is the magnitude of the image shift caused by the refractor. As the refractor is physically rotated at high speed around the optical axis of the VCD lens, the points being measured appear as annular streaks in the image.

Figure 2 shows two examples of the streak effect. The two distinctive circular image streaks are produced depending on whether the point being measured is stationary or moving, In the case where the point being measured is stationary, a circular streak is produced having a diameter inversely proportional to the distance between the actual point and the VCD (see Eq. (1)).

However, nonstationary points describe a spiral streak. If the point being measured is moving from left to right, the spiral streak is drawn from left to right, and the radius of the streak varies depending on the distance to the actual point. The locations and radii of the spiral streaks in the image are related to the three-dimensional locations of the points being measured, i.e., the pitch and size variations of the streaks are directly related to the three dimensional ''velocities'' of the points.

Figure 3 shows an example of the system set-up. Multiple laser spots are projected onto the surface of objects to be measured and these spots are recorded by the circular dynamic stereoscopic system. Figure 4(*a*) shows multiple laser spots projected onto the surfaces of a set of objects and Fig. 4(*b*) shows the circular shifts produced by the system. The smaller annular streaks indicate laser spots on the surfaces of more distant objects, while the bigger annular streaks are indicative of laser spots on nearer objects.

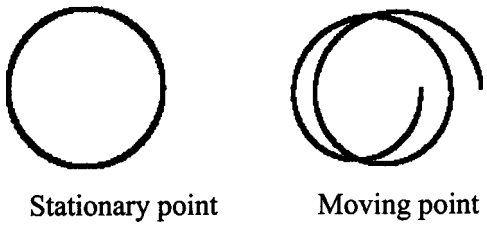

Fig. 2 Spiral image

3 Image Processing

3.1 Analysis of the Streaks in a Single Image. Image processing is relatively easy if the points being measured are relatively sparse. In cases where the points being measured are more densely grouped, for example tracer particles used in Particle Tracking Velocimetry (PTV), the streaks in the image can easily overlap each other. However, by taking into consideration that the segments of annular streaks are concentric, each streak can be extracted automatically using the following procedure.

An intensity gradient is first estimated for all locations in the image and then graded at a certain threshold level in order to extract the positions of the most significant edges of the annular streaks. Vector lines normal to the segment of the annular streak are then generated two-dimensionally. The slope of the normal lines, along the streak edge, can be calculated using the components of intensity gradient for each segment of the annular streaks from:

$$\theta = \tan^{-1}(g_y / g_x) \tag{2}$$

where g_x and g_y are the local components of the intensity gradient.

The calculated point data from along the normal lines are then stored in a cache called a ''Parameter Space.'' Figure 5 shows an example of overlapping annular streaks and edge vector normal lines. Since the edge normal lines converge at the center of the annular streaks, peaks resulting from this data accumulation in the Parameter Space can be interpreted as possible centers. The Parameter Space is then graded at a certain threshold level to extract

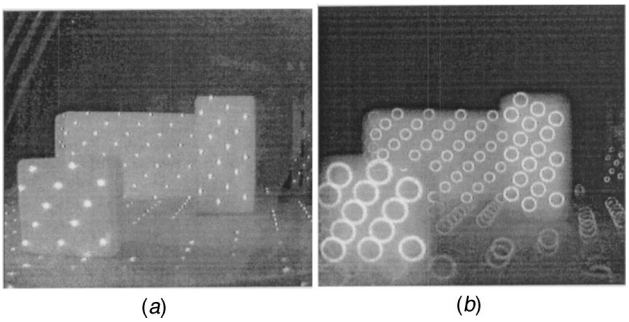

Fig. 4 Example images of multiple laser spots: (*a*) Multiple laser spots projected onto the surfaces of objects; and (*b*) Image with circular shift.

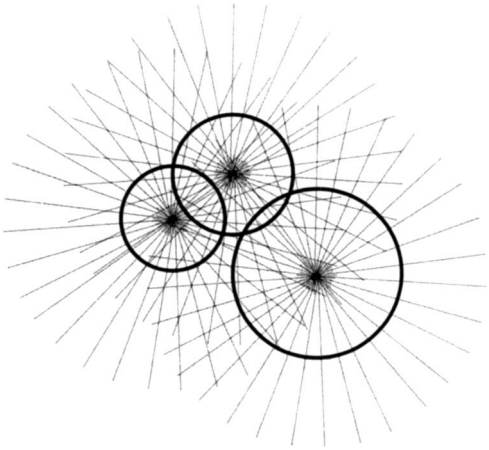

Fig. 5 Annular streaks showing lines projected from edge normals

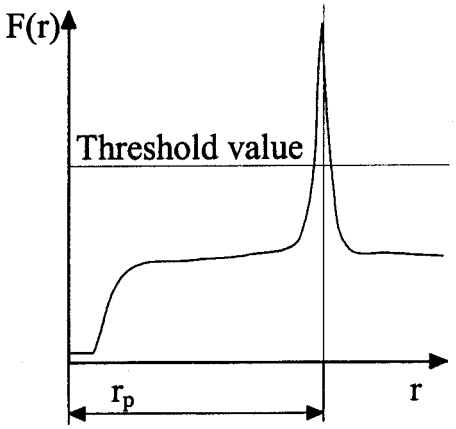

Fig. 7 Accumulation of pixel intensities along a streak

any concentrations of data called ''blobs'' that include a peak. Each concentration blob is then labeled and peaks in each blob are identified as the centers of annular streaks.

The positions of the peaks in the blobs are calculated to sub-pixel accuracy by:

$$x_c=\frac{\Sigma\, x\cdot f_p}{\Sigma\, f_p}\qquad y_c=\frac{\Sigma\, y\cdot f_p}{\Sigma\, f_p}\qquad f_p>\text{certain threshold value} \tag{3}$$

where p is a point located at (x,y) and f_p is the accumulated amount of possible centers at p. Once all of the centers of the annular streaks are found, each streak can then be easily extracted regardless of overlapping.

Since each streak is circular, streak diameter can be measured multiple times at various angles. For improved accuracy the final radius can better to be determined by considering all these radii at various angles. This set of mathematical operations enables highly accurate measurement. To simplify the operation, the following two-step method is adopted in this system.

In the first step, the accumulation of pixel intensity at a distance r from the center point Po is calculated from:

$$F(r)=\sum_{\theta=0}^{2\pi} f(r,\theta) \tag{4}$$

where $f(r,\theta)$ is pixel intensity at (r,θ). This method is also illustrated in Fig. 6.

In the second step, the graph of $F(r)$, as shown in Fig. 7, is plotted from the results of (4). Pixels on the annular streak directly correspond to the center point, i.e., they have the same distance from the center position. The positon of each peak in the graph therefore directly relates to the radius of each annular streak r_p.

The position of each peak in $F(r)$ is calculated to sub-pixel accuracy by:

$$r_p=\frac{\Sigma\, F(r)\cdot r}{\Sigma\, F(r)}. \tag{5}$$

The center (x_c,y_c) and radius r_p of each circular streak obtained using this procedure are converted to world coordinates (x_w,y_w,z_w) by:

$$\begin{bmatrix} x_w \\ y_w \\ z_w \end{bmatrix}=\frac{d}{r_p}\begin{bmatrix} x_c \\ y_c \\ f \end{bmatrix} \tag{6}$$

where d is the magnitude of the shift of the refractor and f is the focal length of the VCD.

3.2 Analysis of Streaks on Consecutive Images. Dynamic information can be obtained by analyzing consecutive images. When the points being measured are in motion, spiral streaks appear in the field image. If the rotation of the refractor is faster than the movement of the points being measured, then the points appear as annular streaks in each successive image, and the approximate center and radius of each streak can be calculated as described in Section 3.1. To process the image data of this type, use is made of the approximation technique as shown in Fig. 8. If the rotational frequency of the refractor is synchronized to the frame rate of the VCD, the streaks and blobs, generated by the accumulation of ''edge normal line'' data, have similar shape and value between consecutive images. The position of the blob indicates the position of point being measured without any circular shift, i.e., its absolute position in space-time. Corresponding matching pairs are determined by using the correlation method between blobs, and in some cases between annular streaks. If the

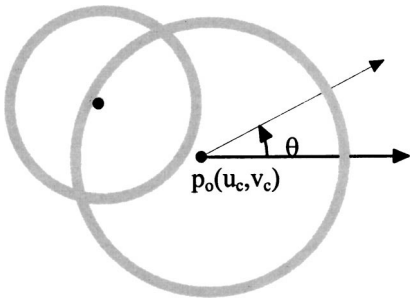

Fig. 6 Measurement of the size of an annular streak

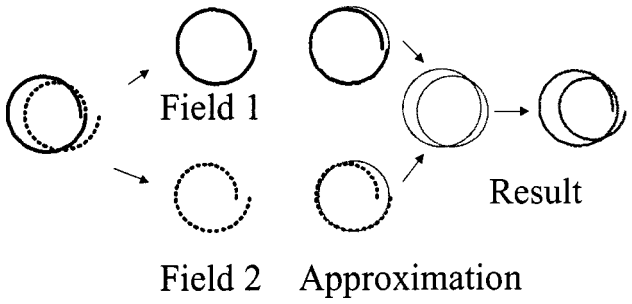

Fig. 8 Analysis of spiral streaks

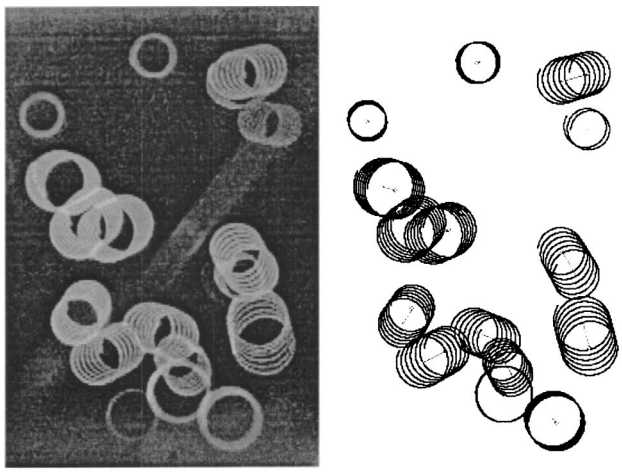

(*a*) (*b*)

Fig. 9 Examples of the streaks associated with tracer particles: (*a*) Recorded image; and (*b*) Analysis result.

points being measured are relatively sparse, the corresponding points can easily be determined by considering the magnitude of the movements and the correlation values between the blobs. However, if the points being measured are densely positioned, some difficulty may exist in accurately determining the correct matching points. In these cases, the size and shape of the annular streaks must be taken into consideration in order to determine the appropriate points.

After identifying the corresponding streaks, spiral equations are generated by considering the radii of streaks, the displacement of blobs between field images, and the rotational frequency of the refractor. Information extracted from the spiral streaks is thus converted into three-dimensional motional data. Figure 9(*a*) shows spiral streaks corresponding to moving tracer particles in flowing water and Fig. 9(*b*) shows the results derived from the analysis from the spiral streaks reconstructed on a computer display.

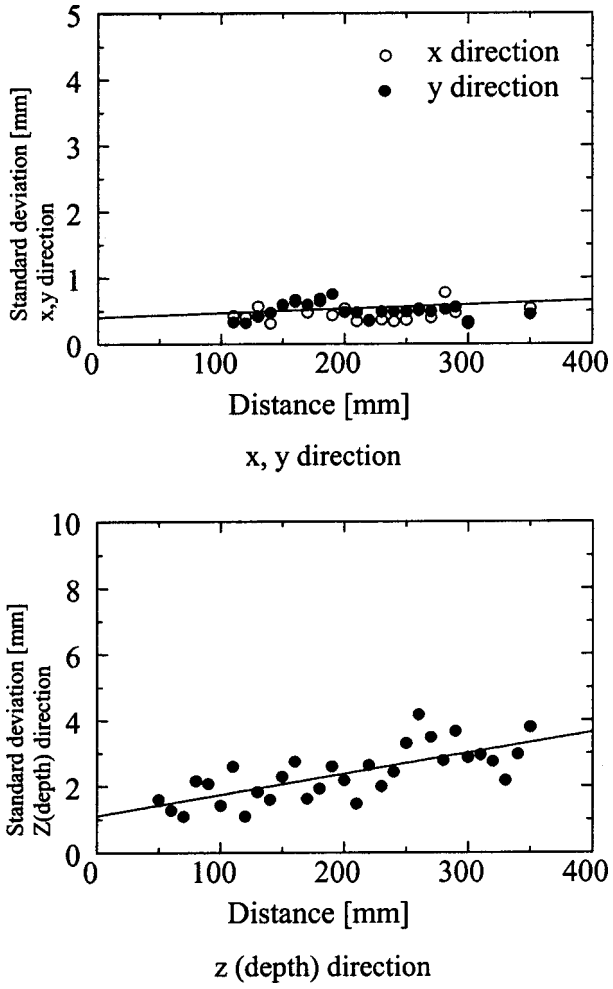

Fig. 10 Accuracy of the measurement system

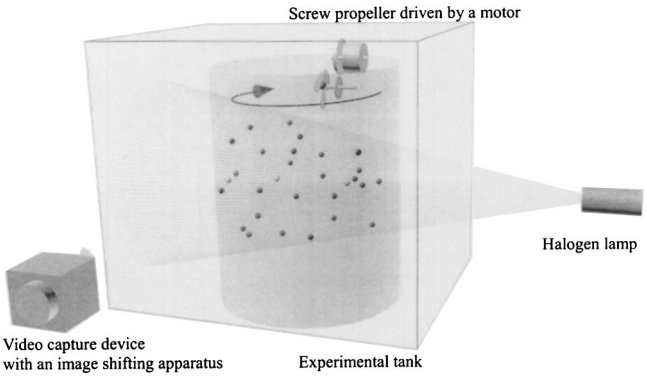

Fig. 11 Experimental setup

4 Experiments

4.1 Evaluation of Measurement Accuracy. To evaluate the feasibility of the system, the following experiment was conducted. A plane board was placed parallel to and at a fixed distance from the image plane of the VCD. Points to be measuring were illuminated on the surface of the board using a laser spot beam. The laser spots were observed as annular streaks using the circular dynamic stereoscopic system. A Pentium III, 800 MHz computer was used to store the image data (at a resolution of 512×512 pixels), and to calculate the positions of the laser spots.

The depth of the board was varied from 50 mm to 350 mm at intervals of 10 mm: the results are shown in Fig. 10. The horizontal and vertical (x,y) measurements, which are parallel to the image plane and relate directly to the center position of the annular streaks, are efficiently determined because the data can be read reliably and directly from the VCD image array. Since the depth (z) is measured from the size of an annular streak, the accuracy is restricted by the resolution and size of the streak.

A small systematic error is also apparent in the original result. It is constant bias, which occurs in the process of calibration; however, by taking some know reference point measurements the bias can be eliminated. Figure 10 shows the results (random error) after eliminating this systematic error. This graph shows the accuracy of the current automatic measurement system and may be improved by applying a more optimized processing algorithm. Almost 10% error as a function of the distance is included in the results, yet the cause of this error is from inaccuracies in data extraction from the streaks due to the overlapping or lack of clarity of the image. If even more accurate results are required, the operator needs to be involved manually in the analysis.

4.2 Particle Tracking Velocimetry Using Circular Dynamic Stereoscopy. Measurement of tracer particles in water is the primary aim of this system (Particle Tracking Velocimetry [14]). By measuring the positions of the tracer particles at different times, the three-dimensional velocity distribution within a flow can be measured. Figure 11 shows the experimental setup used to demonstrate the measuring ability of the system. The dis-

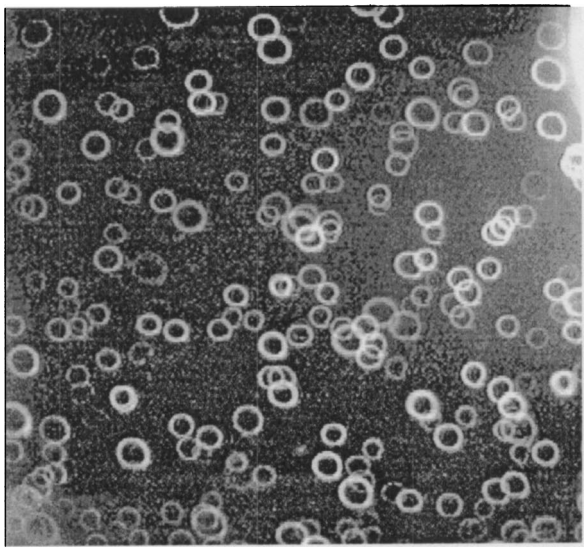

(*a*)

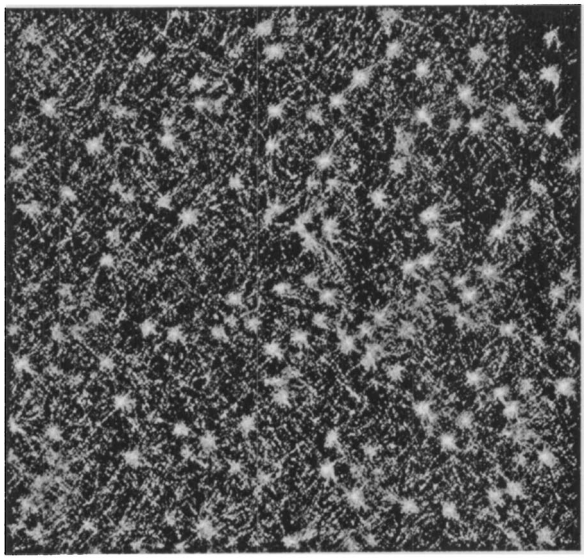

(*b*)

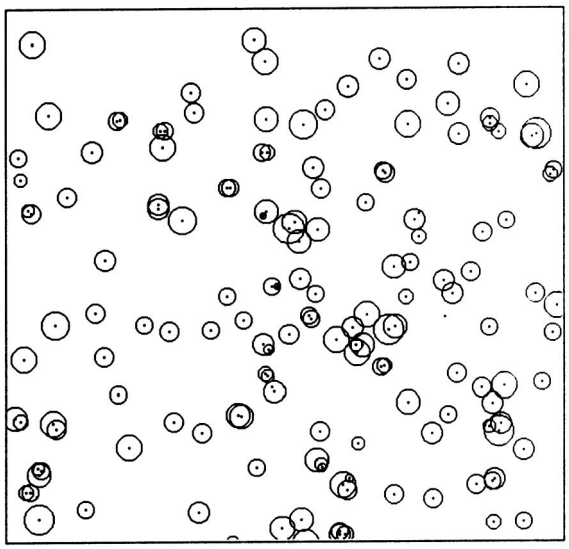

(*c*)

Fig. 12 (*a*) Particle streaks; (*b*) Lines in the direction of edge normal; and (*c*) Estimated center and size of streaks.

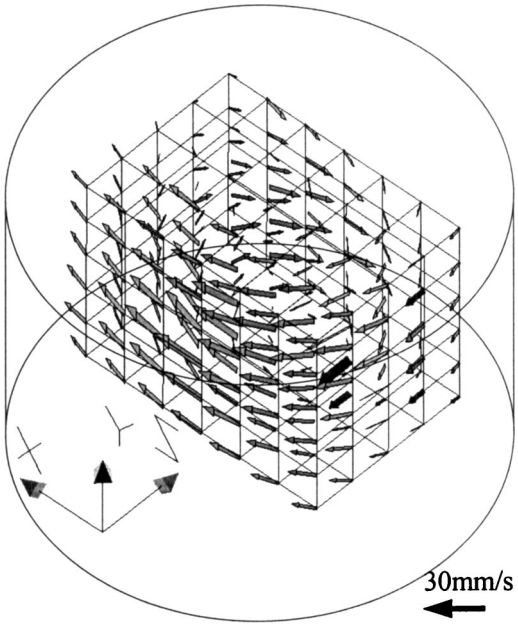

Fig. 13 Velocity distribution within the cylinder tank

tance between the center of the tank and the VCD is approximately 250 mm. Polystyrene tracer particles of 0.2 mm or less in diameter are scattered onto the water. The tracer particles have a specific gravity of 1.03, so that they may be considered neutrally buoyant in water. A cylindrical tank of 200 mm in diameter is placed inside the rectangular tank and both tanks are filled with water to avoid any distortion of the image. Water in the cylinder tank is set into motion via a screw propeller driven by a motor situated on top of the cylinder tank. As the rotation of the refractor on the VCD becomes faster than the movement of the tracer particles, the particles are drawn as annular streaks in the image. An example of the ensuing particles streaks is shown in Fig. 12(*a*). The accumulation of lines in the direction of edge normal is shown on Fig. 12(*b*). Even though the image was dark, due to the conditions of the experiment, 80% of the tracer particles were recognized and there positions measured. The extrapolated information regarding the center of the particle streaks and the size of the streaks is shown graphically in Fig. 12(*c*). The velocity distribution within the cylinder is shown in Fig. 13. Velocity vectors are interpolated by taking into consideration the position of the tracer particles and the velocity vector of each tracer particle. This demonstrates the applicability of the system to Particle Tracking Velocimetry for fluid measurement.

4.3 Surface Measurement of Water Movement. The experimental setup is shown in Fig. 14. Aluminum powder (20 μm) was introduced onto the surface of the water. The powder formed a thin film on the water surface and moved with the wave motion of the water. Multiple laser spots (30 mW) were then projected onto the surface of the water, containing the aluminum powder, which subsequently caused the lights to be reflected. Figure 15(*a*) shows an image of the multiple laser spots on the moving surface and Fig. 15(*b*) shows the resultant stereoscopic image containing the circular shift. Figure 16 shows two consecutive images reconstructions of the surface of the water.

5 Conclusion

Circular dynamic stereoscopy has many advantages that enable three-dimensional measurement using a single VCD. Annular streaks are recorded using this system, with the radii of the annular streaks directly related to the distance from the VCD. Radii of the annular streaks are inversely proportional to distance from the

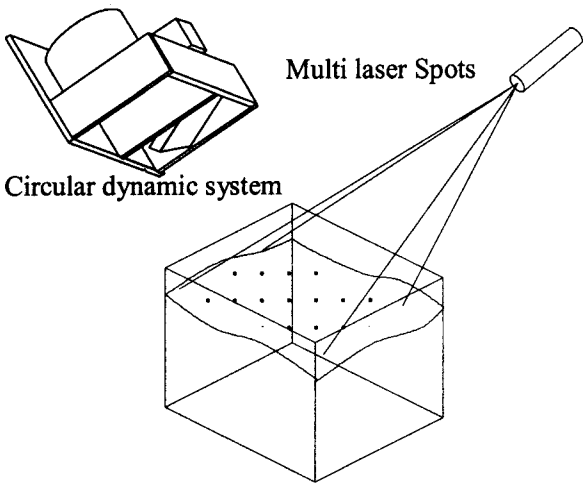

Fig. 14 Experimental setup for measurement of a moving surface

VCD, and this distance can thus be measured using image-processing techniques. Since three-dimensional information can be extracted from a single image, dynamical motion, such as moving particles or a moving surface, can be measured. The system is thus expected to be a useful tool for fluid dynamics such as PTV. Experimental results demonstrate the feasibility of the system.

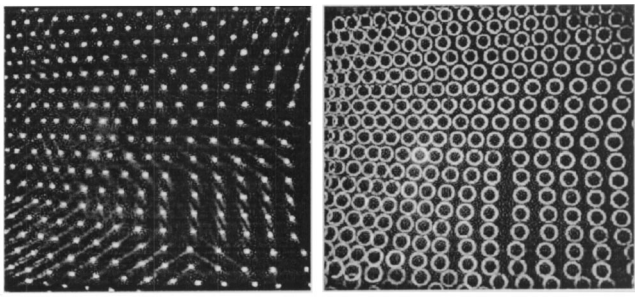

(*a*) (*b*)

Fig. 15 Example images of multiple laser spots on the surface of water: (*a*) Multiple laser spots; and (*b*) Multiple laser spots with circular shift.

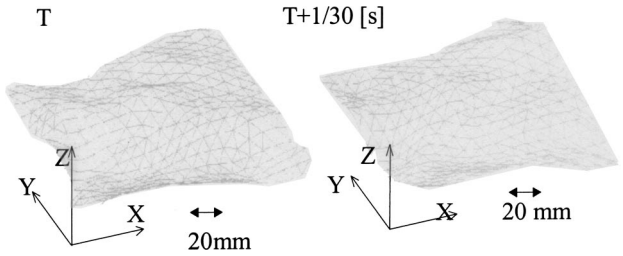

Fig. 16 Experimental results of surface measurement of a water wave

Acknowledgments

This work was partly supported by the Ministry of Education for Scientific Research under grant numbers 11555056 and 11792013.

References

[1] Davies, E. R., 1990, *Machine Vision: Theory, Algorithms, Practicalities*, Academic Press, San Diego, CA.
[2] Torras, C., 1992, *Computer Vision: Theory and Industrial Applications*, Springer-Verlag.
[3] Wu, M. F., and Sheu, H.-T., 1998, ''Representation of 3D Surface by Two-Variable Fourier Descriptors,'' IEEE Trans. Pattern Anal. Mach. Intell., **20**(8), pp. 858–863.
[4] McCallum, B. C., Fright, W. R., Nixon, M. A., and Price, N. B., 1996, ''A Feasibility Study of Hand-Held Laser Surface Scanning,'' *Proceedings of Image and Vision Computing New Zealand*, Lower Hutt, pp. 103–108.
[5] Zhang, X., and Cox, C. S., 1994, ''Measuring the Two-Dimensional Structure of a Wavy Water Surface Optically: A Surface Gradient Detector,'' Exp. Fluids, **17**, pp. 225–237.
[6] Zhang, X., Dabiri, D., and Gharib, M., 1996, ''Optical Mapping of Fluid Density Interface: Concepts and Implementations,'' Rev. Sci. Instrum., **67**(5), pp. 1858–1868.
[7] Zhang, X., 1996, ''An Algorithm for Calculating Water Surface Elevations From Surface Gradient Image Data,'' Exp. Fluids, **21**, pp. 43–48.
[8] Dabiri, D., and Gharib, M., 2001, ''Simultaneous Free-Surface Deformation and Near-Surface Velocity Measurements,'' Exp. Fluids, **30**, pp. 381–390.
[9] Rioux, M., and Blais, F., 1986, ''Compact Three-Dimensional Camera for Robotic Applications,'' J. Opt. Soc. Am. A, **3**(9), pp. 1518–1521.
[10] Willert, C. E., and Gharib, M., 1992, ''Three-Dimensional Particle Imaging With a Single Camera,'' Exp. Fluids, **12**, pp. 353–358.
[11] Kawasue, K., and Ishimatsu, T., 1997, ''3-D Measurement of Moving Particles by Circular Image Shifting,'' IEEE Trans. Ind. Electron., **44**(5), pp. 703–706.
[12] Kawasue, K., Shiku, O., and Ishimatsu, T., 1998, ''Range Finder Using Circular Dynamic Stereo,'' *Proceedings of International Conference of Pattern Recognition*, pp. 774–776.
[13] Kawasue, K., 1998, ''Position and Motion Measurement Using Circular Dynamic Stereo,'' *Proceedings of International Conference on Control, Automation, Robotics and Vision*, pp. 1583–1587.
[14] Kawasue, K., Ishimatsu, T., and Shih, C., 1994, ''Fast Processing Technique of Particle Image Velocimetry,'' *FLUCOME '94*, pp. 209–214.

On the Leak Through a Spiral-Groove Metallic Static Ring Gasket

S. Geoffroy

M. Prat
e-mail: prat@imft.fr

Institut de Mécanique des Fluides de Toulouse,
UMR CNRS-INP/UPS No. 5502
avenue du Professeur Camille Soula
31400 Toulouse, France

The diffusive and viscous leaks through a model spiral groove static ring gasket are studied analytically. This system is characterized by a transition from a leak through radial passages to a leak following the spiral groove as the load increases. The study concentrates on the transition. The results indicate a sharp ("critical") transition with variations of several order of magnitudes in the leak flow rates for small changes in the contact area, i.e. the applied load. It is also shown how results for a diffusive leak and a viscous leak can be combined for identifying the transition. The influence of surface errors of form (waviness) is also considered. Although generally detrimental to tightness, it is however shown that errors of form could be beneficial to tightness for the high loads if their amplitudes are slightly smaller than the groove average depth.
[DOI: 10.1115/1.1637627]

1 Introduction

Metallic static gaskets are used extensively as primary seals in critical joint applications in many industries where severe conditions such as extreme temperature (low temperature associated with cryogenic fluid and high temperature in exhaust lines) impose full metallic parts instead of classical elastomeric O-rings. For instance, these gaskets are widely used in rocket engines, in nuclear power plants to seal the successive fluid circuits as well as in some very specific high tech applications, such as for example high energy accelerators, [1]. Despite their technological importance, studies on static metallic gaskets are scarce in the published literature. Butcher [2] presented the basic principles of static gaskets including the effect of applied load to close up the seal and showed the importance of the plastic displacement of surface roughness. More recently Yanagisawa et al. [3] experimentally studied the leakage of gas through metallic gaskets and they showed that the presence of a soft metal coating is very beneficial. Most of the studies concentrated on the mechanical aspects of the problem (surface roughness deformation, areas of contact between the surfaces, influence of a soft metal coating . . .). The studies on the modelling of the leak are still scarcer and are generally limited to a basic leakage path geometry, typically straight tubes or slots, e.g., [4]. This is not surprising since a thorough prediction of the leak involves a series of difficult operations. First, the topography of the facing surfaces should be obtained, which generally implies careful measurements. The elasto-plastic deformation of the surfaces in contact under given loads must be computed at various scales (from the roughness scale to the ring scale). These computations should give the aperture field between the two surfaces in contact through which the fluid may flow. Then, the leak must be computed solving the flow problem through the aperture field, which can represent a very difficult problem if the system is close to a percolation threshold, [5]. As explained in [6], the accomplishment of this ambitious program has been attempted and is in progress. The results will be presented elsewhere. However, one can refer to [7] for preliminary interesting results. The objectives of the present paper are much more modest and limited to two aspects of the problem. We consider a system characterized by a spiral groove main structure, which is a representative topography of face turned surfaces. As explained in more details below, the leak through this system is circumferential when the flow follows the spiral groove (high loads) and radial when passages exist in the radial direction (low and moderate loads). We first conduct an analysis suggesting that the transition in the type of leak, i.e. circumferential or radial, must be sharp, i.e. occurs over a narrow range of loads. Furthermore, the analysis also suggests that the transition could be confirmed by combining diffusion flux and viscous flow rate measurements. In a second part of the paper, we discuss the influence of errors of form (waviness) on the leak. It is generally admitted that errors or form are detrimental to tightness. We show, however, that the presence of an error of form could improve tightness if its amplitude is slightly smaller than the groove average depth.

2 Geometry Leak Paths

The system under study is schematically shown in Fig. 1. The ring gasket is modelled as a system formed by joining normally a rough textured surface and a smooth one. The rough surface is representative of surfaces obtained by face turning. This machining process classically leads to a textured surface characterized by a spiral groove. As discussed for instance in [8], the regular motion of the cutting tool leads to a quite regular spiral structure. This structure is illustrated in Fig. 2. Naturally, the spiral is however not perfect owing to various phenomena (small vibrations of the cutting tool, local heterogeneities, . . .). As schematically illustrated in Fig. 2, there exist small scale height fluctuations on both the valley and summit (crest) of the groove, see for instance [8] for more details. In particular, this small scale disorder leads to the possibility of radial leak paths as will be discussed further below.

The two surfaces are pressed together by applying a given load. This process leads to the deformation of asperities and reduces the local apertures between the two surfaces. The general problem is then to predict the leak as a function of the applied load. Obviously, increasing the load leads to reduce the distance between the mean planes of the two surfaces. It is therefore qualitatively equivalent to increase the load or to reduce this mean distance. For the sake of simplicity, the analysis presented in this paper is performed using parameters characterizing the distance between the surfaces, rather than the load.

Leak Paths. As illustrated in Fig. 2, for low and moderate loads, leak is possible through passages associated with the local fluctuations of the crest height between two laps of the valley. These passages represent a series of shortcuts forming radial leak

Contributed by the Fluids Engineering Division for publication in the JOURNAL OF FLUIDS ENGINEERING. Manuscript received by the Fluids Engineering Division June 18, 2003; revised manuscript received Sept. 11, 2003. Associate Editor: Y. Tsujimoto.

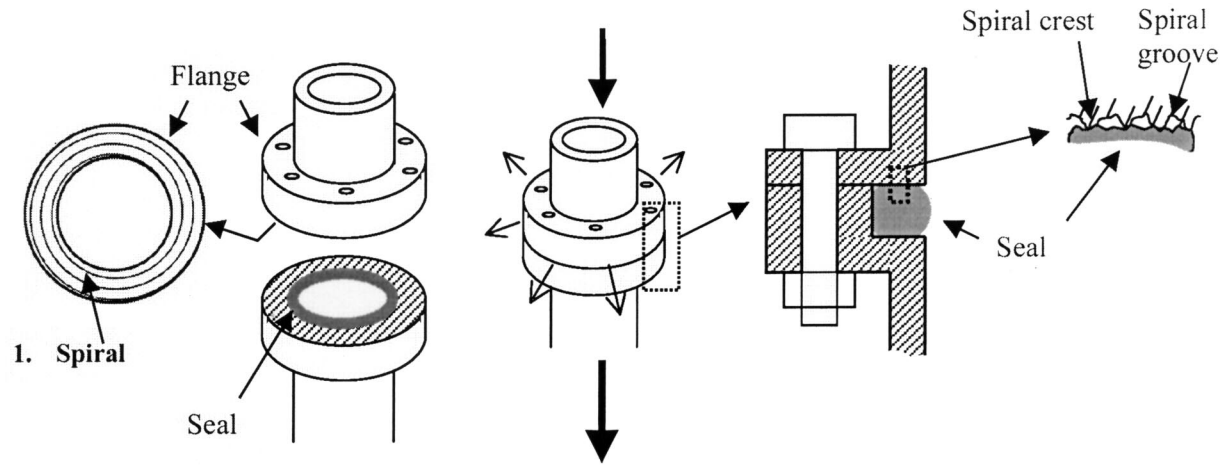

Fig. 1 Schematic illustration of a machine turned static ring gasket

paths. For a sufficient (high) load, the passages on the crest disappear and the only leak path becomes the valley of the spiral. This leak path is termed the circumferential leak path. For intermediate loads the fluid will follow combinations of circumferential leak path sections and radial paths.

Model Gasket. The model ring gasket is depicted in Fig. 3. r_i is the inner radius of the ring, r_e is the outer radius. $\Delta r = r_e - r_i$ is the bearing distance. n is the number of laps of the valley.

The valley is perfect (no height fluctuations) and of sinusoidal shape (Fig. 3). Assuming $\Delta r \ll r_i$, the height variations in the radial direction in the valley is given by:

$$h_1(x) = a \cos\left(\frac{2\pi}{\lambda} x\right) \tag{1}$$

where $x=0$ corresponds to a summit of the crest. a is the amplitude of the spiral groove. λ is the distance between two crest summits in the radial direction ($n\lambda = \Delta r$).

The radial passages are taken into account in an average sense by assuming a uniform small gap εa between the top of the crest and the smooth surface. In this model, the aperture variations in the radial direction are therefore given by:

$$\frac{h(x)}{a} = \varepsilon + 1 - \cos\left(\frac{2\pi}{\lambda} x\right) \quad \text{if } \cos\left(\frac{2\pi}{\lambda} x\right) < 1 + \varepsilon \tag{2}$$

$$h(x) = 0 \quad \text{if } \cos\left(\frac{2\pi}{\lambda} x\right) \geqslant 1 + \varepsilon \text{(which is possible for } \varepsilon \leqslant 0) \tag{3}$$

Note that ε can be <0, in this model. For $\varepsilon<0$, the mean plane of the smooth surface cuts the rough surface as depicted in Fig. 4. As in many previous works on flows through rough fractures with contacts, e.g., [9,10], the tops of the asperities are simply truncated as indicated in Fig. 4. Preliminary results, [11], indicate that

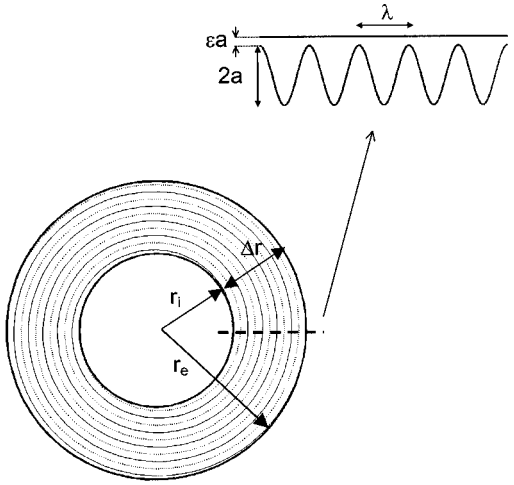

Fig. 3 Model static ring gasket. The ring width Δr is grossly exaggerated for clarity. The thin inner solid line shows the spiral crest. The inner dashed line shows the bottom of the spiral valley. The local slopes are also exaggerated (in fact $a/\lambda \ll 1$).

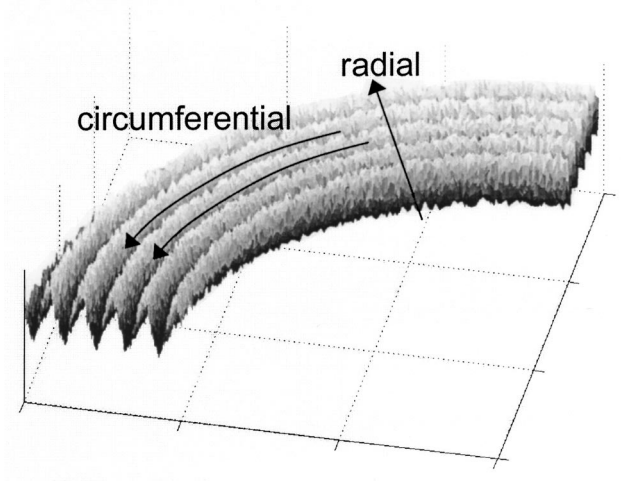

Fig. 2 Schematic illustration of the crest and valley height fluctuations

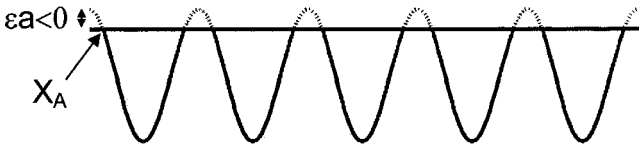

Fig. 4 For $\varepsilon<0$, a simple geometric erosion rule is used as depicted in the figure

this geometrical erosion model is satisfactory in the case of plastic deformation of asperities. It may be surmised that it is also satisfactory when the smooth surface is made of a soft coating. In the present model, the geometrical erosion rule models the deformation of the crest. Deformation of the smaller scale asperities, such as the fluctuations schematically depicted in Fig. 2, is included implicitly in the variation of ε ($\varepsilon \geqslant 0$) since the radial passages are described in an average sense only in the present model.

Another important characteristics of machined surfaces is that the roughness local slopes are small, that is in the present context $a/\lambda \ll 1$.

3 Diffusive Versus Viscous Leaks

In this section, we derive analytical expressions giving the leak trough the model ring gasket for two different transport phenomena. The first one is the transport by diffusion of a species through a stagnant fluid induced by a concentration difference between the ring inner domain and the outer one. Recalling that the roughness local slopes are small and assuming dilute concentration and a binary system, this transport phenomenon can be studied using the following governing equation, see for instance [9] for more details,

$$\nabla \cdot (\mathbf{q}_d) = 0.; \quad \mathbf{q}_d = -\rho D h \nabla c;$$
$$c = c_i \quad \text{at } r = r_i; \quad c = c_e \quad \text{at } r = r_e \tag{4}$$

where $\mathbf{q}_d$ is the diffusive flux (mass flow rate) per unit width. ρ is the density of the stagnant fluid, D is the binary diffusion coefficient of the considered species. c is the mass fraction of the species.

The second one is the incompressible flow of a Newtonian viscous fluid induced by a pressure difference between the ring inner and outer domains. Again, under the assumption of roughness local small slopes, this type of flow is generally modelled using the Reynolds (lubrication) equations,

$$\nabla \cdot (\mathbf{q}_v) = 0.; \quad \mathbf{q}_v = -\frac{h^3}{12\mu} \nabla p; \quad p = p_i \quad \text{at } r = r_i;$$
$$p = p_e \quad \text{at } r = r_e \tag{5}$$

where $\mathbf{q}_v$ is the viscous flux (volume flow rate) per unit width. μ is the viscosity of the fluid, p is the fluid pressure.

It is interesting to note that the main difference in the two problems lies in the dependence of the fluxes with the aperture field, i.e. $\mathbf{q}_d \propto h$ and $\mathbf{q}_v \propto h^3$.

Typically, the apertures are of the order of or less than 1 μm. With the explosion of studies in the domain of microflows in relation with the development of microsystems (MEMS), it is now well-known that special effects associated with the small dimensions may have to be taken into account for modelling a given transport phenomenon properly, see for instance [12] for more details. However, these effects will not modify the essentially qualitative results presented in this paper and are therefore ignored for simplicity.

We now proceed to the estimate of the radial and circumferential fluxes.

Under the assumption $\Delta r \ll r_i$, the radial diffusive and viscous fluxes through the gasket read,

$$Q_r^d = 2\pi \overline{r} \rho D \left[\int_0^{\Delta r} h^{-1} dx \right]^{-1} \Delta c = 2\pi \overline{r} \rho D \overline{h} \sqrt{1-\Gamma_\varepsilon^2} \frac{\Delta c}{\Delta r} \tag{6}$$

$$Q_r^v = \frac{2\pi \overline{r}}{12\mu} \left[\int_0^{\Delta r} h^{-3} dx \right]^{-1} \Delta p = \frac{2\pi \overline{r}}{12\mu} \overline{h^3} \frac{2(1-\Gamma_\varepsilon^2)^{5/2}}{2+\Gamma_\varepsilon^2} \frac{\Delta p}{\Delta r} \tag{7}$$

where $\Delta c = c_i - c_e$, $\Delta p = p_i - p_e$ and $\overline{r} = (r_i + r_e/2) \cdot \overline{h}$ is the average aperture,

$$\overline{h} = a(1+\varepsilon) \tag{8}$$

Γ_ε is defined by

$$\Gamma_\varepsilon = \frac{1}{1+\varepsilon} \tag{9}$$

Carrying out the integrations in Eqs. (6) and (7) involves evaluating Sommerfeld integrals of the form:

$$S_{(m,n)} = \frac{1}{2\pi} \int_0^{2\pi} \frac{\cos^m \chi}{(1+C\cos\chi)^n} d\chi \tag{10}$$

One can refer to appendix A of Ref. [13] for more details.

The circumferential diffusive and viscous fluxes, i.e., the fluxes through a groove of total length $2\pi\overline{r}n$, are easier to evaluate analytically. They read:

$$Q_c^d = \rho D \left(\int_0^\lambda h dx \right) \frac{\Delta c}{2\pi \overline{r} n} = \rho D \lambda \overline{h} \frac{\Delta c}{2\pi \overline{r} n} \quad \text{for } \varepsilon \geqslant 0 \tag{11}$$

$$Q_c^d = \rho D 2 \left(\int_{x_A}^{\lambda/2} h dx \right) \frac{\Delta c}{2\pi \overline{r} n} = \rho D \frac{\Delta c}{\pi \overline{r} n} \left[\overline{h} \left(\frac{\lambda}{2} - x_A \right) + \frac{\lambda a}{2\pi} \sqrt{1-(1+\varepsilon)^2} \right] \quad \text{for } \varepsilon < 0 \tag{12}$$

$$Q_c^v = \frac{\lambda}{12\mu} \overline{h^3} \left(1 + \frac{3}{2} \Gamma_\varepsilon^2 \right) \frac{\Delta p}{2\pi \overline{r} n} \quad \text{for } \varepsilon \geqslant 0 \tag{13}$$

$$Q_c^v = \frac{1}{12\mu} \frac{\Delta P}{2\pi \overline{r} n} \left[2 \left(\frac{\lambda}{2} - x_A \right) \overline{h^3} \left(1 + \frac{3}{2} \Gamma_\varepsilon^2 \right) - \frac{3\lambda a^2 \overline{h}}{2\pi} \sqrt{1-(1+\varepsilon)^2} (1+\varepsilon) - \frac{\lambda a^3}{3\pi} (1-(1+\varepsilon)^2)^{3/2} + \frac{\lambda a}{\pi} (a^2 + 3\overline{h^2}) \sqrt{1-(1+\varepsilon)^2} \right] \quad \text{for } \varepsilon < 0 \tag{14}$$

In Eqs. (12) and (14), x_A is the contact point at which the aperture field becomes zero, see Fig. 4. x_A is given by the equation $a\cos(2\pi/\lambda x_A) = a(1+\varepsilon)$.

Taking as reference fluxes, the circumferential fluxes corresponding to $\varepsilon = 0$, i.e.:

$$Q_{cref}^d = \rho D a \lambda \frac{\Delta c}{2\pi \overline{r} n} \tag{15}$$

$$Q_{cref}^v = \frac{5\lambda a^3}{48\mu} \frac{\Delta p}{\pi \overline{r} n} \tag{16}$$

The radial and circumferential fluxes are compared in Fig. 5 as a function of ε for $r_i = 1.5$ cm, $\Delta r = 0.05$ cm, $a = 2.5\,\mu m$, $n = 5$. For $\varepsilon \leqslant 0$, the leak path is purely circumferential whereas a radial leak becomes possible for $\varepsilon > 0$. As can be seen from Fig. 5, the radial and circumferential fluxes are of the same order of magnitude for extremely small values of ε. This indicates that a few radial passages are sufficient to cause a significant leak compared to the pure circumferential leak. This is consistent with the very large aspect ratio of the groove, i.e. $2\pi\overline{r}n/\lambda \gg 1$. If ε_c is the value of ε corresponding to $Q_r/Q_c \approx 1$, it can be also seen that the value of ε_c in the diffusive case and the viscous case are quite different ($\varepsilon_c^d \sim 5.9\,10^{-13}$ and $\varepsilon_c^v \sim 3.5\,10^{-3}$ respectively). This is a direct consequence of the h and h^3 dependence of the local fluxes in the two transport processes. Hence we have $0 < \varepsilon_c^d < \varepsilon_c^v \ll 1$. We recall that ε characterizes the radial path through the spiral crests in an average sense only. Therefore, it is not unphysical to consider very small values of ε.

Since the radial/circumferential transition occurs for very small values of ε, one can develop general asymptotic approximations

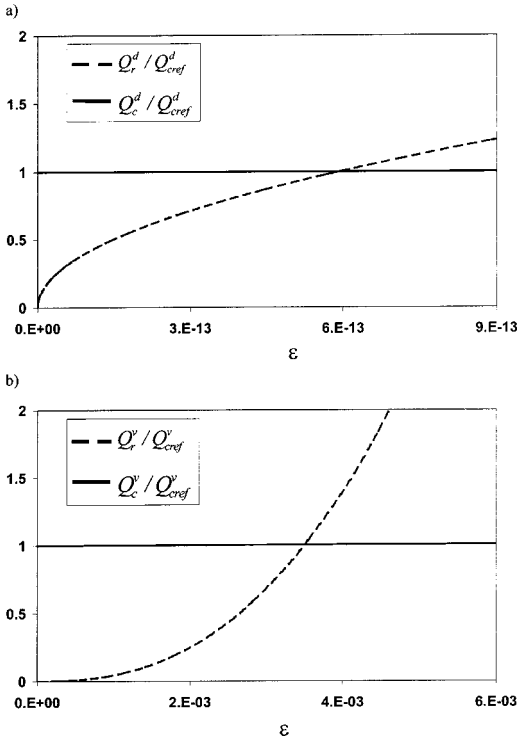

Fig. 5 Radial and circumferential fluxes as a function of ε. (*a*) diffusive fluxes, (*b*) viscous fluxes.

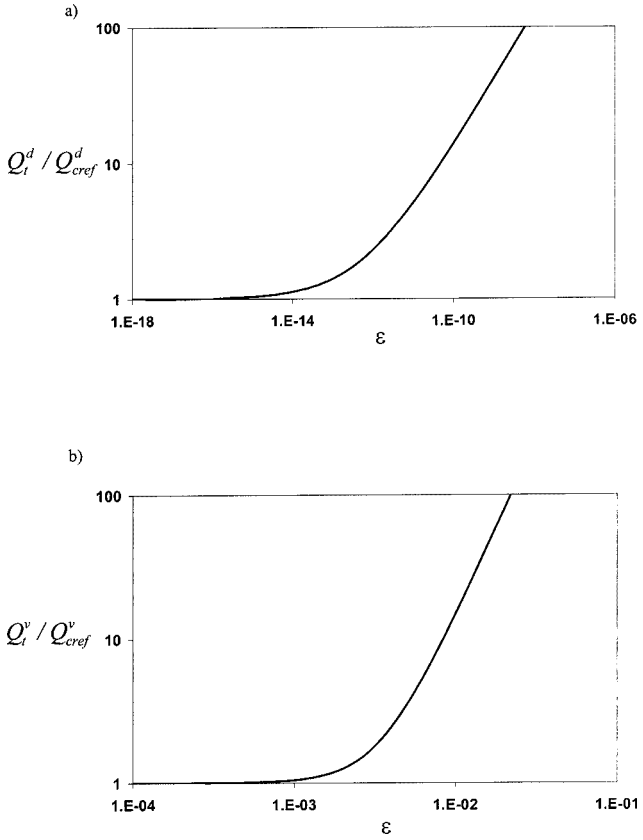

Fig. 6 Total flux (radial+circumferential) as a function of ε. (*a*) diffusive flux, (*b*) viscous flux.

of the radial and circumferential fluxes for $\varepsilon \to 0$. After some calculations (one can refer to [13] for the details), it is found

Asymptotic estimates for radial and circumferential diffusive fluxes:

$$Q_r^d = \rho D a 2\sqrt{2}\pi\bar{r}\varepsilon^{1/2}\frac{\Delta c}{\Delta r} \tag{17}$$

$$Q_c^d = \rho D a \frac{\lambda}{2\pi\bar{r}}\frac{1}{n}\Delta c \tag{18}$$

Asymptotic estimates for radial and circumferential viscous fluxes

$$Q_r^v = \frac{2^{5/2}a^3}{9\mu}\pi\bar{r}\varepsilon^{5/2}\frac{\Delta p}{\Delta r} \tag{19}$$

$$Q_c^v = \frac{5a^3}{24\mu}\frac{\lambda}{2\pi\bar{r}}\frac{1}{n}\Delta p \tag{20}$$

Comparisons (not shown here) between the above estimates and the exact results (for representative values of ring gaskets under study) indicate that the asymptotic estimates can be used safely up to values of ε of the order of 10^{-1} (with a maximum relative error less than 10% for $\varepsilon \sim 10^{-1}$ and less than 1% for $\varepsilon \leqslant 10^{-2}$).

The total fluxes (radial+circumferential) obtained from the above asymptotic estimates are shown as a function of ε in Fig. 6. As can be seen, the leak sharply increases with ε for $\varepsilon \geqslant \varepsilon_c$, as the leak becomes controlled by the radial flux (with $Q_r^d/Q_c^d \propto (\varepsilon/\varepsilon_c^d)^{1/2}$ and $Q_r^v/Q_c^v \propto (\varepsilon/\varepsilon_c^v)^{5/2}$).

The influence of the various geometric parameters on ε_c can be obtained from the asymptotic estimates. ε_c is the value corresponding to radial and circumferential fluxes of the same order of magnitude. From $Q_r^d \approx Q_c^d$ and $Q_r^v \approx Q_c^v$, one obtains:

$$\varepsilon_c^d = \frac{1}{2}\left(\frac{\lambda}{2\pi\bar{r}}\right)^4 \tag{21}$$

$$\varepsilon_c^v = \frac{15^{2/5}}{2^{9/5}}\left(\frac{\lambda}{2\pi\bar{r}}\right)^{4/5} \tag{22}$$

As can be seen, in this model, ε_c only depends on the geometrical parameter $\lambda/2\pi\bar{r}$ (ratio of valley width to gasket perimeter). This parameter is a small parameter of the problem, i.e. $\lambda/2\pi\bar{r} \ll 1$. Thus, for a given average radius of the ring, ε_c only depends on λ, i.e., the radial distance between two crest summits. In particular, ε_c is independent of the number of laps of the spiral. Since $\lambda/2\pi\bar{r}$ is a small parameter, $\varepsilon_c^d \ll 1$ and $\varepsilon_c^v \ll 1$. Also, it may be noted that $\varepsilon_c^d/\varepsilon_c^v \propto (\lambda/2\pi\bar{r})^{3.2}$, i.e. $\varepsilon_c^d \ll \varepsilon_c^v \ll 1$.

We therefore conclude that the sharpness of the radial–circumferential leak transition is a generic feature of this type of system, intimately linked to the existence of the small parameter $\lambda/2\pi\bar{r}$. The exponents of the scaling laws governing the transition, i.e. $Q_r^d/Q_c^d \propto (\varepsilon/\varepsilon_c^d)^{1/2}$ and $Q_r^v/Q_c^v \propto (\varepsilon/\varepsilon_c^v)^{5/2}$ in the present model, are naturally expected to depend on the details of the micro-geometry (smaller scale fluctuations) on the crest top. For example, from the results presented in [14], one expects $Q_r^v/Q_c^v \propto (\varepsilon/\varepsilon_c^v)^2$ if the crest microgeometry in the radial direction can be assimilated to short-range or long-range (fractal) correlated profiles.

Leak Regime Identification. In this section, we explore the possibility of identifying better the type of leak (radial or circumferential) as a function of ε (i.e. in practice the load) from measurements of ''diffusive'' and ''viscous'' leaks. We begin with the definition of the overall diffusivity D and ''transmissivity'' K of the gasket,

$$Q_t^d = Q_r^d + Q_c^d = 2\pi\bar{r}\rho D\frac{\Delta c}{\Delta r} \tag{23}$$

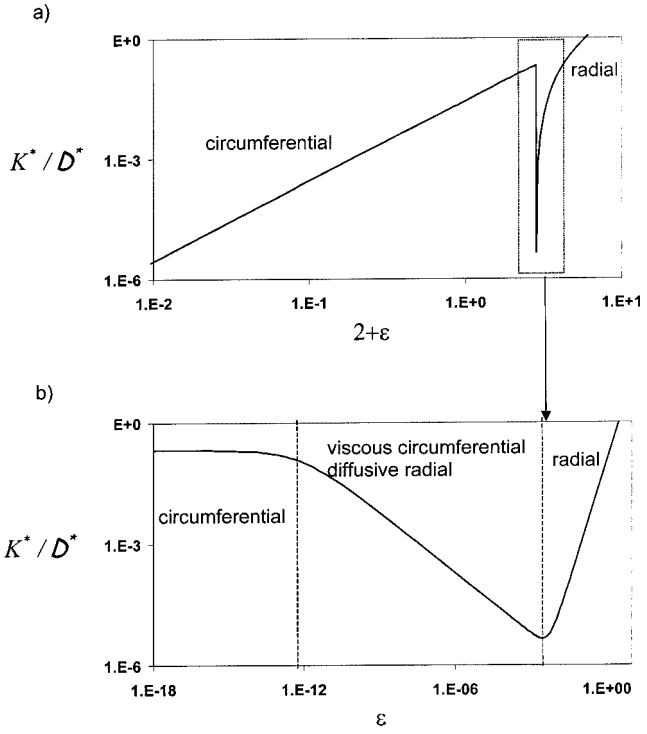

Fig. 7 Evolution of K^*/D^* as a function of ε

$$Q_t^v = Q_r^v + Q_c^v = 2\pi r \frac{K}{\mu}\frac{\Delta p}{\Delta r} \tag{24}$$

Using the estimates (17)–(20) and choosing aD (resp. a^3) as characteristic diffusivity (resp. transmissivity) lead to

$$\frac{K^*}{D^*} = \frac{[K/a^3]}{[D/(aD)]} = \frac{\frac{2^{3/2}}{9}\varepsilon^{5/2} + \frac{5}{24}\left(\frac{\lambda}{(2\pi r)}\right)^2}{2^{1/2}\varepsilon^{1/2} + \left(\frac{\lambda}{(2\pi r)}\right)^2} \tag{25}$$

Figure 7 shows the evolution of K^*/D^* as a function of ε (for $\varepsilon<0$, we have used Eqs. (12) and (14)). As can be seen from Fig. 7, the evolution of K^*/D^* clearly reveals the sharp transition between the radial and circumferential leak regime. Whereas this ratio decreases as ε diminishes (i.e. as the load increases) in the dominant radial regime (larger ε) and the dominant circumferential regime ($\varepsilon<0$), the evolution is the opposite in the transition regime. Also, it may be noted that the variation in the transition regime is of several orders of magnitude. A more detailed view of the evolution in the transition zone is also shown in Fig. 7(*b*). Three main sub-zones can be distinguished, depending on the values of ε. For $\varepsilon<\varepsilon_c^d$, the circumferential contribution is dominant both for the viscous and diffusive leaks. K^*/D^* does not vary significantly with ε in this sub-zone near ε_c^d. For $\varepsilon_c^d<\varepsilon<\varepsilon_c^v$, the dominant leak regime is radial for the diffusive leak but it is still circumferential for the viscous leak. K^*/D^* decreases with ε in this sub-zone. For $\varepsilon_c^v<\varepsilon$, the radial contribution is dominant both for the viscous and diffusive leaks. K^*/D^* increases again with ε in this sub-zone.

The results presented in this section can be summarized as follows;

1. the radial leak is the most critical since it is very sensitive to a small change in the equivalent aperture ε.

2. the radial/circumferential leak transition is sharp (i.e. is expected to occur over a small variation of the applied load). This is a generic feature of the system studied, which is a consequence of the very large aspect ratio of the groove, $2\pi r/\lambda \gg 1$.

3. it is much better to operate the ring gasket in the circumferential regime

4. the radial/circumferential leak regime transition can be detected by combining measurements of diffusive and viscous leak as a function of the load.

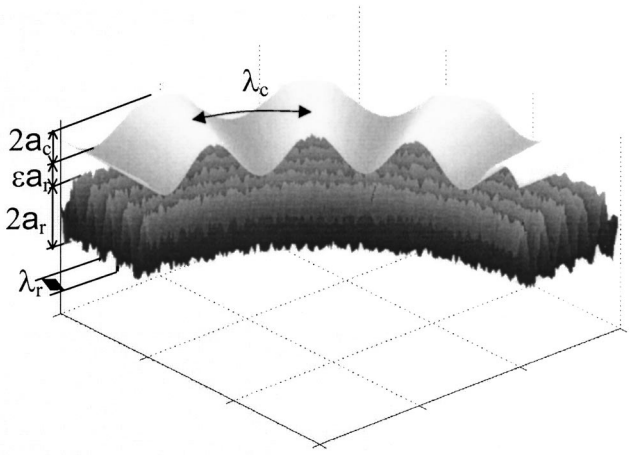

Fig. 8 Schematic view of the model ring gasket with error of form on the top surface. Dimensions within the ring as well as local slopes are grossly exaggerated for clarity.

4 Influence of an Error of Form

Errors of form can be viewed as flatness surface defects, e.g., [15], with characteristic lengths in the plane significantly greater than the roughness length scales. For example, measurements on the facing surfaces of a model ring gasket, [11], revealed a waviness of angular period of about 30 deg and of mean amplitude 1 μm on the metallic rough surface. Consistently with the leak measurements reported in [11,7], the presence of errors of form can presumably favor the existence of radial passages and therefore may be thought as very detrimental to tightness (the issue remains, however, somewhat controversial since it is sometimes argued, [16], that they could become of negligible influence owing to surfaces elastic deformation at the ring scale induced by the applied load; this effect, if any, is ignored in this paper). In this section, we show, however, that the situation may be more subtle. We exhibit a situation where the error of form is in fact beneficial to tightness, at least for the high loads.

The system considered is schematically illustrated in Fig. 8. The rough surface is identical to the one considered in section 3, i.e., height variations of the form $h_1(x)=a_r\cos(2\pi/\lambda_r x)$ in the radial direction where a_r is the amplitude of the spiral groove. λ_r is the distance between two crest summits in the radial direction ($n_r\lambda_r=\Delta r$). The "smooth" surface bears an error of form of wave length λ_c in the circumferential direction. Defining y as a curvilinear co-ordinate in the circumferential direction ($y\approx\overline{r}\theta$ where θ varies between 0 and 2π), the height variations on the "smooth" surface about its mean plane are given by:

$$h_2(y) = a_c\cos\left(\frac{2\pi}{\lambda_c}y\right) \tag{26}$$

where a_c is the amplitude of error of form.

Defining εa_r as the distance between the plane intercepting the top of the rough surface crest and the one intercepting the lower points of the surface bearing the error of form, see Fig. 8, the aperture field between the two surfaces is defined as

$$h(x,y)=\varepsilon a_r+a_r\left(1-\cos\left(\frac{2\pi}{\lambda_r}x\right)\right)+a_c\left(1+\cos\left(\frac{2\pi}{\lambda_c}y\right)\right) \tag{27}$$

if $h(x,y)\geqslant 0$ (otherwise $h(x,y)$ is set to 0; hence again, a simple geometrical erosion rule is applied when the two surfaces are in contact, which corresponds to $\varepsilon\leqslant 0$).

Three main cases can be distinguished depending on the respective values of a_c and a_r. When $a_r \gg a_c$, the error of form does not affect the leak. This case has been studied in section 3. In the opposite case, when $a_r \ll a_c$, the leak is controlled by the error of form and is radial up to full closing of the apertures. Therefore, one expects major leaks and the gasket can be considered as totally defective in this case. The interesting case is therefore when the two amplitudes are of the same order of magnitude.

We now proceed to the estimate of the radial and circumferential fluxes under this circumstance (only the viscous leak is considered, similar results can be obtained for the diffusive leak). In this model, the radial leak is the leak through a series of n_r sinusoidal constrictions (saddle points). The elementary conductance g of this type of constriction has been the subject of a detailed study that will be presented elsewhere. It reads (for sufficiently small h_0),

$$g=\frac{6}{7}h_0^3\sqrt{\frac{h_{xx}}{-h_{yy}}} \tag{28}$$

where h_0 is the aperture at the saddle point, h_{xx} (resp. h_{yy}) is the second derivative with respect to x (resp. y) of the aperture field at the saddle point. g is defined by the relation $Q=g/12\mu\,\delta P$ where Q is the flux (volume flow rate, m^3/s) through the constriction and δP the pressure difference across the constriction.

Making use of Eq. (28) leads to express the radial leak as:

$$Q_r^v=n_c\frac{g}{12\mu}\frac{\Delta p}{n_r}=\frac{1}{12\mu}\frac{6}{7}(2a_c+\varepsilon a_r)^3\sqrt{\frac{a_r}{a_c}}\frac{2\pi\bar{r}}{\Delta r}\Delta p \tag{29}$$

where $\varepsilon a_r+2a_c=h_0$ is the distance between the plane intercepting the spiral crest top and the one intercepting the highest points of the error of form (see Fig. 8). $n_c=2\pi\bar{r}/\lambda_c$ is the number of radial leak paths.

The circumferential leak is estimated as the leak through a series of $n_c\times n_r$ constrictions along the spiral groove. Using again expressions similar to Eq. (28) leads to:

$$Q_c^v=\frac{g}{12\mu}\frac{\Delta p}{n_c n_r}=\frac{1}{12\mu}\frac{6}{7}a_r^3(2+\varepsilon)^3\sqrt{\frac{a_c}{a_r}}\frac{\lambda_r^2}{2\pi\bar{r}\Delta r}\Delta p \tag{30}$$

In what follows, we concentrate on the range of apertures corresponding to $\varepsilon\leqslant 0$, i.e. from the "first contact" ($\varepsilon=0$) where the leak is still radial up to a full circumferential leak (assuming $a_c<a_r$). In order to evaluate the impact of the error of form, we compare the overall transmissivity of the gasket in the presence of the error of form ($a_c>0$) with the transmissivity in the absence of the error of form ($a_c=0$). This comparison is made as a function of the contact area between the two surfaces under the reasonable assumption that the same applied load should lead to the same contact area between the two surfaces. Hence, we compare the transmissivities for identical loads on both surfaces.

The contact surface fraction is defined as

$$A=\frac{S_c}{S} \tag{31}$$

where S is the ring total area, $S=2\pi\bar{r}\Delta r$ and S_c is the contact area. In the absence of error of form, $S_c=n_r 2\pi\bar{r}2x_A=\Delta r 2\pi\bar{r}2x_A/\lambda_r$ where x_A is the contact point between the upper flat surface and the grooved surface (see definition below Eq. (14) and Fig. 4). Hence, in this case,

$$A=2\frac{x_A}{\lambda_r} \tag{32}$$

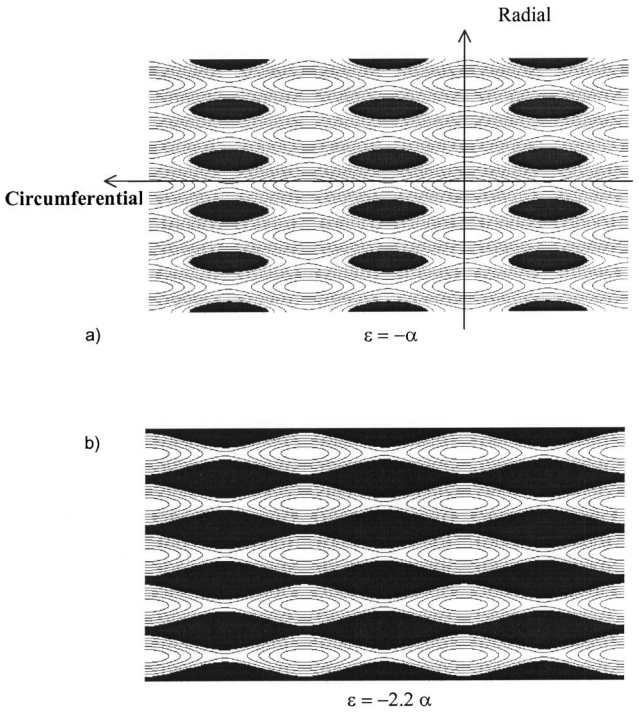

Fig. 9 "Unrolled" view of contact area (in black) and aperture field for the system with error of form. Constrictions along the circumferential and radial paths are shown. For $\varepsilon<-2\alpha$, only a circumferential leak is possible as shown in ε_c^d (b).

Combining Eq. (29) with the equation giving x_A (see below Eq. (11)) leads to the following relationship between A and ε,

$$\varepsilon=(\cos(\pi A)-1) \tag{33}$$

In the presence of error of form, the contact surface fraction has to be determined numerically. As an example, we have taken $\bar{r}=1.5$ cm, $\Delta r=0.05$ cm, $a_r=2.5\,\mu$m, $a_c=0.8a_r$, $n_r=5$ and $n_c=3$. The contact area as a function of ε is computed numerically using a classical Simpson method in 2D. The contact area in this case is illustrated in Fig. 9. Figure 9 shows the constrictions along both the radial and circumferential leak paths. As shown in Fig. 9(*b*), for $\varepsilon=-2\alpha$ (where $\alpha=a_c/a_r$) the system reaches its radial percolation threshold (no radial leak is possible for $\varepsilon\leqslant-2\alpha$). This corresponds to a "critical" contact surface fraction A_{cr} with $A_{cr}\approx 0.41$ in the example studied.

The comparison procedure is finally the following. We compute the total flow rate (circumferential+radial) in the presence of error of form as a function of A using Eqs. (29) and (30) and the relationship between ε and A determined numerically. Then the flow rate in the absence of error of form is determined as a function of A using Eqs. (33) and (14).

The comparison is shown in Fig. 10 (where the case of the diffusive leak is also shown). For $A_{cc}\approx 0.6$, the system reaches its circumferential percolation threshold. For this value of the contact surface fraction, the groove is closed by the error of form and no leak is possible in the presence of the error of form. As discussed above, A_{cr} is the value for which the radial leak path closes up in the presence of the error of form ($A_{cr}\approx 0.41$ in Fig. 10). This value corresponds to the radial percolation threshold. Recalling that the leak is purely circumferential in the absence of error of form in the range of ε studied, the results shown in Fig. 10 can be discussed as follows. For $A\leqslant A_{cr}$, the leak regime is dominantly radial with the error of form. Consistently with the results of section 3, the flow rate is several orders of magnitude greater than in the absence of error of form. Thus, for low and moderate loads,

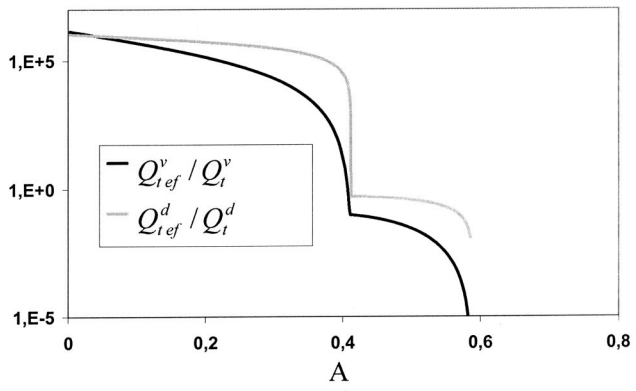

Fig. 10 Influence of an error of form on the flow rate through the ring gasket. A is the contact surface fraction. Q_{ef} is the flux with error of form. Q is the flux without error of form for the same contact surface fraction.

the error of form has a very detrimental effect. However, this is exactly the opposite for high loads corresponding to $A_{cr} \leqslant A \leqslant A_{cc}$ owing to the partial closing of the groove by the error of form. The error of form is then beneficial to tightness. The value A_{cr} corresponds to the radial/circumferential regime transition in the presence of error of form. As in section 3, the transition is rather sharp and characterized by a very large variation of the leak flow rate as a function of the contact area, i.e., the load.

The sharpness of the transition in the presence of the error of form can be discussed in more details from the ratio Q^v_r/Q^v_c. Using Eqs. (29) and (30), this ratio is expressed as

$$\frac{Q^v_r}{Q^v_c} = \left(\frac{2\pi\bar{r}}{\lambda_r}\right)^2 \left(\frac{1}{\alpha}\right) \left(\frac{\varepsilon'}{2(1-\alpha)+\varepsilon'}\right)^3 \tag{34}$$

where $\varepsilon' = \varepsilon + 2\alpha$ (and as before $\alpha = a_c/a_r$). No radial leak is possible for $\varepsilon' \leqslant 0$. In Eq. (34), $(2\pi\bar{r}/\lambda_r) \gg 1$, and $\alpha \approx O(1)$. In the example studied above, $(2\pi\bar{r})/\lambda_r)$ is on the order of 10^3 and can still be much larger in the applications. From Eq. (34), we therefore conclude that the radial/circumferential transition is very sharp since $Q^v_r/Q^v_c \propto (\varepsilon'/\varepsilon'_c)^3$ with $0 < \varepsilon'_c \ll 1$ (where, as before, ε'_c is the value of ε' corresponding to $Q^v_r/Q^v_c \approx 1$).

5 Conclusions

Two aspects of the leak through a model spiral groove ring gasket have been studied. The evolution of the leak flow rate as a function of the load is characterized by a transition from a dominant radial leak (low to moderate loads) to a circumferential leak along the spiral groove (higher loads). Owing to the very large aspect ratio between the total length of the groove and its typical width, it is much better to operate the gasket in the circumferential regime.

Taking advantage of the fact that a diffusive process explores the aperture field whereas a viscous flow explores the cube of this aperture field, it has been shown how diffusive and viscous leak results could be combined for detecting (or confirming) the radial/circumferential transition. Although not shown in this paper, this result also holds in the presence of errors of form.

In general, errors of form are shown to be very detrimental to tightness as they favor radial leaks. However, when the amplitude of the error of form is on the order of the groove depth, it has been shown that they could lead to partial closing of the groove for high loads, which is beneficial to tightness. Hence, contrary to what it is generally thought, errors of form could improve tightness.

In the examples studied, the transition between the radial and circumferential regimes is sharp and characterized by leak flow rate variations of several orders of magnitude for very small expected variations of the contact area. This appears to be a generic feature of the system studied, which is directly related to the very large aspect ratio between the total length of the groove and its typical width. At least qualitatively, it would be very interesting to check whether or not this feature, i.e. the sharp transition, is observed in experiments.

The present study suggests that the fact that such a transition is not observed for a given gasket could be an indication that the leak is predominantly radial over the range of loads imposed.

Naturally, one must keep in mind that the geometrical representation of a face turned surface chosen in the present work is very simplified. Consideration of more realistic models of the surface local geometry is needed. Work in this direction is in progress. Also, it must be emphasized that the analysis presented in this paper is based on a somewhat crude model of surface deformation, i.e., a simple geometrical levelling of the asperities. Further works is certainly needed for assessing the impact of surfaces deformation on the aperture field, notably in the presence of errors of form.

Acknowledgments

The research presented in this paper is supported by GDR 2345 ''Etancheité statique par joints métalliques en conditions extrêmes'' encouraged by CNES, Snecma-Moteur, EDF and CNRS. We thank all the colleagues involved in the GDR for fruitful discussions.

References

[1] Brunet, J. C., Poncet, A., and Thrihle, P., 1994, ''Leak-Tightness Assessment of Demountable Joints for the Super Fluid Helium System of the CERN Large Hadron Collider (LHC),'' *Advances in Cryogenic Enginering*, **39**, pp. 657–662, P. Kittel, ed., Plenum Press, New -York.
[2] Butcher, H., 1973, ''Fundamental Principles for Static Sealing With Metal in High Pressure Field,'' ASLE Trans., **16**, pp. 304–309.
[3] Yanagisawa, T., Sanada, M., Tanoue, H., Koga, T., and Hirabayashi, H., 1990, ''Fundamental Study of the Sealing Performance of a C-Shaped Metal Seal,'' *Proceedings of the 2nd International Symposium on Fluid Sealing*, pp. 389–398, La Baule, France.
[4] Blanc, R., Henry, R. P., and Leclerc, J., 1981, *Guide de l'étanchéité*, Vols. 1 et 2, Société Française du vide, Paris.
[5] Stauffer, D., and Aharony, A., 1992, *Introduction to Percolation Theory*, Taylor & Francis.
[6] Frêne, J., Boccaletto, L., Delaunay, Y., and Pyre, A., 2002, ''Study of Leakage in Static Gasket for Cryogenic or High Temperature Conditions,'' *4th International Conference on Launcher Technology, Space Launcher Liquid Propulsion*, 6 December, Liege, Belgium.
[7] Marie, C., Lasseux, D., Zahouani, H., and Sainsot, P., 2003, ''An Integrated Approach to Characterize Liquid Leakage Through Metal Contact Seal,'' European Journal of Mechanical and Environmental Engineering, Special issue: Launcher Technology, **48**, pp. 81–86.
[8] Robbe-Valloire, F., and Prat, M., 2002, ''A Network Model for Leakage Prediction in a Metallic Static Seal,'' *4th International Conference on Launcher Technology, Space Launcher Liquid Propulsion*, 6 December, Liege, Belgium.
[9] Adler, P. M., and Thovert, J. F., 1999, *Fractures and Fractures Networks*, Kluwer.
[10] Prat, M., Plouraboué, F., and Letalleur, N., 2002, ''Averaged Reynolds Equation for Flow Between Rough Surfaces in Sliding Motion,'' Transport in Porous Media, **48**(3), pp. 291–313.
[11] Marie, C., 2002, ''Fuite Monophasique au Travers d'un Contact Rugueux: Contribution à l'étude de l'étanchéité statique,'' PH.D Thesis, Université de Bordeaux.
[12] Karniadakis, G., and Beskok A., 2002, *Microflows*, Springer Verlag.
[13] Letalleur, N., Plouraboué, F., and Prat, M., 2002, ''Average Flow Model of Rough Surface Lubrication: Flow Factors for Sinusoidal Surfaces,'' ASME J. Tribol., **124**, pp. 539–546.
[14] Plouraboué, F., Prat, M., and Letalleur, N., 2001, ''Sliding Lubricated Anisotropic Rough Surfaces,'' Phys. Rev. E, **64**, pp. 011202-1, 011202-10.
[15] Hamrock, B. J., 1994, *Fundamentals of Fluid Film Lubrication*, McGraw-Hill.
[16] Valentian, D., 2002, Personal Communication.

Unsteadiness of the Port Feed and Jet Flows Within a Gas Turbine Combustion System

N. J. Hughes
Research Associate

J. F. Carrotte
RR Lecturer in Aerospace Propulsion

Rolls-Royce UTC in Combustor Aerodynamics,
Dept of Aeronautical and Automotive Engineering,
Loughborough University,
Loughborough, U.K.

This paper describes an experimental investigation on a gas turbine combustor geometry that is typical of current aerospace applications. The isothermal investigation has concentrated on the flow approaching and passing through a primary port, and the subsequent jet formed by this flow within the flame tube. It is widely accepted that the jet formed by a port in such a geometry is influenced by the mean approach flow conditions. This paper, though, addresses whether the high levels of turbulence and unsteadiness, as is typically found within the approach flow of these systems, can also affect the time dependent jet and flow field generated by the port. Measurements using both hot wire anemometry (HWA) and a three component Laser Doppler Anemometry (LDA) system were therefore used to characterize the flow field. Cross correlation of simultaneous measurements indicated that velocity fluctuations in the feed annulus correlate with fluctuations inside the port and flame tube. The sign and magnitude of the correlations are presented between various feed annulus, port and flame tube spatial locations. The results suggest the time dependent external flow field can influence the flow field within the flame tube and hence, potentially, flame stability, mixing and emissions. [DOI: 10.1115/1.1637629]

1 Introduction

Air issuing from the compressor within a gas turbine engine is initially decelerated by the combustor diffuser system, prior to being distributed around the flame tube to the various porous features. This external flow, together with the flame tube porosity distribution, determines the complex flow field that is generated within the flame tube. For example, air supplied to the flame tube ports is accelerated to form jets within the flame tube that impinge on one another, to create large scale recirculation and mixing regions. If efficient combustion and a satisfactory temperature traverse is to be achieved then it is important that such aerodynamic flow features form the correct mixing patterns and flow fields inside the flame tube. Furthermore, recent developments of ever more stringent emissions legislation necessitates tighter control of fuel/air ratios, while the need to operate at leaner fuel air ratios can lead to problems associated with unsteady heat release. Such developments mean that the need to generate the correct flow field within the flame tube is of increasing significance, but consideration must be given to both the mean and instantaneous flow fields. With this in mind the current paper investigates if unsteadiness, as typically found in the flow supplied to the flame tube ports, can affect the jet characteristics and contribute to unsteadiness of the flow distribution within the flame tube.

Current advanced core engines usually incorporate dump diffusers in which a pre-diffuser, located immediately downstream of the compressor, is followed by a recirculating ''dump'' region which surrounds the flame tube head. Fishenden and Stevens [1] characterized the flow in such systems and noted that large amounts of turbulence are generated in the dump region. This is partly due to the unstable nature of the flow as it passes around the flame tube head and enters each feed annulus. Such effects influence both the mean profile and the turbulence levels within each downstream feed annulus. For example, measurements such as those undertaken by Carrotte et al. [2] indicate feed annulus turbulence intensities that can be in excess of 30%. It is widely accepted that the mean flow field in the feed annulus region affects the subsequent jet formed within the flame tube by the flow which enters the port. For example Lefebvre [3] describes the variation of hole discharge coefficient and initial jet angle based on gross features such as the feed annulus mean dynamic head and the mass flow passing through the port, relative to that approaching the port. Other workers including Griffiths [4] have indicated how local mean flow features within each feed annulus can also influence the jet characteristics. However, very little consideration has been given to the unsteady flow characteristics of the feed annulus and port flows. Furthermore the continuing desire to minimize the pressure drop across the flame tube liner increases the likelihood for potential coupling between the feed annulus flow unsteadiness and the time dependent patterns generated by the port flows within the flame tube.

In this paper results are presented from a program of work which has been conducted on a facility incorporating a modern aerospace gas turbine annular combustor geometry. An experimental facility has been designed in which detailed mean and turbulent measurements can be made of both the external and internal flame tube velocity fields. The experiment has been conducted under isothermal conditions so that an understanding of the aerodynamic processes may be gained in isolation from the complications associated with the combustion process. Both Laser Doppler Anemometry (LDA) and hot wire anemometry (HWA) measurements have been used to characterize the mean and time dependent flow supplied to a primary port, and the subsequent flow field generated by this port flow within the flame tube. Using these data, techniques have been developed to investigate if any unsteadiness of the primary jet correlates with unsteadiness of the feed annulus flow. Such results are not only significant in terms of the potential effect on combustor performance, but also on how numerical simulation of such combustor flow fields should be undertaken.

2 Experimental Facility and Instrumentation

The experimental facility was designed to ensure the aerodynamic features of the test facility were representative of a modern annular combustion system, while allowing instrumentation access to all areas of interest. This latter requirement dictated the

Contributed by the Fluids Engineering Division for publication in the JOURNAL OF FLUIDS ENGINEERING. Manuscript received by the Fluids Engineering Division Sept. 16, 2002; revised manuscript received September 16, 2003. Associate Editor: W. W. Copenhaver.

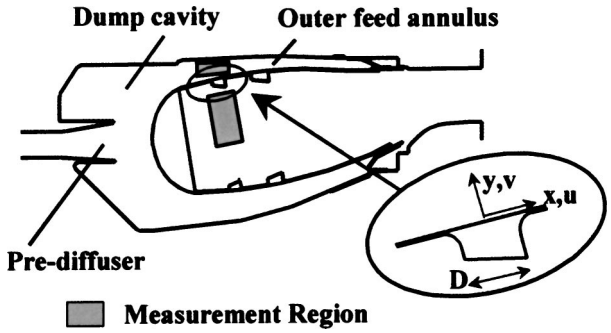

Fig. 1 Test geometry

need for a 45° sector rather than a complete annular combustion system. A detailed description and geometrical definition of the test facility is given by Griffiths [4].

Atmospheric air is drawn into a plenum before entering the vertically mounted test facility via a flared inlet duct. The test section incorporates a three burner sector flame tube segment, obtained from a sectored civil combustion chamber, and this segment is located downstream of a 1.4 area ratio pre-diffuser (Fig. 1). The flame tube incorporates two rows of chuted ports circumferentially positioned so that (i) opposed primary ports are aligned with, and midway between, each fuel injector and (ii) the opposed secondary ports are midway between primary ports. Pressure casings and endwalls are manufactured from Perspex and can incorporate up to ten windows so as to provide optical access to the center burner sector. On exit from the test section air passes into the exhaust plenum, situated directly below the test rig, prior to being expelled to atmosphere. Within the exhaust system two centrifugal fans are incorporated to provide the required pressure rise to draw air through the facility.

For the results reported in this paper the test facility was operated at an inlet Mach number of 0.12. A series of throttles within the bleed ducts, through which air passed to simulate that used for turbine cooling, ensured the correct division of mass flow to the various flame tube features. It should also be noted that great effort was made to reduce the instabilities that are associated with the feed annulus/sector sidewall flows that usually occur within sector rigs. Flow conditioning in these critical regions resulted in the circumferential static pressure gradients within each feed annulus being sufficiently small to indicate negligible flow migration into the central measurement sector due to the side-wall presence (Griffiths [4]).

The data presented in this paper mainly relate to flow in the central burner sector which passes from the outer feed annulus and into the primary port located on the edge of the sector (i.e. midway between fuel injectors). Measurements are also presented that show the subsequent trajectory of this fluid within the combustion chamber. The measurement locations are defined in terms of the port diameter, D, whilst the velocity information is presented in terms of u, v and w components that are relative to the axes of the flame tube (Fig. 1). All the information presented has been obtained using laser doppler anemometry (LDA) and hot wire anemometry (HWA) measurement systems.

The Dantec fibre optic LDA system consists of two probes; the 2-D probe emits two pairs of beams (green and blue), and the 1-D probe emits a single pair (violet), where the colors indicate different wavelengths of light. Processing of the signals is done in the frequency domain using enhanced burst spectrum analysers (BSAs). Most of the data presented were obtained from simultaneous 3-D measurements using both of the probes which resulted in an elliptical measurement volume of major and minor dimensions 300 μm and 150 μm respectively. Further spectral and correlation information was provided by measurements with one or more single hot wire anemometry probes. Note that whereas the LDA system can define three orthogonal velocity components (u,v,w), the single hot wire probe sensor records a single velocity that is sensitive, by varying degrees, to all three velocity components.

3 Data Reduction

The velocity information is presented in terms of the velocity measured in the central passage region at the pre-diffuser inlet (U in), whilst dimensional information is typically expressed in terms of the primary port diameter (D). Further information is presented in terms of velocity correlations and these are defined in the following section.

In order to determine if the flow in one region was dependent on the flow in another, a cross correlation function was used. For a pair of time history records, $u_1(t)$ and $u_2(t)$, for which only the turbulent velocity components are considered then the cross correlation between the signals is:

$$R_{u_1'u_2'}(\tau)=\lim_{T\to\infty}\frac{1}{T}\int_0^T u_1'(t)u_2'(t+\tau)dt \tag{1}$$

As indicated by Lynn [5] this is based on a digital representation of a finite record of the velocity signals. In this paper a nondimensionalized form (see, for example, Bradshaw [6]), is used such that:

$$Cross\ \ Correlation\ \ Function\ \ (CCF)=\frac{R_{u_1'u_2'}(\tau)}{\sqrt{\overline{u_1'^2}\cdot\sqrt{\overline{u_2'^2}}}} \tag{2}$$

Note that, in general, a CCF value of one typically indicates total correlation between the signals while zero indicates no correlation. Furthermore, a positive correlation means that, for example, if u_1 increases then u_2 will also increase τ seconds later. Alternatively a negative correlation suggests an increase in u_1 is accompanied by a decrease in u_2 and vice-versa.

For a single velocity record an auto correlation function can be similarly defined such that:

$$Auto\ \ Correlation\ \ Function\ \ (ACF)=\frac{R_{u_1'u_1'}(\tau)}{\sqrt{\overline{u_1'^2}\cdot\sqrt{\overline{u_1'^2}}}} \tag{3}$$

Hence this function relates a single signal to a shifted version of itself and this can be used to provide an indication of the flow time and length scales in the streamwise direction. In addition the spectral densities, E(f), that are presented indicate how much turbulent energy is contained within a single velocity signal at a given frequency. These were derived using a Discrete Fourier Transform of the original time history, obtained from a single hot wire probe, that was typically split into eight blocks and averaged. The autocorrelation function, $R_{u1u1}(\tau)$, was actually obtained from the derived spectrum using the Wiener-Khinchin relationship, i.e.:

$$R_{u_1'u_1'}(\tau)=\int E(f)e^{i2\pi ft}df \tag{4}$$

4 Experimental Errors

Due to the complex nature of the flow field there is a wide variation in mean velocities and turbulence intensities so no estimate of LDA errors can be made that applies to the entire flow field. The major sources of error associated with the LDA technique take the form of either statistical or systematic errors. The statistical errors arise from the discrete and finite number of samples that are used to determine the mean quantities of a continuous flow. Typically some 10,000 statistically independent samples were used to calculate the time averaged mean and turbulent flow quantities. For a 99% confidence interval and an rms

value of 0.04 U in, this gives an estimated error in the mean values of ±0.01 U in. The systematic errors associated with the measurements include those associated with the finite resolution of the processors (which is relatively small) and the alignment of the laser beams. An estimate of the typical alignment errors (~10 μm) on the transformation matrix used to obtain the derived velocity components suggests errors in the mean value of ±0.005 U in. The systematic errors also include those associated with statistical bias caused by the influence of flow velocity on the number of seed particles passing through the measurement volume. This velocity bias is countered by the use of residence time weighting, as described by Edwards [7], with the correction only becoming significant in regions of very high turbulence intensity. The above analysis suggests errors in the overall measured mean velocities are typically ±0.02 U in and, based on a similar analysis, errors in the fluctuating velocities are thought to be of order ±0.03 U in.

The intrusive nature of the hot wires can introduce errors in the measured mean and fluctuating velocity components. Furthermore errors in the mean quantities can arise where the local turbulence intensity exceeds 30% of the local mean value. For these reasons the LDA system was used to determine the mean and turbulent flow quantities whilst the HWA system was mainly used for determining frequency information or the correlation between two fluctuating velocity signals. The signals were sampled typically at a frequency of 10 kHz over a period of 5 s. Errors in the absolute velocities on these derived spectral and correlation quantities is thought to be relatively small. For the CCF data an indication of the background noise is given experimentally by (i) obtaining a CCF for two points in the test rig that are not correlated and (ii) the values typcally obtained at large time shifts (τ) where the signals are no longer correlated. Both methods suggest that typically the absolute value of a CCF should be greater than 0.05 for some correlation to exist between the two velocity signals.

5 Results and Discussion

The flow distribution approaching the outer sector edge primary port is indicated by measurements in the vicinity of the port leading edge (Fig. 2). Data are presented in the central passage region of the outer annulus, upstream of the port, and at the leading edge of the port. As has been described elsewhere (for example Fishenden and Stevens [1] and Carrotte et al. [8]) the mean velocity profile at entry to the feed annulus can be strongly biased, displaying a peak close to the surface of the flame tube. This bias is clearly evident in the measured data, both upstream of the port and at the leading edge. The biased profile is due to the impingement region on the flame tube head, the resulting wall jet, and the curvature effects around the flame tube head. This unstable flow region, together with the dump cavity recirculation, also generates high levels of turbulence thereby accounting for the relatively large rms velocity values (Fig. 2). Comparison with the mean velocity profile indicates rms levels for each component of between 25% and 50% of the mean velocity, although much greater instantaneous perturbations in velocity are obviously observed. Thus, although the time averaged velocity at all locations is positive, the high turbulence levels indicate the flow undergoes transitory periods of reverse flow across most of the passage height.

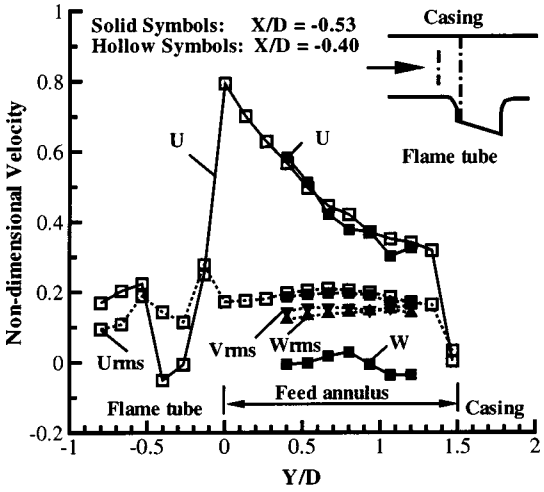

Fig. 2 Time averaged profiles in the port leading edge region

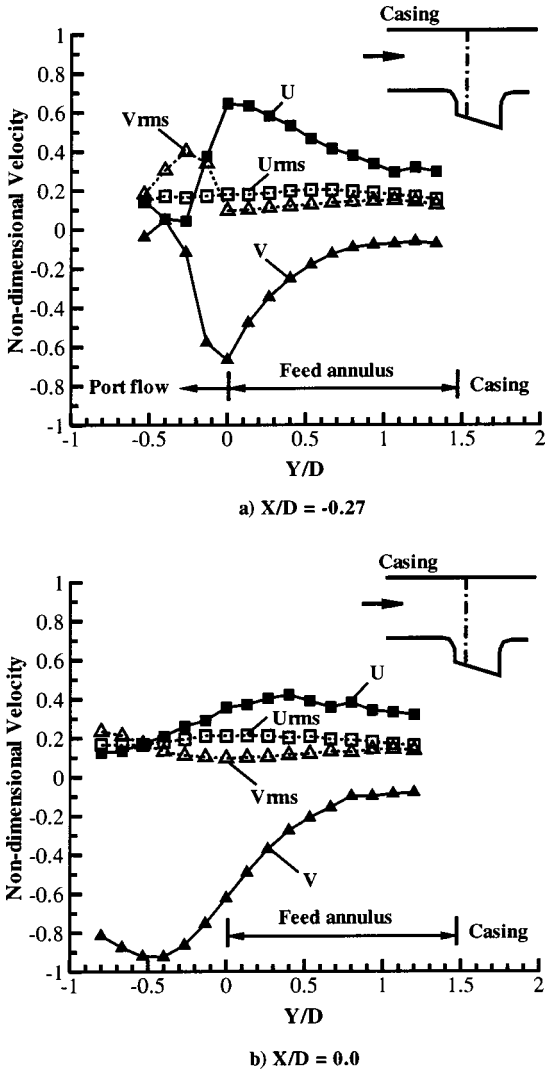

Fig. 3 Feed annulus and port flow profiles: *a*) (X/D=−0.27); *b*) (X/D=0.00)

Circumferential variations in the flow field are present within each feed annulus due to, for example, wakes from burner feed arms (Griffiths [4]). Nevertheless the same basic flow characteristics (i.e. a biased flow distribution with high turbulence levels) are presented to the primary ports at all the various circumferential locations. These characteristics are typical of those found within a modern aerospace combustion geometry.

5.1 Time Averaged Port Flow Data. The passage of flow into the port from the feed annulus has been determined from numerous traverses obtained on an axial plane passing through the center of the sector edge primary port. Information from two such traverses is presented in Fig. 3. Throughout this region, the swirl (W) component is virtually zero and so only the streamwise (U) and radial (V) velocity components are presented.

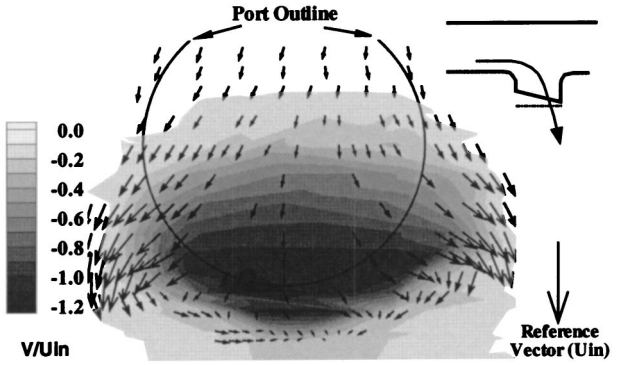

Fig. 4 Port exit plane mean velocity contours and vectors (Griffiths [4])

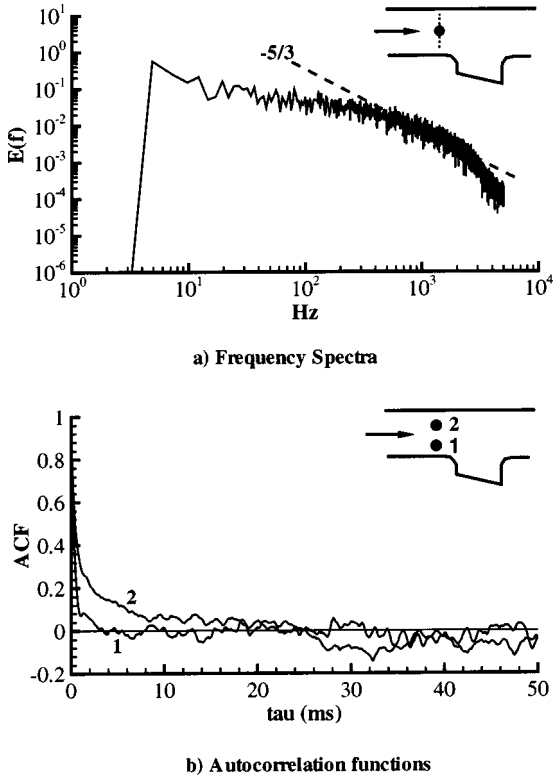

Fig. 5 Feed annulus time dependent characteristics: *a*) frequency spectra; *b*) autocorrelation functions

At X/D=−0.27 the relatively high streamwise (U) velocities at entry (Y/D=0.0) to the port (Fig. 3(*a*)) are remnants of the bias in the approach velocity profile (Fig. 2). In contrast, the increasing magnitude of the radial velocity component in the vicinity of the port reflects the influence of the port on the feed annulus flow. Now clearly for the flow to pass through the port and enter the flame tube, it must undergo a reduction in streamwise momentum and an increase in radial momentum. However, inside the port the mean radial (V) velocity magnitude decreases at this axial location whilst the streamwise (U) velocity decreases and then increases towards the port exit plane. Furthermore, negative streamwise velocities are observed further upstream in the port leading edge region (Fig. 2). This suggests that, despite the hole plunging, flow separation is occurring off the forward lip of the port. This is also supported by an increase in the radial rms velocities in this region. This separated region will be affected by the degree of bias in the approach velocity profile. Flow through the center and in the rear half of the port is more typically indicated by the velocity profile measured at X/D=0.0 (Fig. 3(*b*)). At this location the biased approach profile can no longer be observed as the streamwise velocities within the inner 70% of the feed annulus reduce due to the effect of the port. In addition, the influence of the port on the radial velocity within the feed annulus can also be observed. Inside the port, the streamwise velocity steadily decreases and the radial velocity increases in magnitude up to a maximum value near the port exit plane as would be expected. However, at this exit plane the streamwise velocities are still positive, thereby suggesting that the jet will enter the combustor at an inclined angle rather than perpendicular to the exit plane of the port. In terms of the fluctuating (rms) velocities at the port exit plane these are comparable with those observed in the approach flow.

The supply of flow from the feed annulus and its passage through the port explains many of the features observed in the jet formed by the port. Such features have been described by Griffiths [4] from which contours of mean radial velocity are presented at a port exit plane located within the flame tube, approximately 0.1 D from the trailing edge of the port chute (Fig. 4). In addition, vectors indicating the combined U and W velocity components have been superimposed on this diagram. These vectors indicate a movement of fluid around the jet, with some of this fluid being drawn back upstream towards the port as part of the vortex formation process in the lee of the jet. The radial velocity contours show the location of the jet core, with nearly all of the flow entering through the rear half of the port. Note that the relative jet and combustor velocities mean that this is not due to jet deflection by the combustor flow, thereby confirming the presence of a separated flow region from the leading edge of the port. The finite U components in the core mean the jet enters the combustor at an angle (of between 75° and 80°), as suggested by previous measurements, rather than perpendicular (90°) to the port. Within the jet core, local turbulent (rms) velocity fluctuations are high, up to 30% or 40% of the local mean velocities. This is due to the supply of highly turbulent fluid and its subsequent deflection through the port.

The experimental data presented indicate the changes in streamwise and radial momentum undertaken by the flow as it is deflected to pass through the port. Relative to a plenum fed jet, the effect of the initial streamwise momentum has been indicated in terms of port leading edge separation, initial jet angle etc. However, the fact that the initial mean velocity of the flow in the feed annulus affects the jet issuing from the port into the combustor is not surprising. Parameters such as the hole discharge coefficient and jet angle depend on the approach flow including, for example, the proportion of this approach flow which enters the port (Levebvre [3]). Although such correlations are based on bulk velocity characteristics they do indicate that the mean flow characteristics of the jet are influenced by the feed annulus flow field. However, it is not so easy to determine whether the flow unsteadiness within the feed annulus affects the flow within the flame tube, or whether the pressure drop across the liner is sufficient to de-couple such effects.

5.2 Time Dependent Port Flow Characteristics. The time dependent flow characteristics are mainly presented in terms of the spectra obtained from single hot wire anemometry measurements. As an example a typical spectra observed in the feed annulus upstream of the port is presented (Fig. 5(*a*)) whilst the gradient (−5/3) associated with the inertial subrange of turbulent scales (see for example Bradshaw [6]) is also indicated. The data suggest that the mean frequency associated with the inertial subrange scales is of order 1 KHz at the current operating conditions. Based on the inlet velocity (U in) and the port diameter, this 1 KHz frequency corresponds to a Strouhal number of approximately 0.35. The spectra are broadly similar across the height of the feed annulus with only minor differences being apparent at the lower energy containing frequencies. These differences, though,

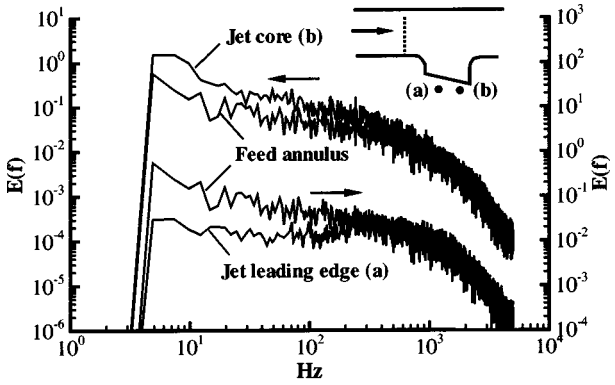

Fig. 6 Feed annulus and jet flow frequency spectra

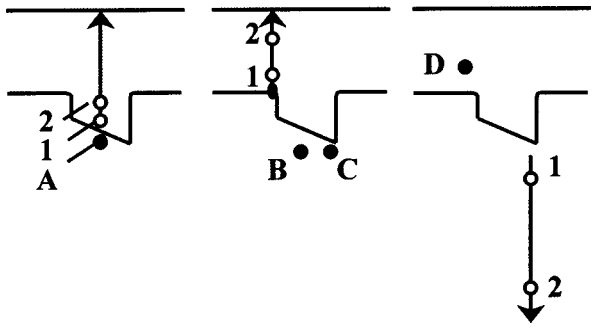

Fig. 8 Cross correlation locations

are more apparent in the auto correlations presented at two locations across the feed annulus (Fig. 5(*b*)). The largest flow time scales are indicated by the time (τ) at which the ACF initially crosses the abscissa, indicating the signal is no longer correlated with itself over this and greater time periods. Hence the correlations indicate that the largest flow time scales are less than 5 ms close to the flame tube, but are greater than 20ms close to the outer casing. Together with the local flow velocity this indicates a length scale, in the streamwise direction, of at least 5 or 10 times the port diameter. In other words, the length scale in the streamwise direction is not comparable with the feed annulus height but is associated with a much larger dimension such as that of the upstream dump cavity.

The feed annulus frequency spectra can be compared with the spectra measured at the port exit plane (Fig. 6). It can be seen that the rms fluctuations at frequencies less than 600 Hz are significantly increased as the flow passes from the feed annulus and through the flame tube port to form the jet core. In comparison the fluctuations are reduced in the jet leading edge region, although there is a small rise in the spectra centerd at approximately 450 Hz. Based on the hole diameter and mean velocity through the port this corresponds to a Strouhal number of approximately 0.15 and is thought to be associated with the flow that separates off the port leading edge. A typical probability density function of velocity about the mean value is also presented for this region (Fig. 7). Note the bi-modal nature of this distribution which was observed at the same location as those obtained by Griffiths [4] using LDA equipment. Whereas the hot wire is sensitive to various velocity components, the LDA measurements indicated that the bi-modal behavior was primarily associated with the radial velocity component. The velocity distributions in the leading edge region may suggest that the jet is moving between two preferred spatial locations. However, the lack of a well defined peak in the frequency spectra indicates this movement is not occurring at a specific frequency.

The mean flow field and some of the turbulent characteristics both within the feed annulus and port exit plane have been defined. By cross correlating some of these measurements it is possible to determine if unsteadiness in the approach flow is influencing the unsteadiness observed at the port exit plane. Furthermore, if this proves to be the case then additional measurements can be used to determine if this feed annulus unsteadiness can influence the flow further within the flame tube.

5.3 Feed Annulus/Port Exit Coupling. The range of spatial locations at which signals were correlated is presented (Fig. 8) with the cross correlations being presented in nondimensionalized form (Eq. (2)). As an example a hot wire probe was held stationary inside the flame tube at the center of the primary port (location A, Fig. 8) whilst a second probe was initially placed close by (within 1 mm). This second probe was then traversed radially outwards through the port into the outer annulus and, for illustration purposes, the cross correlations at two of these locations are presented (Fig. 9). As expected the magnitude of the correlation decreases when the probes move further apart, as the turbulent eddies lose their individuality due to mixing. In addition the time at which the signals correlate also increases due to the increased distance between the probes. In this instance, the time delay (τ) is positive and its magnitude indicates that the correlation is convective rather than, for example, acoustic in nature. Therefore, if a change in velocity occurs at the location of the upstream (traversing) probe then an associated change is observed by the downstream (stationary) probe τ ms later.

The correlation of signals between the outer feed annulus and the port exit plane (locations B and C, Fig. 8) were used to establish if fluctuations of the flow, within the feed annulus, affect the jets issuing into the flame tube. Initial measurements were made with one probe positioned within the port exit plane and towards the front of the port (position B) which, based on the mean flow

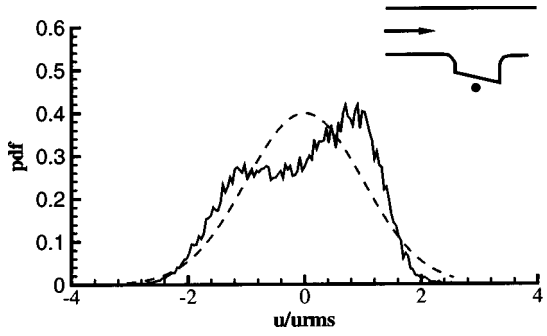

Fig. 7 Instantaneous probability density function in jet leading edge region

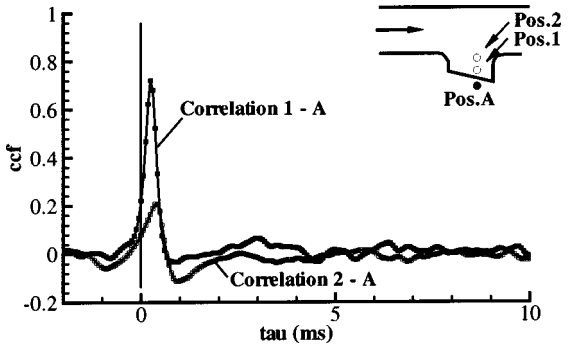

Fig. 9 Cross correlation of 2 fluctuating velocity signals

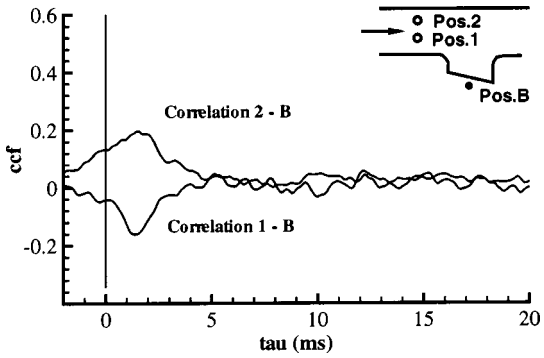

Fig. 10 Cross correlation of feed annulus and jet leading edge velocities

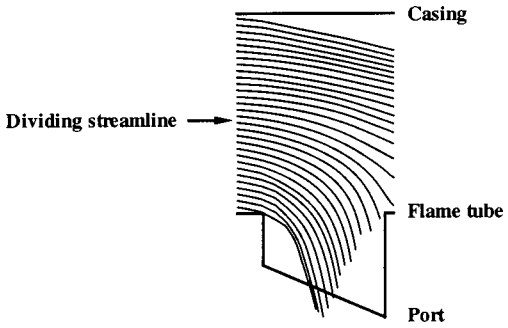

Fig. 12 LDA based time averaged streamlines

field measurements, is in the leading edge region of the jet. The second probe was traversed radially outwards from the flame tube to the outer casing, over a distance of 1.57 port diameters (Fig. 8). A negative correlation was apparent up to Y/D=0.57 followed by a region of negligible correlation (0.57<Y/D<1.29), before a positive correlation was observed beyond Y/D=1.29. As an example the cross correlation functions at two positions are presented (Fig. 10), and indicate CCF values of ±0.2 with these peak values occurring at a time delay (τ) of approximately 1.5ms. These data therefore indicate that the flow in the leading edge region of the jet is negatively correlated with flow that approaches the port from the inner half of the feed annulus closest to the flame tube surface. In other words an increase in the approach velocity of the flow, in this region, results in a decrease of the flow velocity issuing from the center of the port and vice versa. This suggests that, for example, the higher approach velocity near the flame tube results in a larger separation in the port leading edge region and hence a velocity reduction in the jet leading edge region.

The stationary probe was positioned towards the rear of the port (position C, Fig. 8), which corresponds to the jet core region. The second probe was again moved radially outwards within the outer feed annulus. In this case a positive correlation was initially noted (which persisted up to a Y/D location of 0.71), followed by a negative correlation towards the outer feed annulus wall. As an example, cross correlation functions at the two feed annulus locations for which data was previously presented are included (Fig. 11). Note that the correlations are now opposite to that previously observed between positions 1 and 2 and the port exit plane (i.e., 1-C is now positive and 2-C is negative). Comparison with the data in the jet leading edge region indicates that the maximum correlation appears at a similar time delay, reflecting the approximate convection time between the two measurement points. Low correlation levels are also observed over much longer time intervals. It should be noted, though, that the velocities are correlated within a turbulent eddy, and the feed annulus time scales (~10 ms to 20 ms) are much greater than the convection time (~1.5 ms) between the measurement locations. Hence the correlation over longer time intervals indicates that the core flow contains turbulent time scales comparable with those observed in the feed annulus (i.e., flow structures within the feed annulus are passing through the port).

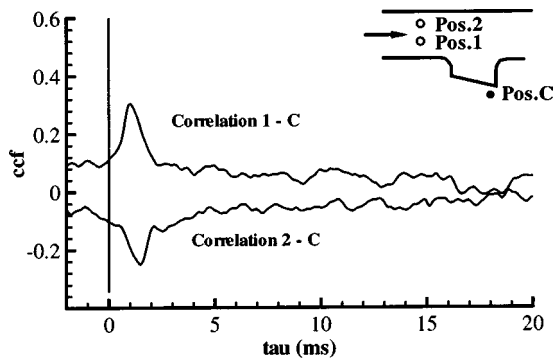

Fig. 11 Cross correlation of feed annulus and jet core regions

The velocity profiles across the annulus can be used in conjunction with the cross correlation results to illustrate the path of the air into the port. The correlations suggest that most of the flow captured by the port originates from the inner half of the feed annulus. It is already known that most of this flow issues through the rear half of the port. As the velocity of the flow in the inner half of the feed annulus increases, the results suggest that:

1. a greater separation region off the leading edge of the plunged hole occurs thereby reducing velocities in the jet leading edge region (hence resulting in a negative correlation) and
2. an increase in velocity of the main jet core issuing through the rear of the port occurs (hence the positive correlation)

The results suggest a possible ''flapping'' motion as the jet moves forwards and backwards in response to flow fluctuations within the feed annulus. In addition, as flow captured by the port increases, the amount of flow by-passing the port and continuing down the feed annulus must reduce. This accounts for the negative correlation between the flow issuing from the port and that in the outer half of the feed annulus. The jet core cross-correlation results suggest that the time averaged dividing streamline would lie at a Y/D location of approximately 0.71. It should be noted that flow streamlines can be derived from tangents to the local time averaged velocity vectors obtained from measurements with the LDA system as illustrated in Fig. 12. The dividing streamline is defined as that which separates the flow captured by the port from that passing downstream. Based on this time averaged dividing streamline it is observed that the size of the streamtube feeding the port is virtually identical to that indicated by the cross correlation measurements.

The described flow field is thought typical of that associated with a primary port where flow enters the port mainly from the upstream direction, with the streamtube captured by the port occupying approximately half the annulus height. Between the upstream and port exit planes mixing causes the turbulent eddies to lose some of their individuality and hence the degree of correlation reduces. Not surprisingly measurements made at the port trailing edge indicate a much smaller degree of correlation with the port exit flow. This is because the correlation is now between streamtubes captured by the port and that by-passing the port, so there is some loss of individuality associated with the turbulent eddies in both streamtubes. It should also be noted that the flow field is significantly different for other types of ports. For example, a dilution port captures a large percentage of the approach

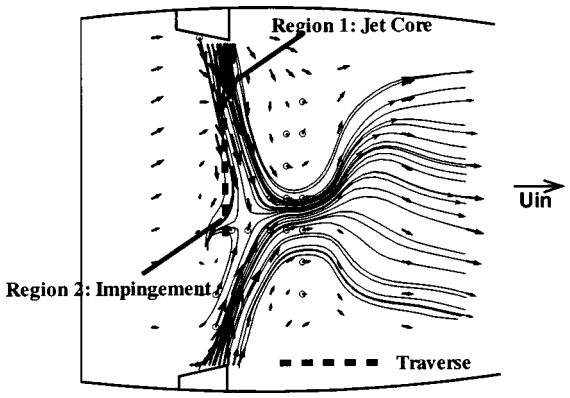

Fig. 13 Flame tube primary jet flow field

flow with only a small amount of flow passing downstream. Hence (i) the captured streamtube may almost fill the feed annulus, (ii) flow may separate from the feed annulus casing to enter the port, and (iii) a portion of the flow typically enters the port from the downstream direction. This different flow field is therefore likely to affect the feed annulus/port exit coupling characteristics.

5.4 Feed Annulus/Flame Tube Coupling. Given the correlation between the feed annulus and the port exit flow, further traverses were performed to investigate the extent to which flow within the flame tube remained correlated with that in the feed annulus.

One probe was positioned at the location (X/D=−0.64, Y/D =0.64), as indicated by position D on Fig. 8, whilst the second probe was traversed radially within the flame tube. A positive correlation was initially apparent, of maximum value 0.32, which remained over the first port diameter from the port exit plane. These points coincide with the high velocity region that is the main core of the jet. This is denoted by region 1 in Fig. 13, obtained from data already presented by Griffiths [4], which shows the time averaged jet trajectory within the flame tube. At slightly greater distances from the port no correlation was indicated, as the probe moved out of the jet (Fig. 13), but towards the flame tube centerline (region 2) a negative correlation was observed with a maximum value of −0.15 (Fig. 14). Compared with region 1 the time delay at which the maximum correlation occurs increases from approximately 1 ms to 3 ms, presumably due to the greater distance between the feed annulus and this location. Region 2, as shown in Fig. 13, encompasses the jet impingement region and the negative correlation can be interpreted in a variety of ways depending on the measurement position relative to the jet impingement. For example, a higher annulus velocity may move the jet further downstream and thereby decrease the magnitude of the upstream velocity component created by the impinging flow. Alternatively, if the probe is outside the impingement region then a higher feed annulus velocity may indicate higher jet momentum and impingement thereby reducing the mainstream approach velocity. Although in physical terms the exact mechanisms cannot therefore be defined the measurements do indicate correlation of the feed annulus and flame tube centerline velocities.

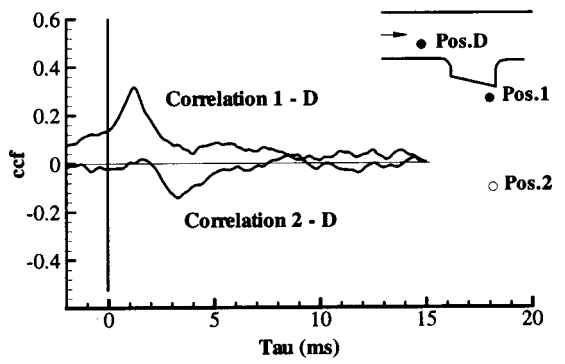

Fig. 14 Feed annulus and flame tube cross correlations

The observed unsteadiness of a primary jet may be due to a variety of reasons including, for example, jet on jet impingement. However, it is clear that some of this unsteadiness correlates with unsteadiness of the flow being supplied to the port. Furthermore, although the time averaged dynamic head in the feed annulus can be relatively small, the instantaneous perturbations about this mean may be large. Consequently, unsteadiness of the flow within the feed annulus can influence flame stability, mixing, and ultimately emissions. The design of the combustion system as a complete unit therefore becomes highly desirable, as does the modelling of the interaction between the feed annulus and the flame tube using CFD.

Conclusions

Measurements have been made of the flow in the vicinity of a primary port within a geometry that is typical of a modern aerospace gas turbine combustion system. Particular emphasis was placed on the time dependent flow field for which the following conclusions have been drawn:

- High levels of turbulence, or unsteadines, are present in the feed annulus flow approaching the port. The rms velocity fluctuations for each component are typically 25–50% of the mean velocity although instantaneous fluctuations can be greater than 100% of the flow mean velocity. In addition length scales which contain most of the flow energy are large relative to the feed annulus height and the port diameter.
- Correlations were observed between the feed annulus velocity fluctuations and those in the jet core at the port exit plane. Typical correlation coefficients of ±0.3 were obtained, depending on spatial location, with smaller values of reverse sign being measured in the jet leading edge region. Unsteadiness of the flow within the feed annulus therefore influences the time dependent characteristics of the jets entering the flame tube.
- Correlation coefficients of 0.3 magnitude were measured between the feed annulus flow fluctuations and the jet core inside the flame tube. Furthermore a correlation of −0.2 was measured between the flame tube centreline, upstream of the jet impingement region, and the feed annulus flow. Unsteadiness of the feed annulus flow therefore affects the time dependent characteristics of the flow on the flame tube centerline.

These conclusions are based on measurements undertaken at atmospheric conditions but the operating condition is well above any critical Reynolds number. Hence the increased Reynolds number within a gas turbine engine, due to higher inlet pressures and temperatures, will have negligible effect on the flow field characteristics. The data therefore indicate that the pressure drop across the flame tube liner, as typically generated within a modern aerospace combustor, is not sufficient to decouple the external fluctuations in velocity from the flame tube internal flow field. Hence both the time averaged and time dependent external flow field can influence the flow within the flame tube and could potentially influence combustion system performance. Furthermore the results imply that, although computationally expensive, numerical modelling should include the interactions between the feed annulus and flame tube. For time dependent calculations this may mean the time varying external flow field needs to be modelled.

Acknowledgments

The authors acknowledge the financial and technical support of Rolls-Royce plc. In addition the authors would like to acknowledge the test rig design and data provided by Dr. J. Griffiths, and Dr. P. Denman's assistance with the hot wire data acquisition software. The authors also acknowledge Messrs. D. Glover, L. Monk, and W. Niven for their assistance in the test rig manufacture.

Nomenclature

ACF = nondimensionalized Auto Correlation Function (Eq. (3))
CCF = nondimensionalized Cross Correlation Function (Eq. (2))
D = port diameter (Fig. 1)
E(f) = power spectral density (Eq. (4))
U_{in} = inlet velocity used for non-dimensionalizing
U,V,W = streamwise, radial, swirl mean velocity components (Fig. 1)
u = instantaneous velocity ($U+u'$)
u' = fluctuating velocity component
PDF = Probability Density Function
$R_{u1u1}(\tau)$ = auto-correlation (Eq. (3))
$R_{u1u2}(\tau)$ = cross-correlation (Eq. (1))
X,Y,Z = streamwise, radial, swirl coordinates (Fig. 1)
τ, tau = time delay

References

[1] Fishenden, C., and Stevens, S. J., 1977, "Performance of Annular Combustor Dump Diffusers," J. Aircr., **14**(1), pp. 60–67.
[2] Carrotte, J. F., Denman, P. A., Wray, A. P., and Fry, P., 1993, "Detailed Performance Comparison of a Dump and Short Faired Diffuser System," ASME Paper No. 93-GT-331.
[3] Lefebvre, A. W., 1983, *Gas Turbine Combustion*, McGraw-Hill, USA.
[4] Griffiths, J. P., 2000, "Measurements of the Flow Field Within a Modern Gas Turbine Combustor," PhD Thesis, Loughborough University, UK.
[5] Lynn, P. A., 1982, *An Introduction to the Analysis and Processing of Signals*, Macmillan, 2nd Ed.
[6] Bradshaw, P., 1971, *An Introduction to Turbulence and Its Measurement*, Pergamon Press.
[7] Edwards, R. V., 1987, "Report of the Special Panel on Statistical Particle Bias Problems in Laser Doppler Anemometry," ASME J. Fluids Eng., **109**, pp. 89–93.
[8] Carrotte, J. F., Bailey, D. W., and Frodsham, C. W., 1995, "Detailed Measurements on a Modern Combustor Dump Diffuser System," ASME J. Eng. Gas Turbines Power, **117**, pp. 678–685.

Analysis of the Influence of Diesel Nozzle Geometry in the Injection Rate Characteristic

J. Benajes

J. V. Pastor

R. Payri*

A. H. Plazas

CMT-Motores Térmicos
Universidad Politécnica de Valencia
Valencia, Spain

An experimental research study was carried out to analyze the influence of different orifice geometries (conical and cylindrical) on the injection rate behavior of a Common-Rail fuel injection system. For that purpose, injection tests in two different injection test rigs were conducted. This behavior of the injection rate in the different nozzles was characterized by using the non-dimensional parameters of cavitation number (K), discharge coefficient (Cd) and Reynolds number (Re). First, some relevant physical properties of the injected fuel were accurately characterized (density, kinematic viscosity and sound speed in the fluid) in a specific test rig as a function of the operating conditions (pressure and temperature). The behavior of both nozzles was analyzed at maximum injector needle lift under steady flow conditions in a cavitation test rig. Injection pressure and pressure at the nozzle discharge were controlled in order to modify the flow conditions. In addition, the nozzles were characterized in real unsteady flow conditions in an injection-rate test rig. From the raw results, the values of the relevant parameters were computed, and the occurrence of cavitation was clearly identified. The results evidenced interesting differences in the permeability of both nozzle geometries and a clear resistance of the conical nozzle to cavitation. [DOI: 10.1115/1.1637636]

Introduction

Performance, efficiency, noise and pollutant emissions in modern diesel engines are extremely dependent on fuel injection, which has a direct influence on the combustion process. This is specially true in high-speed direct-injection diesel engines, where there is a strong connection between pollutant emissions and the characteristics of fuel injection. Relevant characteristics are not only the total amount of fuel injected, but also the instantaneous fuel mass flow rate introduced into the combustion chamber, and the evolution of the spray and its interaction with the air [1,2]. One important phenomenon in this process is the flow behavior across the nozzle holes in the injectors, whose local features are affected by the small geometric details of the holes, and are recognized as being influential on engine performance and emissions [3].

One of the strategies for reducing pollutant emissions is to enhance the atomization of the fuel spray and the mixing of fuel with air, by generating smaller and more dispersed fuel droplets. The most influential parameters on the droplet formation are the fuel injection rate, the effective flow area, the turbulence and cavitation levels, these two last phenomena being represented by the Reynolds number and the cavitation numbers [4].

Due to the strong interconnection between fuel injection rate, spray formation, cavitation, and pollutant emissions [5] many researchers have undertaken investigation work aimed at developing different techniques for characterizing the instantaneous fuel injection process. One of the main difficulties these investigations had to overcome was the small geometrical characteristic of the nozzles, which make it difficult to measure relevant parameters such as the flow velocity in the outlet of the injection orifices.

The flow across the holes of a nozzle is controlled by different factors that can be separated into three categories: operation conditions, orifice geometry and flow properties. In the first category the upstream pressure and the downstream or back pressure one can find, i.e. the actual and time-dependent pressure at the orifice inlet and outlet, respectively. Unfortunately, measuring these pressure values in a real injector in operating conditions is extremely difficult, if not impossible.

One of the main geometric characteristics of the injector orifices is the variation of the cross-section along the length of the orifice. This can be described by the so called *k-factor*, which represents the orifice conicity, expressed by Eq. (1):

$$k = 100\frac{D_i - D_o}{L} \tag{1}$$

The values of *k-factor* can be either positive (convergent conical hole), negative (divergent conical hole) or zero (cylindrical hole).

The radius of the rounding at the orifice inlet is represented by means of the ratio r/D [6–9]. Different researchers have concluded that minor variations in the upstream geometry of the hole can produce changes in the flow across the orifice [6–11]. Nurick [8] found a relation between the ratio r/D and the occurrence of the phenomenon known as *vena contracta*, and he concluded that r/D values larger than 0.14 were required for avoiding this phenomenon.

In a similar manner, the orifice length L is characterized by the non-dimensional aspect ratio L/D. Qin et al. [9] carried out a study changing this parameter and were able to find and describe significant differences in the flow characteristics.

The aim of the present investigation is to shed light on several aspects of the flow behavior (mainly the fuel injection rate) across the holes of conical and cylindrical nozzles, and when possible, to characterize the observed effects by non-dimensional parameters such as Cd, Re, K.

The present paper is structured in four main sections. The purpose of the first part is to discuss some basic aspects of the one-dimensional flow theory of cavitating flows and to define the relevant parameters that will be used throughout the article. The second section is dedicated to the experimental set-up used, in particular the description of the nozzle geometrical characteristics and the three test rigs used (sound speed test rig, cavitation test

*Corresponding author: CMT-Motores Térmicos; Universidad Politécnica de Valencia; C/Camino de Vera s/n; E-46022 Valencia, SPAIN; Phone: +34-963879658; Fax: +34-963877659; e-mail: rpayri@mot.upv.es

Contributed by the Fluids Engineering Division for publication in the JOURNAL OF FLUIDS ENGINEERING. Manuscript received by the Fluids Engineering Division January 17, 2003; revised manuscript received September 16, 2003. Associate Editor: S. L. Cecaio.

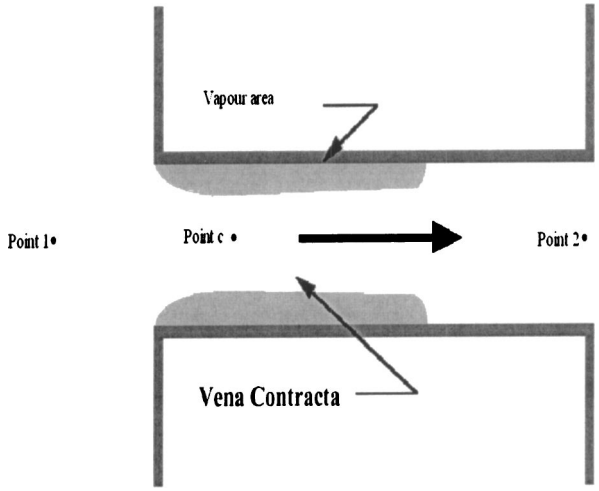

Fig. 1 Cavitation phenomenon in axy-symmetric nozzle

rig, and injection rate test rig). The results section shows the comparison between the results obtained in the different test rigs used in the analysis. Finally, the conclusions from all the experiments carried out are presented.

One-Dimensional Flow Theory

Cavitation is produced due to the low static pressure occurring in the flow under high-speed conditions near the injector hole inlet. If the orifice inlet has a small enough rounding, the flow tends to detach from the boundary layer, thus forming what is known as a ''vena contracta'' within the orifice. This flow contraction at the hole inlet reduces the effective cross-section of the stream, and consequently flow velocity must increase if mass flow rate has to be constant. Furthermore, this flow acceleration across the vena contracta produces a decrease in the static pressure in that zone. This reduced pressure can drop to the value of the vapor pressure for the existing temperature, causing a partial vaporization of the liquid, generating small bubbles or vapor cavities, which give the name cavitation [10]. A simple scheme depicting this phenomenon is drawn in Fig. 1.

The cavitation zone occupies only a fraction of the transversal section of the orifice, and the liquid flows through the remainder of the orifice area, this being the effective cross-section with cavitation, $A \cdot C_c$. The mass flow rate across the orifice under conditions of cavitation is obtained by combining the Bernoulli equation and the mass conservation equation between sections 1 and *C* (Fig. 1), obtaining:

$$\dot{m} = A \cdot C_c \cdot \sqrt{2 \cdot \rho \cdot (P_1 - P_v)} \tag{2}$$

Where P_1 and P_v are pressure values in sections 1 and *C*, respectively, assuming that in section *C* there are cavitation conditions, and pressure is equal to the vapor pressure, (0.08 MPa for the fuel and temperature of the tests), ρ represents the liquid density, and *A* the geometric cross section of the orifice.

A very important consequence derived from Eq. (2) is that the mass flow rate through an orifice under cavitation conditions is independent from the downstream pressure conditions, and for a given geometry of the orifice, the fuel delivery only depends on the upstream pressure, P_1, and the vapor pressure, P_v. In these conditions the model predicts that the orifice is collapsed or under choke state.

A discharge coefficient *Cd* can be defined between sections 1 and 2 in Fig. 1 which represents the orifice permeability in its whole:

$$C_d = \frac{\dot{m}}{A \cdot \sqrt{2 \cdot \rho \cdot (P_1 - P_2)}} \tag{3}$$

Where P_2 is the pressure value at the orifice outlet.

Combining Eqs. (2) and (3), the discharge coefficient becomes:

$$C_d = C_c \cdot \sqrt{\frac{P_1 - P_v}{P_1 - P_2}} \tag{4}$$

Nurick [8] defined the quotient under the square root as a cavitating parameter and he symbolized it as *K*. Using this definition of *K*, the discharge coefficient can be written as:

$$C_d = C_c \cdot \sqrt{K} \tag{5}$$

For high values of *K*, i.e. for small pressure differences, there is no cavitation, the *Cd* value remaining constant or decreasing. In this case *Cd* is independent from *K*, its variation relying solely on the Reynolds number.

Critical Cavitation Number. Cavitation conditions in an injector can be represented using some of the different cavitation numbers proposed in the literature. These are non-dimensional parameters which made it possible to establish whether the relevant flow conditions in the injector nozzle, that is the pressure differential, are favorable or not to the occurrence of cavitation. Definitions of this parameter varies throughout the literature, but they are mainly based on the pressure difference across the injector orifice. In this paper, Nurick's definition will be used:

$$K = \frac{P_1 - P_v}{P_1 - P_2} \tag{6}$$

For cavitating nozzles, the critical cavitation number is defined K_{crit}, corresponding to the pressure drop at which cavitation starts in the injector orifice. This phenomenon happens at a given value of the injection pressure, and it is detected by the stabilization of the mass flow rate across the orifice, despite the further decrease in discharge pressure. Hence, cavitation will not be produced unless the cavitation number, corresponding to these pressure conditions is lower than the critical value (K_{crit}).

Influence on the Discharge Coefficient. For low values of the Reynolds number Re the discharge coefficient increases up to a certain value of Re (critical Re), which depends strongly on the orifice geometry [12]. At this point the discharge coefficient achieves a value close to its maximum (95%), from which the rate of increase is negligible. Taking into account that the Reynolds number is a function of the flow velocity in the orifice, and therefore, it is dependent on the square root of the pressure drop, these parameters are directly proportional [13].

Under cavitating conditions, the discharge coefficient only depends on the cavitation number, not on the Reynolds number [14]

Speed of Sound in Fuel. When determining the injection mass flow rate by means of the Bosch method [15], which has been used in the work reported here, the value of the actual speed of sound in the fuel must be known. The basic equation on which this experimental method relies is:

$$\dot{m} = \frac{A_t}{u} \cdot dP \tag{7}$$

Where A_t is the transversal area of the *Injection Discharge-Rate-Curve Indicator* (IDRCI), *u* is the speed of sound in the fuel and *dP* is the pressure variation in the IDRCI. Since the value of *u* has a direct influence on the calculated mass flow rate, it is of utmost importance to compute its value accurately. For this purpose, it must be kept in mind that speed of sound is mainly dependent on the fuel characteristics, but also on the local values of fuel temperature and pressure [16,17]

Table 1 Basic nozzle characteristics

	Cylindrical nozzle	Conical nozzle
k-factor [−]	0	1.5
Outside hole diameter(mm)	0.155	0.137
L/D [−]	5.96	6.56
Injector nozzle type	Micro sac	Micro sac

Experimental Setup

In order to perform a comprehensive analysis of the involved phenomena, three different test rigs have been employed in this research, with the aim of measuring speed of sound, cavitation and instantaneous injection rate. The details of these systems will be described later.

The injection system used in the experiments is a standard common-rail system; composed of a high-pressure pump, supplying the required injection pressure at the rail, a fuelling system, a control system and an injector holder. The whole system is controlled by a Genotec-impulse-generator. The injector is the typical one from a *Common-Rail*, whose three main components are a control valve, an intensifier plunger and barrel, and a nozzle.

The valve is an electronically controlled solenoid-poppet valve whose purpose is to start and stop the injection process. The characteristic of the two nozzles used in the present study are shown in Table 1:

The fuel used for this experiment was *Repsol CEC RF-06-99* with a density of 835.5 kg/m^3 at 15°C, and a kinematic viscosity of 2.67 mm^2/s at 40°C.

Speed of Sound Test Rig. As commented previously, one of the important variables used for computing instantaneous injection mass flow rate is the speed of sound in the fuel, which is dependent on the fuel properties and on its pressure and temperature. In order to accurately assess the speed of sound in actual injection conditions, a test rig was designed and a methodology conceived.

The methodology is based on producing a pressure perturbation in the fuel and to measure the velocity at which the pressure wave travels through the fuel. This is achieved by measuring the time of travel of the pressure perturbation along a known distance. The pressure propagation is measured in the interior of a pipe filled with fuel at the required values of pressure and temperature. For this purpose, a test rig as shown in Fig. 2 is used.

The fuel is contained in a pipe system with an inner diameter of 2.5 mm. In order to have a long enough distance between two points, 20 m of pipe were rolled into a coil, and two pressure sensors were placed at both extremities. A thermostatic coating controls the fuel temperature in the pipe, while the whole system pressure is kept at the desired value by means of a tank filled with nitrogen and pressurized by an external compressor to a maximum pressure of 10 MPa.

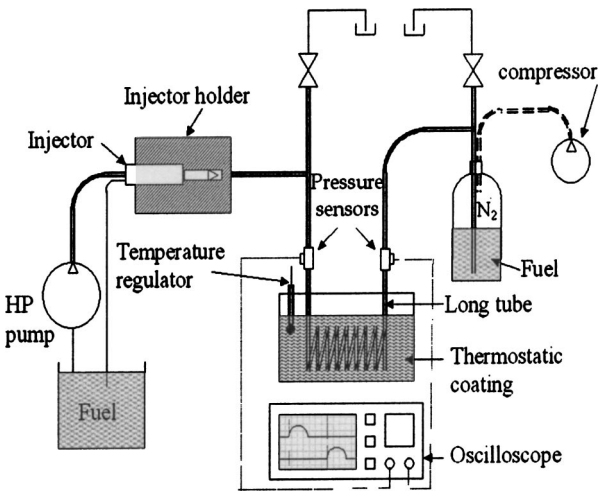

Fig. 2 Sound speed test rig

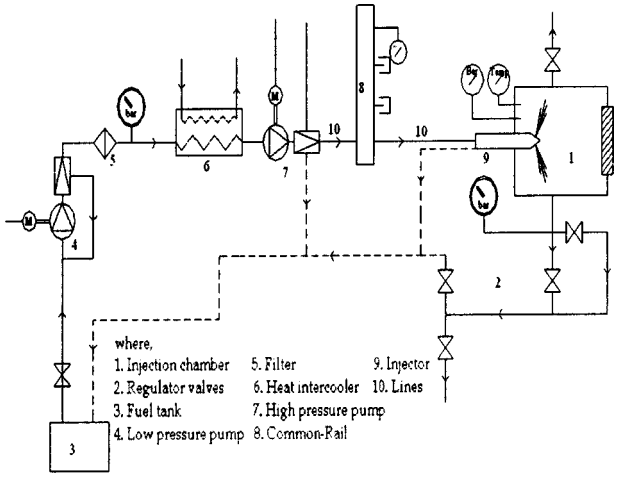

Fig. 3 Cavitation test rig

The pressure perturbation is produced by means of a plain injector and a hand-operated injection pump, and its passage through the pipe is detected by the two pressure sensors. The signals of the sensors is sent to a digital oscilloscope, where the time of travel of the pressure perturbation can be measured, and its propagation speed can be computed. Speed of sound was measured at pressure values of 0.1, 2, 4, 6 and 10 MPa, while fuel temperature was modified between 303 and 333 K in intervals of 5 K.

Cavitation Test Rig. The object of the cavitation test rig is to determine whether choked flow due to cavitation is being produced in the orifices of an injector with steady flow conditions.

For this purpose, the injector nozzle to be tested is installed in a modified injector holder, whose needle can be kept at its maximum lift, thus allowing the inlet of the orifices to always be wide open without the need of an electrical signal input. The injection pressure is controlled by means of the pressure regulator of the standard injection system and can be fixed at different values, up to a maximum dependent on the maximum mass flow that the pump is able to supply. The injector is mounted in a one liter vessel filled with fuel, where pressure is controlled, fixing the injector orifice outlet pressure. A sketch of the installation is shown in Fig. 3.

Pressure difference across the orifice can be kept constant and since geometry is also fixed, steady flow conditions are achieved. In order to carry out the test at different pressure differences, injection pressure, that is pressure at the orifice inlet is kept constant, and the discharge pressure in the vessel is varied.

In order to widely change the flow conditions in the injector orifice, tests were conducted at values of injection pressure, i.e orifice inlet pressure of 10 and 20 MPa, while pressure at the outlet was varied between a minimum value of 0.1 MPa and the injection pressure. After a short stabilization time, when steady flow conditions are achieved, mass flow rate across the injector is measured.

The injection pressure is measured upstream with an AVL piezo-resistive sensor (Reference 310 P1200E-2.0). This discharge pressure is measured with a PMA Gmbh sensor (Reference P40). Both sensors were calibrated before the measurements with a Deadweight Pressure Tester. The uncertainty of the discharge coefficient and critical cavitation number measurements were estimated using a standard procedure, as outlined by Holman [18].

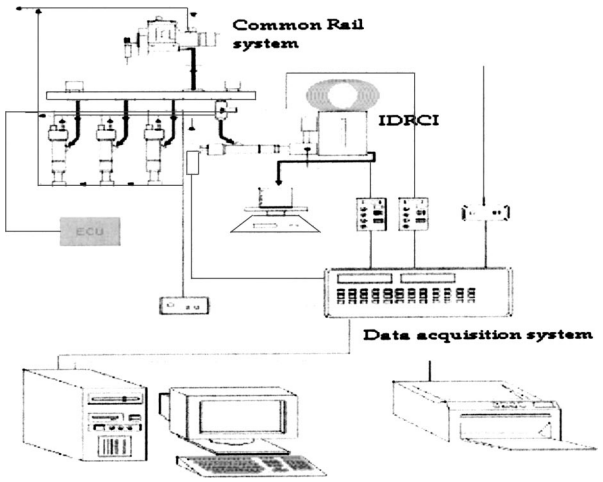

Fig. 4 Injection rate test rig

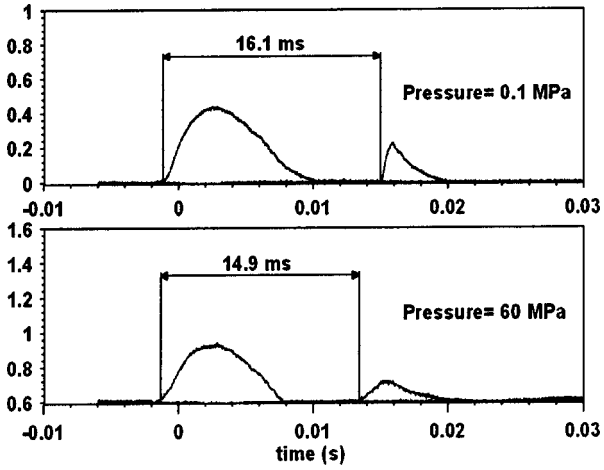

Fig. 5 Pressure influence on the wave gap at 30°C

The uncertainty obtained for the discharge coefficient and cavitation number were around 1.5% and 0.3%, respectively

Injection Rate Test Rig. The test rig where the measurements of injection rate were carried out is a commercial system, called Injection Discharge-Rate-Curve Indicator (IDRCI), depicted in Fig. 4, and it enables the display and recording of the data that describe the chronological sequence of an individual fuel-injection event.

The measuring principle is the Bosch method, which consists of a fuel injector that injects fuel into a fuel-filled measuring tube. The fuel discharge produces a pressure increase inside the tube, which is proportional to the increase in the mass of fuel. The rate of this pressure increase corresponds to the injection rate. A pressure sensor detects this pressure increase, and a data acquisition and display system further processes the recorded data and renders it visible.

A proportional relationship exists between the integral value of the pressure and the injected amount of fuel. This relationship, however, cannot be expressed by means of a constant multiplication factor. Instead, particular interrelationships exist among the absolute quantity, the pump speed of rotation, and fuel temperature.

To have a good estimation of the experimental errors, several repetitive measurements were carried out at the same test point (energizing time, Rail pressure and backpressure) and the obtained dispersion was of about 0.6% respectively with proper calibration of the equipment

In order to determine the momentary mean quantity, a cumulative measurement process must therefore take place downstream from the IDRCI. The mean quantity corresponds to the mean surface area of the pressure integral for a recorded sequence of injection events. Five injection pressure values, fixed at the common rail, were used; 30 MPa, 55 MPa, 80 MPa, 105 MPa and 130 MPa. The backpressure or pressure at the discharge of the injector was changed between 2 MPa and 18 Mpa in order to change the pressure difference across the injector, and thus the flow conditions. For all the measurements taken the injector energizing time was set to 5 ms, which is much longer than the injection event in that engine (typically 0.7 to 1.2 ms). This condition makes it possible to produce a stable injection process and thus to obtain more consistent results for injection rate characterization and analysis.

The injection rate, fuel injection pressure and the energizing time intensity signals were recorded using a data acquisition and display system YOKOGAWA and the in-house developed software TRATASA to obtain the injection rate curves.

Results and Discussion

Measurement of Speed of Sound in the Fuel. As commented above, the methodology for the measurement of the speed of sound in the fuel was carried out with the time of travel across a known distance of a pressure perturbation in the fuel. Figure 5 shows two examples of the pressure perturbations observed in such an experiment, at the two measurement points separated by 20 meters in the pipe filled with fuel. The time of travel has also been plotted in the graphs. The test conditions for this figure correspond to two different pressure values and the same temperature. It can be corroborated how the increase in pressure produces a reduction in the time of travel, that is an increase in the speed of propagation of the pressure perturbations, which is assumed to be the speed of sound.

Figure 6 presents the ensemble of the results obtained in these experiments, where the effect of pressure and temperature are manifest. As expected, the value of speed of sound in the fuel increases with pressure and decreases with temperature.

In order to make this information easier to use, the data obtained for each value of temperature were fitted to a polynomial expression as follows:

$$u = a + b \cdot P + c \cdot P^2 + d \cdot P^3 \tag{8}$$

Where a, b, c y d are the constants of the polynomial, as given in Table 2. The determination coefficient R^2 shows that the greatest

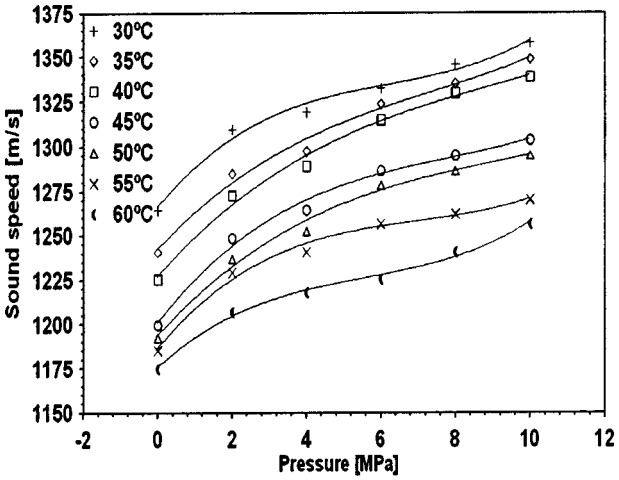

Fig. 6 Sound speed u in the fuel as a function of pressure

Table 2 Polynomial coefficients for Eq. (8) and the determination coefficient

T [°C]	a	b	c	d	R^2
30	1266.2	2.5187	−0.0343	0.00019	0.9875
35	1242.3	2.2613	−0.0217	1E-04	0.9892
40	1227.1	2.3746	−0.0199	7E-05	0.9919
45	1200.9	2.6867	−0.0289	0.00012	0.9922
50	1193.6	2.3161	−0.0202	7E-05	0.991
55	1186.4	2.516	−0.032	0.00015	0.9906
60	1175.6	1.9278	−0.0274	0.00016	0.9944

part of the observed variability of u is associated with the variable P. This means that the obtained polynomial proves a tight relationship between u and P.

Analysis of Cavitation in Steady Flow. In order to characterize the flow across the injector orifice, it is of utmost importance to know the actual local pressure conditions at the orifice inlet and outlet. Since the orifice inlet is not accessible and therefore the pressure at that point is practically impossible to measure, an alternative method was used, based on measuring the pressure drop across the injector holder in a specific preliminary test, and later subtracting this value from the total pressure drop across the complete injector.

For this test, the injector tip was cut off from the injector holder across a normal section just over the orifice inlet, as shown in Fig. 7. The modified injector was installed in the cavitation test rig, and the pressure drop was modified by varying the downstream conditions. In this way, a dependence of the fuel mass flow rate and the pressure drop produced by the injector holder could be obtained, as illustrated in Fig. 8 for the case of 10 MPa constant rail pressure. A relationship yielding the value of pressure drop for a given flow rate can be obtained by a fit to these data, as expressed by Eq. (9):

$$p_i - p_1 = -0.103 + 0.026 \cdot \dot{m} + 0.0089 \cdot \dot{m}^2 \tag{9}$$

These particular results should be obviously dependent on geometry and dimensions of the hydraulic circuit between the rail and the injector orifices. For these tests, the same lines and the same injector holder was used.

The final results applying this methodology to the two orifice geometries, conical and cylindrical, are presented in Fig. 9, where the injection mass flow rate is plotted versus the square root of effective pressure drop across the orifice ($p_1 - p_2$ as shown in Fig. 1) for two values of rail pressure of 10 and 20 MPa. As explained before, these measurements were taken in steady conditions of inlet and outlet pressure.

In the case of the conical orifice, there is a clearly liner dependence of the mass flow rate, while the cylindrical orifice produces an inflexion in this trend at the highest values of pressure drop,

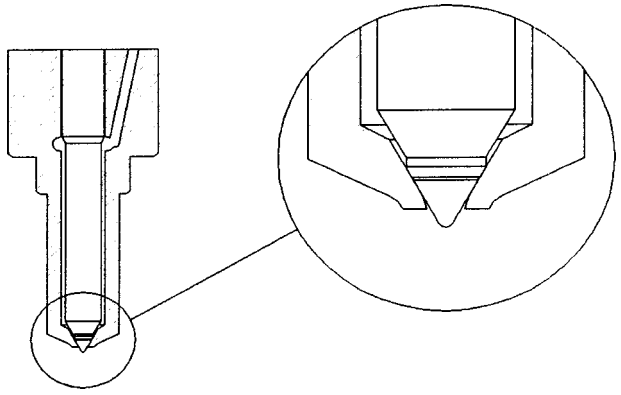

Fig. 7 Nozzle modification (without sac)

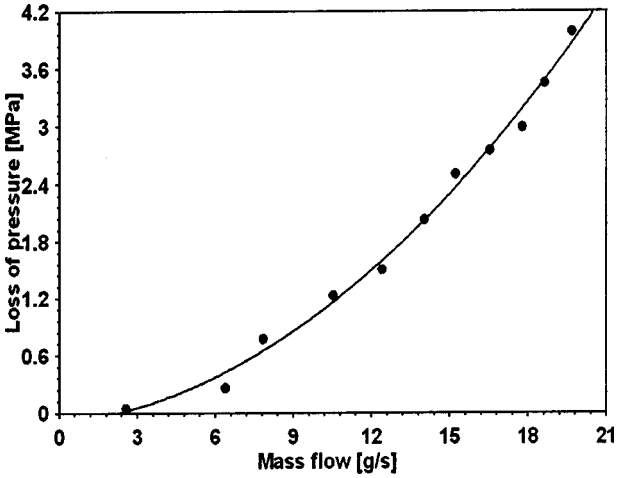

Fig. 8 Pressure loss across the injector holder and the nozzle sac

with almost no increase in mass flow rate. This phenomenon of mass flow rate being independent of the pressure drop evidences a case of choked flow due to the appearance of cavitation. As observed, the higher is the upstream pressure (rail pressure) the larger must be the pressure drop to induce cavitation.

This phenomenon can be identified more clearly using the discharge coefficient C_d across the orifice instead of the mass flow rate. The calculated values of the discharge coefficient by means of Eq. (3) are plotted in Fig. 10 for the same test results. The effect of choking flow in the cylindrical orifice is clearly underscored by the important reduction in the value of C_d at low discharge pressure.

A different way of representing the phenomenon of cavitation are the plots of discharge coefficient C_d versus the square root of the cavitation parameter K, defined by Eq. (6), as done in Fig. 11, again with the same set of results already commented. It should be remembered that as a consequence of the definition of K, cavitation should occur at low values of this parameter, therefore the analysis of these curves should be made from right to left on the horizontal axis.

The curves of Fig. 11 show again the inflexion points where cavitation starts to take place. The case of the cylindrical nozzle presents a region of high K values where no cavitation occurs, and consequently C_d values increase when K diminishes. When a critical value of K is attained, cavitation starts due to the high

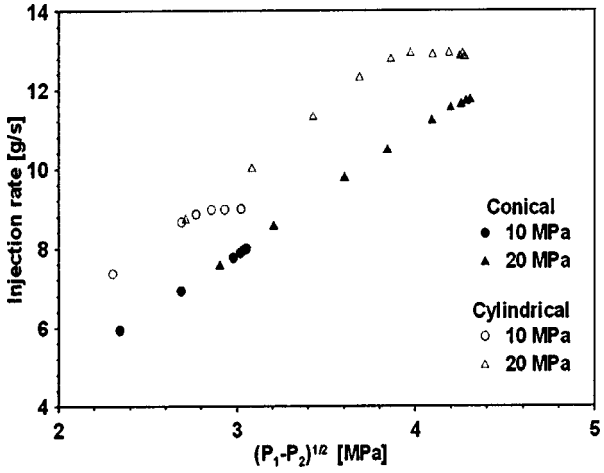

Fig. 9 Cavitation test rig results

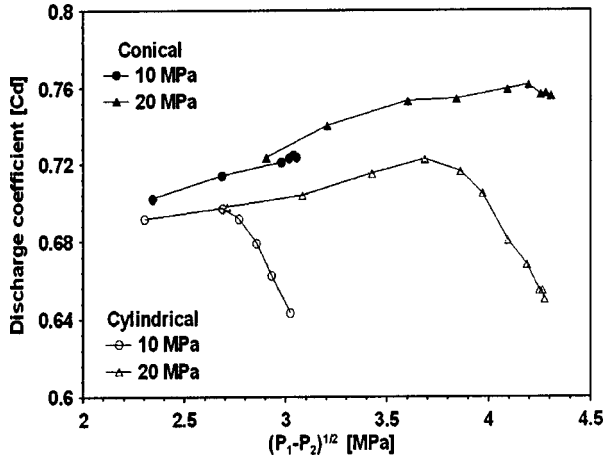

Fig. 10 Discharge coefficient for conical and cylindrical nozzles in the cavitation test rig

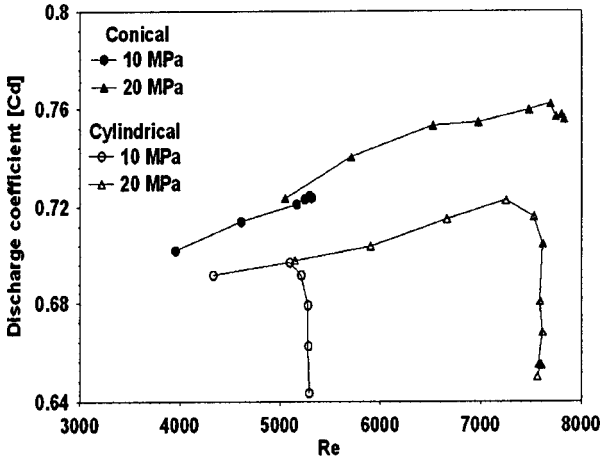

Fig. 12 Discharge coefficient vs. Reynolds number

pressure drop and the value of C_d drops rapidly, as discussed earlier. This zone of falling C_d corresponds to the choked flow state, and according to Eq. (5), the value of the slope corresponds to the value of the contraction coefficient C_c. This value is 0.645 for the case of 10 MPa rail pressure and 0.655 for 20 MPa. The plots corresponding to the conical nozzle confirm the resistance of this geometry against cavitation, since very low values of K are required to produce some slight evidence of cavitation in the case of 20 MPa rail pressure. In this case, a very large pressure drop across the orifice has been forced, as evidenced in Fig. 10.

Figure 12 shows an additional plot that can shed more light on the phenomenon, where Cd is now plotted versus Reynolds number Re. In no-cavitation conditions, it is possible to corroborate that Cd is almost linearly dependent on Re, as seen on the curves of the conical nozzle and in some portion of the curves of the cylindrical nozzle. When cavitation takes place, there is no relationship between these two parameters, and Cd drops practically vertically, that is, at constant Re. This really means that the flow velocity remains practically unchanged, even though pressure drop is being increased. These results substantiate once again that the conical orifice is able to cope with larger values of Re without any signs of cavitation

It should be taken into account that the values of Reynolds numbers produced in these tests are smaller than the maximum values that used to appear in normal injection conditions, mainly because injection pressure is much higher. However, in these cavitation tests in steady conditions, the maximum pressure drop is limited by the flow rate produced by the injection pump. Consequently, it seems opportune to investigate the influence of the higher pressure in real injection conditions.

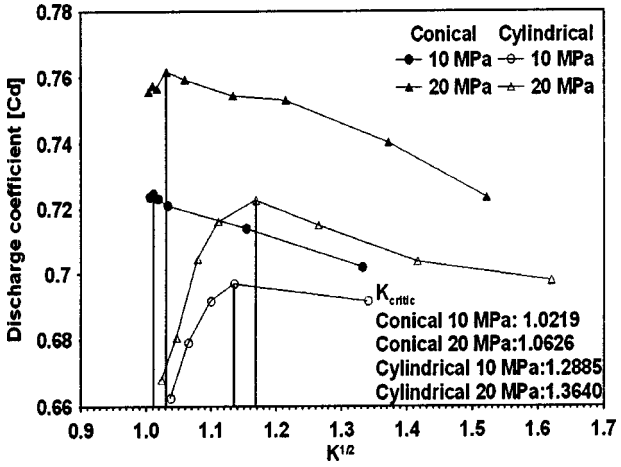

Fig. 11 Critical cavitation number

Real Injection (Injection Rate Test Rig). The results of the tests carried out with both injectors, in terms of instantaneous injection rate versus time, are represented in Fig. 13, in the left column for the cylindrical nozzle geometry and in the right column for the conical geometry. Each row corresponds to one value of injection pressure, and the curves in every plot are produced by modifying the pressure downstream the injector, according to the methodology commented above.

All the plots present the same global shape, with rapid variations during the short periods of needle opening and closing at start and end of the injection respectively. In between, there is a long period of stabilization where a slow decay in the injection rate is produced. The cause of this phenomenon is the decay of the pressure in the rail, as it can be corroborated in Fig. 14, and it is due to the emptying of the rail during the long injection time of 5 ms. This general, slow decay is not relevant for the study, and in the subsequent evaluation, the maximum value of the injection rate will be considered for the quantitative analysis.

A second general result is that for the same injection conditions, the cylindrical geometry produces a larger injection rate. This is due to its larger diameter, as already exposed in Table 1.

When injection pressure at the rail is kept at a low value of 30 and 55 MPa, (first two rows in Fig. 13) the injection rate during the stabilization phase increases with the reduction of the pressure downstream of the injector, that is with the pressure drop across the injector and consequently across the nozzles. In these two injection pressure values, there is a general behavior in both nozzle geometries. However, when injection pressure is raised further, the cylindrical geometry presents a stop in the increase in injection rate, even though the pressure drop is being increased. This is particularly evident in the case of injection pressure 105 and 130 MPa, where the maximum injection rate seems to be choked. The conical geometry shows the same trend, but the choking of the nozzle does not appear, even at the highest injection pressure, i.e. at the highest pressure difference. Comparing both geometries, it is also clear that the relative differences in maximum injection rate practically disappear at high pressure difference, in spite of the larger diameter of the cylindrical geometry.

A better understanding of the results can be gained by plotting the value of maximum injection rate versus the root of the pressure difference across the nozzle, as done in Fig. 15. From that plot, it is clear that some choking of the flow across the cylindrical geometry starts to appear at 55 MPa injection pressure, which is evident by the inflexion of the curves, and that at 105 MPa, the

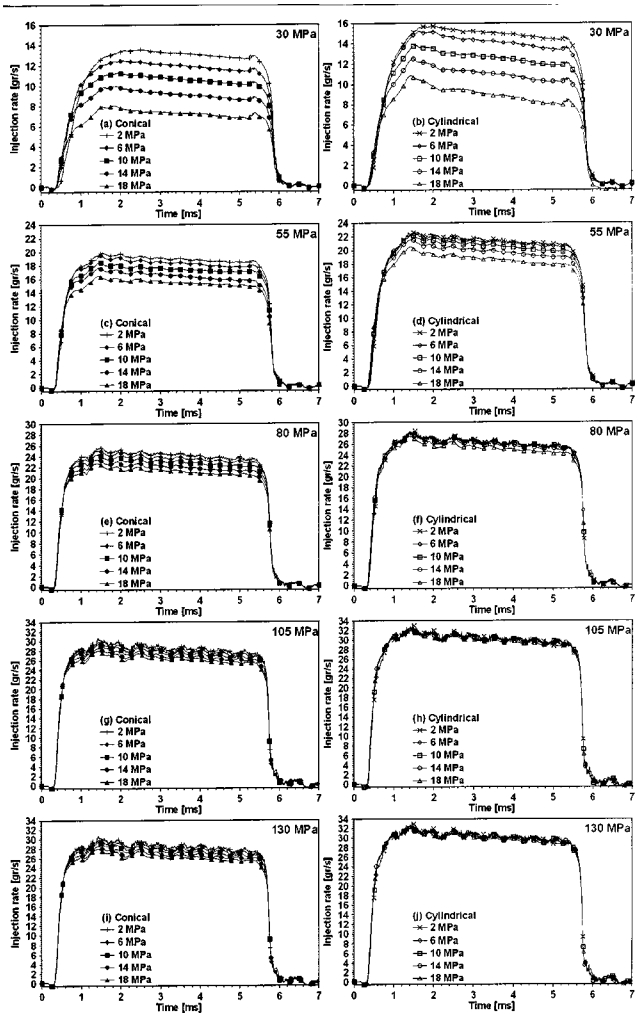

Fig. 13 (a–h) Injection rate curves at different injection pressures

nozzle flow is practically cavitating independently from the pressure value downstream. On the contrary, in the case of the conical geometry, this phenomenon is only slightly visible in the cases of highest pressure difference.

The same results have been plotted in Fig. 16 in terms of discharge coefficient across the injector nozzle for the maximum value of injection rate. In no-cavitation conditions, the discharge coefficient should increase with the pressure difference. This trend

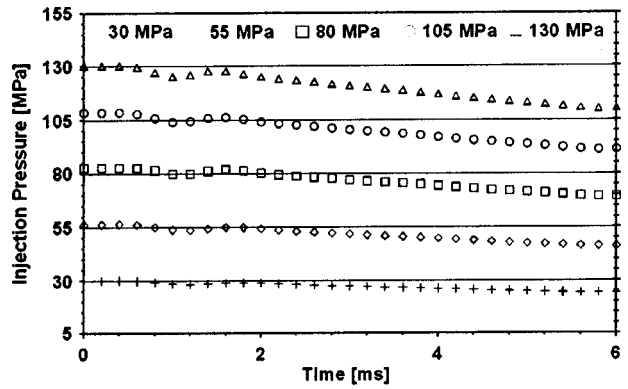

Fig. 14 Pressure drop during an injection event

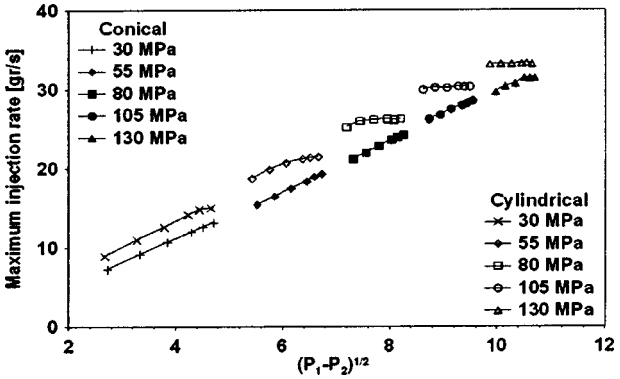

Fig. 15 Maximum injection rate vs. pressure difference

is observed with the conical nozzle, where only at highest values of pressure drop does the discharge coefficient stop growing, entering a transition zone, where cavitation starts. In the case of the cylindrical nozzle, the occurrence of full cavitation is evident by the drop in the discharge coefficient with high pressure difference. An interesting general result is that the conical nozzle exhibits greater discharge coefficients, even in non-cavitating conditions, which demonstrates that this geometry is more efficient.

An additional insight into the phenomenon can be obtained from Fig. 17, where the discharge coefficient has been plotted versus the square root of cavitation number K, as it was done previously for steady flow conditions in Fig. 11. When comparing these two figures, similar behavior can be observed, when injection conditions are comparable. K values close to 1 are required to produce cavitation, observed by the drop in Cd. However, the

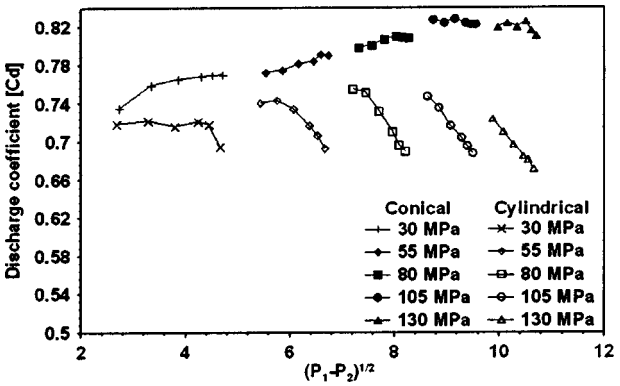

Fig. 16 Maximum discharge coefficient vs. Pressure difference

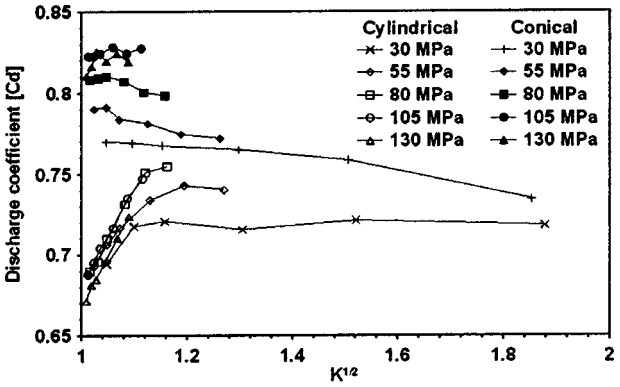

Fig. 17 Discharge coefficient vs. $K^{1/2}$

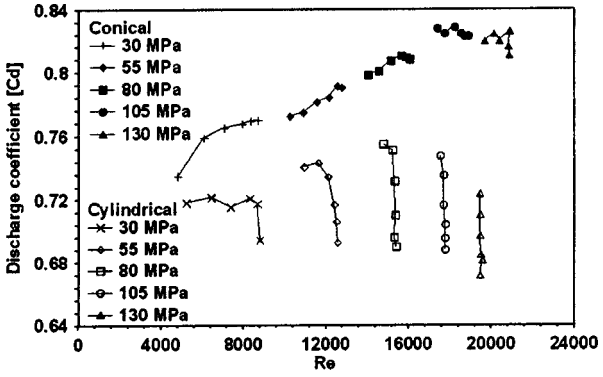

Fig. 18 Discharge coefficient vs. Reynolds number

interesting point is that at equal low values of K, the conical nozzle is more able to resist cavitation than the cylindrical nozzle.

Figure 18 shows again the dependence of Cd with the Reynolds number for the case of maximum value of injection rate. Due to the high injection pressures the real Reynolds numbers are higher than the numbers found in the cavitation test rig, as plotted previously in Fig. 12. Nevertheless, the same basic phenomena discussed earlier for steady-flow conditions are evident: Cd is linearly dependent on Re only in no-cavitation conditions and in fully developed cavitation, Re does not characterize the flow process. In these conditions, K is the controlling parameter, as shown in Fig. 17.

Comparison Between Cavitation Test Rig and Injection Rate Test Rig. In order to shed more light on the set of results from the steady flow in the cavitation test rig and from the unsteady real injection conditions, Fig. 19 compares the values of Cd in the range where similar Re values are available.

At low injection pressure, the cavitation test rig (CTR) produces similar injection conditions as the Injection Rate Test Rig (IRTR). However, since the CTR tests the maximum needle lift is larger, the pressure drop across the injector body is smaller, and the discharge coefficient across the nozzle is higher than in the IRTR.

Another interesting point to analyze is the differences in cavitation occurrence in the cylindrical nozzle, visible in the range of low injection pressures. At equal Reynolds number, there is no evidence of cavitation in the tests in the IRTR, while there is in the CTR. It has been proved in the literature that continuous flow has a strong tendency to cavitate [19].

One plausible reason for this phenomenon could be the requirement of maintaining for a minimum time the conditions of cavitation needed for producing a complete choked flow in the orifice [20]. Since the flow conditions in the CTR are steady, the cavitation conditions are continuous, whereas in the IRTR the unsteady flow causes cavitation conditions during very short periods, so that the requirements for complete choked flow are more difficult to fulfill.

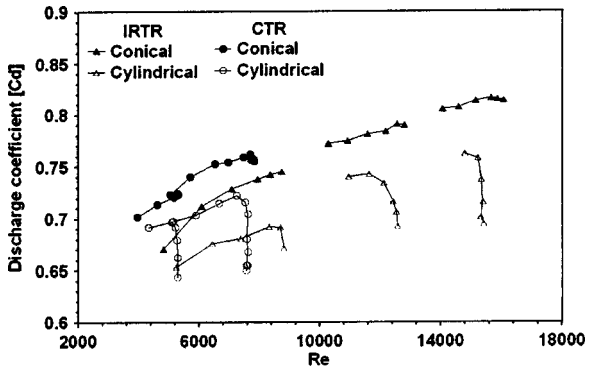

Fig. 19 Comparison between CTR and IRTR

Conclusions

An attempt has been made to compare the flow characteristics produced by two different geometries of injector nozzle holes, cylindrical and conical, based on an analysis of experimental values of Cd, Re and K.

Injector nozzles have been tested in steady flow conditions in a cavitation test rig and in real injection conditions in an injection rate test rig.

Important differences were found between the flow types in the conical and cylindrical nozzles, the most relevant being the following:

1. The values of discharge coefficient are higher in the conical nozzle than in the cylindrical nozzle.
2. The flow in the cylindrical nozzle collapsed at high injection pressure and Re values due to the formation of cavitation, while this phenomenon was not observed in the conical nozzle.

As a general fact for both injector nozzle geometries, it can be concluded that when no cavitation appeared, the discharge coefficient of the nozzle can be well related to the Reynolds number. However, when cavitation appears, Reynolds number is meaningless, and the phenomenon is better characterized by the cavitation number.

Regarding the use of a steady-flow cavitation test rig for characterizing cavitation conditions, the following conclusions can be highlighted:

At the same injection pressure, higher mass flow rate was measured in the cavitation test rig than in unsteady real conditions in an Injection Rate Test Rig. This difference is due to the losses in the needle, which are higher in the Injection Rate test rig, causing the upstream pressure to be lower.

At equal values of Reynolds number, cavitation is more prone to appear in the Cavitation Test Rig than in the Injection Rate Test Rig. This is presumably due to the unsteady flow conditions in the IRTR, which do not allow enough time for cavitation to develop.

Acknowledgment

This research was founded in part by MECD, reference AP2001-2588

Nomenclature

A = nozzle area
A_t = IDRCI transversal area
Cc = contraction coefficient
Cd = discharge coefficient
CTR = Cavitation Test Rig
D = diameter
D_i = hole inlet diameter
D_o = hole outlet diameter
dP = IDRCI pressure rise
$IDRCI$ = Injection Discharge-Rate-Curve Indicator
$IRTR$ = Injection Rate Test Rig
K = cavitation parameter defined by Nurick
k = conicity factor
K_{Critic} = critic cavitation number
L = hole length
$\dot{m}$ = flow injection rate
T = temperature
P = pressure
P_1 = hole upstream pressure
P_2 = hole downstream pressure
P_i = injection pressure

P_v = flow vapor pressure
r/D = standardized ratio
Re = Reynolds number
u = flow sound velocity

Greeks

ρ = flow density

References

[1] Arcoumanis, C., and Baiasad, M. S., 1993, ''Analysis of Consecutive Fuel Injection Rate Signals Obtained by the Zeuch and Bosch Methods,'' SAE Tech. Pap. Ser., 930921.

[2] Ganippa, L. C., Andersson, S., Chomiak, J., and Matsson, A., 2003, ''Combustion Characteristics of Diesel Sprays From Equivalent Nozzles With Sharp and Rounded Inlet Geometries,'' Combust. Sci. Technol., **175**(6), pp. 1015–1032.

[3] Timoney, D. J., and Smith, W. J., 1995, ''Correlation of Injection Rate Shapes With D.I. Diesel Exhaust Emissions,'' SAE Tech. Pap. Ser., 950214.

[4] Arcoumanis, C., Gavaises, M., and French, B., 1997, ''Effect of Fuel Injection Processes on the Structure of Diesel Sprays,'' SAE Tech. Pap. Ser., 970799.

[5] Nishimura, T., Satoh, K., Takahashi, S., and Yokota, K., 1998, ''Effects of Fuel Injection Rate on Combustion and Emission in a DI Diesel Engine,'' SAE Tech. Pap. Ser., 981929.

[6] Koo, J. Y., Hong, S. T., Shakal, J. S., and Goto, S., 1997, ''Influence of Fuel Injector Nozzle Geometry on Internal and External Flow Characteristics,'' SAE Tech. Pap. Ser., 970354.

[7] Schmidt, D. P., Rutland, C. J., and Corradini, M. L., 1997, ''A Numerical Study of Cavitating Flow Through Various Nozzle Shapes,'' SAE Tech. Pap. Ser., 971597.

[8] Nurick, W. H., 1976, ''Orifice Cavitation and its Effect on Spray Mixing,'' ASME J. Fluids Eng., pp. 681–687.

[9] Qin, J. R., Dan, T., Lai, M. C., Savonen, C., Schwartz, E., and Brkyzik, W., 1999, ''Correlating the Diesel Spray Behavior to Nozzle Design,'' SAE Tech. Pap. Ser., 1999-01-3555.

[10] Bergwerk, W., 1959, ''Flow Pattern in Diesel Nozzle Spray Holes,'' Proc. Inst. Mech. Eng., **173**, pp. 655–660.

[11] Goney, K. H., and Corradini, M. L., 2000, ''Isolated Effects of Ambient Pressure, Nozzle Cavitation and Hole Inlet Geometry on Diesel Injection Spray Characteristics,'' SAE Tech. Pap. Ser., 2000-01-2043.

[12] Fox, T. A., and Stark, J., 1989, ''Characteristics of Miniature Short-Tube Orifice Flows,'' Proc. Inst. Mech. Eng., **203**, pp. 351–358.

[13] Sadri, R. M., and Floryan, J. M., 2002, ''Achúrate Evaluation of the Loss Coefficient and the Entrance Length of the Inlet Region of a Channel,'' ASME J. Fluids Eng., pp. 685–693.

[14] Soteriou, C., Andreys, R., and Smith, M., 1995, ''Direct Injection Diesel Spray and the Effect of Cavitation and Hydraulic Flip on Atomization,'' SAE Tech. Pap. Ser., 950080.

[15] Bosch, W., 1966, ''The Fuel Rate Indicator: A New Measuring Instrument for Display of the Characteristics of Individual Injection,'' SAE Tech. Pap. Ser., 660749.

[16] Rodriguez, L. M., Casanova, J., and Tartajos, G., 2000, ''High Pressure Physical Properties of Fluids Used in Diesel Injection Systems,'' SAE Tech. Pap. Ser., 2000-01-2046.

[17] Ball, S. J., and Trusler, J. P. M., 2000. ''The Speed of Sound and Derived Thermodynamic Properties of n-Hexane and n-Hexadecane at Temperatures Between 298 K and 373 K and Pressures up to 100 MPa,'' Fourteenth Symposium on Thermo physical Properties, Boulder, Colorado, USA.

[18] Holman, J. P., 1984. *Experimental Methods for Engineers*, 4th edition., McGraw-Hill, New York.

[19] Ganippa L. C., and Bark G., 2001, ''Comparison of Cavitation Phenomena in Transparent Scaled-up Single-Hole Diesel Nozzles,'' CAV2001: Session A9.005

[20] Kato, M., Kano, H., Date, K., Oya, T., and Niizuma, K., 1997, ''Flow Analysis in Nozzle Hole in Consideration of Cavitation,'' SAE Tech. Pap. Ser., 970052.

J. H. Nie

B. F. Armaly*

Department of Mechanical and Aerospace Engineering,
and Engineering Mechanics
University of Missouri–Rolla,
Rolla, MO 65409

W. Q. Tao

Q. W. Wang

School of Energy and Power Engineering
Xi'an Jiaotong University,
Xi'an 710049, China

Three-Dimensional Turbulent Flow in the Exit Head Section of a Heat Exchanger

Measurements of three-dimensional turbulent flow in the exit head section of a shell-and-tube heat exchanger were performed using three-component laser Doppler velocimeter. The test geometry is half of a hemispherical cap with two outlet-tubes and with a cylindrical inlet section. Distributions of the velocity vector field, the three mean velocity components, and the Reynolds stress components are reported, and the complex nature of flow in the head section and in the neighborhood of the outlet-tube is quantified. The radial and the streamwise velocity components are of the same order of magnitude in the neighboring region of the outlet-tubes, and they are not symmetric relative to the center plane intersection of the outlet-tubes. The friction factor that was measured across the exit head section of the heat exchanger decreases as the Reynolds number increases from 25,000 to 50,000. These results are useful for validating turbulent flow simulation codes and are needed for improving the design of the exit head section of shell-and-tube heat exchangers. [DOI: 10.1115/1.1637635]

Introduction

More than 90% of the heat exchangers that are used in industry (petroleum, chemical, power generation, and heating/air-conditioning engineering) are of the shell-and-tube type design [1]. In such a system, one fluid flows inside the tubes that are encased in a shell, and another fluid flows through the shell and around the tubes. The shell is normally cylindrical in shape and has a hemispherical cap at one end. In the head section, a baffle is normally placed at the center of the hemispherical cap to separate the inlet flow to the tubes that are in the shell from the outlet flow from the tubes as it leaves the shell. In this manner, one half of the hemispherical cap serves as the inlet head section and the other half serves as the exit head section of the heat exchanger. Inlet-tubes are connected to the inlet head section, and outlet-tubes are connected to the exit head section for bringing in and for taking out the fluid that flows through the heat exchangers. The flow characteristics in the inlet head section influence the velocity distribution inside the heat exchanging tubes that are in the shell of the heat exchanger and the flow characteristics in the exit head section influence the velocity distribution in the outlet-tubes that are connected to the exit head section of the heat exchanger. Detailed knowledge of the flow distribution within the heat exchanger and in its head sections helps in the design of reliable and efficient units.

Numerous guidelines and procedures have been published [2–4] for designing and for determining the overall performance of shell-and-tube heat exchangers. In addition, few experimental [5–7] and numerical [8,9] studies have been reported on the overall flow characteristics, heat transfer and fouling performance of these heat exchangers. Unfortunately, most of the reported experimental studies have focused on the overall performance of the heat exchanger and did not report the dynamics of the internal flow and its distribution. Such data and information are needed for the optimization and the design improvements of heat exchangers. In addition, detailed flow measurements inside these heat exchangers are needed for validating simulation codes [10], and the lack of such data motivated the present study.

*Corresponding author.

Contributed by the Fluids Engineering Division for publication in the JOURNAL OF FLUIDS ENGINEERING. Manuscript received by the Fluids Engineering Division September 11, 2001; revised manuscript received September 12, 2003. Associate Editor: J. Katz.

Experimental Apparatus and Test Sections

A schematic of the wind tunnel and the test section is shown in Fig. 1. It is an air tunnel that is composed of five sections: the measurement section, the converging section, the stabilization section, the diverging section, and the power section. The inlet section of the tunnel serves as the test section where velocity measurements are made (section 1), and it is a simplified physical model (half of a hemisphere cap) of an exit head section of a shell-and-tube heat exchanger with two identical outlet-tubes that are symmetric with respect to the symmetry plane of the hemispherical exit head section of the heat exchanger. The volume flow rate through the tunnel is measured with a fluted tube (section 4). This fluted tube has an inner diameter of 50 mm and a length of 2 m, and is equipped with a multiport averaging Pitot tube [11] to measure flow rate. Calibration and use of such fluted tube for measuring flow rate were reported by Wang et al. [12]. The suction of a blower with variable speed electric motor (section 6) was used to control and adjust the air flow rate through the tunnel.

An enlarged schematic of the test section (a simplified model of the exit head section of a shell-and-tube heat exchanger with outlet-tubes) is shown in Fig. 2. It is half of a hemispherical cap mounted with two outlet-tubes and with a cylindrical inlet section at its opening. The vertical wall in the head section is used to separate the inlet flow from the outlet flow of the heat exchanger. The inlet flow enters the inlet head section of the heat exchanger in its way to the tubes that are in the shell of the heat exchanger. The exit flow from the tubes that are in the shell of the heat exchanger enter the exit heat section on its way to the outlet tubes of the heat exchanger. The flow distribution in the exit head section and in the region of the outlet tubes is the subject of this study. Air enters this exit head section of the heat exchanger (the test section), converges into the outlet-tubes, passes through the collection section and the stabilization section where its volume flow rate is measured, and then exits through the diverging section and through the suction blower. Some of the dimensions for the test section are listed as follows, $R_s = 0.149$ m, $R_{in} = 0.145$ m, $l_s = 0.001$ m, $H = 0.200$ m, $H_1 = 0.043$ m, $L = 0.082$ m, and $d = 0.050$ m.

The velocity measurements were performed with dual-probe, six-beam, three-components, backward-scattering laser Doppler velocimeter (LDV). The front lens of the probes has a diameter of 50 mm, and a focal length of 350 mm. The angle between the two

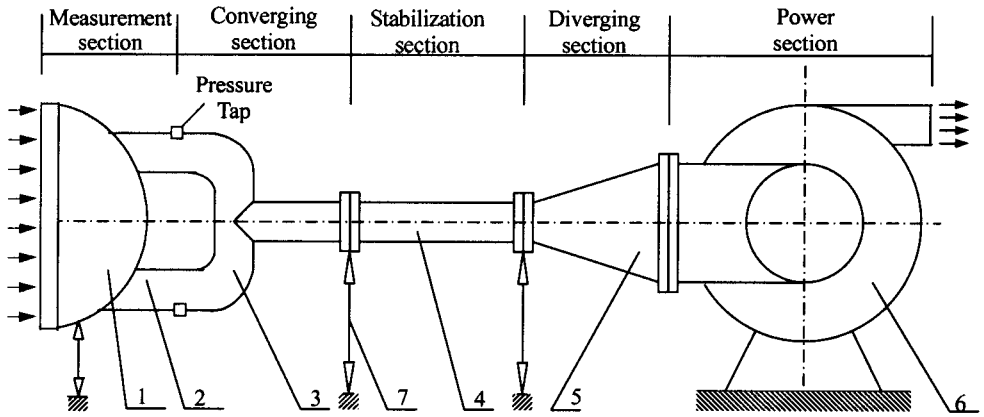

1- heat exchanger head section; 2 - outlet-tube; 3 - converging section; 4 - fluted tube;

5 - diverging section; 6 - blower; 7 - adjustable support

Fig. 1 Schematic of wind tunnel and test section

measuring probes of the LDV system was kept at 30 deg and the Doppler signals were transmitted through fiber optics to a burst spectrum analyzer. The seeding particles (having a mean diameter of less than 2 μm) were generated by a six-jet atomizer, and glycerin was used as the seeding fluid. The laser beams from the LDV system enter from the inlet (x, y) plane of the test section (at $z=0.0$ mm), and the measuring probe volume can be moved to locations inside the test section by the 3D (x, y, z) computer-controlled traversing system. The size of the probe volume was approximately 60 μm in length, and the resolution of the traverse system was 0.03 mm.

The LDV data acquisition system was operated continuously in the ''coincidence'' mode requiring simultaneous detection of samples in three coordinate directions, i.e., from the same scattering particle. If any of the six laser beams from the two probes is blocked by the solid walls of the test section, coincidence measurements could not be performed (data was not acquired for any of the velocity components). Therefore, at the inlet (x, y) plane of the test section $(z=0.0$ mm), the measuring probe volume can be moved to almost any location on that intersecting plane. However, for (x, y) planes that are deeper in the test geometry and in the neighborhood of the outlet-tube (i.e. $z>100$ mm), a limited number of measurements could be made due to one or more of the laser beams being blocked by the solid wall of the test section. For each point, data collection was programmed to acquire 64,000 samples or to measure for a duration of two minutes, whichever came first. Normally, the former criterion was satisfied except in the vicinity of the wall where particle arrival rates were reduced. The LDV software discarded data that was outside the range of $\pm 3\sigma$ from the mean value, and this filtering removed only the spurious data and not the valid turbulence data. The velocity bias correction technique used ensemble analysis as its basis, and applied a weighting function to each data point. The ensemble ''corrected'' values can be obtained through the number of data points and the weighting function. In the current software, the weighting function is determined using the time between data (TBD) points method [13]. In this method, the weighting function is the time between each realization or inter-arrival time. The LDV system was calibrated and the uncertainties for mean velocities were estimated to be less than $\pm 1.5\%$ with a typical inlet average velocity of 2.4 m/s. The results of many measurements at one point inside the flow field were checked at a fixed and steady flow rate and the measured mean velocity was repeatable with deviations of less than ± 0.6 % for the streamwise velocity component (v_z), and $\pm 1.5\%$ for the other two velocities components (v_x and v_y), respectively. Uncertainties of the experimental results were estimated by using the root-sum-square method [14]. From the calibration of the measuring instruments, the uncertainties of mea-

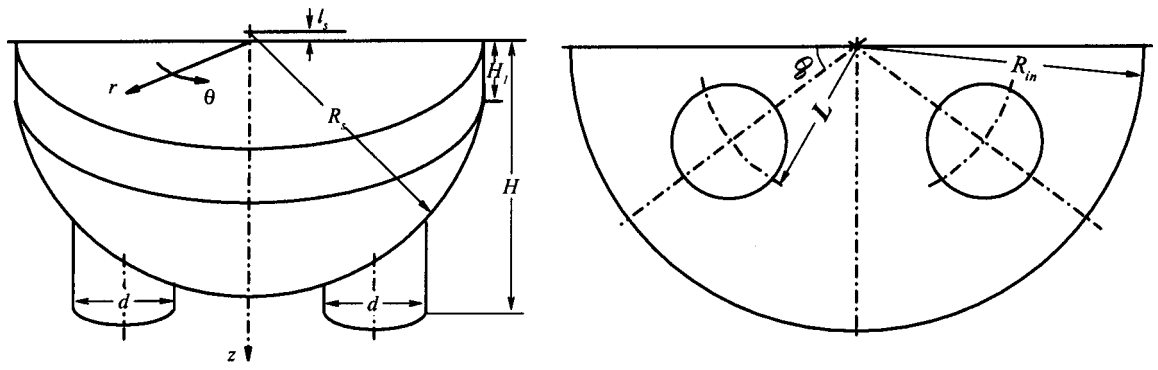

(*a*) Side view (*b*) Top view

Fig. 2 Schematic for the exit head section of the heat exchanger

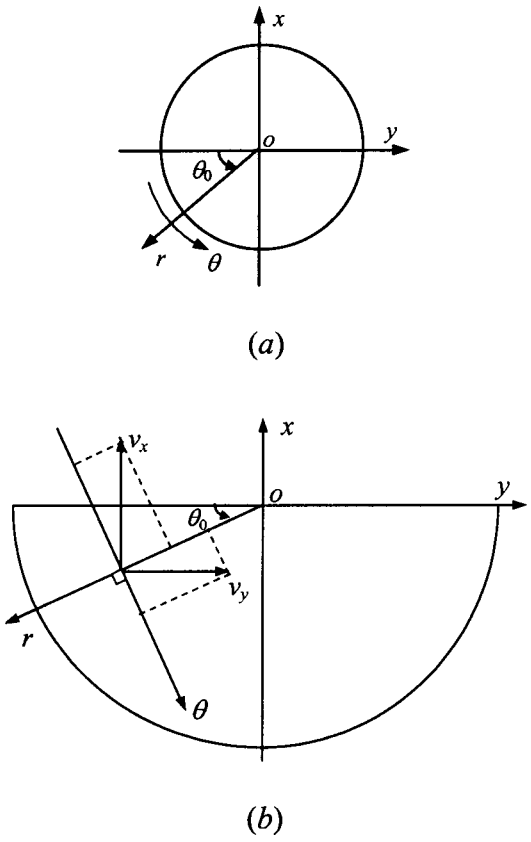

Fig. 3 Coordinates transformations for the traverse system and the measured velocities

sured values for Reynolds number (Re), and friction factor (f), were determined to be 5.6%, and 7.2%, respectively.

The traverse mechanism of the LDV system moved along the Cartesian coordinates (x, y, z), where (x, y) planes represents planes that are parallel to the inlet plane to the test section, and the z-coordinate represents the depth into the test section as shown in Figs. 2 and 3. The measured velocity components (v_x, v_y, v_z) in Cartesian coordinates (x, y, z) are transformed to velocity components (u, v, w) in cylindrical coordinates (r, θ, z), as shown in Fig. 3. It should be noted that the cylindrical coordinate will be used to display the measured fluid velocities and their fluctuations in the investigated cylindrical-hemispherical geometry. The transformation from the Cartesian coordinates system (x, y, z) that describes the movements of the traversing system, to the cylindrical coordinates (r, θ, z) that describes the cylindrical-hemispherical shape of the exit head section geometry of the heat exchanger (the test section), is shown in Fig. 3a for the specific case of $\theta=\theta_0$. Similarly, the measured velocity components (v_x, v_y, v_z) in Cartesian coordinates are transformed to the velocity components (u, v, w) in cylindrical coordinates for the specific case of $\theta=\theta_0$, by using Eq. (1) as shown in Fig. 3b:

$$\left.\begin{aligned} u &= -v_x \cos\theta_0 + v_y \sin\theta_0 \\ v &= -v_x \sin\theta_0 - v_y \cos\theta_0 \\ w &= v_z \end{aligned}\right\} \quad (1)$$

A photograph that shows the laser Doppler system and the inlet test section of the air tunnel (exit head section of the shell-and-tube heat exchanger with two outlet-tubes) is presented in Fig. 4.

Results and Discussions

Due to symmetry in the geometry of the test section, relative to the two outlet-tubes as shown in Fig. 2b, the measuring effort is simplified and reduced by restricting it to only one quarter of the

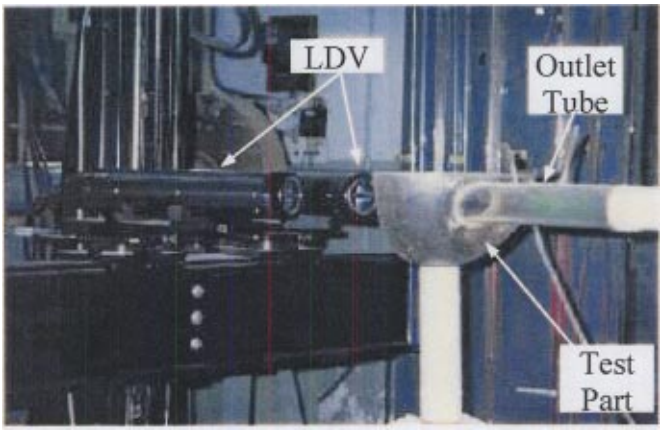

Fig. 4 Laser Doppler system and the test section

hemispherical cap. Laser Doppler velocity measurements were made only on the plane intersection of $\theta=32$ deg with the test section (exit head section of the heat exchanger). This plane is in the radial and vertical directions (r, z) where the tangential coordinate is constant ($\theta=32$ deg). It passes through both the center of the exit head section ($r=0.0$ mm) and the center of the left outlet-tube ($r=82$ mm and $\theta=32$ deg) as shown schematically by a top view as Section A-A in Fig. 5a. A plane view of that intersecting plane (Section A-A in Fig. 5a) is shown in Fig. 5b, and as can be seen it cuts both the hemispherical head section of the heat exchanger and the outlet-tube. All the reported velocity measurements were made on this plane and it will be identified through the text as the measuring plane A-A. In the present study, the Reynolds number (Re) is defined as $\mathrm{Re}=\rho w_{in}(2R_{in})/\mu$, where w_{in} is the average streamwise velocity component at the inlet plane ($z=0.0$ mm) of the test section, the density (ρ) and dynamic viscosity (μ) are taken as constant ($\rho=1.24$ kg/m^3 and $\mu=1.83\times10^{-5}$ kg/m·s). The average inlet air velocity is determined through the expression of $w_{in}=Q/A_{in}$, where Q is the air volumetric flow rate measured by the fluted-tube (section 4 as shown in Fig. 1), and A_{in} is the cross-sectional flow area at the inlet plane of the test section.

The mean and turbulent fluctuating velocity components were measured in the test section on the selected measuring plane A-A, and the measurements of the mean velocity components are reported in Figs. 6 and 7 for Reynolds number of Re=46122. The results in Fig. 6 represent a vector plot of the mean velocity on the measuring plane A-A, and they clearly show how the flow converges to the outlet-tube while velocity vectors change directions and magnitudes due to changes in geometry. The velocity at the inlet of the measuring plane A-A ($z=0.0$ mm) is relatively small and uniform, while the velocity at the inlet of the outlet-tube in

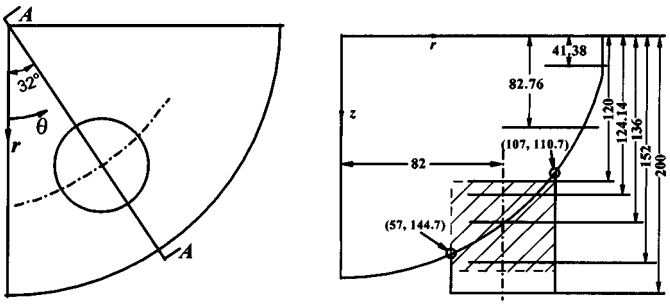

(*a*) Top view (*b*) *A-A* intersection

Fig. 5 Planes where measurements are made

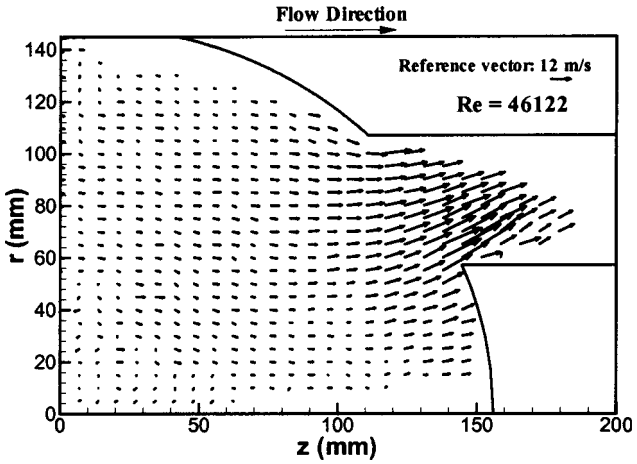

Fig. 6 Velocity vector field on the measuring plane A-A for Re=46,122

the measuring plane A-A is relatively high and nonuniform. The radial velocity component (v) is of the same order of magnitude as the streamwise velocity component (w) in the neighboring region of the outlet-tube on the measuring plane A-A. The streamwise velocity component (w) increases and the radial velocity component (v) decreases gradually as the flow enters the outlet-tube on the measuring plane A-A.

Distributions of the measured three velocity components on the measuring plane A-A are presented in Fig. 7 for Re=46122. It can be seen from Fig. 7(a) that tangential velocity component (u) is small in the whole region of that plane, ranging between -2 to 0.5 m/s and the negative sign means that the velocity is in the reverse θ-direction as denoted in Fig. 3. It is negative on most of that plane, which means that fluid below the measuring plane A-A (i.e., $\theta<32$ deg) rotates in a clockwise direction (as viewed along z axis direction) while fluid that is above the measuring plane A-A ($\theta>32$ deg) rotates in a counterclockwise direction. This is due to the fact that the centerline of the outlet-tube is not symmetric relative to tangential direction in the test section, i.e. the centerline of the outlet-tube is at 58 deg from the top half of the test section and at 32 deg from the bottom half as shown in Fig. 5(a). The larger flow area that exists above the $\theta=32$ deg plane is responsible for making the average tangential velocity component (u) negative on most of this plane. The results in Fig. 7(b) show that the radial velocity component (v) on the measuring plane A-A increases sharply close to the inlet of the outlet-tube due to the abrupt decrease in flow cross sectional area. That velocity component (v) is positive throughout that plane because fluid flows from the larger area at the inlet of that plane ($z=0.0$ mm) toward the smaller area of outlet-tube as shown in Fig. 6. The results in Fig. 7(c) show that the streamwise velocity component (w) on the measuring plane A-A increases gradually from the inlet of that plane to the inlet of the outlet-tube on that plane. On the measuring plane A-A, the maximum of this velocity component occurs at the center of the outlet-tube and its magnitude decreases gradually to zero at the wall of the outlet-tube. These results clearly show that the position of the outlet-tube influences significantly the velocity distribution in the exit head section of the shell and tube heat exchanger. Decreasing the nonsymmetry of the outlet-tube could help in decreasing nonuniformity in the velocity distribution.

The previous results demonstrate that most of the variations in the velocity field on the measuring plane A-A occur in the region where the outlet-tube intersects with the hemispherical exit head section of the heat exchanger. The region of $120\leqslant z\leqslant 160$ mm and $57\leqslant r\leqslant 107$ mm on the measuring plane A-A (the dashed area in Fig. 5(b)) is investigated in more details in order to quantify the velocity field in that region. The radial distributions of the three mean velocity components on three "z" planes at the entrance region of the outlet-tube ($z=120$, 136 and 152 mm) on the measuring plane A-A are shown in Figs. 8, 9 and 10. The solid lines that are shown in these figures represent a best fit to the measured results. The streamwise intersection of $z=120$ mm lies at the beginning of the region where the outlet-tube intersects with the hemispherical exit head section of the heat exchanger. The streamwise intersection of $z=136$ mm lies in the middle of that region, and the streamwise intersection of $z=152$ mm lies at the end of that region as shown schematically in Fig. 5(b).

The results in Fig. 8 show the radial distributions of the three mean velocity components on the measuring plane A-A at $z=120$ mm for Reynolds numbers of 39,524 and 45,057. The tangential velocity component (u) on that plane is negative on this z-line and is relatively uniform until the centerline of the outlet-tube ($r=82$ mm). Its negative magnitude starts to increase sharply as the radial distance (r) continues to increase. The radial velocity component (v) shows a peak value of about 4.5 m/s for Reynolds number of 45057 at $r\approx 73$ mm (a distance smaller than the centerline location of the outlet-tube that is at $r=82$ mm), then decreases as the distance approaches the solid wall boundary of the test section. The streamwise velocity component (w) shows a peak of 15 m/s for Reynolds number of 45057 at approximately $r=82$ mm (the location of the centerline of the outlet-tube), then its magnitude decreases as the distance approaches the solid wall

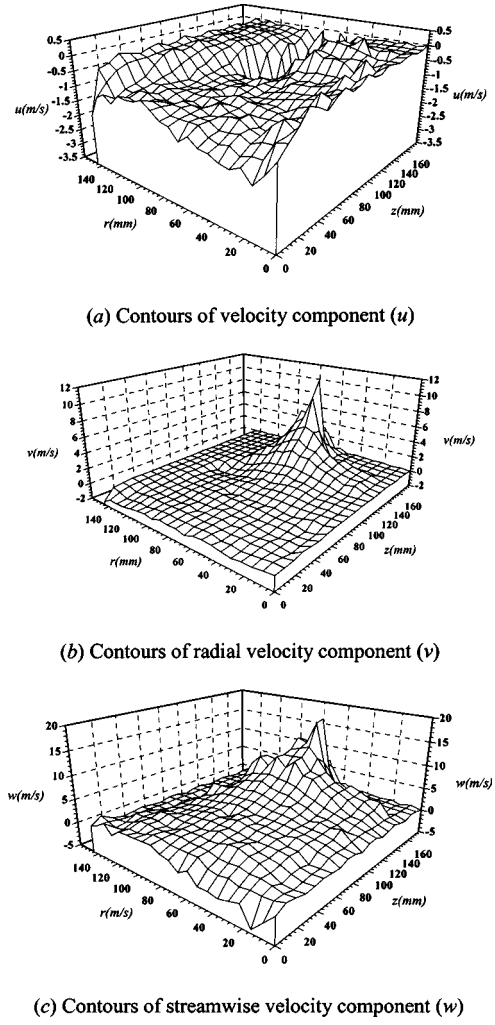

(a) Contours of velocity component (u)

(b) Contours of radial velocity component (v)

(c) Contours of streamwise velocity component (w)

Fig. 7 Distribution of velocity components on the measuring plane A-A for Re=46,122

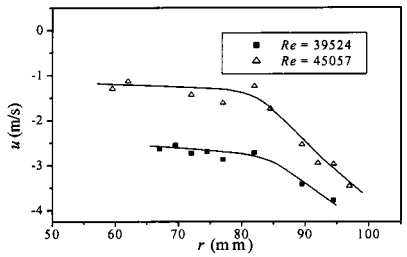

(*a*) Tangential velocity component (u)

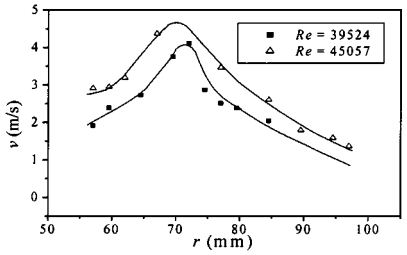

(*b*) Radial velocity component (v)

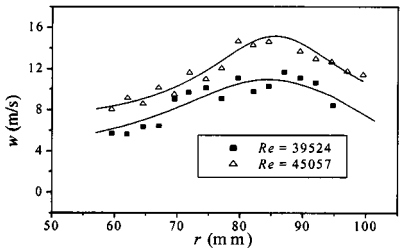

(*c*) Streamwise velocity component (w)

Fig. 8 Velocity distributions on the measuring plane A-A at $z=120$ mm

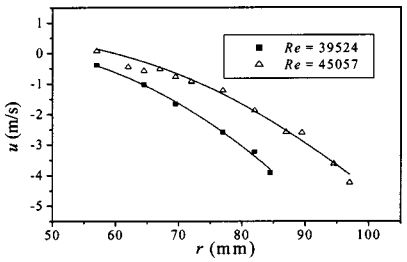

(*a*) Tangential velocity component (u)

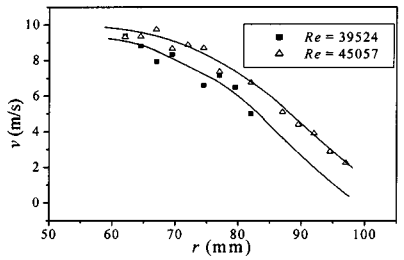

(*b*) Radial velocity component (v)

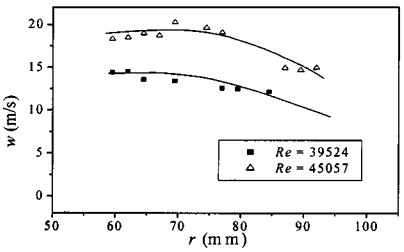

(*c*) Streamwise velocity component (w)

Fig. 9 Velocity distributions on the measuring plane A-A at $z=136$ mm

boundary of the outlet tube. All of these three velocity components (u, v and w) increase in magnitude with the increasing Reynolds number, but they retain approximately the same general distribution. Similar trends in the results can be seen in Fig. 9 for $z=136$ mm on the measuring plane A-A, with the exceptions that the peaks that were observed in two of these velocity distributions in Fig. 8 (for $z=120$ mm) do not appear at this z location. The results presented in Fig. 10 for $z=152$ mm on the measuring plane A-A show similar trends but with peaks in the distributions at roughly $r=65$ mm (a distance smaller than the centerline location of the outlet-tube). It should be noted that the maximum tangential velocity component (u) at $z=152$ mm, is positive and lies in the region of $r=60\sim65$ mm. That velocity component experiences significant variation in its magnitude and direction in this region as the fluid enters the outlet-tube. Baffles or similar structures could be installed in the exit head section of the heat exchanger to improve the quality of the flow in the outlet-tubes.

Radial distributions of the three mean velocity components on the measuring plane A-A are presented in Fig. 11 for three z-locations ($z=41.38$ mm, 82.76 mm and 124.14 mm) for Re $=46122$. The line of $z=41.38$ mm lies in the cylindrical section of the exit head section of the heat exchanger. The line of $z=82.76$ mm lies in the hemispherical region, and the line of $z=124.14$ mm lies in the region where the outlet-tube intersects with the hemispherical cap of the exit head section as shown in Fig. 5*b*. The outer solid wall boundary of the test section at these z-locations are at $r=145$ mm, 125.64 mm, and 107 mm, respectively. Distributions of the three mean velocity components at $z=41.38$ mm and $z=82.76$ mm are similar in nature since these two locations have similar geometries but differ in size. On these two z-lines, the tangential velocity component (u) and the radial velocity component (v) are relatively low, and the streamwise velocity component (w) increases as the flow cross sectional area decreases from that at $z=41.38$ mm to that at $z=82.76$ mm. The streamwise velocity component on the measuring plane A-A at these two locations develops a positive peak value at approximately $r=85$ mm (a distance approximately equal to the centerline location of the outlet-tube). The further decrease in the cross sectional area at the streamwise location of $z=124.14$ mm causes the fluid to accelerate and converge toward the outlet-tube with a maximum tangential velocity component (u) of -3 m/s developing at $r\approx90$ mm. That velocity component is relatively small but positive in the region between $r=20$ to 50 mm, and it is negative for larger radial distances, implying a vortical clockwise type flow into the outlet-tube at this z-plane. Similar conclusion could be drawn from the results that are presented in Fig. 10*a*. The radial velocity component (v) reaches a maximum of about 5 m/s, and the streamwise velocity component (w) reaches a maximum of about 16 m/s at $r\approx70$ mm. The streamwise velocity component experiences the greatest change due to the greatest change in the cross sectional area. Its maximum of about 16 m/s that occurs at $z=124.14$ mm is about four times the maximum that occurs at $z=41.38$ mm.

Radial distributions of the Reynolds normal stresses ($\overline{u'u'}$, $\overline{v'v'}$ and $\overline{w'w'}$) on the measuring plane A-A at three selected streamwise locations ($z=41.38$, 82.76 and 124.14 mm) are shown in Fig. 12 for Re=46122. The interference of the solid wall boundaries of the test section with the laser beams of the LDV

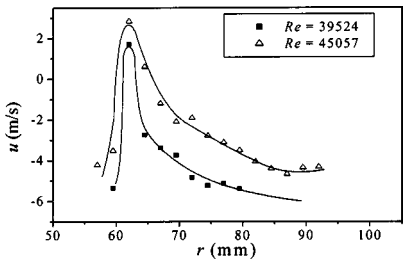

(*a*) Tangential velocity component (u)

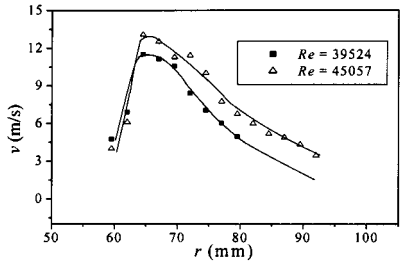

(*b*) Radial velocity component (v)

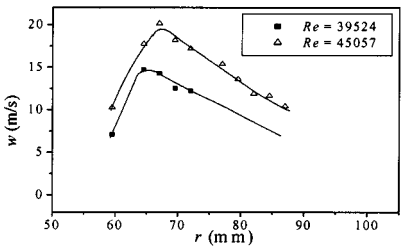

(*c*) Streamwise velocity component (w)

Fig. 10 Velocity distributions on the measuring plane A-A at $z=152$ mm

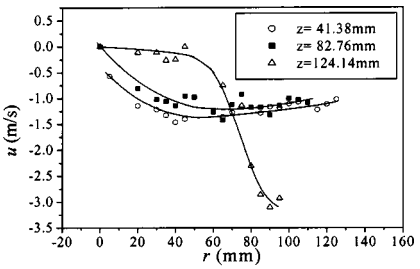

(*a*) Tangential velocity component (u)

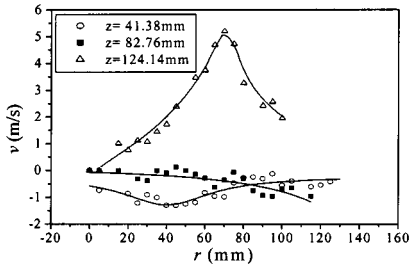

(*b*) Radial velocity component (v)

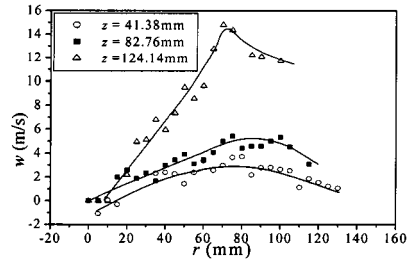

(*c*) Streamwise velocity component (w)

Fig. 11 Radial distribution of mean velocity components on the measuring plane A-A for Re=46,122

system at $z=82.76$ and 124.14 mm limits the number of data points that can be taken on these locations as can be seen from Figs. 11–13. The Reynolds stresses are normalized based on the inlet average streamwise velocity component (w_{in}), which is 2.347 m/s for Re=46122. The solid lines that appear in these figures are an attempt to connect the experimental points while smoothing the transition from one point to the other. Figure 12(*a*) shows that the tangential Reynolds normal stress component, $\overline{u'u'}$, is relatively low on the measuring plane A-A in the whole radial direction at $z=41.38$ and 82.76 mm. At $z=124.14$ mm, a peak appears to develop at $r\approx 65$ mm (near the inner solid wall of the outlet tube that is at $r=57$ mm), and a minimum value appears to develop at $r\approx 75$ mm (near the centerline of the outlet tube that is at $r=82$ mm). The points that appear in the figure on a $z=124.14$ mm and $r>82$ mm are below the orginal hemispherical surface shape of the test section, and are inside the domain of the outlet tube. The tangential velocity component is negative in that region, and the wall of the outlet-tube starts to influence significantly the behavior on the tangential Reynolds normal stress component in that region. Figure 12(*b*) shows that the radial Reynolds normal stress component ($\overline{v'v'}$) is also low on the measuring plane A-A in the whole radial range at $z=41.38$ and 82.76 mm. At $z=124.14$ mm, one peak develops at about $r\approx 65$ mm (close to the inner solid wall of the outlet-tube), and that is in the same general location where the peak tangential Reynolds normal stress component ($\overline{u'u'}$) develops, as seen in Fig. 12(*a*). Another peak appears to develop on this z-location at $r\approx 100$ mm (close to the outer solid wall of the outlet-tube that is at $r=107$ mm). Fig-

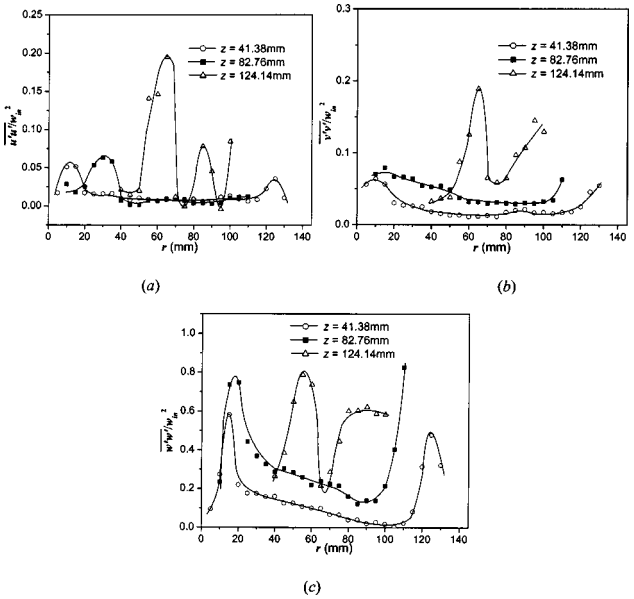

Fig. 12 Radial distribution of Reynolds normal stress components on the measuring plane A-A for Re=46,122

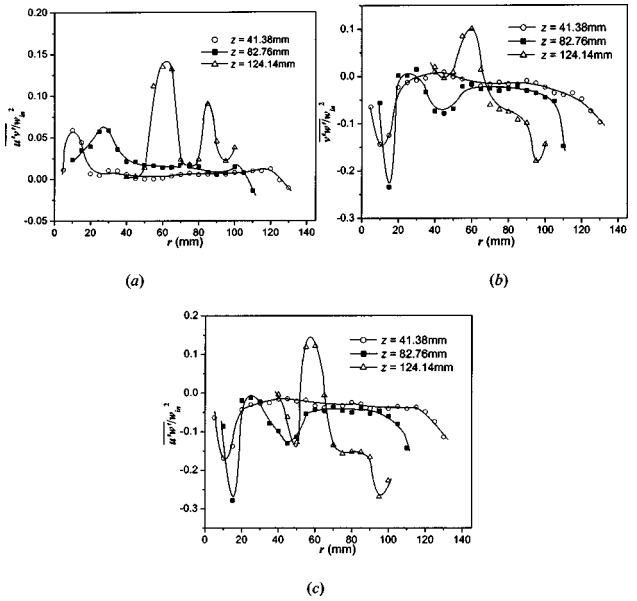

Fig. 13 Radial distribution of Reynolds shear stress components on the measuring plane A-A for Re=46,122

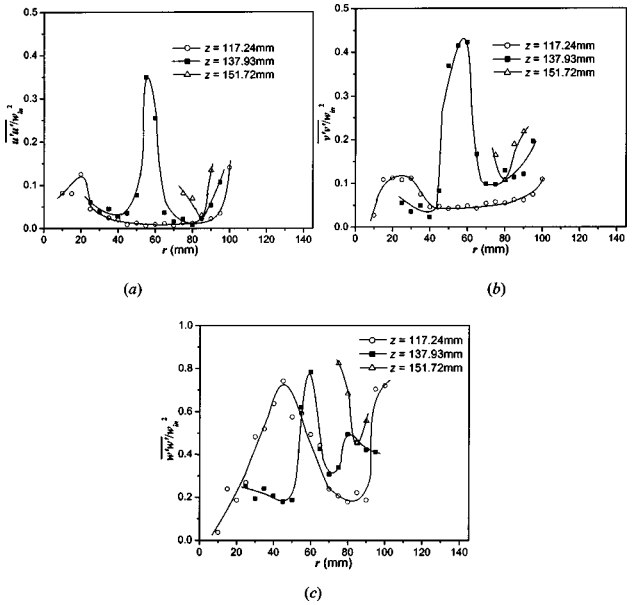

Fig. 14 Radial distribution of Reynolds normal stress components on the measuring plane A-A in the inlet region of the outlet-tube for Re=46,122

ure 12(*c*) shows that the peak values in the distributions of the streamwise Reynolds normal stress component ($\overline{w'w'}$) also develop in the same general regions on $z=124.14$ mm. The maximum value of the streamwise Reynolds normal stress component ($\overline{w'w'}$) is about four times higher than the maximum values of the tangential and the radial Reynolds normal stress components. The peaks that develop in Fig. 12(*c*) at $z=41.38$ mm and 82.76 mm are due to the proximity of these locations to the solid boundary and symmetry line of the hemispherical test section. The solid wall boundary of the test section at these z-locations are at $r=145$ and 125.64 mm, respectively. Radial distributions of the Reynolds shear stress components ($\overline{u'v'}$, $\overline{v'w'}$ and $\overline{u'w'}$) on the measuring plane A-A at three streamwise locations ($z=41.38$, 82.76 and 124.14 mm) are presented in Fig. 13 for Re=46,122. The results for the Reynolds shear stress components are normalized based on the average inlet velocity ($w_{in}=2.347$ m/s for Re =46,122). The Reynolds shear stress component, $\overline{u'v'}$, is relatively low at $z=41.38$ and 82.76 mm. All three shear stress components at $z=124.14$ mm have a positive peak value in the same general radial location of about $r\approx 60$ mm, similar to what was observed for the Reynolds normal stress components on the same z-location as can be seen in Fig. 12. Both $\overline{v'w'}$ and $\overline{u'w'}$ are negative over most of the radial range for $z=41.38$ mm, and 82.76 mm, while at $z=124.14$ mm they exhibit both positive and negative peaks.

Radial distributions of the Reynolds normal stress components ($\overline{u'u'}$, $\overline{v'v'}$ and $\overline{w'w'}$) on the measuring plane A-A are presented in Fig. 14 for three z-locations that are in the neighborhood of the outlet-tube ($z=117.24$, 137.93 and 151.72 mm). The interference of the solid wall boundaries of the test section with the laser beams of the LDV system at these locations, limits the number of measuring data points that can be taken as can be seen from Figs. 14 and 15. Very limited number of measurements could be made at $z=151.72$ mm. The Reynolds normal stress components, $\overline{u'u'}$ and $\overline{v'v'}$, are relatively low in most of the radial range at $z=117.24$ mm. All three Reynold normal stress components develop a peak at $r\approx 60$ mm (near the inner solid wall of the outlet tube) at $z=137.93$ mm. The magnitudes of the Reynolds normal stress components at these z-locations (in the neighborhood of the outlet-tube) are higher than those presented in Fig. 12. One of the common feature in the radial distributions of the Reynolds normal stress components is that they all exhibit a lower value in the region near the centerline of the outlet-tube ($r=82$ mm) at these z-locations. Radial distributions of the Reynolds shear stress components ($\overline{u'v'}$, $\overline{v'w'}$ and $\overline{u'w'}$) on the measuring plane A-A are presented in Fig. 15 for the same z-locations as the ones presented in Fig. 14 ($z=117.24$, 137.93 and 151.72 mm). The results that are presented for $z=137.93$ mm, exhibit a positive peak in the distribution of the Reynolds shear stress $\overline{u'v'}$ component, and negative peaks in the distributions of the other two Reynolds shear stress components $\overline{v'w'}$ and $\overline{u'w'}$ at $r\approx 60$ mm (close to the inner wall of the outlet tube). This roughly the same region where all the three Reynolds normal stress components exhibit a maximum

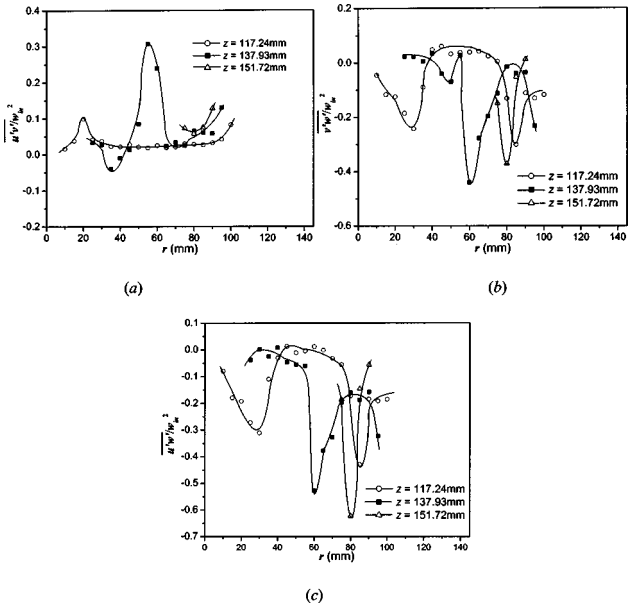

Fig. 15 Radial distribution of Reynolds shear stress components on the measuring plane A-A in the inlet region of the outlet-tube for Re=46,122

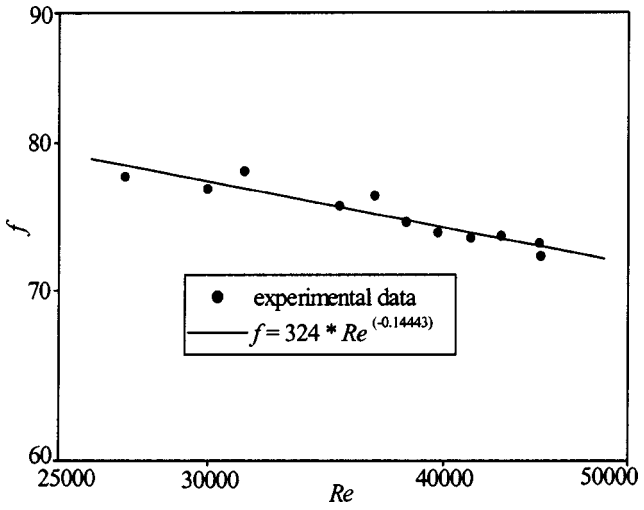

Fig. 16 Variation of the friction factor as a function of Reynolds numbers

at the same z-location, as can be seen in Fig. 14. The magnitudes of the Reynolds shear stress components on these z-locations (in the neighborhood of the outlet-tube) are generaly higher than the one presented in Fig. 13. The pressure drop across the exit head section and the outlet-tube, and the flow rate, were measured and used to calculate the friction factor as a function of Reynolds number. The friction factor is defined as:

$$f=(p_{in}-p_{out}+0.5\rho w_{in}^2-0.5\rho w_{out}^2)/(0.5\rho w_{in}^2) \qquad (2)$$

where p_{in} and p_{out} are static pressures at the inlet and outlet sections respectively, and w_{out} is the mean velocity in the streamwise direction along the outlet-tube (the outlet-tube diameter $d_{out}=0.05$ m). The inlet pressure p_{in} is taken as the atmospheric pressure and the outlet pressure p_{out} is measured through the pressure tap on the wall of the outlet-tube at $z=200$ mm. The results that are presented in Fig. 16 show that the friction factor decreases as the Reynolds number increases in the experimental range, and its behavior can be described by the relation of $f=324\,\mathrm{Re}^{-0.14443}$.

Conclusions

Measurements of the three mean velocity components and the Reynolds stress components are reported for three-dimensional turbulent flow in a model for the exit head section of a shell-and-tube heat exchanger with outlet-tubes. Measurements of velocities in the test section are presented for only one intersecting θ-plane ($\theta=32$ deg) as a function of r and z. The results show that the flow in that measuring plane A-A is nonuniform and complex in the region where the outlet-tubes are connected to the exit head section of the heat exchanger. The fluid converges into the outlet-tube with vortical motion and in that region the velocity components in the radial and streamwise directions are of the same order of magnitude. The velocity distribution in that region is not symmetric in either tangential or radial directions, because the outlet-tubes are not symmetrically located relative to these two directions. The tangential Reynolds normal stress component is relatively low in the whole radial range at $z=41.38$ and 82.76 mm. At $z=124.14$ mm, all of the Reynolds stress components (normal and shear) exhibit a peak at approximately $r=60$ mm (close to the inner solid wall of the outlet-tube). The results that are presented for $z=137.93$ mm, exhibit a positive peak in the distribution of the Reynolds shear stress $\overline{u'v'}$ component, and negative peaks in the distributions of the other two Reynolds shear stress components $\overline{v'w'}$ and $\overline{u'w'}$ at $r\approx 60$ mm (close to the inner solid wall of the outlet-tube). This is roughly the same region where all the three Reynolds normal stress components exhibit a maximum at the same z-location. The magnitudes of the Reynolds normal and shear stress components in the neighborhood of the outlet-tube $z>124.14$ mm are higher than those measured in the hemispherical portion of the test section at $z<124.14$ mm. The measured friction factor decreases as the inlet Reynolds number increases from 27,097 to 45,010.

Acknowledgments

This work was supported in part by grants from the National Science Foundation of China (*NNSFC*) (No. 59676019), the Research Fund for the Doctoral Program of Higher Education (*RFDP*) (No. 9589801), and the US Department of Energy Grant No. DE-FG02-03ER46067.

Nomenclature

A_{in} = inlet cross sectional area of the head section of the heat exchanger
d = inner diameter of the outlet-tube
f = friction factor
p = pressure
Q = volume flow rate
r = radial direction (in cylindrical coordinates)
R_{in} = inlet radius of the heat exchanger head section
R_s = spherical radius of the heat exchanger head section
Re = Reynolds number$=\rho w_{in}(2R_{in})/\mu$
u = velocity component in the θ-direction (in cylindrical coordinates)
$\overline{u'u'}$ = Reynolds normal stress component
$\overline{u'v'}$ = Reynolds shear stress component
$\overline{u'w'}$ = Reynolds shear stress component
v = velocity component in the r-direction (in cylindrical coordinates)
$\overline{v'v'}$ = Reynolds normal stress component
$\overline{v'w'}$ = Reynolds shear stress component
v_x = velocity component in the x-direction (in Cartesian coordinates)
v_y = velocity component in the y-direction (in Cartesian coordinates)
v_z = velocity component in the z-direction (in Cartesian coordinates)
w = velocity component in the z-direction (in cylindrical coordinates)
w_{in} = average inlet streamwise velocity component
w_{out} = average outlet streamwise velocity component
$\overline{w'w'}$ = Reynolds normal stress component
x, y, z = directions of Cartesian coordinates

Greek Symbols

μ = dynamic viscosity
ρ = density
θ = circumferential direction (in cylindrical coordinates)

References

[1] Chrisholm, D., 1980, *Developments in Heat Exchanger Technology—I*, Applied Science Publishers, London, England.
[2] Huppan, T., 2000, *Heat Exchanger Design Handbook*, Marcel Dekker, New York.
[3] Shah, R. K., and London, A. L., 1978, *Laminar Flow Forced Convection in Ducts*, Academic Press, New York.
[4] Kakac, S., and Liu, H. T., 1997, *Heat Exchangers: Selection, Rating, and Thermal Design*, CRC Press, New York.
[5] Bremhorst, K., and Flint, P. J., 1991, "The Effect of Flow Patterns on the Erosion/Corrosion of Shell and Tube Heat Exchangers," Wear, **145**, pp. 123–135.
[6] Yu, B., Nie, J. H., Wang, Q. W., and Tao, W. Q., 1999, "Experimental Study on the Pressure Drop and Heat Transfer Characteristics of Tubes with Internal Wave-Like Longitudinal Fins," Heat Mass Transfer, **35**, pp. 65–73.

[7] Halle, H., Chenoweth, J. M., and Wambsganss, M. W., 1984, ''Shell Side Water Flow Pressure Drop Distribution Measurements in an Industrial-Sized Test Heat Exchanger,'' In: A Reappraisal of Shell Side Tube Flow in Heat Exchangers,'' 22nd Heat Transfer Conference and Exhibition, Niagara Falls, ASME, HTD **36**, pp. 37–48.
[8] Zhang, C., 1994, ''Numerical Modeling Using a Quasi-Three-Dimensional Procedure for Large Power Plant Condensers,'' ASME J. Heat Transfer, **116**, pp. 180–188.
[9] Prithiraj, M., and Andrews, M. J., 1998, ''Three Dimensional Numerical Simulation of Shell-and-Tube Heat Exchangers—Part I: Foundation and Fluid Mechanics,'' Numer. Heat Transfer, Part A, **33**, 799–816.
[10] Tao, W. Q., Nie, J. H., Cheng, P., and Wang, Q. W., 2001, ''Numerical Simulation of Three-Dimensional Turbulent Flow in a Complex Geometry, with LDV Experimental Confirmation,'' Proceedings of 2nd ICHMT Symposium on Advances in Computational Heat Transfer, Queensland, Australia, pp. 1235–1242.
[11] Miller, R. W., 1996, *Flow Measurement Engineering Handbook*, 3rd ed., McGraw-Hill, New York.
[12] Wang, L. B., Tao, W. Q., Wang, Q. W., and He, Y. L., 2001, ''Experimental and Numerical Study of Turbulent Heat Transfer in Twisted Square Ducts,'' ASME J. Heat Transfer, **123**, pp. 868–877.
[13] Barnett, D. O., and Bentley, H. T., 1974, ''Statistical Bias of Individual Realization Laser Velocimeters,'' Proceedings of the Second International Workshop on Laser Velocimetry, Engineering Extension Series, Purdue University, **144**, pp. 428–444.
[14] Moffat, R. J., 1988, ''Describing the Uncertainties in Experimental Results,'' Exp. Therm. Fluid Sci., **1**, pp. 3–17.

Flow at the Centrifugal Pump Impeller Exit With Circumferential Distortion of the Outlet Static Pressure

Soon-Sam Hong
Turbopump Department,
Korea Aerospace Research Institute,
Daejeon 305-333, Korea

Shin-Hyoung Kang
School of Mechanical and Aerospace Engineering,
Seoul National University,
Seoul 151-742, Korea

The effects of circumferential outlet distortion of a centrifugal pump diffuser on the impeller exit flow were investigated. A fence with sinusoidal width variation was installed at the vaneless diffuser exit. The flow field was measured at the impeller exit with and without the fence, using a hot film probe and an unsteady pressure sensor. Flow parameters varied with the circumferential position and the mean flow parameters plotted against the local flow rate at each circumferential position showed loops along the quasi-steady curves, which were obtained from the result without the fence. Simple theoretical calculations were used to predict the velocity components at the impeller exit with the relative flow angle or total pressure assumed. Good result was obtained when the relative flow angle was assumed to vary quasi-steadily, not constant with the local flow rate. The radial velocity was also reasonably predicted when the total pressure was assumed to vary quasi-steadily. A simple method is proposed to predict the impeller exit flow with downstream blockage in two-step sequence: the first step deals with the diffuser alone to obtain static pressure distribution at the diffuser inlet, while the second step deals with the impeller alone to obtain velocity components distribution at the impeller exit.
[DOI: 10.1115/1.1637630]

Introduction

Theoretically, only one operating point can have uniform pressure along the volute or vaned diffuser of centrifugal turbomachines. The non-uniform pressure distribution in the volute or vaned diffuser at off-design points propagates upstream and creates a circumferential flow distortion at the impeller exit. The interaction between the impeller and the downstream flow conditions should be considered in the analysis and design of the impeller, diffuser, and volute.

Extensive studies have been performed on the effects of circumferential outlet flow distortion in centrifugal impellers. Sideris and Van den Braembussche [1] measured detailed velocity and pressure in the vaneless diffuser of a centrifugal compressor with a volute. They discussed the relation between the circumferential variation of pressure and the impeller exit flow, and also made theoretical calculations using an impeller-diffuser interaction model. Fatsis et al. [2] conducted a numerical investigation of the centrifugal compressor impeller response to downstream static pressure distortions using an unsteady three dimensional Euler solver. Hagelstein et al. [3] showed that the asymmetry of the flow in the diffuser could be reduced by using either a throttling ring at the diffuser exit or a vaned diffuser. Sorokes et al. [4] and Sorokes and Koch [5] described experimental and computational analyses of the static pressure distortion caused by the discharge volute in a re-injection centrifugal compressor.

A quasi-steady variation assumption has been applied to the operation of the overall pump system since Knapp [6], but this assumption is also applicable in the calculation of the local rotor response to the circumferential pressure distortion. Van den Braembussche et al. [7] used the slope of the steady impeller performance curve to determine the circumferential variation of the impeller exit velocity components and total pressure at off-design operations for a centrifugal compressor.

The present study aims to investigate the effect of circumferential outlet flow distortion on the impeller exit flow characteristics in a centrifugal pump. Instead of a volute, a fence with non-uniform width is installed at the vaneless diffuser exit. This simple configuration is used for fundamental investigation to develop numerical methods and flow models. The measured impeller exit flow parameters with the fence are compared to those without any blockage. Moreover, impeller-diffuser interaction models are evaluated by comparing predictions and measurements.

Experimental Facility and Instrumentation

Test Rig. An outline of the closed loop test rig is shown in Fig. 1. The water flow rate is measured by a flow nozzle and controlled by a regulating valve. The test section includes an impeller, a vaneless diffuser, and a collector. The shrouded centrifugal impeller has a tip diameter of 260 mm and six blades with 25 deg exit angle from tangential direction. The impeller has a low specific speed of 0.366 (1000 US units). The rotational speed is controlled by an inverter and fixed to 300 rpm for this study, giving a test Reynolds number ($\omega R_2^2/\nu$) of 5.31×10^5. The vaneless diffuser has parallel walls with 330 mm outlet diameter and 14.9 mm width, the same width as that of the impeller exit. The diffuser is followed by a collector, which has a cross sectional dimensions of 300 mm by 300 mm. The axisymmetric collector is used to create a circumferential uniform flow state throughout the stage, unlike the volute that creates circumferential distortions at off-design conditions. The velocity and pressure are measured 3 mm downstream of the impeller exit, or $r=133$ mm, as shown in Fig. 2. Because the measurement location is only 2% away from the actual impeller exit, the measured pressure and velocity components are assumed to be the value at the impeller exit.

To investigate the effect of circumferential outlet distortion on the exit flow of the impeller, a fence with circumferentially non-uniform width is installed at the diffuser exit. The stainless steel

Contributed by the Fluids Engineering Division for publication in the JOURNAL OF FLUIDS ENGINEERING. Manuscript received by the Fluids Engineering Division Nov. 7, 2001; revised manuscript received June 23, 2003. Associate Editor: B. Schiavello.

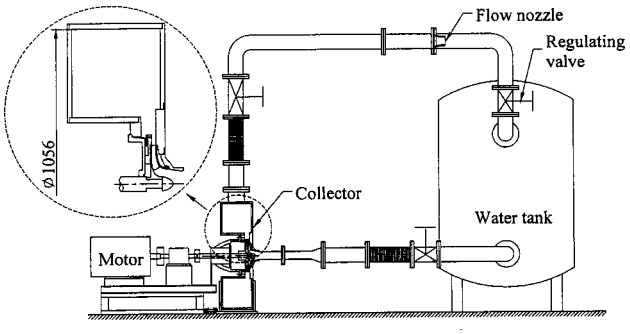

Fig. 1 Schematic view of the test rig

fence with a thickness of 0.5 mm has sinusoidal width distribution to produce a smooth flow variation. A sinusoidal fence with a 360 deg period, which was tested at first, generated excessive flow distortion strength. Therefore, a sinusoidal fence with a 180 deg period, or two sine curves in a circumference, is used for the present study and this is called 2-sine fence hereafter. The diffuser width is 14.9 mm, but the maximum and minimum width of the fence is 14 and 0 mm, respectively, from the diffuser hub wall.

To characterize the unsteadiness, the reduced frequency Ω is specified as follows:

$$\Omega = f \cdot EL / \overline{W_{2\infty}} \tag{1}$$

where f is the excitation frequency, $\overline{W_{2\infty}}$ is the mean of exit relative velocity assuming no flow slip, and EL is the effective length of the flow channel defined as

$$EL = \int_1^2 \frac{A_2}{A} ds \tag{2}$$

The reduced frequency Ω is about 0.9 for the present case of 2-sine fence, therefore, both unsteadiness and quasi-steadiness are important for the present case.

To avoid the difficulty of circumferentially traversing from one measuring position to another, the fence is rotated and the flow field is measured at a single location, stationary on the front wall. It should be noted here that the fence is fixed during a flow measurement and the fence rotation is introduced just for the easy traverse. In Fig. 3 the circumferential angle θ is equal to 0 deg at

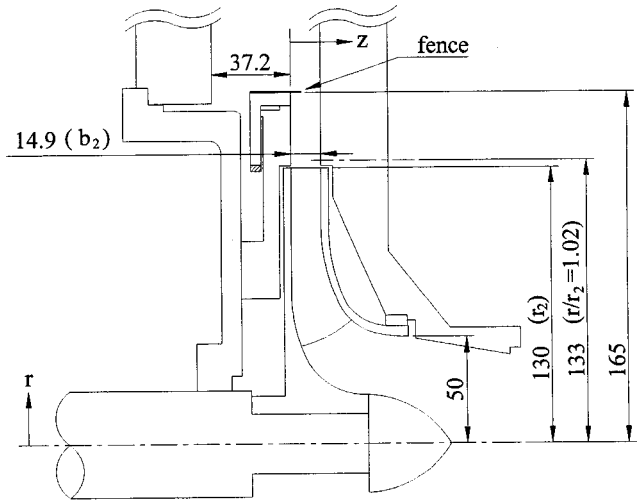

Fig. 2 Measurement location and details of the impeller with the fence

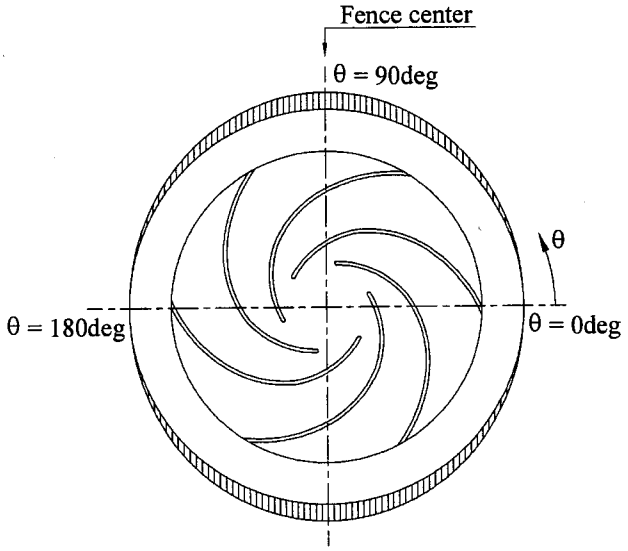

Fig. 3 Definition of circumferential position in the outward-unfolded 2-sine fence

the minimum fence width and 90 deg at the maximum width, or the fence center.

Instrumentation. A single hot film probe of I-type (Dantec 55R11) is used to measure instantaneous velocities and flow directions at the impeller exit. The film probe is calibrated for velocity magnitude and direction. The measured flow is assumed to be two-dimensional, because the axial velocity component is considered to be negligible. According to a calculation at the test impeller exit [8] using a CFD code CFX-TASCflow, the mean magnitude of axial and radial velocity components was 1.8% and 12%, respectively, of the tangential velocity component at the design flow rate in case without the fence. Even in case with the fence, axial velocity component is expected to be still smaller than the radial and tangential ones. Measurements are taken at two probe orientations 60 deg apart. Two outputs, which are phase averaged at each setting, are compared to calculate the flow angle and velocity. This method is similar to the single hot wire probe method used by Inoue and Cumpsty [9]. A fast response pressure transducer (Kulite XTM-190), with natural frequency of 300 kHz given by manufacturer, is used for instantaneous wall static pressure measurements. Static pressure is measured on the shroud side diffuser wall and the total pressure is calculated from the measured static pressure and the velocity.

The sampling rate is 3 kHz, so that 100 data are measured over one blade pitch of six blades at 300 rpm. Since the flow at the impeller exit is highly turbulent, a phase averaging technique is used. From a photo sensor, one pulse is produced per impeller rotation and the pulse is used as a trigger signal for the phase averaging.

The accuracy of the hot film probe measurements is estimated to be 4% in magnitude and 1 deg in direction. The estimated accuracy of the static pressure measurements is 2%. The average flow rate, calculated by integrating the radial velocity at the impeller exit, is compared with that obtained from the flow nozzle. Three test flow rates are investigated as illustrated in Fig. 4. At design and high flow rate condition, the two flow rates agree significantly, being within 4% of each other. At low flow rate condition, however, the integrated flow rate is 15% higher than that from the flow nozzle. Since the absolute flow angle at the low flow rate is about 5 deg from the tangential direction, an angle shift of just 0.5 deg makes approximately 10% deviation of flow rate. For reference, absolute flow angles are 7.2 deg and 9.2 deg

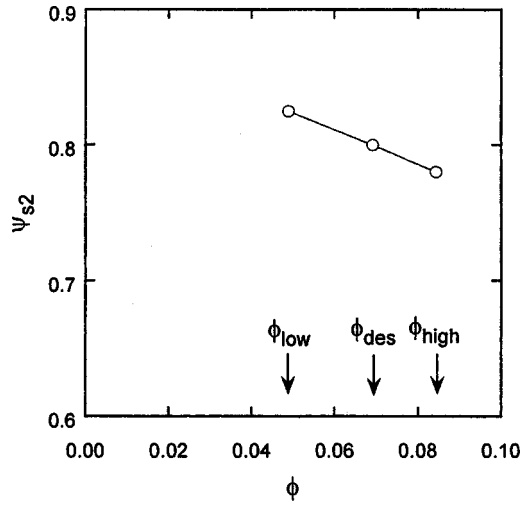

Fig. 4 Static pressure rise at the impeller exit without fence

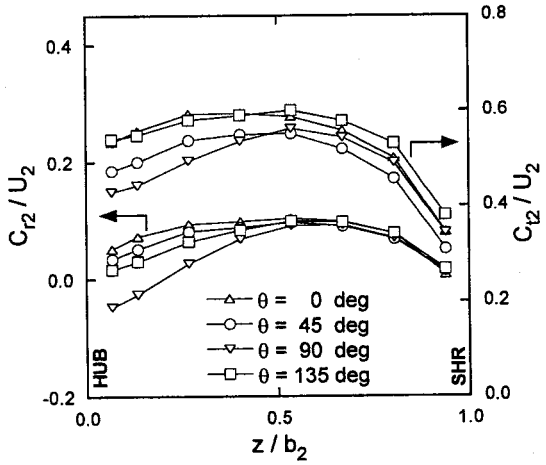

Fig. 6 Distribution of mean radial and tangential velocity at four circumferential positions with 2-sine fence at ϕ=0.069

for design and high flow rate, respectively. Therefore, about 7% and 5% for design and high flow rate, respectively, can be changed by just 0.5 deg.

Results and Discussion

Flow at Impeller Exit. The impeller exit flow field without any fence is measured as base-line data. The static pressure rise versus flow rate is shown in Fig. 4, where the time mean static pressure coefficient is plotted against the flow coefficient. The design flow coefficient ϕ_{des} is 0.069, where the original volute pump with the test impeller had the best efficiency. The static pressure varies almost linearly with the flow rate for narrow range of measurements.

The flow measurements are made at eight locations between the hub and the shroud. Spanwise distributions of mean velocity components, radial and tangential, at three flow rates are shown in Fig. 5. Radial velocity that has a nearly linear spanwise distribution at the high flow rate changes into a symmetric one with boundary layer type profile near hub and shroud at the low flow rate. The radial velocity shows a large change with flow rate at the shroud side. Tangential velocity increases as the flow rate decreases except that for the shroud region.

Measurements with the 2-sine fence are carried out at design flow rate only. Velocity is measured at eight spanwise locations as in the case without the fence. The mean velocity distributions at four circumferential positions are shown in Fig. 6. The radial velocity shows a large change with circumferential position at the hub side, but remains almost constant at the shroud side. The reason for this is that the flow on the hub side is more disturbed by the blockage of the fence installed on the hub side. To see the tangential velocity distribution in Fig. 6, it seems that to spanwise direction the blockage has more effect on the radial velocity than the tangential velocity.

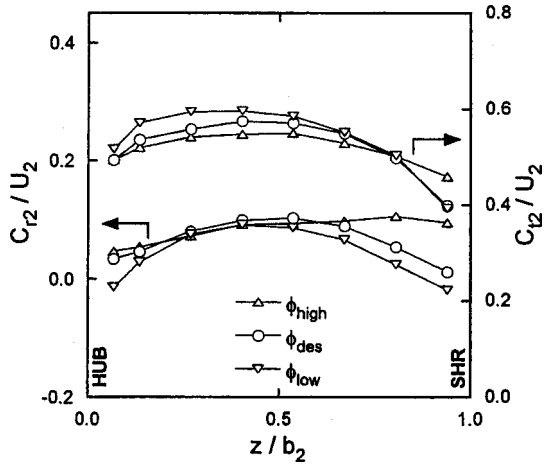

Fig. 5 Distribution of mean radial and tangential velocity at three flow rates without fence

The mean velocity at each circumferential position is mass-averaged through the span to see the dependence of averaged flow parameters on the circumferential position. Distributions of the mass-averaged flow parameters versus θ are shown in Fig. 7. Radial velocity has a minimum at the fence center (θ=90 deg) and tangential velocity has a minimum 30 deg upstream (θ=60 deg) of the fence center. Absolute velocity has nearly the same pattern as the tangential velocity because the radial velocity is typically only about 1/8 of the tangential velocity for present centrifugal impeller. Static pressure has a maximum 15 deg upstream (θ=75 deg) of the fence center and total pressure has a maximum at the fence center (θ=90 deg). It seems that the inertial effect of relative flow in the blade passage is probably the reason for the difference in the circumferential position between the minimum radial velocity and the maximum static pressure.

The pump performance is usually plotted against the overall flow rate. In the same manner, the flow variations can be plotted against the local flow rate, or radial velocity. At ϕ=0.069, which is based on the flowmeter measurement, the local flow parameters versus C_{r2}/U_2 with 2-sine fence are compared with the quasi-steady curves defining flow parameters versus C_{r2}/U_2 in case without the fence. The comparisons are shown in Fig. 8, where the abscissa C_{r2}/U_2 comes from the average of flow traverse for both with and without the fence. Total pressure increases as the local flow rate decreases, but does not follow the quasi-steady curve in Fig. 8(*a*). Static pressure does not follow the quasi-steady curve as well, and shows a loop in Fig. 8(*b*). Tangential velocity, however, shows a trend opposite to that without the fence. Without the fence the tangential velocity increases as the flow rate decreases, but the tangential velocity at θ=90 deg is lower than that at θ=0 deg. The difference in the trend for tangential velocity is attributed to the large flow slip at impeller exit near the fence center. The relative flow angle, on the other hand, follows quasi-steady curve better than other flow parameters as shown in Fig. 8(*d*).

Impeller-Diffuser Interaction Model. Not many theoretical models are available to predict the influence of pressure distortion on the outlet flow of a centrifugal pump impeller. The model used in the present study is the impeller-diffuser interaction model,

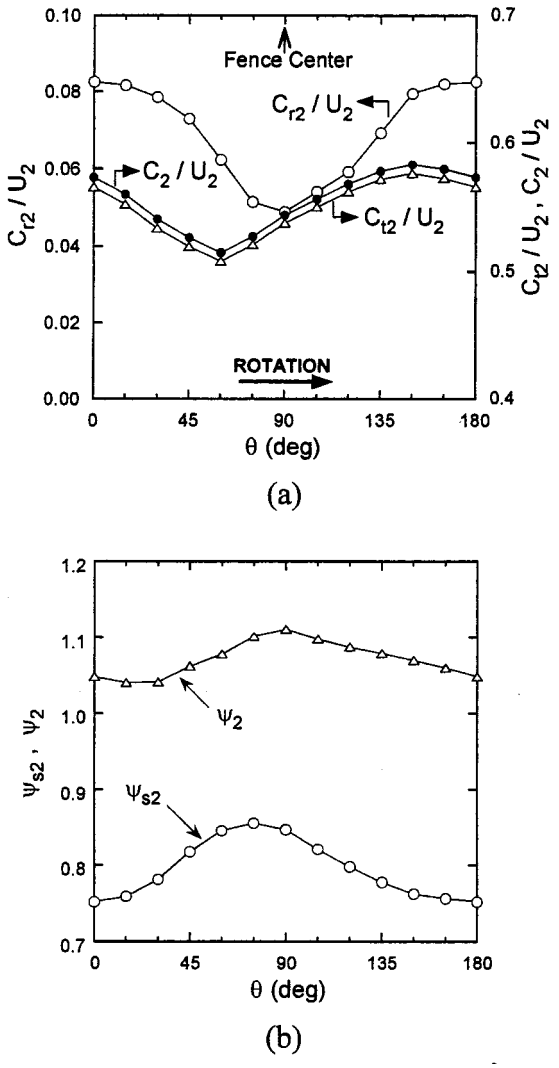

Fig. 7 Distribution of averaged flow parameters with 2-sine fence at ϕ=0.069: (*a*) radial, tangential, and absolute velocity, and (*b*) static and total pressure.

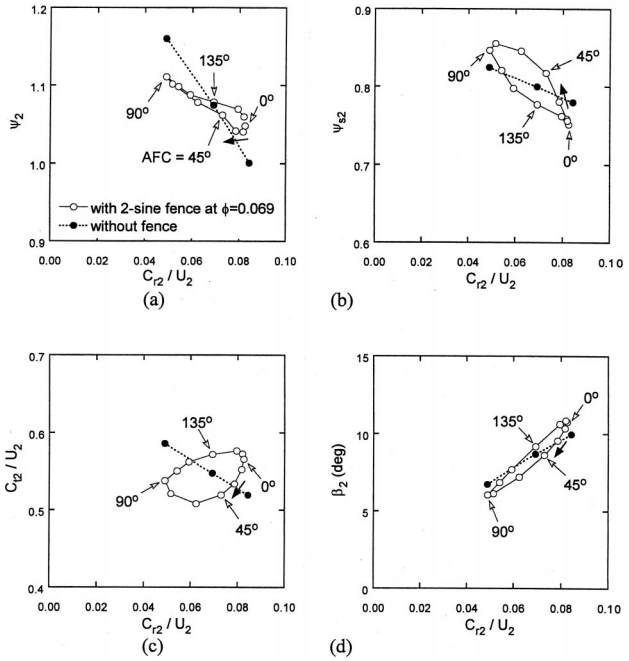

Fig. 8 Distribution of averaged flow parameters plotted against local flow rate with 2-sine fence at ϕ=0.069: (*a*) total pressure, (*b*) static pressure, (*c*) tangential velocity, and (*d*) relative flow angle.

which was used in the rotating stall calculation by Frigne and Van den Braembussche [10]. This model was also used by Sideris and Van den Braembussche [1] to estimate the flow of a centrifugal impeller exit where the static pressure is circumferentially distorted due to the volute. This model assumes that the flow is incompressible, inviscid and two dimensional. The following equation describes the interaction model:

$$\frac{\partial C_{r2}}{\partial t}+\omega\frac{\partial C_{r2}}{\partial \theta}=\frac{\sin\beta_b}{EL}\left(U_2C_{t2}-U_1C_{t1}-\frac{P_2-P_1}{\rho}-\frac{C_{r2}^2+C_{t2}^2-C_1^2}{2}\right) \tag{3}$$

Left term of Eq. (3) represents inertial effect of relative flow in the blade passage. β_b is exit blade angle and EL is the effective length of the flow channel as defined in Eq. (2). The tangential velocity is calculated from the velocity triangle.

$$C_{t2}=U_2-C_{r2}/\tan\beta_2 \tag{4}$$

If the distribution of the outlet static pressure is imposed, the radial velocity can be calculated from integration of Eq. (3) with respect to time. This integration is repeated until the steady state solution is obtained. The inlet swirl is assumed to be zero and the inlet total pressure be constant. The effective length used in the calculation is the real impeller channel length. This is three-eights of the overall blade length from leading edge to trailing edge in the present study because of low solidity and high stagger. A single step explicit Lax-Wendroff scheme (e.g., [11]), which is second order accurate in space and time, is used for the numerical integration as follows:

$$C_{r2,i}^{n+1}=C_{r2,i}^n-\frac{CFL}{2}(C_{r2,i+1}^n-C_{r2,i-1}^n)+\frac{CFL^2}{2}(C_{r2,i+1}^n-2C_{r2,i}^n+C_{r2,i-1}^n)+\frac{\sin\beta_b}{EL}\Delta t\left[U_2C_{t2,i}^n-U_1C_{t1,i}^n-\frac{P_{2,i}^n-P_1}{\rho}-\frac{1}{2}(C_{r2,i}^{n\,2}+C_{t2,i}^{n\,2}-C_1^2)\right] \tag{5}$$

where $CFL=\omega\Delta t/\Delta\theta$ must be smaller than one.

As to the relative flow angle β_2, a simple approach assumes constant value of β_2 around the circumference. Sideris and Van den Braembussche [1] used this assumption. They could obtain the better prediction by imposing the measured β_2 to the calculation. In the present study, the variation of measured β_2 follows the quasi-steady curve fairly well as illustrated in Fig. 8(*d*), and therefore β_2 can be assumed to vary quasi-steadily. In Fig. 9 are shown the predicted results using two assumptions for β_2; first, β_2 is assumed to be constant as the value (β_2=8.7 deg) measured without the fence at ϕ=0.069; second, β_2 is assumed to vary quasi-steadily with C_{r2}/U_2, which is obtained from the curve fitting β_2 versus C_{r2}/U_2 in case without the fence. When β_2 is assumed to be constant, the curve of the predicted radial velocity agrees with the measured data; however, the predicted amplitude is smaller than the measured one. For the tangential velocity the predicted amplitude agrees with the measured one, but the phase shows a shift from the measured data. Radial and tangential velocity can be better predicted when β_2 is assumed to vary quasi-steadily. The above results suggest that the assumption of quasi-steadily varying β_2 is more effective than the assumption of constant β_2.

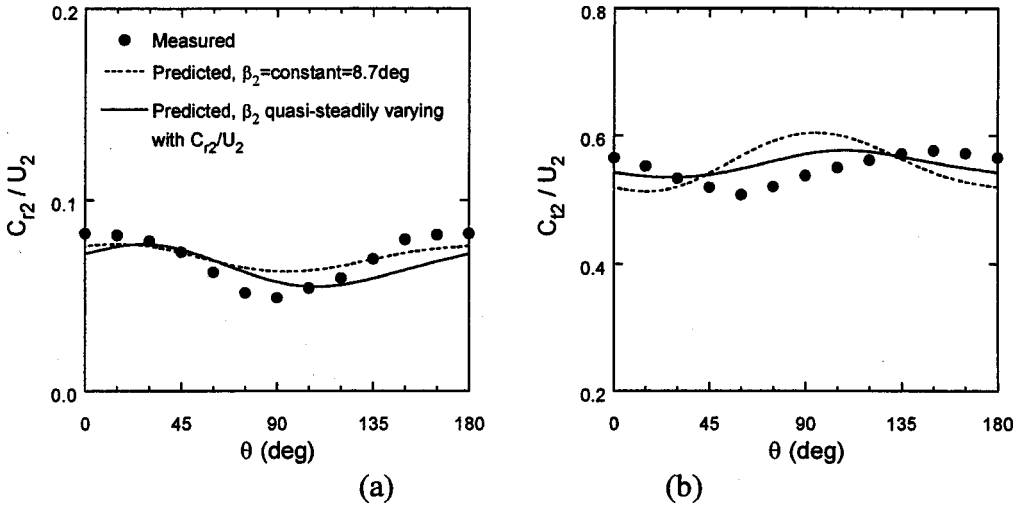

Fig. 9 Measured and predicted velocity components with 2-sine fence (parameter=β_2) at ϕ=0.069: (*a*) radial velocity, and (*b*) tangential velocity.

Equation (3) can be also represented using the total pressure as follows:

$$\frac{\partial C_{r2}}{\partial t}+\omega\frac{\partial C_{r2}}{\partial \theta}=\frac{\sin\beta_b}{EL}\left(U_2C_{t2}-U_1C_{t1}-\frac{P_{t2}-P_{t1}}{\rho}\right) \quad (6)$$

where $P_{t2}-P_{t1}$ is a total pressure rise. Another equation is derived from the definition of the total pressure rise:

$$C_{t2}^2=C_1^2+2\left(\frac{P_{t2}-P_{t1}}{\rho}-\frac{P_2-P_1}{\rho}\right)-C_{r2}^2 \quad (7)$$

Now, Eqs. (3) and (4) are replaced by Eqs. (6) and (7). As the relative flow angle β_2 is an important parameter in the former equation set, so is the total pressure P_{t2} in the latter one. With regard to P_{t2}, the assumption that P_{t2} varies quasi-steadily with C_{r2}/U_2 is used here and the results are shown in Fig. 10. The predicted radial velocity agrees very well with the measurement and also the prediction of tangential velocity is satisfactory.

To note, the previously mentioned models need static pressure distribution around the impeller periphery. In many cases, static pressure can be predicted with reasonable accuracy from steady state calculation without rotor-stator interaction. The steady state flow calculation was attempted in case with 2-sine fence by using a commercial CFD code STAR-CD. The calculation domain does not include the impeller, but only includes the vaneless diffuser, 2-sine fence, and collector. The turbulent viscosity was calculated using the standard k-ε model. Second order accurate schemes were used for the discretization of the Navier-Stokes equations. The inlet conditions into the vaneless diffuser, e.g., radial and tangential velocity components are assumed constant from hub to shroud and circumferentially uniform. The input velocity components are the values at design flow rate in the case without the fence. For the inlet condition of static pressure an arbitrary value is given to a calculation grid. After the computation with the inlet conditions, static pressure level of all the grids is shifted by the same amount so that the mean of the computed static pressure can be equal to the value at the design flow rate in the case without the fence. The value of the static pressure used in the inlet condition has no effect on the final result in the present incompressible water flow. The calculated static pressure, including circumferential angle for the pressure maximum, agrees very well with the measurement as shown in Fig. 11. It is found that a CFD calcula-

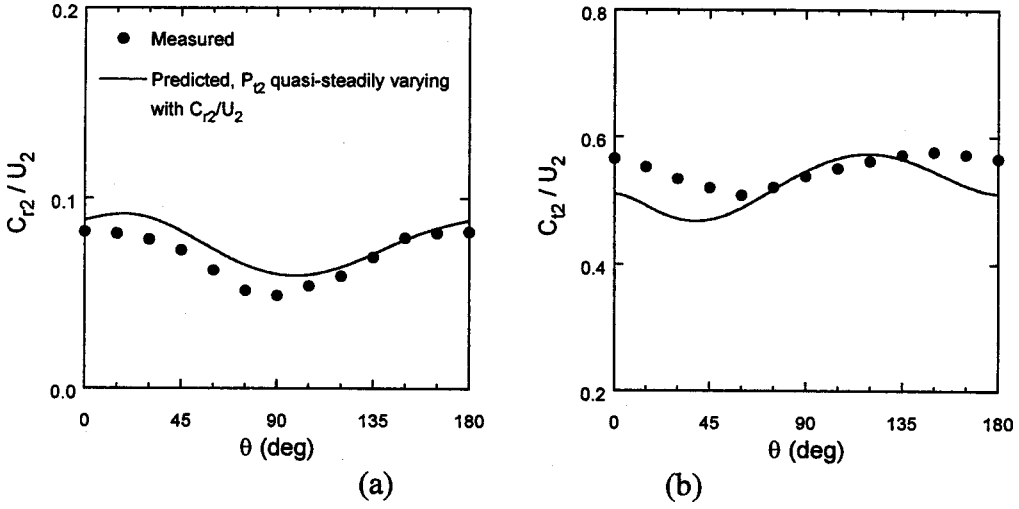

Fig. 10 Measured and predicted velocity components with 2-sine fence (parameter=P_{t2}) at ϕ=0.069: (*a*) radial velocity, and (*b*) tangential velocity.

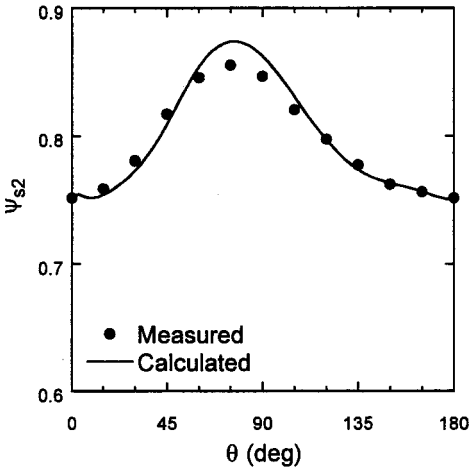

Fig. 11 Static pressure calculated by CFD with 2-sine fence at ϕ=0.069: impeller excluded in CFD.

tion, which is based on steady state flow condition without interaction between the impeller and the fence, can make a good prediction for the static pressure.

Now a simple method, which does not need a simultaneous CFD coupling of impeller and diffuser, is proposed to predict the impeller-diffuser interaction in two-step sequence. First, only diffuser part is calculated to find the circumferential distribution of static pressure at the vaneless diffuser inlet by performing the steady state numerical calculation, which has a uniform inlet velocity condition. The impeller is excluded in the first step. Second, the circumferential distribution of velocity components at the impeller exit is predicted by using the impeller-diffuser interaction models. The second step deals with only the impeller. The static pressure calculated from the first step is the input to the interaction model of the second step.

Conclusions

Exit flow field of a centrifugal pump impeller was measured when the circumferential pressure was distorted due to a nonuniform fence located at the vaneless diffuser outlet. The mean flow parameters, e.g., static pressure, total pressure, and flow angles were strongly dependent on the circumferential position. The flow parameters plotted against the local flow rate at each circumferential position showed loops along the quasi-steady curves obtained from the result without the fence.

Simple theoretical calculations were used, instead of more accurate but complex and unsteady CFD, to predict the velocity components at the impeller exit with imposed static pressure. The assumption of quasi-steadily varying relative flow angle at impeller outlet was more effective than that of constant relative flow angle for the velocity prediction. Another model in which the total pressure is the parameter was also evaluated. Good prediction of radial velocity was obtained with the assumption of quasi-steadily varying total pressure.

A simple method is proposed to predict the impeller exit flow with downstream blockage in two-step sequence: the first step deals with the diffuser alone, while the second step deals with the impeller alone. This more simple method can be used as enough accurate alternative to the complex and unsteady CFD.

Nomenclature

A = cross-section area normal to a streamline
b = passage width
C = absolute velocity
C_r = radial velocity
C_t = tangential velocity
EL = effective length
P = static pressure
P_t = total pressure
s = distance along a streamline
SHR = shroud
U = peripheral velocity of impeller
z = axial distance from hub
β = relative flow angle from tangential direction
β_b = exit blade angle from tangential direction
ϕ = flow coefficient, C_{r2}/U_2
ν = kinematic viscosity
θ = circumferential angle
ω = angular speed of the impeller
ψ = total pressure coefficient normalized by $\rho U_2^2/2$
ψ_s = static pressure coefficient normalized by $\rho U_2^2/2$

Subscript

1 = impeller inlet
2 = impeller exit

References

[1] Sideris, M. T., and Van den Braembussche, R. A., 1987, ''Influence of a Circumferential Exit Pressure Distortion on the Flow in an Impeller and Diffuser,'' ASME J. Turbomach., **109**, pp. 48–54.
[2] Fatsis, A., Pierret, S., and Van den Braembussche, R., 1997, ''Three-Dimensional Unsteady Flow and Forces in Centrifugal Impellers With Circumferential Distortion of the Outlet Static Pressure,'' ASME J. Turbomach., **119**, pp. 94–102.
[3] Hagelstein, D., Van den Braembussche, R. A., Keiper, R., and Rautenberg, M., 1997, ''Experimental Investigation of the Circumferential Static Pressure Distortion in Centrifugal Compressor Stages,'' ASME Paper No. 97-GT-50.
[4] Sorokes, J. M., Borer, C. J., and Koch, J. M., 1998, ''Investigation of the Circumferential Static Pressure Non-Uniformity Caused by a Centrifugal Compressor Discharge Volute,'' ASME Paper No. 98-GT-326.
[5] Sorokes, J. M., and Koch, J. M., 2000, ''The Influence of Low Solidity Vaned Diffusers on the Static Pressure Non-Uniformity Caused by a Centrifugal Compressor Discharge Volute,'' ASME Paper No. 2000-GT-0454.
[6] Knapp, R. T., 1937, ''Complete Characteristics of Centrifugal Pumps and Their Use in the Prediction of Transient Behavior,'' Trans. ASME, **59**, pp. 683–689.
[7] Van den Braembussche, R. A., Ayder, E., Hagelstein, D., Rautenberg, M., and Keiper, R., 1999, ''Improved Model for the Design and Analysis of Centrifugal Compressor Volutes,'' ASME J. Turbomach., **121**, pp. 619–625.
[8] Shim, C. Y., Hong, S. S., and Kang, S. H., 2000, ''Flow Evaluations of Centrifugal Pump Impeller Using Commercial Code,'' *Proceedings of the Korean Fluid Machinery Association Annual Meeting*, Busan, Dec. 1–2, pp. 285–292.
[9] Inoue, M., and Cumpsty, N. A., 1984, ''Experimental Study of Centrifugal Impeller Discharge Flow in Vaneless and Vaned Diffusers,'' ASME J. Eng. Gas Turbines Power, **106**, pp. 455–467.
[10] Frigne, P., and Van den Braembussche, R. A., 1985, ''A Theoretical Model for Rotating Stall in the Vaneless Diffuser of a Centrifugal Compressor,'' ASME J. Eng. Gas Turbines Power, **107**, pp. 507–513.
[11] Hoffmann, K. A., and Chiang, S. T., 1993, *Computational Fluid Dynamics for Engineers*, Engineering Education System, Wichita, Kansas.

Yury A. Semenov[1]
e-mail: relcom@semenov.dp.ua

Akira Fujii
e-mail: a-fujii@me.es.osaka-u.ac.jp

Yoshinobu Tsujimoto
e-mail: tujimoto@me.es.osaka-u.ac.jp

Osaka University,
Graduate School of Engineering Science,
1-3 Machikaneyama, Toyonaka 560-8581,
Osaka, Japan

Rotating Choke in Cavitating Turbopump Inducer

During the development stage of the liquid hydrogen turbopump for the main engine LE-7A of the H-IIA rocket, a new type of cavitation instability was observed. This instability occurs at lower cavitation numbers where the head of the inducer starts to decrease due to choke. The disturbance rotates around the rotor at about 50% of the inducer rotational speed. So, it is called "rotating choke." In order to predict the instability, a cavity model with a cavity wake is developed. The region of instability and the frequency predicted by the model are in agreement with experiment. Discussions are made as to the relationship between rotating choke and rotating cavitation. [DOI: 10.1115/1.1637926]

1 Introduction

During the firing test of the LE-7A LOX/LH2 engine of the HIIA rocket, a large amplitude rotor vibration of the fuel turbopump occurred at a frequency of about 350 Hz which is about one-half of the shaft rotational frequency $\Omega = 700$ Hz. The vibration occurred when the pump inlet pressure was reduced. This vibration caused the failure of the bolts fastening the bearing cartridge. To investigate into this phenomenon, a series of tests were conducted at full speed with liquid hydrogen and the results are reported by Shimura et al. [1].

It was found that the shaft vibration is associated with a pressure pattern rotating around the rotor at about one half of the rotational speed of the impeller. This is similar to rotating stall but non-cavitating inducers with small blade angle never stall since the angle of attack does not exceed the small blade angle even if the local flow rate becomes zero. This is different also from rotating cavitation in which the disturbance rotates faster than impeller.

The most important feature of this instability is that it occurs at the inlet pressure where the head is decreased due to cavitation. This is quite different from cavitation surge and rotating cavitation which occur at higher cavitation number where the head is not affected by cavitation. They are both caused by positive mass flow gain factor and physically explained as follows (Tsujimoto et al., [2]). When the flow rate is increased, the angle of attack to a rotor blade is decreased. If the value of mass flow gain factor is positive, the cavity volume will also decrease since the mass flow gain factor is defined as the ratio of the cavity volume decrease to the corresponding angle of attack decrease. If the cavity volume is decreased, the flow into the rotor will increase to fill up the space occupied by the decreased cavity volume. Thus, the increase of flow rate results in further increase of flow rate. This mechanism of instability depends only on the continuity relation and is not associated with the head degradation due to cavitation. From this reason, rotating cavitation and cavitation surge can be predicted by a 2-D potential flow stability analysis where the head drop due to cavitation is totally neglected (Horiguchi et al., 2000, [3]).

It is well known that surge and rotating stall are caused by the positive slope of performance curve due to blade stall at lower flow rate (Greitzer, E.M., 1976, [4]). With a positive slope, the head is increased if the flow rate is increased. The increased head accelerates the flow and the flow rate is increased further. Detailed examination of the suction performance of the pump inducer shows that the performance curve has a positive slope in the region where the instability is observed. This suggests that the instability is caused by the positive slope of the performance curve due to cavitation at lower inlet pressure. The present study is intended to confirm theoretically if such explanation can be applied to the new instability observed in the fuel turbopump inducer for LE-7A. In order to take account of the head drop due to cavitation, a cavity model with a cavity wake is developed and used for the stability analysis.

2 Experimental Observation of Rotating Choke Cavitation

Figure 1 shows the suction performance and the amplitude of the shaft vibration for two groups of flow rates $Q/Q_d \fallingdotseq 0.98$ and $Q/Q_d \fallingdotseq 0.95$. For $Q/Q_d \fallingdotseq 0.95$, the amplitude becomes larger at the cavitation number where the inducer head drops rapidly. The head is kept nearly constant, above and below the breakdown cavitation number. For $Q/Q_d \fallingdotseq 0.98$, the head decreases smoothly and the shaft vibration does not increase (not shown). The sudden head drop for $Q/Q_d \fallingdotseq 0.95$ is not caused by the instability since the head drop is not recovered at smaller cavitation number where the amplitude of vibration is smaller again. At a cavitation number σ_{high} higher than the breakdown cavitation number, the head is larger for smaller flow rate and the performance curve has a nega-

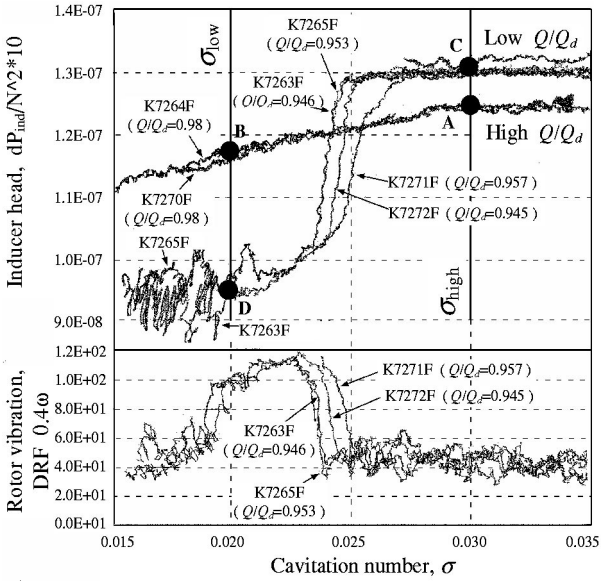

Fig. 1 Suction performance of the inducer of the LE-7A LH2 turbopump. Uncertainties: $\sigma \pm 0.002$, $dP_{ind}/N\,\hat{}\,2*10 \pm 0.03E-07$ and $DRF \pm 0.2E+02$

[1]On leave from the Institute of Technical Mechanics of the NAS and NSA of Ukraine, 15 Leshko-Popel' St., Dniepropetrovsk, 49005, Ukraine.

Contributed by the Fluids Engineering Division for publication in the JOURNAL OF FLUIDS ENGINEERING. Manuscript received by the Fluids Engineering Division July 25, 2002; revised manuscript received September 10, 2003. Associate Editor: S. L. Ceccio.

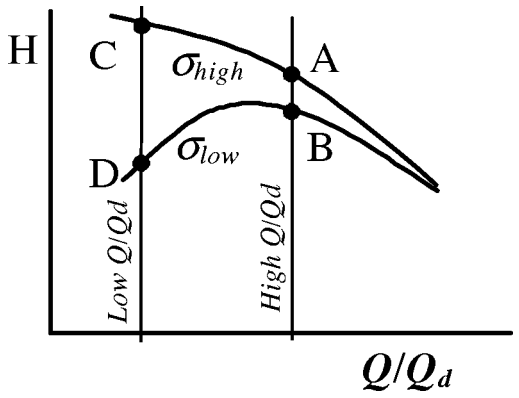

Fig. 2 Head dependence for low and high cavitation number

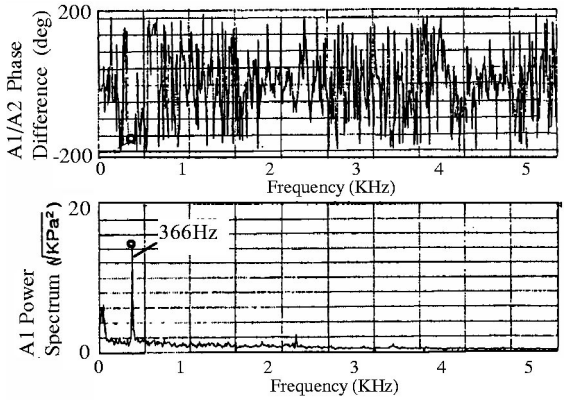

Fig. 4 The spectrum of the inlet pressure fluctuation and the phase difference of the signals from two pressure transducers located apart by 144 degrees circumferentially. Uncertainties: frequency ±2 Hz, phase difference ±5 degree

tive slope in the flow rate vs. head plane. On the other hand, at a cavitation number σ_{low} lower than the breakdown, the head is smaller for smaller flow rate and the performance curve has a positive slope. These situations are sketched in Fig. 2. For compressors and fans, it is well known that the positive slope of the performance curve can cause surge and rotating stall at smaller flow rate.

Without cavitation, inducers with smaller blade angle from tangent never stall and the performance curve has positive slope for all flow rate. On the other hand, the head starts to decrease when the cavity extends into the flow channel between blades. It was shown by Stripling and Acosta [5] that the head drop can be evaluated by the mixing loss downstream of the cavity terminus. This is called ''choke (by cavitation).'' The cavity thickness is larger for smaller flow rate as shown in Fig. 3. At σ_{high} where the cavity is shorter than the circumferential blade spacing, the cavity does not block the main flow and the head drop is not significantly increased with the decrease of the flow rate. On the other hand, at σ_{low} where the cavity extends into the throat, the ''blockage'' due to cavitation will be increased at lower flow rate and hence the head drop due to the mixing loss or the increase of relative velocity will be increased. If the increase of the head loss associated with the reduction of flow rate is larger than the increase of Euler's head, the performance curve will have a positive slope. So, it is quite possible that the positive slope at smaller cavitation number is caused by the choke.

Figure 4 shows the spectrum of the inlet pressure fluctuation and the phase difference of the signals from two pressure transducers separated by 144 degrees circumferentially [1]. The pressure transducers are located on the casing wall, about (1/12) diameter upstream from the leading edge of the blade, at the tip. The rotational frequency of the impeller is 723 Hz. The phase difference at the spectrum peak, 366 Hz, is 147 deg, which is close to the angular distance of 144 deg. This suggests that a disturbance with one cell is rotating around the rotor at 366 Hz, with the rotational speed ratio 366/723=0.506. Since the head drop due to cavitation is caused by choke, it is appropriate to call the instability ''rotating choke.'' All reported cavitation instabilities occur in a range of cavitation number where degradation of performance due to cavitation is limited. So, this is a new type of cavitation instability caused by the positive slope of pressure performance due to cavitation choke. We should note there that the positive slope of suction performance has a stabilizing effect, as shown by Young et al. [6] for surge mode oscillation.

3 Theoretical Analysis of Rotating Choke

In order to take the head drop due to cavity blockage into account, we adopt a cavity model with a wake as shown in Fig. 5. We consider a cavity wake ***AETFF'CGH*** behind the cavity ***OAH***. The boundary of external inviscid flow is shown by ***OADD'C***. According to the concept of viscous/inviscid interaction [13], we

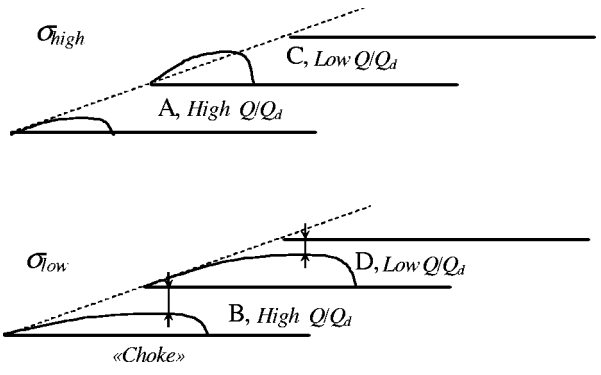

Fig. 3 The "choke" phenomenon

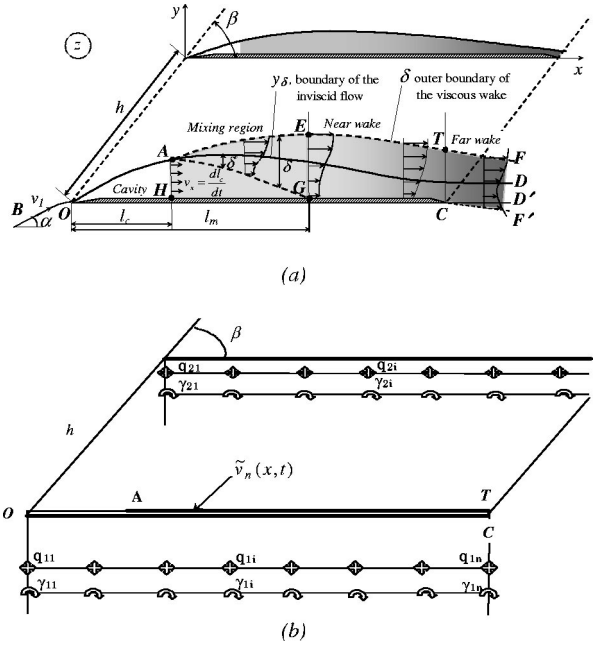

Fig. 5 Scheme of the cavity-wake flow: *a*) physical plane: the cavity OAH; the mixing region AEGH; the near wake region ETCG; *b*) linearized plane

assume that the inviscid flow velocity at the boundary $y=y_\delta$ is identical to the viscous flow velocity at the outer boundary of the turbulent wake $y=\delta$. The cavity wake is further divided into mixing region ***AEGH***, near wake ***ETCG***, and far wake ***TFF'C***.

3.1 Problem for the External Inviscid Flow. We consider an inducer with N blades and assume that the flow is periodical with the periodicity of N blades. Following the work [3], the flow complex potential can be represented as the superposition of the complex potentials:

$$W(z,t)=Ue^{-i\alpha}z+\tilde{S}e^{\lambda t}e^{-i\beta}z+\sum_1^N \overline{w}_n(z)+\sum_1^N \tilde{w}_n(z)e^{\lambda t}, \tag{1}$$

where $Ue^{-i\alpha}z$ is the complex potential of the uniform flow; $\tilde{S}e^{\lambda t}e^{-i\beta}z$ is the complex potential of uniform perturbation; $\overline{w}_n(z)$ and $\tilde{w}_n(z)e^{\lambda t}$ are the complex potentials of the steady and unsteady perturbation respectively, induced by the n^{th} blade of the cascade; $\lambda=\mu+j\omega$ is Laplace's variable. The complex potentials $\overline{w}_n(z)$ and $\tilde{w}_n(z)$ are defined so that the perturbations vanish at the upstream infinity.

The velocity disturbances due to the blades are represented by sources q_n and vortices γ_n along the profiles as shown in Fig. 5(*b*) ($n=1,N$). The complex conjugate velocity can be represented as follows:

$$\frac{dW}{dz}=v_x-iv_y=Ue^{-\alpha}+\tilde{S}e^{\lambda t}e^{-i\beta}+\sum_1^N \overline{\theta}_n(z)+\sum_1^N \tilde{\theta}_n(z)e^{\lambda t}, \tag{2}$$

where

$$\overline{\theta}_n(z)=\frac{1}{2\pi}\int_0^c \overline{q}_n(x)f_n(z,x)dx+\frac{1}{2\pi i}\int_0^c \overline{\gamma}_n(x)f_n(z,x)dx,$$

$$\tilde{\theta}_n=\frac{1}{2\pi}\int_0^c \tilde{q}_n(x)f_n(z,x)dx+\frac{1}{2\pi i}\int_0^c \tilde{\gamma}_n(x)f_n(z,x)dx+\frac{1}{2\pi i}\int_c^\infty \tilde{\gamma}_{tn}(x)f_n(z,x)dx$$

$$f_n(z,x)=\frac{\pi}{h}\exp(-i\beta)\left\{\cot\left[\frac{\pi}{h}(z-x-he^{-i\beta(n-1)})\right]+i\right\},$$

and $\overline{q}_n(x)$ and $\overline{\gamma}_n(x)$ are source and vortex distributions inducing the steady complex velocity perturbations $\overline{\theta}_n(z)$; $\tilde{q}_n(x)$ and $\tilde{\gamma}_n(x)$ are source and vortex distributions inducing the unsteady complex velocity perturbations $\tilde{\theta}_n(z)e^{\lambda t}$. $\tilde{\gamma}_{tn}(x)e^{\lambda t}$ is the trailing vortex behind the n^{th} blades. It is assumed that $\tilde{S}$, $\overline{\theta}_n(z)$ and $\tilde{\theta}_n(z)$ are much smaller than U and the linearization is made based on this assumption.

Boundary conditions. On the cavity surface ***OA*** and the cavity closure contour ***AD***, the steady and unsteady components of the tangential velocity are given from the linearized Bernuoli's equation and from the solution for the viscous wake problem:

$$\overline{v}_n(x)=\begin{cases} U+\dfrac{\sigma U}{2}, & 0<x<\overline{l}_{cn} \\ \overline{v}_{\delta n}(x), & \overline{l}_{cn}<x<c \end{cases}, \tag{3}$$

$$\tilde{v}_n(x)=\begin{cases} \tilde{v}_{on}e^{-\lambda x/U}, & 0<x<\overline{l}_{cn} \\ \tilde{v}_{\delta n}(x), & \overline{l}_{cn}<x<c \end{cases}, \tag{4}$$

where $\tilde{v}_{on}$ is the complex amplitude of the tangential velocity perturbation at the leading edge ***O***, $\tilde{v}_{\delta n}(x)$ is the complex amplitude of the velocity perturbation along the boundary ***AD***. The velocity perturbation $\tilde{v}_{on}$ can be found from the unsteady Bernuolli's equation applied between the leading edge $z_{n0}=(n-1)he^{i\beta}$ of the n^{th} blade and at some distance $x=-L$ upstream where pressure p_{-L} is assumed to be constant:

$$\left.\frac{\partial\phi_n}{\partial t}\right|_{-L}+\frac{v_{-L}^2}{2}+\frac{p_{-L}}{\rho}=\left.\frac{\partial\phi_n}{\partial t}\right|_0+\frac{v_{0n}^2}{2}+\frac{p_v}{\rho}, \quad n=1,N$$

Linearizing the above equation on the assumption of small perturbation and taking into account the relations:

$$\left.\frac{\partial\phi_n}{\partial t}\right|_{-L}=\lambda\left[-L\tilde{S}\cos\beta+\mathrm{Re}\left(\sum_{k=1}^N \tilde{w}_k(-L)\right)\right]$$

$$=-\lambda L\tilde{S}\cos\beta, \quad v_{-L}=U+\tilde{S}\cos\beta, \quad \left.\frac{\partial\phi_n}{\partial t}\right|_0=\lambda\tilde{\phi}_{n0},$$

$$\tilde{\phi}_{n0}=\sum_{k=1}^N \mathrm{Re}[\tilde{w}_k(z_{n0})],$$

we obtain:

$$\lambda(\tilde{\phi}_{n0}+L\tilde{S}\cos\beta)-U\tilde{S}\cos\beta+U(1+\sigma/2)\tilde{v}_{0n}=0. \tag{5}$$

On the other hand, with using Eq. (2) on the cavity surface ***OA*** and the boundary of viscous and inviscid flow ***AD***, we obtain:

$$\mathrm{Re}[\overline{\theta}_n(z)]-\frac{\overline{\gamma}_n(x)}{2}=\overline{v}_n(x)-U, \quad 0<x<c, \quad n=1,N, \tag{6}$$

$$\tilde{S}\cos\beta+\mathrm{Re}[\tilde{\theta}_n(z)]-\frac{\tilde{\gamma}_n(x)}{2}=\tilde{v}_n(x), \quad 0<x<c, \quad n=1,N, \tag{7}$$

where $z=x+h(n-1)\exp(i\beta)$.

If we put Eq. (3) and (4) into Eq. (6) and (7), we obtain integral equations with respect to $\overline{q}_n(x)$, $\overline{\gamma}_n(x)$, $\tilde{q}_n(x)$ and $\tilde{\gamma}_n(x)$.

On the pressure side of the profiles, the non-passage condition takes the form:

$$-U\alpha+\mathrm{Im}[\overline{\theta}_n(z)]-\frac{\overline{q}_n(x)}{2}=0, \quad 0<x<c, \quad n=1,N \tag{8}$$

$$\tilde{S}\sin\beta+\mathrm{Im}[\tilde{\theta}_n(z)]-\frac{\tilde{q}_n(x)}{2}=0, \quad 0<x<c, \quad n=1,N \tag{9}$$

which, combined with Eq. (2), also provide integral equations with respect to the singularities.

We assume that the pressure is continuous at the trailing edge of the blades (Kutta's condition). By integrating the momentum equation along the blades, this condition can be represented for steady and unsteady components as follows:

$$\overline{\gamma}_n(c)=0, \tag{10}$$

$$\frac{\lambda}{U}\int_0^c \tilde{\gamma}_n(x)dx+\tilde{\gamma}_n(c)=0, \quad n=1,N. \tag{11}$$

We assume that the upper and lower boundaries of the far wake in $x>c$ are parallel with each other and we assume no sources there. In order to have a continuous velocity at the trailing edge, we need to require:

$$\overline{q}_n(c)=0, \quad \tilde{q}_n(c)=0, \quad n=1,N. \tag{12}$$

The mass conservation for unsteady flow requires:

$$\lambda Nh\tilde{S}+\sum_{n=1}^N \int_0^c q_n(x)dx=0 \tag{13}$$

Equations (5)–(13) allow to determine the flow disturbance as well as steady cavity length $\overline{l}_c$ and fluctuation of the cavity length $\tilde{l}_c$, if the velocity perturbation $\overline{v}_{\delta n}(x)$ $\tilde{v}_{\delta n}(x)$ along the boundary of viscous and inviscid flow are known.

The steady and unsteady cavity shape and the contour of interaction ***AD*** can be calculated from [3]:

$$\overline{y}(x)=\frac{1}{U}\int_0^x \overline{q}(x)dx,$$

$$\tilde{y}_n(x)=\frac{1}{U}e^{-\lambda x/U}\int_0^x \tilde{q}_n(x)e^{\lambda x/U}dx.$$

$$y=y_\delta=\overline{y}(x)+\tilde{y}(x)e^{\lambda t}$$

defines the unsteady boundary of the inviscid flow.

3.2 Unsteady Flow Model of the Wake. The cavity wake is divided into three subregions as shown in Fig. 5: the mixing region ***AEGH*** where the velocity profile is under development, the near wake region ***ETCG*** interacting with the inviscid flow under the completely developed velocity profile, and the far wake ***TFF'C*** starting from the trailing edge ***C*** of the blade ***OC***. The terms ''mixing region,'' ''near wake'' and ''far wake'' are used after the boundary-layer theory for cavitation-free separated flows [9,13]. In the ''mixing region'' and ''near wake,'' the development of the wake is calculated by taking account of the pressure gradient of the outer inviscid flow and neglecting the shear stress exerted by the blade surface. Once the location of the inviscid flow boundary $y=y_\delta$ is determined from the outer inviscid flow analysis, the wake model provides tangential velocity v_δ on the wake surface, which is used as a boundary condition for the external inviscid flow. For the steady component, outer inviscid flow and inner wake flow is solved successively until the convergence is obtained. For the unsteady component, both flows are solved simultaneously by linearizing the problem based on the assumption of small unsteady disturbance. The far wake is assumed to have no effect on the inviscid flow and hence no wake model is provided.

Mixing region. We consider a mixing region where the velocity profile across the wake is under formation. The flow downstream of the cavity is highly unsteady, turbulent and two-phase [7]. The velocity of the liquid is substantially smaller than the main flow velocity [8]. Under the influence of the pressure gradient a re-entrant flow appears. The interaction of the re-entrant flow and main flow cause large scale vortices and high turbulent stress. The liquid flow into the cavity decreases the cavity length and increases the density of the two-phase medium. The outflow from the cavity on the contrary increases the cavity length and decreases the density in the mixing region. From the above considerations, we assume that the flow velocity u_0 and the density ρ_0 at the beginning of the mixing region can be correlated with the cavity length l_c as follow:

$$u_0=\frac{dl_c}{dt}, \tag{14}$$

$$r_0=\rho_0/\rho=1-\frac{l_c}{l_{c\,\max}} \tag{15}$$

where $l_{c\,\max}$ is the maximum partial cavity length just before extending to super cavity. When the cavity length approaches zero $l_c\to 0$, the non-dimensional density should approach one $r_0\to 1$, which corresponds to the cavitation-free flow. Equation (15) is a linear interpolation of these two limiting cases. We assume that the non-dimensional density r of the fluid in the mixing region is transported with the flow velocity v_δ at the outer boundary of the mixing region:

$$\frac{dr}{dt}=\frac{\partial r}{\partial t}+v_\delta\frac{\partial r}{\partial x}=0. \tag{16}$$

From the features of the flow in the mixing region mentioned above, we assume that we can neglect the convective terms in the x-component of the momentum equation. It gives:

$$\frac{\partial u_0}{\partial t}=-\frac{\partial p}{\partial x}+\frac{\partial \tau}{\partial y}, \tag{17}$$

The gradient of the shear stress is approximated by:

$$\frac{\partial \tau}{\partial y}\approx\frac{\tau_m}{h},$$

where the shear stress τ_m between the upper and lower boundaries of the mixing layer is determined by $-\tau_m=\chi_1\rho_0(v_\delta-u_0)^2$; χ_1 is the turbulence factor and h is the blade spacing used as a characteristic length. The value $\chi_1=0.4$ has been used in the present calculations. Taking Eq. (14) into account, we can rearrange Eq. (17) as follows:

$$\frac{\partial v_\delta}{\partial t}+v\frac{\partial v_\delta}{\partial x}+\frac{\chi_1 r}{h}\left(v_\delta-\frac{dl_c}{dt}\right)^2-r\frac{d^2l_c}{dt^2}=0. \tag{18}$$

Eq. (18) provides the tangential velocity v_δ on the wake surface which is used as a boundary condition for the external inviscid flow.

It is favorable that we can justify each assumptions of Eqs. (14)–(17). However, from the complexity of the flow near the cavity closure, it is difficult to examine the validity of each assumption and we need to depend on the final results for the validation of the model.

Unsteady near cavity wake. The flow in the near cavity wake is characterized by the velocity profile formed under the action of the longitudinal pressure gradient and the shape of the inviscid flow boundary. The velocity profile $u(y)$ across the wake is represented by using the form parameter m and an universal function of velocity defect $f(\overline{y})$:

$$\frac{u}{v_\delta}=1-m(x,t)f(\overline{y}) \tag{19}$$

where m is the form parameter of the velocity profile, $\overline{y}=y/\delta$ is the non-dimensional coordinate across the wake, v_δ is the velocity at the outer boundary of the viscous wake. The function $f(\overline{y})=2\overline{y}^3-3\overline{y}^2+1$ is the universal velocity defect function for the turbulent free mixing layers [9]. Equation (19) gives $u=v_\delta$ at the outer boundary $\overline{y}=1$ and $u=u_0\equiv(1-m)v_\delta$ on the blade $\overline{y}=0$. We assume that there is a thin laminar sublayer at $\overline{y}=0$ where the velocity changes from zero to the value u_0. We assume that the thickness of the laminar sublayer is so small that the momentum in it can be neglected. We also assume that the laminar shear stress in it can be neglected. From Eq. (19), the displacement thickness δ^* and the momentum thickness δ^{**} are given by:

$$\delta^*=\int_0^\delta\left(1-\frac{\rho_0 u}{\rho v_\delta}\right)dy=\delta H^*(m,r)=\delta\left(1-r+\frac{rm}{2}\right),$$

$$\delta^{**}=\int_0^\delta\frac{\rho_0 u}{\rho v_\delta}\left(1-\frac{u}{v_\delta}\right)dy=\delta H^{**}(m,r)=\delta\frac{rm}{2}\left(1-\frac{26}{35}m\right) \tag{20}$$

von Karman's integral momentum equation integrated over the whole wake and the differential momentum equation applied at $y=0$ are used:

$$\frac{1}{v_\delta}\frac{\partial[\delta^*-(1-r)\delta]}{\partial t}+\frac{\delta^*}{v_\delta}\frac{\partial \ln v_\delta}{\partial t}+\frac{\partial \delta^{**}}{\partial x}+(2\delta^{**}+\delta^*)\frac{\partial \ln v_\delta}{\partial x}=0 \tag{21}$$

$$r\frac{\partial u_0}{\partial t}+ru_0\frac{\partial u_0}{\partial x}=\frac{\partial v_\delta}{\partial t}+v_\delta\frac{\partial v_\delta}{\partial x}+\frac{1}{\rho}\frac{\partial \tau}{\partial y}\bigg|_{y=0} \tag{22}$$

In the integral momentum equation (21), the shear stress is neglected both on the upper ($y=\delta$) and lower ($y=0$) boundaries of the wake. In the differential momentum Eq. (22), the shear stress

in the wake is considered to take account of the momentum transfer within the wake. The gradient of shear stress is evaluated by:

$$\left.\frac{\partial \tau}{\partial y}\right|_{y=0} = \frac{\tau_n}{\delta},$$

where $\tau_n = \chi_2 \rho_0 (v_\delta - u_0)^2$ with $v_\delta = u(\delta)$ and $u_0 = u(0)$. The empirical factor $\chi_2 = 0.03$ has been used in the present calculations.

It is assumed that the direction of the wake flow velocity at the outer-wake boundary ($y = \delta$) is identical to the slope of the inviscid flow boundary [13]. This condition can be represented as follows, by integrating the continuity equation across the wake:

$$\left(\frac{v_y}{v_x}\right)_\delta = \frac{\partial y_\delta}{\partial x} = \frac{\partial \delta^*}{\partial x} - (\delta - \delta^*)\frac{\partial \ln v_\delta}{\partial x} - \frac{\delta}{v_\delta}\frac{\partial r}{\partial t}, \qquad (23)$$

where v_x and v_y are the wake velocity components in x and y directions.

The length of mixing region l_m is determined from the condition of the flow attachment:

$$\delta^*(l_m) = y_\delta(l_m), \qquad (24)$$

where $\delta^* = \delta H^*(1, r_0)$ is the displacement thickness of the mixing layer. Equations (23) and (24) show that y_δ corresponds to the displacement thickness in the mixing region but differs slightly from the displacement thickness in the near-wake region. In the mixing region, we assume that the thickness δ of the mixing layer shown in Fig. 5 is determined from the relationship obtained for free jet boundary layers [11]:

$$\frac{\partial \delta}{\partial x} = b r_0,$$

where $b = 0.098$ is used in the present calculations, determined from Görtler's theory [11].

The mixing layer reaches the blade surface at point ***G*** (Fig. 5) where the near wake starts. Downstream of the cross section ***GE*** the density of the fluid increases rapidly due to higher pressure there ($p > p_v$) and the absence of the recirculating flows. In this region it is assumed that the density of the fluid increases [10] following the relation:

$$\frac{dr}{dt} = \frac{\partial r}{\partial t} + v_\delta \frac{\partial r}{\partial x} = v_\delta \frac{1 - r}{L_r}, \qquad (25)$$

where the scale of relaxation $L_r = 0.2h$ is used in the present calculations.

The system of Eqs. (22–25) can be used to determine the wake variables v_δ, δ, m and r when the shape of the external inviscid flow $y_\delta(x,t)$ is given from the inviscid flow analysis. Rather elaborate wake model used in the present analysis is intended to obtain reasonable agreement of steady suction performance with experiment [12].

3.3 Linear Stability Analysis. The vortex and source distributions are discretized along the blades at the locations x_i^n, $i = 1, M$ as shown in Fig. 5*b*. Using linear interpolation between the points x_i^n the inviscid flow problem is reduced to a system of linear equations related to the strength of souces q_i^n and vortex γ_i^n at these points.

Representing the flow parameters in the wake as a sum of steady and unsteady components $P(x,t) = \overline{P}(x) + \tilde{P}(x)e^{\lambda t}$, where $P = \{m_n, v_{\delta n}, y_{\delta n}, r_n\}$, $n = 1, N$ and linearizing the Eqs. (14–16), (18), and (21–25), we can obtain a system of linear ordinary differential equations in terms of the complex amplitudes of oscillations. The system of equations for steady components of the parameters in the wake is nonlinear. An iterative procedure coupling the steady viscous and inviscid flow is used in order to determine the steady shape of the boundary of interaction and the tangential velocity on this boundary.

The linear system of ordinary differential equations of the unsteady viscous flow is discretized at the locations x_i^n mentioned above. The derivatives are approximated by using finite differences and the obtained system of linear equations is added to the system of the inviscid flow. The joint system of the linear equations of the unsteady viscous and inviscid flow can be represented as follows

$$\left[\overline{A}(\lambda, \sigma, \alpha)\right] \begin{bmatrix} \tilde{q}_i^n \\ \tilde{\gamma}_i^n \\ \tilde{v}_{\delta i}^n \\ \tilde{m}_{\delta i}^n \\ \tilde{l}_n \\ \tilde{v}_{0n} \\ \tilde{S} \end{bmatrix} = [0] \qquad (26)$$

Here, it is assumed that the outlet flow rate does not oscillate. The eigen value problem related with Laplace's variable λ is $\det|\overline{A}(\lambda, \sigma, \alpha)| = 0$. By solving this characteristic equation we obtain the eigen frequencies of various kinds of cavitation instabilities.

4 Results and Discussion

Figure 6 shows the suction performance predicted by the present model. The static head coefficient is estimated from

$$\psi_{st} = \frac{p_2 - p_1}{\rho U^2} = 0.5(1 + \phi^2)\left(1 - \frac{\overline{v}_{\delta 2}^2}{v_1^2}\right),$$

where p_1 and p_2 are the pressure at the inlet and outlet correspondently, $v_{\delta 2}$ is the velocity at the outlet of the cascade, $v_1^2 = U^2 + v_m^2 = U^2(1 + \phi^2)$ is the mean velocity at the inlet, v_m is the meridional (axial) velocity, ϕ is the flow coefficient. The head decrease due to cavitation is associated with the increase of relative velocity $v_{\delta 2}$ caused by the displacement effect of the cavity wake. On the suction performance curves, the occurrence of rotating cavitation is shown by open symbols, while the onset of rotating choke is shown by closed symbols. We note that the rotating cavitation occurs mainly in the range where the performance degradation is insignificant, while rotating choke occurs where the head is decreased due to cavitation.

The performance curve in the flow coefficient vs. head plane is shown in Fig. 7, where the occurrence of rotating cavitation and rotating choke is also shown by open and closed symbols respectively. The same observations as with Fig. 6 are evident also in this figure. Rotating choke occurs typically in the region with positive slope of the performance curve, which is quite different

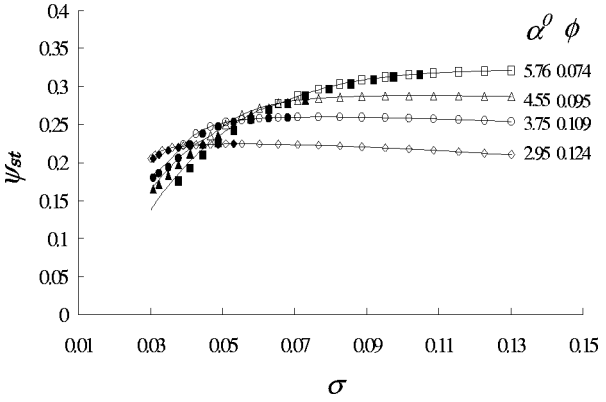

Fig. 6 Cavitation performances of the cascade and region of instability for various angles of attack: stagger angle 80 deg, solidity 2.35. Uncertainty $\psi_{st} \pm 0.005$.

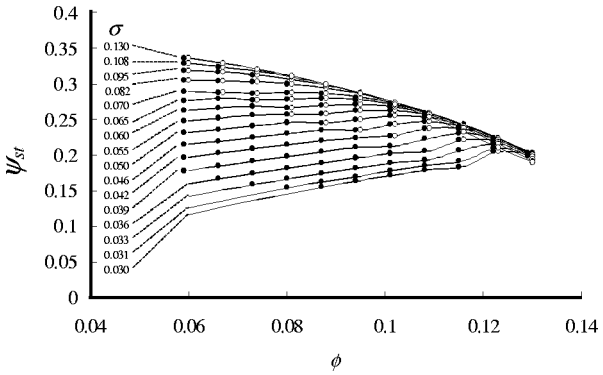

Fig. 7 Head performance of the cascade for various values of cavitation number and region of instability: stagger angle 80 deg, solidity 2.35. Uncertainty $\psi_{st} \pm 0.005$.

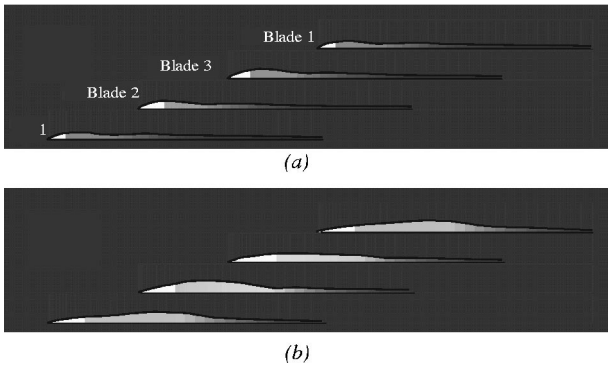

Fig. 9 The unsteady cavity shapes at the onset point of cavitation instability; $\phi = 0.095$; stagger angle 10 deg; solidity of the cascade 2.35. The amplitude of oscillation of cavity length is assumed to be $\tilde{l}_c = 0.3\bar{l}_c$. Cavity is shown by white area and the density in the mixing region and wake is shown by the darkness. Uncertainties: $x/h \pm 0.001$, $y/h \pm 0.001$. *a*) rotating cavitation ($\sigma = 0.26$); *b*) rotating choke ($\sigma = 0.077$)

from rotating cavitation. This suggests that rotating choke is caused by the positive slope of the performance curve associated with choke.

Figure 8 shows the propagation velocity ratio ω/Ω of rotating cavitation and rotating choke, defined as the ratio of the propagation velocity ω of the instabilities observed in a stationary frame to the rotational speed Ω of the impeller. Rotating choke is found only at smaller σ. Rotating cavitation rotates faster than impeller speed but rotating choke rotates about a half of the impeller speed. This agrees with experimental observations. With the present wake model, it cannot be shown analytically that the instabilities depend on $\sigma/(2\alpha)$. However, the numerical results show that the $\sigma/(2\alpha)$ rule found for linear closed cavity [3] practically applies to the present case, for both rotating choke and rotating cavitation.

Figure 9 shows the cavity shapes with rotating cavitation and rotating choke at their onset points (the largest cavitation number). For rotating choke the mixing region extends to the throat of the blade channel. Rotating stall in impellers with longer blade rotates with a speed only slightly smaller than impeller speed, caused by the inertia effect of the fluids in the impeller. Lower speed of the rotating choke may be caused by the decrease of the inertia effect due to cavitation. On the other hand, rotating cavitation starts to occur with much shorter cavity. With a closed cavity model, it has been shown that various types of cavitation instability start to occur when the cavity length reaches about 65% of the spacing [3]. The results shown in Fig. 9 suggest that the total length of cavity plus mixing region plays an important role in the present model.

Figure 10 shows the steady cavity length l_c of closed model and the total length of cavity and mixing region l_m, normalized by the blade spacing h, plotted against $\sigma/(2\alpha)$. The regions of rotating cavitation and rotating choke occurrence are also shown. It is clearly shown that rotating cavitation starts to occur when the cavity length (closed model) or the total length of cavity and mixing region (wake model) exceeds 65% of the blade spacing, h. This can be explained by the interaction of the local flow near the cavity closure with the leading edge of the next blade [3]. On the other hand, rotating choke starts to occur when the total length of cavity and mixing region exceeds 150% of the spacing.

Thus, the present model can simulate two important characteristics of rotating choke, the onset condition and frequency. However, predicted suction performance shown in Fig. 6 is significantly different from the experimental curve as shown in Fig. 1. Positive slope and hence rotating choke are unusual and not observed for many inducers. This may be caused by nonlinear and/or three dimensional effects. On the same reasons, we cannot expect quantitative agreement of the range of rotating choke and rotating cavitation in the present linear 2-D calculations. The model includes a series of empirical coefficients the values of which were chosen from the previous analysis of the predicted and experimental cavitation performances of inducers [11]. If we change some of these oefficients, we may obtain better quantitative agreement between the calculated and test results. However, we did not make such attempts since the goal of the study is to give a physical explanation of the new type of cavitation instability. Further research is needed for the complete understanding of rotating choke.

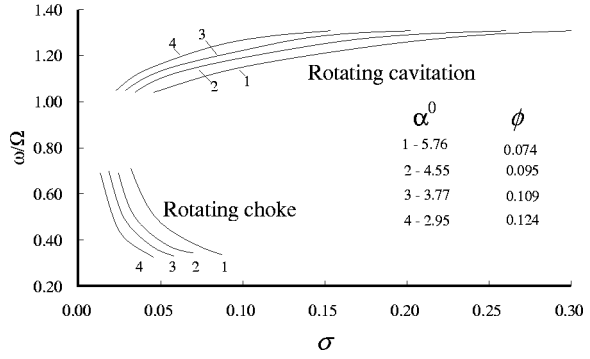

Fig. 8 Propagation velocity ratio for the rotating cavitation and rotating choke. Uncertainty $\omega/\Omega \pm 0.01$

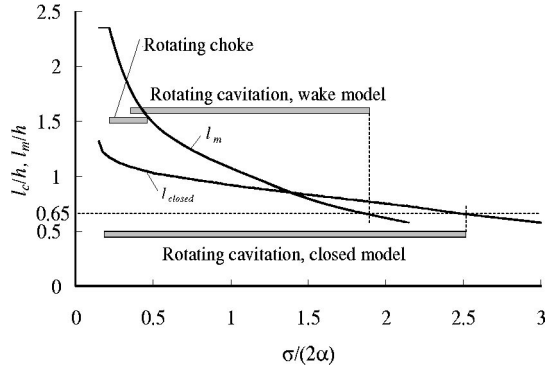

Fig. 10 Cavity length (closed model, l_{closed}) and total length of cavity and mixing region (wake model, l_m) versus parameter $\sigma/(2\alpha)$; the gray bars show the range of instability; blade angle 10 deg, solidity 2.35, angle of attack 4 deg. Uncertainties: $l_c/h \pm 0.001$, $l_m/h \pm 0.001$

Conclusions

Rotating choke is analyzed by using a cavity model with a cavity wake. It was shown that the model proposed can predict not only rotating choke but also rotating cavitation. Rotating choke is predicted in the region where the performance curve has positive slope due to choke. Predicted propagation velocity is 0.3–0.6, which agrees with experimental observation. From these results, we can conclude that rotating choke is a two dimensional local flow instability caused by the positive slope of performance curve due to the choking of flow passage with cavitation. This mechanism is completely different from other cavitation instabilities such as cavitation surge and rotating cavitation, that are caused by positive mass flow gain factor.

Acknowledgments

The present paper is based on the extensive tests reported in [1] conducted by National Aerospace Laboratory (NAL) and National Aerospace Development Agency (NASDA). Their contribution is highly appreciated. This study was supported by the JSPS.

Nomenclature

- c = chord length
- b = free mixing layer spreading factor
- h = cascade pitch
- F_c = area of the wake
- i = imaginary unit in space, $i^2=-1$
- j = imaginary unit in time, $j^2=-1$
- l_c = cavity length
- l_m = total length of the cavity and mixing region
- L = upstream conduit length
- m = form parameter of velocity profile or an integer number
- N = number of blades
- n = blade index
- p, p_v = pressure and vapor pressure
- q = strength of sources
- r = non-dimensional density
- u = x-component velocity in the wake
- v = velocity modulus for inviscid flow
- U = circumferential velocity
- $\tilde{S}$ = perturbation of axial velocity
- t = time
- W = complex potential
- w = perturbation of complex potential
- x = location of discrete point on coordinate x
- y_δ = boundary of inviscid flow
- z = physical plane $=x+iy$
- Q = volumetric flow rate
- Q_d = design volumetric flow rate
- α = angle of attack
- β = blade angle
- χ = coefficient of turbulent viscosity
- δ = thickness of viscous layer
- δ^* = displacement thickness
- δ^{**} = momentum thickness
- $\lambda=\mu+j\omega$ = Laplace's variable
- θ = complex velocity perturbation
- ϕ = flow coefficient, potential
- γ = strength of vortex
- ρ = liquid density
- σ = cavitation number
- τ = tangential stress
- ψ_{st} = static head coefficient
- ω = frequency of oscillations
- Ω = shaft rotational frequency

Superscript and Subscript

- $-$ = steady component
- $\sim$ = complex amplitude of unsteady component
- $_n$ = blade index
- $_\delta$ = parameters at outer boundary of viscous layer
- $_0$ = parameters at the suction side of the profile

References

[1] Shimura, T., Yoshida, M., Kamijo, K., Uchiumi, M., Yasutomi, Y., 2002, "Cavitation Induced Vibration Caused by Rotating-stall-type Phenomenon in LH2 Turbopump," *Proc. of the 9th International Symposium on Transport Phenomena and Dynamics of Rotating Machinery*, Honolulu, Hawaii, February 10–14.

[2] Tsujimoto, Y., Kamijo, K., Brennen, C., 1999, "Unified Treatment of Flow Instabilities of Turbomachinaries," AIAA paper 99-2678.

[3] Horiguchi, H., Watanabe, S., Tsujimoto, Y., Aoki, M., 2000, "A Theoretical Analysis of Alternate Blade Cavitation in Inducers," J. Fluids Eng., **122**(1), pp. 156–163.

[4] Greitzer, E. M., 1976, "Surge and Rotating Stall in Axial Flow Compressors, Part 1; Theoretical Compression System Model, Part 2; Experimental Results and comparison Theory," ASME J. Eng. Power, **98**, pp. 190–217.

[5] Stripling, L. B., and Acosta, A. J., 1962, "Cavitation in Turbopump—Part 1," ASME J. Fluids Eng., **84**(3), pp. 326–338.

[6] Young, W. E. et al., 1972, "Study of Cavitating Inducer Instabilities," Final Report, NACA-CR-123939, 1972-8.

[7] Knapp, R. T., Daily, J. W., and Hammit, F. G., 1970, "Cavitation," McGraw-Hill, New York.

[8] Furness, R. A., Hutton, S. P., 1975, "Experimental and Theoretical Studies on Two-dimensional Fixed-type Cavities," ASME J. Fluids Eng., **97**(4), pp. 515–522.

[9] Gogish, L. V., and Stepanov, G. Yu., 1979, "Turbulent Separated Flows" (in Russian), Moscow, Nauka.

[10] Gogish, L. V., and Stepanov, G. Yu., 1982, "Turbulent Separated flows," (in Russian), Izvestija AN USSR Ser. Mechanika Zhidkosti i Gazov, **2**, pp. 32–47.

[11] Schlichting, H., 1960, "Boundary layer theory," McGraw-Hill, New York.

[12] Semenov, Yu., and Tsujimoto, Y., 2003, "A Cavity Wake Model Based on the Viscous/Inviscid Interaction Approach and Its Application to Non-symmetric Cavity Flows in Inducers," ASME J. Fluids Eng., **125**(5), pp. 758–766.

[13] Crocco, L., and Lees, L., 1952, "A mixing theory for the interaction between dissipative flows and nearly isentropic streams," J. Aerosol Sci., **19**(10), pp. 649–676.

An Experimental Study of Unsteady Partial Cavitation

Jean-Baptiste Leroux

Jacques André Astolfi[1]
Assistant Professor
e-mail: astolfi@ecole-navale.fr

Jean Yves Billard
Professor

Ecole Navale/IRENAV,
Institute de Recherche de l'Ecole Navale,
BP 600,
29240 Brest-Armee, France

Unsteady partial cavitation can cause damage to hydraulic machinery and understanding it requires knowledge of the basic physics involved. This paper presents the main results of a research program based on wall-pressure measurements aimed at studying unsteadiness in partial cavitation. Several features have been pointed out. For cavity lengths that did not exceed half the foil chord the cavity was stated to be stable. At the cavity closure a peak of pressure fluctuations was recorded originating from local cavity unsteadiness in the closure region at a frequency depending on the cavity length. Conversely, cavities larger than half the foil chord were stated to be unstable. They were characterized by a cavity growth/destabilization cycle settled at a frequency lower than the previous ones. During cavity growth, the closure region fluctuated more and pressure fluctuations traveling in the cavity wake were detected. When the cavity was half the foil chord, cavity growth was slowed down and counterbalanced by large vapor cloud shedding. When the cavity length was maximum ($l/c \sim 0.7–0.8$), it was strongly destabilized. The reason for such destabilization is discussed at the end of the paper. It is widely believed that the cavity instability originates from a process involving the shedding of vapor clouds during cavity growth, a re-entrant jet, and a shock wave phenomenon due to the collapse of a large cloud cavitation. [DOI: 10.1115/1.1627835]

Introduction

Partial cavitation is commonly encountered on lifting surfaces such as hydrofoils or blades on propellers and pumps. It generally occurs in the vicinity of the leading edge in incidences for which a pressure peak takes place on the suction side and is reduced below the liquid vapor pressure. In some cases, partial cavitation exhibits instabilities that can cause severe damage to hydraulic systems. Partial cavitation is unsteady by nature; however, at the early phases of development the location of the cavity closure does not vary very much and the cavity is often stated steady and stable. As the cavity grows, the variation of the cavity closure location increases leading to unsteadiness effects. Under some conditions, the unsteadiness leads to cavity destabilization and breakdown. Under destabilization, the cavity alternates strongly between a small partial cavity and a large cavity. The destabilization process results in the shedding of large bubbly vapor structures, called ''cloud cavitation,'' which is known to induce high-level pressure pulses and to be a destructive form of cavitation, [1]. Although many interesting works have been published to understand the physical mechanisms involved, they are not yet fully understood, [2]. A mechanism of cavity destabilization and transition to cloud cavitation was often attributed to a re-entrant jet at the end of the cavity, [3–8]. However, several complex features can be involved in partial cavitating flow such as bubbly flow, laminar, transition or turbulent flow, detached and reattached flow, shear layer and vortical structures, deforming surface. Consequently, more than one type of partial cavity has to be considered. Also, other mechanisms can lead to cavity instability such as bubbly flow shock wave, instability of the shear layer on the cavity surface, deforming surface instability, transitional instability between partial and super cavitation or surge instability. For instance, Laberteaux and Ceccio [9] observed two types of partial cavities with two distinct behaviors: *closed* re-entrant partial cavities formed on a two-dimensional NACA0009 hydrofoil, and *open* partial cavities without re-entrant flow (although recirculation flow was detected for some cases) on a plano-convex hydrofoil. A *closed* partial cavity has a clear interface, a cavity closure relatively free of bubbles and a re-entrant jet at the cavity closure. Conversely, an *open* cavity is typically ''frothy'' and has a periodically varying length associated with the shedding of vapor clouds. Kawanami et al. [10] also observed two types of cavity depending on whether the boundary layer is of a burst type or nonburst type. The burst type corresponds to a laminar separation in a long bubble whereas the nonburst type corresponds to a short separation bubble with the flow reattaching in the vicinity of the leading edge, [11]. The shape, fluctuations in length and type of partial cavities are quite different whether the boundary layer along a foil section will burst or not. Callenaere et al. [8] identified a transition between short and long cavities, with those instabilities originating from a re-entrant jet or surge-type instability, respectively.

Although unsteady partial cavitating flow has complex features, substantial efforts have been made in modeling cavitating flow to understand unsteady partial cavitation and transition to cloud cavitation. Kubota et al. [12], using a bubble two-phase flow model showed that cloud cavitation can result in the separation and the rollup of the boundary layer at the cavity leading edge meaning that the instability of the shear layer may produce the cavitation cloud. The re-entrant jet exists at the cavity trailing-edge region but plays a less important role in the separation mechanism of the cavitation cloud. Chahine and Hsiao [13] using a coupled RANSE-BEM method showed that cavity shape oscillations might occur due to the formation of a re-entrant jet or to the development of a wave over the cavity surface with amplitude large enough to cut the cavity into two parts. These might occur simultaneously under some flow conditions. Arndt et al. [14] based on LES simulations and experiments indicate that depending on $\sigma/(2\alpha)$, two mechanisms are found for cloud cavitation. At high values of $\sigma/(2\alpha)$, a re-entrant jet dominates, whereas at low values, a bubbly flow shock wave dominates. The transition was found to occur for $\sigma/(2\alpha)=4$. From a theoretical analysis, Watanabe et al. [15] show theoretically that although cavity shedding and re-entrant jet are not taken into account, instability can originate from the transitional cavity oscillation between partial and super cavities. A brief review of these recent works indicates that fundamental knowledge of the basic physics resulting in cavity destabilization and transition to cloud cavitation is still progressing and need to be documented. Particularly, the complex flow near the cavity closure region requires close examination. Follow-

[1]To whom correspondence should be addressed.

Contributed by the Fluids Engineering Division for publication in the JOURNAL OF FLUIDS ENGINEERING. Manuscript received by the Fluids Engineering Division November 21, 2002, revised manuscript received June 30, 2003. Associate Editor: S. L. Ceccio.

ing previous works, [16,17], the present paper focuses on the unsteadiness and instability of partial cavitation. This is achieved by means of wall-pressure measurements using an instrumented hydrofoil equipped with wall-pressure transducers. The experimental investigation was performed ranging from conditions close to inception to the conditions where an unstable cavity arose. For stable cavities, transducers in the vicinity of the cavity closure are used to characterize the unsteadiness of this region. For unstable cavities, the cavity break by the re-entrant jet, the main vapor cloud emission and the residual cavity evolution, are captured by ten aligned transducers. Measurements of lift and drag were also performed.

Experimental Setup

The experiments were carried out in the Ecole Navale Cavitation Tunnel, fitted with a 1 m long and 0.192 m wide square cross test section. In this device, velocities of up to 15 m/s and pressures between 30 mbar and 3 bars can be achieved. A regulation system sets the pressure and the velocity to prescribed values, which lead to the cavitation number values of the measurements. The designed foil for this project was a two-dimensional cambered foil of the NACA66 series, for which the theoretical coordinates are given in Table 1. The relative maximum thickness was $\tau=12\%$ at 45% from the leading edge and the relative maximum camber was 2% at 50% from the leading edge. The chord length was $c=0.150$ m and the span was 0.191 m. The material for the hydrofoil was polished stainless steel. Two identical hydrofoils were fabricated. One was equipped with wall-pressure transducers. Except for lift and drag measurements, the hydrofoil was clamped on both sides of the tunnel walls. The angle of incidence was given with respect to the zero angle of incidence. The latter was adjusted by aligning the foil chord to the horizontal top of the test section taken as a reference surface. This was achieved by positioning the trailing edge with respect to the top of the test section using a special mechanical gauge. The foil incidence was driven by a step-by-step DC motor, resulting in a precision on the angle readings of $\pm 1/60$ deg.

Pressure measurements were carried out using seventeen piezoresistive transducers (Keller AG 2 MI PAA100-075-010) of 10 bars maximum pressure. The pressure transducers were mounted into small cavities with a 0.5 mm diameter pinhole at the foil surface (see Fig. 1(*a*). The Helmoltz natural frequency of the cavity is 85 kHz in water. The transducer locations are given on Fig. 1(*b*). As shown, one set of ten transducers was aligned along the chord on the suction side from $x/c=0.05$ up to the trailing $x/c=0.90$ with a step of $0.10\,c$ from $x/c=0.10$. Two sets of three transducers were arranged parallel to this line in order to analyze three-dimensional effects. One transducer was also mounted on the opposite face in order to analyze the effect on the pressure side of cavitation developing on the suction side. Before mounting the hydrofoil in the test section, the pinhole, just upper each transducer, was water filled using a syringe. An *in-situ* calibration was performed to take transducer assembly into account. The transducers were calibrated simultaneously by decreasing the static pressure in the test section from 1.5 bars to 0.05 bars with a step of 0.05 bars at zero flow velocity. The transducers responses were found to be linear (see Fig. 2) and the coefficients of the linear regression were used to convert Volts in Pascals. To control any deviation during the experiments, the calibration procedure was performed systematically before and after each series of measurements.

Signals from the wall-pressure transducers were amplified, filtered and collected through a 16-channel 16-bit A/D digitizer VXI HPE1432A, at simultaneous sample with a maximum available sample frequency of 51.2 kHz. The control and the measurement data storage were performed by a PC through an HPE8491A/IEE1394 PC link to VXI. The acquisition programs were developed *in-situ* and the signal processing was developed using MATLAB® software. Two nominal sample frequencies, 51.2 kHz and 1.024 kHz, were selected, corresponding to samples of 0.64 s and 4.00 s, respectively. Spectral analysis was obtained from the average of eight individual spectra.

Finally, lift and drag were also measured using a resistive gauge

Table 1 Coordinates of the tested hydrofoil

x/c	y/c	x/c	y/c
0,000000	0,000000	0,000000	0,000000
−0,000173	0,002046	0,000123	−0,000530
0,000246	0,004647	0,001125	−0,002977
0,001346	0,007110	0,002705	−0,005255
0,003148	0,009593	0,004941	−0,007456
0,005551	0,012035	0,007885	−0,009478
0,008995	0,014762	0,012011	−0,011509
0,013509	0,017653	0,017255	−0,013475
0,019545	0,020864	0,024086	−0,015482
0,027070	0,024273	0,032440	−0,017467
0,036197	0,027872	0,042411	−0,019444
0,046867	0,031575	0,053931	−0,021377
0,059025	0,035312	0,066930	−0,023242
0,072601	0,039049	0,081336	−0,025035
0,087531	0,042754	0,097080	−0,026756
0,103750	0,046389	0,114097	−0,028391
0,121195	0,049922	0,132317	−0,029933
0,139799	0,053343	0,151675	−0,031393
0,159495	0,056643	0,172102	−0,032772
0,180221	0,059786	0,193536	−0,034041
0,201918	0,062725	0,215911	−0,035169
0,224521	0,065435	0,239160	−0,036161
0,247963	0,067921	0,263218	−0,037034
0,272179	0,070179	0,288017	−0,037790
0,297102	0,072199	0,313493	−0,038414
0,322671	0,073961	0,339581	−0,038910
0,348822	0,075431	0,366214	−0,039267
0,375488	0,076615	0,393327	−0,039470
0,402604	0,077522	0,420855	−0,039540
0,430107	0,078104	0,448731	−0,039410
0,457932	0,078300	0,476890	−0,039042
0,486010	0,078085	0,505264	−0,038453
0,514276	0,077477	0,533788	−0,037652
0,542662	0,076471	0,562395	−0,036640
0,571101	0,075059	0,591019	−0,035423
0,599524	0,073243	0,619594	−0,034009
0,627866	0,071022	0,648054	−0,032405
0,656057	0,068390	0,676334	−0,030630
0,684030	0,065358	0,704371	−0,028722
0,711719	0,061944	0,732100	−0,026703
0,739054	0,058133	0,759457	−0,024586
0,765966	0,053929	0,786385	−0,022480
0,792374	0,049272	0,812828	−0,020500
0,818200	0,044138	0,838712	−0,018533
0,843402	0,038681	0,863964	−0,016484
0,867937	0,033027	0,888517	−0,014315
0,891756	0,027250	0,912300	−0,012005
0,914812	0,021431	0,935248	−0,009564
0,937060	0,015648	0,957425	−0,006953
0,958581	0,009949	0,978894	−0,004146
0,979449	0,004342	1,000000	−0,001178
1,000000	−0,001178		

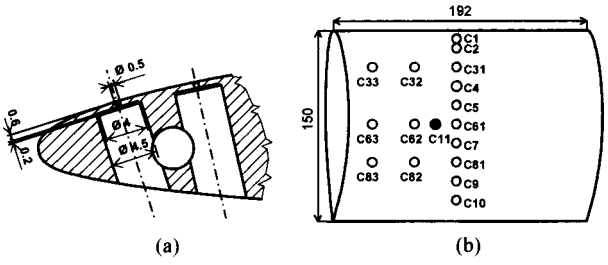

Fig. 1 (*a*) Transducer mounting. (*b*) Location and nomenclature of the pressure transducers, filled symbol is on the pressure side. Units in millimeter.

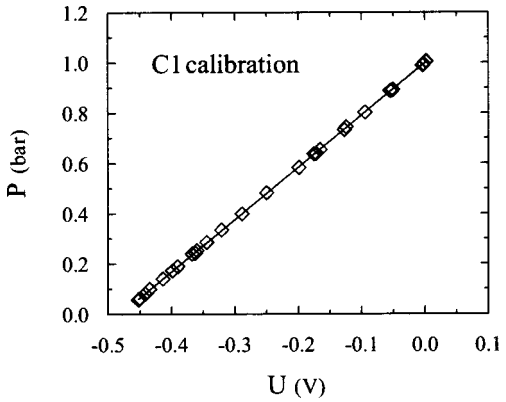

Fig. 2 Example of pressure transducer calibration curve

hydrodynamic balance carefully calibrated in our laboratory. In that case, the measurements were carried out on the hydrofoil without pressure transducers.

For the experiments, the nominal freestream velocity U was 5.33 m/s, corresponding to a Reynolds number based on the foil chord length $\mathrm{Re}=0.8\times10^6$. The nominal angle of incidence α of 6° was selected, but a control using the lift measurements showed that the effective angle was 6.5 deg. This value corresponds to an angle for which partial cavity clearly developed. Figure 3 shows an example of stable cavity studied in the present experiment. As shown, the cavity leading edge is formed of blunt ''glossy'' fingers. The cavity surface experiences a transition close to the leading edge and it is ''frothy'' over the major part of the cavity length. Characteristic horseshoe shaped cavitating structures are observed in the cavity wake. This suggests an open cavity as classified by Labertaux and Ceccio [9].

Uncertainties

Part of uncertainty is inherent in the flow conditions: the flow velocity, the pressure in the test section, the cavitation number and the angle of incidence. The uncertainty on the mean flow velocity is about 2%. The uncertainty on the pressure is about 3%. The resulting cavitation number variability is estimated to be $\Delta\sigma=\pm0.05$. However during the experiments, great care was taken to record the samples at the prescribed values of σ, with a variability less than $\Delta\sigma=\pm0.02$. The uncertainty of α is mainly due to the uncertainty of the zero angle of incidence (taken as a reference) and although care was taken to control it, the uncertainty was estimated to be as large as $\Delta\alpha=\pm0.2$ deg. For the pressure transducers calibration, the recorded noise was $P_{\mathrm{rms}}=150$ Pa and the deviation toward linearity was about 250 Pa (0.25% of the measurement range). The noncavitating pressure measurements show good reproducibility, with $\Delta C_p<0.03$. Finally, after the balance calibration measurements, the lift and drag uncertainties were estimated by testing several loads on the calibration device, leading to $\Delta L=\pm5N$ and $\Delta D=\pm1N$, corresponding to $\Delta C_L=\pm0.012$ and $\Delta C_D=\pm0.002$ using the nominal free stream velocity (respectively ~1% and ~5% of the measurement ranges).

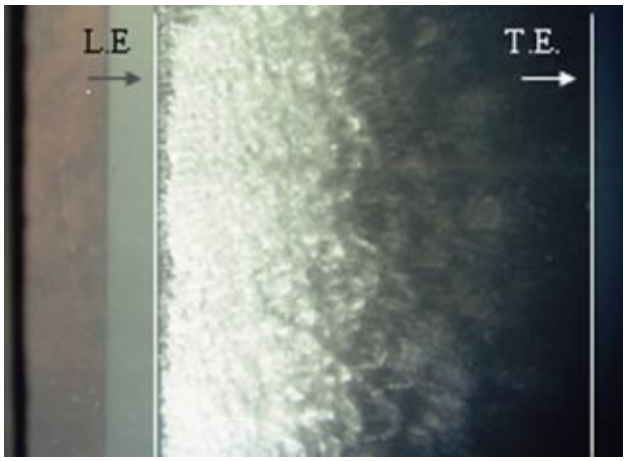

Fig. 3 Aspect of the cavity. Flow is from the left.

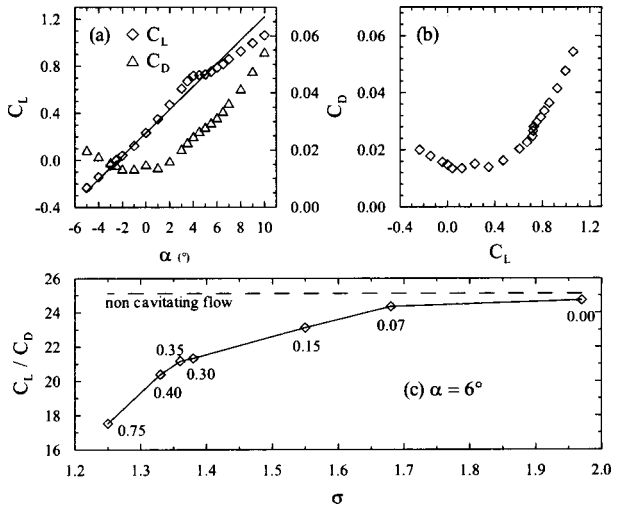

Fig. 4 (*a*) (*b*) Measured lift and drag coefficient for the non cavitating flow, straight line on (*a*) is the theoretical value $C_L=0.1097(1-0.83\tau)(\alpha+2.35)$ (inviscid unbounded calculation with viscous corrections, [18]). (*c*) Lift to drag ratio for various cavity lengths, labels are the mean relative cavity lengths (see also Table 2).

Results

The measured lift and drag coefficients are given on Fig. 4. The zero lift angle is found to be −2.5 deg compared to the unbounded theoretical value of −2.35 deg, [18]. As shown, the lift coefficient increases linearly and is closed to the theoretical value up to 2 deg. Then, it is larger and exhibits a ''plateau'' behavior with a quasi-constant value between 4 deg and 6 deg and increases again beyond. The ''plateau'' in the lift evolution between 4 deg and 6 deg is associated with an increase in the drag (See Fig. 4(*b*)) and often assumed to be due to viscous effects of a separation bubble at the leading edge, [11]. It was found that the plateau extent tends to be reduced as the velocity increases. The meanpressure coefficient for the noncavitating flow is shown in Fig. 5. The isolated point corresponds to the transducer on the pressure side. The figure includes several measurement series and shows a satisfactory reproducibility of the measurements ($\Delta C_p<2.5\%$ of the measurement range). It must be pointed out that the

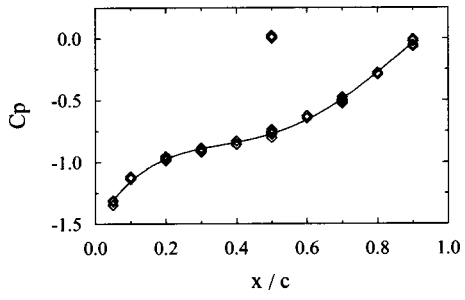

Fig. 5 Pressure coefficient for the noncavitating flow, α=6.5 deg

Table 2 Measured lift and drag coefficient for various cavity lengths, α=6 deg, Re=0.8×10^6

l/c	C_L	C_D
0.00	0.791	0.032
0.07	0.776	0.032
0.15	0.802	0.035
0.30	0.864	0.041
0.35	0.865	0.041
0.40	0.875	0.043
0.75	0.877	0.050

pressure coefficient peak of -1.4 at $x/c=0.05$ is not the minimum pressure coefficient, which occurs closer to the leading edge, [16].

When partial cavitation developed, two cases were observed. For cavity lengths smaller than half the foil chord, the closure cavity location experienced small variations and the cavity was unsteady but was stated to be ''stable.'' Conversely, when the cavity length was larger than about half the foil chord, a cavity growth/destabilization cycle was observed: the cavity pulsated and its length varied periodically from the vicinity of the leading edge, up to a maximum value of $x/c\sim0.7-0.8$. In that case, the cavity was stated to be ''unstable.'' If the cavitation number decreased more, the cavity extended periodically from the trailing edge ($l/c=1$) up to the leading edge inducing a large and low frequency vibration of the hydrofoil that was transmitted to the surrounding structures. If the cavitation number was decreased more then the partial cavity transited to super cavitation.

The hydrodynamic coefficient measurements in cavitating flow are given on Table 2 and Fig. 4(*c*). As shown both the lift and the drag coefficients increase leading to a loss in the hydrofoil efficiency, C_L/C_D. For stable cavities ($l/c<0.5$), Figs. 6(*a–c*) shows that the pressure coefficient is constant in the cavity and very close to the opposite of the cavitation number. At the cavity closure, the pressure coefficient experiences an adverse pressure gradient, and recovers the noncavitating value downstream. The vertical bars on Fig. 6 show that the recompression is accompanied by an increase in the intensity of pressure fluctuations. The relative intensity of pressure fluctuations is clearly depicted on Fig. 7 for various cavity lengths. As shown, a pressure peak is located at the cavity closure. The peak level increases as the cavitation number decreases (and cavity increases) within 10 to 19% of the dynamic pressure. Within the cavity ($x/c<l/c$), the intensity of the pressure fluctuations is fairly constant and lower than the noncavitating flow. A net increase in the pressure fluctuations is recorded in the cavity wake. For $l/c\sim0.4$, a spectral analysis revealed that the increase of the pressure fluctuations intensity at the cavity closure is associated with a frequency of 19 Hz (see Fig. 8 for $x/c=0.4$). As shown, this frequency still exists at $x/c=0.5$ but it spreads at $x/c=0.6$ in the cavity wake and is no longer detected at $x/c=0.7$. On the other hand, a secondary frequency (40 Hz) about double as the dominant frequency is detected in the cavity wake (see Fig. 8 for $x/c=0.6$). The main frequency in the closure region was also observed for others cavity lengths. The peak frequency decreased as the cavity length increased. It was 23 Hz for $l/c\sim0.3$ and 14 Hz for $l/c\sim0.5$. When l/c was closed to 0.5, a lower frequency about 5 Hz was also detected together with the higher frequency of about 40 Hz.

At this stage a slight decrease in the cavitation number leads to an unstable cavity characterized by a cavity growth/destabilization cycle (see photographs on Fig. 9). The frequency of the cycle was smaller than the previous ones and increased linearly with the velocity leading to a Strouhal number $fc/U\sim0.11$ (see Table 3). A secondary frequency, twice as high as the fundamental one, was always detected in the power pressure spectra. The periodic change of cavity length yields to the pressure coefficient on Fig. 6(*d*) showing that, from the leading edge up to $x/c\sim0.5$, the mean

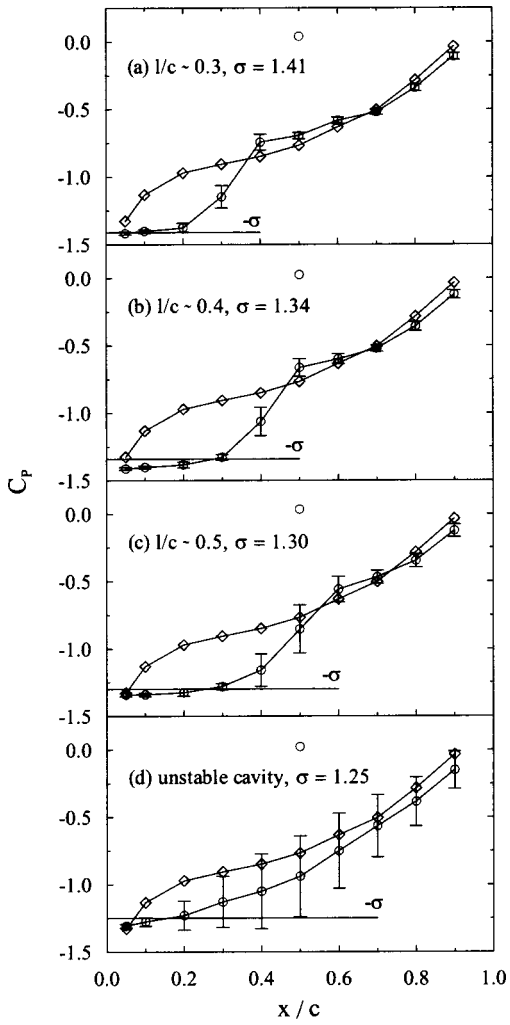

Fig. 6 Pressure coefficient for various cavity lengths, (*a*) (*b*) (*c*) stable cavity, (*d*) unstable cavity ($l/c>0.5$). Vertical bars are $\pm P_{rms}/q$.

pressure coefficient is approximately an average value between the cavitation number (vapor) and the noncavitating pressure coefficient (liquid).

An increase in pressure fluctuation intensity all along the suction side with a maximum at $x/c\sim0.5$ can be observed on Fig. 7 (for $\sigma=1.25$). Figure 10 depicts the instantaneous pressure signals during two cycles of cavity growth/destabilization on the suction side together with the pressure on the pressure (last signal, C11). As shown, on the suction side the transducers (between x/c

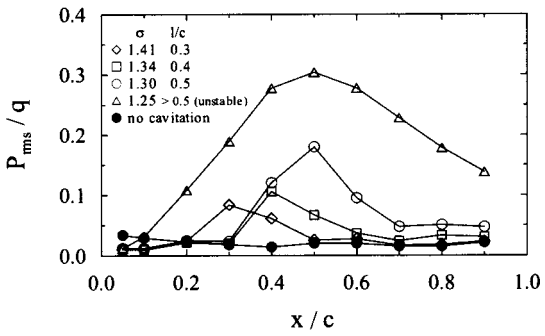

Fig. 7 Pressure fluctuation intensity for various cavity lengths

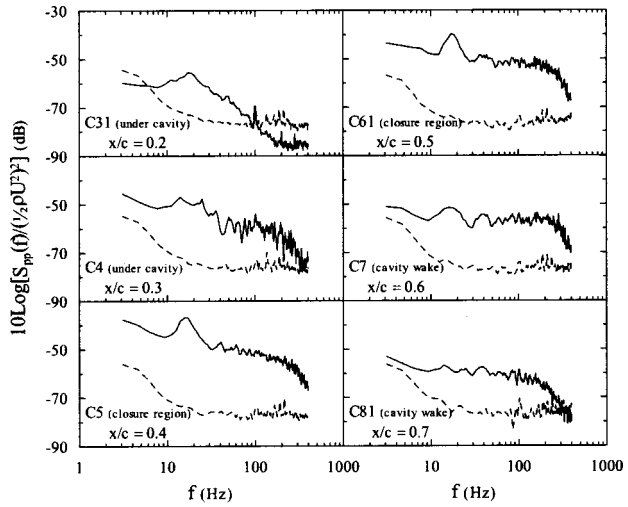

Fig. 8 Power spectral density, dashed line is the noncavitating flow, $\sigma=1.34$, $l/c\sim0.4$

$=0.1$ to $x/c=0.7-0.8$) pass alternately from the vapor pressure to the noncavitating pressure. This corresponds to the low frequency of 3.625 Hz of Table 3. For $t\in[0.13\,\text{s},0.17\,\text{s}]$ (resp. $t\in[0.41\,\text{s},0.46\,\text{s}]$) the pressure increases over the whole suction side (see dashed vertical lines on Fig. 10 for C31 to C81): the cavity is destabilized and disappears. During $t\in[0.17\,\text{s},0.41\,\text{s}]$ (resp. $t\in[0.46\,\text{s},0.64\,\text{s}]$) the cavity length increases. As the cavity

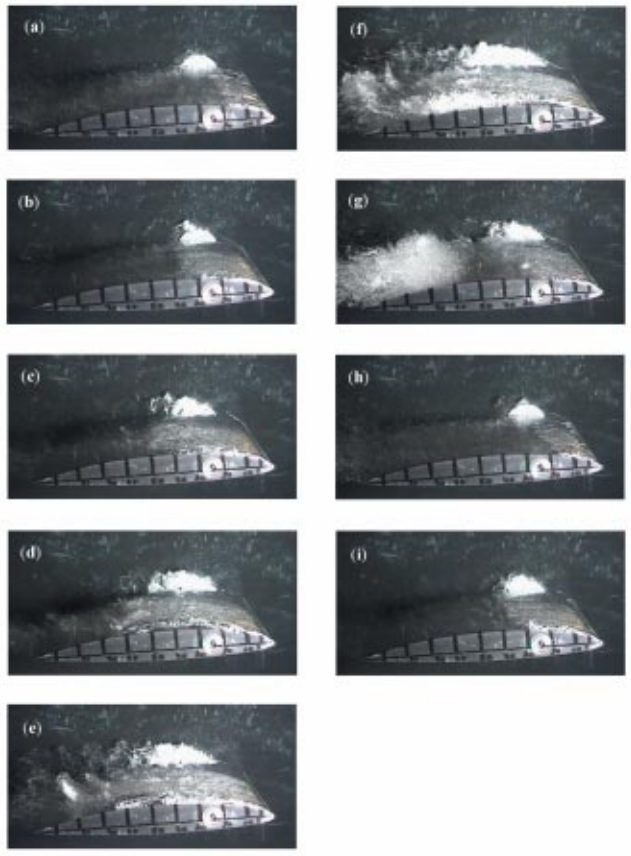

Fig. 9 Photographs of partial cavitation during cavity growth/destabilization cycle. Time between two consecutive images is 1/25[e] s.

Table 3 Frequency of oscillation of the cavity as a function of the velocity

U (m/s)	f (Hz)	fc/U
5,33	3,625	0,102
6,66	5,250	0,118
8,00	6,250	0,117
10,00	8,125	0,121

grows, the transducers experience, one after another, an increase in pressure fluctuations before falling to the vapor pressure (see arrows on Fig. 10 for C4, C5, C61, and C7): This corresponds to the cavity closure passing over the transducers. It is observed that when the cavity length is half the foil chord, the decrease in pressure is more gradual and more fluctuating (see Fig. 10, C61). At that time, pressure fluctuations are convected in the cavity wake (see, for instance, labels (*a*) and (*b*) on Fig. 10). This corresponds to the shedding of vapor clouds, which are known to be detectable by a pressure transducer as a decrease in pressure near the vapor pressure, followed by an increase in pressure fluctuations, [19]. So, it appears that when the cavity is half the foil chord, the cavity growth is slowed and is counterbalanced by vapor cloud shedding. The cloud shedding sequences (*a*) and (*b*) are depicted on Fig. 11 showing the spatial-temporal pressure distribution. The frequency of cloud shedding was estimated at roughly 40 Hz and their convection velocity was 3.2 m/s, about half the velocity of the non cavitating flow at $x/c\sim0.8$. As the cavity length increased more ($l/c>0.5$), the intensity of the pressure fluctuations associated to cloud shedding increased. When the cavity length was maximum ($l/c\sim0.7-0.8$), a major pressure perturbation was observed at approximately the middle of the cavity and destabilized the cavity (see label (*c*) on Fig. 10 and Figs. 9(*f–g*)). The destabilization process is clearly depicted on Fig. 12, which shows the spatial-temporal pressure distribution on the suction side corresponding to label (*c*). As shown the major pressure perturbation occurs for $x/c\sim0.4$ (see $t=0.411$ s) and cuts the cavity into two parts: a partial cavity and a large cloud cavitation (see also Fig. 9(*g*)). The cloud cavitation moves downstream (see arrows on Fig. 12). During this time the cavity tends to continue its growth. When the cloud cavitation reaches the trailing edge, the cavity length decreases suddenly and the pressure increases passing over the noncavitating value (see for $t=0.450$ s on Fig. 12) before a new growth/destabilization cycle begins again. The filled symbols on Fig. 12 show that little three-dimensional effects exist during cavity destabilization. We have to point out that, as far as this experiment is concerned, the pressure transducers did not detect the front of the re-entrant jet, as a pressure wave which travels upstream, prior to cloud shedding and destabilization. However, the re-entrant jet development was observed by top view visualizations. It is also interesting to observe that the pressure measured on the pressure side (see Fig. 10, C11) varies significantly during the destabilization phase.

Discussion

For $l/c<0.5$, relatively small oscillations of the cavity length were observed and the cavity was stated to be stable. The dominant frequency corresponding to the cavity closure oscillation gives a constant Strouhal number $fl/U=0.2$ in agreement with the Strouhal number found by Callenaere et al. [8] using wall-pressure measurements, but differs from the value close to 0.3 found by others using impedance probes, [6], or based on high-speed visualizations, [5]. The reason for such a difference is not clearly understood but George et al. [20], using electrical impedance probes, found Strouhal numbers ranging between 0.23–0.45 meaning that a given range of Strouhal number is probable. On the other hand, the secondary frequency (~40 Hz) detected in the cavity wake for $l/c=0.4$ corresponds to a Strouhal number $fl/U=0.45$. It is 0.29 using the cavity length and $U\sqrt{1+\sigma}$ as a veloc-

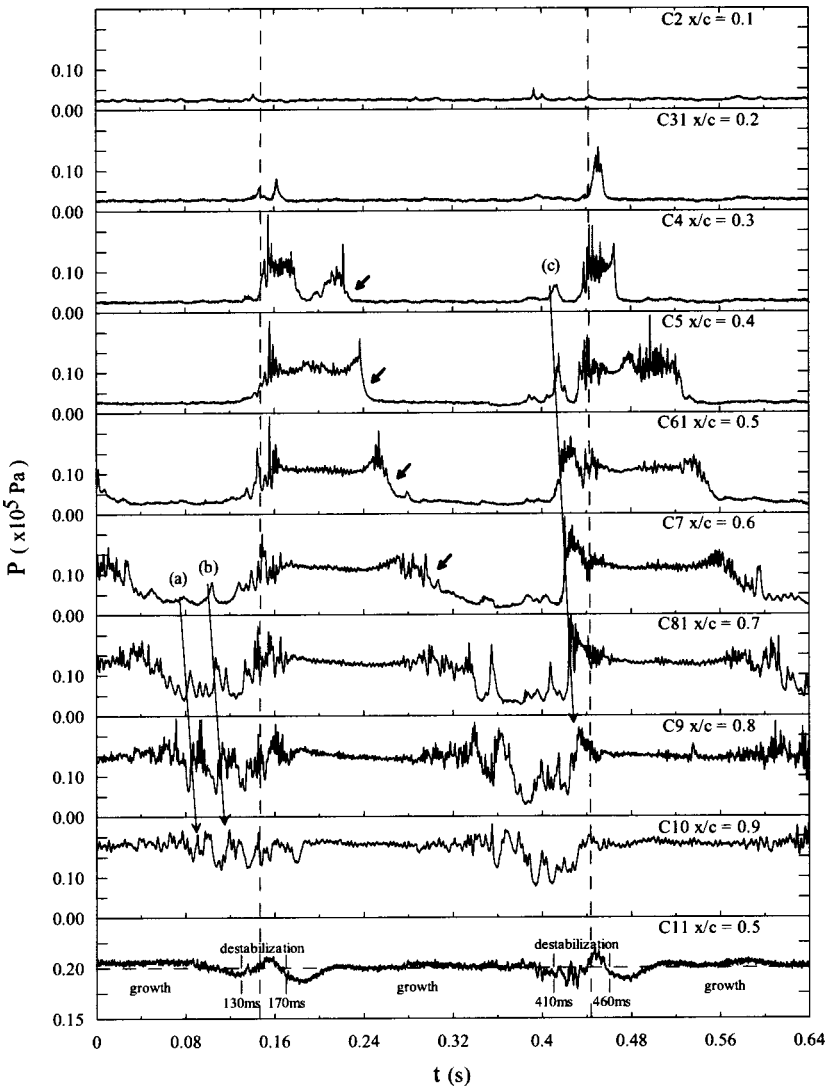

Fig. 10 Instantaneous pressure signals during cavity growth/destabilization cycle, σ=1.25, C11 is the instantaneous pressure signals on the pressure side

ity scale. The value of 0.2–0.3 is often attributed to the presence of a re-entrant jet. Here, the pressure measurements did not detect a clear sign of a reverse flow such as a pressure wave traveling from the cavity closure towards the leading edge. This is consistent with the model of an open cavity—without re-entrant jet—suggested by the "frothy" aspect of the cavity, [9]. However, to be clearly detected the re-entrant jet must have an extent larger than the spacing between two consecutive transducers. As the cavity closure oscillates with small amplitude the capability of the wall-pressure transducer arrangement to detect a re-entrant jet with small amplitude can be questioned.

For $l/c>0.5$, the cavity varied periodically from a small ($l/c \sim 0.1$) to a long cavity ($l/c \sim 0.7-0.8$) producing large cloud cavitation and was stated to be unstable. In certain cases, the cavity could disappear totally on the foil surface ($l/c \sim 0$). The frequency of the phenomenon was lower than the previous ones. It increased linearly with the velocity and corresponded to a constant value of the Strouhal number, $fc/U=0.11$. A secondary frequency, twice as high as the fundamental one, was also observed. The low Strouhal number $fc/U=0.11$ is close to low theoretical values for transition between partial cavitation and supercavitation found by Watanabe et al. [15], without modeling re-entrant jets or cloud shedding in their simulations. Contrary to Watanabe who found that the oscillation of the cavity length ranged between 0.2 and 1.5 chord length, in the present experiments the maximum length of the partial cavity never exceeded 0.75–0.8 of the chord length and it was observed that the cavity growth stopped and was supplanted by cloud shedding. Arndt et al. [14] showed that, depending on $\sigma/(2\alpha)$, two competitive mechanisms can be responsible for cloud cavitation. For large values a re-entrant jet was found to dominate whereas for smaller values of $\sigma/(2\alpha)$ bubbly flow shock waves dominated. The transition was found to occur for $\sigma/(2\alpha)=4$. The data which we observed during the transition between stable and unstable cavity are plotted on Fig. 13 using $2(\alpha-\alpha_o)$ instead of 2α (this is equivalent to Arndt et al. [14] using a symmetrical hydrofoil, $\alpha_o=0$). It is very interesting to observe that the transition is consistent with the transition given by $\sigma/2(\alpha-\alpha_o)=4$. Moreover, the relative frequency $fc/U=0.11$ of the unstable cavity ($l/c>0.5$) agrees with 0.15 found by Kjeldsen et al. [21] thus attributing the instability to shock wave physics. Song and Qin [22] observed numerically that a cloud cavity generated by a long sheet cavity might emit rarefaction waves on the pressure side before collapsing. In the present case, the dynamics of cavity growth/destabilization cycle are the following: (1) for small cavity length ($l/c \sim 0.1-0.2$) the cavity increases without shedding vapor cloud structures; (2) as the cavity continues to increase, it begins to shed vapor clouds; (3) when $l/c \sim 0.5$, the cavity growth is slowed, unsteadiness of the closure

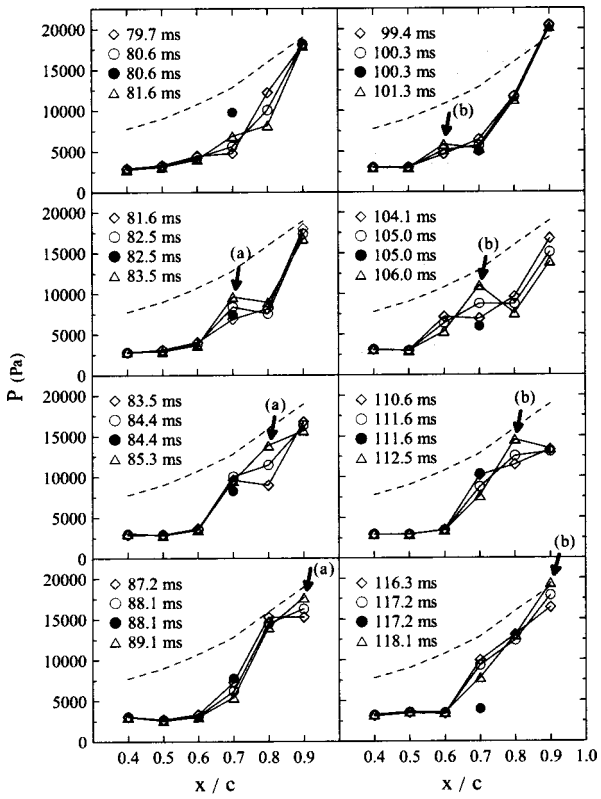

Fig. 11 Spatial-time history of wall pressure in the cavity wake during cavity growth and vapor cloud shedding, σ=1.25. Figures on the left (resp. right) depict the sequence (*a*) (resp. (*b*)) on Fig. 10, filled symbol is transverse transducer C82.

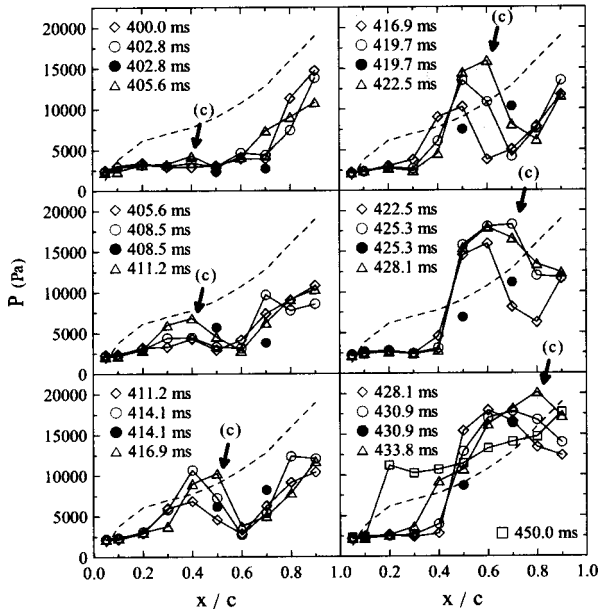

Fig. 12 Spatial-time history of wall pressure during cavity destabilization and cloud cavitation (label (*c*) on Fig. 10), σ=1.25, dashed line is the noncavitating flow, filled symbols are transverse transducers C62 and C82

increases and the cavity produces larger vapor clouds; (4) when $l/c \sim 0.7-0.8$, a pressure peak occurs towards the middle of the cavity surface and is strong enough to cut the cavity into two parts—a residual partial cavity still attached to the leading edge ($l/c \sim 0.3-0.4$) and a large cloud cavitation which is convected downstream; (5) during the convection motion of the cloud, the residual cavity tends to continue its growth; (6) when the cloud reaches the trailing edge, it collapses, and the residual cavity length suddenly decreases (in some cases the hydrofoil could be free of cavitation). At this point, a new cavity appears at the leading edge and a new cycle of cavity growth/destabilization is initiated. Point (3) is consistent with the development of a re-entrant jet, which interacts with the cavity interface, as it was observed by Callenaere et al. [23], in the case of a thin cavity. The numerical simulations of Arndt et al. [14] reveal a high pressure zone where the re-entrant jet breaks the cavity. Hence the high pressure peak described point (4) is a probable signature of the re-entrant jet in the present experiments. The last signal (C11) on Fig. 10, shows a decrease of the pressure on the pressure side when cavity length is maximum ($l/c \sim 0.7-0.8$) just before cavity destabilization. The decrease of the pressure on the pressure side, as observed here, is consistent with the rarefaction wave found by Song and Qin [22]. Moreover, they observed the radiation of strong pressure waves from the nose of the foil, and suspected this to be due to the shifting of the stagnation point when the flow is highly unsteady. In our opinion, this shifting can be equivalent to a variation of the angle of attack. Let us considered that the pressure wave on the pressure side on Fig. 10 is comparable to that which would be induced by a change of the angle of attack. In the present experiment, it was possible to convert the pressure signal of the pressure side to the corresponding angle of attack (Fig. 14). This was done using a linear relationship that we measured between the pressure on the pressure side and the angle of attack. As shown in Fig. 14, just before cavity destabilization, the angle of attack decreases significantly to a value of about 4 deg. It was observed that for the operating cavitation number σ=1.25, 4 deg was close to the angle of cavitation inception and then small enough to destabilize the cavity, [16]. This indicates that the pressure wave can be strong enough to induce cavity destabilization. Furthermore, such shock waves, caused by a low pressure cloud arriving at the trailing edge and the collapse, can explain points (5) and (6) of the cycle. In our opinion, in this particular case of cloud cavitation, a re-entrant jet and a shock wave phenomenon are both responsible for the cavity destabilization. Moreover, the Strouhal number is lower than 0.2–0.3, because the re-entrant jet is slowed by its interaction with the cavity interface, and because the collapse of the cloud influences and slows the development of the residual cavity.

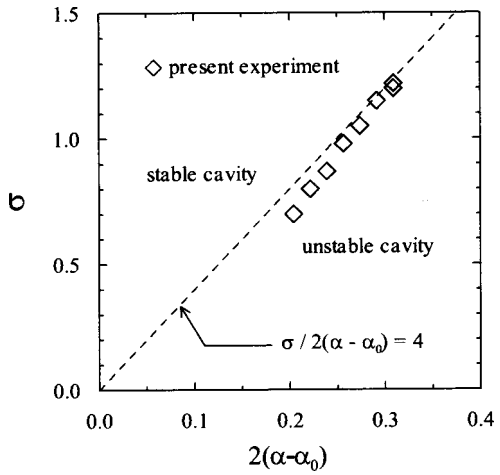

Fig. 13 Limit for which stable cavity transits to unstable cavity in the plane $(\sigma, 2(\alpha-\alpha_o))$. The dashed straight line is Arndt et al.'s criteria given by $\sigma/2(\alpha-\alpha_o)=4$ (with $\alpha_o=0$). Angles are in radians.

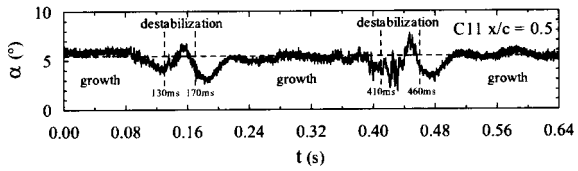

Fig. 14 Variation of the angle of attack equivalent to the variation of the pressure on the pressure side during the growth/destabilization cycle, σ=1.25

Further studies, which are necessary to address these points, have already begun. First, the re-entrant jet has been clearly observed by numerical videos. Secondly, similar measurements have been performed up to an angle of incidence of 8 deg, in order to investigate the transition between the two mechanisms of cloud cavitation, which are mentioned by Arndt et al. [14].

Conclusion

An investigation of partial leading edge cavitation unsteadiness was carried out based on wall-pressure measurements. For cavities that did not exceed half the foil chord, the cavity was stable. In that case the pressure was very close to the liquid vapor pressure inside the cavity and it recovered the noncavitating flow value outside. At the closure of the cavity, the pressure fluctuation intensity increased significantly. Conversely, when the cavity length was larger than half the chord length, the cavity was unstable and exhibited a growth/destabilization cycle at a lower frequency. As the cavity grew to about half the length of foil chord, the cavity growth slowed and was counterbalanced by the shedding of larger cloud cavitation. When the cavity length was maximum ($l/c \sim 0.7-0.8$), a major pressure perturbation occurred cutting the cavity into two parts: a partial cavity still attached to the leading edge and a large cloud cavitation, which was convected downstream. During the convection of the cloud cavitation, the cavity tended to grow again until a disappearance of the cavity occurred suddenly. This is believed to be due to a shock wave phenomenon when the large cloud cavitation collapsed. A pressure wave on the pressure side is observed when the cavity length is maximum and just before cavity destabilization and breakdown. It is widely believed that the cavity instability originates from a process involving the cavity growth, the shedding and the collapse of cavitation clouds during cavity growth which originate from the interaction between the re-entrant jet and the cavity surface, and a shock wave phenomenon due to the collapse of a large cloud cavitation at the end of the cycle. Further work is necessary to study this point and particularly to study in more detail the flow on the pressure side during the cavity growth/destabilization cycle.

Acknowledgments

The authors wish to express their deep appreciation for the continuous support of the Ecole Navale, Ministry of Defense (France) and of the technical staff of the IRENav.

Nomenclature

c = foil chord length=0.150 m
$C1, C2, \ldots$ = label of pressure transducers
C_L, C_D = lift and drag coefficient=L/qS, D/qS
C_p = pressure coefficient
l = cavity length
$L.E., T.E.$ = leading edge, trailing edge
P_o = test section pressure
P_{rms} = root mean square of pressure fluctuations
P_v = vapor pressure
q = dynamic pressure=$0.5\rho U^2$
Re = Reynolds number=Uc/v
S = foil area=0.150*0.192 m^2
$S_{pp}(f)$ = pressure power spectral density
U = freestream velocity
α = angle of incidence
α_o = zero lift angle
σ = cavitation number=$(P_o - P_v)/q$
τ = relative foil thickness=12%

References

[1] Le, Q., Franc, J. P., and Michel, J. M., 1993, "Partial Cavities: Pressure Pulse Distribution Around Cavity," ASME J. Fluids Eng., **115**, pp. 249–254.
[2] Franc, J. P., 2001, "Partial Cavity Instabilities and Re-Entrant Jet," CAV2001 Fourth International Symposium on Cavitation, June 20–23, 2001, Pasadena, CA.
[3] Furness, R. A., and Hutton, S. P., 1975, "Experimental and Theoretical Studies of Two-Dimensional Fixed-Type Cavities," ASME J. Fluids Eng., **Dec., pp.** 515–522.
[4] Stutz, B., and Reboud, L., 1997, "Experiments on Unsteady Cavitation," Exp. Fluids, **22**, pp. 191–198.
[5] Kawanami, Y., Kato, H., Yamaguchi, H., Tagaya, Y., and Tanimura, M., 1997, "Mechanism and Control of Cloud Cavitation," ASME J. Fluids Eng., **119**, pp. 788–794.
[6] Pham, T. M., Larrarte, F., and Fruman, D. H., 1999, "Investigation of Unstable Sheet Cavitation an Cloud Cavitation Mechanisms," ASME J. Fluids Eng., **121**, pp. 289–296.
[7] Dang, J., and Kuiper, G., 1999, "Re-entrant Jet Modeling of Partial Cavity Flow on Two-Dimensional Hydrofoils," ASME J. Fluids Eng., **121**, pp. 773–780.
[8] Callenaere, M., Franc, J. P., Michel, J. M., and Riondet, M., 2001, "The Cavitation Instability Induced by the Development of a Re-Entrant Jet," J. Fluid Mech., **444**, pp. 223–256.
[9] Laberteaux, K. R., and Ceccio, S. L., 2001, "Partial Cavity Flows. Part 1. Cavities Forming on Models Without Spanwise Variation," J. Fluid Mech., **431**, pp. 1–41.
[10] Kawanami, Y., Kato, H., Yamaguchi, H., and Maeda, M., 1995, "An Experimental Investigation of Flow Field Around Sheet Cavity on Foil Section," private communication. Société hydrotechnique de France, Section cavitation, Réunion du 26 Oct., LEGI, Grenoble, France.
[11] Gaster, M., 1969, "The Structure and Behavior of Laminar Separation Bubbles," NPL Aero. Report No. 1181 (revised).
[12] Kubota, A., Kato, H., and Yamaguchi, H., 1992, "A New Modeling of Cavitating Flows: A Numerical Study of Unsteady Cavitation on a Hydrofoil Section," J. Fluid Mech., **240**, pp. 59–96.
[13] Chahine, G. L., and Hsiao, C. T., 2000, "Modeling 3D Unsteady Sheet Cavities Using a Coupled UnRANS-BEN Code," Proceedings of 23rd Symposium on Naval Hydrodynamics, Sept. 17–22, Val de Reuil, France.
[14] Arndt, R. E. A., Song, C. C. S., Kjeldsen, M., He, J., and Keller, A., 2000, "Instability of Partial Cavitation: A Numerical/Experimental Approach," Proceedings of 23rd Symposium on Naval Hydrodynamics, Sept. 17–22, Val de Reuil, France.
[15] Watanabe, S., Tsujimoto, Y., and Furukawa, A., 2001, "Theoretical Analysis of Transitional and Partial Cavity Instabilities," ASME J. Fluids Eng., **123**, pp. 692–697.
[16] Astolfi, J. A., Leroux, J. B., Dorange, P., Billard, J. Y., Deniset, F., and De la Fuente, S., 2000, "An Experimental Investigation of Cavitation Inception and Development on a Two Dimensional Hydrofoil," J. Ship Res., **44(4)**, pp. 259–269.
[17] Leroux, J. B., Astolfi, J. A., and Billard, J. Y., 2001, "An Experimental Investigation of Partial Cavitation on a Two Dimensional Hydrofoil," CAV2001 Fourth International Symposium on Cavitation, June 20–23, Pasadena, CA.
[18] Valentine, D. T., 1974, "The Effect of Nose Radius on the Cavitation Inception Characteristics of Two-Dimensional Hydrofoils," Report 3813 of the *Naval Ship Research and Development Center*, Bethesda, MD.
[19] Caron, J. F., Farhat, M., and Avellan, F., 2000, "On the Leading Edge Cavity Development of an Oscillating Hydrofoil," Proceedings of ASME FEDSM'00, ASME 2000 Fluid Engineering Division Summer Meeting, June 11–15, Boston, MA.
[20] Georges, D. L., Iyer, C. O., and Ceccio, S. L., 2000, "Measurement of the Bubbly Flow Beneath Partial Attached Cavities Using Electrical Impedance Probes," ASME J. Fluids Eng., **122**, pp. 151–155.
[21] Kjeldsen, M., Arndt, R. E. A., and Effertz, M., 2000, "Spectral Characteristics of Sheet/Cloud Cavitation," ASME J. Fluids Eng., **122**, pp. 481–487.
[22] Song, C. C. S., and Qin, Q., 2001, "Numerical Simulation of Unsteady Cavitating Flow," CAV 2001, Fourth International Symposium on Cavitation, June 20–23, Pasadena, CA.
[23] Callenaere, M., Franc, J. P., and Michel, J. M., 1998, "Influence of Cavity Thickness and Pressure Gradient on the Unsteady Behavior of Partial Cavities," CAV1998 Third International Symposium on Cavitation, Apr., Grenoble, France.

Analysis of Two-Phase Homogeneous Bubbly Flows Including Friction and Mass Addition

Marat Mor[1]
Graduate Student

Alon Gany
Professor,
Lena and Ben Fohrman Chair in Aeronautical Engineering Mem. ASME
e-mail: gany@tx.technion.ac.il

Department of Aerospace Engineering,
Technion-Israel Institute of Technology,
Haifa 32000, Israel

The present work is a theoretical investigation of two-phase bubbly flows. The main objective is to get a better insight of the basic phenomena associated with such flows through nozzles via physical modeling and mathematical formulation. Introducing Mach number into the flow equations, we find novel, closed-form analytical solutions and expressions for homogeneous bubbly flows including the influence of wall friction and mass addition. The expressions obtained demonstrate an analogy to those of classical, single-phase gas flows. The study deals with homogeneous flows, however, its approach and results can also be applied to investigate flows with unequal phase velocities, to study instability phenomena, as well as to design and analyze water jet propulsion systems. [DOI: 10.1115/1.1637628]

Introduction

Although two-phase bubbly flows have been extensively studied for many years, they continue to be of great interest. There are two major reasons for this. First, there is a continually growing use of engineering devices that contain bubbly flows, for example, nuclear power-stations, liquid rocket engines, and submarine and boat propulsion systems. The second reason is that despite continuing studies, there are still fundamental aspects of two-phase flows, whose physical description and modeling may give insufficient insight, while existing theoretical solutions often do not agree with experimental results.

The processes, which take place in two-phase bubbly flows, are quite complicated. Their mathematical formulation requires a system of non-linear differential equations. Because of the complex nature of the two-phase gas/liquid flow phenomena and their practical applications, bubbly-flow analyses have yet to reach the mature stage of single-flow theories. Instead, numerical solutions using heavy computational means replaced theoretical analyses at a relatively early stage, substituting the physical evaluation of the effects of major parameters by multi-variable numerical presentations. Computational fluid dynamics (CFD) codes are commercially available. Most of them were originally developed for single-phase flows. However, modified versions can treat two-phase flows as well. Some special computer programs have been specifically developed for bubbly flows, for example the VORT code [1], which solves 2-D slow bubbly flows.

While the use of CFD codes enables the solution of complex flow-fields, one loses much insight into the dominant parameters and processes that could be gained via analytical treatment. To reduce the degree of complexity of the physical description and mathematical formulation and at the same time to increase understanding of the fundamental phenomena, much effort has been devoted to one-dimensional or quasi-one-dimensional flows. Nevertheless, even so, most of these cases have been treated numerically.

The complexity of the problem starts with the sound speed equations, which are found in closed analytical form only for certain special cases [2–4] and depend on the relative motion between the phases as well as on bubble parameters. There is also the complexity in solving the system of non-linear differential equations.

The simplest case of a two-phase bubbly flow is a frictionless, homogeneous, isothermal flow. The formulation and basic analysis of such flow were performed by Tangren et al. [5] and later by Muir et al. [6], Wijngaarden [7] and Brennen [8]. The problem becomes more complicated when a relative motion between the two phases is introduced, by means of a bubble momentum equation. Many models exist for this equation [1,7–15]. They differ in the expression for virtual mass (which has been the subject of many papers [1,16–18]), and in interphase drag [1,13–15,19–22]. Even without the inclusion of mass transfer, change in bubbles number, change in temperature, and pressure differences between the phases, the solution accounting for different phase velocities describes well the true picture in nozzle flows (without drastic phenomena such as shock waves), hence it has been widely used for analyzing propulsion systems [20–22].

If the phases are introduced with different initial conditions, the problem becomes very complex. A formulation of such a problem, including heat and mass transfer, was presented by Albagli and Gany [22] and treated numerically. In their work they show that for different initial conditions, both the pressures and the temperatures of the phases become almost equal at a very short distance.

It is worth noting that for over a hundred years the fluid dynamic sciences have come up with closed-form expressions for single-phase gas flows, establishing the basic characteristics and fundamental relations for the ideal case. Most useful both for the understanding and practical applications of flow systems are, for instance, the relations associated with perfect-gas isentropic flows through nozzles, flow properties ratios across shock waves, flows through ducts with heat addition or friction, etc. As stated above, such expressions are scarce for two-phase bubbly flows. This is the background that has stimulated the present research. The objectives of this research were to investigate the basic phenomena associated with two-phase, bubbly, steady, quasi-1-D flows through nozzles, obtaining novel analytical solutions for homogeneous flows with and without wall friction as well as mass addition.

[1]Presently, Post-Doctoral Fellow, Dept. of Aeronautics and Astronautics, University of Washington, Seattle, WA.

Contributed by the Fluids Engineering Division for publication in the JOURNAL OF FLUIDS ENGINEERING. Manuscript received by the Fluids Engineering Division October 25, 2002; revised manuscript received September 3, 2003. Associate Editor: S. Balachandar.

Formulation of the Problem of Air Bubbles in Water

For the basic investigation of two-phase bubbly flows through nozzles, we will reduce the three-dimensional problem to a quasi-1-D one, and develop a model for a homogeneous flow.

For further simplification of the mathematical formulation and solution, a number of physical assumptions are used and justified by their minor effects on the overall development of a high speed flow through a nozzle:

a. Equal temperatures of the two phases and no change of temperature along the nozzle (isothermal flow). As stated before [22], it was found that even in the case of different initial temperatures of the two phases, they quickly attain thermal equilibrium. The substantially small air mass flow rate (by three orders of magnitude) than that of the water and the large thermal capacity of the water, should result in an almost constant temperature over the entire flow field.

b. No mass transfer between the phases. The air and water phases are practically insoluble, and no evaporation or condensation of the water is taken into account, as is implied by the constant temperature assumption.

c. The pressures of both phases are the same. This assumption holds well in the entire flow-field (see Albagli and Gany [22]), except in the vicinity of a shock wave or during the process of mixing between two phases with different initial conditions.

d. Equal velocities of the two phases. This assumption finally leads to the case of homogeneous flow, which provides fairly good results in the case of large interphase drag, typical to flows with small radius bubbles. The other limit case concerns nonhomogeneous flow with no interphase drag, predicting fairly well the flow behavior in instances of low velocities or large bubbles. This case will be dealt with in a separate study.

Based on the above physical description, the following set of equations results:
Water Mass Conservation:

$$(1-\alpha)\rho_w UA=\dot{m}_w \tag{1}$$

where α is the volume fraction of air, ρ-density, U-velocity, $\dot{m}$-mass flow rate (which may be a function of x for mass addition), and A is the cross-section area of the nozzle. The indices a and w denote air and water, respectively, but can generally represent gas and liquid, respectively.
Air mass conservation:

$$\alpha\rho_a UA=\dot{m}_a=\mu\dot{m}_w \tag{2}$$

where μ is the air/water mass flow rate ratio (a function of x if mass is added).
Single bubble mass conservation:
If assuming spherical bubbles with no coalescence or fragmentation, then:

$$m_b=\frac{4}{3}\pi r^3\rho_a=\text{const}\Rightarrow\rho_a r^3=\text{const} \tag{3}$$

where r is the radius of the bubble. The no-coalescence assumption is realistic for small air volume fractions, while spherical bubbles and no-fragmentation are typical for small velocity differences between the phases as well as for small bubbles (both conditions indicate small Weber numbers [19]). Nevertheless, the homogenous two-phase flow model is independent of these assumptions, accounting only for the overall fraction of each phase.
Total momentum conservation:

$$(1+\mu)\dot{m}_w\frac{d}{dx}U=-A\frac{d}{dx}P-4\frac{\tau}{d} \tag{4}$$

where P is the pressure and $4\tau/d$ is the drag term due to wall friction. d is the cross-section diameter, τ is the stress which is applied by the walls of the nozzle on the flow. It can be defined as follows:

$$\tau=\frac{1}{2}\rho_w U_w^2 f\cdot\Phi^2 \tag{5}$$

Here f is the wall friction coefficient and Φ^2 is the correction factor due to air bubbles.
Equation of state of air:

$$P=\rho_a RT \tag{6}$$

where T is temperature and R is the specific gas constant.
Water is incompressible, hence:

$$\rho_w=\text{const} \tag{7}$$

An analytical treatment of these equations, including some closed-form solutions, is revealed in the ensuing sections.

Analysis and Results

Frictionless Flow. In order to make the problem analytically tractable we seek to introduce Mach number into the governing equations. As we shall demonstrate, this also reveals a strong similarity between one-phase airflow solution and the new solution for bubbly flow. The speed of sound, which can be easily derived from Eqs. (1), (2), and (6), is given by:

$$a=\sqrt{\frac{dP}{d\bar{\rho}}}=\frac{\beta}{\phi\alpha} \tag{8}$$

where

$$\bar{\rho}=\alpha\rho_a+(1-\alpha)\rho_w \tag{9}$$

is the mean density of the mixture. The parameters β and ϕ are defined as follows:

$$\beta=\sqrt{\mu RT} \tag{10}$$

$$\phi=\sqrt{1+\mu} \tag{11}$$

Then Mach number is:

$$M=\frac{U}{a}=\frac{\phi\alpha U}{\beta} \tag{12}$$

From Eqs. (1), (2), and (6) together with Eq. (10) we find:

$$\frac{P}{\beta^2\rho_w}=\frac{1}{\alpha}-1 \tag{13}$$

Then, substituting Eq. (13) into Eq. (12) gives:

$$U=\frac{\beta}{\phi}M\left(1+\frac{P}{\beta^2\rho_w}\right) \tag{14}$$

Substituting Eqs. (13,14) into Eq. (1) and Eq. (4) (without friction) one can obtain the following useful expressions:

$$\left(\frac{1}{M^2}-1\right)d\ln(M)=-\left(1+\frac{P}{\beta^2\rho_w}\right)d\ln(A) \tag{15}$$

$$\left(\frac{1}{M^2}+\frac{P}{\beta^2\rho_w}\right)d\ln(P)=-\left(1+\frac{P}{\beta^2\rho_w}\right)d\ln(M) \tag{16}$$

According to Eq. (15) the critical area for which $M=1$ appears to be the nozzle throat area (as expected [1,2]), as it is for isentropic one-phase gas flow. Using Eqs. (1–7) and Eqs. (15) and (16) we can deduce the behavior of various two-phase bubbly flow characteristics as a function of nozzle geometry and Mach number, as is presented in Fig. 1. The schematic picture is identical to the one for isentropic airflow.

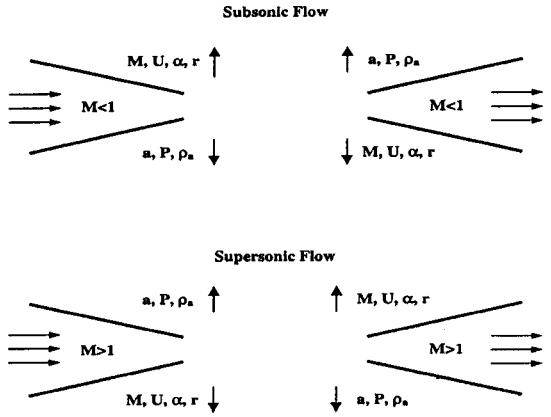

Fig. 1 Two-phase homogeneous bubbly flow behavior in nozzle

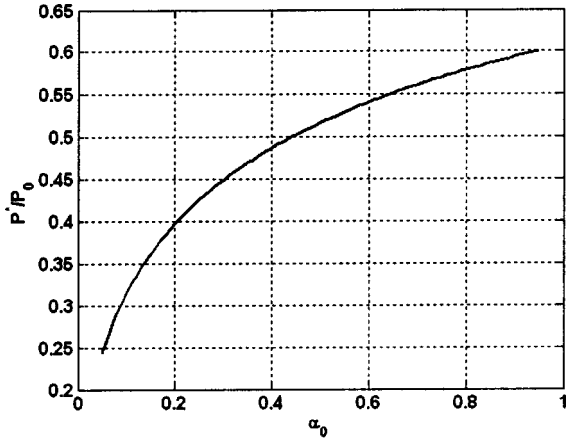

Fig. 3 Choking curve vs. air void fraction at stagnation point

Equation (16) contains pressure, Mach number and other flow characteristics such as water density and the parameter β, which contains the flow temperature, mass flow rate ratio, and the specific air constant. However, substituting Eq. (13) into Eq. (16), we obtain a differential equation for the void fraction and Mach number only:

$$\left(\frac{1}{M^2}+\frac{1}{\alpha}-1\right)d\ln\left(\frac{1}{\alpha}-1\right)=-\frac{1}{\alpha}d\ln(M) \tag{17}$$

From Eq. (17) we can conclude that the solution for the air volume fraction depends on Mach number and the air volume fraction at one specified Mach number. We choose the stagnation point, namely $M=0$, as this specified Mach number. Therefore, based on Eq. (13), the ratio P_1/P_2 of two points in the flow also depends on Mach numbers at those points and on the air volume fraction at the stagnation point only. Similarly, we can deduce the same conclusion for the rest of the flow parameters.

As is well known, for one-phase, isentropic perfect gas flow, the static to stagnation pressure ratio P/P_0 depends only on Mach number and the type of gas:

$$\frac{P}{P_0}=\left(1+\frac{\gamma-1}{2}M^2\right)^{\gamma/(1-\gamma)} \tag{18}$$

Therefore, for a given γ there is only one curve of pressure ratio versus Mach number. However, in the case of two-phase homogeneous flow a set of curves is relevant, as shown in Fig. 2. Each curve describes the ratio between the static and stagnation pressures (as a function of Mach number) for a specific void fraction at the stagnation point α_0.

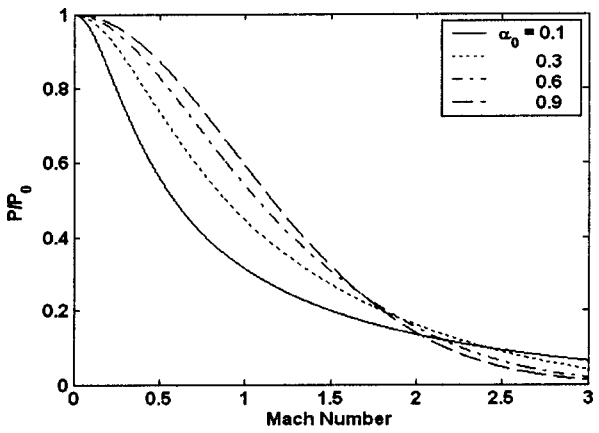

Fig. 2 Behavior of pressure ratio as a function of Mach number and air void fraction at stagnation point

Solving Eqs. (13) and (17) we can derive a choking curve (instead of a choking point as in one-phase flow), P^*/P_0, which is presented in Fig. 3. Here P^* denotes the pressure at the cross-section where $M=1$, coinciding with the throat of a choked nozzle [23]. Typically Mach number at this cross-section is unity. The ratio P^*/P_0 is a function of the air volume fraction at the stagnation point only, and can be approximated by the following expression (obtained by curvefitting a numerical solution):

$$\frac{P^*}{P_0}=f(\alpha_0)=\frac{1}{\sqrt{e}}\alpha_0^{0.213}e^{-[0.175\ln(\alpha_0)]^2} \tag{19}$$

The pressure ratio predicted by the homogeneous flow model (Eq. (19)) underestimates the experimental results obtained by Muir and Eichhorn [6]. However, according to Wang and Chen [14], the inclusion of slip motion between the phases implies only small changes compared to the homogeneous flow model prediction. This suggests that at least for the nozzle used by Muir and Eichhorn (having a 60 deg inlet angle), other influences, such as the high dimensional effects, may be responsible for the discrepancies between model predictions and experiments.

The mathematical analysis of the homogeneous bubbly flow model presented above can be applied for any range of the void fraction α (except of the vicinity of zero and one, where the speed of sound can no longer be represented by Eq. (8)). However, it is worth noting that, in a two-phase flow consisting of monodisperse bubbles, there is a geometric limit for the gas volume fraction. This limit corresponds to a face centered cubic lattice configuration, or ''orange pile'' packing, $\alpha=\pi/\sqrt{18}\cong 0.74$ (see Devlin [24]). If one deals with the above mentioned flow regime of water flow with air bubbles, the air void fraction limitation of $\alpha=0.74$ also leads to a restriction on Mach number. Figure 4 shows the behavior of Mach number in a bubbly flow constrained by $\alpha=0.74$. The limit value of Mach number in such a case, $M(\alpha=0.74)$, becomes a function of α_0 only. It can be seen that the condition of $\alpha\leqslant 0.74$ imposes severe restrictions on the achievable maximum Mach number, particularly in the high α_0 range.

So far, the results of the investigation show an analogy between the behavior of an isentropic airflow and that of an air-water bubbly homogenous flow. Another analogous point lies in the character of the mathematical solution. We recall the well-known solution for isentropic airflow presented in Eq. (18). Let us assume an analogous solution for a bubbly flow:

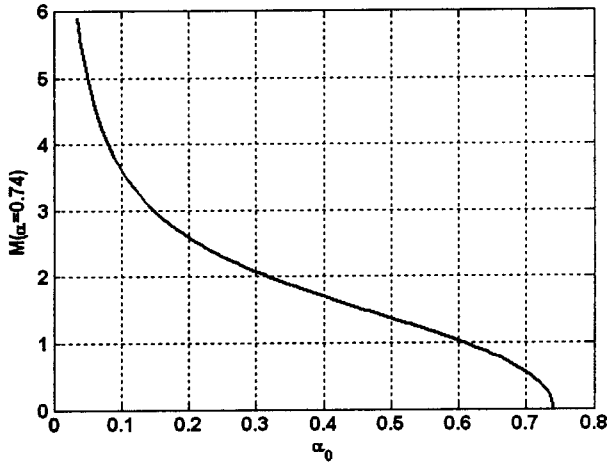

Fig. 4 Limit value of Mach number $M(\alpha=0.74)$ for gas volume fraction restriction of $\alpha=0.74$ as a function of α_0

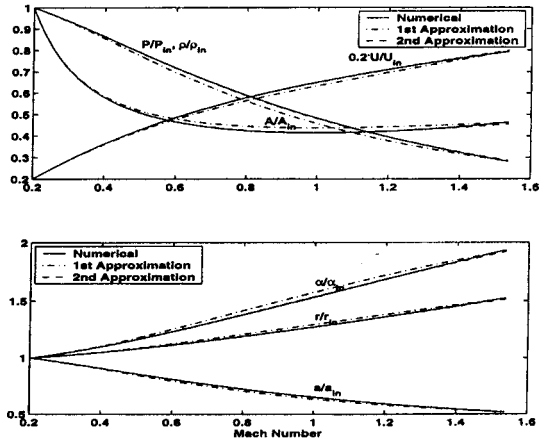

Fig. 5 Numerical solution and analytical approximations for flow through a converging-diverging (Laval) nozzle. Initial conditions: $A_{in}=13.2$ cm^2, $P_{in}=3.5$ atm (0.35 MPa), $T=293$ K, $\mu=0.002$, $M_{in}=0.2$. (Relative variation of bubble radius, r/r_{in}, is presented as indication for the case of monodisperse spherical bubbles.)

$$P=P_0\prod_{n=1}^{\infty}(1+a_nM^2)^{b_n} \tag{20}$$

Each member of this product series is analogical to the expression, which is a solution for one-phase isentropic airflow. Comparison of both the first approximation:

$$P^{(1)}=P_0(1+a_1M^2)^{b_1} \tag{21}$$

and, more so, the second one

$$P^{(2)}=P_0(1+a_1M^2)^{b_1}(1+a_2M^2)^{b_2} \tag{22}$$

with a numerical solution of the governing equations reveals an excellent agreement. The parameters a_n and b_n (that depend on the volume fraction at the stagnation point), are evaluated by solving a system of equations, derived as follows: Substituting the relevant approximation in Eqs. (21–22) into Eq. (16), we use a Taylor series expansion in the Mach number of the relevant approximation to obtain the necessary equations, by taking the first term of the series for the first approximation and the first three terms for the second approximation. To complete the system we use the choking condition criteria to receive the additional equation. For $M=1$, Eq. (16) takes the following form:

$$\frac{d}{dM}\ln(P)\bigg|_{M=1}=-1 \tag{23}$$

Then substituting Eqs. (21–22) into Eq. (23), for the first approximation we finally write:

$$\begin{cases} a_1=\dfrac{1}{\alpha_0}-1 \\ b_1=-\dfrac{1}{2}\left(\dfrac{1}{1-\alpha_0}\right) \end{cases} \tag{24}$$

Knowing the void fraction at stagnation point the coefficients a_1, b_1 can be easily evaluated from the system above. However, the stagnation conditions are usually unknown, so an additional equation for α_0 (see Eq. (13)) has to be solved together with Eqs. (24):

$$\alpha_0=\frac{1}{1+\dfrac{P_0}{\beta^2\rho_w}}=\frac{1}{1+\dfrac{1-\alpha_{in}}{\alpha_{in}(1+a_1M_{in}^2)^{b_1}}} \tag{25}$$

The index *in* represents initial conditions.

For the second approximation:

$$\begin{cases} a_1=\dfrac{1}{8}\dfrac{8-7\alpha_0+\varphi}{\alpha_0} \\ a_2=\dfrac{1}{8}\dfrac{8-7\alpha_0-\varphi}{\alpha_0} \\ b_1=-\dfrac{1}{2\varphi(1-\alpha_0)}\dfrac{(4-5\alpha_0+\varphi)^2}{16-9\alpha_0+3\varphi} \\ b_2=-16\dfrac{1-\alpha_0}{\varphi}\dfrac{2+3\alpha_0}{(8-7\alpha_0-\varphi)\cdot(4-5\alpha_0+\varphi)} \end{cases} \tag{26}$$

where:

$$\varphi=\sqrt{32-32\alpha_0+\alpha_0^2} \tag{27}$$

and for unknown stagnation void fraction:

$$\alpha_0=\frac{1}{1+\dfrac{1-\alpha_{in}}{\alpha_{in}(1+a_1M_{in}^2)^{b_1}(1+a_2M_{in}^2)^{b_2}}} \tag{28}$$

Figure 5 shows some flow characteristic distributions in a converging-diverging (Laval) nozzle versus Mach number for the two first approximations and a comparison with a numerical solution. We see that the first approximation gives a relatively good match for results in the subsonic region up to the low supersonic flow range. Calculations show that at higher Mach numbers the error of the first approximation tends to increase. However, the second approximation reduces the maximum error (in pressure[2]) from 6% (for the first approximation) to less than 1%(!).

Wall Friction Influence. In this section, we introduce wall friction effects that are generally not included in numerical solutions of bubbly flows through nozzles. Substituting Mach number definition (Eq. (12)) into Eq. (2) for air mass conservation and using Eq. (6) together with the definitions for β and ϕ one can obtain the following relation:

[2]It can be easily proved that the relative errors in pressure, density and cross-sectional area are equal. The relative errors in the other flow characteristics are smaller.

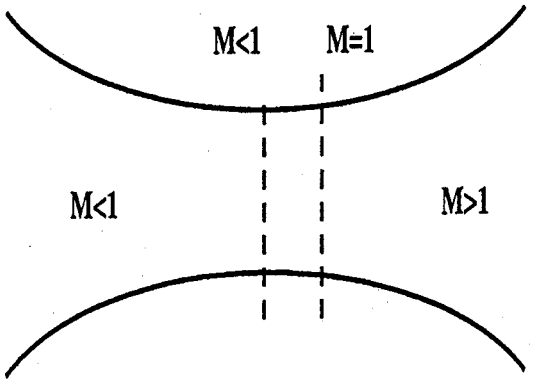

Fig. 6 Nozzle flow with friction

$$P \cdot M \cdot A = \phi \beta \dot{m}_w \tag{29}$$

Also defining parameter ν as:

$$\nu \cdot A = \frac{\phi \dot{m}_w}{\beta \rho_w} = \text{const} \tag{30}$$

we can obtain from Eqs. (13), (29), and (30):

$$\alpha = \frac{1}{1 + \frac{\nu}{M}} \tag{31}$$

and from Eqs. (12) and (31):

$$U = \frac{\beta}{\phi}(M + \nu) \Rightarrow \frac{d}{dx}U = \frac{\beta}{\phi}\left(\frac{d}{dx}M - \nu \frac{1}{A^2}\frac{d}{dx}A\right) \tag{32}$$

Differentiating Eq. (29) and substituting it together with Eqs. (30) and (32) into the total momentum conservation equation (Eq. (4)) we finally obtain the following equation:

$$\frac{1 - M^2}{M^2}\frac{d}{dx}M + \frac{1}{A}\left(\nu + \frac{1}{M}\right)\frac{d}{dx}A = \Omega^2(\nu + M)^2 \tag{33}$$

where:

$$\Omega^2 = \frac{2}{\phi^2}\frac{f}{d \cdot \nu} \tag{34}$$

When substituting the expression for the wall shear stress τ (Eq. (4)) to yield Eq. (33), it was simplified by assuming a value of unity to the correction factor due to air bubbles (Φ^2, Eq. (5)). Hence, the correction factor does not show up in Eq. (34). The use of $\Phi^2 = 1$ is a reasonable representation particularly for relatively small values of α. It is further justified by the view of Wallis [25] (e.g. p. 28 and Ch. 9), that the wall friction in a turbulent bubbly flow is basically due to the liquid phase.

According to Eq. (33) Mach number reaches unity in the diverging part of the nozzle (see Fig. 6) and not at the nozzle throat (this phenomenon is identical to the one which occurs in a single-phase gas flow with friction). Direct integration of Eq. (33) in its global form is not possible. However, analytical solutions can be found for some special cases, such as flow through a constant area duct or flow through a nozzle with a constant Mach number. These special cases will be discussed below.

Flow Through a Constant Area Duct With Friction: Analogy to Fanno-line. In this case $A = \text{const}$, therefore Eq. (33) simplifies to a simple differential equation:

$$\frac{d}{dx}M = \Omega^2 \frac{M^2}{1 - M^2}(M + \nu)^2 \tag{35}$$

From this equation we can conclude:

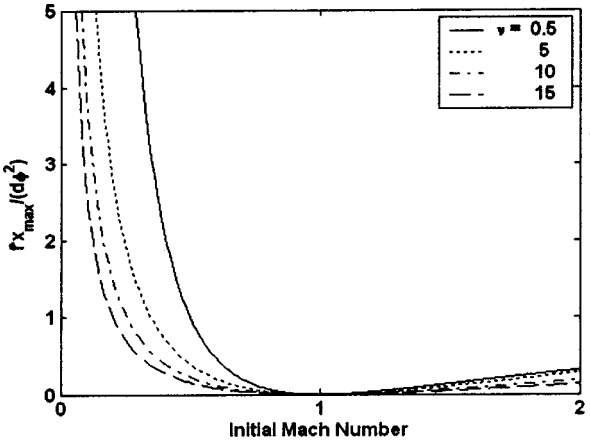

Fig. 7 $fx_{max}/d\phi^2$ vs. initial Mach number–analogy of Fanno-line in a two-phase bubbly flow

$$\begin{cases} \dfrac{d}{dx}M > 0, & M < 1 \\ \dfrac{d}{dx}M < 0, & M > 1 \end{cases} \tag{36}$$

The result of Eq. (36) is identical to that of a one-phase airflow. If the flow is subsonic, the wall friction of the duct causes the flow to accelerate until it chokes at $M = 1$. For a supersonic flow, however, the friction slows it down until $M = 1$.

Integrating Eq. (35) between 0 and x one gets an expression for the location x as a function of Mach number:

$$\frac{2}{\nu}\ln\left(1 + \frac{\nu}{M}\right) + \frac{\nu^2 - \frac{\nu}{M} - 2}{M + \nu} = \theta_1 x + \theta_2 \tag{37}$$

where:

$$\theta_1 = \nu^2 \Omega^2 = \frac{2}{\phi^2}\nu \frac{f}{d}$$

$$\theta_2 = \frac{2}{\nu}\ln\left(1 + \frac{\nu}{M_{in}}\right) + \frac{\nu^2 - \frac{\nu}{M_{in}} - 2}{M_{in} + \nu} \tag{38}$$

This solution includes the parameter ν which, according to Eq. (30), depends on flow characteristics such as the temperature, water density, etc. However, using Eq. (31) for a constant area duct we can write:

$$\nu = \text{const} = \left(\frac{1}{\alpha_{in}} - 1\right) M_{in} \tag{39}$$

Therefore the solution for $f \cdot x/(d \cdot \phi^2)$, Eqs. (37) and (38), depends only on the air void fraction and Mach number at the initial point, and Mach number at point x.

It is interesting that the behavior of the bubbly flow under external friction influence is similar to the so-called Fanno-line of a single-phase gas flow. Figure 7 shows a variation of Fanno-line (similar to figures presented in Shapiro [23]), where x_{max} is the maximal possible length of a duct where $M = 1$.

From the figure we can conclude that the higher the parameter ν (namely, lower α_{in} for the same initial Mach number), the shorter the distance to attain the choked cross-section. This can be explained using Eq. (30). Indeed, if ν increases, then (under the same conditions) a greater water mass-flux has to be introduced and this, of course, reduces the value of x_{max}.

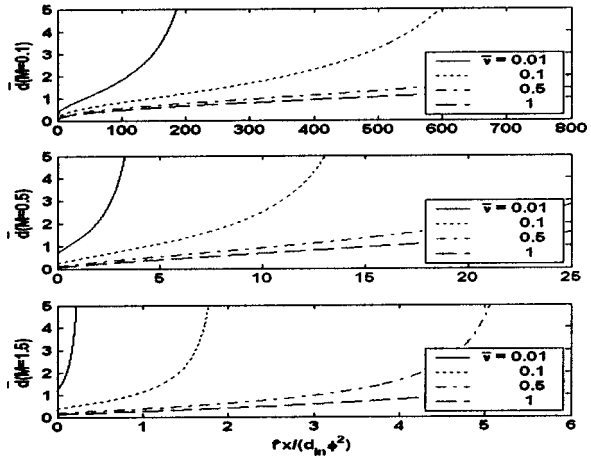

Fig. 8 Behavior of cross-section dimensionless diameter as a function of location for various $\bar{\nu}$ and Mach number values

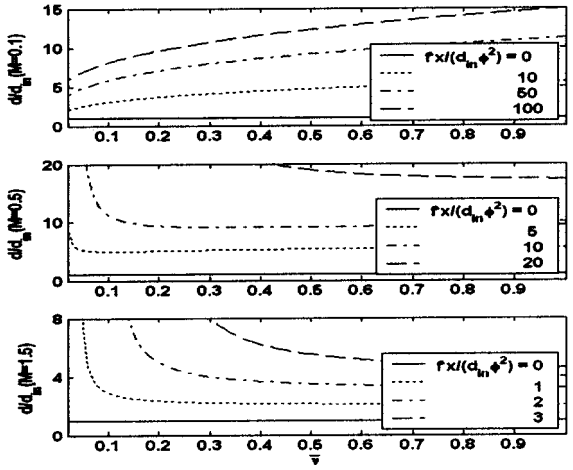

Fig. 9 Behavior of cross-section diameter as a function of $\bar{\nu}$ for various locations and Mach number values

Interesting relationships can be obtained between the flow characteristics at some point x and their values at $M=1$. According to Eq. (32):

$$\frac{U}{U^*}=\frac{M+\nu}{1+\nu} \tag{40}$$

In the case of $\nu\rightarrow 0$, Eq. (40) reduces to:

$$\frac{U}{U^*}=M \tag{41}$$

In addition, from Eq. (29) we obtain:

$$\frac{P}{P^*}=\frac{\rho}{\rho^*}=\frac{1}{M} \tag{42}$$

The expressions in Eqs. (41) and (42) are identical to those of one-phase ideal gas flow through a constant area duct with friction, when substituting $\gamma=1$ (unreal case). This case is identical to isothermal gas flow conditions, which are actually similar to the conditions in our case of a bubbly flow.

Flow Through a Nozzle With Friction and Constant Mach Number. In this case $M=\text{const}$, therefore Eq. (33) can now be rewritten as follows:

$$\frac{1}{A}\left(\nu+\frac{1}{M}\right)\frac{d}{dx}A=\Omega^2(\nu+M)^2 \tag{43}$$

Substituting Eqs. (30) and (34) into Eq. (43), and supposing a nozzle of a circular cross-section, we obtain a differential equation for the cross-section diameter:

$$\frac{\bar{\nu}}{\bar{d}^2}\frac{\dfrac{\bar{\nu}}{\bar{d}^2}+\dfrac{1}{M}}{\left(\dfrac{\bar{\nu}}{\bar{d}^2}+M\right)^2}\cdot\frac{d}{dx}d=\frac{f}{\phi^2} \tag{44}$$

where:

$$\bar{\nu}=\frac{4}{\pi}\nu\cdot A=\frac{4}{\pi}\frac{\phi\dot{m}_w}{\beta\rho_w}=\text{const} \tag{45}$$

Integrating Eq. (44) as before, the following solution is obtained:

$$\frac{M^2+1}{M^2}\arctan(\bar{d})+\frac{M^2-1}{M^2}\frac{\bar{d}}{1+\bar{d}^2}=\theta_1 x+\theta_2 \tag{46}$$

where

$$\theta_1=2\frac{f}{\phi^2}\sqrt{\frac{M}{\bar{\nu}}}$$

$$\theta_2=\frac{M^2+1}{M^2}\arctan(\bar{d}_{in})+\frac{M^2-1}{M^2}\frac{\bar{d}_{in}}{1+\bar{d}_{in}^2} \tag{47}$$

and $\bar{d}$ is a dimensionless diameter which is defined as:

$$\bar{d}=\sqrt{\frac{M}{\bar{\nu}}}\cdot d \tag{48}$$

As is known from the literature [26], in a single-phase airflow with friction the change in cross-section diameter is linear with x:

$$d=\frac{\gamma M^2}{4}f\cdot x+d_{in} \tag{49}$$

However, in a bubbly flow the solution is characterized by strong non-linearity. This can also be seen in Figs. 8 and 9. Figure 8 presents the behavior of the dimensionless diameter $\bar{d}$ as a function of the parameter $f\cdot x/(d_{in}\cdot\phi^2)$ for various values of $\bar{\nu}$ and M. It is obvious that the higher the Mach number the faster the growth of the dimensionless diameter (this also applies to dimensional diameter) in order to keep the Mach number constant. In addition, for the same x, an increase in $\bar{\nu}$ causes a reduction of $\bar{d}$. However, such a strict conclusion cannot be applied to the dimensional diameter d (see Fig. 9).

In order to understand the behavior of d with $\bar{\nu}$, we return to the definition of $\bar{d}$[3]:

$$\bar{d}=\sqrt{\frac{M}{\bar{\nu}}}\cdot d=M^{1/2}\left(\frac{4}{\pi}\frac{\phi\dot{m}_w}{\beta\rho_w}\right)^{-1/2}\cdot d$$

$$=M^{1/2}\left(\frac{4}{\pi}\frac{\phi(1-\alpha)\rho_w\cdot\dfrac{\beta M}{\phi\alpha}\cdot\dfrac{\pi}{4}d^2}{\beta\rho_w}\right)^{-1/2}\cdot d=\sqrt{\frac{\alpha}{1-\alpha}} \tag{50}$$

Now, according to Eq. (45) an increase in $\bar{\nu}$ (which causes a reduction in $\bar{d}$) causes an increase in the water mass flow rate $\dot{m}_w$. This does not dictate an increase in the cross-section area.

Indeed, according to Eq. (50) a reduction in $\bar{d}$ causes a reduction in the air void fraction α which will increase the flow velocity

[3]Equation (50) is obtained using Eqs. (45) and (48) for $\bar{\nu}$ and $\bar{d}$, and Eqs. (1) and (12) for $\dot{m}_w$, U and A.

U (see Eqs. (31) and (32) for a constant Mach number). Therefore, the expression $\dot{m}_w/A=(1-\alpha)\rho_w U$ will increase too. So, the increase in mass flow rate may be a result of either an increase in velocity or a decrease in air void fraction and not necessarily an increase in cross-section area. For low Mach numbers the influence of changes in α and U on mass flow rate is not considerable, and so an increase in $\overline{\nu}$ strictly causes cross section area growth. However, for higher Mach numbers an increase in $\overline{\nu}$ comes strictly from α and U, in which case the cross section area can also decrease (see Fig. 9).

Flow With a Distributed Mass Addition of Air and Water. To complete the discussion about homogeneous, bubbly flows, the case of the influence of mass addition to a flow was originally investigated. Due to injected air bubbles and water, the mass flow rate of both phases increases and is a function of the location along the duct:

$$\dot{m}_a=\dot{m}_{a_{in}}(1+f(x)) \tag{51}$$

and

$$\dot{m}_w=\dot{m}_{w_{in}}(1+g(x)) \tag{52}$$

We assume $x_{in}=0$, so $f(0),g(0)=0$. Neglecting the momentum of the introduced air and water, the total momentum equation can now be written as follows

$$\frac{d}{dx}[(1+\mu)\dot{m}_w U]+A\frac{d}{dx}P=0 \tag{53}$$

where the mass flow rate ratio is determined using Eqs. (51,52):

$$\mu(x)=\mu_{in}\frac{1+f(x)}{1+g(x)} \tag{54}$$

Considering a case of flow through a constant area duct (which can be solved analytically), one can investigate the basic phenomena of the influence of mass addition. Substituting Eq. (54) into Eqs. (10) and (11) one obtains:

$$\beta(x)=\beta_{in}\sqrt{\frac{1+f(x)}{1+g(x)}} \tag{55}$$

$$\phi(x)=\phi_{in}\sqrt{1+\frac{\mu_{in}}{1+\mu_{in}}\cdot\frac{f(x)-g(x)}{1+g(x)}} \tag{56}$$

Let us define (similar to Eq. (30)):

$$\nu=\frac{\phi_{in}}{\beta_{in}}\frac{\dot{m}_{w_{in}}}{A\rho_w} \tag{57}$$

Then, integrating Eq. (53) and using Eqs. (12), (13), and (31) together with Eqs. (55–57), we finally can write a simple second order equation for Mach number:

$$M^2+\Gamma_2(x)\left(\nu(\Gamma_1^2(x)-1)-\frac{M_{in}^2+1}{M_{in}}\right)M+1=0 \tag{58}$$

where

$$\Gamma_1(x)=\frac{\phi}{\phi_{in}}\frac{\dot{m}_w}{\dot{m}_{w_{in}}}=\sqrt{\frac{1+g(x)}{1+\mu_{in}}[1+g(x)+\mu_{in}(1+f(x))]} \tag{59}$$

and

$$\Gamma_2(x)=\frac{\beta_{in}}{\beta}\frac{1}{\Gamma_1(x)}=\sqrt{\frac{1+g(x)}{1+f(x)}}\frac{1}{\Gamma_1(x)} \tag{60}$$

Differentiation of Eq. (58) provides:

$$\frac{d}{dx}M=\frac{M^2}{1-M^2}\frac{d}{dx}\left[\Gamma_2(x)\left(\nu(\Gamma_1^2(x)-1)-\frac{M_{in}^2+1}{M_{in}}\right)\right] \tag{61}$$

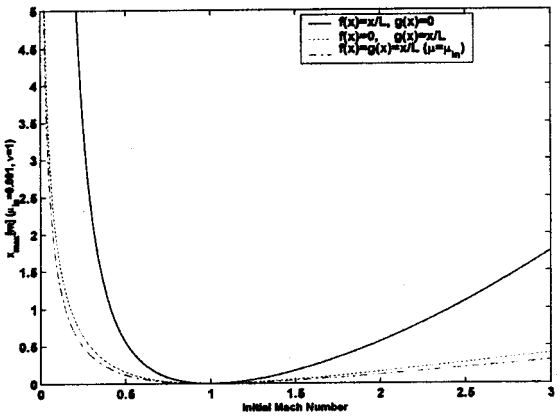

Fig. 10 Location of the choking point (x_{max}) vs. initial Mach number for different mass addition distributions

Analyzing the RHS expression of Eq. (61), we find (after much algebra):

$$\frac{d}{dx}\left[\Gamma_2(x)\left(\nu(\Gamma_1^2(x)-1)-\frac{M_{in}^2+1}{M_{in}}\right)\right]>0 \tag{62}$$

Therefore, similar to the case of flow with friction (see Eq. (36)), for a subsonic flow, the injection of air bubbles causes the flow to accelerate until it chokes, whereas for a supersonic flow Mach number decreases until $M=1$.

The solution of Eq. (58) for different mass addition distributions of air bubbles and water is presented in Figs. 10–11.

Figure 10 presents the location of the choking point along a constant area duct vs. initial Mach number for different mass addition distributions. For illustration, the parameter ν was taken to be equal to 1, and according to Eq. (39) it represents the initial volume fraction ratio between the water phase and the air bubbles phase. According to Fig. 10, the behavior of the flow due to injection of water and/or air is similar to the behavior when influenced by external drag (due to wall friction). More detailed aspects of behavior of the flow are presented in Fig. 11. The injection of bubbles (for a constant mass flow rate of water) increases the mass flow rate ratio $\mu(x)$. Yet the mass flow rate of the air phase is negligible compared to the water. However, the change in mass flow rate ratio directly causes a change in the value of air volume fraction. The injection of water, on the other

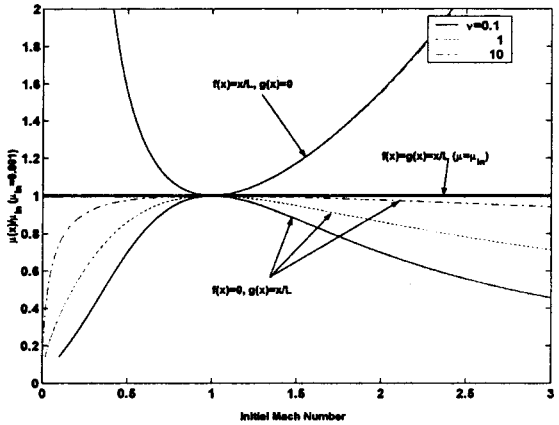

Fig. 11 Normalized mass flow rate ratio at the choking point vs. initial Mach number for different values of ν and mass addition distributions

hand, directly influences the total mass flow rate, and apparently such an influence causes a more substantial change in flow parameters (see also Fig. 10).

Finally, according to Fig. 11 the influence of the parameter ν on the flow in the case of injection of air bubbles only (no added water) is negligible. From Eq. (58) the influence of the parameter ν depends on the expression $\Gamma_1^2(x)-1$. Expanding this expression to a Taylor series, one obtains:

$$\Gamma_1^2(x)-1=g(x)+\frac{1}{2}[f(x)-g(x)]\mu_{in}+O(\mu_{in}^2) \qquad (63)$$

If water is injected, the parameter ν is multiplied by $g(x)$, so its influence is considerable. However, if only air is injected ν is multiplied by μ_{in}, therefore there are almost no differences between the curves (presented in Fig. 11) in such a case.

Conclusion

A new analytical approach for the investigation of two-phase homogeneous bubbly flows was developed and presented. Closed-form analytical solutions were obtained for typical flow regimes including the influences of wall friction and mass addition. The investigation of the homogeneous bubbly flow revealed close analogy to the classical expressions of single-phase airflows.

The analytical expressions give a better insight into the basic phenomena associated with bubbly flows. These expressions can be used, for example, to examine the instability of homogeneous bubbly flows as well as for the design and performance prediction of marine propulsion systems such as waterjets. In addition, the technique used here can be applied to the case of two-phase bubbly flows with unequal phase velocities. The results of such investigations are the subject of other presentations.

Acknowledgments

The authors thank Prof. J.B. Greenberg of the Faculty of Aerospace Engineering, Technion-Israel Institute for Technology for his constructive comments. The support of J. and J. Gringorten Aeronautical Research Fund and the Fund for Promotion of Research at the Technion is acknowledged as well.

Nomenclature

A = cross-section area
a = speed of sound
$a_1, a_2, \ldots a_n$ = coefficients of the product series, Eq. (20)
$b_1, b_2, \ldots b_n$ = coefficients of the product series, Eq. (20)
d = cross-section diameter
$\overline{d}$ = dimensionless diameter defined in Eq. (48)
f = wall friction coefficient
$f(x), g(x)$ = functions describing mass flow rate addition of air and water, respectively Eqs. (51) and (52)
M = mach number
m_b = mass of a single bubble
$\dot{m}$ = mass flow rate
P = pressure
R = specific gas constant
r = radius of the bubble
T = temperature
U = velocity
x = longitudinal coordinate
α = air volume fraction (void fraction)
β = parameter defined in Eq. (10)
$\Gamma_1(x), gG_2(x)$ = functions defined in Eqs. (59) and (60)
γ = specific heat ratio
μ = mass flow rate ratio
ν = parameter defined in Eq. (30)
$\overline{\nu}$ = parameter defined in Eq. (45)
Φ = correction factor Eq. (5)
ϕ = parameter defined in Eq. (11)
φ = parameter defined in Eq. (27)
θ_1, θ_2 = parameters defined in Eqs. (38) and (47)
ρ = density
$\overline{\rho}$ = mean density
τ = stress
Ω = parameter defined in Eq. (34)

Subscripts

a = air phase
in = initial conditions
max = Maximal value
t = nozzle throat
w = water phase
0 = stagnation conditions

Superscripts

(1) = first approximation
(2) = second approximation
* = conditions at Mach number of unity

References

[1] Cook, T. L., and Harlow, F. H., 1984, "VORT: A Computer Code for Bubbly Two-Phase Flow," Los Alamos National Lab., LA-10021-MS.
[2] Crespo, A., 1969, "Sound and Shock Waves in Liquids Containing Bubbles," Phys. Fluids, **12**(11), pp. 2274–2282.
[3] McWilliam, D., and Duggins, R. K., 1970, "Speed of Sound in Bubbly Liquids," Proc. Inst. Mech. Eng., **184/3C**, pp. 102–107.
[4] Gregor, W., and Rumpf, H., 1975, "Velocity of Sound in Two-Phase Media," Int. J. Multiphase Flow, **1**(6), pp. 753–769.
[5] Tangren, R. F., Dodge, C. H., and Seifert, H. S., 1949, "Compressibility Effects in Two-Phase Flow," J. Appl. Phys., **20**, pp. 637–645.
[6] Muir, J. H., and Eichhorn, R., 1963, "Compressible Flow of an Air-Water Mixture Through a Vertical, Two-Dimensional, Converging-Diverging Nozzle," *Proc. 1963 Heat Transfer and Fluid Mechanics Institute*, Stanford, pp. 183–204.
[7] Van Wijngaarden, L., 1972, "One-Dimensional Flow of Liquids Containing Small Gas Bubbles," Annu. Rev. Fluid Mech., **4**, pp. 369–394.
[8] Brennen, C. E., 1995, *Cavitation and Bubble Dynamics*, Oxford University Press, New York, pp. 172–177.
[9] Biesheuvel, A., and Van Wijngaarden, L., 1984, "Two-Phase Flow Equations for a Dilute Dispersion of Gas Bubbles in Liquid," J. Fluid Mech., **148**, pp. 301–318.
[10] Presperetti, A., and Van Wijngaarden, L., 1976, "On the Characteristics of the Equations of Motion for a Bubbly Flow and the Related Problem of Critical Flow," J. Eng. Math., **10**, pp. 153–162.
[11] Nishikawa, H., Matsumoto, Y., and Ohashi, H., 1991, "The Numerical Calculation of the Bubbly Two-Phase Flow Around an Airfoil," Comput. Fluids, **19**, p. 453.
[12] Yonechi, H., Suzuki, M., Ishii, R., and Morioka, S., 1992, "Bubbly Flows Through a Convergent-Divergent Nozzle," Mem. Fac. Eng. Kyoto Univ., **45**, p. 3.
[13] Ishii, R., Umeda, Y., Murata, S., and Shishido, N., 1993, "Bubbly Flows Through a Converging-Diverging Nozzle," Phys. Fluids A, **5**(7), pp. 1630–1643.
[14] Wang, Y., and Chen, E., 2002, "Effects of Phase Relative Motion on Critical Bubbly Flows Through a Converging-Diverging Nozzle," Phys. Fluids, **14**(9), pp. 3215–3223.
[15] Witte, J. H., 1969, "Predicted Performance of Large Water Ramjets." AIAA Paper 69-406, *AIAA 2nd Advanced Marine Vehicles and Propulsion Meeting*, Seattle, Washington.
[16] Van Wijngaarden, L., 1976, "Hydrodynamic Interaction Between Gas Bubbles in Liquid," J. Fluid Mech., **77**, pp. 27–44.
[17] Cook, T. L., and Harlow, F. H., 1984, "Virtual Mass in Multiphase Flow," Int. J. Multiphase Flow, **10**, pp. 691–696.
[18] Biesheuvel, A., and Spoelstra, S., 1989, "The Added Mass Coefficient of a Dispersion of Spherical Gas Bubbles in Liquid," Int. J. Multiphase Flow, **15**, pp. 911–924.
[19] Soo, S. L., 1990, *Multiphase Fluid Dynamics*, Science Press, Beijing.
[20] Amos, R. G., Maples, G., and Dyer, D. F., 1973, "Thrust of an Air-Augmented Waterjet," J. Hydronautics, **7**(2), pp. 64–71.
[21] Muench, R. K., and Ford, A. E., 1961, "A Water-Augmented Air Jet for the Propulsion of High-Speed Marine Vehicles," NASA N D-991, Langley Research Center.
[22] Albagli, D., and Gany, A., 2003, "High Speed Bubbly Nozzle Flow with Heat, Mass, and Momentum Interactions," Int. J. Heat Mass Transfer, **46**, pp. 1993–2003.
[23] Shapiro, A. H., 1953, *The Dynamics and Thermodynamics of Compressible Fluid Flow*, John Wiley & Sons, New York, pp. 159–173.
[24] Devlin, K. J., 1994, *Mathematics—the Science of Patterns*, Scientific American Library, New York, p. 157.
[25] Wallis, G. B., 1969, *One-Dimensional Two-Phase Flow*, McGraw-Hill, New York.
[26] John, J. E. A., 1969, *Gas Dynamics*, Allyn and Bacon, Inc., Boston, pp. 174–177.

A Phase-Averaged Analysis of Droplet Dispersion in the Wake of a Square Cylinder in a Uniform Stream

S. Fohanno
Laboratoire de Thermomécanique-UTAP (E.A. 2061), Faculté des Sciences
Université de Reims Champagne-Ardenne,
B.P. 1039, 51100 Reims, France

R. J. Martinuzzi
Department of Mechanical and Materials Engineering, Faculty of Engineering,
The University of Western Ontario, London, Ontario, Canada, N6A 5B9

Time-averaged and phase-averaged size and velocity distributions of water droplets in the turbulent wake of a square cross-section cylinder, measured with a phase-Doppler anemometer, are presented for a Reynolds number $\mathrm{Re}_D = 18{,}500$*, based on the free stream velocity,* U_∞*, and cylinder side dimension, D. It is shown that the coherent motion strongly influences the particle distribution and that the mean flow representation can be misleading in interpreting mixing. The results show that small particle concentration is largest in the very near wake. The mean particle distributions are homogeneous as early as 4D downstream of the cylinder, but the influence of vortex shedding on instantaneous distributions persists much longer. It is also observed that at the point of maximum mean streamline curvature, which also coincides with the region of maximum streamwise velocity fluctuations, particle separation is most effective.* [DOI: 10.1115/1.1637637]

Introduction

The transport of aerosols in the wake of bluff bodies is important for many industrial applications such as drying and combustion processes where mixing characteristics are critical. Growing environmental concern and stricter regulatory legislation has promoted renewed interest in controlling dispersion of contaminants in the wakes of free-standing structures. The wake flow of tall structures or flow control devices in incinerators or driers may be approximated by the flow around a two-dimensional bluff body immersed in a stream. These flows give rise to separated shear layers and regions of reverse flow, which affect scalar transport. Amplification of shear layer instabilities causes large velocity fluctuations in the wake, which tend to redistribute scalar quantities normal to the flow. Particles, for example, can thus be convected by the main stream or be entrained into the reverse flow towards the obstacle before being re-entrained into the shear layer and finally convected downstream. These competing mechanisms result in complex flow patterns and mixing characteristics, which are of interest both fundamentally and for simulation purposes.

The single-phase flow field around two-dimensional bluff bodies has been the subject of several studies. The structure of the flow around a square cross-section cylinder suspended in a uniform stream, for example, is independent of the Reynolds number for $10{,}000 < \mathrm{Re}_D < 100{,}000$, with Re_D based on the side dimension of the cylinder (D) and the freestream velocity of the flow (U_∞). The wake flow is characterized by high levels of velocity fluctuations, which Lyn et al. [1] discuss in terms of incoherent turbulence, concentrated along the two opposite shear layers, and *quasi*-regular passage of large-scale coherent structures, *i.e.* shed vortices. They show that the coherent fluctuations can account for up to 50% of the total velocity fluctuations.

Lyn et al. [1], Durao et al. [2] and Wu and Martinuzzi [3] found that the mean wake recirculation extended roughly 1D downstream of the trailing face. Along the centerline, the streamwise velocity component increases rapidly behind the obstacle up to 2D downstream of the trailing face where it reaches $0.5U_\infty$. The downstream recovery is much slower. Lyn et al. [1] and Wu and Martinuzzi [3] report approximately $0.65U_\infty$ at 6D from the trailing face. Durao et al. [2] report substantially higher values. However, in the latter study, the blockage ratio (13.6%) is much higher than in the other studies (5.5% [3] and 8% [1]).

Both streamwise (U_{RMS}) and cross-stream (V_{RMS}) velocity fluctuations are large in the near-wake. The maximum U_{RMS} appoaches $0.6U_\infty$ and occurs in the shear layer at approximately 0.5D downstream of the trailing edges (roughly 0.6D above and below the centerline). This location coincides with the maximum mean streamline curvature. Along the centerline, U_{RMS} is roughly constant at $0.5U_\infty$ in the recirculation region, and drops further downstream. The cross-stream fluctuations are also largest in the recirculation region but decrease more slowly in the wake. The maximum, $0.9U_\infty$, occurs along the centerline at the mean location of the saddle point marking the end of the recirculation region. Lyn et al. [1] found that shedding contributes about 50% to V_{RMS} and less than 30% to U_{RMS}.

Bearman and Obasaju [4] report a base pressure coefficient, based on the ambient reference pressure and U_∞, of -1.6 and pressure fluctuation root-mean-square (rms) coefficients of 0.3. On the side faces, the mean and rms coefficients are -1.6 and 0.63, respectively. Haidn et al. [5] obtain similar results, but also show that there exists an underlying long-wave disturbance which modifies the shedding frequency. This phenomenon is shown to be related to the frequency jitter reported, for example, by Lyn et al. [1] in wake velocity measurements. A general consensus in the literature indicates a drag coefficient of approximately 2.1.

In the case of particle-laden flows, shed vortices have a significant effect on the particle distribution and may lead to preferential concentration depending on the particle size and local turbulence levels [6]. Numerical and experimental studies on particle dispersion in free shear flows have focused on mixing layers [7–13], wake [14–21] and jet flows [22–24]. Crowe et al. [7] point to the importance of large-scale structures, compared to incoherent, small-scale turbulence, on particle dispersion and discuss the importance of inertial effects in term of the particle Stokes number, St, defined as the ratio of the aerodynamic response time, τ_A, to a characteristic time scale for the fluid motion (τ_F) [7], generally related to the scale of coherent motion. The particle response time, τ_A, can be approximated from Stokes drag formula. Peak particle dispersion is observed for St of order unity. Particles in this size range are centrifuged out of vortical structures and tend to disperse more [7,25]. Sufficiently small particles ($St < 0.01$) follow

Contributed by the Fluids Engineering Division for publication in the JOURNAL OF FLUIDS ENGINEERING. Manuscript received by the Fluids Engineering Division Jan 17, 2003; revised manuscript received Sept. 16, 2003. Associate Editor: J. Katz.

closely the fluid motion, while very large particles ($St \gg 1$) carry sufficient inertia to cross the vortical structures with little trajectory modification. Several mixing layer experiments report similar behaviors [8,9].

Several numerical studies show that the influence of the particle Stokes number on mixing in bluff body wakes can be very important. Laitone [14] shows that particles with $St=1$ which originate upstream of a circular cylinder essentially do not penetrate the mean recirculation region. Chein and Chung [15] also note this effect on particles with $1 \leqslant St \leqslant 25$, released upstream of a flat plate normal to the flow and suggest that inertia keeps the particles from entering the cores of large-scale vortices. For $St=0.5$, particles are shown to be captured in the wake recirculation. A different behavior is observed when particles are released directly into the obstacle wake. Chein and Chung [15] found that, in the range $10 \leqslant St \leqslant 50$, particle dispersion was inversely proportional to both the Stokes number and the particle initial velocity. Tang et al. [16] and Crowe et al. [19] show that, in the extreme case where $St=1$, ''demixing'' occurs as particles are concentrated in a thin layer on the outer edge of vortices.

Bachalo et al. [17] and Bachalo [18] investigated experimentally the distribution of water droplets in the wake of a circular cylinder for three Reynolds numbers. The flow was seeded with steam droplets, with diameters ranging up to 20 μm, in a stream approximately 4 cylinder diameters wide. They observed that large-scale vortices serve to entrain fluid containing high concentrations of drops into the wake. In the recirculation region, extending to about 2D downstream of the cylinder, droplets of up to 20 μm could be found for $\mathrm{Re}_D=16{,}000$. For larger Reynolds numbers ($\mathrm{Re}_D=80{,}000$ and 122,000), only droplets smaller than 10 μm could be found in the recirculation region. Upon reprocessing these data, Bachalo et al. [17] showed that droplets entering the recirculation region typically correspond to Stokes numbers of order 0.1, while droplets with larger St remained on the outside of the recirculation region.

The aforementioned results show that large particles ($St>1$) released upstream of the obstacle do not enter the recirculation wake. Numerical [15] and experimental [17,18] studies show that particles with lower Stokes number can be captured in the near wake. Mixing layer studies [7–9] show that mixing is related to the influence of coherent structures and is thus difficult to determine from time-averaged flow properties. Performing a Fourier analysis on the time series, Bachalo et al. [17] observed larger concentration at the same frequency as the shedding.

These results confirm that coherent structures (shed vortices) play an important role in mixing, but fail to provide a detailed description of the phenomenon. The present study aims to provide such detailed information on the influence of shed vortices on the wake mixing characteristics of droplets released upstream of a square cross-section cylinder. This geometry was selected because the shear layer separation point, occuring at the leading edges, is well defined. When compared to the circular cylinder, the square cylinder wake width and the maximum velocity in the shear layer are larger. The contributions of the coherent motion to U_{RMS} and especially V_{RMS} are also greater. As a consequence, the flow will feature stronger streamline curvature, larger velocity fluctuations and the droplet Stokes number will evolve significantly in time and space. Tests were conducted at a Reynolds number of $\mathrm{Re}_D=18{,}500$, based on the cylinder side dimension, D. The particle size distribution resulted in particle Stokes number ranging up to a maximum of order unity for a 30 μm-droplet in the shear layer region, which allows to investigate the efficiency of the entrainment of particles in the wake as a function of size during the shedding cycle. This paper first presents data analyzed in terms of the time-averaged mean field for five droplet size classes. Then, a phase-averaging technique based on the double decomposition representation of Hussain [26] is used to extract the influence of the coherent structures (shed vortices) on particle motion as a function of size and location.

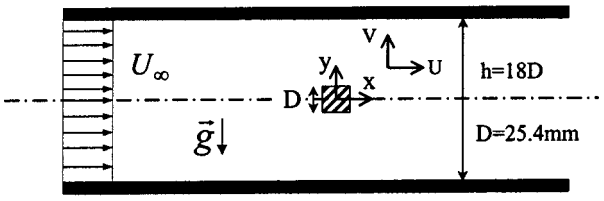

Fig. 1 Schematic of the experimental geometry and nomenclature

Experimental Set-Up

Experiments were conducted in a suction-type, open-circuit, subsonic wind-tunnel in which a square cylinder was placed at the working-section mid-height, as shown schematically in Fig. 1. The airflow is uniform and the Reynolds number is about 18,500, based on the freestream velocity and obstacle side dimension, D. The freestream turbulence intensity, measured at $x/D=-5$, is less than 3% and the nominal blockage is 5.5%. Water droplets are generated with a spray nozzle located about 100D upstream of the cylinder. These droplets range in size from 0 to 100 μm, with a number mean diameter, measured at $x/D=-5$, of $d_{10} \approx 16\ \mu$m, and Sauter mean diameter of $d_{32} \approx 40\ \mu$m. The overall droplet concentration is at maximum of order 10^{-6} in the regions of high concentrations such as the shear layers so that we may consider a dilute regime. Typical droplet number densities at $x/D=-5$ and $x/D=-1$ are provided for three vertical locations in Fig. 2. The number density (Nd_k) for the kth droplet size class is given by $Nd_k=(1/V_k \cdot T_S)\Sigma_{j=1}^{n_k}\tau_{kj}$ where τ_{kj} is the residence time of the jth particle of the kth droplet size class, n_k is the number of particles of this size class measured during the sampling time T_S, and V_k is the effective volume of the optical probe for this size class. V_k is determined by using the burst length model [27]. No significant differences are observed both between transverse locations and between the two streamwise locations, except for the largest droplets. The latter seems to be subject to a not negligible gravitational settling effect. Note that the terminal velocity of the largest droplets in air is of the order of 0.1 to 0.2 m/s, which may become important in stagnation or recirculation regions. Furthermore, the number mean diameter measured at $x/D=-1$ is also close to 16 μm, indicating negligible evaporation between the two upstream locations. A two-component Phase-Doppler Particle Analyzer was used to simultaneously measure particle size, streamwise and vertical velocity components. A liquid spray is well suited to this measurement technique as droplets are nearly spherical. Measurements were performed in forward scattering mode. The receiving optics was positioned at an angle of 30 deg with respect to the optical axis. Both receiving and transmitting lenses had a nominal focal length of 400 mm. The light source was a 300 mW Ar-Ion laser operating with wavelengths of 514.5 nm (green) and 488 nm (blue). A Bragg cell was used to shift the frequency and permit measurements in reverse flow. Signals detected by the receiving

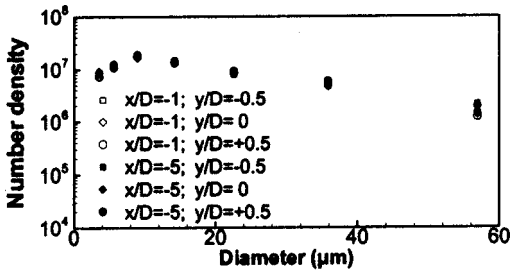

Fig. 2 Droplet number density distribution upstream of the cylinder

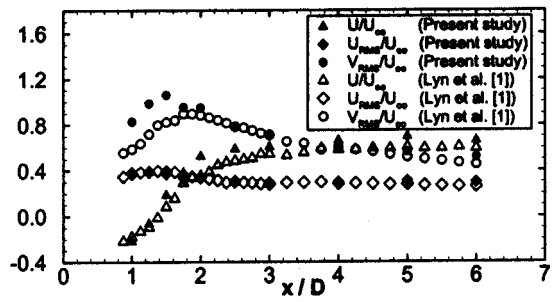

Fig. 3 Centerline ($y/D=0$) streamwise velocity (U/U_∞) and streamwise (U_{RMS}/U_∞) and cross-stream (V_{RMS}/U_∞) velocity fluctuations downstream of the obstacle. Comparison between present study and results of Lyn et al. [1]

optics were processed using the Multi PDA 58N80 Signal Processor and the Fiber PDA 58N70 Detector unit of DANTEC.

Uncertainty. The average flow statistics (velocity moments) were estimated using interarrival time weighting. The uncertainty estimates for the velocity field were calculated as in Wu and Martinuzzi [3], based on the method of Abernethy et al. [28] and the criteria for Laser Doppler Anemometry outlined in Edwards [29]. The statistical contribution to the experimental error was obtained based on Benedict and Gould [30]. The maximum uncertainty occurs in the shear layer, where the velocity gradients and fluctuations are largest. It is estimated to be $\pm 0.03U_\infty$ and $\pm 0.07U_\infty$ for the mean and root-mean-square (RMS) quantities, respectively. For the coherent (phase-averaged) velocities, additional sources of uncertainty were the resolution of the peak detection algorithm (about 1% of the period) and the reduced number of samples per phase and size bin. The maximum uncertainty for the velocity components is estimated to range from $0.05U_\infty$ for the smallest to $0.15U_\infty$ for the largest particles size classes.

A sufficiently large sample size of droplets is required to obtain reliable statistical results. Therefore, phase-averaged properties were determined on larger size classes than those used for time-averaged properties. In that first case, it may still be assumed, with some caution, that results from the smallest particle size class ($\overline{d_p}=3.6\ \mu$m) provide a good approximation of the continuous phase properties. The trends and values obtained in these measurements are similar to those reported in the literature as discussed in the introduction.

The absolute uncertainty for the particle size and concentration measurements from the PDA system could not be assessed reliably. The operating conditions were set to optimize the validation rate, which typically ranged from 70%-80%. The signal to noise rejection criterion was set at 0 dB, the sphericity at 0.90. The size bin resolution was 0.8 μm. Variance measured in the uniform flow upstream of the obstacle is used to assess reproducibility. For the data shown in Fig. 2, for $d_{10}\approx 10\ \mu$m, the variance is $\sigma\approx 1.5\ \mu$m, and for $d_{32}\approx 40\ \mu$m, $\sigma\approx 6\ \mu$m.

Time-Averaged Properties

The mean and fluctuating (rms) velocity estimates for small particles of mean diameter $\overline{d_p}=3.6\ \mu$m mostly agreed within experimental uncertainty with flow field data reported in previous studies [1,3]. Figure 3 shows the centerline downstream streamwise velocity and the streamwise and cross-stream velocity fluctuations as a brief comparative summary. Except for some differences noted in the cross-stream velocity fluctuations in the close near-wake, it is concluded that velocity measurements with this class of particles approximate well the fluid flow field.

Figure 4 shows the upstream time-averaged velocity characteristics at $x/D=-1$. Streamwise and transverse velocity profiles clearly indicate that larger droplets will be less deflected and, as expected and observed, that impingement on the obstacle will

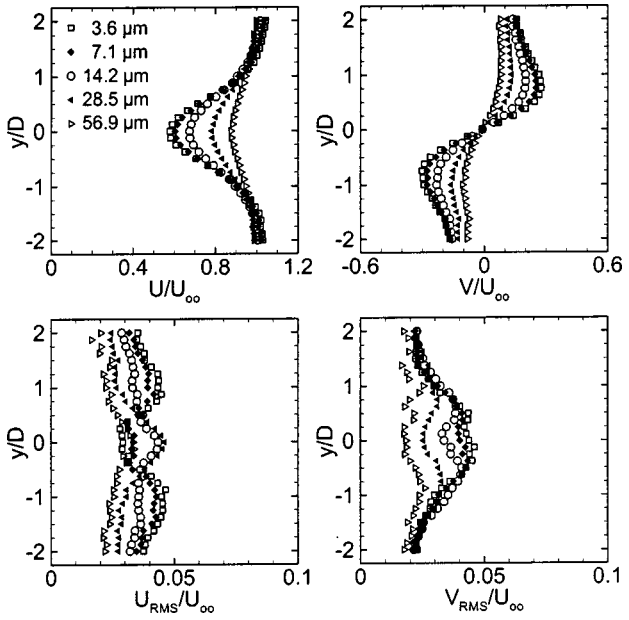

Fig. 4 Approaching flow conditions at $x/D=-1$

occur. In order to reduce the possible occurrence of secondary atomization in the wet, solid cylinder corners, the obstacle was regularly wiped during the experiments. This also attenuated the effect of particle deposition and re-entrainment in the downstream side of the cylinder due to the near-wake recirculation, which might induce droplet distribution modifications.

Particle Number Distribution. Figure 5 shows the particle number mean diameter (d_{10}) as a function of the streamwise location (x/D) for several vertical locations. Figure 6 provides the particle concentration per size class compared to the freestream value (C_∞) of the corresponding class as a function of the streamwise location (x/D) and for several transverse locations. The particle concentration (C_k) for the kth droplet size class is given by $C_k=Nd_k\cdot(\pi/6)(D_{30_k})^3$ where Nd_k and D_{30_k} are respectively the number density and the volume mean diameter for the kth droplet size class. At $x/D=+1$, d_{10} is lowest in the region close to the centerline (directly behind the cylinder), which indicates a higher relative concentration of small sized particles, as seen in Fig. 6. The number mean diameter increases away from the centerline and reaches a maximum for $y/D\approx\pm 1$ and decreases slightly for $|y/D|>1$ (Fig. 5). Thus two regions exist: (i) the recirculation region between $y/D\approx -1$ and $y/D\approx +1$, characterized by the nearly exclusive presence of small sized droplets ($\overline{d_p}=3.6\ \mu$m and, in a lesser extent, $\overline{d_p}=7.1\ \mu$m), and an external region where the particle distribution is essentially that of the ambient stream. This behavior is similar to that observed by Bachalo et al. [17]. At

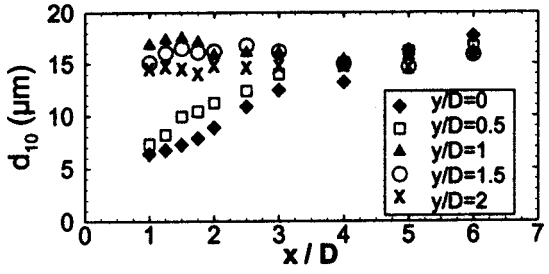

Fig. 5 Particle number mean diameter (d_{10}) as a function of the streamwise location (x/D) at several vertical locations (y/D)

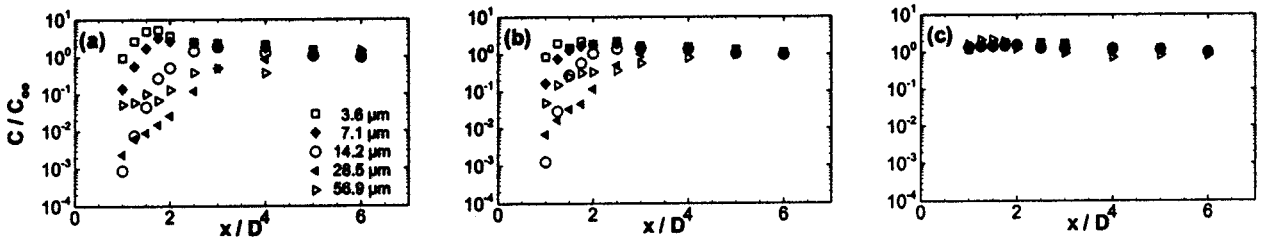

Fig. 6 Non-dimensional particle concentration (C/C_∞) as a function of the streamwise location (x/D^4) and particle size classes for three vertical locations. (a) $y/D=0$ (b) $y/D=0.5$ (c) $y/D=1$

$y/D \approx \pm 0.6$, the relative concentration of small particles is maximum. This location coincides with the largest mean streamline curvature and maximum U_{RMS}. In this region, particle separation would be greatest due to two effects. First, the inertial slip of the larger particles would also be largest so that particles deflected on the front face would concentrate along the shear layer. Second, centrifugal "demixing" [16,19] concentrates particles along the outer rim of the recirculation.

As x/D increases, d_{10} increases along the centerline to a value of 16 μm at $x/D \approx 5$ and remains nearly constant downstream. In Fig. 6, it can be seen that the relative proportion of larger particles rapidly increases along the centerline as x/D increases. Thus, the increase in d_{10} is due to the influx of larger particles entrained by the shear layer towards the centerline. A similar trend is observed along $y/D=0.5$, but until $x/D=4$, the mean diameter is somewhat larger than along the centerline. However, it is also noted that the smaller the particles are, the earlier is their influx.

From the point-of-view of particle mixing, the near-wake region, where particle segregation is clearly evident, is upstream of $x/D \approx 3$ (Figs. 5 and 6). For x/D=2 and x/D=3, relative concentration of the smaller particles ($\overline{d_P}=3.6$ and 7.1 μm for $x/D=2$ and also $\overline{d_P}=14.2$ μm for $x/D=3$) is higher about the centerline ($|y/D| \leq 0.6$). Further downstream ($x/D>4$), the streamwise gradients of the velocity and Reynolds stress field are small so that the mean particle distribution changes slowly and the droplet distribution, in a mean sense, appears homogeneous for x/D=6. However, it will be shown below that these "smooth" profiles are artefacts of the averaging operation. A phase-averaged analysis will show that the passage of each vortex is associated with sharp changes in particle size distribution both temporally and spatially.

Droplet Mean and Fluctuating Velocities. Figures 7–10 give non-dimensional, time-averaged mean and fluctuating streamwise ($U/U_\infty, U_{RMS}/U_\infty$) and vertical ($V/U_\infty, V_{RMS}/U_\infty$) particle velocity profiles for several downstream locations. Recall that the velocity characteristics of particle size class $\overline{d_p}=3.6$ μm should match those of the continuous phase (air). The periodic passage of large-scale coherent structures (shed vortices) results in high velocity fluctuations, especially close to the centerline ($y/D=0$). The contribution to the vertical velocity fluctuation by the coherent motion due to the passage of shed vortices accounts for up to 50% of V_{RMS} [1]. In the near and intermediate wakes ($1<x/D<20$), the center of these vortices move roughly parallel to the locus of points of maximum shear rate, $\partial u/\partial y$, in each of the opposite shear layers. The distance between opposite loci is symmetric about $y/D=0$ and increases in the streamwise direction to asymptotically approach a classical wake spreading rate. The vertical spread of the V_{RMS} profile is consistent with these observations. Between the loci, the flow is strongly influenced by vortices in both shear layers, explaining that the maximum V_{RMS} always occurs at the center, and not along the lines of maximum shear rate as is the case for U_{RMS}.

At x/D=1 (Fig. 7), negative mean streamwise velocities can be observed close to the centerline (y/D=0). This indicates the presence of the recirculation in the close near-wake. These negative velocities are observed for $|y/D|<0.4$, which is similar to earlier results [1–3,31] for the same location. Outside this recirculation region, droplet mean streamwise velocities (U) quickly increase across the shear layer to a maximum of approximately $1.3U_\infty$ at $|y/D| \approx 1.0$. All particle size classes feature similar velocity profiles. However, the number of large particles is low close to the centerline upstream of $x/D=2$ (Fig. 6), which reinforces the view that the streamline curvature is sufficiently strong to prevent entrainment of nearly all particles larger than about 10 μm into the recirculation vortex core. The net effect is that migration of larger particles towards the centerline is delayed downstream as a consequence of trajectory modification and weaker streamline curva-

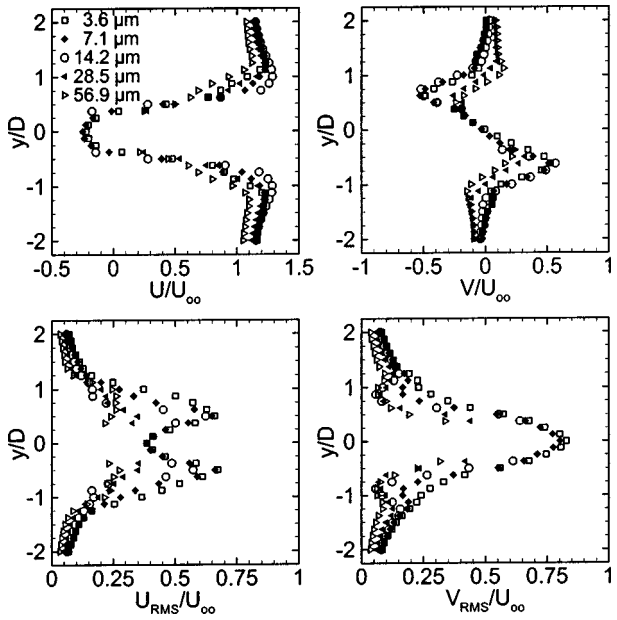

Fig. 7 Time-averaged non-dimensional flow conditions at $x/D=+1$

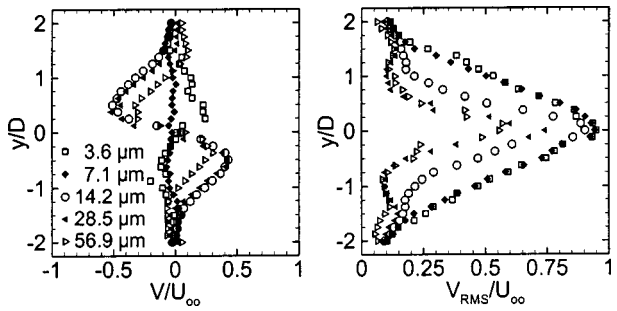

Fig. 8 Time-averaged non-dimensional transverse velocity conditions at $x/D=2$

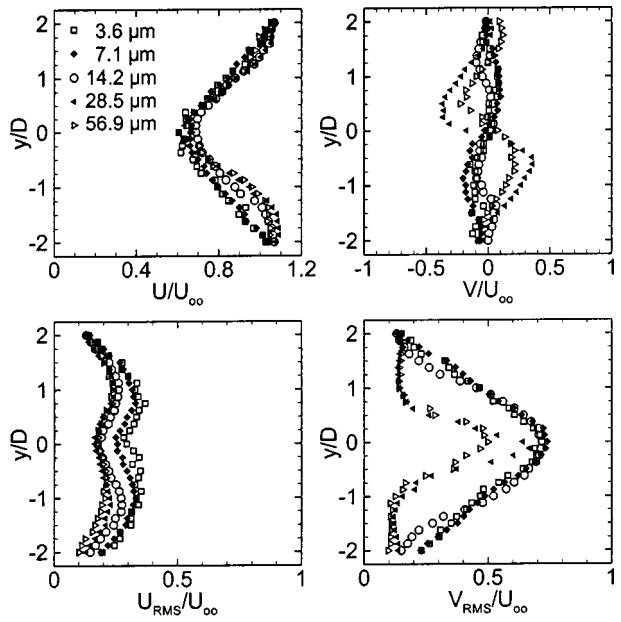

Fig. 9 Time-averaged non-dimensional flow conditions at $x/D=+3$

ture downstream. The relative importance of inertial effects for heavier particles also leads to the attenuation in U_{RMS}, for example around $|y/D|=0.6$.

At $x/D=2$ (Fig. 8), it can be seen that the fluctuating (V_{RMS}) vertical velocity characteristics for small particle size classes ($\overline{d_p}=3.6$ and 7.1 μm) are very similar. Mean particle velocities (V) are also close to zero for both classes. However, segregation based on particle size can be observed for larger particles ($\overline{d_p}=14.2$, 28.5 and 56.9 μm). The vertical velocities (V and V_{RMS}) depart significantly from those for smaller particles. For the two larger size classes, minima of V_{RMS} occur at $|y/D|\approx 0.9$. A strong attenuation of the fluctuations is noted in the upper and lower regions corresponding to $0.5<|y/D|<1.5$, whereas higher transverse velocity magnitudes are observed in the same time. The sign

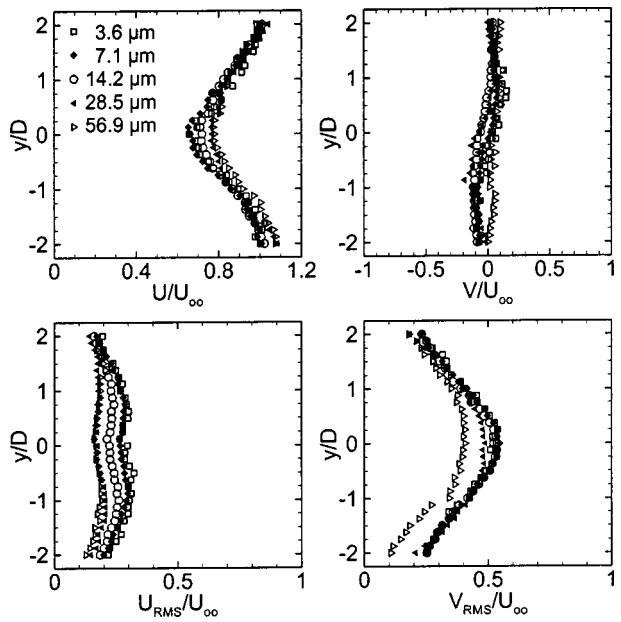

Fig. 10 Time-averaged non-dimensional flow conditions at $x/D=+6$

of the tranverse velocity component indicates a motion in the direction of the centerline. As a result, the larger particles seem to be globally entrained towards the centerline. This behavior will be further documented in the phase-averaged analysis.

Differentiation based on particle size is very subtle based on U, but is clearly visible for the other components for $x/D=3$ (Fig. 9). The profiles are also close for small particle size classes ($\overline{d_p}=3.6$ and 7.1 μm), but lower fluctuations are still observed for larger particles. Inertial effects persist far downstream. At $x/D=6$ (Fig. 10), U_{RMS} for larger particles is still clearly lower than those of the flow. The vertical particle velocity component illustrates different stages of evolution of the particle velocity field. In the region of maximum flow vertical fluctuation ($2\leqslant x/D\leqslant 3$), the downstream location at which the particle V and V_{RMS} matches that of the flow field is delayed proportionately with size class. Inspection of Fig. 9 shows that, as for $x/D=2$, the magnitude of vertical velocity of larger particles is also larger than that of the flow at $x/D=3$. The lower V_{RMS} observed at the same streamwise locations is consistent with a global transverse entrainment of larger particles ($\overline{d_P}=28.5$ and 56.9 μm) towards the centerline, as previously suggested by results at $x/D=2$. At $x/D=6$, segregation according to size cannot be made based on V or V_{RMS}, except for $\overline{d_P}=56.9$ μm. This suggests, as in Fig. 6, a homogeneous redistribution. The phase-averaged analysis of this flow, shown next, suggests that this conclusion may be misleading.

Phase-Averaged Properties

The importance of the coherent structure passage in describing turbulence management generally, and specifically the evolution of the particle size distribution, requires a strategy to isolate the influence of shed vortices. In the obstacle wake, the fluid (continuous phase) velocity field is characterized by the passage of shed vortices, which influence the dispersed phase velocity and concentration characteristics differently depending on droplet size. Counter-rotating vortices are alternately formed and shed from opposite cylinder faces. The core of the shed vortices are convected downstream. The average convective speed (U_C) was shown by Lyn et al. [1] to be $U_C\approx 0.43U_\infty$ in the base region ($x/D<4$) and to increase rapidly to $0.78U_\infty$ for $x/D>4$. The coherent motion results in large velocity fluctuations, especially in the vertical direction, at each vortex passage upon which turbulent (incoherent) fluctuations are superimposed. The average characteristic frequency (f_S) of the coherent fluctuations corresponds to a Strouhal number of $St_D=f_SD/U_\infty=0.132\pm 0.003$ [1–3,5].

Hussain [26] proposes that the influence of the coherent motion can be represented in terms of a ''typical'' or average cyclical passage of a coherent structure subject to the double decomposition written for the generalized flow variable ψ:

$$\psi(t)=\langle\psi\rangle+\psi'$$

where $\psi(t)$ represents the instantaneous value, $\langle\psi\rangle$ is the phase averaged value and ψ' the turbulent (incoherent) fluctuation contribution. For periodic events, $\langle\psi\rangle$ represents simply the average value of the coherent velocity at a given phase of the cycle so that $\psi=\overline{\langle\psi\rangle}$, where the overbar indicates the time average. The aim of phase-averaging is to obtain a statistical description of the flow during a ''typical'' cycle. Experimentally, this requirement implies measurements of a sufficient number of cycles, typically over 200. Depending on the data acquisition rate (generally a few kHz), the data is then subdivided into finite phase bins, the size of which is determined by the desired sample size. As reported by many researchers, there is a slight cycle-to-cycle variation, or phase jitter, due to turbulence and transient three dimensional instability. A cycle will be considered to occur between two peaks of the vertical velocity. The peak occurrence is determined by filtering the original signal (time series for the vertical velocity component) with a bandpass filter about the average shedding frequency (determined from Fourier analysis) and then applying a peak detector

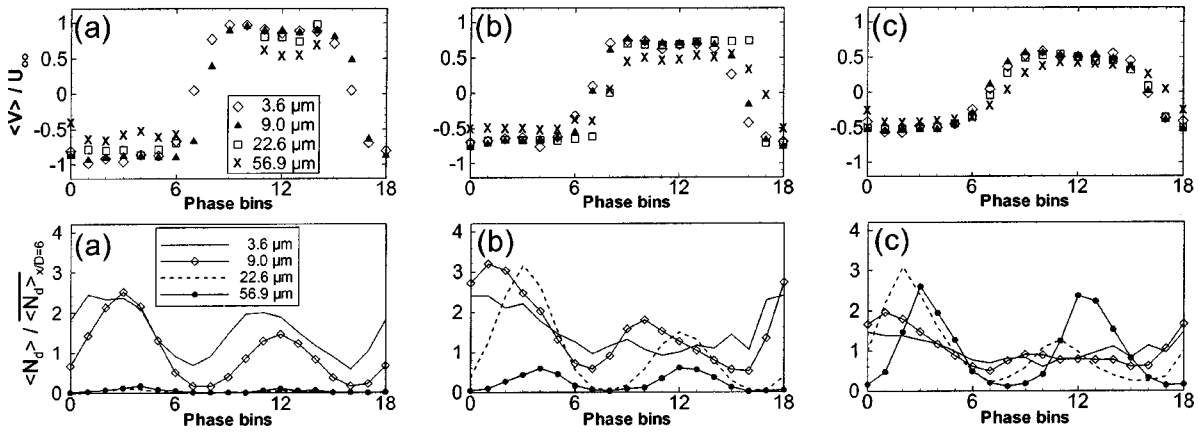

Fig. 11 Phase-averaged non-dimensional vertical velocity (top) and droplet number density distribution (bottom) at the centerline ($y/D=0$) for three streamwise locations. (a) $x/D=2$ (b) $x/D=3$ (c) $x/D=6$

on this enhanced signal to determine the beginning and the end of each cycle. Subsequently, each cycle is subdivided in a number of bins (NB), or phase intervals, of equal lengths, i.e. (time between the two peaks)/NB. In this study, NB=18, corresponding to phase bins of 20 deg. The phase-averaged streamwise and vertical velocity components, incoherent turbulent fluctuations and the number of droplets in each bin can then be deduced.

As indicated in the literature, the particle Stokes number, St, is an important parameter to characterize the effect of particle size on dispersion. To determine St, the particle response time, τ_A, can be approximated from $\tau_A=\rho_P d_p^2/18\mu f$ where ρ_P is the particle density, d_P is the particle diameter, μ is the fluid dynamic viscosity and f is a coefficient linking the Stokes drag to the actual drag so that $C_D=f24/\mathrm{Re}_P$. For $\mathrm{Re}_P<1000$, a good approximation of f is given by $f=1+.15\,\mathrm{Re}_P^{0.687}$ [6]. Following Bachalo et al. [17], based on the similarity between the circular and the square cylinder wakes, the characteristic fluid motion time scale is approximated by $\tau_F=D/U_R$, where $U_R=U-U_C$. Using these definitions, it is found that for 30 μm droplets the Stokes number is in the critical range, being of the order unity in the region of maximum U_{RMS} in the shear layer and dropping to order 0.1 downstream. Thus, the existing particle size distribution will result in a sufficiently large St-range to study particle entrainment efficiency.

Results on the Centerline. The non-dimensional phase averaged vertical velocity component ($\langle V\rangle/U_\infty$) at the centerline ($y/D=0$) and at x/D=2, 3 and 6 is shown in Fig. 11 as a function of particle size. A sufficiently large sample size is required to get reliable statistical results. Therefore, phase-averaged properties were determined for a reduced number of size classes whose mean diameters ($\overline{d_p}$) are 3.6 μm, 9.0 μm, 22.6 μm and 56.9 μm, respectively. Like for the time-averaged analysis, velocity measurements corresponding to the class of the smallest particles ($\overline{d_p}=3.6\,\mu$m) may be assumed to approximate the fluid flow field. The origin of the cycle is arbitrarily chosen at an instant such that the magnitude of the vertical velocity is a maximum for this size class. As concerns particle concentration, number densities have been used to account for velocity induced bias. For a given size class, results are presented as the particle number density ($\langle N_d\rangle$) compared to the average particle number density ($\overline{\langle N\rangle}_{dx/D=6}$) of the corresponding size class computed on a complete cycle at $x/D=6$ and for the same vertical location (y/D).

At $x/D=2$, the phase-averaged vertical velocity has a square-wave shape, which shows the alternate presence of shed vortices coming either from the upper or lower side of the cylinder. The combined effect of these alternate vortices results in an apparent upward motion (i.e. $\langle V\rangle>0$) when one is located just upstream of the upper vortex and just downstream of the lower vortex, and a downward motion ($\langle V\rangle<0$) when located just downstream of the upper vortex and just upstream of the lower one. Transitions with a transverse velocity component close to zero occur when one is located just above or below vortices' cores. Note that only partial data are provided for $\overline{d_p}=22.6\,\mu$m and 56.9 μm as insufficient numbers of particles were detected for some phase bins at this location. This flow pattern suggests that shear layer *flapping* abruptly redirects the particle stream into the wake region with similar velocity magnitudes observed in both directions for a given size class. Moreover, a slight phase lag is observed for larger particles. This effect is more pronounced for $x/D=3$ and indicates that inertial effects are present for $\overline{d_p}=22.6\,\mu$m and 56.9 μm. The inertial effect is also evidenced by the relative low number density of droplets with $\overline{d_p}=22.6\,\mu$m and 56.9 μm at both these locations ($x/D=2$ and 3) as seen in Fig. 11. Further downstream, at $x/D=6$, droplets up to $\overline{d_p}=22.6\,\mu$m have similar flow characteristics. However, the phase lag is still observed for the largest droplets ($\overline{d_p}=56.9\,\mu$m).

The influence of the fluctuations associated with the coherent motion on the local, instantaneous, droplet concentration is characterized by large changes and two peaks in the particle number density distribution during the shedding cycle. These peaks occur close to the middle phase of either the upward or downward motion. This behavior is consistent with the observed shear layer dynamics. The poorer mean mixing characteristics in the very near wake region observed from the mean particle distributions seem directly related to particle slip as the shed vortices cause reorientation of the shear layer. The oncoming particles directly upstream of the cylinder are deflected preferentially along the separated shear layer. As these shear layers are redirected in the wake, they convect these high particle concentrations towards the center line. Particle trajectory deflections towards the centerline depend on particle inertia with a better response of small, i.e. low Stokes number, particles to the reorientation of the shear layer. A more detailed description of particle behavior in the shear layer region is provided later.

Due to the large droplet size range and in order to keep a sufficient number of large particles all along the flow despite gravitational effects, some asymmetry in droplet concentrations could not be avoided, as observed just downstream of the cylinder at $x/D=1$ (Fig. 12). The importance of this asymmetry is size-dependent. Considering that the region in between, and including, the shear layers contains the particles contributing to the feeding at the centerline, droplet concentrations at $x/D=2$ and for each size class may be corrected by taking the ratio between the average droplet number densities above and below the centerline at $x/D=1$ (Fig. 13). Time-averaged vertical velocity profiles (Fig. 7)

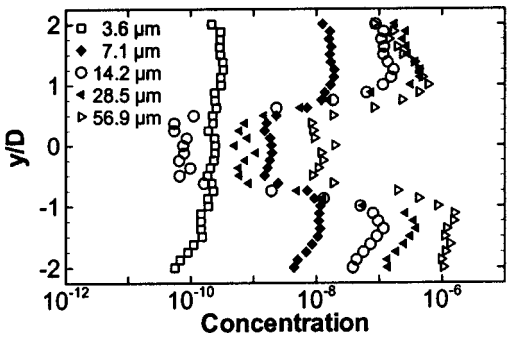

Fig. 12 Time-averaged droplet concentration distributions in the close near-wake at $x/D=1$

indicates that this inner region is roughly delimited by $|y/D| \leq 1.25$. Symmetry is recovered for three of the four size classes. However, for the larger particles, the influence of gravity is still not negligible, giving the particles a net downward settling motion. The number density profiles are smoother for the smaller droplets ($\overline{d_p}=3.6\,\mu$m and 9.0 μm, Types I & II). These tend to follow the streamline curvature better so that small particles (Type I) are found during the complete cycle, even if not at the same concentration. Once these particles have been entrapped in vortices, one would expect to find them distributed homogeneously all along the shedding cycle. However, a substantial modulation is observed leading to small number of particles near the velocity transitions. The use of a single Stokes number based on the characteristic time-scale of the vortex motion appears to be insufficient if one wants to consider the behavior of a particle located close to the vortex core. In that case, when the particle is at a shorter distance from the core than the characteristic length scale of the vortex motion, the flow time-scale, and subsequently the corresponding Stokes number, change. In such a situation, heavy particles (i.e. such that $\rho_P \gg \rho_F$) tend to be centrifuged out as observed and described by several authors [6,13,25]. This results in depleted vortex cores and leads to the observed large nonhomogeneities in the temporal distribution. Type III droplets ($\overline{d_p}=22.6\,\mu$m) appear only intermittently in the near wake and are not observed during the transitions between upward and downward motions, which indicates important slip velocity effects.

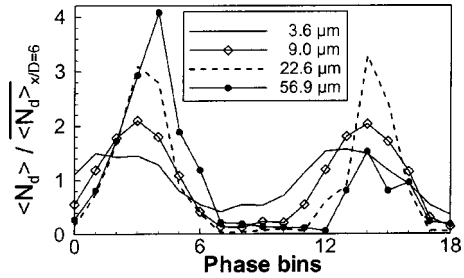

Fig. 13 Corrected and normalized phase-averaged droplet number density distribution at the centerline ($y/D=0$) and for $x/D=2$

Further downstream (x/D=3 and 6), no correction is applied for droplet concentration results. If needed, comparisons will be done with uncorrected droplet concentrations at $x/D=2$. However, qualitative as well as quantitative results (phase lags between density peaks, for example) are obtained and will help in detailing the underlying mechanisms of droplet dispersion in this plane wake. At x/D=3 (Fig. 11), Type III droplets are observed at nearly any phase of the cycle, whereas Type I particles tends towards a more homogeneous temporal distribution. Type IV droplets ($\overline{d_p}=56.9\,\mu$m) also appear intermittently, especially when the downward and upward motions are the most intense, but not during the transitions (similar behavior as Type III droplets at x/D=2). Due to the ejection process, these larger droplets are confined at the very outer edge of vortices so that, during a typical shedding cycle, they are not present during most of the passage of either vortex. Another noticeable characteristic of the droplet distribution is the slight shift of the location of the maximum concentration with increasing droplet size, which, together with the observed response lag to velocity fluctuations, is consistent with the ejection phenomenon. At $x/D=6$, Type I as well as Type II particles feature rather homogeneous distributions, while two peaks are still observed in the number density distributions of the larger particles ($\overline{d_p}=22.6\,\mu$m and 56.9 μm) indicating that the phenomenon of ejection of the entrapped droplets towards the outer edges of vortices is still prominent for these sizes and is indicative of particle "demixing" as noted by Tang et al. [16] or Crowe et al. [19].

Droplet Characteristics Away From the Centerline. Figure 14 shows the vertical velocity at $y/D=0.5$ and for three streamwise locations ($x/D=2$, 3 and 6) as a function of droplet size and shedding phase. At x/D=2, Type III and IV droplets are mainly present when the downward motion occurs. This downward motion lasts longer and the transition towards the upward motion is smoother, or *smeared*, indicating slip. Such size-dependent phase lags in particle motion characteristics were also observed in the

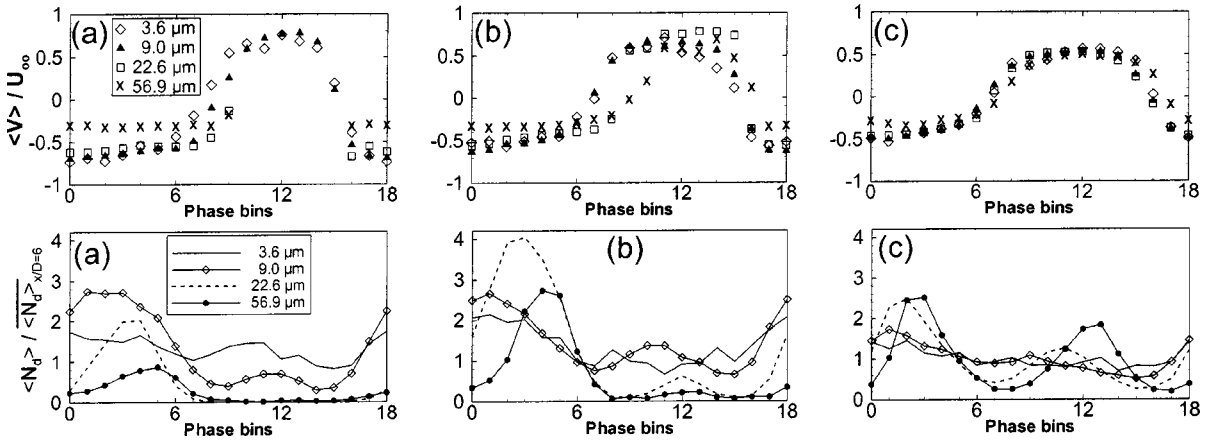

Fig. 14 Phase-averaged non-dimensional vertical velocity (top) and droplet number density distribution (bottom) half a diameter above the centerline ($y/D=0.5$) for three streamwise locations. (a) $x/D=2$ (b) $x/D=3$ (c) $x/D=6$

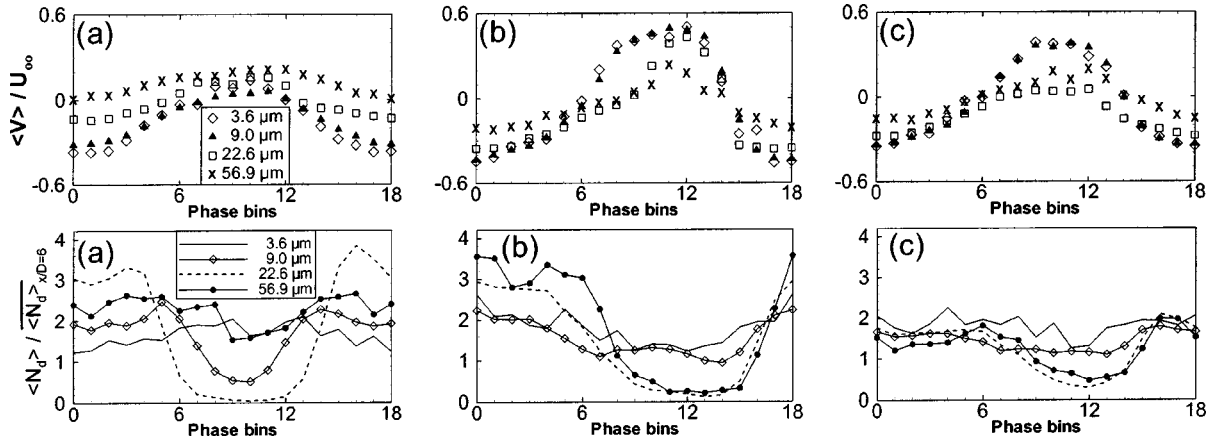

Fig. 15 Phase-averaged non-dimensional vertical velocity (top) and droplet number density distribution (bottom) for three locations close to the shear layer region. (a) $x/D=1$, $y/D=1$ (b) $x/D=3$, $y/D=1$ (c) $x/D=3$, $y/D=1.25$

phase-averaged results of Kiger and Lasheras [12] in their study of a mixing layer. This is accompanied by delayed peaks in the number densities. Phase lags between the number density peaks of Types II, III and IV particles and the number density peak of Type I particles are about 40, 70 and 100 deg, respectively. A significant lower magnitude of the particle vertical velocity is also observed for the largest droplets ($\overline{d_P}=56.9\ \mu$m) during this downward motion. Note that, during the upward motion of the flow, some velocity data are not provided for Types III and IV droplets due to limited sample sizes.

Further downstream, at $x/D=3$, both Type I and Type II droplets are found throughout the cycle. Types III and IV particles also appear during the upward motion. For example, the transition between the two kinds of motion (upward and downward) occurs later for Types III and IV particles. The vertical velocity magnitude is still lower for Type IV particles in the case of the downward motion. As droplets are entrained from the upper shear layer towards the centerline, the smallest droplets follow more easily the strong curvature of the vortex and have a more intense downward motion than larger droplets whose trajectories are less deflected. For the upward motion, higher vertical velocity magnitudes are observed for the larger droplets. This motion may be due to the passage of the trailing edge of the upper vortex with a peak in Type III droplet concentration occurring earlier than for Type IV. Then, this upward motion is maintained by the subsequent passage of the leading edge of the lower vortex, which will continue to provide large droplets. The leading edge of the lower vortex should then be able to feed with droplets the trailing edge of the previous upper vortex, resulting in the formation of particle streaks in the region between the two vortices similar to those observed in the experiments of Longmire and Eaton [23] and Lazaro and Lasheras [10,11] or the numerical study of Martin and Meiburg [13]. Furthermore, this means that droplets must be located in the outer edge of the vortices. Very large concentrations of large droplets (especially Types III and IV) are observed in the middle of the downward motion. This phenomenon may be explained by the fact that the upper vortex feeds from the upper separated shear layer containing high droplet concentrations. These droplets are convected downwards along the leading edge of the upper vortex. Important phase lags are also observed. Whereas the passage of negative to positive velocity is close for the smallest particles (Types I and II), the change occurs 30 and 40 deg later for Types III and IV droplets, respectively. Such a lag is also evidenced by particle number densities temporal evolutions during a shedding cycle. Although lower than at x/D=2, phase lags of about 50 and 80 deg are still observed for Type III and Type IV particles, respectively.

Further downstream ($x/D=6$, Fig. 14), the three first types of droplets have nearly identical velocity profiles. Only the largest droplets ($\overline{d_p}=56.9\ \mu$m) feature slightly different flow characteristics. However, the droplet concentrations do not evolve similarly. As was observed at the centerline, two characteristic peaks in the number density distributions during a cycle remain for the larger droplets ($\overline{d_p}=22.6$ and $56.9\ \mu$m) due to the preferential concentrations of these droplets combined with the alternating upward and downward flow induced by the vortices, but the mixing that has occurred upstream tends to smear the distribution. The peaks are more pronounced with the larger droplets and phase lag is still pronounced. The distribution characteristics observed for large particles are similar to those for smaller particles further upstream. Finally, a uniform droplet distribution during a complete cycle is not yet totally achieved at $x/D=6$ (Fig. 14), even for the smallest droplets. This illustrates how conclusions drawn from time-averaged results alone, where droplet concentration is on average uniform along the vertical, can be misleading. It is concluded that redistribution or mixing is still active, which explains intra-cycle differences. The averaged results are weighted more to the events at which peak concentrations occur.

Droplet Characteristics in the Shear Layer. As discussed for $x/D=2$ and $x/D=3$, larger particles enter the centerline region during a preferential phase of the shedding cycle. Consequently, the velocity of the large particles is biased towards peak-$\langle V\rangle$ and the particle V_{RMS} is lower, as observed in Figs. 8 and 9. Particles originating upstream of the obstacle are initially concentrated in the shear layer. Particle trajectory modifications due to shed vortices in the wake, and thus entrainment towards the centerline, depend on particle inertia and local fluid motion characteristics, i.e. their local Stokes number. Figure 15 shows the phase-averaged vertical velocity for three vertical locations close to or in the shear layer at $x/D=1$ for $y/D=1$, and at $x/D=3$ for $y/D=1$ and 1.25. These locations span regions where minima of the V_{RMS} were observed for the larger particles ($\overline{d_p}=14.2\ \mu$m at $x/D=1$, $\overline{d_p}=28.5\ \mu$m and $56.9\ \mu$m at $x/D=1$ and $x/D=3$, Figs. 7 and 9). The smallest droplets ($\overline{d_p}=3.6\ \mu$m) are well mixed throughout the shear layer as is indicated by the nearly uniform particle number density throughout the shedding cycle at the three locations.

The largest particles ($\overline{d_p}=22.6\ \mu$m and $56.9\ \mu$m) have Stokes numbers of the order unity, or larger, throughout the shedding cycle. They tend to follow the flow less well as can be seen from the phase-averaged particle velocity profiles at $y/D=1$ for both streamwise locations ($x/D=1$ and 3). At $x/D=1$, the low cross-stream velocity magnitudes indicate that both types of particles

are subject to little lateral motion during the cycle. For Type III particles ($\overline{d_p}=22.6\ \mu$m), this weak lateral motion is accompanied by a very high droplet number density for about half of the cycle followed by a near total absence of droplets for the other half. This suggests that Type III particles are confined in a very thin layer close to $y/D=1$. This behavior evokes particle ''demixing'' or ''focusing'' in the outer edges of vortices previously described by Tang et al. [16] or Crowe et al. [19] for particles with $St\approx 1$. As concerns Type IV particles ($\overline{d_p}=56.9\ \mu$m), whose Stokes number is roughly six times that of Type III particles, they appear to be more scattered in the shear layer and to be less influenced by the coherent motion. Inertial effects remain important for those largest particles. This ''demixing'' effect may explain the minimum relative concentration observed in Fig. 6 in the near-wake recirculation region, just downstream of the cylinder, in the intermediate size class ($\overline{d_p}=14.2\ \mu$m) with higher relative concentrations of larger particles ($\overline{d_p}=28.5\ \mu$m and 56.9 μm) both at $y/D=0$ and $y/D=0.5$.

Mixing is also not totally achieved for Type II particles ($\overline{d_p}=9.0\ \mu$m) at $x/D=1$, as it can be inferred from the lack of uniformity of the number density profile. Further downstream, at $x/D=3$, this mixing is achieved for Type II particles, which feature similar velocity and concentration profiles with Type I particles (Figs. 15b and 15c). At $y/D=1$ (Fig. 15b), both Type III and Type IV particles are strongly influenced by the coherent motion. The droplet number density is very high during the downward motion of the deflected upper shear layer and very low during the subsequent upward motion. No number density peak is observed during the latter motion. The lower vortex has no longer any effect so far from the centerline so that droplet feeding from the lower vortex may no longer occur at that location. However, high droplet concentrations are convected with the downward motion of the deflected shear layer, which may be sufficient to feed the centerline region ($y/D\approx 0$) with large droplets and would explain the sharp increase in the concentration of the larger droplets observed downstream of the recirculation region (Fig. 6). The droplet motion will decelerate under the influence of the subsequent upward motion. However, because of their larger inertia, larger particles will decelerate less quickly than the smaller ones. At $y/D=1.25$ (Fig. 15c), cross-stream velocity and number density profiles of Type III and Type IV particles still differ significantly from those of the fluid (Type I). Low cross-stream velocity magnitudes, as well as lower concentrations, are noticed during the upward motion.

Conclusion

The results for an investigation on the dispersion of droplets in the near-wake of a square cylinder have been presented. The effect of shed vortices on the particle size and velocity distributions in the wake of a square-cross-section cylinder were measured with a phase-Doppler anemometer. Results were first given in terms of time-averaged properties, and then analyzed by phase-averaging using double decomposition for a fully turbulent flow. The mechanism for entraining larger particles towards the cylinder centerline ($y/\mathrm{D}=0$), and thus improving mixing, was described from wake flow velocity characteristics. It is found that the coherent motion has a strong influence on the particle trajectory and that particle slip velocity cannot be neglected for droplets larger than 10 μm diameter, that is for Stokes numbers larger than 0.1.

The flow is mainly composed of two regions, which can roughly be separated by the streamline associated with the maximum streamwise velocity. This leads to an inner-wake region where particle statistics depend strongly on their size, and an outside region where these statistics are similar for all studied droplet diameters (up to $\overline{d_p}=56.9\ \mu$m). In the near wake ($x/\mathrm{D}<4$), poor lateral mixing is observed. High streamline curvatures and high streamwise velocities accentuate inertial effects. In the recirculation region directly behind the cylinder, only particles smaller than 10 μm were found. Larger particles tend to be concentrated along the outer side of the shear layer. The ejection process of heavy particles from vortices' cores is an essential additional phenomenon complementing the description of the droplet dispersion process. These effects result in clearly identifiable lag between particle motion and flow field, which is significant for particles bigger than 15 μm. The spatial reorganization and redistribution of particles due to the vortex motion is very strong in the very near-wake, as expected, but also persists far downstream. The effect of the coherent motion results in instantaneous, nonhomogeneous spatial distributions. However, since time-averaged statistics are inherently biased towards peak concentration events, the mean distributions are fairly homogeneous, for which interpretation can be misleading and thus to be treated with caution.

References

[1] Lyn, D. A., Einav, S., Rodi, W., and Park, J.-H., 1995, ''A Laser-Doppler Velocimetry Study of Ensemble-Averaged Characteristics of the Turbulent Near Wake of a Square Cylinder,'' J. Fluid Mech., **304**, pp. 285–319.

[2] Durao, D. F. G., Heitor, M. V., and Pereira, J. C. F., 1986, ''A Laser Anemometry Study of Separated Flow Around a Squared Obstacle,'' in *Laser Anemometry in Fluid Mechanics III* (Ed. R. J. Adrian et al.), LADOAN-IST, Lisbon, Portugal.

[3] Wu, K. C. Q., and Martinuzzi, R. J., 1997, ''An Experimental Investigation of the Flow Around a Two-Dimensional Square Prism in the Proximity of a Solid Wall: Effect of the Gap Size,'' *Proc. 11th Symposium on Turb. Shear Flows*, Grenoble, France, pp. 1116–1121.

[4] Bearman, P. W., and Obasaju, E. D., 1982, ''An Experimental Study of Pressure Fluctuations on Fixed and Oscillating Square-Section Cylinders,'' J. Fluid Mech., **119**, pp. 297–321.

[5] Haidn, O. J., Bailey, S. C. C., and Martinuzzi, R. J., 1999, ''Relating Pressure Field and Vortex Shedding Suppression for a Square Cylinder in the Vicinity of a Solid Wall,'' *Proc. 1st Int. Symposium on Turbulence and Shear Flow Phenomena*, Santa Barbara, U.S.A., pp. 1039–1044.

[6] Eaton, J. K., and Fessler, J. R., 1994, ''Preferential Concentration of Particles by Turbulence,'' Int. J. Multiphase Flow, **20** (Supplement), pp. 169–209.

[7] Crowe, C. T., Chung, J. N., and Troutt, T. R., 1988, ''Particle Mixing in Free Shear Flows,'' Prog. Energy Combust. Sci., **14**, pp. 171–194.

[8] Lazaro, B. J., and Lasheras, J. C., 1989, ''Particle Dispersion in a Turbulent, Plane, Free Shear Layer,'' Phys. Fluids A, **1**, pp. 1035–1044.

[9] Wen, F., Kamalu, N., Chung, J. N., Crowe, C. T., and Troutt, T. R., 1992, ''Particle Dispersion by Vortex Structures in Plane Mixing Layers,'' ASME J. Fluids Eng., **114**, pp. 657–666.

[10] Lazaro, B. J., and Lasheras, J. C., 1992, ''Particle Dispersion in the Developing Free Shear Layer. Part 1. Unforced Flow,'' J. Fluid Mech., **235**, pp. 143–178.

[11] Lazaro, B. J., and Lasheras, J. C., 1992, ''Particle Dispersion in the Developing Free Shear Layer. Part 2. Forced Flow,'' J. Fluid Mech., **235**, pp. 179–221.

[12] Kiger, K. T., and Lasheras, J. C., 1995, ''The Effect of Vortex Pairing on Particle Dispersion and Kinetic Energy Transfer in a Two-Phase Turbulent Shear Layer,'' J. Fluid Mech., **302**, pp. 149–178.

[13] Martin, J. E., and Meiburg, E., 1994, ''The Accumulation and Dispersion of Heavy Particles in Forced Two-Dimensional Mixing Layers. I. The Fundamental and Subharmonic Cases,'' Phys. Fluids, **6**(3), pp. 1116–1132.

[14] Laitone, J. A., 1981, ''A Numerical Solution for Gas-Particle Flows at High Reynolds Numbers,'' J. Appl. Mech., **48**, pp. 465–471.

[15] Chein, R., and Chung, J. N., 1988, ''Particle Dynamics in a Gas-Particle Flow Over Normal and Inclined Plates,'' Chem. Eng. Sci., **43**(7), pp. 1621–1636.

[16] Tang, L., Wen, F., Yang, Y., Crowe, C. T., Chung, J. N., and Troutt, T. R., 1992, ''Self-Organizing Particle Dispersion Mechanism in a Plane Wake,'' Phys. Fluids A, **4**(10), pp. 2244–2251.

[17] Bachalo, W. D., Bachalo, E. J., Hanscom, J., and Sankar, S. V., 1993, ''An Investigation of Spray Interaction With Large-Scale Eddies,'' Proc. *AIAA 31st Aerospace Sciences Meeting*, Reno, NV, paper AIAA 93-0696.

[18] Bachalo, W. D., 1994, ''Experimental Methods in Multiphase Flows,'' Int. J. Multiphase Flow, **20** (Supplement), pp. 261–295.

[19] Crowe, C. T., Troutt, T. R., Chung, J. N., Davis, R. W., and Moore, E. F., 1995, ''A Turbulent Flow Without Particle Mixing,'' Aerosol Sci. Technol., **22**, pp. 135–138.

[20] Burns, T. J., Davis, R. W., and Moore, E. F., 1999, ''A Perturbation Study of Particle Dynamics in a Plane Wake Flow,'' J. Fluid Mech., **384**, pp. 1–26.

[21] Borée, J., Ishima, T., and Flour, I., 2001, ''The Effect of Mass Loading and Inter-Particle Collisions on the Development of the Polydispersed Two-Phase Flow Downstream of a Confined Bluff Body,'' J. Fluid Mech., **443**, pp. 129–165.

[22] Chung, J. N., and Troutt, T. R., 1988, ''Simulation of Particle Dispersion in an Axisymmetric Jet,'' J. Fluid Mech., **186**, pp. 199–222.

[23] Longmire, E. K., and Eaton, J. K., 1992, ''Structure of a Particle-Laden Round Jet,'' J. Fluid Mech., **236**, pp. 217–257.

[24] Sakakibara, J., Wicker, R. B., and Eaton, J. K., 1996, ''Measurements of the Particle-Fluid Velocity Correlation and the Extra Dissipation in a Round Jet,'' Int. J. Multiphase Flow, **22**(5), pp. 863–881.

[25] Raju, N., and Meiburg, E., 1997, ''Dynamics of Small, Spherical Particles in

Vortical and Stagnation Point Flow Fields,'' Phys. Fluids, **9**(2), pp. 299–314.
[26] Hussain, A. K. M. F., 1983, ''Coherent Structures—Reality and Myths,'' Phys. Fluids, **26**(10), pp. 2816–2850.
[27] Saffman, M., 1987, ''Automatic Calibration of LDA Measurement Volume Size,'' Appl. Opt., **26**(13), pp. 2592–2597.
[28] Abernethy, R. B., Benedict, R. P., and Dowdell, R. B., 1985, ''ASME Measurement Uncertainty,'' ASME J. Fluids Eng., **107**, pp. 161–164.
[29] Edwards, R. V., 1987, ''Report of the Special Panel on Statistical Particle Bias Problems in Laser Anemometry,'' ASME J. Fluids Eng., **109**, pp. 89–93.
[30] Benedict, L. H., and Gould, R. D., 1996, ''Towards Better Uncertainty Estimates for Turbulence Statistics,'' Exp. Fluids, **22**, pp. 129–136.
[31] Saha, A. K., Biswas, G., and Muralidhar, K., 2001, ''Two-Dimensional Study of the Turbulent Wake Behind a Square Cylinder Subject to Uniform Shear,'' ASME J. Fluids Eng., **123**, pp. 595–603.

Donghong Gao*
Neil B. Morley
Vijay Dhir

Department of Mechanical and Aerospace Engineering,
University of California,
Los Angeles, CA 90095

Understanding Magnetic Field Gradient Effect From a Liquid Metal Droplet Movement

A two-dimensional liquid metal droplet moving into magnetic field gradient regions in a vacuum space in the absence of gravity has been simulated in VOF-CSF method. The general one-fluid VOF model for tracking free surfaces, and associated CSF model for applying surface tension to free surfaces are formulated. The calculations show us that the droplet encounters strong magnetohydrodynamics (MHD) drag from the field gradient along moving path. Interaction of liquid motion with a magnetic field induces electrical currents and Lorentz force on the droplet. The force is always to oppose the liquid motion in both increased and decreased field conditions. More attention is given to understanding the MHD equations and numerical results. [DOI: 10.1115/1.1637638]

Introduction

Interest in liquid metal magnetohydrodynamics (MHD) arises from the possibility of utilizing liquid metal film flows or droplet curtains in future magnetic confined fusion for protection of solid structures from the thermonuclear plasma [1]. Interaction between magnetic field and electrically conducting flow induces electrical currents in the flow. Steady duct MHD flows in a uniform magnetic field have been well understood in regard to the Hartmann layers and side layers [2,3]. Quite different from Hartmann-type problems where the closure of induced currents is in the plane perpendicular to streamwise, the currents induced by a potential variation of velocity or magnetic field along flow direction encircle in the plane parallel to stream-wise. Some studies on the induction effect from velocity field variation can be found in references [2,4]. Recently, the studies by Sellers and Walker [5], Gao et al. [6,7] and Morley et al. [8] pay more attention to spatial field variations due to the fact that potential field gradients exist in fusion environment. Now, 3-D numerical modeling and experimental study for MHD free-surface flows in complex fusion-like magnetic environment can be found in a recent article by Morley et al. [9]; interim reports are available on website www.fusion.ucla.edu/apex, where the works by Neil Morley et al. are more-closely about the liquid metal MHD. A 2-D modeling with focus on the field gradient can be found in the dissertation by Gao [10].

The purpose of this study is to improve our understanding of the field gradient induction effect through simulations of droplet movement in field gradient regions in a 2-D regime. The droplet is given an initial uniform velocity in the absence of gravity. Without magnetic field, the droplet simply moves like a solid ball at a constant velocity. However, when a magnetic field gradient is applied along its moving path, complex interaction between magnetic field and flow field makes it too difficult for us to obtain an analytical solution to the seemingly simple droplet movement. In the case here, the numerical simulation is a useful tool to understanding physical principles because we can concentrate on one factor, but experimental settlement is difficult or impossible. Moreover, the experimental results are often the visualization of all physical principles.

We choose to simulate the time-dependent governing equations by the finite volume scheme using a volume-of-fluid (VOF) free surface tracking method. The VOF method [11–13] is based on fixed staggered grid and widely used in the free surface simulation. The VOF method, instead of tracking free surfaces explicitly, tracks the volume fraction of fluid in each cell to avoid topological restriction which happens for most direct surface tracking method. Scardovelli and Zaleski [13] provided a comprehensive and informative review on numerical methods for tracking interface and applying discontinuity conditions at the interface with emphasis on VOF methods. They provided formulations from several aspects and summarized problems with VOF methods. In the present work, the projection method is used for solving the Navier-Stokes equations. The van Leer second-order accurate convection scheme is adopted from RIPPLE [11]. The split operator scheme from Puckett et al. [14] is used for the VOF advection. The dynamic conditions at free surface are numerically implemented through the continuum surface force (CSF) model [11,15] in conjunction with VOF method. The general CSF model often results in so-called spurious currents [13,16] at neighborhood of free-surface. A more accurate representation of surface tension term can be found in [16].

Some advantages of this case are listed in the following respects. One is that we do not need to concern boundary conditions. The boundary condition in the VOF method does not matter when the droplet moves in vacuum. Also, in the absence of magnetic field and gravity field, the solution is known, but calculation for such a simple case is still presented for checking the numerical scheme in some senses and for comparison with MHD droplet movement. For a MHD droplet moving in a field gradient region, the electromagnetic force is the only external force acting on the droplet. Changing the magnetic conditions, we should be able to see easily the corresponding changes. From these simulation results at various properly designed magnetic field conditions, we can understand the MHD effect to some extent.

Governing Equations

The velocity field $\mathbf{V}=(u,v,0)$ and the *del* operator $\nabla=(\partial/\partial x,\partial/\partial y,0)$ are considered two-dimensional in the x-y plane. The applied magnetic field $\mathbf{B}_a=(0,0,B[x,y,t])$ is aligned in the z-direction and can in general vary both temporally and spatially in the x-y plane. The field gradient interacts with liquid metal motion, producing electrical currents and thereby the Lorentz force in x-y plane [2]. The induced currents in turn build their own magnetic field B_i, which is also aligned in z-direction. We actually use scalar variables B_a and B_i to represent the applied and induced field because only one component of a vector is involved here. The field gradient effect can be studied by the 2-D model

*Corresponding author e-mail: donghong@seas.ucla.edu; mail: Mechanical and Aerospace Engineering Dept., 43-133 Engineering IV, University of California Los Angeles, Los Angeles, CA 90095.

Contributed by the Fluids Engineering Division for publication in the JOURNAL OF FLUIDS ENGINEERING. Manuscript received by the Fluids Engineering Division January 9, 2003; revised manuscript received September 3, 2003. Associate Editor: S. Balachandar.

[6,10] (other variants of this infinite and/or axisymmetric 2-D model can be seen in [8]). In a VOF model, two immiscible fluids in the computational area are considered, and interfaces, or free-surfaces, are no longer grid boundaries. The surface tension term at an interface is transformed to a volume force F_{sv} which is only non-zero within a limited thickness of interface region. The scalar field f is defined to denote the volume fraction of the fluid whose dynamics we really want to know. The f follows fluid motion and satisfies the advection equation. Therefore, in a VOF method, the incompressible liquid metal flow is described by the time-dependent electromagnetic induction equation [8], momentum equation, mass conservation, and VOF advection [11,13]:

$$\frac{\partial B_i}{\partial t}+(\mathbf{V}\cdot\nabla)B_i=\frac{1}{\mu_m}\nabla\cdot\left(\frac{1}{\sigma_e}\nabla B_i\right)-(\mathbf{V}\cdot\nabla)B_a-\frac{\partial B_a}{\partial t}, \quad (1)$$

$$\frac{\partial \mathbf{V}}{\partial t}+(\mathbf{V}\cdot\nabla)\mathbf{V}=-\frac{1}{\rho}\nabla p+\frac{1}{\rho}\nabla\cdot(2\mu\mathbf{D})+\frac{1}{\rho}\mathbf{F}_{sv}+\frac{1}{\rho\mu_m}(\nabla\times B_i\hat{z})B_a\hat{z}, \quad (2)$$

$$\nabla\cdot\mathbf{V}=0, \quad (3)$$

$$\frac{\partial f}{\partial t}+\nabla\cdot(f\mathbf{V})-f\nabla\cdot\mathbf{V}=0, \quad (4)$$

where $\mathbf{D}$ is the strain-rate tensor $\mathbf{D}_{ij}=1/2(\partial_j u_i+\partial_i u_j)$, p the pressure, and ρ, μ, σ_e, μ_m are respectively density, dynamic viscosity μ, electrical conductivity σ_e, magnetic permeability. The μ_m can be considered to be constant for non-ferromagnetic material. The gravity is set to zero here in order to highlight the MHD effect. The properties of the mixture are estimated by the volume-weighted average of two fluids:

$$\rho=f\rho_1+(1-f)\rho_2, \quad (5)$$

$$\mu=f\mu_1+(1-f)\mu_2, \quad (6)$$

$$\sigma_e=f\sigma_{e,1}+(1-f)\sigma_{e,2}, \quad (7)$$

For the free-surface flows in vacuum or light-gas surrounding, the dynamics of this side can be ignored, and a two-fluid VOF model is simplified to one-fluid/void model where ρ_2, μ_2, $\sigma_{e,2}$ are zero.

As a matter of fact, B_i is very small (about 10^{-4} times the applied field as will be shown in the calculations) for the liquid metal MHD. Its real role is to represent induced current density $\mathbf{j}$ because of:

$$\mathbf{j}=\frac{\nabla\times B_i\hat{z}}{\mu_m}. \quad (8)$$

The B_i contours function as streamlines of induced currents. The induction equation, Eq. (1), reveals that the source term of induced magnetic field (electrical currents) comes from the spatial or temporal variation of the applied magnetic field; it does not depend at all on the absolute value of applied field. The inducted currents are also transported by diffusion and convection as in general transport equation. The induced currents are confined in liquid flow, in other words, $j_n=0$. The condition is interpreted as B_i=Constant along free-surfaces, and thus B_i is set to zero for convenience in calculations.

The surface tension is taken into account by incorporating a volume force F_{sv} into the momentum equations. At an interface the normal stress is balanced by capillary force, and the shear stress vanishes for the liquid with constant properties. The volume force F_{sv} is defined in the VOF-CSF model [11,13,15].

$$\mathbf{F}_{sv}=\sigma\kappa\nabla f, \quad (9)$$

where σ is the surface tension coefficient, and κ is the curvature of surface. The relation shows that F_{sv} is concentrated on interface regions; away from interfaces it is zero due to $\nabla f=0$. The interface characteristic values: the outward normal $\mathbf{n}$ and curvature κ, are calculated as:

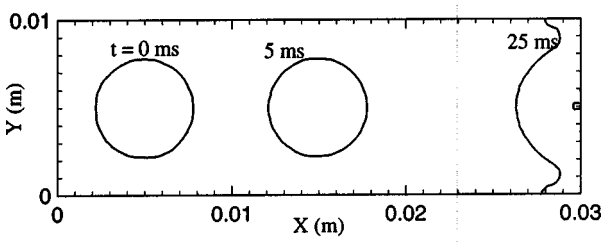

Fig. 1 Droplet movement in the absence of magnetic field and gravity

$$\mathbf{n}=(n_x,n_y)=-\nabla f, \quad \hat{n}=\mathbf{n}/|\mathbf{n}| \quad (10)$$

$$\kappa=(\nabla\cdot\hat{n})=-\frac{1}{|\mathbf{n}|}\left[\left(\frac{\mathbf{n}}{|\mathbf{n}|}\cdot\nabla\right)|\mathbf{n}|-(\nabla\cdot\mathbf{n})\right]=-\frac{1}{|\mathbf{n}|}\left[\frac{n_x^2}{|\mathbf{n}|^2}\frac{\partial n_x}{\partial x}+\frac{n_x n_y}{|\mathbf{n}|^2}\left(\frac{\partial n_x}{\partial y}+\frac{\partial n_y}{\partial x}\right)+\frac{n_y^2}{|\mathbf{n}|^2}\frac{\partial n_y}{\partial y}-\frac{\partial n_x}{\partial x}-\frac{\partial n_y}{\partial y}\right] \quad (11)$$

The VOF advection equation, Eq. (4), is adopted from Puckett et al. [14]. As indicated by Scardovelli and Zaleski [13], the VOF advection equation can not be differentiated as we do to a general partial differential equation, such as Navier-Stokes equation. Actually, it is only well-defined in integrals, expressing the volume (mass) conservation during interface (free-surface) advection. Therefore, an approximate free-surface needs to be constructed from the volume fraction data when we solve Eq. (4). Here, a curvy free-surface is represented as segment straight lines. A line function is determined by its slope and intersection length in its local x-y coordinates with the origin at cell center. The slope is obtained from surface normal $\mathbf{n}$ and the intersection is determined by the volume fraction of liquid in the cell f and the slope. More details about implementation of the VOF model and verification for the numerical scheme are available in Refs. [10,17]. The computation time step is controlled by parameters such as velocity, surface tension, viscosity and mesh size, and encoded in the code. The most time-consuming part is the solving of the pressure Poisson equation, which is done by using the LU factorization solver residing in ESSL and IMSL math library on RS/6000 cluster machines.

Results and Discussion

The liquid Lithium droplet is given the initial velocity 1 m/s to move into several different field gradient regions in a vacuum space without gravity. The velocity is chosen to easily show MHD effect since the intensity of induced currents increases with moving velocity. The computational area is 3 cm in x-direction and 1 cm in y-direction, the grid number is 120 in x-axis and 40 in y-axis. The droplet originally sits at (0.5 cm, 0.5 cm).

The ordinary droplet in the absence of magnetic field is first calculated. The positions and shapes of the droplet at a series of moments are shown in Fig. 1. The solution is well agreed with our expectation that the ordinary droplet moves in vacuum at the constant speed.

The droplet is then shot into a field gradient region between $x=[1,1.5]$ cm, where the magnetic field linearly increases from zero at $x=1$ cm to 1 T at $x=1.5$ cm. B_a is zero in $x<1$ cm, and remains 1 T after $x>1.5$ cm. The field gradient is 200 T/m in x-direction, which is a very large gradient. The droplet movement is modified by induced electromagnetic force as shown in Fig. 2. Here and in the following, the applied magnetic field gradient region is marked by the two vertical lines. It is apparent that the droplet has moved much shorter distance than the ordinary droplet in 25 ms. It encounters opposition so-called MHD drag. For better understanding the MHD drag, contours of the induced field B_i are shown in Fig. 3. The magnitude of B_i decreases with the depth

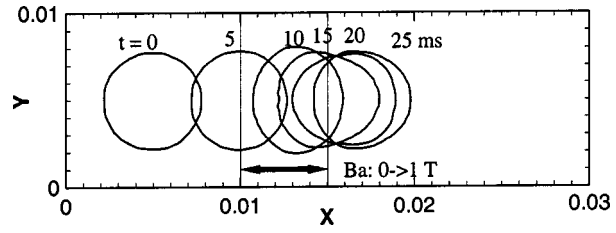

Fig. 2 Droplet movement in the field increasing from 0 T to 1 T at $x=[1,1.5]$ cm

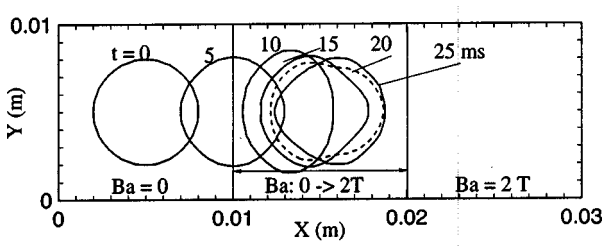

Fig. 4 Droplet movement in the field increasing from 0 T to 2 T at $x=[1,2]$ cm

into center with the biggest ($Bi_{\max}=0$) at the outermost surface. As state by Eq. (8), the B_i contours reflect the electrical current field. The strength of a current field is indicated by the density of contour lines. The currents encircle clockwise following the droplet shape, and thus the resultant electromagnetic force presses the droplet into inside. But the force is not uniformly distributed due to the spatially varying field. In an increased field region, the backward electromagnetic force acting on the front-half is larger than the forward force acting on the rear-half, resulting in the MHD drag effect. The droplet is also squeezed into the elongated shape as shown in Fig. 2 for $t=10$ ms.

The strength of induced currents is proportional to the magnitude of velocity field. This can be seen from the decreasing minimum value of B_i, i.e., $Bi_{\min}$ in the figure, as the movement is slowed down. When the droplet still has dominant forward-moving velocity, the electrical currents should close co-centered as shown by B_i contours in Fig. 3, According to induction Eq. (1), the source of generating currents is located inside the field gradient region. After the droplet comes out of field gradient region, it will keep moving at the velocity obtained at the end of field gradient region, but the shape may change because the relative velocity is already generated inside the droplet.

As the field gradient region is elongated to 1 cm, the droplet with the initial velocity may be stopped by MHD drag as shown in Fig. 4. The droplet almost does not change position after 20 ms, but it indeed changes the shape. This behavior implies the velocity field is not zero everywhere like a solid ball. There must be relative velocities between different parts of fluid inside the droplet. This can be confirmed from the contours of B_i shown in Fig. 5, where the non-co-centered B_i contours occur. In contrast, at the beginning when the droplet has dominant forward velocity and negligible relative velocity, the B_i contours are co-centered. The problem of spurious velocity field [16] due to the CSF representation of surface tension may contribute to the oscillation at the stopping state. But the relative velocity field is also dictated by physics in the case here. The spurious velocity problem is more difficult to identify because of the complex coupling between velocity field and magnetic field. Popinet and Zaleski [16] pointed out the spurious velocity may cause computational difficulty, but we did not encounter any numerical convergence problem for this work. This may be due to the one-fluid model so that the coefficients of discretized pressure Poisson equation are adjusted to yield zero pressure in void side.

The increased and decreased field gradients put same resistance on the droplet movement. The droplet is put in the opposite magnetic field distribution, where B_a decreases from 2 T to zero in $x=[1,2]$ cm, and $B_a=2$ T at $x<1$ cm, $B_a=0$ at $x>2$ cm. The result is shown in Fig. 6. Comparing with the preceding case with increased field, we see the very similar deceleration of movement from the decreased field region. A little difference is that the droplet here is decelerated slightly faster than the preceding one. This is caused by the larger absolute value of applied field here around $x=1$. At the same velocity field and same field gradient, the induction equation model states that the same magnitude currents except current directions will be induced, but the electromagnetic force generated by the cross product of induced current and mag-

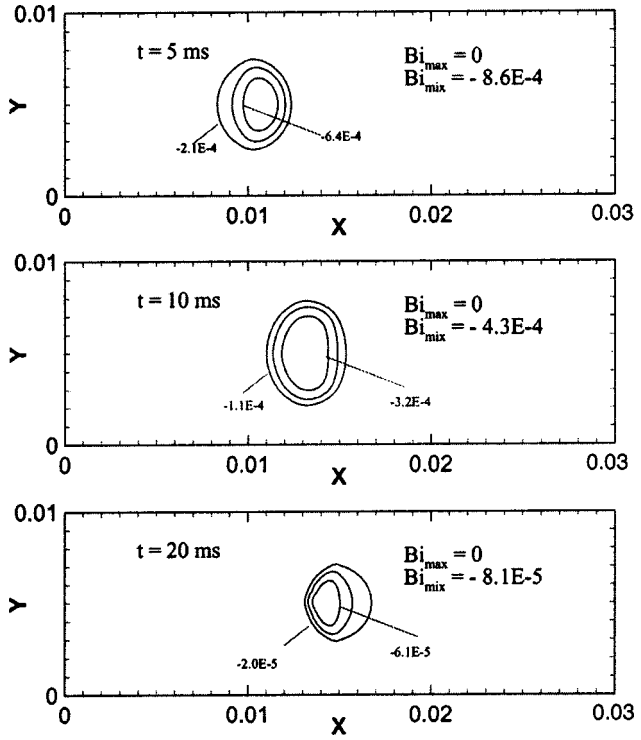

Fig. 3 B_i contours for the droplet in field increasing from 0 T to 1 T at $x=[1,1.5]$ cm

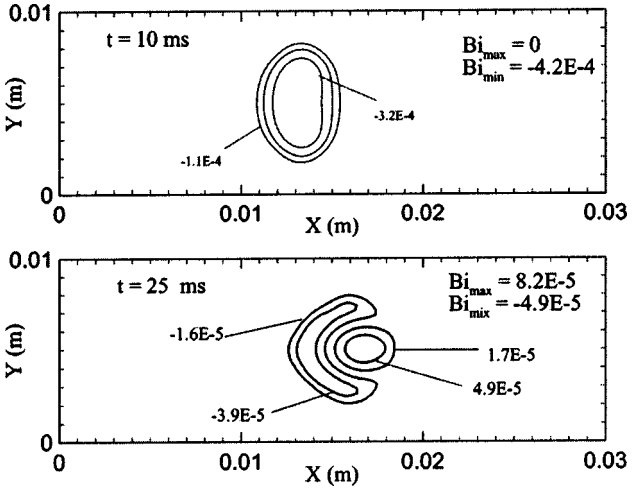

Fig. 5 B_i contours for the droplet in field increasing from 0 T to 2 T at $x=[1,2]$ cm

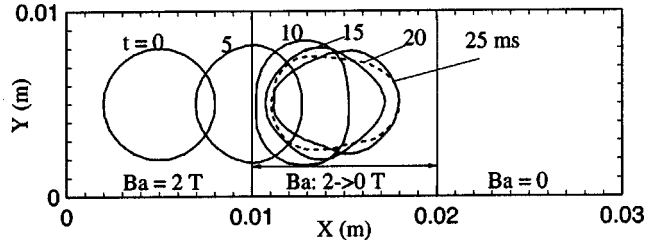

Fig. 6 Droplet movement in the field decreasing from 2 T to 0 T at $x=[1,2]$ cm

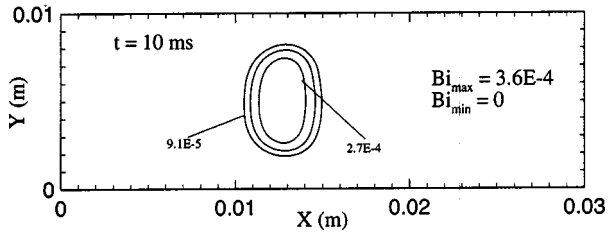

Fig. 7 B_i contours at 10 ms for field decreasing from 2 T to 0 T at $x=[1,2]$ cm

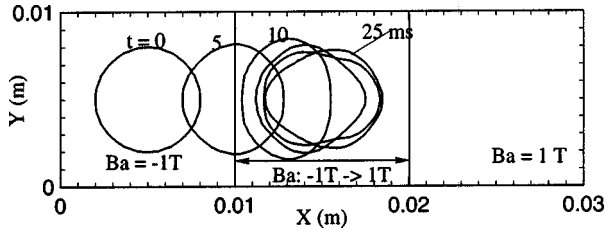

Fig. 8 Droplet movement in the field increasing from −1 T to 1 T at $x=[1,2]$ cm

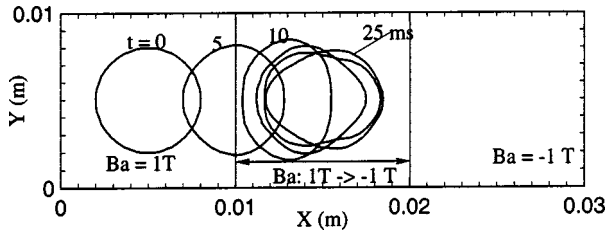

Fig. 9 Droplet movement in the field decreasing from 1 T to −1 T at $x=[1,2]$ cm

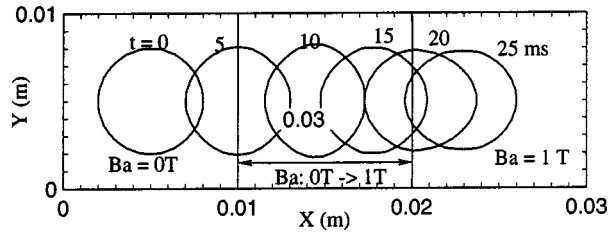

Fig. 10 Droplet movement in the field increasing from 0 T to 1 T at $x=[1,2]$ cm

netic field is proportionally larger for the larger field, resulting in larger drag at beginning of the course. The induced currents at 10 ms are illustrated in Fig. 7, and it is shown that the B_i is nearly the counterpart of the B_i in Fig. 5. The B_i here in the decreased field represents counterclockwise currents instead of clockwise currents in an increased field. $Bi_{max}-Bi_{min}=3.6E-4$ here is a little bit smaller than $Bi_{max}-Bi_{min}=4.2E-4$ for the last case because at 10 ms, the droplet already moves slower than the droplet in the last case.

As another example to see the same MHD drag from increased field and decreased field, we have computed the droplet movements in the magnetic field increasing from −1 T to 1 T in the region of $x=[1,2]$, and in the field decreasing from 1 T to −1 T in the same region. The only difference for the two conditions is the direction of field gradient. The results are shown in Figs. 8 and 9. The positions and shapes of the droplet at a series of moments are nearly the same for these two conditions,

All the above cases have the field gradient 200 T/m. To clearly show that the MHD drag is more than linearly related to field gradient, the movement of the droplet in the magnetic field which linearly increases from 0 T to 1 T in the region of $x=[1,2]$ cm is shown in Fig. 10. Compared with Fig. 4, it is shown that in this smaller field gradient the droplet encounters much less resistance so that it can come through the field gradient region. Indeed, from our understanding of preceding results shown in Figs. 2 and 3, strength of induced currents is linearly proportional to the magnitude of field gradient, and MHD drag magnitude is quadratic to the increase of field gradient.

Conclusions

We have calculated the 2-D (x-y) liquid metal droplet movement in different magnetic field gradient conditions. A VOF-CSF numerical method is used to deal with free-surfaces advection and application of discontinuity conditions at free surfaces. The basic numerical model and a 2-D MHD model have been presented. The results point to the field gradient opposition effect on liquid metal movement. Interaction of liquid metal motion with the field gradient induces electrical currents, thereby creating Lorentz force on the droplet. The strength of induced current field is proportional to field gradient magnitude and velocity magnitude, but independent of the absolute value of field. Due to the spatial field gradient, the backward electromagnetic force is always larger than the forward force in both increased field and decreased field conditions, causing the MHD drag from field gradient along moving direction. The drag increases quadratically with the increase of field gradient. The MHD drag decelerates the droplet and may stop it, placing cautions for possible engineering applications.

Acknowledgments

The authors would like to gratefully acknowledge the support of U.S. Department of Energy through Grant No. DE-FG03-86ER52123, and the support of Professor Mohamed Abdou at UCLA.

References

[1] Abdou, M. A., Ying, A., Morley, N. et al., 2001, ''On the Exploration of Innovative Concepts for Fusion Chamber Technology-APEX Interim Report Overview,'' Fusion Eng. Des., **54**, pp. 181–247.

[2] Branover, H., 1978, *Magnetohydrodynamic Flows in Ducts*, Israel University Press, Jerusalem, Israel.

[3] Hunt, J. C. R., and Shercliff, J. A., 1971, ''Magnetohydrodynamics at High Hartmann Number,'' Annu. Rev. Fluid Mech., **3**, pp. 37–62.

[4] Lielausis, O., 1975, ''Liquid-Metal Magnetohydrodynamics,'' At. Energy Rev., **13**, pp. 527–581.

[5] Sellers, C. C., and Walker, J. S., 1999, ''Liquid Metal Flow in an Electrically Insulated Rectangular Duct With a Non-Uniform Magnetic Field,'' Int. J. Eng. Sci., **37**(5), pp. 541–552.

[6] Gao, D., and Morley, N. B., 2002, ''Equilibrium and Initial Linear Stability Analysis of Liquid Metal Falling Film Flows in a Varying Spanwise Magnetic Field,'' Magnetohydrodynamics, **38**, pp. 359–375.

[7] Gao, D., Morley, N. B., and Dhir, V., 2002, ''Numerical Study of Liquid Metal Film Flows in a Varying Spanwise Magnetic Field,'' Fusion Eng. Des., **63–64**, pp. 369–374.

[8] Morley, N. B., Smolentsev, S., and Gao, D., 2002, ''Modeling Infinite/Axisymmetric Liquid Metal Magnetohydrodynamic Free Surface Flows,'' Fusion Eng. Des., **63–64**, pp. 343–351.

[9] Morley, N. B., Smolentsev, S., Munipalli, R., Ni, M.-J., Gao, D., and Abdou, M., 2003, ''Modeling of Liquid Metal Free Surface MHD Flow for Fusion Liquid Walls,'' Fusion Eng. Des.

[10] Gao, D., 2003, ''Numerical Simulation of Surface Wave Dynamics of Liquid Metal MHD Flow on an Inclined Plane in a Magnetic Field With Spatial Variation,'' Ph.D. Dissertation, University of California, Los Angeles.

[11] Kothe, D. B., Mjolsness, R. C., and Torrey, M. D., 1991, ''RIPPLE: A Computer Program for Incompressible Flows With Free Surfaces,'' LA-12007-MS, Los Alamos National Laboratory.

[12] Rider, W. J., and Kothe, D. B., 1998, ''Reconstructing Volume Tracking,'' J. Comp. Physiol., **141**, pp. 112–152.

[13] Scardovelli, R., and Zaleski, S., 1999, ''Direct Numerical Simulation of Free-Surface and Interfacial Flow,'' Annu. Rev. Fluid Mech., **31**, pp. 567–603.

[14] Puckett, E. G., Almgren, A. S., Bell, J. B. et al., 1997, ''A High-Order Projection Method for Tracking Fluid Interfaces in Variable Density Incompressible Flows,'' J. Comput. Phys., **130**, pp. 269–282.

[15] Brackbill, J. U., Kothe, D. B., and Zemach, C., 1992, ''A Continnum Method for Modeling Surface Tension,'' J. Comput. Phys., **100**, pp. 335–354.

[16] Popinet, S., and Zaleski, S., 1999, ''A Front-Tracking Algorithm for Accurate Representation of Surface Tension,'' Int. J. Numer. Mech. Fluids, **30**, pp. 775–793.

[17] Gao, D., Morley, N. B., and Dhir, V., 2003, ''Numerical Simulation of Wavy Falling Film Flows Using VOF Method,'' J. Comput. Phys., to appear.

P. V. Skudarnov

C. X. Lin*

M. A. Ebadian

Hemispheric Center for Environmental Technology,
Florida International University,
10555 W. Flagler St., EC 2100,
Miami, FL 33174

Double-Species Slurry Flow in a Horizontal Pipeline

Slurry transport experiments were performed with five double-species slurries composed of glass beads and water. The double-species glass beads were various combinations of beads having two widely different densities and three narrow particle size distributions. Pressure gradients for double-species slurries were compared to those for individual components at the same solids volume concentrations. Effect of mean particle diameter on pressure gradient of double-species slurry in the pipe was studied. Experiments were performed in a horizontal pipe flow loop of 23 mm internal diameter. Obtained data are useful for pipeline systems design and also valuable for verification of numerical simulations of the slurry flows. [DOI: 10.1115/1.1637925]

1 Introduction

Pipeline systems are widely used in the transportation of coal, iron ore, mineral concentrates, ore tailings, and sewage sludge [1,2]. In many of these applications, transported slurries are complex multi-species mixtures containing solids with different densities and particle sizes. In the past, most of the theoretical and experimental studies dealt with only single-species slurries such as sand- or coal-water mixtures [1–3]; little is known about multi-species slurries. Several multi-species slurries were tested at Saskatchewan Research Council [4,5]; however, tested slurries were very specific in composition to simulate uranium ore, and no systematic study was undertaken to study the effect of individual components on overall slurry transportation properties. Roco and Shook [6] developed a space/time averaged approach to model multi-species slurry flow numerically, but their model was only tested for coal-water slurry with coal particles having different densities in the narrow range of 1310 kg/m^3 to 1730 kg/m^3. Several studies were dedicated to the effect of particle size in single-species slurries on pipeline flow [7–11]; these slurries contained solids of the same density but different particle sizes. In contrast, the effect of particle size in multi-species slurry with solids of different densities is unknown.

The current design of pipeline systems based on the studies of single-component slurries causes substantial limitation of safety and efficiency. Thus, there is a significant need to study multi-species slurry transportation in order to build a scientific basis for better pipeline system design in the future.

For this paper, we studied double-species slurries composed of well-characterized spherical glass beads of various mean particle diameters and densities. Pressure gradient in a pipe versus flow velocity relationships for several double-species slurries were measured experimentally in the horizontal pipeline flow loop. Obtained data are useful for pipeline systems design and also valuable for verification of numerical simulations of the slurry flows since the solid particles of the tested slurries are spherical and closely sized.

2 Experimental Facility

2.1 Flow Loop. Measurements of slurry transport characteristics were performed in a flow loop of a closed type (with mixture returning from the loop directly into a pump inlet). The schematic diagram of the flow loop used in this study is shown in Fig. 1. The loop is constructed out of 25 mm O.D. (I.D. $D=23$ mm) stainless steel circular tubing. The slurry is circulated in the loop with a Svedala MM25 centrifugal slurry pump equipped with a variable speed drive. The loop has a 68-liter conical supply tank. The loop is also equipped with a heat exchanger and constant temperature bath to maintain slurry temperature constant. There are two *K*-type thermocouples installed near the loop inlet and outlet to measure slurry temperature. The loop is 17 m long and has two 130 *D* flow development sections followed by pressure drop measurement sections. The length of the flow development sections was chosen to ensure that the flow is fully developed when it enters the measurement section; minimum flow development section should be at least 50 *D* [1,12]. Pressure drops in the two 158 *D* horizontal straight measurement sections of the flow loop are measured with Rosemount 3051 differential pressure transmitters. The volume and mass flow rates as well as slurry density are measured with a Micro Motion T-100 Coriolis mass flow meter. The pressure transmitters, the thermocouples, and the flow meter are connected to a National Instruments data acquisition system, which is controlled by a LabView program. The data acquisition system allows simultaneous measurement of pressure gradients, mass and volume flow rates, and slurry temperature. The same LabView program is used to calculate solids volume concentration in the slurry from known solids and liquid densities and measured slurry density:

$$C_v=\frac{\rho_{sl}-\rho_l}{\rho_s-\rho_l} \tag{1}$$

The experimental procedure for each test run consists of the following. First, the supply tank is filled with carrier fluid (water), and the pump is started. Next, while water is circulating in the loop at a flow velocity well above the stationary bed velocity, the solids are gradually introduced into the loop through the supply tank, and the slurry concentration is monitored with the Coriolis mass flow meter. The solids are added until the desired slurry concentration is reached. The slurry then is allowed to circulate in the loop for some time to obtain homogeneous solids distribution. The pressure gradient measurements are taken with a stepwise decrease of the flow rate from the maximum flow rate to the minimum. The flow rate is controlled by the rotation rate of the pump.

It was estimated that the accuracy of the flow velocity measurements is $\pm 5\times 10^{-3}$ m/s; that of the slurry density is ± 2.0 kg/m^3; and that of the pressure gradient is ± 50 Pa/m. The roughness value of the flow loop tubing was determined experimentally to be 32 μm. The flow loop was calibrated by performing clear water runs. Comparison of measured pressure gradients for water with predictions of Wood's [13] empirical correlation from Eq. (2) for

*Corresponding author: Phone: 305-348-1596; Fax: 305-348-1852; e-mail: lin@hcet.fiu.edu

Contributed by the fluids Engineering Division for publication in the JOURNAL OF FLUIDS ENGINEERING. Manuscript received by the Fluids Engineering Division November 11, 2002; revised manuscript received September 11, 2003. Associate Editor: S. L. Ceccio.

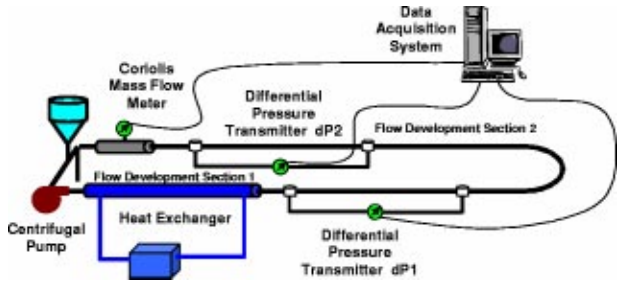

Fig. 1 The schematic diagram of the flow loop

turbulent flow in a pipe with a rough wall is shown in Fig. 2. Good agreement between our measurements and Wood's correlation indicates that the results obtained in the flow loop are reliable:

$$f = a + b \cdot \mathrm{Re}^{-c}, \quad \text{where} \quad a = 0.0026\left(\frac{e}{D}\right)^{0.225} + 0.133\left(\frac{e}{D}\right);$$

$$b = 22\left(\frac{e}{D}\right)^{0.44}; \quad \text{and} \quad c = 1.62\left(\frac{e}{D}\right)^{0.134} \tag{2}$$

2.2 Slurry Characterization. In this study five double-species slurries were used. The solid component of the slurries was glass spheres, and the carrier fluid was water. The double-species mixtures were 50% by 50% by volume mixtures of two different kinds of glass spheres. The glass spheres were obtained from Potters Industries Inc.[1] and from Flex-o-Light[2]. These glass beads were of two different densities (2490 kg/m^3 and 4200 kg/m^3) and three different mean particle diameters (140 μm, 260 μm, and 530 μm). Out of five double-species mixtures, three had solids of the same mean particle size but different densities, while the other two had solids with different mean particle sizes and different densities. Detailed properties of solid component of all double-species slurries are summarized in Table 1.

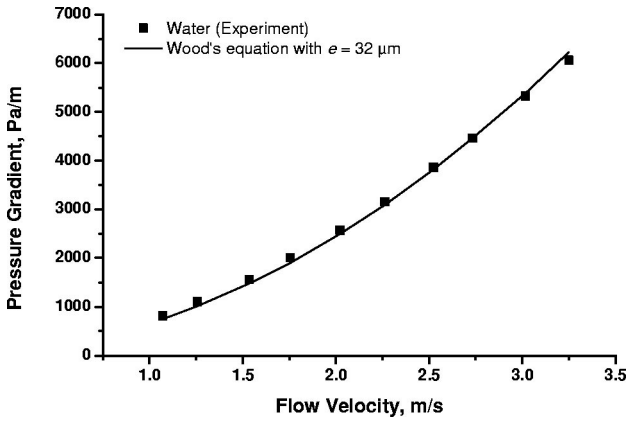

Fig. 2 Comparison of experimental data for clear water flow with prediction of Wood's [12] empirical equation

3 Results

3.1 Comparison of Double-Species and Single-Species Slurries. Prior to our experiments with double-species slurries, we performed tests with single-species slurries consisting of each individual component of the double-species slurries. Single-species results are reported in detail elsewhere [14]. In this section we compare double-species slurry transport characteristics with those of individual components of each slurry at the same solids volume concentrations.

3.1.1 Double-Species Slurries Consisting of Particles of the Same Mean Diameter but of Different Densities. First, we consider double-species slurries consisting of particles of the same mean diameter but of different densities. Figures 3–5 show the pressure gradient versus flow velocity curves for such slurries for three different mean diameters. These figures confirm that the pressure gradient curve for a double-species slurry is always between the curves for its individual components. However, double-species curves are not exactly in the middle between the single-species curves, which indicates that the pressure gradient of double-species slurry is not the average of the pressure drops of individual components. To illustrate the difference between double-species and the average between the single-species slurries more clearly, we fitted all our experimental data with second-order polynomials and then created difference curves between pressure gradient for double-species slurries and average pressure gradient for single-species slurries according to the formula:

$$\%\ \text{deviation} = \frac{\Delta P_{\text{double-species}} - \Delta P_{\text{average}}}{\Delta P_{\text{average}}} \cdot 100\% \tag{3}$$

where $\Delta P_{\text{double-species}}$ is the pressure gradient of a double-species slurry, and $\Delta P_{\text{average}}$ is the average of the pressure gradients of single-species slurries of individual components.

The results are shown in Fig. 6. On this figure, the position of the difference curve close to zero indicates that the pressure gradient of double-species slurry is close to the average of the pressure drops of individual components; the position of the difference curve above zero indicates that the pressure gradient of double-species slurry is closer to that of the denser component (Flex-o-

[1]Potters Industries Inc., P.O. Box 840, Valley Forge, PA 19482-0840, USA. www.pottersbeads.com

[2]Flex-O-Lite Inc., 125 Cassens Ct., Fenton, MO 63026, USA

Table 1 Properties of solid components of double-species slurries and test conditions.

Components	Component Density, kg/m^3	Component Mean Particle Diameter, mm	Component Particle Size Range, μm	Tested solids volume concentrations, %	Tested Flow Velocity Range, m/s
1. Potters P-0060 2. Flex-O-Light (100/140 mesh)	2490 4200	140 140	100–150 100–150	5, 10, 15	0.7–3
1. Potters P-0120 2. Flex-O-Light (50/70 mesh)	2490 4200	260 260	210–300 210–300	5, 10, 15	1–3
1. Potters P-0230 2. Flex-O-Light (30/40 mesh)	2490 4200	530 530	430–600 430–600	5, 10	0.7–3
A. Potters P-0060 B. Flex-O-Light (30/40 mesh)	2490 4200	140 530	100–150 430–600	5, 10	1–3
C. Potters P-0230 D. Flex-O-Light (100/140 mesh)	2490 4200	530 140	430–600 100–150	5, 10, 15	0.7–3

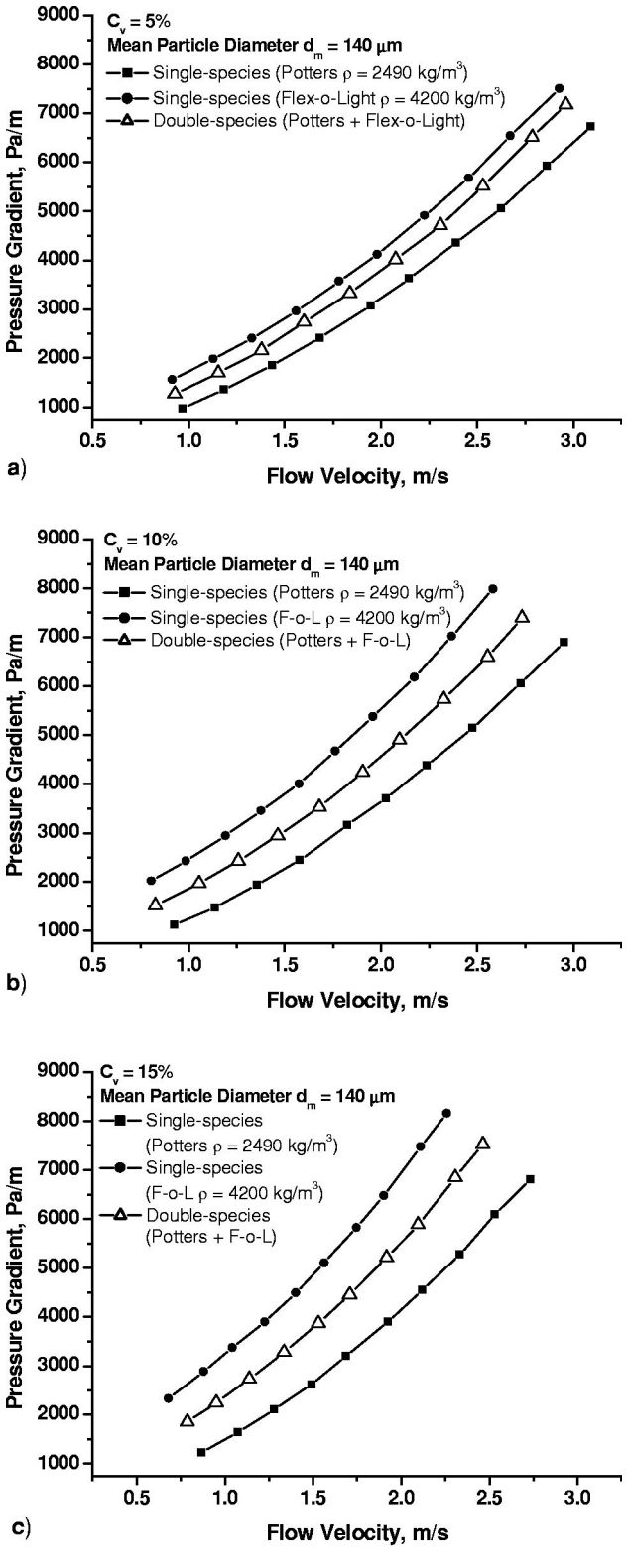

Fig. 3 Comparison of pressure gradients of double-species slurry with single-species slurries. Mean particle diameter 140 μm: *a*) C_v=5%; *b*) C_v=10%; *c*) C_v=15%

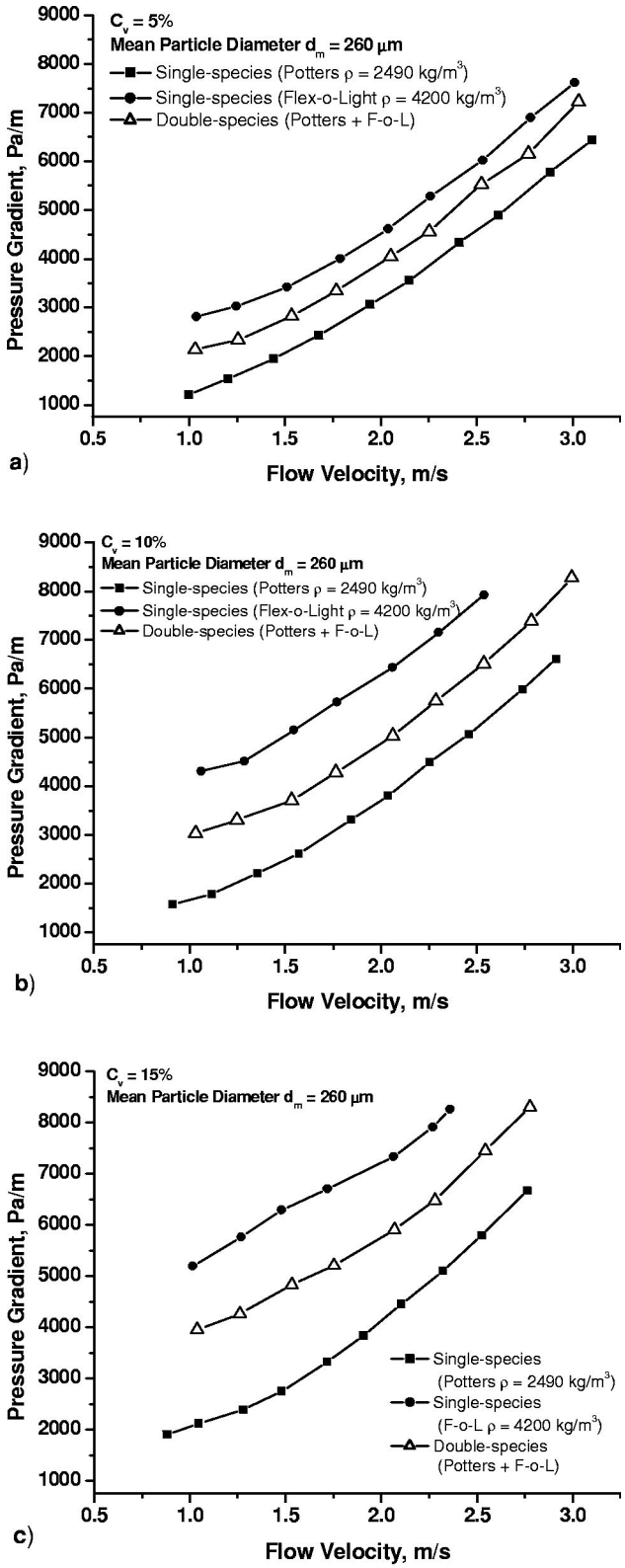

Fig. 4 Comparison of pressure gradients of double-species slurry with single-species slurries Mean particle diameter 260 μm: *a*) C_v=5%; *b*) C_v=10%; *c*) C_v=15%

Light), and the position of the difference curve below zero indicates that the pressure gradient of double-species slurry is closer to that of the less dense component (Potters).

Figure 6 shows that for a mean particle diameter of 140 μm and 5% concentration, the double-species slurry pressure gradient is above the average of the pressure drops of individual components, i.e., closer to the pressure gradient of denser (Flex-o-light) slurry. However, when the concentration increases, the double-species slurry pressure gradient becomes very close to the average pressure gradient of individual components.

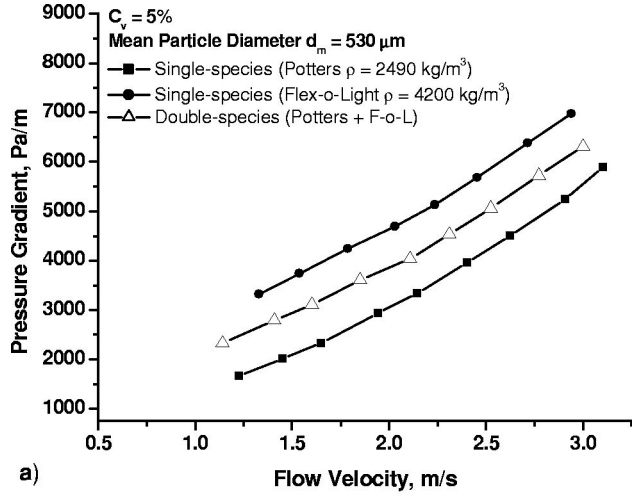

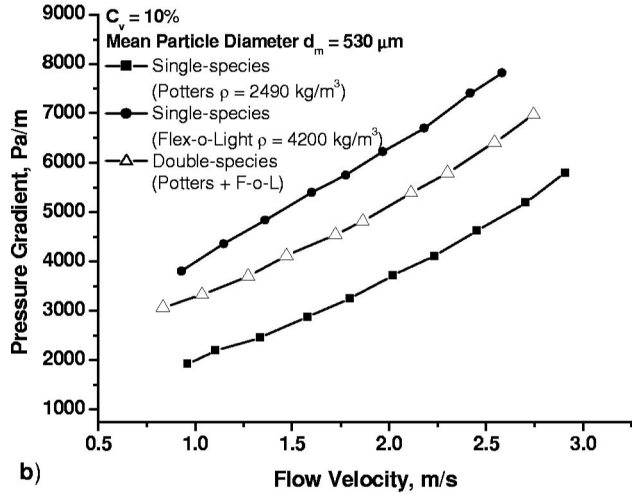

Fig. 5 Comparison of pressure gradients of double-species slurry with single-species slurries. Mean particle diameter 530 μm: *a*) C_v=5%; *b*) C_v=10%

For a mean particle diameter of 260 μm, the 5% and 15% concentration slurries display pressure gradients above the average of the pressure drops of individual components, while the 10% slurry has pressure gradients below the average of individual components, except for flow velocities below 1.25 m/s. Thus, in contrast to smaller particles slurry, the d_m=260 μm double-species slurry pressure gradient does not become close to the average pressure gradient of individual components with the increasing concentration.

For still larger mean particle diameter of 530 μm slurry and C_v=5% and 10%, the double-species slurry pressure gradient is above the average of the pressure drops of individual components. However, for C_v=5%, this is true only for flow velocities below 2.5 m/s; for higher flow velocities, the double-species slurry pressure gradient is below the average.

3.1.2 Double-Species Slurries Consisting of Particles of Different Mean Diameters and Different Densities. Second, we consider double-species slurries consisting of particles of different mean diameters and different densities. Figures 7 and 8 show the pressure gradient versus flow velocity curves for slurries composed of such particles. Figure 7 shows pressure gradients for a slurry composed of small particles having low density (Component A) mixed with large particles of higher density (Component B). Figure 8 shows pressure gradients for a slurry composed of large particles having low density (Component C) mixed with small particles of higher density (Component D). Both figures show that, as for double-species slurries with particles of the same mean diameter, the pressure gradient curve for double-species slurry is always between the curves for its individual components.

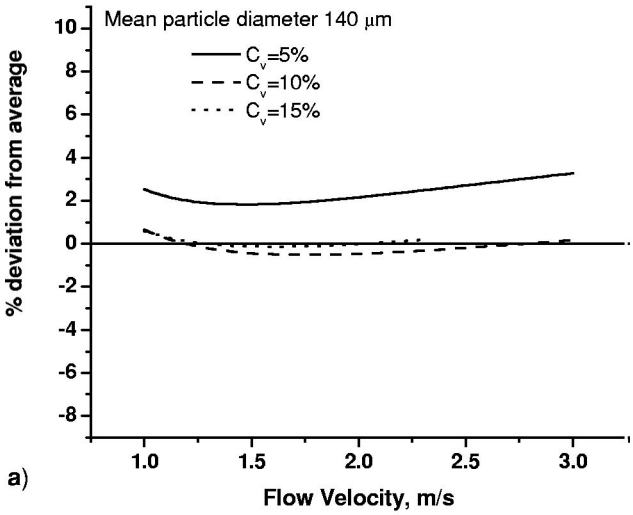

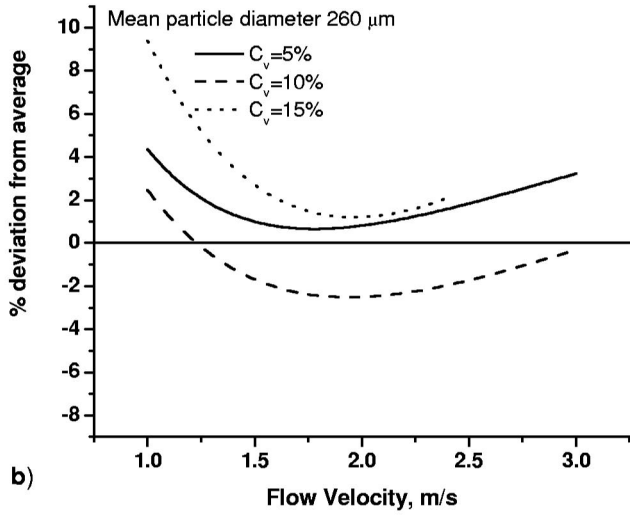

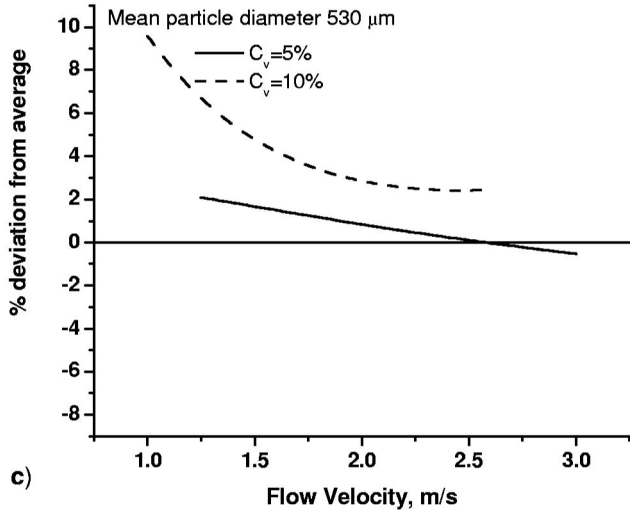

Fig. 6 Difference between pressure gradients for single- and double-species slurries: *a*) d_m=140 μm; *b*) d_m=260 μm; *c*) d_m=530 μm

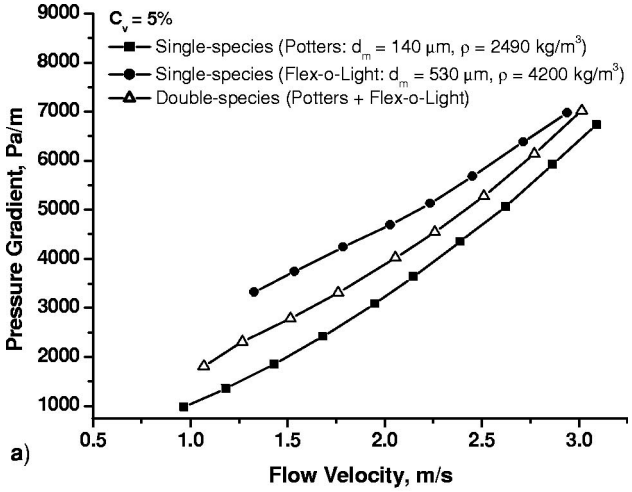

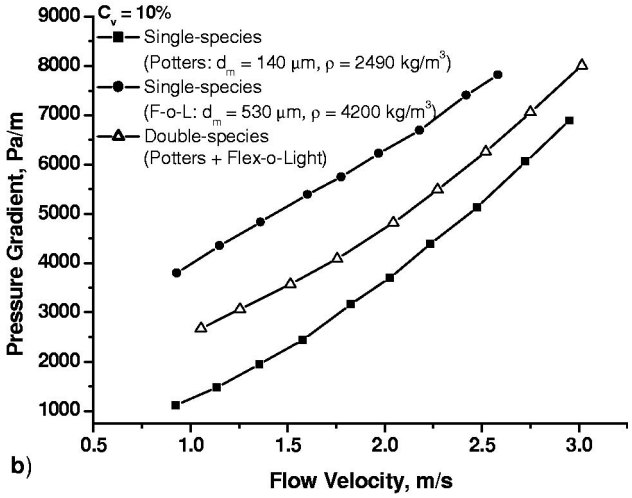

Fig. 7 Comparison of pressure gradients of double-species slurry with single-species slurries Slurry composed of d_m = 140 μm, ρ = 2490 kg/m^3 and d_m = 530 μm, ρ = 4200 kg/m^3 particles: *a*) C_v = 5%; *b*) C_v = 10%

The difference curves between pressure gradient for double-species slurries and average pressure gradient for single-species slurries of individual components are shown in Fig. 9. Figure 9(a) shows that for the slurry composed of small particles having low density mixed with large particles of higher density, pressure gradients are below the average pressure gradient of individual components and closer to that of Component A, except for C_v = 5% slurry for flow velocities above 2.25 m/s for which the effect is opposite. Figure 9(b) shows that for the slurry composed of large particles having low density mixed with small particles of higher density, for C_v = 5% the pressure gradients are above the average and closer to that of Component D; for C_v = 10% the pressure gradients for flow velocities below 1.5 m/s and above 2.25 m/s are above the average; for other flow velocities, the pressure gradients are below the average, and for C_v = 15% the pressure gradients are below the average.

In general, for most of the slurries tested, the difference curves have parabolic shape with a minimum at flow velocity between 1.75 and 2 m/s. The pressure gradient for double-species slurries composed of particles of the same size but different densities behaves similarly for all tested slurries. This pressure gradient is above the average pressure gradient of individual components for low flow velocities, goes through a minimum for intermediate velocities going below the average for some slurries, and again

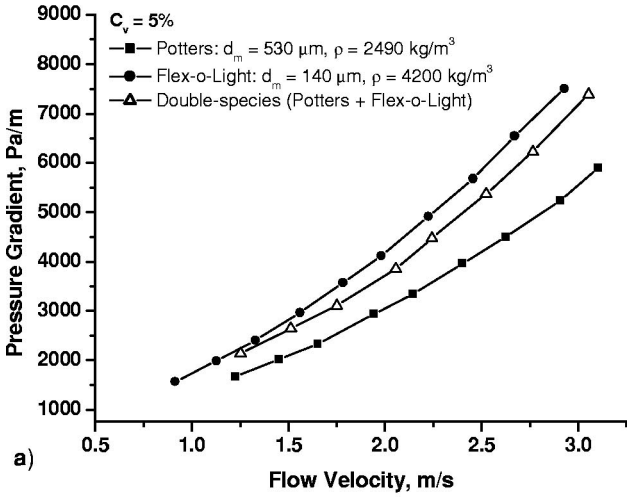

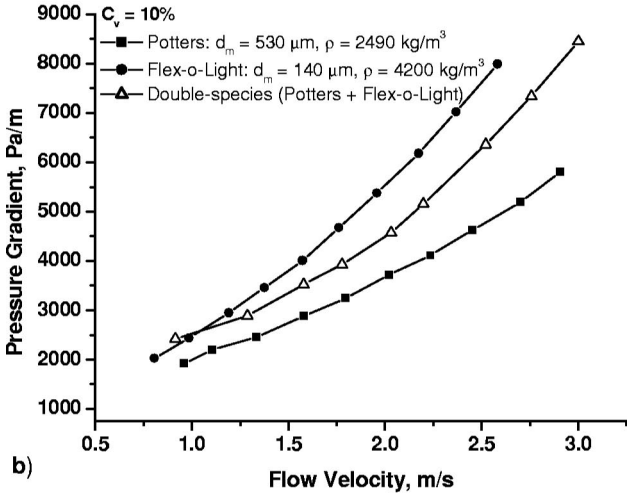

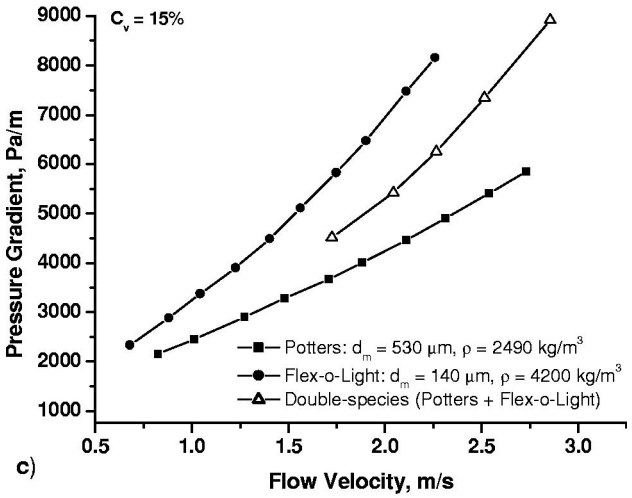

Fig. 8 Comparison of pressure gradients of double-species slurry with single-species slurries Slurry composed of d_m = 530 μm, ρ = 2490 kg/m^3 and d_m = 140 μm, ρ = 4200 kg/m^3 particles: *a*) C_v = 5%; *b*) C_v = 10%; *c*) C_v = 15%

becomes above the average for high flow velocities. Similar behavior is observed for double-species slurry composed of Components C and D. The double-species slurry composed of Components A and B displays different behavior for different solids concentrations: For C_v = 10%, it behaves similarly to other

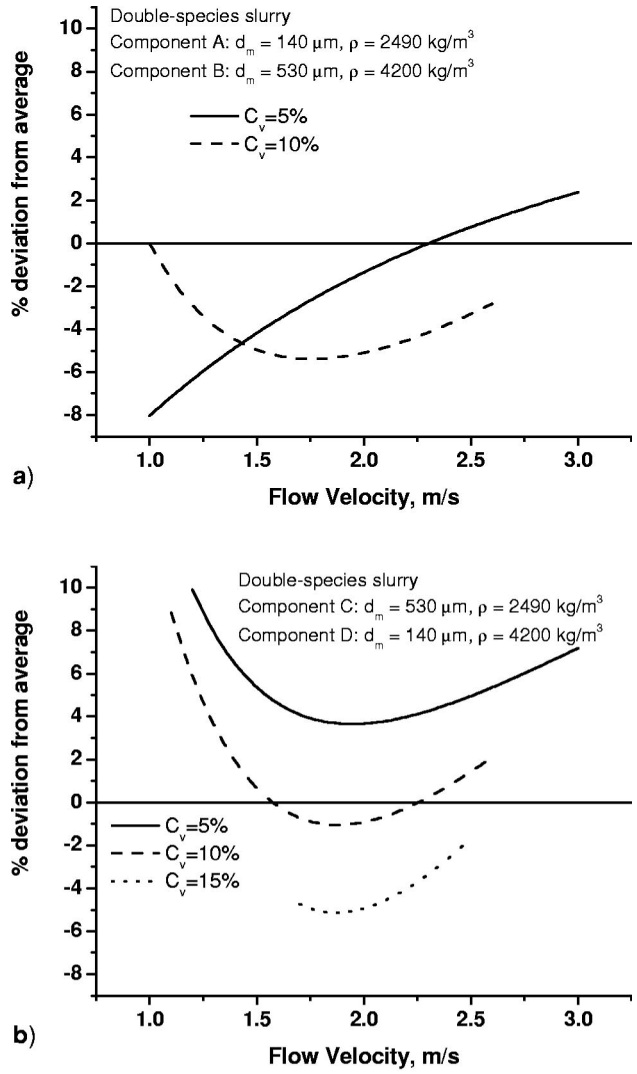

Fig. 9 Difference between pressure gradients for single- and double-species slurries: *a*) Slurry composed of $d_m=140\ \mu$m ($\rho=2490$ kg/m^3) and $d_m=530\ \mu$m ($\rho=4200$ kg/m^3) particles; *b*) Slurry composed of $d_m=530\ \mu$m ($\rho=2490$ kg/m^3) and $d_m=140\ \mu$m ($\rho=4200$ kg/m^3) particles

double-species slurries, while for $C_v=5\%$, its pressure gradient is below average for low flow velocity and increases with flow velocity until it becomes higher than average for velocities above 2.25 m/s.

The fact that the pressure gradient of double-species slurry is not the average of the pressure drops of individual components indicates that there is an interaction between the components that contributes to the overall pressure gradient. As indicated by Figs. 6 and 9, this interaction is dependent on flow velocity, particle size, and solids concentration and thus is quite complex. For slurries composed of particles of the same size but different densities (Fig. 6), in most of the cases double-species slurry pressure gradient is higher than the average pressure gradient indicating that denser component probably contributes more to the overall pressure gradient. For double-species slurries consisting of particles of different mean diameters and different densities (Fig. 9), the trend is more complex with several cases of double-species slurry pressure gradient below the average pressure gradient. These cases may be an object of future studies of identifying combinations of slurry components that would produce lower pressure gradient when pumped though a pipe.

The maximum deviation of double-species slurry pressure gradient from the average pressure gradient of individual components is about 10% and is always found at the lowest studied flow velocities. Thus, for practical applications, the pressure gradient of a double-species slurry can be approximated (within 10% accuracy) as the average pressure gradient of individual components at the same solids volume concentrations.

3.2 Particle Size Effect. The effect of the solid particle mean diameter on the pressure gradient-flow velocity relationship for double-species slurry was studied by comparing the data obtained for three slurries each composed of particles of the same mean diameter. Studied mean particle diameters were 140 μm, 260 μm, and 530 μm. Pressure gradient-flow velocity relationships for these slurries are compared in Fig. 10 for the three solids volume concentrations of $C_v=5$, 10, and 15%. The figure shows that with the increase of the mean particle diameter, the pressure gradient for low flow velocities increases, while for high flow velocities, it decreases. Similar behavior was observed for single-species slurries composed of the same particles [14]. If linear fit is used for pressure gradient data, the slope of fitted lines for $C_v=5\%$ and 10% decreases almost linearly with the mean particle diameter as shown in Fig. 11. Figure 11 also shows that the change in the slope of pressure gradient curves due to mean particle diameter is higher for $C_v=10\%$ than it is for 5%. The available data on Fig. 10(c) suggest that the change in slope at $C_v=15\%$ should be even higher than at 10%. Thus, the change in slope of pressure gradient curves due to change of mean particle diameter is increasing with solids volume concentration in the slurry. For all three concentrations tested, pressure gradient curves intersect at approximately the same point. This point shifts in the direction of higher velocities as slurry concentration increases from 5% to 10%.

4 Numerical Modeling

Detailed model description and modeling result are presented in a separate paper [15]. Only brief model description and some results are presented in this section for comparison and discussion purposes.

Eulerian Granular Multiphase (EGM) model [16] was employed to model double-species slurry flow numerically. In this model momentum and continuity equations are solved for each phase, and a single pressure is shared by all phases. Coupling is achieved through the pressure and interface exchange coefficients. The multiphase flow is described as an inter-penetrating continuum using the concept of phasic volume fractions. Volume fractions represent the space occupied by each phase, and the laws of conservation of mass and momentum are satisfied by each phase individually. EGM model was used in conjunction with k-ε turbulence model to simulate slurry flow in circular pipe. The 3-D cylindrical computational domain was used in the model with dimensions corresponding to those of the flow loop tubing.

Figure 12 compares pressure gradient predicted by the EGM model and measured experimentally for double-species slurry with $d_m=140\ \mu$m and $C_v=15\%$. As seen from the figure, predicted pressure gradient curve has the same shape as the experimental one; however, the numerical model under-predicts pressure gradient observed in the experiment. Possible reasons for this discrepancy are that interface exchange coefficients used in the model are not capturing all the interactions between different phases and that the wall function and roughness constant used in the turbulence model were developed for single-phase flow and may need modification for multiphase system.

5 Conclusions

Slurry transport experiments were performed with five double-species slurries composed of various combinations of glass beads with two widely different densities and three narrow particle size

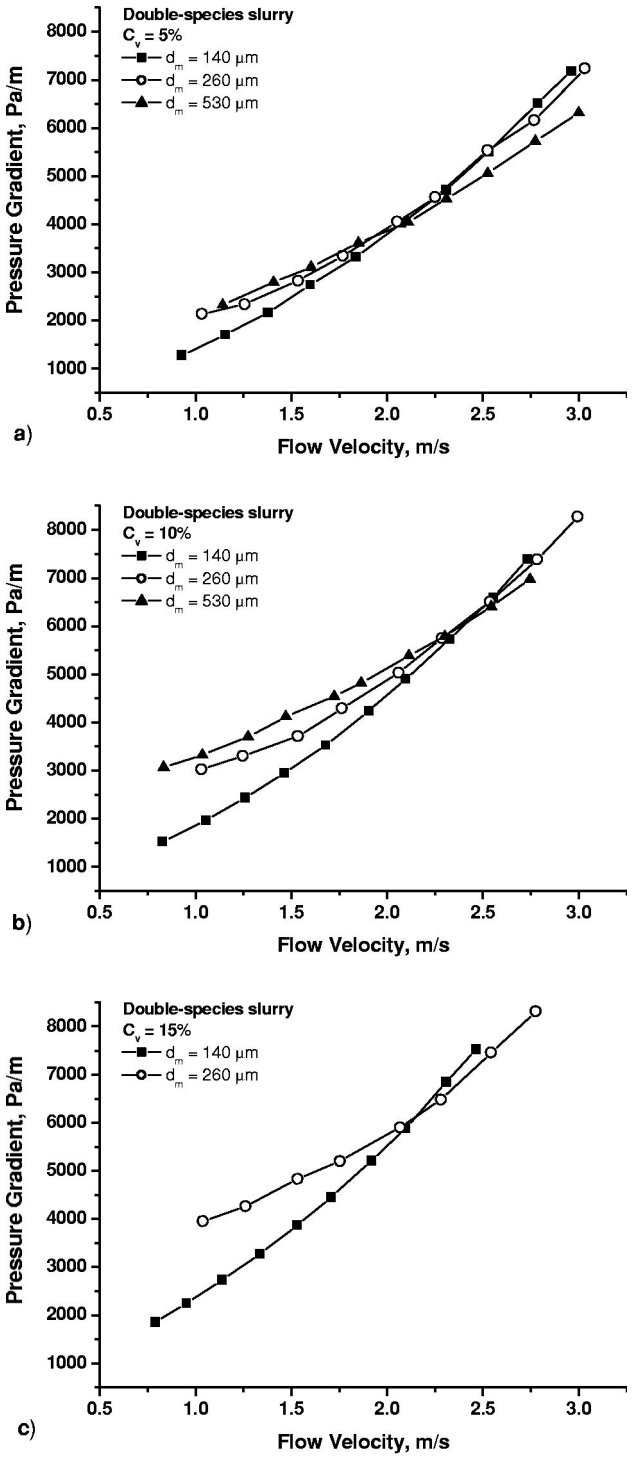

Fig. 10 Particle size effect on pressure gradient of double-species slurry: *a*) C_v=5%; *b*) C_v=10%; *c*) C_v=15%

distributions. Pressure gradients for double-species slurries were compared to those for individual components at the same solids volume concentrations.

The effect of mean particle diameter on pressure gradient of double-species slurry in the pipe was studied. It was found that the pressure gradient curve for double-species slurry is always between the curves for individual components. However, double-species curves are not exactly in the middle between the single-species curves but exhibit complex behavior depending on mean particle diameters of individual components. For practical applications, the pressure gradient of a double-species slurry can be approximated (within 10% accuracy) as the average pressure gradient of individual components at the same solids volume concentrations.

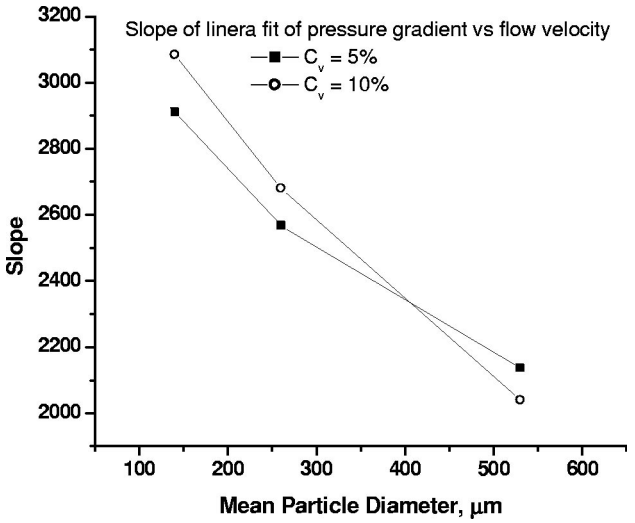

Fig. 11 Variation of the slope of linear fit of pressure gradient vs. flow velocity curves with mean particle diameter

The effect of particle size in double-species slurries on pressure gradient is similar to that for single-species slurries. An increase in the solids mean particle diameter from 140 to 530 μm results in higher pressure gradients for low flow velocities but lower pressure drop for high flow velocities. The slope of linear fit of pressure gradient data decreases linearly with mean solid particle diameter, and the decrease is higher for slurries with higher solids concentration.

Eulerian Granular Multiphase model fairly well predicted the shape of the pressure gradient curve, but consistently underpredicted the pressure gradient values. Further analysis and modification of model constants and coefficients are needed to obtain better predictions.

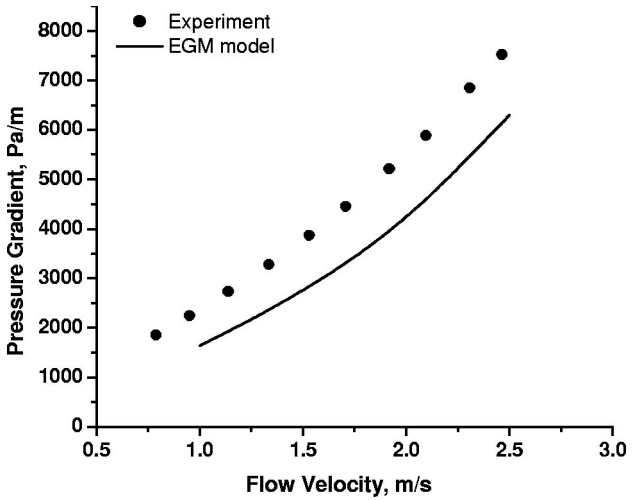

Fig. 12 Comparison of pressure gradient predicted by the EGM model and measured experimentally for double-species slurry with d_m=140 μm and C_v=15%

Acknowledgment

This material is based upon work supported by the National Science Foundation under Award No. CMS-0085645.

Disclaimer

Any opinions, findings, and conclusions or recommendations expressed in this publication are those of the authors and do not necessarily reflect the views of the National Science Foundation.

Nomenclature

C_v = volume concentration, %
D = internal diameter of a pipeline, m
d_m = mean particle diameter, μm
e = pipeline roughness, m
f = $(\Delta P/l)\cdot D/(2\cdot\rho\cdot V^2)$ friction factor, dimensionless
Re = $\rho VD/\mu$ Reynolds number, dimensionless
V = mean velocity, m/s
ρ = density, kg/m^3
μ = dynamic viscosity, Pa·s

Subscripts

l = liquid
s = solid
sl = slurry

References

[1] Wasp, E. J., Kenny, J. P., and Gandhi, R. L., 1979, Solid-Liquid Flow: Slurry Pipeline Transportation, *Gulf Publishing Co.*, Houston, Texas, 9–16.
[2] Brown, N. P., and Heywood, N. I., 1991, Slurry Handling: Design of Solid-Liquid Systems, *Elsevier Science Publishing Co., Inc.*, New York, NY 10010, USA, 625–625.
[3] Govier, G. W., and Aziz, K., 1977, The Flow of Complex Mixtures in the Pipes, *Robert E. Krieger Publishing Company, Inc.*, Malabar, FL, 642–661.
[4] McKibben, M. J., Gilles, R. G., and Shook, C. A., 1996, Pipeline Flow Testing of Simulated Uranium Ore Slurries Using SRC's 53 mm Pipeloop, *Saskatchewan Research Council Publication* No. R-1620-5-C-96.
[5] McKibben, M. J., and Gilles, R. G., 1997, Simulated Coarse Uranium Ore Slurries in SRC's 105 mm Diameter Pipeline, *Saskatchewan Research Council Publication* No. R-1620-3-C-97.
[6] Roco, M. C., and Shook, C. A., 1985, Turbulent flow of incompressible mixtures, J. Fluids Eng., **107**, 224–231.
[7] Parzonka, W., Kenchington, J. M., and Charles, M. E., 1981, Hydrotransport of solids in horizontal pipes: Effects of solids concentration and particle size on the deposit velocity, The Canadian J. of Chem. Eng., **59**, 291–296.
[8] Shook, C. A., Gilles, R., Haas, D. B., Husband, W. H. W., and Small, M., 1982, Flow of coarse and fine sand slurries in pipelines, J. Pipelines, **3**, 13–21.
[9] Wilson, K. C., Clift, R., Addie, G. R., and Maffett, J., 1990, Effect of Broad Particle Grading on Slurry Stratification Ratio and Scale-up, Powder Technology, **61**, 165–172.
[10] Ni, F., and Matousek, V., 1999, Flow of aqueous mixture of sand composed of fractions of different particle size, Hydrotransport, **14**, BHR Group, 31–43.
[11] Matousek, V., 2002, Pressure Drops and Flow Patterns in Sand-Mixture Pipes, Exp. Therm. Fluid Sci., **26**, 693–702.
[12] Glillies, R. G., 1991, Flow Loop Studies, in "Slurry Handling: Design of Solid-Liquid Systems," Brown, N. P., and Heywood, N. I., eds., *Elsevier Science Publishing Co., Inc.*, New York, NY 10010, USA, 625–625.
[13] Wood, D. J., 1966, *Civil Eng.*-A.S.C.E. 36 (12), 60. Cited in Govier, G. W., and Aziz, K., 1977, The Flow of Complex Mixtures in Pipes, *Robert E. Krieger Publishing Company, Inc.*, Malabar, FL, 166, 181.
[14] Skudarnov, P. V., Lin, C. X., and Ebadian, M. A., 2002, Slurry Particles Density and Size Effects on Pressure Losses for Single-Species Solid-Liquid Slurry Flow in a Horizontal Pipeline, *Submitted to* Int. J. Multiphase Flow, in press.
[15] Ling, J., Skudarnov, P. V., Lin, C. X., and Ebadian, M. A., 2002, Numerical Investigations of Double-Species Solid-Liquid Flow in a Straight Pipe, *Submitted to* Int. J. Multiphase Flow, in press.
[16] Ding, J., and Gidaspow, D., 1990, A Bubbling Fluidization Model Using Kinetic Theory of Granular Flow, AIChE J., **36**, 523–538.

Oil Sands Slurry Flow in Flexible Pipe

Samuel Frimpong
e-mail: frimpong@ualberta.ca

Oluropo Rufus Ayodele*
e-mail: oayodele@ualberta.ca

Jozef Szymanski
e-mail: szymanski@ualberta.ca

School of Mining and Petroleum Engineering,
Civil and Environmental Engineering Department,
220 CEB, University of Alberta, Edmonton,
Alberta, Canada T6G 2G7

Production cost and efficiency optimization for the Athabasca oil sands is a key to securing North America's energy supply. Current oil sands production cost is about $13/bbl compared with $1.25/bbl for conventional crude oil. The effort to reduce production cost must focus on truck haulage because it contributes the dominant component of the production cost of about 26%. Toward this objective, hydraulic transportation has become a competitive means for materials handling. There is a desire to extend the hydraulic transport system to production faces using mobile train of flexible pipelines to optimize the system efficiency and cost. This flexible arrangement introduces a unique set of hydraulic transport problems, which must be addressed through rigorous modeling and analysis. This paper provides multiphase oil sand slurry models in flexible pipelines. New mathematical models are developed to characterize the multi-phase flow of oil sands slurry. The models combine the effects of dispersed particles and the carrier continuous phases. The coupled equations of each field are solved numerically for flexible pipe configuration. The models yield the productivity and deliverability of bitumen slurry between two mine facilities. The flexible arrangement allows modeling in elbow-type joint at different angles and in conventional linear pipelines, enabling adaptation of pipelines to various mine outlays. Numerical examples are presented to show the applicability of the new model and to ascertain optimum operational conditions of the flexible pipes in mine layouts.
[DOI: 10.1115/1.1637929]

Introduction

Frimpong et al. [1] presented a detailed review of slurry flow in pipes. They also presented the mechanics of oil sands slurry flow in a flexible pipeline system termed grand articulating pipeline (GAP). The GAP system is made up of pipelines connected together with flexible joints in each pipe sections. This allows deflection, thereby avoiding the torsional stress from the adjoining frames. They consider the problem as a single-phase flow modeling of slurry in flexible pipe in one-dimension. Changirwa et al. [2] presented details of different flexible pipe arrangement being considered by Syncrude Canada Limited. This study deals with one of the options recommended by Changirwa et al. [2], that is, the use of FlexRite flexible pipeline.

FlexRite provides alternate way of slurry conveyance in a flexible pipe arrangement. With FlexRite, the pipeline can span several meters without any need for any flexible joints. The flow across the FlexRite pipeline can change in any direction due to the flexible nature of the pipeline system. This change in flow direction at the bend points should be investigated to determine its effect on throughput. In considering slurry mixture flow in FlexRite pipes, many interactions can take place. The flexible pipe can bend to a maximum angle of 60 deg. The material content of the flexible pipe enables this bending characteristic. FlexRite pipes are more flexible than conventional steel pipes and provide maximum bending with smooth flow of materials. Two types of particles/mixtures impingement can occur including (i) straight horizontal flexible pipe and (ii) bend (from 0 deg to 60 deg deflection) flexible pipe. These two types of pipe configurations are considered in this paper. Direct impingement occurs in the bend configuration while random impingement occurs in the horizontal arrangement as reported in Edward et al. [3] and illustrated in Fig. 1. The advantage of investigating flexible pipe that might result into elbow-type configuration is that, this type of configuration allows for the adaptation of the transport line to different mine layouts.

Changirwa et al. [2] observed that the most rigorous approach in modeling slurry flow is to model the dispersed and continuous phases as distinct, separate interacting continua, such that the continua have their properties including velocity concentration and pressure fields. The work presented here uses the FlexRite pipeline arrangement for comprehensive modeling and analysis. The main objectives include mathematical modeling of the multiphase slurry through the flexible pipelines. Numerical models examples are also presented to ascertain optimum operational conditions for flexible pipes, when used in the design of hydraulic transportation system in a oil sands mine layout.

Mathematical Modeling Assumptions

The basic assumptions underlining the equations described in this section are:

1. Multiphase flow of incompressible and immiscible phases (water, oil, and solid phases). The solid (sand particles) phase is dispersed or suspended and carried continuously in the slurry mixture. The presence of trapped air is neglected.
2. Uniform distribution of phases through the pipeline (homogeneous).
3. Sand particles are dispersed and do not settle at the bottom along the pipe length to form stationary bed. These conditions are not quite rigid and the particles' behavior can change intermittently between settling and non-settling. For an average size of sand particles, there is a tendency for the solids in the slurry mixture to settle. Centrifugal pumps create adequate energy to ensure that the conveying velocity is above the settling velocity to maintain operational stability [4].
4. Density of each phase is constant and different from the density of other phases.
5. Velocity for each phase is assumed constant over the whole region.
6. Pipe wall shear stress is constant irrespective of the phase in contact with the pipe surface.

*Corresponding author.
Contributed by the Fluids Engineering Division for publication in the JOURNAL OF FLUIDS ENGINEERING. Manuscript received by the Fluids Engineering Division Dec. 6, 2002; revised manuscript received Sept. 21, 2003. Associate Editor: D. Siginer.

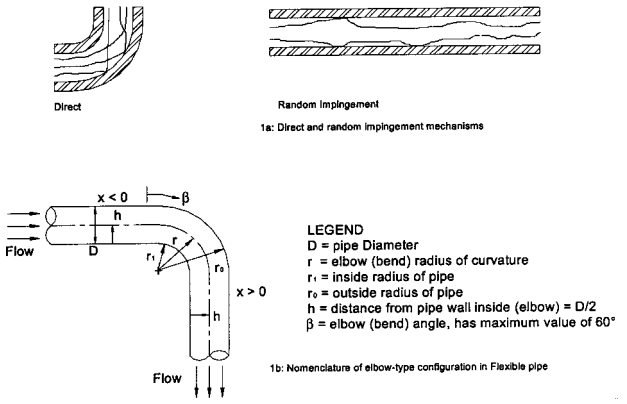

Fig. 1 Impingement and Nomenclature in Flexible Pipes (Sources: Edwards et al., 2001)

7. Hot water and bitumen are the continuous immiscible phases. This assumption is quite reasonable because hot water reduces bitumen viscosity to a continuous viscous fluid.
8. Bitumen temperature is assumed approximately constant through the pipe length.
9. Average sizes of sand particles are less than 2 inches.
10. Mixture properties: Solid particles (density of 2650 Kg/m^3), bitumen (API<10 deg and density of 995 Kg/m^3) and water/hot water (density of 1000 Kg/m^3), [5–6].
11. The slurry mixture flow is continuous from one end to the other end.
12. Flow can be horizontal or inclined depending on the flexible pipe bend angle.
13. Laminar or turbulent flow.

Continuity Equation

Considering the elemental portion of the pipe in Fig. 1(b), three possible flow directions are axial, radial and tangential. Axial flow is considered in this study. Radial and tangential flows can be neglected since they are often very small. The flow between two ends of the pipeline can be modeled with the continuity and momentum equations, which give the conservation of mass between two ends. This can be extended to predict flow pattern at every point along the pipes. The two ends must be connected by a streamline where the conditions are known. The continuity equation for the control volume of solid particles and two continuous phases can be written as follows [7]:

$$\frac{\partial q_s}{\partial t}+\frac{\partial q_s V_s}{\partial z}=0 \tag{1}$$

$$-\frac{\partial q_s}{\partial t}+\frac{\partial}{\partial z}((1-q_s-q_{c2})V_{c1}+(1-q_s-q_{c1})V_{c2})=0 \tag{2}$$

$$\frac{\partial j}{\partial z}=0 \tag{3}$$

$$j=q_s V_s+(1-q_s-q_{c2})V_{c1}+(1-q_s-q_{c1})V_{c2} \tag{4}$$

$$q=q_s+q_{c1}+q_{c2}=1 \tag{5}$$

$$q_c=q_{c1}+q_{c2} \tag{6}$$

The definitions of all the variables are given in the nomenclature.

Momentum Equation

Considering axial flow direction, the momentum equation can be written in the form presented by Hewitt and Hall-Taylor [8] in Eq. (7):

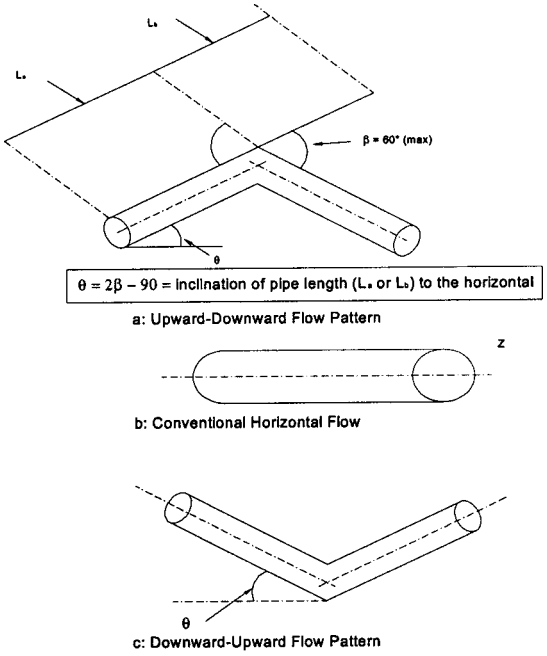

Fig. 2 Pipe Flow Configuration

$$\frac{dP}{dz}=\frac{S}{A}\tau_o+\frac{\dot{Q}}{A}\frac{d}{dz}[q_s\rho_s V_s+(1-q_s-q_{c2})\rho_{c1}V_{c1}+(1-q_s-q_{c1})\rho_{c2}V_{c2}]+\ldots+g\cdot\sin\theta[q_s\rho_s+(1-q_s-q_2)\rho_{c1}+(1-q_s-q_1)\rho_{c2}] \tag{7}$$

In Eq. (7), P is the pressure in the mixture at a given point in the cross-section at axial position, z, τ_o is the wall shear stress at a point around the periphery, S. For round or circular cross-section, S equals $4/D$ and D is the pipe diameter. $\dot{Q}$ is the total volumetric flow rate of the mixture, ρ is the density, g is the acceleration due to gravity, θ is the pipe inclination angle, A is the pipe cross sectional area, the subscripts and other terms are as previously defined, all in Sl units. From Eq. (4), j is given by Eq. (8) or Eq. (9):

$$j=\lambda=[q_s\rho_s+(1-q_s-q_{c2})\rho_{c1}+(1-q_s-q_{c1})\rho_{c2}] \tag{8}$$

$$\lambda=q_s\rho_s+\lambda_c=\lambda_s+\lambda_c \tag{9}$$

$$\lambda_c=q_{c1}\rho_{c1}+q_{c2}\rho_{c2} \tag{10}$$

$$\lambda_s=q_s\rho_s \tag{11}$$

$$V_c=V_{c1}+V_{c2} \tag{12}$$

Hence, Eq. (7) becomes:

$$\frac{dP}{dz}=\frac{S}{A}\tau_o+\frac{\dot{Q}}{A}\frac{d}{dz}[\lambda_s V_s+\lambda_c V_c]+g\cdot\sin\theta(\lambda_s+\lambda_c) \tag{13}$$

The problem associated with solving Eqs. (7) or (13) is that detailed information on the local mass flux, velocity, and density is seldom available. Data on the profiles of these variables through the pipeline is required. The profiles depend on the phase, their physical properties, and the pipe geometry. The unknown variables, which are functions of position, z through the pipe cross-section are ρ_i, V_i, and q_i. Based on the assumptions given previously, these reduce to q_is$(q_{c1i}, q_{c2i}, q_{si})$.

As shown in Figs. 2(a), 2(b), and 2(c), the flexible pipeline can be in upward-downward mode (positive), horizontal (conven-

tional) mode, or downward-upward dissipation mode (negative). The inclination angles for the downward and upward sections are the same. In Figs. 2(a) and 2(c), the equations above are solved at the discretized intervals up to the upward or downward point to investigate the effects at the bend ends. The results are then used as input for the downward or upward sections. By combining Eqs. (1) to (6) with Eqs. (7) or (13), solutions are obtained for the possible downward and upward flow patterns through the flexible pipeline. Various solution maps for the deliverability are generated at every point along the pipe length.

Numerical Scheme and Solution

Equation (13) was solved for all variables to give deliverability and performance at any point along the pipe especially at the bent points at various geometrical orientations as given or formulated below. Boundary and initial conditions are:

$$\dot{Q}(0)=\dot{Q}(z=0 \ \ to \ \ L) \tag{14}$$

$$P_{(inlet)}=P_o \tag{15}$$

$$\left(\frac{\partial P}{\partial z}\right)_{(inlet)}=\left(\frac{\partial P}{\partial z}\right)_0 \tag{16}$$

$$\rho_s(z=0)=\rho_s(z=0 \ \ to \ \ L)=\rho_s \tag{17}$$

$$\rho_{c1}(z=0)=\rho_{c1}(z=0 \ \ to \ \ L)=\rho_{c1} \tag{18}$$

$$\rho_{c2}(z=0)=\rho_{c2}(z=0 \ \ to \ \ L)=\rho_{c2} \tag{19}$$

$$V_s(z=0)=V_s(z=0 \ \ to \ \ L)=V_s \tag{20}$$

$$V_{c1}(z=0)=v_{c1}(z=0 \ \ to \ \ L)=V_{c1} \tag{21}$$

$$V_{c2}(z=0)=v_{c2}(z=0 \ \ to \ \ L)=V_{c2} \tag{22}$$

$$q_{c1}(z=0)=q_{c1} \tag{23}$$

$$q_{c2}(z=0)=q_{c2} \tag{24}$$

$$q_s(z=0)=q_s \tag{25}$$

The vector k, the average momentum flux density, can be written as:

$$k=\rho_s q_s V_s+\rho_c(1-q_s)V_c \tag{26}$$

$$q_c=1-q_s \tag{27}$$

Substituting Eq. (26) into Eq. (13) leads to:

$$\frac{dP}{dz}=\frac{S}{A}\tau_o+\frac{\dot{Q}}{A}\frac{d}{dz}[\rho_s q_s V_s+\rho_c(1-q_s)V] + g\cdot\sin\theta(q_s\rho_s+(1-q_s)\rho_c) \tag{28}$$

With the assumptions of constant density and velocity for each phase, Eq. (28) gives:

$$\frac{dP}{dz}=\frac{S}{A}\tau_o+\frac{\dot{Q}}{A}\left[\rho_s V_s\frac{dq_s}{dz}+\rho_c V_c\frac{d}{dz}(1-q_s)\right] + g\cdot\sin\theta(q_s\rho_s+(1-q_s)\rho_c) \tag{29}$$

Hence, with the known boundary and initial conditions, Eq. (29) can be discretized and solved using finite difference approximation, resulting in a system of linear equations as follows:

$$\frac{dP}{dz}=\frac{S}{A}\tau_o+\frac{\dot{Q}}{A}\left[\rho_s V_s\frac{q_{s_{i+1}}-q_{s_i}}{\Delta z}+\rho_c V_c\frac{q_{c_{i+1}}-q_{c_i}}{\Delta z}\right]+g \cdot\sin\theta(q_{s_i}\rho_s+(1-q_{s_i})\rho_c) \tag{30}$$

Equation (30) can be rearranged as:

$$A_i q_{s_{i+1}}+B_i q_{s_i}=C_i \quad i=1,2,3\ldots n \tag{31}$$

Equation (31) is a system of linear equation that can be solved by back-substitution method based on the boundary conditions specified above. In Eq. (31):

$$A_i=(\eta_o\rho_s V_s-\eta_o\rho_c V_c) \tag{32}$$

$$B_i=(\eta_o\rho_c V_c-\eta_o\rho_s V_s+\rho_s g\cdot\sin\theta+\rho_c g\cdot\sin\theta) \tag{33}$$

$$C_i=-\left(\left(\frac{dp}{dz}\right)_i+\rho_c g\cdot\sin\theta+\eta_1\right) \tag{34}$$

$$\eta_o=\frac{\dot{Q}}{\Delta z A} \tag{35}$$

$$\eta_1=\frac{S}{A}\tau_o \tag{36}$$

$$\tau_o=\frac{D}{4}\left(-\left(\frac{\partial P}{\partial z}\right)_i-(\rho_c+\rho_s)g\sin\theta\right) \tag{37}$$

For practical field applications, the expression, $(\partial P/\partial z)_i$, in Eq. (37) can be neglected along the pipe length at any point in the pipe wall, because it is always small when compared with the expression, $(\rho_c+\rho_s)g\sin\theta$, that is:

$$(\rho_c+\rho_s)g\sin\theta\gg\left(\frac{\partial P}{\partial z}\right)_i \tag{38}$$

Hence, Eq. (37), becomes:

$$\tau_o=\frac{D}{4}(-(\rho_c+\rho_s)g)\sin\theta \tag{39}$$

The coefficients of the unknown terms can be obtained from the given initial and boundary conditions. Pressure gradient values are only specified at the inlet and outlet. Hence the pressure gradient values must be known at least in either of those points. As a rule, whenever the pressure is specified at any point in the boundary, q_s must be specified too at that point for the system of equations to be solvable. Alternatively, if the q_s's are given at the boundaries, the pressure gradient values must be known at the boundaries otherwise the matrix will be ill-conditioned. In the numerical examples given below, the characteristics of the flexible pipe, such as the range of diameter, elbow angle, etc. and other flow properties and parameters, used as input are within the operational limits of the flexible pipe.

Numerical Examples of Slurry Flow in Flexible Pipe System

The mathematical models are applied to solve a real-world slurry flow problem in a flexible pipe system. The mathematical models are translated into computer simulation codes using MS-Excel. Table 1 contains the input data for the computer simulation models. The computer models are used to examine three critical areas of the flexible pipe flow, which affect the flow efficiency. These areas include variations in (i) the elbow angle; (ii) pipe diameter; and (iii) low and high elbow angles. The results from these experiments are discussed below.

Numerical Results and Discussion

Elbow Angle Variation. Table 1 contains the input data to the simulator. These are based on field data as well as on experience from field observations. In this example, the effect of varying the elbow angle on the flow pattern is considered. The angle is varied from 0 to 60 deg at an increment of 10 deg and the outputs of the simulator are shown graphically in Figs. 3 and 4. The results show that as the elbow angle increases the fraction volume of the solid phase along the pipe length decreases. The decrements are less far

Table 1 Input Data

L_a	50.00 m	$\theta_{\text{first-upward}}$	11.20 deg	Q_t	120.00 m^3/s	V_{c2}	9.60 m/s
L_b	50.00 m	Range of β	0–50.60 deg	τ_o	−337.21 N/m^2	V_s	70.80 m/s
$\beta_{\text{first-upward}}$	50.60 deg	η_1	−485,200.18 Nm^{-5}	$P(0)$	1,400.00 N/m^2	Δz	5.00 m
ρ_o	995 kg/m^3	S	26.67 m^{-1}	D	0.1524 n	A	0.02 m^2
ρ_s	2,650 kg/m^3	$q_{\text{s inlet}}$	0.59	n	10	$dP/dZ_{(\text{inlet})}$	1,000 N/m
ρ_w	1,000 kg/m^3	$\theta_{\text{first-downward}}$	11.20 deg	V_{c1}	39.60 m/s	$dP/dZ_{(\text{oulet})}$	700 N/m
$\beta_{\text{first-downward}}$	50.60 deg						

away from the elbow joints and more rapid or abrupt at the elbow corner. On the other hand, as the elbow angle increases, the volume fraction of the combined mixture of the continuous phases increases. Again such increments are less noticeable far away from the elbow joints and more noticeable at the elbow corner as shown in Fig. 4. These observed phenomena can be attributed to the fact that the continuous phase mixture has lower specific gravity and generally required less energy per unit volume to move through the flexible pipeline than the solid phase. Also, as can be seen in Figs. 3 and 4, the Equilibrium State of the elbow angle can be ascertained. This equilibrium position falls in the 30 to 40 ranges. In this interval, reasonable fractional volumes of the phases are being delivered through the pipes at optimized conditions. Hence for practical field design, flexible pipe operations should be design to fall in such elbow configuration ranges in majority of the mines' layout.

Pipe Diameter Variation. The total flow, elbow angle, and other parameters are kept constant while the diameter is varied. Because the diameter varies, A also vary. That is, Q is constant while Q/A changes. The pipe diameter was varied from about 0.1 ft to 11 ft. The input data are the same as those in Table 1, except that the elbow angle is kept constant at 35 deg for each of the pipe diameters. The results are shown in Fig. 5. From the figure, generally, the distribution of q_s follows the pipe shape. The distribution of q_s remains fairly constant at lower values of diameter. As the diameter increases, q_s reduces along the pipe length until the bent points where q_s rises till the end of the pipe. Ultimately at the pipe end, q_s is much higher at higher values of the diameter. This shows that the higher pipe diameter, the higher the quantity of the solid phase that will be delivered eventually although less quantity is being transported at the first half of the pipe. Another deduction from Fig. 5 is that the pipe diameter of about 3 ft gives the best or optimum deliverability of the solid and the continuous phases. This is because this is the diameter at which the fractional concentration of the solid phase and the combined continuous phase remained fairly uniform.

Flow at Low and High Elbow Angles. For this example, input values are the same as those of Table 1 but the flow rate values vary from 100 to 135 m^3/s and the elbow angles of 30 deg

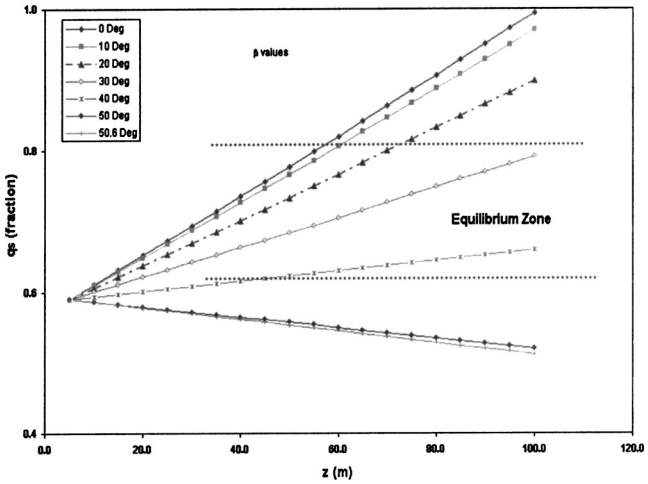

Fig. 3 Plot of q_s Profile (Elbow Angle Variation)

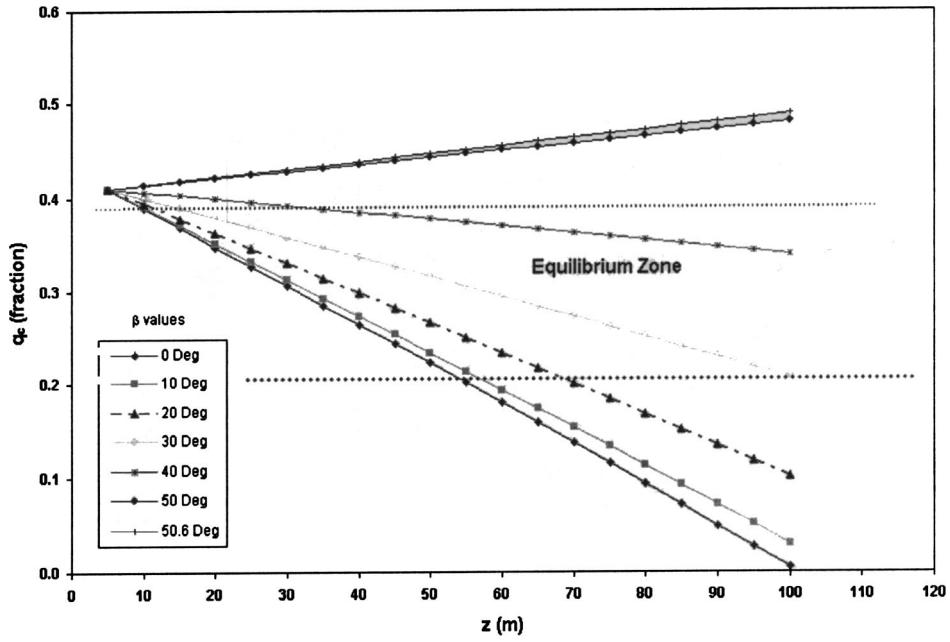

Fig. 4 Plot of q_c Profile (Elbow Angle Variation)

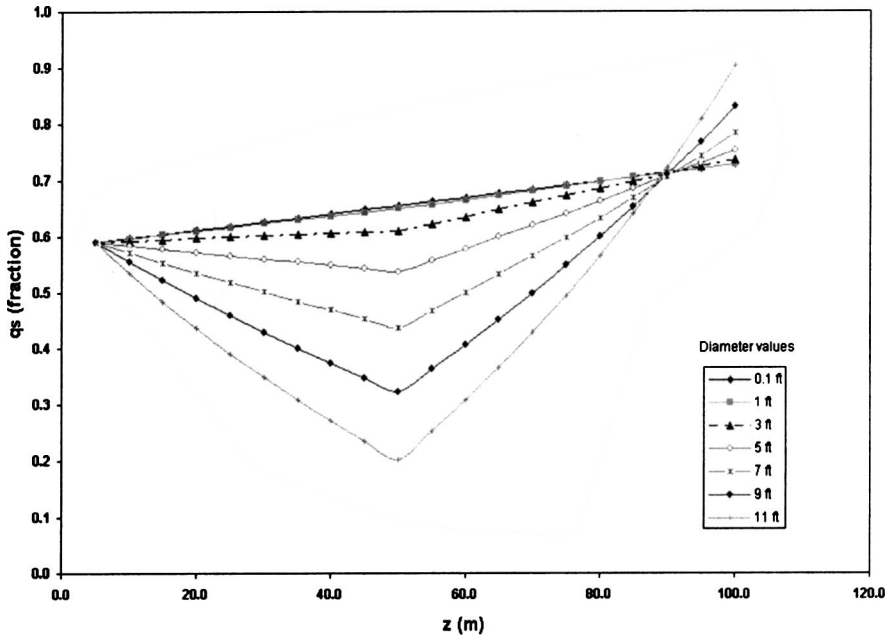

Fig. 5 Plot of q_s Profile (Diameter Variation)

(low) and 60 deg (high) were considered as indicated in Figs. 6 and 7. Figure 6 shows the variation of the total flow rate with q_s along the pipe length. The values of q_s increase along the pipe for each of the total flow rate values investigated. But as the total flow rate increases, q_s reduces. This can be attributed to the low elbow joint angle. This low angle contributes negatively to the solid phase throughput along the pipe length. On the other hand, at high elbow angle of 60 deg, as the total flow rate increases, the q_s values increase along the pipe length. This is due to the positive contribution of the elbow angle. From these, it can be concluded that a high elbow angle favors a high percentage of the solid phase transportation through the pipeline while a low elbow angle favors transportation of a higher percentage of the continuous phases.

Conclusion

New mathematical models are developed for modeling the multi-phase flow of oil sand slurry in a flexible pipeline train. The equations yield the productivity and deliverability of bitumen slurry between two mine facilities. The models combined the effects of dispersed particles and the carrier continuous phases as opposed to the single-phase assumptions. The flexible arrangement allows modeling in elbow-type joint at different angles and in conventional linear pipelines, enabling adaptation of pipelines to various mine outlays. Numerical results show that the optimum elbow angle for the effective oilsand slurry delivery is about 30 to 40 deg. A pipe diameter of about 3 ft was found to be adequate for

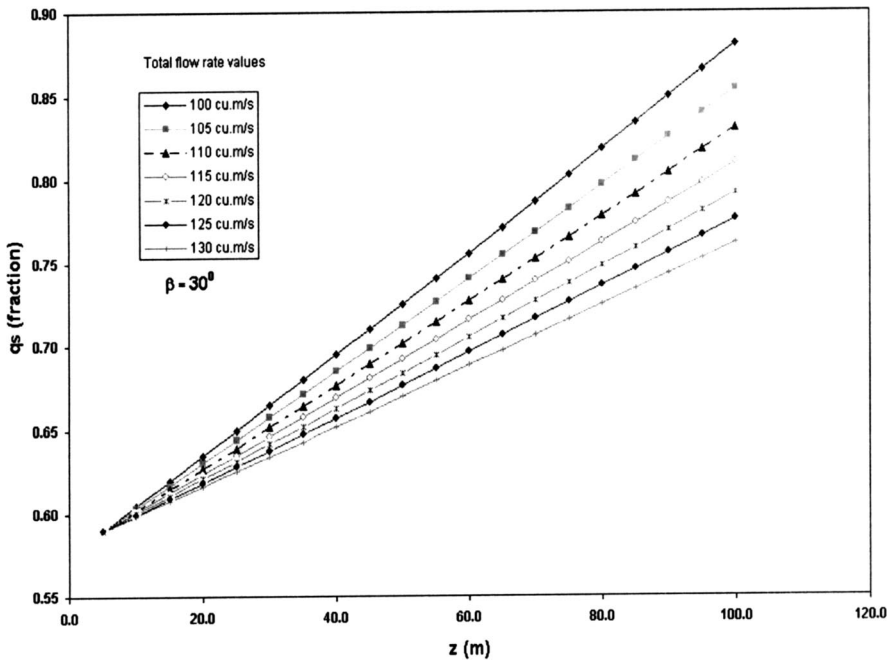

Fig. 6 Plot of q_s Profile (Total Flow Rate Variation at Low Elbow Angle)

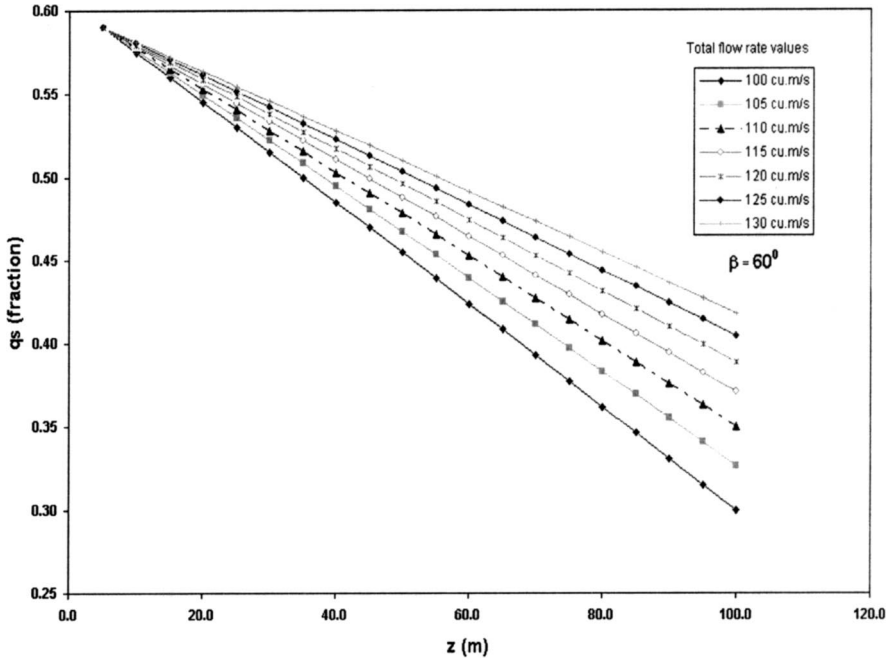

Fig. 7 Plot of q_s Profile (Total Flow Rate Variation at High Elbow Angle)

optimized bitumen delivery under the model assumptions, although other pipe diameters can be used. High elbow angle gives a higher deliverability of the solid phase while a low elbow angle favors a higher deliverability of the continuous phases. In addition, maintaining a higher ratio of the inlet to outlet pressure gradient was found to be fairly appropriate for continuous phase deliverability.

Nomenclature (Units are in SI Units)

A = the pipe cross sectional area
D = the pipe diameter
g = the acceleration due to gravity
j = the volume-averaged velocity
k = the average momentum flux density
P = the pressure in the mixture at a given point in the cross-section at axial position, z
q = the total volume fraction of all phases
q_c = the total volume fraction of the two continuous phases (water and bitumen)
q_{c1} = the volume fraction of water
q_{c2} = the volume fraction of oil (bitumen)
q_s = the total volume fraction of the solid particles
Q = the total volumetric flow rate of the mixture
S = $4/D$, (For round or circular cross-section)
V_{c1} = velocity of the first continuous phase (water)
V_{c2} = velocity of the second continuous phase (oil)
V_s = average velocity of q_s
z = axial position along the pipe
ρ = density
θ = pipe inclination angle
τ_o = wall shear stress at a point around the periphery, S
λ_i = $q_i\rho_i$, i=solid phase or continuous phase (oil or water or mixture of both)

References

[1] Frimpong, S., Changirwa, R. M. M., Asa, E., and Szymanski, J., 2002, ''Mechanics of Oil Sands Slurry Flow in a Flexible Pipeline System,'' Int. J. of Surface Mining, **16**(2), pp. 105–121.
[2] Changirwa, R., Frimpong, S., Szymanski, J., Coward, J., McTurk, J., and Batty, P., 2000, ''Collaborative Research on the At-Face Slurrying (AFS) Technology—NSERC-Syncrude-U of A: AFS Recommended Options,'' Progress Report # NSERC/SCL/CRD00001 Submitted to Syncrude Canada Limited. January 2000.
[3] Edward, J. K., McLaury, B. S., and Shirazi, S. A., 2001, ''Modeling Solid Particle Erosion in Elbows and Plugged Tees,'' ASME J. Energy Resour. Technol., December, pp. 277–284.
[4] Addie, G. R., 1982, ''Slurry Pipeline Design Manual by GIW Industries Inc.,'' pp. 1–4, Miller #2200 Rev. 6/01.
[5] McDonell, B., 2002, ''Slurry Systems: Design and Equipment Selection With Examples From Syncrude's Operation,'' MIN E 420 Seminar (March 2002).
[6] Ghazi, H., 2002, ''Measurement of Gas Content in Slurries,'' M. Eng. Project, University of Alberta, Canada.
[7] Greenspan, H. P., and Nigam, M. S., 2001, ''A Note on Separation of a Bimodal Mixture in Pipe Flow,'' Int. J. Multiphase Flow, **27**, pp. 2015–2021.
[8] Hewitt, G. F., and Hall-Taylor, N. S., 1970, ''Annular Two-Phase Flow,'' Pergamon Press, USA.

Flow Through a Finite Packed Bed of Spheres: A Note on the Limit of Applicability of the Forchheimer-Type Equation

Agnès Montillet
Laboratoire de Génie des Procédés appliqués à l'Environnement et l'Agroalimentaire,
C.R.T.T., Bd de l'Université, BP 406-44602
Saint-Nazaire Cedex-France
e-mail: montill@crttsn.univ-nantes.fr

The variation of the pressure drop measured as a function of the fluid velocity through a packed bed of spheres is presented and discussed in the range of particle Reynolds number 30–1500. Based on previous studies, the observed limit of validity of the so-called Forchheimer law may be attributed to the concomitant effects of the finite character of the tested bed and of the transition of flow regime which is marking the beginning of the fully developed turbulent flow regime. The limit of validity of the Forchheimer-type law was formerly noticed by several authors. [DOI: 10.1115/1.1637928]

1 Introduction

Numerous experimental and theoretical studies have been conducted on single phase flow through porous media. Since the well-known works of Darcy or Forchheimer, in particular, many experimental studies have focused on the pressure drop variation as a function of the fluid velocity. In the early years, between 1930 and 1950, a great amount of interesting experimental data were gathered and published. These data were mostly discussed on the basis of an empirical dimensional analysis and analogies were suggested with flow through tubes and singularities. More recent experimental works, based on various experimental techniques, have focused mainly on proposing a more refined cartography of flow regimes. In the mean time, theoretical works developed different approaches to the way of modeling the pressure drop. The main features of this cartography, i.e. the different flow regimes, are now generally accepted: the Darcy regime, the steady nonlinear laminar flow regime, the unsteady laminar flow regime and the unsteady and chaotic flow regime [1], also called turbulent flow regime.

The present objective of this paper is to examine and discuss the pressure drop evolution in the transition domain of the flow regime which occurs between the unsteady laminar flow regime and the turbulent flow regime. This point still remains obscure. Kuwahara et al. [2] observe that experimental works dealing with this particular transition domain are few and suggest that this transition is probably difficult to observe in practice. Theoretical studies which are modeling the pressure drop in this transition domain are basically relying on two recent experimental works: that of Fand et al. [3] and that of Kececioglu and Jiang [4]. The problem is that these two references are not in accordance with each other concerning the localization of this transition domain and that the localization of such a transition cannot be identified solely from the evolution of the pressure drop. In this paper, a new set of data is presented, obtained from an experimental apparatus especially designed for the study of the flow in the expected transition zone between the unsteady laminar flow regime and the turbulent flow regime. Then the localization of this transition is discussed.

Contributed by the Fluids Engineering Division for publication in the JOURNAL OF FLUIDS ENGINEERING. Manuscript received by the Fluids Engineering Division March 27, 2001; revised manuscript received June 23, 2003. Associate Editor: L. Mondy.

2 Experimental Variation of the Pressure Drop During the Flow Through a Bed of Spheres

2.1 Experimental Details. An experimental apparatus was equipped in order to study the pressure drop in the transition domain between the unsteady laminar flow regime and the turbulent flow regime. The choice of the equipment was based on previous works by Seguin et al. [5,6] who studied the flow regime transitions in packed beds of various particles using electrochemical microprobes. In packed beds of 5 mm diameter spheres, the authors observed a significant change of the fluctuating rate of the current intensity, TFi, measured at the probes for a particle Reynolds number, Re_{part}, close to 100. This step was analyzed as marking the end of the purely laminar flow regime. The quick variation of TFi was followed by a slow increase of the fluctuating rate of the velocity gradient, TFs, and then by its stabilization. This stabilization was explained as an effect of the establishment of a fully turbulent flow. Statistically, the stabilization of TFs at the different microprobes is not observed for the same value of Re_{part}. The authors suggest that the turbulent flow can be considered as fully established in the bed when the stabilization of TFs is obtained at 90% of the microprobes, i.e. for $Re_{part} \approx 530$.

Based on these results, experiments were conducted in a bed, the geometry of which is the same as that of the bed used by Seguin et al. [5,6]. A cylindrical column was filled with identical glass beads (mean diameter $d_{part} = 4.92$ mm). The bed diameter, D, is 60 mm and its total height is 160 mm. The overall porosity, ε, is 0.367. The static specific surface area of the spheres, avs, calculated per volume of spheres, is 1220 m^{-1}. According to Zou and Yu [7], the geometry meets expectations considering the thickness effects. The flow of demineralized water was studied over a range of velocities corresponding to a Re_{part} range of 30–1500. The difficulty of the experiments consisted in measuring the pressure drop in the same thickness of the bed with an acceptable accuracy in the above whole range of Re_{part}. Therefore, the pressure drop was measured in the same central part of the bed, 30 mm in thickness, using a membrane pressure-meter (Delta bar 0–25 mbar, Hendress & Hauser), as well as inclined and straight U-manometers. Two centrifugal pumps were used. One was equipped with a velocity variator and is especially used for high flow rates. Suitable electro-magnetic flow-meters were used, depending on the flow rate value (TecMag DN15 and PicoMag DMI 6530 DN4, Hendress & Hauser). The experimental set-up is depicted in Fig. 1. The measurement uncertainty of the different manometers is given in Fig. 2. According to the manufacturer, the measurement uncertainty of the flow rates is ±1%. Measurements

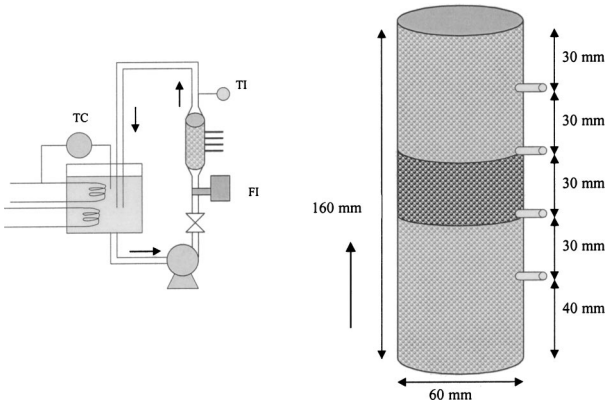

Fig. 1 Schematic diagram of the experimental apparatus. On the right: the packed bed. (the test section is the delimited by the two central pressure taps). On the left: the experimental device. FI: electromagnetic flow meter, TI: temperature probe (Pt 100), TC: temperature controller.

were made after ensuring that a complete saturation of the bed by the fluid was achieved. The reproducibility of measurements was verified by setting the flow rate in a random order. As much as possible, some ranges of velocities were covered with two of the above-mentioned devices, so as to verify their reliability. The temperature was usually correctly regulated, except for highest flow rates. Thus, the temperature was systematically read and encountered in the calculations. The data are presented in a dimensionless form or converted to a single temperature if a presentation of the pressure drop versus the superficial velocity is needed.

2.2 Experimental Results. In Fig. 3, data are presented in a dimensionless form as a function of Re_{part}. Knowing that for $Re_{part} > 30$ conditions are beyond the Darcy regime [8], if the so-called Forchheimer law (equation 1) was valid in the whole range of tested Re_{part}, a linear variation of the experimental data should be observed, which is not the case.

$$\frac{\Delta P}{H} = aUo + bUo^2 \tag{1}$$

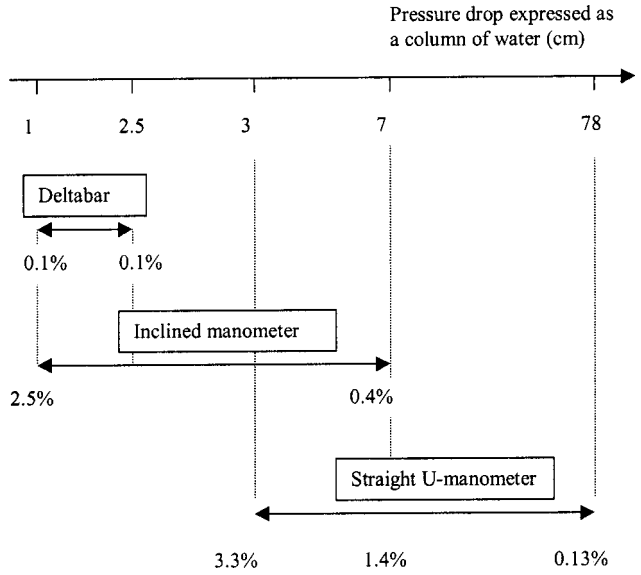

Fig. 2 Schematic diagram of the measurement uncertainty of the different manometers used in this work

This phenomenon has already been observed in the past. The limited validity of Eq. (1) was reported early on by Carman [9], who mentioned a few works in which the phenomenon was noticed. Carman suggested using an equation allowing the calculation of a Blake function where Re_{part} has a power of 0.1. Later, Rose [10–12] proposed an empirical equation of the form:

$$f = \frac{\Delta P}{H}\frac{d_{part}}{\rho Uo^2} = f(\varepsilon)\left\{\frac{1000}{Re_{part}} + \frac{60}{(Re_{part})^{1/2}} + 12\right\} \tag{2}$$

where f is a modified friction factor and $f(\varepsilon)$ is an empirical function of the porosity, the value of which is 1 for $\varepsilon = 0.4$. Using an arbitrary value of 1.294 for $f(\varepsilon)$, this equation is in keeping with our data as can be seen in Fig. 4. The mean relative scatter between the experimental data and Eq. (2) is 1.7%:

$$ERM = \frac{1}{n}\sum_{i=1}^{n}\frac{|(\Delta P/H)_{measured} - (\Delta P/H)_{calculated}|}{(\Delta P/H)_{measured}} \tag{3}$$

In Fig. 4, some other recent experimental data from Wahyudi [13] are presented which also concern a packed bed of 5 mm diameter glass beads. The bed diameter is larger (100 mm), the ratio D/d_{part} is 20 and the wall effects are generally considered to be negligible for this value of the ratio in the Forchheimer regime. The limit of validity of the Forchheimer law is also noteworthy, even though the author has not mentioned it in his work.

Then, the equation of a capillary-type model (Comiti and Renaud [14]) is added in Fig. 4. In this model, a capillary-type representation of the flow in a tortuous model pore is made. The pressure drop is expressed as the sum of two terms; the resulting equation is a Forchheimer-type equation. The first term of the model accounts for the wall friction in the pore and at the bed wall, while the second considers the energy loss due to flow direction variation. The constants a and b of Eq. (1) are obtained using the Poiseuille law and the Nikuradsee friction coefficient respectively. The second term also accounts for wall effects. Each term of the equation of the model is given as a function of three structural parameters: the porosity, the dynamic specific surface area (avd), and the tortuosity (τ). This model has been successfully tested with various porous media made of packed particles of various shapes or synthetic foams. It can be used in the permeametry technique in order to determine avd and τ. The equation of the model has been used in Fig. 4 in order to predict the pressure drop, using avd=avs and $\tau = 1.44$. According to Fig. 4, the equation of the model is showing a discrepancy with experimental data for a velocity greater than 0.12 m s^{-1}, i.e. for $Re_{part} \approx 580$.

The equation of the Forchheimer-type proposed by Fand et al. [3] for the turbulent flow regime is presented in Fig. 4. It is not closer to the experimental data than the Comiti and Renaud model.

In Fig. 5, the modified friction factor defined in Eq. (2) is presented as a function of Re_{part}. In this figure the discrepancy between the capillary-type model appears in a more significant way beyond $Re_{part} \approx 600$. In this representation, the limit of f predicted by the model when the particle Reynolds number tends to the infinite is 20. It is 25% greater than that calculated from the empirical Eq. (2). An example of the variation of the fluctuation rate of the velocity gradient, TFs, measured by Seguin [15] at a microprobe located in a packed bed of spheres, is presented in Fig. 5. As can be noticed, the relative stabilization of TFs coincides with the appearance of the discrepancy between the modified friction factor predicted by the capillary-type model and the experimental data.

3 Discussion

The progressive evolution of the pressure drop from the Darcy regime to the laminar flow regime is generally described with the Darcy law and then with a Forchheimer-type equation (Eq. (1)) in which the constant a is taken as equal to the single constant of the Darcy law. In the particle Reynolds number range 30–1500, about

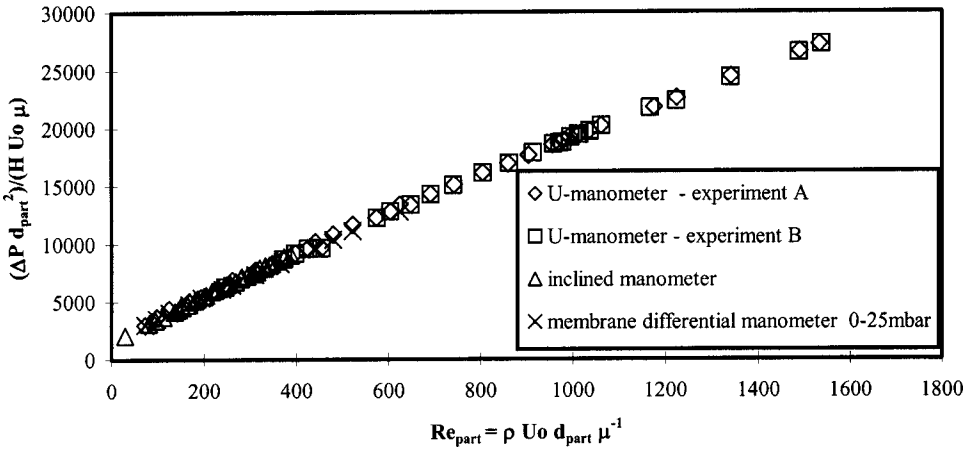

Fig. 3 Experimental data expressed in a dimensionless form

the regime transition presently studied, we saw that the pressure drop can be correctly described with an empirical equation of the form:

$$f = \frac{\alpha}{Re_{part}} + \beta + \frac{\gamma}{Re_{part}^{\delta}} \tag{4}$$

with $\delta = 1/2$. In this equation, the constant β cannot be calculated from the quadratic term of the Ergun equation nor from that of the model of Comiti and Renaud [14]. As a matter of fact, the value of the friction coefficient which is used in the model of Comiti and Renaud for the calculation of the constant of the quadratic term is too high beyond $Re_{part} \approx 500-600$. This coefficient could be corrected in order to integrate the natural variation of the modified friction factor. Thus, the classical equations proposed for the Forchheimer-Darcy regime cannot be properly used in their present state to predict the pressure drop at higher particle Reynolds numbers. Moreover, the experimental pressure drop is lower than that predicted by classical models and it seems difficult to give a physical explanation to this phenomenon.

Rose and Rizk [16] present an interesting set of curves showing the variation of wall effects for beds of spherical materials. These curves are partly based on experimental data and on calculations. They show that beyond $Re_{part} = 400$ the influence of the wall effects is not negligible and that it tends to affect the pressure by a factor lower than 1, whereas under $Re_{part} = 400$, the wall effects affect the pressure drop by a factor greater than 1. As expected, for a given Reynolds number, the influence of the wall effect decreases with the D/d_{part} ratio, but this influence is difficult to evaluate at large Reynolds numbers for $D/d_{part} > 10$ due to a lack of information. The great difficulty of implementing experiments in these zones must be emphasized. At this stage of the investigations, it cannot be excluded that the finite character of tested beds may be an explanation or a partial explanation to the limit of validity of the Forchheimer-type equation.

In the empirical Eq. (4), a third term has been introduced by Rose, where the particle Reynolds number appears at the power $-1/2$. To our knowledge, the value of this exponent has no theoretical explanation. We have tried to optimize its value as well as those of β and γ while fixing α and calculating it from the model of Comiti and Renaud [14]. The following correlating equation was then found:

$$f = \frac{1410}{Re_{part}} + 16 + \frac{45}{Re_{part}^{0.45}} \tag{5}$$

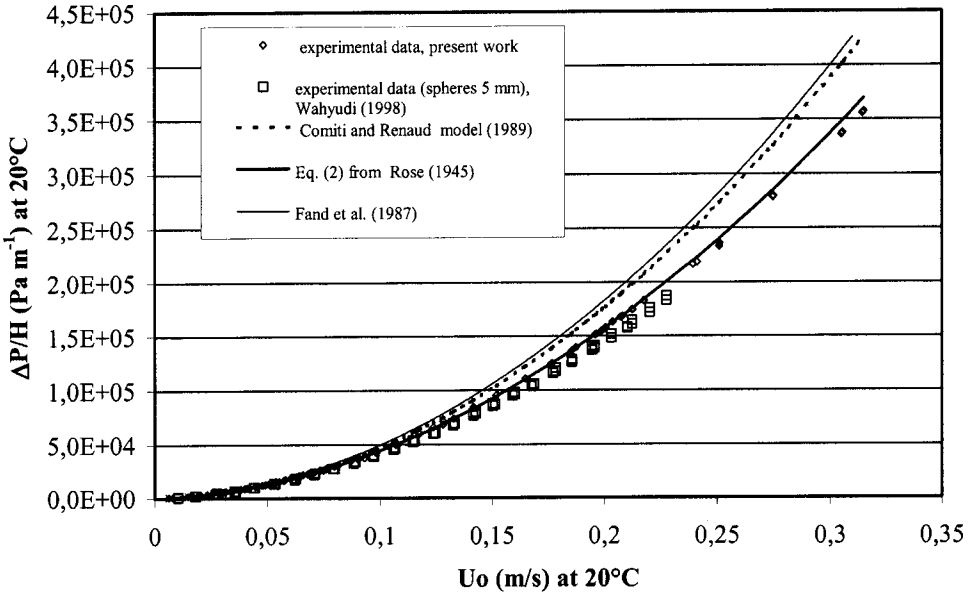

Fig. 4 Comparison of experimental data with different predictive equations

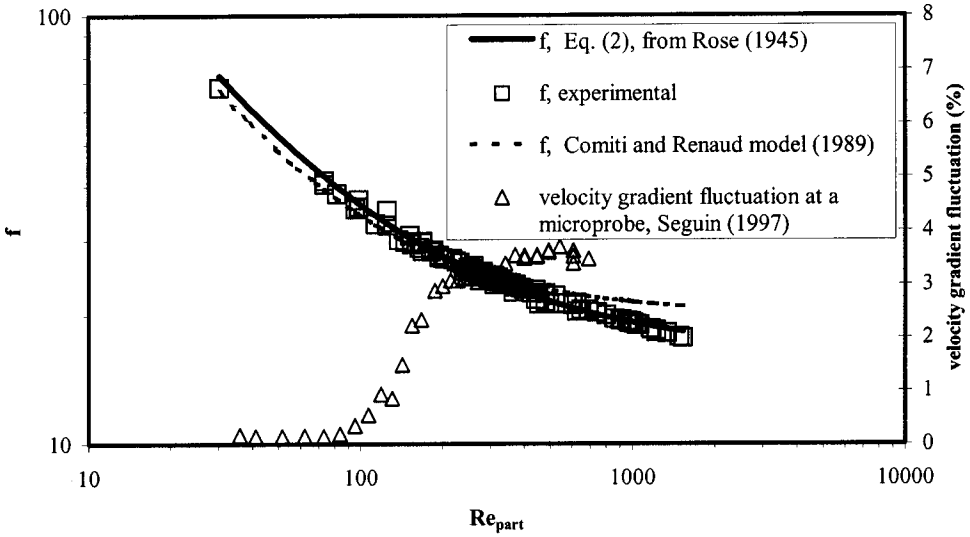

Fig. 5 Evolution of the modified friction factor as a function of the particle Reynolds number. Comparison with the variation of the fluctuation rate of the velocity gradient measured at a microprobe inside a similar packed bed by Seguin (1997).

It fits the experimental data with a low value of the mean relative scatter, ERM=2.0%.

If the original Eq. (2) of Rose is considered again, a way of using it as a predictive equation can be to propose a correlating equation for $f(\varepsilon)$ which would also take into account for the effect of the D/d_{part} ratio. This function is now designated as $f(\varepsilon, D/d_{part})$. Using the present experimental data, that of Wahyudi [13] and the fitting equations of the six experimental sets of data from Fand et al. [3], the following equation has been found:

$$f\left(\varepsilon, \frac{D}{d_{part}}\right) = 0.066\left(\frac{D}{d_{part}}\right)^{0.17}\left(\frac{1-\varepsilon}{\varepsilon^3}\right) \tag{6}$$

The mean relative errors between the experimental data and the calculated ones are given in Table 1. This is an attempt to propose a general predictive equation but, obviously, more sets of experimental data are needed to confirm its usefulness.

As observed above, the so-called Forchheimer law loses its validity beyond $Re_{part} \approx 500-600$. This phenomenon coincides with the establishment of a fully developed turbulent regime in the whole bed as observed by Seguin et al. [6] in a bed of the same geometry. This is in contradiction with the laminar/turbulent transition domain proposed in the cartography of Fand et al. [3] which is comprised in the Re_{part} range 80–120. This is also in contradiction with the transition domain proposed more recently by Kececioglu and Jiang [4] which is $Re_{part} \approx 25$. Moreover, in these two papers, the transition is presented, from the point of view of pressure drop fitting, as the succession of two different Forchheimer type-laws. One may notice that in these two papers, the transition domain is determined on the simple basis of the observation of the pressure drop evolution. A change of slope in the pressure drop evolution does not prove that the turbulent regime has been achieved. Seguin [15] has noticed that in the assumed domain of the fully developed turbulent regime, most spectral representations of the velocity gradient fluctuation present a $-5/3$ slope, which is not the case in the laminar flow regime nor in the transition domain. This slope value is characteristic of a turbulent and probably isotropic flow [17] in the vicinity of the microprobe.

4 Conclusion

The objective of this paper was to discuss a remaining obscure aspect of single phase flow through porous media: the pressure drop evolution in the flow regime transition ranging from the end of the unsteady laminar flow to the establishment of a fully developed turbulent regime. An experiment was carefully conducted in a packed bed of spheres. The pressure drop was measured in a large range of the particle Reynolds number (30–1500). The evolution of the pressure drop pointed out a limit of the validity of the Forchheimer-type equation which confirms the experimental ob-

Table 1 Mean relative errors between experimental data of f and values calculated from Eqs. (2) and (6)

	System:				
Author(s)	d (mm)	ε	D/d_{part}	Range of Re_{part}	ERM (%)
Fand et al. (1987) [3]	2	0.357	41.3		3.4
	3	0.360	28.2		4.0
	4	0.359	21.5	120–440	7.9
	3.69 (mixed spheres)	0.348	23.5		6.7
	3.27 (mixed spheres)	0.344	26.4		5.1
	2.76 (mixed spheres)	0.342	31.4		3.3
Wahyudi (1998) [13]	4	0.392	25.2	140–905	2.7
	5	0.377	19.9	140–1130	4.3
	2.69 (mixed spheres)	0.318	37.2	120–620	1.3
Montillet (present work)	5	0.367	12.2	120–1540	1.6
Montillet (not published)	3.1 (2 and 5 mixed)	0.327	19.3	120–450	6.9

servations of earlier works [9,10,12] and which coincides with the localization of the transition unsteady laminar flow regime/turbulent flow regime proposed by Seguin et al. [6]. This work confirms that, for the turbulent flow regime, the pressure drop in a finite packed bed is no longer a power 2 term in velocity. The limit of validity of the Forchheimer-type equation may be attributed to a concomitant effect of the transition to a new regime and of the finite character of the bed. Further experiments are needed in order to determine precisely if the regime transition is marked or not by a limit of validity of the Forchheimer law in the case of a quasi-infinite bed. Then, based on these results, the modeling of pressure drops in the fully developed turbulent flow regime should be attempted.

Nomenclature

- a = first Forchheimer constant, Eq. (1)
- avs = specific static surface area (per volume of particles)
- avd = specific dynamic surface area (per volume of particles)
- b = second Forchheimer constant, Eq. (1)
- d_{part} = mean particle diameter
- D = diameter of the bed
- ERM = mean relative scatter, Eq. (3)
- f = modified friction factor$=(\Delta P d_{part})/(H\rho Uo^2)$, Eq. (2)
- H = thickness of the porous medium at which the pressure drop is measured
- Re_{part} = particle Reynolds number$=(\rho Uo d_{part})/\mu$
- Uo = superficial velocity
- ΔP = pressure drop
- α = constant, Eq. (4)
- β = constant, Eq. (4)
- δ = constant, Eq. (4)
- ε = bed porosity
- γ = constant, Eq. (4)
- μ = dynamic viscosity of fluid
- ρ = fluid density
- τ = tortuosity

References

[1] Dybbs, A., and Edwards, R. V., 1984, "A New Look at Porous Media Fluid Mechanics—Darcy to Turbulent," *Fundamentals of transport phenomena in porous media*, Martinus Nishoff publishers, pp. 199–256.

[2] Kuwahara, F., Kameyama, Y., Yamashita, S., and Nakayama, A., 1998, "Numerical Modeling of Turbulent Flow in Porous Media Using a Spatially Periodic Array," J. Porous Media, **1**, pp. 47–55.

[3] Fand, R. M., Kim, B. Y. K., Lam, A. C. C., and Phan, R. T., 1987, "Resistance to the Flow of Fluids Through Simple and Complex Porous Media Whose Matrices are Composed of Randomly Packed Spheres," J. Fluids Eng., **109**, pp. 268–274.

[4] Kececioglu, I., and Jiang, Y., 1994, "Flow Through Porous Media of Packed Spheres Saturated With Water," J. Fluids Eng., **116**, pp. 164–170.

[5] Seguin, D., Montillet, A., and Comiti, J., 1998, "Experimental Characterization of Flow Regimes in Various Porous Media—I: Limit of Laminar Flow Regime," Chem. Eng. Sci., **53**, pp. 3751–3761.

[6] Seguin, D., Montillet, A., Comiti, J., and Huet, F., 1998, "Experimental Characterization of Flow Regimes in Various Porous Media—II: Transition to Turbulent Regime," Chem. Eng. Sci., **53**, pp. 3897–3909.

[7] Zou, R. P., and Yu, A. B., 1995, "The Packing in a Cylindrical Container: The Thickness Effect," Chem. Eng. Sci., **50**, pp. 1504–1507.

[8] Comiti, J., Sabiri, N. E., and Montillet, A., 2000, "Experimental Characterization of Flow Regimes in Various Porous Media—III: Limit of Darcy's or Creeping Flow Regime for Newtonian and Purely Viscous Non-Newtonian Fluids," Chem. Eng. Sci., **55**, pp. 3057–3061.

[9] Carman, P. C., 1937, L'écoulement des gaz à travers les milieux poreux. P.U.F.

[10] Rose, H. E., 1945, "An Investigation Into the Laws of Flow of Fluids Through Beds of Granular Materials," Proc. Inst. Mech. Eng., **153**, pp. 141–148.

[11] Rose, H. E., 1945, "The Isothermal Flow of Gazes Through Beds of Granular Materials," Proc. Inst. Mech. Eng., **153**, pp. 148–153.

[12] Rose, H. E., 1945, "On the Resistance Coefficient-Reynolds Number Relation-Ship for Fluid Flow Through Beds of Granular Materials," Proc. Inst. Mech. Eng., **153**, pp. 154–161.

[13] Wahyudi, I., 1998, "Ecoulement Dans les sols granulaires saturés en Régimes permanent et transitoires," *doctorat*, Université de Nantes—Ecole Centrale de Nantes.

[14] Comiti, J., and Renaud, M., 1989, "A New Model for Determining Mean Structure Parameters of Fixed Beds From Pressure Drop Measurements: Application to Packed Beds With Parallelepipedal Particles," Chem. Eng. Sci., **44**, pp. 1539–1545.

[15] Seguin, D., 1997, "Contribution à l'étude du transfert de matière et des régimes d'écoulement dans des milieux poreux de structures variées," *doctorat*, Université de Nantes.

[16] Rose, H. E., and Rizk, A. M. A., 1949, "Further Researches in Fluid Flow Through Beds of Granular Material," Proc. Inst. Mech. Eng., **160**, pp. 493–503.

[17] Lesieur, M., 1994, "La Turbulence," Presses Universitaires de Grenoble.